✓VOLUME 76 NOVEMBER 9, 1972 NUMBER 23

JPCHAx

THE JOURNAL OF PHYSICAL CHEMISTRY

PUBLISHED BIWEEKLY BY THE AMERICAN CHEMICAL SOCIETY

THE JOURNAL OF

PHYSICAL CHEMISTRY

AMERICAN CHEMICAL SOCIETY, *1155 Sixteenth St., N.W., Washington, D. C. 20036*

Books and Journals Division
JOHN K CRUM, *Director*
JOSEPH H. KUNEY, *Head, Business Operations Department*
RUTH REYNARD, *Assistant to the Director*

 Published biweekly by the American Chemical Society at 20th and Northampton Sts., Easton, Pa. 18042. Second-class postage paid at Washington, D. C., and at additional mailing offices.

All manuscripts should be sent to *The Journal of Physical Chemistry*, Department of Chemistry, University of Minnesota, Minneapolis, Minn. 55455.

Additions and Corrections are published once yearly in the final issue. See Volume 75, Number 26 for the proper form.

Extensive or unusual alterations in an article after it has been set in type are made at the author's expense, and it is understood that by requesting such alterations the author agrees to defray the cost thereof.

The American Chemical Society and the Editor of *The Journal of Physical Chemistry* assume no responsibility for the statements and opinions advanced by contributors.

Correspondence regarding accepted copy, proofs, and reprints should be directed to Editorial Production Office, American Chemical Society, 20th and Northampton Sts., Easton, Pa. 18042. Manager: CHARLES R. BERTSCH. Assistant Editor: EDWARD A. BORGER. Editorial Assistant: JOSEPH E. YURVATI.

Advertising Office: Centcom, Ltd. (formerly Century Communications Corporation), 142 East Avenue, Norwalk, Conn. 06851.

Business and Subscription Information

Remittances and orders for subscriptions and for single copies, notices of changes of address and new professional connections, and claims for missing numbers should be sent to the Subscription Service Department, American Chemical Society, 1155 Sixteenth St., N.W., Washington, D. C. 20036. Allow 4 weeks for changes of address. Please include an old address label with the notification.

Claims for missing numbers will not be allowed (1) if received more than sixty days from date of issue, (2) if loss was due to failure of notice of change of address to be received before the date specified in the preceding paragraph, or (3) if the reason for the claim is "missing from files."

Subscription rates (1972): members of the American Chemical Society, $20.00 for 1 year; to nonmembers, $60.00 for 1 year. Those interested in becoming members should write to the Admissions Department, American Chemical Society, 1155 Sixteenth St., N.W., Washington, D. C. 20036. Postage to Canada and countries in the Pan-American Union, $5.00; all other countries, $6.00. Single copies for current year: $3.00. Rates for back issues from Volume 56 to date are available from the Special Issues Sales Department, 1155 Sixteenth St., N.W., Washington, D. C. 20036.

This publication and the other ACS periodical publications are now available on microfilm. For information write to: MICROFILM, Special Issues Sales Department, 1155 Sixteenth St., N.W., Washington, D. C. 20036.

Notice to Authors last printed in the issue of June 22, 1972

THE JOURNAL OF
PHYSICAL CHEMISTRY

Volume 76, Number 23 November 9, 1972

JPCHAx 76(23) 3303–3508 (1972)

AUTHOR INDEX

In papers with more than one author the name of the author to whom inquiries about the paper should be addressed is marked with an asterisk in the by-line.

THE JOURNAL OF
PHYSICAL CHEMISTRY

VOLUME 76, NUMBER 23 NOVEMBER 9, 1972

The Reaction of Ethyl Radicals with Nitric Oxide. Nitrosoethane and Triethylhydroxylamine Formation[1]

by Hiok-Seng Tan and F. W. Lampe*

Whitmore Laboratory, Department of Chemistry, The Pennsylvania State University, University Park, Pennsylvania 16802
(Received June 7, 1972)

Publication costs assisted by the Petroleum Research Fund

Ethyl radicals, formed by photolysis of azoethane, react with nitric oxide by successive addition to yield nitrosoethane and triethylhydroxylamine. Nitrosoethane is the sole product until the nitric oxide concentration has been reduced to very low levels, at which time the addition reaction to form the triethylhydroxylamine takes place in competition with the combination and disproportionation reactions of ethyl radicals. In the absence of ethyl radicals, or in experiments with initial nitric oxide concentrations above 6%, the dimerization of nitrosoethane is observed. Kinetic analysis of the data subsequent to depletion of nitric oxide affords an evaluation of specific reaction rates for the addition of ethyl radicals to monomeric nitrosoethane and for the reversible dimerization of monomeric nitrosoethane. The ionization potential of monomeric nitrosoethane was determined from a study of the photolytic growth rate dependence of $C_2H_5NO^+$ on electron energy.

Introduction

For many years nitric oxide has been used as a free-radical scavenger in mechanistic studies of gas-phase reactions involving free radicals.[2-5] The ideal scavenger is a substance that reacts so rapidly with free radicals that other reactions of the radicals are completely eliminated by very low concentrations of scavenger; moreover, the product of the scavenging reaction should be stable. It is generally accepted[3-5] that the scavenging reaction of nitric oxide is addition to form the nitroso compound, *viz.*

$$R + NO + M \longrightarrow RNO + M \qquad (1)$$

It has also been found[6,7] that this reaction is sufficiently rapid to allow essentially complete scavenging at nitric oxide concentrations of several per cent or less. However, there is no doubt[3-5] that the product of (1), namely RNO, is not stable and does react further in practically all systems studied. Hence, if scavenging techniques using nitric oxide are to lead to unambiguous conclusions, it is essential that the details of the reactions involving RNO under scavenging conditions be understood.

Under the usual scavenging conditions of low nitric oxide concentrations (a few per cent or less), and at temperatures near room temperature, (1) has been shown to be followed by (2) and (3) for R = H,[8,9] CH_3,[6,10-12] and $(CH_3)_2\dot{C}CN$.[13,14] If the concentra-

(1) U. S. Atomic Energy Commission Document COO-3416-3.

(2) L. A. K. Stavely and C. N. Hinshelwood, *J. Chem. Soc.*, 1568 (1937).

(3) B. G. Gowenlock, *Progr. React. Kinet.*, **3**, 173 (1965).

(4) J. Heicklen and N. Cohen, *Advan. Photochem.*, **5**, 157 (1968).

(5) Y. Rees and G. H. Williams, *Advan. Free Radical Chem.*, **3**, 199 (1969).

(6) D. E. Hoare, *Can. J. Chem.*, **40**, 2012 (1962).

(7) M. I. Christie and J. S. Frost, *Trans. Faraday Soc.*, **61**, 468 (1965).

(8) F. C. Kohout and F. W. Lampe, *J. Amer. Chem. Soc.*, **87**, 5795 (1965).

(9) F. C. Kohout and F. W. Lampe, *J. Chem. Phys.*, **46**, 4075 (1967).

(10) B. Bromberger and L. Phillips, *J. Chem. Soc.*, 5302 (1961).

(11) A. Maschke, B. S. Shapiro, and F. W. Lampe, *J. Amer. Chem. Soc.*, **85**, 1876 (1963).

tion of R· relative to RNO is sufficiently low, dimeriza-

$$R\cdot + RNO \xrightarrow{(M)} R_2NO\cdot \quad (2)$$

$$R\cdot + R_2NO \xrightarrow{(M)} R_2NOR \quad (3)$$

tion of RNO, (4), can compete with (2) and (3). Such dimerizations have been reported for R = CH_3,[15-23]

$$RNO + RNO \longrightarrow (RNO)_2 \quad (4)$$

C_2H_5,[20] n-C_3H_7,[20] and s-C_3H_7.[20] In the case of R = H the dimer is unstable and dissociates to water and nitrous oxide.[8,9,24-28] Other reactions of RNO[3-5] do not seem to be significant under the radical scavenging conditions mentioned above.

This paper describes mass spectrometric studies of the reactions of ethyl radicals with nitric oxide and the subsequent reactions of nitrosoethane.

Experimental Section

Ethyl radicals were generated in the presence of a few per cent of nitric oxide by the photolysis of azoethane with light of wavelength greater than 3100 Å. The reactions were carried out in a photolysis cell containing a pinhole leak leading directly into the ionization chamber of a somewhat-modified Bendix Model 14-101 time-of-flight mass spectrometer. Three pinhole leaks were used, having first-order leak rate constants[9,23] of $1.2 \pm 0.1 \times 10^{-3}$, $5.0 \pm 0.5 \times 10^{-4}$, and $2.7 \pm 0.2 \times 10^{-4}$ sec^{-1}. The photolysis cell was 8.35 cm in length with a diameter of 2.10 cm and was connected *via* 3-mm stainless steel and 6-mm Pyrex tubing to a large reservoir (5-12 l.) containing the reactants, azoethane and nitric oxide.

The first set of experiments at nitric oxide concentrations of 6.8% and 3.0% were carried out under conditions identical with those described in earlier reports.[9,12,23,29] The temperature of the photolysis cell under these conditions was found to be 56 ± 3°. This temperature proved to be too high for quantitative measurements of the dimerization reaction of nitrosoethane. Accordingly, the photolysis cell was jacketed to provide for some dissipation of the heat transferred to it from the hot filament of the ionization chamber. The last set of experiments were conducted in this jacketed cell at a temperature of 41 ± 3°.

High-pressure mercury arcs were used as light sources in this work. In most of the experiments an Osram HBO-100 lamp was employed. The spectral emission of this lamp and the wavelength dependence of the azomethane absorption coefficient are such that the average effective photolytic wavelength was about 3660 Å. A few experiments were conducted using an Illumination Industries Type 110 high-pressure mercury lamp with a similar spectral emission. Both lamps were operated at 5.2 A. The power supply for both lamps was obtained from the George W. Gates Co. (Model P109); with this power supply, the lamp operating current could be reproduced to within ±2%.

Azoethane was purchased from Merck Sharp and Dohme, Ltd. It was purified to greater than 99% purity by repeated freeze–pump–thaw cycles in a cold finger immersed in methanol slush (−97.8°). This purification procedure was carried out at least twice prior to preparing a sample for photolysis. Nitric oxide, having a stated purity of 98.5 mol %, was purchased from the Matheson Co. It was purified by freezing the gas onto silica gel at −295° and allowing a slow temperature increase of the condensed gas to occur. An initial and a final fraction of the gas distilling from the silica gel were discarded and the procedure was repeated once more.

Results and Discussion

1. Photolysis of Pure Azoethane. When pure azoethane at 5-10 Torr was photolyzed under our conditions the only observable product was n-butane, as indicated by the growth of the ion currents at m/e 43 and 58 relative to that at m/e 86 (parent peak of azoethane) with photolysis time. Ethane and ethylene were undoubtedly formed, and at a rate of about $^1/_3$ that of n-butane,[30] by the disproportion of ethyl radicals. However, the mass peaks from ethane and ethylene, as well as those due to nitrogen, were obscured by the peaks from the much more abundant azoethane. Although a search was made for mass peaks characteristic of products of combination reactions of $C_2H_5N{=}N\cdot$ radicals and of the addition of ethyl radicals to azoethane, such products, if formed, were present at concentrations below our detection sensitivity.

(12) A. Maschke, B. S. Shapiro, and F. W. Lampe, *J. Amer. Chem. Soc.*, **86**, 1929 (1964).

(13) B. A. Gingras and W. A. Waters, *Chem. Ind. (London)*, 615 (1953).

(14) B. A. Gingras and W. A. Waters, *J. Chem. Soc.*, 1920 (1954).

(15) H. W. Thompson and J. W. Linnett, *Trans. Faraday Soc.*, **33**, 874 (1937).

(16) C. S. Coe and T. F. Doumani, *J. Amer. Chem. Soc.*, **70**, 1516 (1948).

(17) H. T. J. Chilton, B. G. Gowenlock, and J. Trotman, *Chem. Ind. (London)*, 538 (1955).

(18) B. G. Gowenlock and J. Trotman, *J. Chem. Soc.*, 4190 (1955).

(19) M. I. Christie, *Proc. Roy. Soc. Ser. A*, **249**, 258 (1958).

(20) M. I. Christie, J. S. Frost, and M. A. Voisey, *Trans. Faraday Soc.*, **61**, 674 (1965).

(21) J. G. Calvert, S. S. Thomas, and P. L. Hanst, *J. Amer. Chem. Soc.*, **82**, 1 (1960).

(22) T. Johnston and J. Heicklen, *J. Phys. Chem.*, **70**, 3088 (1966).

(23) F. A. Thomassy and F. W. Lampe, *ibid.*, **74**, 1188 (1970).

(24) P. Harteck, *Ber.*, **66**, 423 (1933).

(25) H. A. Taylor and C. Tanford, *J. Chem. Phys.*, **12**, 47 (1944).

(26) M. Z. Hoffman and R. B. Bernstein, *J. Phys. Chem.*, **64**, 1753 (1960).

(27) A. Serewicz and W. A. Noyes, Jr., *ibid.*, **63**, 843 (1959).

(28) O. P. Strausz and H. E. Gunning, *Trans. Faraday Soc.*, **60**, 347 (1964).

(29) E. Kamaratos and F. W. Lampe, *J. Phys. Chem.*, **74**, 2267 (1970).

(30) A. F. Trotman-Dickenson, "Gas Kinetics," Academic Press, Inc., New York, N. Y., 1955, p 121.

These facts are in accord with previous work on photolysis of azoethane[31] and are completely analogous to our earlier studies of azomethane in the same apparatus.[11,12] It is thus indicated that the photolysis of pure azoethane under our conditions is described adequately by reactions 5–7, *viz.*

$$C_2H_5N{=}NC_2H_5 + h\nu \longrightarrow 2C_2H_5 + N_2 \quad (5)$$

$$C_2H_5 + C_2H_5 \longrightarrow C_4H_{10} \quad (6)$$

$$C_2H_5 + C_2H_5 \longrightarrow C_2H_6 + C_2H_4 \quad (7)$$

Ethyl radicals are present in this system at concentration levels much below our detection sensitivity because of the very large contributions of azoethane to the peak at m/e 29. However, from the known specific reaction rates of (6) and (7) and our leak rate constants and light intensities, it may be shown that the ethyl radical concentration reaches a steady-state level determined only by (5)–(7). Moreover, this steady-state concentration is attained in times very short compared to our time resolution of about 1 sec. Therefore, in a kinetic treatment of our flow system we need not consider the leakage of ethyl radicals from the photolysis cell into the ion source of the mass spectrometer.

Considering ethyl radicals to be in a steady state at all photolysis times, we may write for the change of concentration of azoethane in the photolysis chamber

$$\frac{d[C_2H_5N{=}NC_2H_5]}{dt} = \lambda[C_2H_5N{=}NC_2H_5]_0 - (\phi I_0\alpha + \lambda)[C_2H_5N{=}NC_2H_5] \quad (8)$$

where ϕ is the quantum yield of (5), α is the average absorption coefficient, I_0 is the light flux incident in the photolysis cell, λ is the specific leakage rate through the pinhole, and $[C_2H_5N{=}NC_2H_5]$ is the instantaneous concentration in the photolysis chamber. $[C_2H_5N{=}NC_2H_5]_0$ is the initial concentration in the photolysis chamber which is equal to the azoethane concentration in the reactant reservoir at all times, since the pressure decrease in the reservoir during a run is negligible. The first term on the right-hand side of (8) thus represents the flow rate of azoethane into the photolysis cell.

Integration of (8) yields the result shown by (9).

$$\frac{[C_2H_5N{=}NC_2H_5]}{[C_2H_5N{=}NC_2H_5]_0} = \frac{\lambda + \phi I_0\alpha e^{-(\lambda+\phi I_0\alpha)t}}{\lambda + \phi I_0\alpha} \quad (9)$$

Since azoethane is the only contributor to the peak at m/e 86, we may replace the concentration ratio in (9) by the corresponding ratio of intensities, $i_{86}(t)/i_{86}(0)$, and utilize the decrease in this ratio with photolysis time to determine the specific photodissociation rate, $\phi I_0\alpha$. It is clear that the concentration ratio in (9), or the equivalent peak-intensity ratio, $i_{86}(t)/i_{86}(0)$, will decrease with photolysis time to a steady-state value of $\lambda/\lambda + \phi I_0\alpha$. While one may, in principle, determine $\phi I_0\alpha$ from measurement of the steady-state concentration of azoethane, its magnitude is too small relative to that of λ to be a practical method.

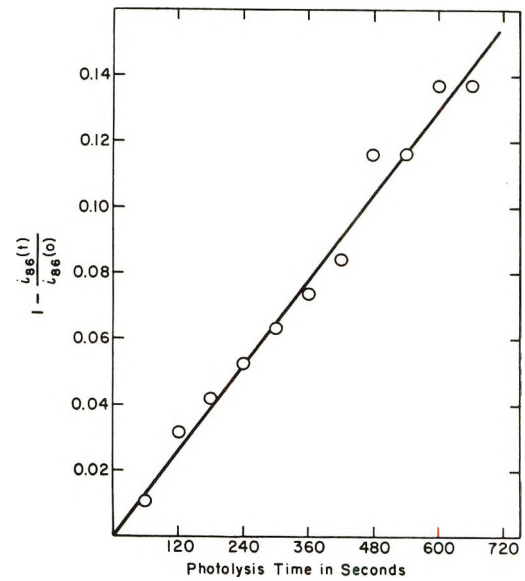

Figure 1. Dependence of azoethane concentration on photolysis time; $\phi I_0\alpha = 2.2 \pm 0.1 \times 10^{-4}$ sec^{-1}; $\lambda = 2.7 \pm 0.2 \times 10^{-4}$ sec^{-1}.

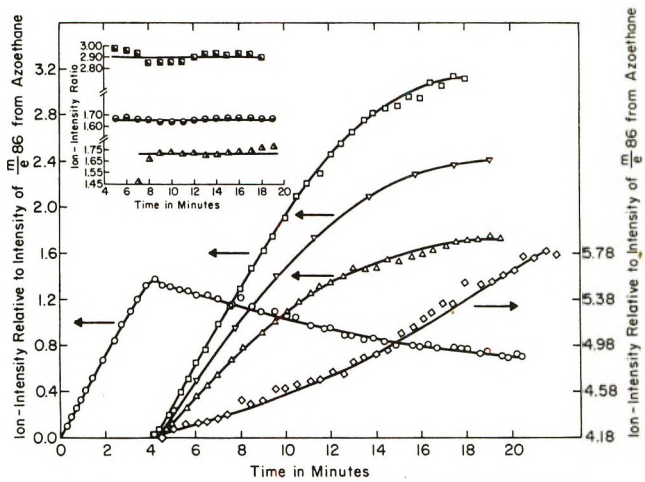

Figure 2. Dependence of ion intensities on photolysis time of 6 Torr of NO (3%) in azoethane: ○, $i_{59} \times 25$; □, $i_{88} \times 25$; ▽, $i_{102} \times 33$; △, $i_{117} \times 40$; ◇, $i_{58} \times 25$; ◪, i_{88}/i_{117}; ◒, i_{102}/i_{117}; ◭, i_{74}/i_{117}.

However, the decrease in concentration of azoethane at short photolysis time does provide a practical means to determine the quantity $\phi I_0\alpha$. If we replace the concentration ratio in (9) by the corresponding peak intensity ratio and expand the exponential with retention of only the linear term, we obtain the result in (10).

$$\frac{i_{86}(t)}{i_{86}(0)} = 1 - \phi I_0\alpha t \quad (10)$$

In Figure 1 is shown a typical plot of the data accord-

(31) J. G. Calvert and J. N. Pitts, "Photochemistry," Wiley, New York, N. Y., 1966, p 463.

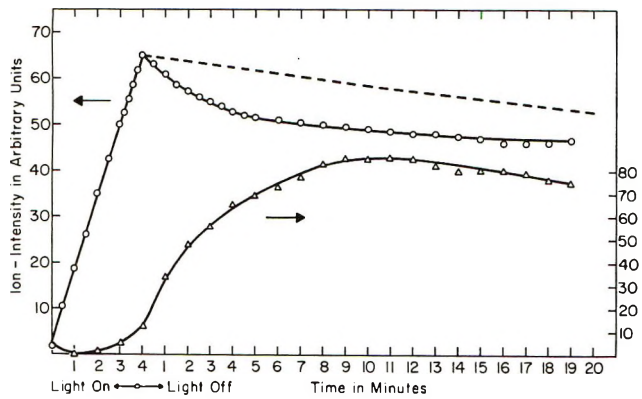

Figure 3. Dimeric nitrosoethane formation after termination of photolysis of 4.3 Torr of NO (6.8%) in azoethane: ○, $i_{59} \times 1$; △, $i_{118} \times 40$; represents the decay rate of a chemically stable product.

ing to (10); the linearity is in accord with our treatment and the slope yields a value of $\phi I_0 \alpha = 2.2 \pm 0.1 \times 10^{-4}$ sec^{-1}. As we found, not unexpectedly, that this value decreased with time, owing to aging of the lamps, the value of $\phi I_0 \alpha$ was redetermined before each set of experiments. Over a period of seven months, for example, the intensity from a given lamp decayed to approximately $^1/_2$ that provided when it was new.

2. Photolysis of Azoethane–Nitric Oxide Mixtures. When mixtures of azoethane and nitric oxide (at 3–11 mol %) are photolyzed, the only product mass peak observed in the initial stages is at m/e 59, an ion which can only be $C_2H_5NO^+$. As shown in Figure 2, which refers to photolysis of 6 Torr of a mixture containing 3% nitric oxide, the intensity of $C_2H_5NO^+$ increases to a maximum at a photolysis time of about 4 min. At about the same time as the maximum in $C_2H_5NO^+$ there is an onset in the formation of ions with m/e values of 117, 102, 88, 74, and 58, of which all but m/e 74 are shown in Figure 2. The absence of a time dependence of the relative intensities of m/e 117, 102, 88, and 74, as shown in the inset of Figure 2, suggests strongly that these ions arise from electron impact on the same reaction product. Moreover, the shapes of the formation curves indicate this precursor molecule to m/e 117, 102, 88, and 74 to be a molecular species whose concentration is increasing at a decreasing rate. By contrast, the ion at m/e 58 is from a precursor molecule whose concentration is increasing at an increasing rate.

If the photolysis is stopped, thus removing ethyl radicals almost instantaneously, the intensities of the peaks at m/e 117, 102, 88, 74, and 58 decay in a manner characteristic of stable products in this flow system. However, as shown in Figure 3, the intensity of m/e 59 ($C_2H_5NO^+$) decreases initially much more rapidly than does the intensity from a stable product and this rapid decrease is accompanied by a simultaneous increase in intensity of a peak at m/e 118.

The ions having m/e values of 117, 102, 88, and 74 are with little doubt due to $(C_2H_5)_2NOC_2H_5^+$, $(C_2H_5)_2NOCH_2^+$, $(C_2H_5)_2NO^+$, and $CH_3NOC_2H_5^+$, respectively, although no significance should be attached to the structures implied for the fragment ions. These ions are expected to be predominant ions in the mass spectrum of triethylhydroxylamine and, since they arise in this system from a common molecular precursor whose kinetic behavior is identical with that of trimethylhydroxylamine in the analogous reaction of methyl radicals with nitric oxide,[11,12] we conclude that this common precursor is, indeed, triethylhydroxylamine.

The ion with m/e 58, whose intensity in Figure 2 increases at an increasing rate, simultaneously with the depletion of $C_2H_5NO^+$ (m/e 59), can only be $C_4H_{10}^+$, derived from n-butane produced in (6). A behavior similar to that of the m/e 58 peak is observed for the m/e 43 peak (the major ion in the mass spectrum of n-butane) but this latter peak is greatly obscured by contribution to m/e 43 from azoethane. Thus, in a manner completely analogous to the methyl radical–nitric oxide system,[11,12] these facts lead to the conclusion that nitric oxide effectively inhibits reactions 6 and 7 until the formation of nitrosoethane has so depleted the nitric oxide concentration that the ethyl radicals may react with nitrosoethane and with each other. Since the nitrosoethane is depleted by reaction with ethyl radicals (produced photolytically at an essentially constant rate), the probability of ethyl radicals reacting with each other, rather than with nitrosoethane, increases with time and is reflected in the different shape of m/e 58 as compared with the ions from triethylhydroxylamine, namely m/e 117, 102, 88, and 74. That nitric oxide is greatly depleted may be seen from the behavior of m/e 30 shown in Figure 4. Consideration of the contribution to m/e 30 from azoethane indicates that in the experiment depicted in Figure 4, depletion of nitric oxide is approximately 90–95% at the maximum in the intensity of m/e 59. The time independence shown in the inset of Figure 4 suggests strongly that the ion with m/e 60 is also an ion produced by electron impact on triethylhydroxylamine.

The rapid decrease in intensity of $C_2H_5NO^+$, shown in a subsequent section to be second order, and the simultaneous increase in the intensity of m/e 118, $(C_2H_5NO)_2^+$, after irradiation is stopped (Figure 3) is clearly due to the dimerization of nitrosoethane.[20] The mass spectrometric observation here is completely analogous to the recent study of nitrosomethane dimerization.[23]

All the experimental observations discussed above and contained in Figures 2–4 point clearly to the reaction mechanism being (5)–(7) in addition to (11)–(14).

$$C_2H_5 + NO \longrightarrow C_2H_5NO \quad (11)$$

$$C_2H_5 + C_2H_5NO \longrightarrow (C_2H_5)_2NO \quad (12)$$

$$C_2H_5 + (C_2H_5)_2NO \longrightarrow (C_2H_5)_2NOC_2H_5 \quad (13)$$

$$C_2H_5NO + C_2H_5NO \rightleftharpoons (C_2H_5NO)_2 \quad (14)$$

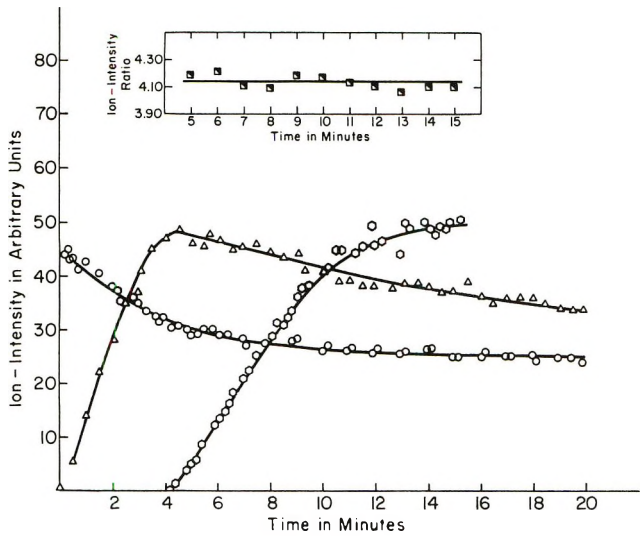

Figure 4. Nitric oxide depletion in photolysis of 5 Torr of 6.8% NO in azoethane: ○, i_{30}; □, i_{58}; △, i_{59}; ○, i_{117}; ◥, i_{60}/i_{117}.

The formation of triethylhydroxylamine is interesting in that a search of the literature reveals this work to represent the first documented observation of the compound. In an attempt to prepare *O*,*N*-diethylhydroxylamine from *O*-ethylhydroxylamine, Lossen[32] reported the probable formation of triethylhydroxylamine, but the meager detail given is very unconvincing. Jones and Major[33] reported unsuccessful attempts to prepare triethylhydroxylamine by synthetic procedures analogous to those that had been successful in the preparation of trimethylhydroxylamine and *O*,*N*-diethyl-*N*-methylhydroxylamine. No other pertinent mention of triethylhydroxylamine has been found.

In accord with the fact that in recent years a considerable number of nitroxide radicals have been observed and prepared,[3,5] we write the addition of ethyl radicals to nitrosoethane as a two-step process, (12) and (13) with (12) being rate-determining. We have not observed the nitroxide radical, $(C_2H_5)_2NO\cdot$, in our system; this was not unexpected, since it would undergo sufficiently rapid combination with ethyl radicals (13) to prevent it reaching detectable concentrations.

3. Specific Rates of Nitrosoethane Reactions. In order to obtain specific reaction rates from the mass spectrometric data, it is first necessary to obtain the relationship between peak intensity and partial pressure or concentration of monomeric nitrosoethane. The relationship between partial pressure of nitric oxide and the intensity of the peak at *m*/*e* 30 in the azoethane–nitric oxide mixtures is made directly by observation of the mass spectra of these mixtures as a function of known partial pressures.

In the initial stages of the photolysis, wherein nitrosoethane is the sole product, we may write

$$-\left(\frac{d[NO]}{dt}\right)_0 = \left(\frac{d[C_2H_5NO]}{dt}\right)_0 = 2\phi I_0\alpha[A]_0 \quad (15)$$

where $[A]_0$ is the initial concentration of azoethane and $\phi I_0\alpha$ has been determined, as described previously, by measurement of the decrease in the concentration of azoethane. Writing $\beta_{m/e}(X)$ as the proportionality factor between concentration and peak intensity, (15) becomes

$$-\beta_{30}(NO)\left(\frac{di_{30}}{dt}\right)_0 = \beta_{59}(C_2H_5NO)\left(\frac{di_{59}}{dt}\right)_0 \quad (16)$$

and since $\beta_{30}(NO)$ is known, we obtain $\beta_{59}(C_2H_5NO)$.

We assume in this calibration that contribution of nitrosoethane dimer to the peak at *m*/*e* 59 is negligible. This would, at first sight, appear to be inconsistent with the recent mass spectrum of nitrosoethane reported by Eastmond and Pratt.[34] These authors admitted dimeric nitrosoethane (trans) to their mass spectrometer and obtained only very small peaks (5% or less of the base peak) at *m*/*e* values greater than 59. We believe that at the pressures and temperatures obtaining in their ion source most of the nitrosoethane was present predominately as monomer. The values for the equilibrium constant between monomer and dimer reported by Christie, Frost, and Voisey,[20] and determined in this work, are in accord with this belief. Also in accord is our observation that the appearance potential of the ion with *m*/*e* 59 that is formed *initially* and which, therefore, can represent only the onset energy of the process

$$C_2H_5NO + e \longrightarrow C_2H_5NO^+ + 2e \quad (17)$$

is identical, within experimental error of ±0.2 eV, with the appearance potential of *m*/*e* 59 found by Eastmond and Pratt.[35]

Assuming that the radical-combination reaction (13) is very rapid, the rate-determining step in the formation of triethylhydroxylamine is (12). We may evaluate the specific reaction rate of (12) by kinetic analysis of the photolyzing mixture *after* the maximum in the concentration of C_2H_5NO, assuming: (1) the maximum in the concentration of C_2H_5NO corresponds to complete consumption of NO; and (2) the contribution of dimerization (14) to the decrease in C_2H_5NO concentration after the maximum is negligible. Analysis of the relative amount of dimer formation during photolysis, and of the times required to reach the maximum in C_2H_5NO concentration as a function of the light intensities and partial pressures of reactants used, indicates these two assumptions to be satisfactory for initial partial pressures of NO below 0.4 Torr.

To evaluate the specific reaction rate of (12) from the experimental data after the maximum in $[C_2H_5NO]$, it is first necessary to convert the ion intensities of experiments such as shown in Figures 2 and 4 to con-

(32) W. Lossen, *Ann. Chem.*, **252**, 233 (1889).

(33) L. W. Jones and R. T. Major, *J. Amer. Chem. Soc.*, **50**, 2742 (1928).

(34) G. B. M. Eastmond and G. L. Pratt, *J. Chem. Soc., A*, 2337 (1970).

centrations of C_2H_5NO. It is known that trimethylhydroxylamine has a significant mass peak at m/e 45 (CH_3NO^+)[10] and it is, therefore, likely that triethylhydroxylamine has a significant peak at m/e 59, corresponding, of course, to $C_2H_5NO^+$. This means that, after the maximum in $[C_2H_5NO]$, the increasing contribution of triethylhydroxylamine to m/e 59 will compensate for the decreasing contribution from nitrosoethane, and the ion-current m/e 59 must be corrected in order to obtain the concentration of nitrosoethane. Unfortunately, the mass spectrum of triethylhydroxylamine is not known, in contrast to our studies with nitrosomethane,[12] and this correction must be made indirectly and approximately as follows.

We assume that at the maximum in $[C_2H_5NO]$, *all* the ethyl radicals react either with nitrosoethane or with each other. Since ethyl radicals are always at a steady state, this means that at the maximum in $[C_2H_5NO]$ the sum of the formation rates of triethylhydroxylamine and butane are equal to one-half of the formation rate of ethyl radicals. In terms of the relationship between ion current and concentration, we have then

$$\beta_{117}((C_2H_5)_2NOC_2H_5)\left(\frac{di_{117}}{dt}\right)_{max} + \beta_{58}(C_4H_{10})\left(\frac{di_{58}}{dt}\right)_{max} = \phi I_0 \alpha[C_2H_5N{=}NC_2H_5]_{max} \quad (18)$$

Since the slopes are measurable and $\beta_{58}(C_4H_{10})$ and $\phi I_0 \alpha[C_2H_5N{=}NC_2H_5]_{max}$ are known, we may obtain easily β_{117} and, hence, the concentration of triethylhydroxylamine as a function of time.

Recognizing that the only fates awaiting nitrosoethane are leakage out of the cell and conversion to triethylhydroxylamine, and that triethylhydroxylamine can only leak out of the cell, it is easy to show that (19) applies, *viz.*

$$[C_2H_5NO] = [C_2H_5NO]_{max}e^{-\lambda t} - [(C_2H_5)_2NOC_2H_5] \quad (19)$$

$[C_2H_5NO]_{max}$ may with less than 10% error be taken to be equal to $[NO]_0$, for initial partial pressures of NO less than 0.4 Torr, and $[(C_2H_5)_2NOC_2H_5]$ may be calculated from the time dependence of the intensity of m/e 117. Hence (19) permits calculation of $[(C_2H_5NO]$ as a function of time after the maximum in this species. The rate of depletion of C_2H_5NO is described by (20) while the steady-state concentration of ethyl radicals after the $[C_2H_5NO]$ maximum is given by (21).

$$-\frac{d[C_2H_5NO]}{dt} = k_{12}[C_2H_5][C_2H_5NO] + \lambda[C_2H_5NO] \quad (20)$$

$$[C_2H_5] = \frac{1}{2(k_6 + k_7)}\{(k_{12}^2[C_2H_5NO]^2 + 4(k_6 + k_7)\phi I_0 \alpha[C_2H_5N{=}NC_2H_5])^{1/2} - k_{12}[C_2H_5NO]\} \quad (21)$$

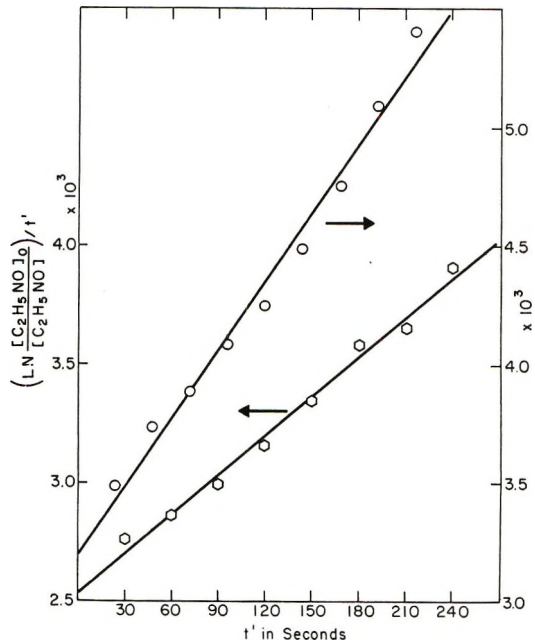

Figure 5. Kinetic description of nitrosoethane depletion after consumption of nitric oxide: (eq 23) O, 6.2 Torr of NO(3% in azoethane; ○, 5.0 Torr of NO(6.8%) in azoethane.

From an initial guess that k_{12} is the same as for the corresponding reaction in the nitrosomethane system, and using reported values for k_6 and k_7,[30,35] the steady-state $[C_2H_5]$ can be computed from (21) as a function of $[C_2H_5NO]$ and, hence, as a function of time, from (19). When this is done it is found that over an appreciable range of time, beginning with about 20 sec after the $[C_2H_5NO]$ maximum, the calculated steady-state $[C_2H_5]$ is a linear function of time. Hence we may write for this time range

$$[C_2H_5] = a + bt' \quad (22)$$

where t' is the reaction time less some convenient time, t_0, and a and b are empirical constants. Substituting (22) into (20) and integrating, we obtain the result shown in (23)

$$\frac{1}{t'}\ln\frac{[C_2H_5NO]_0}{[C_2H_5NO]} = k_{12}a + \lambda + \frac{1}{2}k_{12}bt' \quad (23)$$

where $[C_2H_5NO]_0$ is the nitrosoethane concentration at t_0. Thus a plot of the left-hand side of (23) *vs.* t' should be linear with a slope of $^1/_2k_{12}b$ and an intercept of $k_{12}a + \lambda$. Such plots for initial partial pressures of nitric oxide of 0.34 and 0.18 Torr are shown in Figure 5. Using the first values of a and b, as determined by computation using (21) and (22), a first-improved k_{12} may be obtained. The process may be repeated until no significant change in k_{12} occurs on successive iterations.

The linearity of the plots according to (23), shown in

(35) K. J. Ivin and E. W. R. Steacie, *Proc. Roy. Soc., Ser. A*, **208**, 25 (1951).

Figure 5, attests to the validity and internal consistency of the method. The values obtained for k_{12} at 56° are 1.6 ± 0.2 × 10^{-14} cm³/molecule-sec at $P_0(NO)$ = 0.34 Torr and 2.4 ± 0.1 × 10^{-14} cm³/molecule-sec at $P_0(NO)$ = 0.18 Torr. The apparent dependence on initial pressure of nitric oxide is very probably real and is due to the assumption that, after the maximum in $[C_2H_5NO]$, [NO] = 0. Actually, in this flow system, the concentration of nitric oxide cannot be zero because it is continually flowing into the photolysis cell from the reactant reservoir where it is at the initial concentration throughout any experiment. As discussed previously,[12] the net result is that k_{12} determined by this procedure is a lower limit. In principle, the true value of k_{12} could be determined by extrapolation to zero initial nitric oxide concentration. However, the dependence on nitric oxide concentration is a complicated function and a reliable extrapolation is not feasible.

The dimerization of monomeric nitrosoethane is shown clearly in Figure 3 by the simultaneous rapid decrease of $C_2H_5NO^+$ (m/e 59) and increase of $(C_2H_5NO)_2$ (m/e 118), when the photolysis is stopped, thereby removing ethyl radicals. This behavior is completely analogous to that reported recently for nitrosomethane.[23] The dimer will be formed in the cell only until the monomer that produces it is effectively consumed and thereafter its concentration must decay. Hence, the intensity of $(C_2H_5NO)_2^+$ goes through a maximum.

After the light is shut off, we may write for the rate of disappearance of monomeric nitrosoethane

$$-\frac{d[C_2H_5NO]}{dt} = 2k_{14}[C_2H_5NO]^2 + \lambda[C_2H_5NO] \quad (24)$$

which upon integration and substitution of the calibration relation, $[C_2H_5NO] = \beta_{59}(C_2H_5NO)i_{59}$, yields the result shown in (25), *viz.*

$$\frac{e^{-\lambda t}}{i_{59}} = \frac{1}{i_{59}^0} + \frac{2k_{14}\beta_{59}(C_2H_5NO)(1 - e^{-\lambda t})}{\lambda} \quad (25)$$

In (25), i_{59}^0 is the ion current at m/e 59 at the instant the photolysis is terminated, and i_{59} is the same ion current at time t subsequent to the termination; we have also assumed that the dimer makes no contribution to the intensity of m/e 59. A typical plot of data, such as shown in Figure 3, according to (25) is shown in Figure 6. The plot is linear for times not too far removed from the time of photolysis termination and, since λ and $\beta_{59}(C_2H_5NO)$ are known, we obtain k_{14} from the slope. The deviation from linearity at the longer times in Figure 6 is no doubt due to a breakdown of the assumption of no dimer contribution to m/e 59 and to reformation of monomer by dimer dissociation (not included in (24)). The value obtained for k_{14} from five determinations at 41° and for initial partial pressures of NO of 1.3 Torr and 0.34 Torr is 5.0 ± 0.5 × 10^{-20} cm³/molecule-sec. This is smaller by a factor

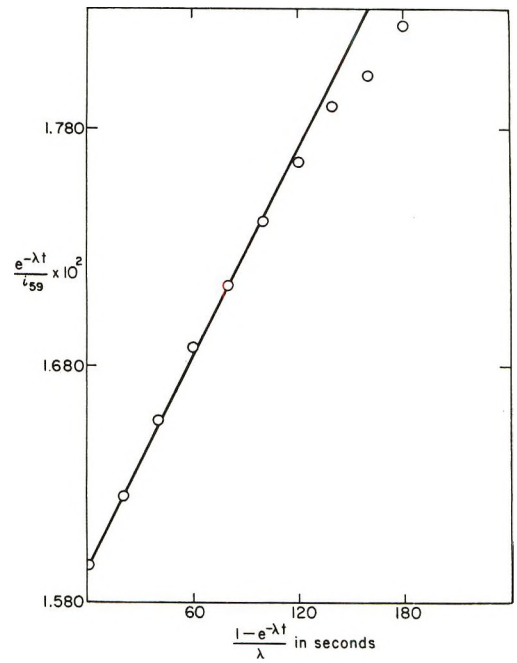

Figure 6. Kinetic description of nitrosoethane dimerization (eq 25).

of about 3 from the value given by Christie, Frost, and Voisey.[20] We are unable to account for the disagreement but considering the great difference in conditions and method, this magnitude of disagreement is perhaps not too surprising.

It is to be noted in Figure 3 that after the maximum in the concentration of $(C_2H_5NO)_2$, the decay of $(C_2H_5NO)_2$ is slower than that of C_2H_5NO. Since any mass dependence of λ due to the system being in a transition region between viscous and molecular flow[9] would operate in the opposite direction, a chemical reaction producing C_2H_5NO at the expense of $(C_2H_5NO)_2$ is indicated. We conclude that, as the total concentration of nitrosoethane in the photolysis cell decreases, the reversible reaction (14) is shifted to the left, in accord with LeChatelier's principle.

After termination of photolysis we may write, then, for the time dependence of $(C_2H_5NO)_2$ concentration

$$\frac{d[(C_2H_5NO)_2]}{dt} = k_{14}[C_2H_5NO]^2 - \lambda[(C_2H_5NO)_2] - k_{-14}[(C_2H_5NO)_2] \quad (26)$$

where t is the time after illumination ceases. At the maximum in the concentration of $(C_2H_5NO)_2$, the derivative in (26) is zero. Therefore, using the notation described previously for the relationship between ion current at a given m/e and concentration, we obtain from (26) the result shown in (27), *viz.*

$$k_{-14} = k_{14}\frac{\beta_{59}^2(C_2H_5NO)}{\beta_{118}((C_2H_5NO)_2)}\left(\frac{i_{59}^2}{i_{118}}\right)_{max} - \lambda \quad (27)$$

We may assume (Figure 3) that at the instant of termination of illumination the contribution of $(C_2H_5$-

Table I: Specific Rates of Nitrosoethane and Nitrosomethane Reactions[a]

	k^d (ref 12)	k (ref 20)[b,c]	$k^{b,c}$ (ref 23)	$k^{c,d}$ (this work)
$CD_3NO + CD_3 \rightarrow (CD_3)_2NO$	$\geq 6.5 \times 10^{-14}$	...	...	...
$CH_3NO + CH_3NO \rightarrow (CH_3NO)_2$	...	9.5×10^{-20}	$3.6 \pm 0.08 \times 10^{-20}$	...
$(CH_3NO)_2 \rightarrow CH_3NO + CH_3NO$	...	1.8×10^{-4}	...	...
$C_2H_5NO + C_2H_5 \rightarrow (C_2H_5)_2NO$	...	...	...	$\geq 2.4 \times 10^{-14}$
$C_2H_5NO + C_2H_5NO \rightarrow (C_2H_5NO)_2$	...	1.7×10^{-19}	...	$5.0 \pm 0.5 \times 10^{-20}$
$(C_2H_5NO)_2 \rightarrow C_2H_5NO + C_2H_5NO$	...	4.0×10^{-4}	...	$4.1 \pm 0.6 \times 10^{-3}$

[a] Units of first-order reactions are sec^{-1} and of second-order reactions are cm^3 molecule^{-1} sec^{-1}. [b] The rate constants for dimerization are defined by $-d[RNO]/dt = 2k[RNO]^2$. [c] Nitrosomethane dimerization and the reverse refer to a temperature of 50°; nitrosoethane dimerization and the reverse to 41°. [d] The radical addition to nitrosomethane and nitrosoethane refer to 56°.

$NO)_2$ to the intensity of the ion at m/e 59 is negligible. Since monomer and dimer are stoichiometrically related by (14) simple consideration of the time derivatives of the intensities of ions at m/e 59 and m/e 118 leads to (28), *viz.*

$$\frac{\beta_{118}}{\beta_{59}}\frac{((C_2H_5NO)_2)}{(C_2H_5NO)} = -\frac{1}{2}\frac{\left(\frac{di_{59}}{dt}\right)_0 + \lambda i_{59}^0}{\left(\frac{di_{118}}{dt}\right)_0 + \lambda i_{118}^0} \qquad (28)$$

where $(di_{m/e}/dt)_0$ and $i_{m/e}^0$ represent time derivatives of ion intensities and ion intensities, respectively, at $t = 0$, that is, at the instant of termination of the irradiation. Since λ and $\beta_{59}(C_2H_5NO)$ are known, we obtain from (28), and data such as shown in Figure 3, a value for $\beta_{118}((C_2H_5NO)_2)$. We may then utilize (27) and the ion intensity at the maximum in the concentration of $(C_2H_5NO)_2$ to evaluate k_{-14}; the value obtained from five experiments at 41° and for initial partial pressures of NO of 0.34 Torr and 1.3 Torr is $4.1 \pm 0.6 \times 10^{-3}$ sec^{-1}. This is higher by a factor of 10 than the value of 4.0×10^{-4} sec^{-1} reported by Christie, Frost, and Voisey.[20] The disagreements in the forward and reverse rates of the dimerization lead to our value for the equilibrium constant of (14) at 41°, namely

$$k_{14} = \frac{k_{14}}{k_{-14}} = 1.2 \pm 0.2 \times 10^{-17} \text{ cm}^3/\text{molecule}$$

being more than an order of magnitude smaller than the value of Christie, Frost, and Voisey.[20]

In our work we have calculated K_{14} from experimental measurements of k_{14} and k_{-14} as contrasted with the work of Christie, Frost, and Voisey in which k_{-14} was calculated from measurements of k_{14} and K_{14}. We believe that our error limits on k_{14} and k_{-14} are realistic and the disagreement between our results and those of Christie, Frost, and Voisey[20] is therefore disturbing. Unfortunately, these latter authors do not report error limits for their experimental values nor do they discuss the accuracy of their results other than to remark about "the difficulty of determining absolute concentrations of nitrosomethane."

For convenience, the specific rates for the reactions of nitrosoethane studied in our work are tabulated in Table I, where they are compared with specific rates for analogous reactions of nitrosomethane.

4. Ionization Potentials of C_2H_5NO and $C_2H_5N{=}NC_2H_5$. Since during the initial stages of photolysis the $(C_2H_5NO)_2$ is present in very low concentration relative to C_2H_5NO (*cf.* Figure 3), we may study, in a manner similar to that of Kohout and Lampe for HNO,[36] the growth curves of m/e 59 as a function of electron energy to obtain the ionization potential of C_2H_5NO.

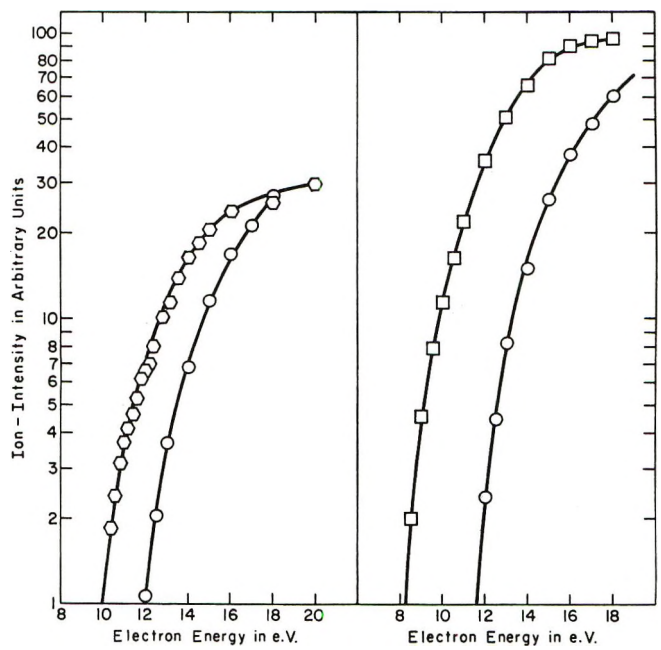

Figure 7. Ionization efficiency curves: ○, $C_2H_5NO^+$; □, $C_2H_5N{=}NC_2H_5^+$; ○, Xe^+.

Thus for all conditions of the photolysis held constant, the initial slope of the intensity of m/e 59 *vs.* time will depend on the ionizing electron energy in the same manner as does the ionization cross section. A plot of these initial slopes *vs.* electron energy yields a typical ionization efficiency curve, as shown in Figure 7. Using

(36) F. C. Kohout and F. W. Lampe, *J. Chem. Phys.*, **45**, 1074 (1966).

xenon as an internal standard we find the result: $I_z(C_2H_5NO) = 10.1 \pm 0.2$ eV. Also shown for comparison is an ionization efficiency curve for formation of $C_2H_5N{=}NC_2H_5^+$ which leads to a value of $I_z(C_2H_5N{=}NC_2H_5) = 8.7 \pm 0.1$ eV. This value may be compared with the value of 8.65 ± 0.2 eV for the ionization potential of azomethane reported by Prasil and Forst;[37] the agreement suggests that the lowest ionization potential of azoalkanes involves removal of a nonbonding electron on one of the nitrogen atoms.

Acknowledgment. This work was supported in part by the U. S. Atomic Energy Commission under Contract No. AT(11-1)-3416 and in part by the Petroleum Research Fund of the American Chemical Society under Grant No. 3298-A5. We also thank the National Science Foundation for providing funds to assist in the original purchase of the time-of-flight mass spectrometer.

(37) Z. Prasil and W. Forst, *J. Amer. Chem. Soc.*, **90**, 3344 (1968).

Absolute Rate Constants for the Addition and Abstraction Reactions of Atomic Oxygen with 1-Butene over the Temperature Range 190–491 K[1]

by Robert E. Huie,

Chemistry Department, University of Maryland, College Park, Maryland, and National Bureau of Standards, Washington, D. C.

John T. Herron,

National Bureau of Standards, Washington, D. C.

and Douglas D. Davis*[2]

Chemistry Department, University of Maryland, College Park, Maryland *(Received February 15, 1972)*

Publication costs assisted by the Petroleum Research Fund

Using the technique of flash photolysis–resonance fluorescence, absolute rate constants have been measured for the reaction of ground-state atomic oxygen with 1-butene over the temperature range 190–491 K. With a measured precision of 3–5% at each temperature, it was found that the data could not be fit by a single straight line. It was concluded that the curvature in the Arrhenius plot was due to concurrent abstraction and addition reactions, the former process representing approximately 15% of the total reaction at 300 K and 39% at 500 K. The rate expressions derived were $k_{addition} = (3.7 \pm 1.8) \times 10^{-12} \exp(-50 \pm 210 \text{ cal mol}^{-1}/RT)$ cm^3 molecule^{-1} sec^{-1} and $k_{abstraction} = (1.6 \pm 0.9) \times 10^{-11} \exp(-1970 \pm 430 \text{ cal mol}^{-1}/RT)$ cm^3 molecule^{-1} sec^{-1}.

In a recent paper,[3] absolute rate constants were reported for the reaction of atomic oxygen, O(^{3}P), with 1-butene over the temperature range 259–493 K. An activation energy for this reaction of 760 cal mol^{-1} was derived. More recently, Kurylo[4] has studied the reaction of atomic oxygen with propene, also a terminal olefin, and found an activation energy of 73 cal mol^{-1}. Since O(^{3}P) addition to propene and 1-butene might be expected to have similar activation energies (both being terminal olefins), we have extended our previous measurements to lower temperatures to investigate the possibility that abstraction of the internal α-hydrogens in 1-butene might have been important at the higher temperatures.

The apparatus and technique used in this work have been described previously[3,5] and will not be discussed here. For the 1-butene reaction, rate constants have been determined from 190 to 491 K with the results

(1) From a dissertation submitted to the Graduate School, University of Maryland, in partial fulfillment of the requirements for the Ph.D. degree in Chemistry. The research reported on was performed at the University of Maryland.

(2) Acknowledgment is made by this author to the donors of The Petroleum Research Fund, administered by the American Chemical Society, for support of this research.

(3) R. E. Huie, J. T. Herron, and D. D. Davis, *J. Phys. Chem.*, **75**, 3902 (1971).

(4) M. J. Kurylo, *Chem. Phys. Lett.*, **14**, 117 (1972).

(5) D. D. Davis, R. E. Huie, J. T. Herron, M. J. Kurylo, and W. Braun, *J. Chem. Phys.*, **56**, 4868 (1972).

Table I: Rate Constants for the Reaction of Atomic Oxygen with Propene and 1-Butene

T, K	Olefin, mTorr	O_2, Torr	Total pressure, Torr, Ar	Flash energy,[a] J	First-order k, (s^{-1})	$k \times 10^{12}$, cm^3 molecule^{-1} sec^{-1}
			Propene			
215	5.47	1	20	31	892	3.43
257	5.30	1	20	26	801	3.77
298	5.30	1	20	18	730	3.99
			1-Butene			
190	...	1	20	45	79	...
190	6.65	1	20	45	1168	3.23
200	...	1	20	31	66	...
200	1.81	1	20	45	394	3.73
200	2.67	1	20	31	467	3.12
200	6.65	1	20	20	1155	3.40
200	6.65	1	20	130	1100	3.24
200	7.98	1	20	31	1272	3.13
215	...	1	20	31	51	...
215	2.68	1	20	31	467	3.47
215	7.93	1	20	31	1316	3.56
226	...	1	20	29	51	...
226	...	1	200	29	296	...
226	1.84	1	20	26	311	3.31
226	3.10	1	200	29	996	3.10
226	5.31	1	20	10	820	3.47
226	5.31	1	20	80	757	3.19
226	10.7	1	20	26	1530	3.24
248	...	1	40	45	41	...
248	2.77	1	40	45	397	3.62
259	...	0.5	100	45	46	...
259	2.53	0.5	100	45	364	3.38
272	...	1	20	45	51	...
272	...	2	200	45	191	...
272	2.21	1	20	45	357	3.91
272	5.37	1	200	45	934	3.90
272	7.10	1	20	22	972	3.68
272	7.10	1	20	100	919	3.45
272	12.6	1	20	45	1670	3.61
274	...	1	40	30	64	...
274	2.77	1	40	30	455	3.62
298	...	0.5	10	40	81	...
298	...	1	20	45	44	...
298	...	1	200	40	130	...
298	1.29	1	200	18	282	3.73
298	2.63	0.5	10	20	424	4.10
298	2.71	1	20	18	444	4.57
298	5.26	1	20	32	689	3.84
298	5.26	1	20	18	730	4.10
298	5.26	1	20	8	747	4.20
298	5.26	1	200	26	777	3.86
298	8.20	1	20	18	1156	4.20
298	8.25	1	20	28	1110	3.99
298	12.9	1	200	18	1895	4.20
343	...	1	200	20	59	...
343	2.63	1	200	20	396	4.69
370	...	1	20	45	60	...
370	3.3	1	20	39	437	4.38
370	6.38	1	20	39	810	4.52
370	13.7	1	20	39	1670	4.51
403	...	1	200	20	44	...
403	2.63	1	200	20	366	5.27
472	...	1	20	29	196	...
472	3.26	1	20	29	556	5.41
472	6.18	1	20	29	891	5.51
472	11.1	1	20	29	1350	5.14
484	...	1	20	36	187	...
484	3.26	1	20	36	566	5.74
484	6.61	1	20	18	950	5.79
484	6.61	1	20	100	928	5.62
484	13.3	1	20	36	1613	5.38
491	...	1	200	45	111	...
491	7.3	1	200	45	961	5.92

[a] A flash energy of 45 J corresponds to an incident light intensity of about 8×10^{12} photons/cm^2 at the reaction cell at wavelengths <1800 Å.

presented in Table I. Excluded is the data point at 493 K reported previously[3] and now thought to have been in error. At several temperatures, reactant concentration, total pressure, and flash intensity were varied to ascertain that no secondary reactions were taking place, as has been described previously.[5] In Figure 1, the data are presented in Arrhenius form. The points shown are average values at temperatures where three or more measurements were made. It can be seen that these data can only be fit by a curved line. This curve, however, can be approximated by the sum of two straight lines—one of which can be assumed to correspond to the addition of atomic oxygen to the double bond and the other to the abstraction of the internal α-hydrogens. Thus, the following two rate expressions may be derived.

$$k_{\text{addition}} = (3.7 \pm 1.8) \times 10^{-12} \times \exp\left(\frac{-50 \pm 210 \text{ cal mol}^{-1}}{RT}\right) \text{cm}^3 \text{ molecule}^{-1} \text{ sec}^{-1}$$

$$k_{\text{abstraction}} = (1.6 \pm 0.9) \times 10^{-11} \times \exp\left(\frac{-1970 \pm 430 \text{ cal mol}^{-1}}{RT}\right) \text{cm}^3 \text{ molecule}^{-1} \text{ sec}^{-1}$$

The expression for the addition reaction was obtained by a straight line fit to the lower temperature data (<260 K). The expression for the abstraction reaction was determined by subtracting the values predicted for the addition reaction from the higher temperature data and fitting this difference to a straight line. The stated uncertainties in the Arrhenius expressions were derived from a consideration of the lines with the max-

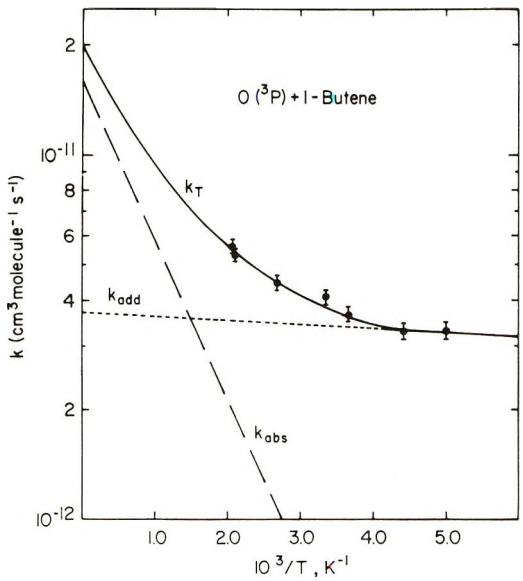

Figure 1. Arrhenius plot for the reaction of atomic oxygen with 1-butene.

imum and minimum slopes drawn through the attached error bars (3–5%). In addition to the measurements reported here, Kurylo has also made several measurements of the rate constant for reaction of O(³P) with 1-butene and found the values to be in good agreement (±5%) with ours.[6]

In the case of the reaction of O(³P) with propene, single measurements were made in this study at 216, 257, and 298 K. These results are also given in Table I and are within 6% of those rate constants reported by Kurylo at comparable temperatures.[4] Although these data do not establish that both addition and abstraction reactions are taking place in the 1-butene reaction, the derived Arrhenius parameters are consistent with this interpretation. A comparison of the activation energy for reaction of O(³P) with propene and 1-butene shows that for the addition reaction very similar values are obtained, 76 *vs.* 50 cal/mol. The reasonableness of these values has recently been demonstrated in a related study by Klemm and Davis[7] in which the activation energies for addition of S(³P) to propene and 1-butene were both found to be 360 cal/mol. It is also noteworthy that in the study by Klemm and Davis[7] no curvature was observed in the Arrhenius plot for the S(³P)–1-butene system over the temperature range 216–475 K. This result is in keeping with the known higher activation energy required for H atom abstraction from hydrocarbons by S(³P) *vs.* O(³P).

For the O(³P)–1-butene abstraction reaction, it is observed that the preexponential factor is in good agreement with those observed for atomic oxygen–alkane reactions (1–3 × 10^{-11} cm^3 $molecule^{-1}$ sec^{-1}) in which hydrogen abstraction is the most probable reaction.[8,9] The activation energy for this process is lower than the activation energies measured for most alkane reaction,[8,9] but is consistent with the very low C–H bond strength for internal α-hydrogens (82 kcal/mol) recently reported by Tsang.[10]

The conclusion that the curvature in the Arrhenius plot is due to concurrent abstraction and addition reactions is supported further by comparison with the equivalent situation involving atomic hydrogen. From an analysis of the reaction products, Falconer and Sunder[11] concluded that 1.6% of the H + 1-C_4H_8 reaction proceeded by the abstraction of the α-hydrogen at room temperature. The addition and abstraction component lines presented in Figure 1 indicate that for atomic oxygen, 15% of the reaction proceeds by abstraction at 298 K and 39% at 500 K. However, the lower error limit given in the Arrhenius expression for abstraction predicts ~1% of the total reaction is due to abstraction at 298 K and 20% at 500 K. The correct value at each temperature undoubtedly lies somewhere between these two sets of numbers.

(6) M. J. Kurylo, private communication.

(7) R. Klemm and D. D. Davis, *Int. J. Chem. Kinet.*, in press.

(8) J. T. Herron and R. E. Huie, *J. Phys. Chem.*, **73**, 3327 (1969).

(9) R. E. Huie and J. T. Herron, *J. Res. Nat. Bur. Stand.*, **76A**, 77 (1972).

(10) W. Tsang, *Int. J. Chem. Kinet.*, **1**, 245 (1969).

(11) W. E. Falconer and W. A. Sunder, *ibid.*, **4**, 315 (1972).

The Bond Dissociation Energy of the C–H Bond in Ethanol. A Kinetic Study of the Reaction I_2 + Ethanol[1a]

by Ze'ev B. Alfassi[1b] and David M. Golden*

Department of Thermochemistry and Chemical Kinetics, Stanford Research Institute, Menlo Park, California 94025 *(Received May 30, 1972)*

The reaction of iodine with ethyl alcohol has been studied in a static system in the temperature range 203–252° and in the pressure range 30–750 Torr. The rate-determining step of this reaction has been found to be $I + CH_3CH_2OH \xrightarrow{1} CH_3\dot{C}HOH + HI$ and k_1 is given by the equation $\log (k_1/M^{-1}\,\mathrm{sec}^{-1}) = (11.5 \pm 0.3) - (22.7 \pm 0.6)/\theta$, $\theta = 2.303RT$ kcal mol^{-1}. From the activation energy and the assumption $E_{-1} = 1 \pm 1$ kcal mol^{-1}, it has been calculated that $D[CH_3CH(OH)-H] = 93.0 \pm 1.0$ and $\Delta H_f^\circ(CH_3\dot{C}HOH,g) = -15.2 \pm 1.0$ kcal mol^{-1}. The data of the reaction $I_2 + CH_3OH$ are reinterpreted, increasing log A by 0.3.

Introduction

The first values of the bond dissociation energies (BDE's) of C–H bonds in alcohols were measured by Whittle and coworkers[2,3] using photobromination techniques. They found $D[CH_2(OH)-H] \leq 92$ kcal/mol and $D[CH_3CH(OH)-H] \leq 90$ kcal/mol. Two years later Walsh and Benson[4] studied the reaction of iodine with 2-propanol and found $D[(CH_3)_2C(OH)-H] = 90.3 \pm 1.1$ kcal/mol. The similarity of the strengths of the tertiary C–H bonds in isobutane and in 2-propanol led them to suggest that "the inductive effect of hydroxyl group is the same as that of a methyl group with respect to homolytic bond breaking at the α-carbon position." This suggestion would lead to $D[CH_2(OH)-H] = 98$ kcal/mol and $D[CH_3CH(OH)-H] = 95$ kcal/mol. Cruickshank and Benson[5] have measured the BDE of the C–H bond in methanol and found $D[CH_2(OH)-H] \geq 95.9$.[5,6] These discrepancies lead to the present situation in which the C–H bond strengths in alcohols are not too well known. In order to resolve these discrepancies, more data are needed. The kinetics of gas-phase iodine atom reactions have been found to be a reliable source of bond dissociation energies.[6] This work deals with the reaction of iodine with ethanol in order to measure $D(CH_3CH(OH)-H]$.

Experimental Section

Iodine (Mallinkrodt) was resublimed and degassed at liquid nitrogen temperature before use. Ethanol (Rossville, Gold Shield) and acetaldehyde (Matheson Coleman and Bell) were distilled and found to be more than 99.9% pure by gas chromatography (F and M, Model 810), using a 25-ft column of 20% Carbowax, 20 M, on Chromosorb, W. AW 60–80 mesh.

The Cary 15 spectrophotometer modified for use with a heated reaction vessel has been described previously.[7] Iodine was introduced into the reaction vessel at the desired pressure, first, and the spectrophotometer was set to record the absorbance as a function of time at a wavelength between 502 and 440 mμ, according to the I_2 pressure. The wavelength was chosen such that the initial absorption was 1.7–1.9 OD, except in one experiment where the amount of I_2 was too low and the absorption at the peak was 0.95 OD. In some of the experiments the absorptions at 270 and 235 mμ were also measured in order to measure the amount of HI formed.

In order to minimize surface effects, the vessel was coated with Teflon by polymerization of 150–200 Torr of C_2F_4 catalyzed by 1–5 Torr of *tert*-butyl peroxide at 185°.[8] Initial rates were measured by following the rate of disappearance of 5–10% of the original iodine absorption.

Results

The initial rates of the reactions of iodine with organic compounds have been found[6] to obey the equation

$$-\frac{d(I_2)}{dt} = k_{obsd}(I)(RH) = k_{obsd}K_{I_2}^{1/2}(I_2)^{1/2}(RH) \quad (1)$$

where RH is the organic compound and K_{I_2} is the equilibrium constant for the dissociation of iodine molecules

(1) (a) This work was supported, in part, by Grant No. AP 00353-08 from the Environmental Protection Agency. (b) Postdoctoral Research Associate.

(2) (a) E. Buckley and E. Whittle, *Trans. Faraday Soc.*, **58**, 529 (1962); (b) E. Buckley and E. Whittle, *ibid.*, **58**, 536 (1962).

(3) A. M. Tarr and E. Whittle, *Trans. Faraday Soc.*, **60**, 2039 (1964).

(4) R. Walsh and S. W. Benson, *J. Amer. Chem. Soc.*, **88**, 3480 (1966).

(5) F. R. Cruickshank and S. W. Benson, *J. Phys. Chem.*, **73**, 733 (1969).

(6) D. M. Golden and S. W. Benson, *Chem. Rev.*, **69**, 125 (1969).

(7) D. M. Golden, R. Walsh, and S. W. Benson, *J. Amer. Chem. Soc.*, **87**, 4053 (1965); R. Walsh and S. W. Benson, *ibid.*, **88**, 3480 (1966).

(8) R. K. Solly, D. M. Golden, and S. W. Benson, *Int. J. Chem. Kinet.*, **2**, 381 (1970).

$$I_2 + M \overset{K_{I_2}}{\rightleftharpoons} 2I + M$$

The results for the reaction of iodine with ethanol given in Table I show that this reaction is governed by the same rate law, since sixfold changes in iodine pressure and more than tenfold changes in ethanol pressure give the same k_{obsd} (calculated according to eq 1) within experimental error. The dependence of k_{obsd} on the temperature in the range 203.2–252.0° is given by $\log (k_{obsd}/\text{l. mol}^{-1} \text{ sec}^{-1}) = (11.5 \pm 0.3) - (22.7 \pm 0.6)/\theta$, where θ equals $2.303RT$ kcal/mol, and the quoted errors are standard deviations. This Arrhenius plot is shown in Figure 1.

Table I: The Observed Rate Constants for the Reaction of Iodine with Ethanol: $k_{obsd} = (-d(I_2)/dt)_{initial}/(I)(C_2H_5OH)$

Run no.	Temp, °C	(I_2), Torr	(EtOH), Torr	$1/K_{I_2}^{1/2}$, Torr$^{-1/2}$	$k_{obsd} \times 10^{-1}$ l. mol^{-1} sec^{-1}
1	203.0	21.0	689	1.66×10^4	1.185
2	203.0	24.1	425	1.66×10^4	1.20
3	203.2	22.8	743	1.64×10^4	1.09
4	203.2	20.1	689	1.64×10^4	1.12
5	213.5	5.85	535	1.089×10^4	1.55
6	213.5	15.3	362		1.71
7	213.5	20.4	122.5		1.55
8	213.5	21.8	629		1.84
9	225	2.62	579	7.03×10^3	2.84
10		5.6	540		2.81
11		16.7	527		2.85
12		17.8	38		3.05
13		21.8	27.4		2.78
14		24.5	603.5		3.13
15	236.5	3.9	633	4.59×10^3	4.72
16		5.71	494		4.25
17		11.8	367		4.44
18		17.1	96		5.55
19		25.6	447		5.00
20	252	8.65	354	2.74×10^3	9.9
21		13.4	169		10.9
22		18.6	195		10.8
23		22.4	277		11.1
24	212.8[a]	19.5	303	1.10×10^4	2.01
25		20.9	536		1.66
26	244[a]	16.6	185	3.55×10^3	7.15
27		18.4	280.5		6.30
28		22.4	146		7.75
29	215[b]	14.5	519.5	1.025×10^4	1.76
30	217[b]	18.7	221	9.40×10^3	2.45

[a] Measurements done in packed vessel. [b] Measurements done in uncoated packed vessel.

The possibility of a heterogeneous contribution to the disappearance of I_2 was checked by measuring the rate of the reaction in a packed vessel in which the surface to volume ratio is about 14 times larger than in the usual vessel. The results of these measurements given in Table I and in Figure 1 show that the disappearance of I_2 is homogeneous. In the study of the reaction of I_2 with methanol[5] it was found that the surface catalyzed the disappearance of I_2. In order to check if the difference in the surface effects is caused by the different alcohols or by the fact that our surfaces have been Teflonized, the Teflon coating was decomposed by heating to 400° (the decomposition is verified by the decrease of the absorbance (scattering) of light in the reaction vessel). Two measurements were done in the un-Teflonized packed vessel. The results of these measurements (*cf.* Table I and Figure 1) show that a quartz surface does not catalyze the reaction between I_2 and ethanol either.

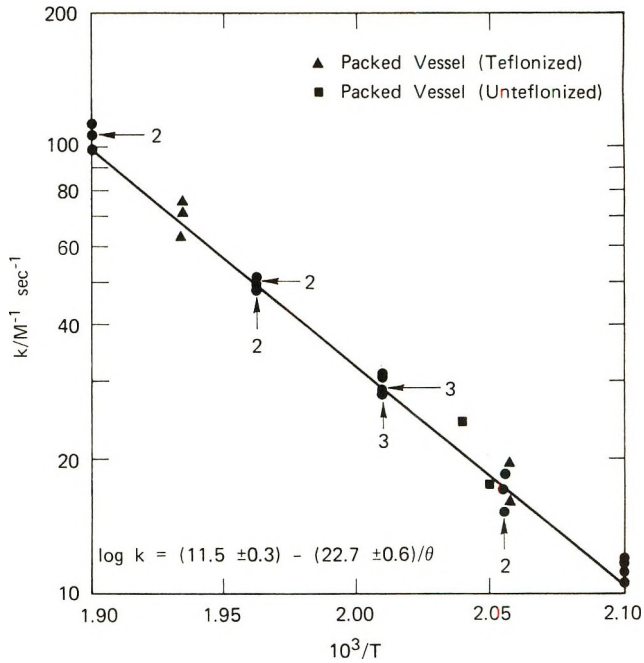

Figure 1. Arrhenius plot for the reaction $I + CH_3CH_2OH \rightarrow CH_3\dot{C}HOH + HI$.

Discussion

Following the mechanism found for methanol,[5] the scheme of reactions in the case of ethanol will be

$$I_2 \overset{K_{I_2}}{\rightleftharpoons} 2I\cdot$$

$$I\cdot + CH_3CH_2OH \overset{1}{\rightleftharpoons} CH_3\dot{C}HOH + HI$$

$$CH_3\dot{C}HOH + I_2 \overset{2}{\rightleftharpoons} CH_3CHIOH + I$$

$$CH_3CHIOH \overset{3}{\longrightarrow} HI + CH_3CHO$$

$$CH_3CHO + I \overset{4}{\rightleftharpoons} HI + CH_3\dot{C}O$$

$$CH_3\dot{C}O + I_2 \overset{5}{\rightleftharpoons} CH_3COI + I$$

In the case of methanol, it was assumed that, since reactions 3 and 4 are much faster than reaction 1, for every molecule of CH_3OH which reacts, two molecules of I_2 will be consumed, and hence $k_{obsd} = 2k_1$. This assumption has to be considered carefully since, although the rate constant k_4 is larger than k_1, the con-

centration of the alcohol is usually much higher than that of the aldehyde.

The rate constant for the abstraction of hydrogen from acetaldehyde by an iodine atom was measured previously at one temperature[9] and the Arrhenius parameters were chosen by assuming a reasonable A factor. In order to be sure of our comparison of k_1 and k_4, we measured k_4 for one of the temperatures for which k_{obsd} was measured (225°); the results are given in Table II. Comparison with the results of k_{obsd}

Table II: The Reaction of I_2 with Acetaldehyde at 225°

$(I_2)_0$	$(CH_3CHO)_0$, Torr	$\left(\frac{-d(I_2)}{dt}\right)_{in.}$, Torr sec^{-1}	$1/K_{I_2}^{1/2}$, Torr$^{-1/2}$	k_4, l. mol^{-1} sec^{-1}
19.4	42.8	1.71×10^{-3}	7.03×10^3	1.98×10^3
20.3	24.5	9.25×10^{-3}	7.03×10^3	1.90×10^3

which is either k_1 (if reaction 3 or 4 do not occur), or twice k_1 (if these reactions are completed) shows that k_4/k_1 is between 67 and 134. The initial rates are measured up to 10% change in the $(I_2)_0$ concentration and thus the concentration of the acetaldehyde, which is equal or less than the amount of the iodine consumed, is given by $(CH_3CHO) \leq 0.1(I_2)_0$. The ratio of the rates of reactions 4 and 1 will be

$$\frac{\text{rate 4}}{\text{rate 1}} \leq \frac{k_4}{k_1} \times \frac{0.1(I_2)_0}{(C_2H_5OH)_0} \leq 13.4 \frac{(I_2)_0}{(C_2H_5OH)_0}$$

This value of 13.4 is a high upper limit including the assumption that $k_{obsd} = 2k_1$ and that the amount of acetaldehyde present is equal to the amount of reacted iodine. These are contradictory assumptions and a more reasonable relation is obtained by using the value 67 for the ratio of the rate constants. Thus

$$\frac{\text{rate 4}}{\text{rate 1}} \leq 6.7 \frac{(I_2)_0}{(C_2H_5OH)_0} \quad \text{(at 225°)}$$

The results of Table I show that at 225° the ratio $(I_2)_0/(C_2H_5OH)_0$ has been varied in the range of 7.9×10^{-1} to 4.5×10^{-3} without any noticeable change in k_{obsd}. For the cases of higher values of this ratio (7.9×10^{-1} and 4.7×10^{-1}), almost all the acetaldehyde formed would have had to react and thus $k_{obsd} = 2k_1$, while for the runs with low $(I_2)_0/(C_2H_5OH)_0$ ratios only a very small fraction of the acetaldehyde would have reacted with iodine and $k_{obsd} = k_1$. The fact that in both cases we get the same result for k_{obsd} shows that $k_{obsd} = k_1$ in all the runs. This same conclusion can be reached for the methanol[5] experiments when the data are reevaluated. In this latter study, the authors[5] assumed that, since the reaction of I with formaldehyde (reaction 4 in their paper) is much faster than the reaction with methanol (the ratio of the rate constants is about 500), every molecule of formaldehyde formed would have reacted, and they did not consider the ratio of the concentrations of the aldehyde and alcohol.

The rate constant of the reaction I + CH_3OH has been found to be log (k_1/l. mol^{-1} sec^{-1}) = 11.5 − 26/θ and of the reaction of iodine atoms with formaldehyde[10] log k_4 = 10.9 − 17.4/θ, and hence, $k_4/k_1 = 10^{-0.6+8.6/\theta}$. For runs 11–13 (the numbers are the numbers of the runs in the original paper[5]), θ = 2.64 and $k_4/k_1 = 10^{2.66}$. A similar expression to the one derived previously for ethanol will, in this case, be

$$\frac{\text{rate 4}}{\text{rate 1}} \leq \frac{k_4}{k_1} \frac{0.1(I_2)_0}{(CH_3OH)_0} = 45.6 \frac{(I_2)_0}{(CH_3OH)_0}$$

Thus, for runs 12 and 13 where the ratio of the pressures is about unity, reaction 4 would be much faster than reaction 1, and hence $k_{obsd} = 2k_1$, since the overall reaction would be $2I_2 + CH_3OH \rightarrow CO + 4HI$. Whereas for run 11, where the ratio $(I_2)_0/(CH_3OH)_0 = 1.5 \times 10^{-2}$, the rate of reaction 4 would be smaller than that of reaction 1 and $k_{obsd} < 2k_1$. The solution of the rate equations (Appendix A) shows that in run 11 for 10% consumption of I_2 only about 28% of the newly formed formaldehyde would have reacted, thus $k_{obsd} = 1.28k_1$, while in run 12, 98.5% of the formaldehyde would have been consumed by I_2, and thus $k_{obsd} = 2k_1$. Yet the experimental results of k_{obsd} for runs 11–13 are the same, within the experimental error, meaning that in both cases $k_{obsd} = k_1$, and reaction 4 does not occur. The same results for $CH_3OH + I_2$ are found for runs 15–17. In run 16, after consumption of 10% of the iodine, only 18% of the newly formed HCHO will have reacted, while in run 17, 78% will have reacted, meaning that in run 16, $k_{obsd} = 1.18k_1$, and in run 17, $k_{obsd} = 1.78k_1$; yet the experimental results are the same, leading to the conclusion that no iodine at all has been consumed by the aldehyde.

The reason that no iodine has been consumed by the aldehyde, although in the reaction of iodine with pure aldehyde iodine is consumed, is either that no aldehyde is formed or that the iodine consumed by the aldehyde is regenerated. Rollefson and Faull[11] found that in the reaction of iodine with acetaldehyde and propionaldehyde the I_2 disappeared in the first step, but at the end of the reaction the original amount of iodine is regenerated. These studies were done at higher temperatures (>300°), and the mechanism for this regeneration, proposed by O'Neal and Benson,[12] does not predict the same phenomena at 225°. More than that, both Walsh and Benson,[9] at 208°, and the present authors, at 225°, found that the absorption of iodine

(9) R. Walsh and S. W. Benson, *J. Phys. Chem.*, **70**, 3751 (1966).

(10) R. Walsh and S. W. Benson, *J. Amer. Chem. Soc.*, **88**, 4570 (1966).

(11) G. K. Rollefson and R. F. Faull, *ibid.*, **59**, 625 (1937).

(12) E. O'Neal and S. W. Benson, *J. Chem. Phys.*, **40**, 302 (1964).

reaches an equilibrium value and does not return to the original absorption, at least in the time range of our experiments (2–4 hr). Thus the remaining explanation is that the iodohydrin is not in a steady-state concentration, and the concentration of the aldehyde is lower than that calculated by assuming a steady state of the iodohydrin. This must mean that the iodohydrin is more stable than previously assumed,[5] and the lower limit of k_3 which can be deduced from these results is compared with a theoretical calculation in Appendix II. The fact that CO has been found to be one of the products[5] and the existence of an accompanying pressure increase do not contradict the conclusion concerning lack of formation of aldehyde in the initial steps. The iodohydrin reaches its steady-state concentration after the initial steps and then the aldehyde is formed. This sort of behavior has been observed in the reaction of iodine with methyl ethyl ketone,[13] where in the initial step 2-iodo-3-butanone is formed, and only later does this intermediate decompose to give methyl vinyl ketone by elimination of hydrogen iodide.

In the case of ethyl alcohol, there is still another possibility, namely, that the iodohydrin decomposes to water and vinyl iodide (instead of the hydrogen iodide and acetaldehyde). This possibility does not seem to be favored by the calculation of its homogeneous rate constant (Appendix II), but it might be the predominant reaction as a result of heterogeneous catalysis. Some support for this possibility is the fact that in two runs carried out at 271°, after the absorption of the iodine goes to a minimum value and remains at this value for some time, it starts to increase again. A mass spectrometric analysis of the mixtures shows, besides C_2H_5OH, I_2, and HI, the presence of water, ethane, and ethylene. Ethane and ethylene have previously been found to be the products of the reaction of vinyl iodide and hydrogen iodide.[14]

The conclusion that in the case of the reaction of I_2 with methanol, $k_{obsd} = k_1$ and not $k_1 = k_{obsd}/2$, as was postulated before, leads for that system to $\log k_1 = 11.8 - 26/\theta$.

The Bond Dissociation Energy, $D(CH_3CH(OH)-H)$. The reaction of hydrogen iodide with radicals is usually assumed (and in some cases has been proven[6]) to have an activation energy of 1 ± 1 kcal/mol, and thus

$$\Delta H(1) = E_1 - E_{-1} = 22.7 - 1 = 21.7 \text{ kcal/mol}$$

This enthalpy is for 502°K, the average temperature at which the reaction has been studied. Since the average heat capacity is small, it can be neglected and $\Delta H_{298}(1) = 21.7$ kcal mol^{-1}.[15] The enthalpy of reaction is the difference between the BDE of the broken bond $D(CH_3CH(OH)-H)$ and that of the newly formed bond, $D(H-I)$, thus

$$D(CH_3CH(OH)-H) = 21.7 + D(H-I) = 21.7 + 71.3[16] = 93.0 \text{ kcal mol}^{-1}$$

This value is larger than the value found by Tarr and Whittle[3] by photobromination studies ($\leq$90 kcal mol^{-1}), but it is close to the value predicted by Golden and Benson as a result of both bromination and iodination studies[6] (~92 kcal mol^{-1}). An interesting observation is that the iodination method gives higher results for the BDE of C–H bonds in alcohols than the photobromination method. A possible good way to check this discrepancy might be through a study of the kinetics of thermal bromination, which may eliminate some of the problems connected with photosensitization.

This value of the bond dissociation energy can be used to calculate the heat of formation of the radical $CH_3\dot{C}HOH$.

$$D[CH_3CH(OH)-H] = \Delta H_f^\circ(CH_3\dot{C}HOH) + \Delta H_f^\circ(H) - \Delta H_f^\circ(CH_3CH_2OH)$$

The heats of formation of a hydrogen atom and of the ethyl alcohol molecule at 298°K are 52.1[17] and −56.1[18] kcal mol^{-1}, respectively; thus the heat of formation of the hydroxyethyl radical at 298°K is −15.2 ± 1.0 kcal mol^{-1}.

Appendix A

Solution of the Rate Equations for the Reaction of I_2 with Methanol

$$I + CH_3OH \xrightarrow{1} \dot{C}H_2OH + HI$$

$$\dot{C}H_2OH + I_2 \xrightarrow{2} CH_2IOH + I$$

$$CH_2IOH \xrightarrow{3} CH_2O + HI$$

$$CH_2O + I \xrightarrow{4} \dot{C}HO + HI$$

Assuming steady state for $\dot{C}H_2OH$ and CH_2IOH gives

$$(CH_2IOH)_{ss} = \frac{k_1}{k_3}(I)(CH_3OH)$$

(13) R. K. Solly, D. M. Golden, and S. W. Benson, *Int. J. Chem. Kinet.*, 2, 381 (1970).

(14) A. S. Rodgers, D. M. Golden, and S. W. Benson, unpublished results.

(15) The values used for heat capacity are: I, $C_p^\circ_{298} = 5.0$; $C_p^\circ_{502} = 5.0$ gibbs mol^{-1} (S. W. Benson, "Thermochemical Kinetics," Wiley, New York, N. Y., 1968, p 195); C_2H_5OH, $C_p^\circ_{298} = 15.64$; $C_p^\circ_{502} = 22.80$; HI, $C_p^\circ_{298} = 6.97$, $C_p^\circ_{502} = 7.11$ (D. R. Stull, E. F. Westrum, Jr., and G. C. Sinke, "The Chemical Thermodynamics of Organic Compounds," Wiley, New York, N. Y., 1969, pp 228, 423); $CH_3\dot{C}HOH$, $C_p^\circ_{298} = 14.0$, $C_p^\circ_{502} = 20.3$ calculated by deduction from the value of ethyl alcohol, the values for the three missing vibrations (H–C–H scissors, C–C–H rocking, and C–H stretching) and for the hindered rotation (S. W. Benson, "Thermochemical Kinetics," Wiley, New York, N. Y., 1968, p 44). $\Delta\Delta C_p^\circ = (0.42 - 0.34)/2 = 0.04$ eu.

(16) B. deB Darwent, "Bond Dissociation Energies in Simple Molecules," NSRDS-NBS 31 (1970).

(17) S. W. Benson, "Thermochemical Kinetics," Wiley, New York, N. Y., 1968, p 195.

(18) D. R. Stull, E. F. Westrum, Jr., and G. C. Sinke, "The Chemical Thermodynamics of Organic Compounds," Wiley, New York, N. Y., 1969, p 423.

$$\frac{d(CH_2O)}{dt} = k_3(CH_2IOH) - k_4(I)(CH_2O)$$

$$= k_1(I)(CH_3OH) - k_4(I)(CH_2O)$$

and for the initial steps ($\Delta(I_2) \leq 0.1(I_2)_0$)

$$(CH_2O) = \frac{k_1}{k_4}(CH_3OH)(1 - e^{-k_4(I)t})$$

The total amount of formaldehyde formed (both the amount present and the amount already consumed) is given by

$$(CH_2O)_{total} = k_1(CH_3OH)(I)t$$

and the fraction of the formaldehyde consumed by the reaction with iodine F, is given by

$$F = \frac{(CH_2O)_{total} - (CH_2O)}{(CH_2O)_{total}} = 1 - \frac{(CH_2O)}{(CH_2O)_{total}}$$

$$= 1 - \frac{1 - e^{-k_4(I)t}}{k_4(I)t}$$

The maximum value for $k_4(I)t$ can be calculated by the upper limit of the measured disappearance of iodine, *i.e.*, $\Delta(I_2) = 0.1(I_2)_0$

$$\Delta(I_2) = k_1(CH_3OH)(I)\cdot t$$

$$0.1(I_2)_0 = k_1(CH_3OH)(I)\cdot t$$

$$k_4(I)t = \frac{0.1k_4(I_2)_0}{k_1(CH_3OH)}$$

and

$$F = 1 - \frac{1 - \exp\left[\frac{0.1k_4(I_2)}{k_1(CH_3OH)}\right]}{\frac{0.1k_4(I_2)}{k_1(CH_3OH)}}$$

Appendix B

Estimated Upper Limit Value for k_3 and Comparison to the Theoretical Estimation

The upper limit value of k_3 can be estimated by assuming that, in the region where the initial rate law applies ($\Delta(I_2) \sim 0.1(I_2)$), the iodohydrin reaches its stationary-state concentration. This can be calculated by assuming that the iodohydrin steady-state concentration is equal to the amount of the iodine which has been consumed ($0.1(I_2)$). The steady-state concentration of the iodohydrin is given by $k_1/k_3(I)(ROH)$ [Appendix A], where (I) and (ROH) are the concentration of the iodine atoms and the alcohol, respectively. Thus the upper limit value of k_3 is given by

$$0.1(I_2) = \frac{k_1}{k_3}(I)(ROH)$$

$$k_3 = \frac{k_1(I)(ROH)}{0.1(I_2)} = \frac{k_1\cdot K_{I_2}^{1/2}(ROH)}{0.1(I_2)^{1/2}}$$

For $I_2 + CH_3OH$, run 12, where we expect the reaction of the aldehyde to have the most effect, $T = 574.2°K$, $K_{I_2} = 10^{-10.13}\ M$, $(I_2) = 3.1 \times 10^{-4}\ M$, $(ROH) = 2.9 \times 10^{-4}\ M$, and $k_1 = 10^{1.55}\ M^{-1}\ sec^{-1}$, and thus $k_3 = 10^{-4.30}\ sec^{-1}$. For $I_2 + C_2H_5OH$, run 13, $T = 498°K$, $K_{I_2}^{1/2} = 8.07 \times 10^{-7}\ M^{1/2}$, $(I_2) = 7.0 \times 10^{-4}\ M$, $(ROH) = 8.85 \times 10^{-4}\ M$, and $k_1 = 2.9 \times 10^{1}\ M^{-1}\ sec^{-1}$, and thus $k_3 = 10^{-5.10}\ sec^{-1}$.

The rate constant for the HI elimination from the iodohydrin can be calculated theoretically, as suggested by Cruickshank and Benson.[5] The A factor is calculated by O'Neal and Benson's method[19] for four- and six-center unimolecular elimination as $\Delta S^{\ddagger} \approx -2$ eu, and thus $A = 10^{13.1}$. The activation energy is calculated from the activation energy for the reverse reaction, the four-center addition of HX to the carbonyl double bond, calculated by Benson and Haugen's method,[20] and adding the endothermicity of the elimination reaction. The endothermicity is calculated from the known bond dissociation energies

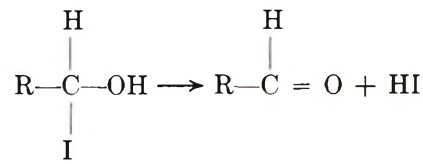

$\Delta H = D(O\text{-}H) + D(C\text{-}I) - D(C{=}O, \pi\ bond) - D(H\text{-}I)$ and using the values $D(O\text{-}H) = 104.0, 105.0$, $D(C\text{-}I) = 53.5, 56.0$, $D(C{=}O) = 76, 73$, and $D(H\text{-}I) = 71.3$ (the first value is for ethanol iodohydrin and the second is for methanol iodohydrin), thus $\Delta H = 10.2$, 16.7 kcal mol^{-1}, respectively. The activation energies were calculated by using the data in Benson and Haugen's paper, and $\alpha_{CH_3CHO} = 3.60$ Å^3, $\alpha_{CH_2O} = 3.56$ Å^3,[21] $\mu_{CH_3CHO} = 2.690$,[22] $\mu_{CH_2O} = 2.330$,[22] $r_{O=H} = 0.96$ Å,[23] $r_{C-I} = 2.14$ Å.[23] The C–O bond distance in the transition state has been taken as the average value between double and single C–O bond lengths, 1.33 Å.[23] The activation energies calculated thus are for CH_3CHIOH and CH_2IOH, 31.5 and 38.7 kcal mol^{-1}, respectively. Thus k_3 for formaldehyde iodohydrin at 574°K is $10^{-1.7}\ M^{-1}\ sec^{-1}$, much higher than our upper limit estimate and the same is true for acetaldehyde

(19) H. E. O'Neal and S. W. Benson, *J. Phys. Chem.*, **71**, 2903 (1967).

(20) S. W. Benson and G. R. Haugen, *J. Amer. Chem. Soc.*, **87**, 4036 (1965); *J. Phys. Chem.*, **70**, 3336 (1966).

(21) The molar refraction, R, was calculated from those of n-butylaldehyde and propylaldehyde (K. G. Denbigh, *Trans. Faraday Soc.*, **36**, 936 (1940)), assuming additivity of molar refraction. The molar polarizability is calculated from the equation $\alpha = 3R/4\pi N$, and the ratio longitudinal to total polarizability is taken to be equal to those of propane and ethylene, respectively (J. O. Hirschfelder, C. F. Curtiss, and R. B. Bird, "Molecular Theory of Gases and Liquids," Wiley, New York, N. Y., 1954, p 950).

(22) A. L. McClellan, "Tables of Experimental Dipole Moments," W. H. Freeman, San Francisco, Calif., 1963, pp 41, 64.

(23) "C. R. C. Handbook of Chemistry and Physics," 51st ed, 1970–1971, p F-157.

iodohydrin. The conclusion thus is that the Benson and Haugen calculation cannot be applied to four-center addition to a carbonyl bond, unless further modification would be done, such as enlarging the HI bond distance in the transition state more than in the transition state for addition to olefins (The ground state bond length + 0.40 Å.[20]).

The rate constant for the elimination of water from acetaldehyde iodohydrin can be calculated by the same method, using Haugen and Benson's calculations[24] for addition of water to olefinic double bonds, which gives $k = 10^{13.6-64.2/\theta}$, which is much smaller than the calculated rate constant for HI elimination.

(24) G. R. Haugen and S. W. Benson, *Int. J. Chem. Kinet.*, 2, 235 (1970).

Epoxidation of Alkenes in the Gas Phase

by D. J. M. Ray and D. J. Waddington*

Department of Chemistry, the University of York, Heslington, York Y01 5DD, England *(Received April 13, 1972)*

It is suggested that the retardation of acetaldehyde oxidation by alkenes is due to addition of peracetyl radicals to the alkene. This leads to the formation of the corresponding epoxide from the alkene. Addition of 2,3-dimethylbut-2-ene leads to long induction periods before acetaldehyde is oxidized and this may be due to interaction of peracetic acid with the alkene, leading to enhanced suppression of chain branching. The addition reaction between peracetyl radicals and *cis*-but-2-ene is calculated as 2×10^3 m^3 mol^{-1} sec^{-1} at 457 K.

In a previous paper,[1] we reported that many aliphatic alkenes retard the gas-phase oxidation of acetaldehyde. By comparing the relative retardation coefficients of the alkenes and by considering the products formed from the alkenes, we suggested that the alkene reacted with acetylperoxy radicals (formed during the propagation reactions in acetaldehyde oxidation[2]), the resulting alkene–acetylperoxy radicals being stabilized by hyperconjugation. The addition reaction (reaction 1) is able to compete with the alternative reaction (reaction 2). However, 2-methyl-2-butene and 2,3-dimethyl-2-butene are added. The addition of these alkenes gives rise to the different types of behavior noted. The apparatus, procedures, and methods of analysis are described in the earlier paper.[1]

$$CH_3CO_3\cdot + >C{=}C< \longrightarrow >\dot{C}{-}C(O_2CCH_3)< \longrightarrow >C(O)C< + CH_3\cdot + CO_2 \quad (1)$$

$$CH_3CO_3\cdot + CH_3CHO \longrightarrow CH_3CO_3H + CH_3\dot{C}O \quad (2)$$

The nature and amount of product from the oxidation of acetaldehyde are unaltered by the addition of *cis*-2-butene; the main difference between these two systems is the lower rate at which the aldehyde is oxidized in presence of the alkene (Table I). The principal products from *cis*-2-butene are *trans*- and *cis*-butan-2,3-epoxides; the isomers are formed in the ratio of 1.3:1 throughout the reaction.[1] In the presence of a similar concentration of 2,3-dimethyl-2-butene, on the other hand, the maximum oxidation rate of acetaldehyde is not reached until the concentration of alkene is comparatively low. Again, the corresponding epoxide is the major product from the alkene, but, unlike the butan-2,3-epoxides, most of the 2,3-dimethylbutan-2,3-epoxide is formed before the maximum rate of acetaldehyde consumption. There is also a significant difference in the proportion of peracetic acid to acetic acid formed. The detection of acetic acid *vs.* peracetic acid suggests that 2,3-dimethyl-2-butene is methyl-2-butene behave differently from the other alkenes studied. The maximum rate of oxidation is not retarded to the extent expected and long induction periods, during which only a small pressure decrease occurs, are observed.

We have therefore compared the oxidation products of acetaldehyde when *cis*-2-butene and 2,3-dimethyl-

(1) D. J. M. Ray and D. J. Waddington, *Symp. (Int.) Combust., [Proc.], 13th*, 1970, 261 (1971).

(2) J. F. Griffiths and G. Skirrow, *Oxid. Combust. Rev.*, 3, 47 (1968).

Table I: Formation of Products during the Oxidation of Acetaldehyde at 457 K[a]

Alkene added	Reaction time, min	Reactants consumed, kN m^{-2}		Products formed, kN m^{-2}						
		Alkene	Acetaldehyde	Epoxides	Peracetic acid	Formaldehyde	Methanol	Carbon monoxide	Carbon dioxide	Acetic acid
	1		2.5		1.3	<0.1	0.5		0.3	
	1.5		2.8		1.7	<0.1	0.6	<0.1	0.5	
	2		3.7		2.7	0.1	0.7	<0.1	0.7	0.2
	4		5.5		3.4	0.3	1.2	0.1	1.6	
	6		6.0		3.4	0.7	1.7	0.3	2.0	0.1
	8		6.2		3.4	0.8	1.8	0.5	2.3	0.1
cis-2-Butene	4	0.3	1.2	0.22	0.8	<0.1	0.3		0.2	
(1.2 kN m^{-2})	6	0.5	2.3	0.30	2.0	<0.1	0.4	<0.1	0.5	
	10	0.7	3.9	0.37	3.4	<0.1	0.8	<0.1	1.2	0.2
	15	0.9	5.5	0.60	3.5	0.3	1.4	0.2	1.6	0.1
	18	1.0	5.9	0.67	3.5	0.6	1.8	0.2	1.8	0.2
	20	1.1	6.2	0.72	3.6	0.7	1.9	0.3	2.0	0.2
2,3-Dimethyl-2-butene	20	0.03	0.1	0.03	<0.1	...	...	...	...	...
(1.2 kN m^{-2})	45	0.06	0.1	0.06	<0.1	...	...	...	...	...
	65	0.1	0.1	0.1	<0.1	...	...	...	...	...
	80	0.2	0.3	0.2	<0.1	...	...	...	...	...
	95	0.3	0.4	0.2	<0.1	...	...	...	...	...
	125	0.6	0.6	0.4	<0.1	...	...	...	...	...
	140	1.0	1.2	0.6	0.1	...	...	...	...	1.3
	150	1.1	1.7	0.9	0.5	...	...	...	...	1.5
	180	1.2	6.7	0.9	2.2	...	...	...	...	1.5

[a] Acetaldehyde, 6.7 kN m^{-2}; oxygen, 6.7 kN m^{-2}. (...) indicates analyses were not performed.

not only reacting by reaction 1 but also with peracetic acid. The latter reaction is analogous to the liquid-phase epoxidation of alkenes by peracetic acid[3] and the cooxidation of alkenes and benzaldehyde in solution, in which the epoxide is considered to be produced by reaction between the hydrocarbon and perbenzoic acid.[4] Thus, we suggest that 2,3-dimethyl-2-butene is reacting with peracetic acid by a similar molecular mechanism. Compared with reaction 1, reaction 3 leads to

$$Me_2C{=}CMe_2 + CH_3CO_3H \longrightarrow \underset{Me_2C\text{——}CMe_2}{\overset{O}{\diagup\diagdown}} + CH_3CO_2H \quad (3)$$

further suppression of chain branching and thus accounts for the difference in behavior on adding aliphatic alkenes of different structures on the oxidation of acetaldehyde. It appears that the presence of three or four methyl groups attached directly to the π bond results in a high-electron density being donated to the bond, facilitating electrophilic attack by peracetic acid as well as addition of peracetyl radicals by reaction 1.

From the analysis we are able to assume that the overall reactions for the peracetyl radical in the presence of *cis*-2-butene are (1) and (2). Thus

$$\frac{d[\text{epoxide}]}{d[\text{peracetic acid}]} = \frac{k_1[\text{alkene}]}{k_2[\text{acetaldehyde}]}$$

We estimate that, under these conditions, k_2/k_1 = 1.5 ± 0.1. The Arrhenius parameters for reaction 2 have been determined from a study of acetaldehyde oxidation,[5] log A_2 = 6.3 (A/m^3 mol^{-1} sec^{-1}), E_2 = 30.2 kJ mol^{-1}. However, Griffiths and Skirrow[2] have pointed out that the data were obtained over a narrow temperature range 293–313 K, and that, in a subsequent study,[6] at temperatures up to 413 K, E_2 was determined as 28.5 ± 4.2 kJ mol^{-1}. This value is similar to that obtained for the corresponding reaction in propionaldehyde oxidation[5] (log A = 6.7 (A/m^3 mol^{-1} sec^{-1}), E_2 = 28.5 kJ mol^{-1}). As the observed rates of oxidation of acetaldehyde and propionaldehyde are similar over a wide range of temperatures, Griffiths, Skirrow, and Tipper have used values of k_2 computed by averaging the data from these studies, confirming their reliability when using them in a numerical analysis study of acetaldehyde oxidation.[7] Using this technique, we obtain a value at 457 K for k_2 of 3 × 10^3 m^3 mol^{-1} sec^{-1}, giving a value of 2 × 10^3 m^3 mol^{-1} sec^{-1} for k_1 at this temperature.

Acknowledgment. We thank the Science Research Council for a research studentship (D. J. M. R.).

(3) D. Swern, *J. Amer. Chem. Soc.*, **69**, 1692 (1947).

(4) F. Tsuchiya and T. Ikawa, *Can. J. Chem.*, **47**, 3191 (1969).

(5) C. A. McDowell and L. K. Sharples, *ibid.*, **36**, 251, 268 (1958).

(6) L. M. Postnikov, V. Ya. Shlyapintokh, and M. N. Shumilina, *Kinet. Katal.*, **6**, 161 (1965).

(7) J. F. Griffiths, G. Skirrow, and C. F. H. Tipper, *Combust. Flame*, **12**, 360 (1968).

Ionic Reactions in Monosilane. Some Radiation Chemistry Implications[1]

by Tung-Yang Yu, Tom M. H. Cheng, V. Kempter, and F. W. Lampe*

Whitmore Laboratory, Department of Chemistry, The Pennsylvania State University, University Park, Pennsylvania 16802 *(Received January 12, 1972)*

Publication costs assisted by the U. S. Atomic Energy Commission

The ion–molecule reactions occurring in ionized monosilane have been studied by high-pressure mass spectrometry up to about 0.5 Torr and by tandem mass spectrometry in both 90 and 180° configurations. Relative cross sections of the second-order primary ion and secondary ion reactions have been determined at relative kinetic energies of reactants near 1 eV. Rate constants of both second- and third-order primary ion reactions have also been measured. It is suggested that $Si_2H_7^+$, $Si_3H_9^+$, and $Si_4H_{11}^+$, whose abundance reaches 35% of the ions present, are responsible for the large yield of disilane in the radical-scavenged radiolysis.

A previous study[2] of the ion–molecule reactions occurring in monosilane at pressures below 0.012 Torr indicated the ionic products to be SiH_3^+, Si_2H^+, $Si_2H_2^+$, $Si_2H_3^+$, $Si_2H_4^+$, and $Si_2H_5^+$; it was further concluded that the sole reactant ion forming all these product ions was SiH_2^+. Subsequent studies[3] of the electron impact ionization and dissociation of disilane lead to the firm conclusion that reactions of SiH_2^+ with SiH_4 to form Si_2H^+ and $Si_2H_3^+$ are energetically unfeasible (endothermic by 25 and 16 kcal/mol, respectively) under the conditions of the earlier investigation. In fact, the thermochemical results[3] indicate that the only primary ion capable, energetically, of producing $Si_2H_3^+$ and Si_2H^+ is SiH^+. In view of these contradictions and the rather small pressure range of our earlier work,[2] it was thought desirable to carry out more detailed mass spectrometric studies of the ion–molecule reactions occurring in ionized monosilane. The results and conclusions of these investigations comprise the subject matter of this paper. Since completing our work, the existence of an ion-cyclotron resonance study[4] of ion–molecule reactions in monosilane has come to our attention. The results of this latter study[4] and of our work reported herewith are generally in agreement and are complementary at low pressures.

Experimental Section

Studies of the variation of ionic abundances with ion-source pressures were carried out in a Nuclide Associates 12-90G sector-field mass spectrometer. This instrument has been described previously,[5–8] although in the studies reported herewith the entrance and exit slits of the ion source were made appreciably smaller to achieve source pressures up to about 0.5 Torr. The energy of the ionizing electron beam was 100 eV, the trap current very small and not measured, and the ion-accelerating voltage was 2500 V. In all experiments the repeller field was 6.25 V/cm leading to an ion-exit energy of 2.1 eV. The temperature of the ion source was approximately 70° in all experiments.

Ion-source pressures in the Nuclide mass spectrometer were read directly from a McLeod gauge that was connected *via* $^5/_{16}$-in. diameter tubing to the ion source. Measurement of the pressure dependence of CH_5^+ in ionized CH_4, which occurs with a known specific reaction rate,[9–13] demonstrated our pressure readings to be accurate to within ±10%.

Experiments to identify the reactant ions leading to various ionic products and to examine the kinetic energy dependence of the reactions were carried out in a tandem mass spectrometer recently constructed in this laboratory.[13] The spectrometer consists basically of two quadrupole mass filters, separated by a collision chamber and ion-lens systems, which can be mounted either in-line, as shown in the diagram in Figure 1, or in a 90° configuration. The quadrupole mass filters were of a design by Schmeltekopf,[14] consisting of stainless steel segmented rods,[15] 10 cm in length, 0.53 cm in diameter, and mounted so that the distance between surfaces of opposite rods is 0.46 cm. The ion source to provide ions for injection into the first mass filter is

(1) U. S. Atomic Energy Commission Document No. COO-3416-2.

(2) G. G. Hess and F. W. Lampe, *J. Chem. Phys.*, **44**, 2257 (1966).

(3) P. Potzinger and F. W. Lampe, *J. Phys. Chem.*, **73**, 3912 (1969).

(4) J. M. S. Henis, G. W. Stewart, M. K. Tripodi, and P. P. Gaspar, *J. Chem. Phys.*, **57**, 389 (1972).

(5) P. Potzinger and F. W. Lampe, *J. Phys. Chem.*, **74**, 587 (1970).

(6) P. Potzinger and F. W. Lampe, *ibid.*, **74**, 719 (1970).

(7) J. J. DeCorpo and F. W. Lampe, *ibid.*, **74**, 3939 (1970).

(8) P. Potzinger and F. W. Lampe, *ibid.*, **75**, 13 (1971).

(9) V. L. Talroze and E. L. Frankevich, *Zh. Fiz. Khim.*, **34**, 2709 (1960).

(10) C. W. Hand and H. von Weyssenhoff, *Can. J. Chem.*, **42**, 195 (1964).

(11) J. L. Franklin, Y. Wada, P. Natahis, and P. M. Hierl, *J. Phys. Chem.*, **70**, 2353 (1966).

(12) S. K. Gupta, E. G. Jones, A. G. Harrison, and J. J. Myber, *Can. J. Chem.*, **45**, 3107 (1967).

(13) V. Kempter and F. W. Lampe, U. S. Atomic Energy Commission Annual Progress Report, NYO-3570-18, June 1971.

(14) A. L. Schmeltekopf, private communication, Nov 1969.

(15) W. M. Brubaker, *Advan. Mass Spectrom.*, **4**, 293 (1968).

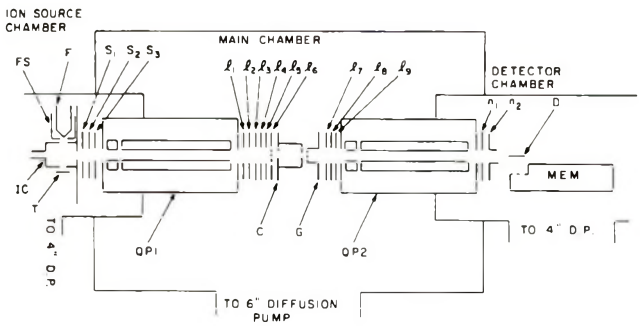

Figure 1. Tandem quadrupole mass spectrometer: F, filament; FS, filament shield; IC, ionization chamber; T, electron trap; l_i, s_i, n_i, focussing lenses; C, collision chamber; G, ion extractor; D, ion deflector; MEM, electron multiplier; QP, quadrupole mass filter.

similar to that described by Iden.[16] Ions are detected by a Bendix M306 magnetic electron multiplier, mounted off the axis of the second mass filter to avoid interference from fast neutral particles.

The radiofrequency power supplies for the quadrupole mass filters are also of Schmeltekopf's design[14] and produce ac voltages variable from 20 to 150 V at frequencies of 1, 2, 4, and 8 MHz, at appropriate and constant ratios of dc to ac voltages.

Typical operation of the tandem spectrometer, with reference to Figure 1, is as follows. Ions from IC are focussed into the first quadrupole filter by the electrodes S_1, S_2, and S_3, under such conditions that the ion energy in the mass filter is about 4 eV. After selection of the reactant ion, the electrodes l_1–l_6 focus the ions into the collision chamber C, with the ion energy being determined, of course, by the potential difference between IC and C. Ions are extracted from C by G and focussed into the second quadrupole by electrodes l_7–l_9, again under such conditions that the ion energy in the filter is about 4 eV. Ions emerging from the second quadrupole are accelerated by electrode n_2, deflected by the ground plate D and accelerated to the cathode of the magnetic electron multiplier (MEM). Ionizing electron energies in the IC of 100 eV are used with trap currents of 20–40 μA. Typical potentials for an experiment with 3 eV (laboratory energy) impacting ions are as given in Table I. Under such conditions, the current of SiH_2^+ ions reaching the collision chamber is of the order of 10^{-11} A. The energy spread of the reactant ion beam is about 1 eV.

The collision chamber is well shielded, with calculations[17] indicating potential penetration into the reaction zone to be negligible. Satisfactory operation of the apparatus was confirmed by measurement of the cross section of the reaction $O^+ + N_2 \rightarrow NO^+ + N$ for O^+ kinetic energies in the range 1–27 eV (laboratory energy). Within experimental error the dependence of the reaction cross section on kinetic energy of O^+ was identical with that reported by Giese.[18]

The resolutions of the two quadrupole mass filters are set separately, by adjustment of the dc/ac ratio to yield unit resolution at the base line. Ultimate resolution of the quadrupoles, limited by the radiofrequency generators, appears to be about 200.

Table I: Typical Potential Configuration for 3-eV Energy Ions

Element (Figure 1)	Potential, V	Elements (Figure 1)	Potential, V
IC	20	C	17
S_1, S_2	−5	G	Ground
S_3, QP1, l_1	−16	l_7, l_8	−19
l_2, l_3	−13	l_9, QP2, m_1	16
l_4	−19	m_2	−250
l_5	−13	D	Ground
l_6	0	MEM	−1800

Collision chamber pressures were measured with a Granville-Phillips capacitance manometer. In the studies reported herein the collision chamber pressures were varied from 10^{-3} to about 10^{-2} Torr.

Monosilane was purchased from the J. T. Baker Chemical Co., and also prepared in the laboratory by the action of $LiAlH_4$ on $SiCl_4$ in di-*n*-butyl ether solution; monosilane-d_4 was prepared similarly by the action of $LiAlD_4$ on $SiCl_4$. Disilane was prepared by a similar reduction of Si_2Cl_6 in the ether solution. $SiCl_4$ and Si_2Cl_6 were obtained from Peninsular Chemical Co., and $LiAlH_4$ and $LiAlD_4$ from Alpha Inorganics and Merck. All gases were fractionated on the vacuum line and checked mass spectrometrically for satisfactory purity before use.

Results and Discussion

1. Pressure Variation Studies. Single Mass Spectrometer. The pressure dependence of the ion intensities in monosilane is depicted in Figures 2–5 in which the ion abundances, as per cent of total ionization, are plotted *vs.* ion source pressure. All ion intensities refer to the ^{28}Si isotope, the necessary corrections having been made.

Contrary to the conclusions of the earlier study[2] and in agreement with the results of Henis, *et al.*,[4] it is clear from Figure 2 that the primary ions Si^+ and SiH^+ do react with SiH_4. Energetic considerations[3] indicate that the only second-order reaction of Si^+ with SiH_4 that is energetically feasible is that to form $Si_2H_2^+$. As comparison of Figures 2 and 3 reveals, up to a pressure of about 60 μ the loss of Si^+ is almost exactly counterbalanced by the increase in $Si_2H_2^+$. Thus, it is strongly suggested that, in the low pressure region ($P < 60$ μ), $Si_2H_2^+$ arises almost exclusively from reaction of Si^+

(16) C. R. Iden, Ph.D. Thesis, The Johns Hopkins University, Baltimore, Md., 1971.

(17) R. P. Feynman, R. B. Leighton, and M. Sands, "The Feynman Lectures on Physics," Vol. II, Addison-Wesley, Reading, Mass., 1964, p 7–11.

(18) C. F. Giese, *Advan. Chem. Ser.*, **No. 58**, 20 (1966).

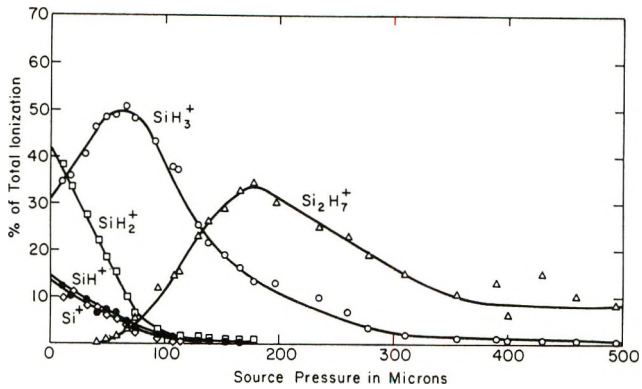

Figure 2. Ionic abundance as a function of source pressure: ○, SiH_3^+; □, SiH_2^+; ●, SiH^+; ◇, Si^+; △, $Si_2H_7^+$.

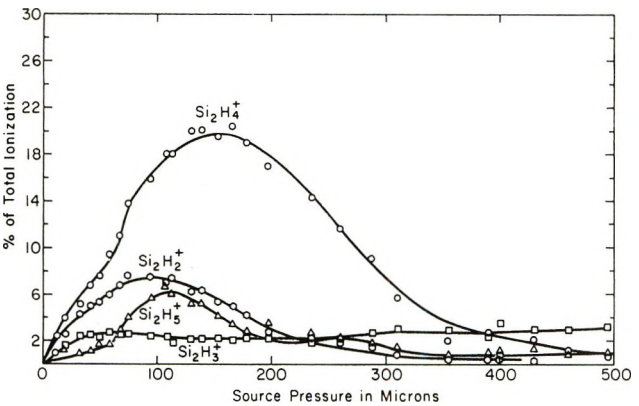

Figure 3. Secondary ion abundance as a function of source pressure: △, $Si_2H_5^+$; ○, $Si_2H_4^+$; □, $Si_2H_3^+$; ○, $Si_2H_2^+$.

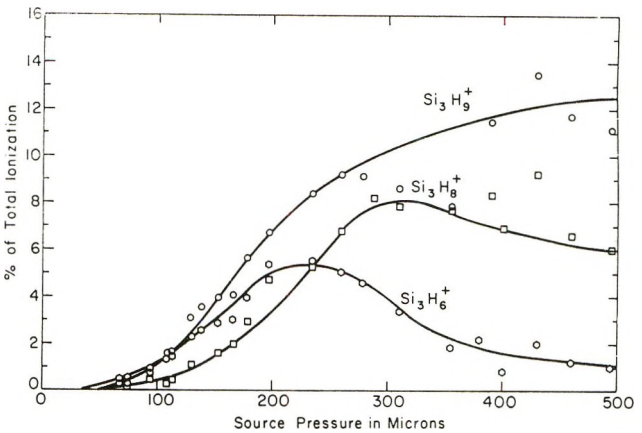

Figure 4. Tertiary ion abundance as a function of source pressure: ○, $Si_3H_9^+$; □, $Si_3H_8^+$; ○, $Si_3H_6^+$.

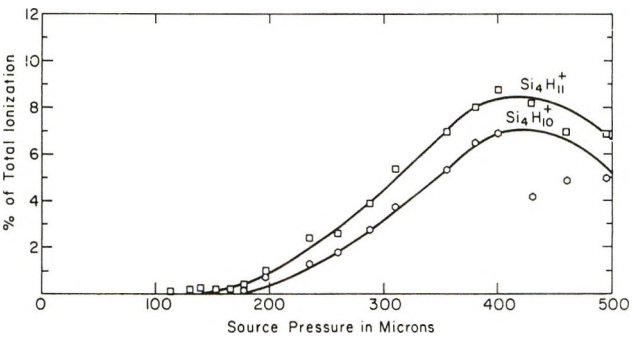

Figure 5. Quaternary ion abundance as a function of source pressure: □, $Si_4H_{11}^+$; ○, $Si_4H_{10}^+$.

with SiH_4. It has already been mentioned that SiH^+ is the only primary ion energetically capable of forming $Si_2H_3^+$. The same applies to the formation of Si_2H^+, although this is a minor product ion and is not shown in Figure 3. Comparison of Figures 2 and 3 shows that SiH^+ is consumed faster than $Si_2H_3^+$ is formed, and faster than the sum of the formation rates of $Si_2H_3^+$ and Si_2H^+; in fact, about 80% of the SiH^+ reacting is accounted for by formation of $Si_2H_3^+$ and Si_2H^+. Thus, while the pressure-dependence studies and energetic considerations establish the reactions 1–3, *viz.*

$$Si^+ + SiH_4 \longrightarrow Si_2H_2^+ + H_2 \quad (1)$$

$$SiH^+ + SiH_4 \longrightarrow Si_2H_3^+ + H_2 \quad (2)$$

$$SiH^+ + SiH_4 \longrightarrow Si_2H^+ + 2H_2 \quad (3)$$

in agreement with the conclusions of Henis, *et al.*,[4] the consumption of about 20% of the SiH^+ is not accounted for. Most likely this extra depletion of SiH^+ is due to H^- ion transfer from SiH_4 as shown by (4), a reaction that is probably exothermic by 5–10 kcal/mol.[3] Al-

$$SiH^+ + SiH_4 \longrightarrow SiH_2 + SiH_3^+ \quad (4)$$

though (4) was not reported by Henis, *et al.*,[4] we have, in fact, observed it in our tandem mass spectrometric experiments to be described in a later section.

As shown in Figure 2, the major reactant ion in monosilane at source pressures less than about 60 μ is SiH_2^+. The primary ion SiH_3^+ exhibits an increase in intensity at pressures below 60 μ and the magnitude of this increase, taking into consideration the foregoing discussion of the major depletion of Si^+ and SiH^+ *via* (1)–(3), points unambiguously to the occurrence of reaction 5, *viz.*

$$SiH_2^+ + SiH_4 \longrightarrow SiH_3 + SiH_3^+ \quad (5)$$

a conclusion in agreement with other studies.[2,4] The negative of the initial slope of the SiH_2^+ curve is greater than the initial slope of the SiH_3^+ curve, indicating that SiH_2^+ is undergoing at least one reaction in addition to (5). Inspection of Figure 3, within the framework of the earlier discussion, suggests that the predominant possibilities are reactions to form $Si_2H_4^+$ and $Si_2H_5^+$. Ion-cyclotron resonance studies[4] and tandem mass spectrometric studies, to be described in a later section, show conclusively that at the kinetic energies obtaining in our pressure study (2.1-eV ion-exit energy), $Si_2H_5^+$ is not a major product of SiH_2^+ reactions while $Si_2H_4^+$ definitely is. Thus reaction 6, *viz.*

$$SiH_2^+ + SiH_4 \longrightarrow Si_2H_4^+ + H_2 \quad (6)$$

is established as a principal loss channel of SiH_2^+, in addition to (5).

The behavior of SiH_3^+ in Figure 2, at pressures below 60 μ, is that of a product ion, in accordance with (4) and (5). Actually, as demonstrated by ion-cyclotron resonance[4] and our tandem mass spectrometric experiments, SiH_3^+ reacts in this low-pressure region by the second-order processes 7 and 8, *viz.*

$$SiH_3^+ + SiH_4 \longrightarrow SiH_4 + SiH_3^+ \quad (7)$$

$$SiH_3^+ + SiH_4 \longrightarrow Si_2H_5^+ + H_2 \quad (8)$$

Since (7) does not change the abundance of SiH_3^+, the net initial increase in SiH_3^+ intensity shown in Figure 2 shows that (4) and (5) are faster than (8).

The results of the pressure studies up to 60 μ are in accord with the results of Henis, *et al.*,[4] and, with regard to the major reactions, not seriously in disagreement with earlier work.[2] However, as the pressure is increased above 60 μ one sees from Figure 2 that the abundance of SiH_3^+ reaches a maximum and then decreases, becoming essentially zero at about 400 μ. This behavior is accompanied by a parallel increase and a subsequent decrease in abundance of $Si_2H_7^+$. This latter ion is the only product ion that increases sufficiently with pressure above 60 μ to account for the decrease of the SiH_3^+ ion, and, up to about 200 μ pressure, the magnitude of the increase in $Si_2H_7^+$ intensity matches very well the magnitude of the decrease in SiH_3^+ intensity. Moreover, as will be discussed in a subsequent section, the decrease in SiH_3^+ and the equal increase in $Si_2H_7^+$ are third-order processes. One may conclude, therefore, that the reaction depleting SiH_3^+ and forming $Si_2H_7^+$ is (9), *viz.*

$$SiH_3^+ + 2SiH_4 \longrightarrow Si_2H_7^+ + SiH_4 \quad (9)$$

which we picture as occurring *via* collisional stabilization of the energetic association product, $Si_2H_7^{+*}$.

It is of interest to note in Figure 3 the changes of slope in the formation curves of $Si_2H_4^+$ and $Si_2H_5^+$ at $\sim$60 μ, which reflect the appearance of additional measurable contributions from reactions other than (6) and (8), respectively. These additional processes must be of higher order than (6) and (8) and, by analogy to (9) we propose them to be (10) and (11), *viz.*

$$Si^+ + 2SiH_4 \longrightarrow Si_2H_4^+ + SiH_4 \quad (10)$$

$$SiH^+ + 2SiH_4 \longrightarrow Si_2H_5^+ + SiH_4 \quad (11)$$

both of which also occur *via* collisional stabilization of the respective energetic association products.

As shown in Figures 4 and 5, significant amounts of ions containing three and four silicon atoms are observed at pressures above 200 μ, with the species $Si_3H_9^+$ and $Si_4H_{11}^+$ predominating. Although not shown in Figures 4 and 5, the ions $Si_3H_3^+$, $Si_3H_4^+$, $Si_3H_5^+$, $Si_3H_7^+$, $Si_4H_3^+$, $Si_4H_4^+$, $Si_4H_5^+$, $Si_4H_6^+$, $Si_4H_7^+$, $Si_4H_8^+$, and $Si_4H_9^+$ were observed, but at lower intensities. At the highest pressures employed, small amounts of $Si_5H_{11}^+$, $Si_5H_{12}^+$, and $Si_5H_{13}^+$ were also detected. Other than to note the obvious fact of a consecutive reaction system in which $Si_2H_X^+$ ions are giving rise to $Si_3H_Y^+$, etc., little can be said from the pressure studies alone concerning the actual reactions involved. As will be seen in the next section, however, some information on this polymerization sequence can be obtained from the tandem mass spectrometric experiments.

At pressures above 200 μ there appear in the spectra ions having m/e values of 49, 79, 109, 139, and 169. The intensities of these ions increase more-or-less identically with increasing pressure and the sum of their intensities accounts for about 40% of the ions at 500 μ. The masses of these ions correspond to protonated silanols, $Si_nH_{2n+1}OH_2^+$ (n = 1–5). Although we do not understand in detail their appearance in the spectra at the higher pressures, it seems clear that the parent silanols (or siloxanes) arise from reaction of SiH_4 with H_2O on the walls of the inlet system. The hydrolysis of SiH_4 to SiH_3OH and subsequent disproportionation to SiH_3OSiH_3 is well documented.[19]

2. *Tandem Mass Spectrometric Studies. A. Secondary Ion Formation.* No repeller field is used in the collision chamber of the tandem mass spectrometer and, therefore, when it is operated in the 90° mode, ions with any appreciable component of momentum in the direction of the incident reactant ion are strongly discriminated against and not detected. The result is that, even at the lowest incident ion-energy studied (E_{lab} = 1 eV), only charge transfer, proton transfer, or hydride transfer and, at higher collision chamber pressures, reactions subsequent to these will be observed. Such effects have been noted before[20] in 90° tandem mass spectrometers.

Thus, when SiH_3^+ ions are incident on SiH_4, only SiH_3^+, $Si_2H_5^+$, and $Si_2H_7^+$ are observed, having relative intensities that depend on the collision chamber pressure but which are independent of ion energy. When SiH_3^+ ions are injected into SiD_4, only SiD_3^+, $Si_2D_5^+$, and $Si_2D_7^+$ are observed, and these exhibit the same collision chamber pressure dependence as in the SiH_3^+–SiH_4 experiments. It is, therefore, clear that the reactions occurring are (7) followed by (8) and (9). In Figure 6a is shown the relative ion abundance as a function of collision chamber pressure for an experiment in which SiH_3^+ ions having 4.5 eV kinetic energy (laboratory system) are incident on SiH_4.

Results essentially identical with those shown in Figure 6a are observed when SiH_2^+ ions of the same energy are injected into SiH_4, a fact that clearly indicates the occurrence of (5) followed by (8) and (9). When SiH^+ is the incident ion, much lower product ion intensities result, but SiH_3^+ is clearly observed to be a product, demonstrating the occurrence of (4), a reac-

(19) E. A. V. Ebsworth, "Volatile Silicon Compounds," Pergamon Press, Elmsford, N. Y., 1963, pp 33–35.

(20) P. Wilmenius and E. Lindholm, *Ark. Fys.*, 21, 97 (1962).

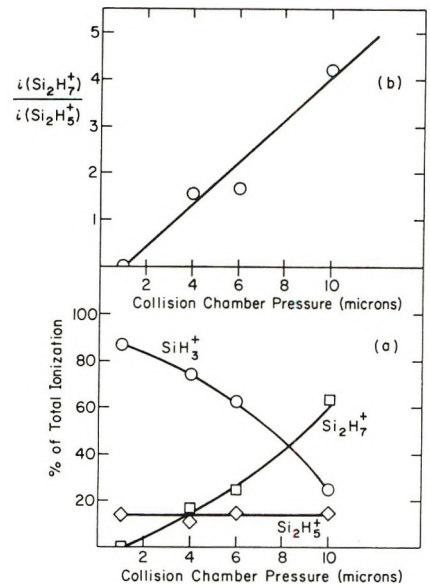

Figure 6. Formation of SiH_3^+, $Si_2H_5^+$, and $Si_2H_7^+$ by reaction of SiH_3^+ with SiH_4.

tion which was inferred from the pressure-dependence studies in the single-source mass spectrometer.

With the tandem mass spectrometer operated in the 180° configuration, as shown in Figure 1, product ions having momentum that is imparted to them from the incoming reactant primary ions are observed, such ions in the monosilane system being Si_2H^+, $Si_2H_2^+$, $Si_2H_3^+$, $Si_2H_4^+$, and $Si_2H_5^+$. To compare the results from the tandem mass spectrometric study with the secondary ion formation in the single spectrometer pressure study, shown in Figure 2, it is convenient to fix the second quadrupole mass filter to pass a given product ion and scan the first quadrupole mass filter through the various primary reactant ions. For a given product ion, one thus obtains the relative contributions to that product from the possible reactants at the predetermined reactant ion energy. An example of such measurements for 6-eV reactant ions is shown in Figure 7, in which the intensities of product ions are plotted *vs.* the mass numbers of their primary ion precursors. Combination of data such as shown in Figure 7 with the primary beam distribution of ions then yields relative reaction cross sections. We have carried out such measurements for ion energies in the range 2–15 eV, but the results at the lowest energies are of principal interest in this paper.

The percentage contributions of the various primary ions to the secondary ions produced, at the lowest ion energy studied for each product, are shown in Table II. As mentioned earlier, the ion-exit energy used in the pressure study in the single mass spectrometer was 2.1 eV, so that the data in Table II for the formation of ions of m/e = 58, 59, 60, and 61 correspond reasonably closely to the conditions pertinent to Figures 2 and 3.

Applying appropriate isotope corrections based on the natural abundances (^{28}Si = 92.2%), ^{29}Si = 4.7%, and ^{30}Si = 3.1%), it is easily shown that in Table II the

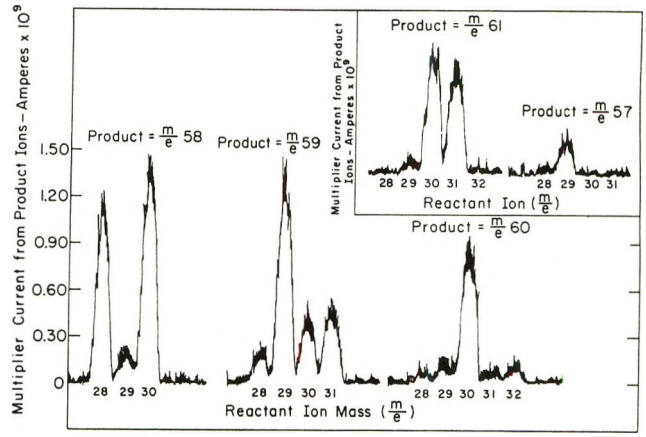

Figure 7. Primary ion contributions to secondary ion formation at 6-eV ion energy.

formation of m/e 60 from m/e 29 results entirely from reaction of $^{28}SiH^+$ with $^{29}SiH_4$ to form $^{28}Si^{29}SiH_3^+$, while formation of m/e 61 from m/e 29 results entirely from the reaction of $^{28}SiH^+$ with $^{30}SiH_4$ to form $^{28}Si^{30}SiH_3^+$. The only other isotope correction of any importance indicates that the reaction of $^{28}Si^+$ with $^{29}SiH_4$ to form $^{28}Si^{29}SiH_2^+$ accounts for about 16% of the formation of m/e 59 from m/e 28.

Table II: Secondary Ion Formation at Low Energy

Product ion (m/e)	Contribution from primary ion, %			
	m/e 28 (15)[c]	m/e 29 (20)[c]	m/e 30 (68)[c]	m/e 31 (68)[c]
57[a]	9	91	0	0
58[b]	57.9	7.9	34.2	0
59[b]	9.3	60.5	20.8	9.4
60[b]	0	9.5	90.5	0
61[b]	0	7.7	46.1	46.1

[a] Ion energy in laboratory system = 4 eV. [b] Ion energy in laboratory system = 2 eV. [c] Relative intensity of primary ion.

The tandem mass spectrometric results at low energy, shown in Table II and those discussed earlier in this section for the experiments in the 90° configuration allow one to identify unambiguously the reactions shown in Table III as those responsible for the secondary ions in monosilane. Also shown in Table III are the enthalpy changes of the reactions, the relative kinetic energy obtaining in our low-energy experiments, relative reaction cross sections at this energy, and the reaction cross sections reported by Henis, *et al.*[4] Because each experiment was performed with a fixed product ion and, therefore, at different times, the relative cross sections for different products from a given reactant ion may not be very accurate. Comparison with the data of Henis, *et al.*,[4] however, indicates satisfactory agreement with the sole exception of the reaction of SiH_2^+ to form $Si_2H_4^+$. For a given product ion, the relative cross sections are precise to within ±5%.

Table III: Secondary Reactions in Monosilane

Reaction no.	Reaction	ΔH, eV	C.M. energy, eV	Relative cross section	Cross section, Å² (Henis, *et al.*[4])
12	$Si^+ + SiH_4 \rightarrow Si_2H^+ + H_2 + H$	0.7	2.1	12[a]	Not obsd
3	$SiH^+ + SiH_4 \rightarrow Si_2H^+ + 2H_2$	−2.3	2.1	88[a]	15
1	$Si^+ + SiH_4 \rightarrow Si_2H_2^+ + H_2$	−0.4	1.1	100	99
13	$SiH^+ + SiH_4 \rightarrow Si_2H_2^+ + H_2 + H$	1.2	1.1	10.2	Not obsd
14	$SiH_2^+ + SiH_4 \rightarrow Si_2H_2^+ + 2H_2$	0.0	1.0	13.0	12
15	$Si^+ + SiH_4 \rightarrow Si_2H_3^+ + H$	0.3	1.1	15.8	Not obsd
2	$SiH^+ + SiH_4 \rightarrow Si_2H_3^+ + H_2$	−2.6	1.1	95.2	59
16	$SiH_2^+ + SiH_4 \rightarrow Si_2H_3^+ + H_2 + H$	0.7	1.0	9.3	Not obsd
17	$SiH_3^+ + SiH_4 \rightarrow Si_2H_3^+ + 2H_2$	0.3	1.0	4.2	1.5
6	$SiH_2^+ + SiH_4 \rightarrow Si_2H_4^+ + H_2$	−0.9	1.0	17.5	53
18	$SiH_2^+ + SiH_4 \rightarrow Si_2H_5^+ + H$	−0.3	1.0	11.0	Not obsd
8	$SiH_3^+ + SiH_4 \rightarrow Si_2H_5^+ + H_2$	−0.7	1.0	11.0	5.2
4	$SiH^+ + SiH_4 \rightarrow SiH_2 + SiH_3^+$	−0.3	2.4	...	Not obsd
5	$SiH_2^+ + SiH_4 \rightarrow SiH_3 + SiH_3^+$	0.0	2.4	...	230
7	$SiH_3^+ + SiH_4 \rightarrow SiH_4 + SiH_3^+$	0.0	2.4	...	290

[a] These cross sections refer to a higher ion energy and should not be compared with the other values in this column.

The agreement of our results with those of Henis, *et al.*,[4] is, in general, very satisfactory, especially when one considers that different relative kinetic energies obtain in the two studies. Although exact ion energies are not given by Henis, *et al.*,[4] it is likely from previous ion-cyclotron resonance studies[21-24] that their relative kinetic energies were near thermal energy; it is, therefore, not surprising that reactions 12, 13, 15, and 16 were not observed by these workers[4] because they are endothermic by at least 0.3 eV. We do not understand their failure to observe reactions 4 and 18, both of which would appear from thermochemical data[3] to be exothermic. In any event, we find no reason to mistrust our results and we, therefore, conclude that at the kinetic energies obtaining in our experiments the reactions shown in Table III occur in ionized monosilane.

Cross-section measurements as a function of relative energy have been carried out for the reactions of SiH_2^+ with SiH_4, and the results are shown in Figure 8. The results at low energy make it quite clear that the relative cross section for reaction 6 given in Table III is low compared with those of reactions 14, 16, and 18, being, in actuality, about four times the cross section for reaction 18, in agreement with Henis and coworkers.[4]

The initial decrease, with increasing energy, of the cross sections for formation of $Si_2H_4^+$ and $Si_2H_2^+$ indicates the involvement of exothermic processes, in accord with the thermochemical data[3] for reactions 6 and 14 in Table III. However, the cross section for reaction 6 exhibits a minimum at ~5 eV, subsequently increasing to a maximum at ~7 eV. Similarly, the cross section for reaction 14 exhibits a minimum at ~4 eV and a maximum at ~8 eV. This behavior is indicative of the onset of contributions from endothermic reactions to the formation of $Si_2H_4^+$ and $Si_2H_2^+$ ions. It is tempting to think that these endothermic processes

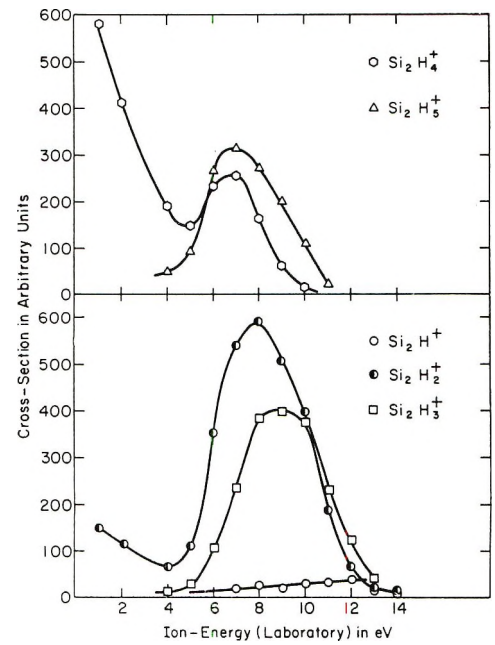

Figure 8. Dependence of cross section on ion energy for reaction of SiH_2^+ with SiH_4.

might simply involve dissociation of the molecular hydrogen product, as illustrated by (19). However, reaction 19 would be expected[3] to exhibit an *onset*

$$SiH_2^+ + SiH_4 \longrightarrow Si_2H_4^+ + 2H \qquad (19)$$

of 7 eV in the laboratory system, whereas a *maximum* at 7 eV is observed. Similarly, an analog to (19) for

(21) J. D. Baldeschwieler, *Science*, 159, 263 (1968).

(22) M. T. Bowers and D. D. Elleman, *J. Chem. Phys.*, 51, 4606 (1969).

(23) A. A. Herod, A. G. Harrison, R. M. O'Malley, A. J. Ferrer-Correia, and K. R. Jennings, *J. Phys. Chem.*, 74, 2720 (1970).

(24) J. M. S. Henis, *J. Chem. Phys.*, 52, 282 (1970).

formation of $Si_2H_2^+$ would be expected[3] to exhibit an onset of ~8.5 eV, whereas a maximum of ~8 eV is observed. While it is possible that the energy spread of 1 eV may explain these energy differences, we cannot rule out the possibility that internal excitation of $Si_2H_2^+$ and $Si_2H_4^+$ is the explanation of the onset of the endothermic processes.

The formation of $Si_2H_3^+$ *via* reaction 16 is endothermic by 0.7 eV[3] and the cross section shows the expected behavior, with the laboratory energy onset being at least consistent with the value of 1.4 eV calculated. The onset for Si_2H^+ is predicted on thermochemical grounds[3] to be 2 eV in the laboratory system. Although the intensity of this ion is low at all energies, the data in Figure 8 are not inconsistent with this predicted onset.

The formation of $Si_2H_5^+$ *via* reaction 18 is thought to be exothermic[3] by 0.3 eV. However, the behavior of the cross section with ion energy indicates reaction 18 to be slightly endothermic. The endothermicity of reaction 18 is supported by the fact that Henis, *et al.*,[4] did not observe it and is not inconsistent with the combined error limits on the heats of formation of all reactants and products involved.

B. Tertiary Ion Formation. As shown in Figures 3 and 4, the secondary ions react further with monosilane to produce tertiary ions containing three silicon atoms. Tandem mass spectrometric experiments in which primary ions containing two silicon atoms (produced by electron impact ionization of disilane) were impinged upon monosilane in the collision chamber yielded the data shown in Table IV. These allow one to conclude that the principal reactions for tertiary ion formation are those shown in Table V. Also presented in Table V are the relative cross sections in arbitrary units at the relative kinetic energy given. Isotope corrections were not made. The products of reactions of $Si_2H_5^+$ at these kinetic energies produced signals too small for measurement in these experiments, although $Si_2H_5^+$ obviously does react with SiH_4, as shown in Figure 3, by the decrease in its intensity with increasing pressure above 100 μ.

The origin of many of the tertiary ions observed is shown in Table V, although $Si_3H_7^+$, $Si_3H_8^+$, and $Si_3H_9^+$ are not accounted for. These ions are most probably formed by association reactions of $Si_2H_3^+$, $Si_2H_4^+$, and $Si_2H_5^+$ with SiH_4, which become probable at the higher pressures used in the single mass spectrometer study. However, even granting this, there is not sufficient $Si_2H_5^+$ to account for the amount of $Si_3H_9^+$ formed (Figures 3 and 4). We therefore conclude that the reaction depleting $Si_2H_7^+$ (Figure 2) is (30), *viz.*

$$Si_2H_7^+ + SiH_4 \longrightarrow Si_3H_9^+ + H_2 \qquad (30)$$

The much lower cross sections for the reactions of $Si_2H_4^+$ with SiH_4, as compared with those for $Si_2H_3^+$, $Si_2H_2^+$, and Si_2H^+, are in accord with the appearance of maxima in the intensities of these latter ions (Figure 3) at lower pressures.

Table IV: Tertiary Ion Formation at Low Energy

Product ion *m/e*	Contribution from primary ion (arbitrary units) *m/e* 56 (16)[a]	*m/e* 57 (31)[a]	*m/e* 58 (71)[a]	*m/e* 59 (31)[a]	*m/e* 60 (131)[a]
84	17	0	0	0	0
85	0	31	0	0	0
86	13	0	20	0	0
87	0	13	0	9	0
88	0	0	19	0	4.5
89	0	0	0	11	0
90	0	0	0	0	4.5

[a] Relative intensity of primary ion.

Table V: Tertiary Ion Formation in Monosilane

Reaction no.	Reaction	C.M. energy, eV	Cross section, arbitrary units
20	$Si_2^+ + SiH_4 \rightarrow Si_3^+ + 2H_2$	1.1	11
21	$Si_2^+ + SiH_4 \rightarrow Si_3H_2^+ + H_2$	1.1	8.1
22	$Si_2H^+ + SiH_4 \rightarrow Si_3H^+ + 2H_2$	1.1	10
23	$Si_2H^+ + SiH_4 \rightarrow Si_3H_3^+ + H_2$	1.1	4.2
24	$Si_2H_2^+ + SiH_4 \rightarrow Si_3H_2^+ + 2H_2$	1.1	2.5
25	$Si_2H_2^+ + SiH_4 \rightarrow Si_3H_4^+ + H_2$	1.1	2.4
26	$Si_2H_3^+ + SiH_4 \rightarrow Si_3H_3^+ + 2H_2$	1.1	2.9
27	$Si_2H_3^+ + SiH_4 \rightarrow Si_3H_5^+ + H_2$	1.1	3.6
28	$Si_2H_4^+ + SiH_4 \rightarrow Si_3H_4^+ + 2H_2$	1.4	0.34
29	$Si_2H_4^+ + SiH_4 \rightarrow Si_3H_6^+ + H_2$	1.4	0.34

3. Kinetic Considerations and Specific Reaction Rates. The decay of the primary ions with increasing source pressure up to ~60 μ (Figure 2) may be used to evaluate total second-order rate constants for the reactions of SiH_2^+, SiH^+, and Si^+. Above 60 μ third-order reactions begin to be superimposed significantly on the second-order processes. Thus, semilogarithmic plots of the ion abundances of SiH_2^+, SiH^+, and Si^+ *vs.* ion-source pressure (up to 60 μ) are linear and, when combined in the usual way[23] with the pertinent reactant ion residence time (1.73×10^{-6} sec for SiH_2^+), yield the total second-order rate constants shown in Table VI.

Noting that our tandem mass spectrometric results and the ion-cyclotron resonance results of Henis, *et al.*,[4] show that $Si_2H_2^+$ is formed at low energy only from SiH_2^+, it is easily shown that (31) applies, *viz.*

$$\frac{Y_{Si_2H_4^+}}{Y^0_{SiH_2^+} - Y_{SiH_2^+}} = \frac{k_6}{k_{SiH_2^+}} \qquad (31)$$

where Y represents per cent abundance, Y^0 is the per cent abundance in the limit of zero pressure, and $k_{SiH_2^+}$ is the second-order rate constant for the decay of SiH_2^+. This ratio is constant within ±5% at pressures below 60 μ and, since $k_{SiH_2^+}$ is known, we

Table VI: Second-Order Specific Reaction Rates

Reaction no.	Reaction	$k \times 10^{10}$ cm³/molecule-sec		
		This work	Ref 2	Ref 4
8	$SiH_3^+ + SiH_4 \rightarrow Si_2H_5^+ + H_2$	0.07 ± 0.02	...	0.24 ± 0.05
Total SiH_2^+	$SiH_2^+ + SiH_4 \rightarrow$ products	4.0 ± 0.4	4.1 ± 0.6	...
18	$SiH_2^+ + SiH_4 \rightarrow Si_2H_5^+ + H$	0.08 ± 0.02	0.07 ± 0.01	Not obsd
6	$SiH_2^+ + SiH_4 \rightarrow Si_2H_4^+ + H_2$	1.1 ± 0.1	1.1 ± 0.1	2.5
14	$SiH_2^+ + SiH_4 \rightarrow Si_2H_2^+ + 2H_2$	0.31 ± 0.06	0.67 ± 0.07	0.55 ± 0.075
5	$SiH_2^+ + SiH_4 \rightarrow SiH_3^+ + SiH_3$	2.5 ± 0.3	1.7 ± 0.7	10.7 ± 0.2
Total SiH^+	$SiH^+ + SiH_4 \rightarrow$ products	2.9 ± 0.3	...	...
2	$SiH^+ + SiH_4 \rightarrow Si_2H_3^+ + H_2$	2.0 ± 0.3	...	2.8 ± 0.07
13	$SiH^+ + SiH_4 \rightarrow Si_2H_2^+ + H_2 + H$	0.3 ± 0.1	...	Not obsd
3	$SiH^+ + SiH_4 \rightarrow Si_2H^+ + 2H_2$	...	...	0.7 ± 0.2
4	$SiH^+ + SiH_4 \rightarrow SiH_2 + SiH_3^+$	0.6 ± 0.1	...	Not obsd
Total Si^+	$Si^+ + SiH_4 \rightarrow$ products	3.6 ± 0.4	...	...
15	$Si^+ + SiH_4 \rightarrow Si_2H_3^+ + H$	0.40 ± 0.2	...	Not obsd
1	$Si^+ + SiH_4 \rightarrow Si_2H_2^+ + H_2$	3.2 ± 0.3	...	4.8 ± 0.6

may easily obtain k_6. The specific reaction rates for reactions 14 and 18 in Table VI were obtained using the relative cross sections for reactions of SiH_2^+ at 2 eV (laboratory energy) shown in Figure 8. The value of the rate constant for reaction 5 was obtained by difference from the total reaction rate of SiH_2^+ ions and was in excellent agreement with the value obtained from the ratio of initial slopes for SiH_3^+ formation and SiH_2^+ decay. The second-order rate constants for reactions 1, 2, 13, and 15 were obtained from the rate constants for loss of Si^+ and SiH^+ and the relative reaction cross sections at 1 eV (C.M.) given in Table III. Since no data for Si_2H^+ formation are available at this low energy and its intensity is very low, we were unable to evaluate a specific reaction rate for reaction 3.

Also shown in Table VI for comparison are specific reaction rates determined by Hess and Lampe,[2] using the pulsed mass spectrometric technique, and by Henis and coworkers[4] using ion-cyclotron resonance. The rate constants determined in the present study refer to an average ion energy of about 1 eV (laboratory energy) while those of the earlier papers to essentially thermal ion energies. Considering the diverse nature of the experiments, the agreement is generally quite satisfactory, particularly when one recalls that Hess and Lampe[2] attributed all reaction to the SiH_2^+ ion. The one exception to the generally satisfactory agreement is the specific reaction rate for reaction 5, hydride ion transfer to SiH_2^+. The rate constants for total second-order reaction of SiH_2^+ determined in the present work and by Hess and Lampe[2] agree very well, with the value obtained simply not large enough to support the high value reported by Henis, *et al.*,[4] for reaction 5. One might argue that the difference of ion energy is responsible for the disagreement; however, the reported concordance[23] of rate constants determined by the pulsed mass spectrometric method and the ion-cyclotron resonance method and the agreement of the present value with that of Hess and Lampe,[2] as well as the satisfactory agreement of other specific reaction rates shown, would seem to refute it.

The abundance curves of $Si_2H_4^+$ and $Si_2H_5^+$, shown in Figure 3, exhibit onsets of other formation processes at ion-source pressures of about 60 μ. This is the same region of pressure in which the third-order formation of $Si_2H_7^+$ begins to be significant and, moreover, it is the same pressure region at which semilogarithmic decay curves of the abundances of Si^+ and SiH^+ indicate the onset of a higher-order removal process. We conclude, therefore, that above ion-source pressures of 60 μ the ions Si^+ and SiH^+ are being removed not only by second-order processes (Table VI) but also by the third-order reactions 10 and 11.

Attributing the loss of Si^+ above 60 μ to the sum of the second-order processes in Table VI and to (10), it may easily be shown that (32) applies, *viz.*

$$\frac{1}{[SiH_4]t} \ln \frac{Y^0_{Si^+}}{Y_{Si^+}} = k_1 + k_{15} + k_{10}[SiH_4] \qquad (32)$$

where t is the residence time of Si^+ ions, Y_{Si^+} is the per cent of Si^+ ions in the source, and $Y^0_{Si^+}$ is the corresponding value in the limit of zero pressure. A similar equation applies for the decay of SiH^+ above 60 μ. Figure 9a shows a plot of the decay data for Si^+ according to (32), the line drawn through the points having an intercept corresponding to the second-order decay rate shown in Table VI and a slope obtained as the average value given by the points and this intercept. A similar plot is obtained for the SiH^+ decay above 60 μ. The third-order rate constants obtained from the slope of Figure 9a and from a corresponding plot for SiH^+ are shown in Table VII.

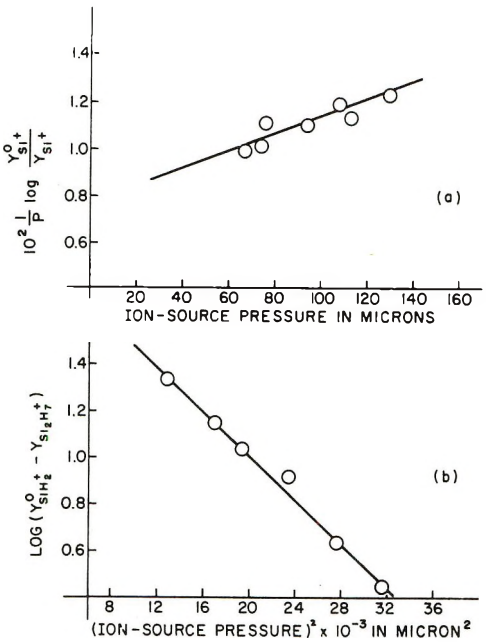

Figure 9. Third-order kinetic plots: (a) formation of $Si_2H_4^+$ from Si^+; (b) formation of $Si\,H_7^+$ from SiH_3^+.

Table VII: Third-Order Ionic Reactions in Monosilane

Reaction no.	Reaction	k, $\times 10^{26}$, cm⁶/molecule²-sec
10	$Si^+ + 2SiH_4 \rightarrow Si_2H_4^+ + SiH_4$	1.4 ± 0.6
11	$SiH^+ + 2SiH_4 \rightarrow Si_2H_5^+ + SiH_4$	1.3 ± 0.5
9	$SiH_3^+ + 2SiH_4 \rightarrow Si_2H_7^+ + SiH_4$	1.8 ± 0.7

A somewhat different treatment must be used to obtain the specific reaction rate of (9) because at low pressures the reactant ion SiH_3^+ exhibits a net formation, mainly *via* hydride ion transfer from SiH_4 to SiH_2^+. As shown in Figure 2, at ion-source pressures of about 110 μ SiH_2^+ has been reduced to very low abundance and hence no further formation of SiH_3^+ will occur as the pressure is raised above 110 μ. It may be shown that in the pressure region 110–180 μ (below the maximum in $Si_2H_7^+$) the sum of the abundances of SiH_3^+ and $Si_2H_7^+$ is constant, indicating that in this pressure region all the SiH_3^+ that reacts appears as $Si_2H_7^+$ and that further reaction of $Si_2H_7^+$ is negligible. Under these conditions it is easily shown that (33) applies, *viz.*

$$\ln (Y^0_{SiH_3^+} - Y_{Si_2H_7^+}) = \ln Y^0_{SiH_3} - k_9[SiH_4]^2 t \quad (33)$$

where $Y^0_{SiH_3^+}$ is the per cent abundance of SiH_3^+ at 110 μ. A plot of the data, according to (33), in this pressure region is shown in Figure 9b; the plot is seen to be linear and thus permits evaluation of k_9 from the slope. The value obtained is also shown in Table VII.

The value of t which is applicable to the pressure regime of (32) and (33) is not the collision-free residence time[25] used earlier. Rather in this pressure region, a value of 7.5×10^{-6} sec was calculated from our average E/P value of ~42 V/cm-Torr, our source dimensions, and the drift velocity results of Warneck[26] for N_2^+, an ion of similar mass to Si^+. The approximate nature of this reaction time (estimated to be uncertain to ±40%) is the major reason for the rather large uncertainties in the third-order specific reaction rates.

We have mentioned earlier that the third-order formation of $Si_2H_7^+$ may be viewed as a collisional stabilization of the energetic association product of SiH_3^+ and SiH_4. Thus, we picture the process to be as described by (34)–(36), *viz.*

$$SiH_3^+ + SiH_4 \underset{k_a}{\overset{k_a}{\rightleftharpoons}} Si_2H_7^{+*} \quad (34)$$

$$Si_2H_7^{+*} \xrightarrow{k_d} Si_2H_5^+ + H_2 \quad (35)$$

$$Si_2H_7^{+*} + SiH_4 \xrightarrow{k_s} Si_2H_7^+ + SiH_4 \quad (36)$$

It is easily shown from this model that a plot of the intensity ratio $i(Si_2H_7^+)/i(Si_2H_5^+)$ *vs.* $[SiH_4]$ should be linear with a slope equal to the rate constant ratio k_s/k_d. Such a plot from the single spectrometer ion-intensity data is not feasible because of complications due to presence of so many other ions. However, in the tandem experiments in which SiH_3^+ or SiH_2^+ is injected into SiH_4, only SiH_3^+ produced by hydride transfer and products of its reaction with SiH_4 are observable (*cf.* Figure 6a). A plot of the ratio $i_{Si_2H_7^+}/i_{Si_2H_5^+}$ *vs.* collision chamber pressure is shown in Figure 6b, the slope of which yields the value (at 300°K) $k_s/k_d = 1.5 \times 10^{-14}$ cm³/molecule.

A value of this ratio may also be derived from the specific reaction rates determined in the pressure studies with the single mass spectrometer. Thus viewing $Si_2H_5^+$ and $Si_2H_7^+$ formation in the framework of (34)–(36), it is easily shown that

$$k_9 = \frac{k_a k_s}{k_{-a} + k_d} = 1.8 \times 10^{-26} \text{ cm}^6/\text{molecule}^2\text{-sec}$$

$$k_8 = \frac{k_a k_d}{k_{-a} + k_d} = 7 \times 10^{-12} \text{ cm}^3/\text{molecule-sec}$$

and, hence, the ratio k_9/k_8 is, in terms of the reaction model

$$\frac{k_9}{k_8} = \frac{k_s}{k_d} = 0.3 \times 10^{-14} \text{ at } 343°\text{K}$$

Considering the fact that an increase in temperature will tend to reduce k_s and increase k_d, the agreement between the two determinations of k_s/k_d in very different apparatus is quite satisfactory. It should be mentioned that the magnitudes of both k_8 and k_9 de-

(25) F. W. Lampe, J. L. Franklin, and F. H. Field, *Progr. React. Kinet.*, 1, 67 (1961).

(26) P. Warneck, *J. Chem. Phys.*, 46, 502 (1967).

mand that in the stabilization model, $k_{-a} >> k_d$; that is to say, dissociation of the encounter complex, $Si_2H_7^{+*}$, to the original reactants is much faster than dissociation to products.

4. Radiation Chemistry Implications. The radiolysis of monosilane at 300°K[27-29] results in the formation of hydrogen, disilane, trace amounts of higher Si_nH_{2n+2} homologs and a polymeric substance of empirical formula $(SiH_2)_x$. In a recent study[29] of the γ-ray radiolysis it was shown that the initial 100-eV yields of $G(H_2) = 17.0$ and $G(Si_2H_6) = 5.3$ were reduced, with increasing dose, to plateau values of 12.5 and 1.7, respectively; moreover, these plateau values were nearly identical with the G values found for hydrogen and disilane, respectively, under conditions of complete free-radical scavenging by ethylene or nitric oxide. It was thus concluded[29] that 65% of the hydrogen and 38% of the disilane are produced by reactions not involving free radicals. These nonradical reactions were proposed to be ionic, although some of the specific ionic reactions proposed at that time (1966)[2] are now known to be unfeasible on energetic grounds[3] and, in fact, do not occur at the ion energies obtaining in the radiolysis.

The formation of appreciable amounts of hydrogen in the radical-scavenged radiolysis is not surprising when one considers the large number of fast reactions of primary and secondary ions that produce larger ions and molecular hydrogen (*cf.* Tables V and VI). Indeed, a very similar result is observed in the radical-scavenged radiolysis of methane.[30] The very appreciable yield of disilane in the radical-scavenged radiolysis[29] is in contrast, however, to the high degree of inhibition of ethane formation in the radiolysis of methane.[30]

The most striking feature of the ionic distribution in monosilane at the higher pressures is the dominance of the protonated molecules $Si_2H_7^+$, $Si_3H_9^+$, $Si_4H_{11}^+$, and $Si_5H_{13}^+$, these ions comprising over 30% of the total ionization at 0.5 Torr. Such an effect is not observed in the high-pressure spectrum of methane,[31] the corresponding protonated molecules making up only a minor contribution. We suggest that it is the dominance of such species in monosilane that is the principal reason for the observation of appreciable yields of disilane in the radical-scavenged radiolysis.

The abundance of $Si_2H_7^+$ reaches a plateau of about 10% of the total ionization at 0.5 Torr (*cf.* Figure 2). Although plateaus are not particularly evident for $Si_3H_9^+$ and $Si_4H_{11}^+$ in Figures 4 and 5, it has been pointed out that most of these latter ions must be formed by reaction of $Si_2H_7^+$ with SiH_4. It is, therefore, reasonable to assume that at the pressures obtaining in the radiolysis[29] the species $Si_2H_7^+$, $Si_3H_9^+$, $Si_4H_{11}^+$, and $Si_5H_{13}^+$, in a distribution similar to that shown in Figures 2, 4, and 5, comprise the ions that are sufficiently stable towards reaction with monosilane to undergo neutralization reactions, either with electrons or with negative ions.

As shown by Figure 2 and Table VI, about 60% of the primary SiH_2^+ ions react to form SiH_3^+, and, at the pressures obtaining in the radiolysis, essentially all of the SiH_3^+ will result in $Si_2H_7^+$, which will produce subsequently $Si_3H_9^+$, $Si_4H_{11}^+$, and $Si_5H_{13}^+$; therefore, about 60% of the total ions produced in primary events lead to the formation of $Si_2H_7^+$ and its subsequent products. Assuming the energy required to produce an ion pair in monosilane to be the same as in methane[32] leads to a 100-eV yield of 2.2 ions/100 eV for the formation of $Si_2H_7^+$ and its subsequent products. If all of these ions ($Si_2H_7^+$, $Si_3H_9^+$, $Si_4H_{11}^+$, and $Si_5H_{13}^+$) neutralized to form Si_2H_6, $G(Si_2H_6) = 2.2$ is predicted; this is to be compared with the observed value of 1.7. The approximate agreement is not compelling but is in accord with our suggestion that in the radical-scavenged radiolysis disilane is formed by neutralization of protonated molecules. We suggest the reactions to be of the form shown by (37) and (38) with the radical products of these reactions being rapidly scavenged

$$Si_2H_7^+ + e^- \longrightarrow Si_2H_6 + H \quad (37)$$

$$Si_3H_9^+ + e^- \longrightarrow Si_2H_6 + SiH_3, \text{ etc.} \quad (38)$$

Some formation of Si_3H_8 and Si_4H_{10} might be expected from such neutralization reactions, but yields of these products were always so low that they were not measured.[29]

Acknowledgment. This work was supported by the U. S. Atomic Energy Commission under Contract No. AT(11-1)-3416. We also wish to thank the National Science Foundation for providing funds to assist in the original purchase of the Nuclide mass spectrometer.

(27) W. Ando and S. Oae, *Bull. Chem. Soc. Jap.*, **35**, 1540 (1962).

(28) G. J. Mains and T. Tiernan, U. S. Atomic Energy Commission Report NYO-2007-8 (1965).

(29) J. F. Schmidt and F. W. Lampe, *J. Phys. Chem.*, **73**, 2706 (1969).

(30) K. Yang and P. J. Manno, *J. Amer. Chem. Soc.*, **81**, 3507 (1959).

(31) F. H. Field and M. S. B. Munson, *ibid.*, **87**, 3289 (1965).

(32) C. E. Clots, "Fundamental Processes in Radiation Chemistry," P. Ausloos, Ed., Interscience, New York, N. Y., 1968, p 40.

Recoil and Charging Contributions to Organic Incorporation of Radiobromine Atoms Following Neutron Activation

by K. E. Collins, G. D. Robinson, Jr.,* and C. H. Collins

Department of Chemistry, State University of New York at Buffalo, and Research Department, Western New York Nuclear Research Center, Buffalo, New York 14214
(Received September 13, 1971)

Publication costs assisted by UCLA Laboratory of Nuclear Medicine and Radiation Biology

Radiobromine atoms from n,γ activation events in bromine–carbon tetrachloride solutions appear to form carbon–bromine bonds solely as a result of electronic processes initiated by the inner-shell vacancies which accompany internal conversion. Organic yield data from the n,γ reactions are used to evaluate the probabilities of internal conversion accompanying these nuclear activations. A general notation relating certain nuclear factors which may influence the chemical fate of transformed atoms is introduced.

Introduction

Most of the 6–8 MeV of nuclear excitation energy which a nucleus acquires upon capture of a thermal neutron is rapidly ($<10^{-14}$ sec) lost as a set of γ-ray photons, causing the product nucleus to experience a momentum impulse (recoil), the magnitude of which is determined by the momenta of the individual photons and by the angular distribution of their emission.[1] In some fraction of the deexcitation cascades, an intermediate nuclear state may decay with internal conversion rather than photon emission.[1,2] When this occurs, the excitation energy of that nuclear state is transferred to an inner-shell electron, usually in the K or L shell, which then carries away as kinetic energy the nuclear excitation energy minus the atomic binding energy of the electron. The atom in which the inner-shell vacancy has occurred has a high probability of losing several more electrons as the result of Auger cascades and, as a result, acquires several units of positive charge.[1,3] A direct indication of the charging accompanying n,γ activation of bromine was made by Wexler and Davies using gaseous ethyl bromide irradiated in an electrical field.[4] From their data, it was estimated that approximately 12% of ^{80m}Br, 18% of ^{80g}Br, and 25% of ^{82g}Br atoms resulting from n,γ activations were charged by internal conversion processes.[4]

The chemical reactions occurring as a result of this internal conversion might be expected to provide some estimation of the probability of conversion accompanying a particular n,γ activation. However, this approach to the determination of the probability of charging is complicated by the difficulty of distinguishing the chemical effects of internal conversion from those presumed to result from the local deposition of nuclear recoil energy. A clear cut difference in chemical product yields from pure internal conversion events and from n,γ events would seem to be a necessary, if not sufficient, criterion for possible chemical determination of the probability of internal conversion accompanying n,γ activation.

Several studies have shown that organic yields from converted isomeric transition (IT) processes occurring in bromine nuclides are higher than organic yields from n,γ processes.[5] Bohlman and Willard found that the organic yield from the ^{80m}Br(IT)^{80g}Br process was greater than that from the ^{79}Br(n,γ)^{80m}Br activation by a factor of at least 1.4 for bromine–carbon tetrachloride solutions and by a factor of 2.2 for bromine–tetrachloroethylene solutions.[6] Rack and his coworkers have found organic yields from the ^{82m}Br(IT)-^{82g}Br process exceed those of the ^{79}Br(n,γ)^{80m}Br activation by factors of 1.7–1.8 for solutions of bromine in several aliphatic hydrocarbons.[7] The greater organic yields from IT events were attributed to a "more highly reactive hot atom zone."[8]

On the other hand, only very slight differences have

* Address correspondence to this author at UCLA Laboratory of Nuclear Medicine and Radiation Biology, Los Angeles, Calif. 90024. (This work was supported by U. S. A. E. C. Contract No. AT(04-1) GEN-12.)

(1) (a) S. Wexler in "Actions Chimiques et Biologiques des Radiations," M. Haissinsky, Ed., Huitieme Ser., Masson et Cie, Paris, 1965, p 106; (b) I. G. Campbell, *Advan. Inorg. Nucl. Chem.*, 5, 135 (1963).

(2) T. von Egidy in "Neutron Capture Gamma-Ray Spectroscopy," IAEA, Vienna, 1969, p 541.

(3) (a) S. Wexler, *J. Chem. Phys.*, 36, 1992 (1962); (b) T. A. Carlson and R. M. White, *ibid.*, 38, 2075 (1963).

(4) S. Wexler and T. H. Davies, *ibid.*, 20, 1688 (1952).

(5) The *organic yield* of radiobromine from a given type of nuclear transformation is the fraction of the bromine atoms tagged by the transformed (radiobromine) nuclei which attain stable carbon–bromine bonds.

(6) E. G. Bohlman and J. E. Willard, *J. Amer. Chem. Soc.*, 64, 1342 (1942).

(7) J. A. Merrigan, J. B. Nicholas, and E. P. Rack, *Radiochim. Acta*, 6, 94 (1966).

(8) J. A. Merrigan, W. K. Ellgren, and E. P. Rack, *J. Chem. Phys.*, 44, 174 (1966).

been observed in the product distributions resulting from isomeric transition processes and from n,γ recoil processes in bromine containing solutions.[9-11] Such a similarity in product distribution, even when the total organic yield differed, led Willard to suggest that "... a controlling factor {in the reactivity of bromine from (n,γ) activation} may be charge neutralization following internal conversion occurring near the end of the track of the recoil atom."[12] This idea has been further developed by Geissler and Willard[13] and by Rack and his coworkers.[7,14,15] However, as an alternative explanation, Kazanjian and Libby view the similarity in product distributions from n,γ and IT processes as resulting from mechanical recoil, the recoil occurring in the isomeric transition case as an assumed result of coulombic repulsion between positive ions from the initially affected molecule after the initial loss of Auger electrons.[16] By contrast, Shaw and his coworkers conclude that the products from n,γ activation are largely produced as a consequence of recoil, while the products from IT processes are produced by charging, with the quantitative similarities being fortuitous.[17,18]

The present paper uses the organic yield data from the several nuclear transformations of bromine occurring in bromine–carbon tetrachloride solutions in an attempt to clarify the relative roles of mechanical recoil and Auger charging (from internal conversion) in determining this yield. The data also appear to permit estimation of the probability of internal conversion occurring during n,γ activations of ^{79}Br and ^{81}Br.

Experimental Section

Chemicals. Carbon tetrachloride (J. T. Baker) was purified by illuminating 100-ml portions containing 0.05 mole fraction of Br_2 for 24 hr at 12 in. from a 300-W Sun Lamp (General Electric). Reducible, aqueous extractable material was removed by washing with 0.1 *N* Na_2SO_3 until no bromine color remained. Immediately before use, 1-ml portions were passed through a 3 m × 9 mm gas chromatography column packed with 20% Apiezon N on 45–60 mesh Chromosorb P at 75°. The resulting carbon tetrachloride had no detectable impurities (thermal conductivity detection).

Bromine (Mallinckrodt) was purified by treating 1-ml portions with finely divided KBr for 2–3 hr and then subliming twice under vacuum. The purified bromine was stored in ampoules under vacuum until needed.

Potassium ferrocyanide (Mallinckrodt) was purified by precipitation from a saturated aqueous solution at 80° by the addition of methanol. The vacuum-filtered powder was dried at 105°.

Other reagents were used without further purification.

Neutron Irradiations. Neutron irradiations at ambient reactor temperature (35–40°) and at −78° were performed in a pneumatic conveyor of the reactor at the Western New York Nuclear Research Center, Inc., at a neutron flux of 6×10^{12} n cm^{-2} sec^{-1} and a γ-ray exposure dose rate of 1.0×10^7 rads hr^{-1}.

Determination of the Organic Yield from the $^{79}Br(n,\gamma)^{80m}Br$ Transformation. Samples were prepared from stock solutions made by mixing appropriate volumes of freshly purified CCl_4 and Br_2. The concentration of each stock solution was determined spectrophotometrically. The stock solutions were stored frozen(−196°) and protected from incident light between uses. Individual samples (0.5 ml) were sealed under vacuum in precleaned quartz ampoules after being degassed by at least four freeze–evacuate–thaw cycles. The samples were stored at −196° until being thawed immediately prior to a 1-min irradiation at ambient reactor temperature. Following irradiation, the samples were refrozen and stored in the dark until analysis by a modification of the potassium ferrocyanide technique.[19,20] Counting of the ^{80g}Br β particles using a planchet-type Geiger–Müller counting system was carried out after the ^{80m}Br–^{80g}Br secular equilibrium had been established. Volatilization of the samples was prevented by freezing them with liquid nitrogen. The counting data were corrected for solution density effects, and the organic yield was calculated by relating the activity of the organic phase to the total activity (summed organic and inorganic activities) of the sample.

Determination of the Organic Yield from the $^{81}Br(n,\gamma)(IT)^{82g}Br$ Transformation Sequence. Degassed samples were prepared from stock solutions as described above. Following a 1-min irradiation at ambient reactor temperature, the liquid samples were stored at room temperature (20–25°) for 2 hr to allow completion of the isomeric transition (6.1-min half-life) in the liquid state before being frozen to await analysis by the $K_4Fe(CN)_6$ adsorption technique. The activity of the samples was determined by conventional NaI(Tl) γ-ray scintillation counting at least 48 hr after the irradiation.

(9) G. Levy and J. E. Willard, *J. Amer. Chem. Soc.*, **78**, 2351 (1956).
(10) J. E. Willard, *Annu. Rev. Phys. Chem.*, **6**, 141 (1955).
(11) G. D. Robinson, Jr., C. H. Collins, and K. E. Collins, manuscript in preparation.
(12) J. E. Willard in "Chemical Effects of Nuclear Transformations," Vol. 1, IAEA, Vienna, 1961, p 222.
(13) P. R. Geissler and J. E. Willard, *J. Phys. Chem.*, **67**, 1675 (1963).
(14) J. A. Merrigan and E. P. Rack, *ibid.*, **69**, 2806 (1965).
(15) R. M. Lambrecht and E. P. Rack, *J. Chem. Phys.*, **48**, 3735 (1968).
(16) A. R. Kazanjian and W. F. Libby, *ibid.*, **42**, 2778 (1965).
(17) A. J. Cole, M. D. Mia, G. E. Miller, and P. F. D. Shaw, *Radiochim. Acta*, **6**, 150 (1966).
(18) M. D. Mia and P. F. D. Shaw, *ibid.*, **6**, 172 (1966).
(19) W. E. Harris, *Can. J. Chem.*, **39**, 121 (1961).
(20) Z. Abedinzadeh, R. Radicella, K. Tanaka, and M. Milman, *Radiochim. Acta*, **12**, 4 (1969).

Determination of the Organic Yield from the ^{82m}Br-(IT)^{82g}Br Transition. Each sample for this determination was individually prepared from freshly purified CCl_4 and Br_2. CCl_4 (0.25 ml) was degassed in a quartz ampoule by several freeze–evacuate–thaw cycles and then frozen under vacuum. While the CCl_4 was still immersed in liquid nitrogen, a vacuum ampoule containing a predetermined amount of Br_2 was broken in an attached flask and a thin layer of bromine was deposited, essentially instantaneously, on the surface of the degassed CCl_4. The resulting two-phase samples were then sealed and kept frozen until after irradiation (15 sec) in the solid state. The bromine concentration was measured spectrophotometrically at the time of radiochemical analysis. Use of this modification of the sample preparation procedure of Merrigan, Ellgren, and Rack[8] eliminated the small amount of organic incorporation seen by these authors in solid-state irradiations at low concentrations of bromine.[21]

Determination of the Organic Yield from the ^{81}Br-$(n,\gamma)^{82m+82g}Br$ Transformation. Degassed samples were prepared from the stock solutions. Exactly 30 sec after the midpoint of a 15-sec irradiation in the liquid state, the samples were immersed in liquid nitrogen to prevent additional organic incorporation from the $^{82m}Br(IT)^{82g}Br$ transition from occurring.[8,21] After storage for 48 hr the samples were analyzed for ^{82g}Br as described above.

The ^{82m}Br atoms which decay after the samples were frozen do not change the organic yield.[8,21] However, the 6% of the ^{82m}Br atoms which decay before the samples are frozen tend to increase the organic yield slightly. The true organic yield can be obtained by correcting for this isomeric transition contribution, as will be discussed later in the text.

Results and Discussion

Definition of Organic Yield. Prior to a discussion of experimental results, it will be useful to consider the definition of the organic yield as an experimental quantity and to introduce a general notation relating certain nuclear factors which may influence the chemical fate of an atom whose nucleus undergoes a nuclear transformation (such as radiative neutron capture). In general, the yield of labeled product species, i, resulting from chemical reactions following a given nuclear transformation is the sum of several individual contributions to that yield

$$Y_i = \sum_j f_j P_{i,j} \qquad (1)$$

where f_j is the fraction of the nuclear transformation events which are of a given type, j, and $P_{i,j}$ is the probability that a type j event will give rise to the product i. The condition $\Sigma_j f_j = 1$ is an obvious constraint. Using this expression, the organic yield, Y_{org}, is the sum of *all* of the organic products tagged by radiobromine atoms which have undergone the transformation of interest

$$Y_{org} = \sum_j f_j P_{org,j} \qquad (2)$$

We shall consider those types of radiative neutron-capture events which may contribute to the organic yield. One category includes those events which occur with recoil but with *no* internal conversion. This fraction, f_r, corresponds to "recoil only" events and reflects the results of high kinetic energy reactions occurring in the absence of vacancy cascades.[1] The second category of events, fraction f_c, corresponds to events in which an internal conversion occurs to produce charging. Using these classifications, the organic yield is given by

$$Y_{org} = f_r P_{org,r} + f_c P_{org,c} \qquad (3)$$

For isomeric transition events, with *all* of the relevant chemistry initiated by internal conversion (charging), $f_c = 1$ ($f_r = 0$). The probability of organic incorporation from internal conversion is therefore given directly by the organic yield.

Measured Organic Yields. Figure 1 shows organic yield data, as a function of (mole fraction of $Br_2)^{1/2}$, for three of the nuclear transformations of bromine which can occur in bromine–carbon tetrachloride solutions. The linear dependences indicated by these data suggest the use of the zero-bromine intercept to characterize the data from a given transformation. This intercept, nominally the organic yield at "infinitely dilute" bromine concentration,[22] Y^0_{org}, is readily obtained by

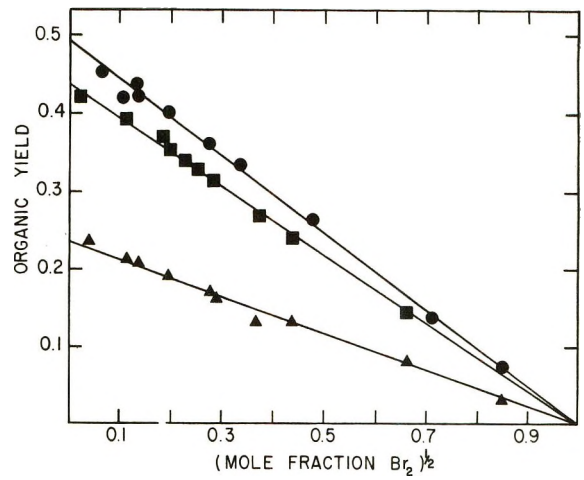

Figure 1. Organic yields of radiobromine in carbon tetrachloride as a function of (mole fraction of $Br_2)^{1/2}$: $^{79}Br(n,\gamma)^{80m}Br$ transformation (▲), $^{82m}Br(IT)^{82g}Br$ transition (●), $^{81}Br(n,\gamma)^{82m}Br(IT)^{82g}Br$ and $^{81}Br(n,\gamma)^{82g}Br$ transformations (■).

(21) G. D. Robinson, Jr., Ph.D. Thesis, State University of New York at Buffalo, 1970.

(22) The organic yield at "infinite dilution" for the system discussed in the present paper is presumably the probability that a bromine atom, initially present in an isolated bromine molecule in carbon tetrachloride, becomes bonded to a carbon atom as a consequence of the nuclear transformation event which has involved the nucleus of that atom.

least-squares analysis.[23] Table I lists the Y^0_{org} values from the Figure 1 data as well as corresponding values from other bromine transformations occurring in the bromine–carbon tetrachloride system. Included for comparison are Y^0_{org} values which we have calculated from data reported in other studies on this solution system.[8,24,25]

Table I: Organic Yields at Infinite Dilution (Y^0_{org}) from Several Nuclear Processes in Bromine–Carbon Tetrachloride Solutions

Nuclear transformation	Y^0_{org} values[a] This work	Other
$^{79}Br(n,\gamma)^{80m}Br$	0.236 ± 0.005	0.25[b]
$^{81}Br(n,\gamma)^{82m+82g}Br$	0.226 ± 0.006[c]	0.22[b,c]
$^{81}Br(n,\gamma)(IT)^{82g}Br$	0.438 ± 0.005	0.43,[b] 0.45[d]
$^{82m}Br(IT)^{82g}Br$	0.495 ± 0.005	0.49,[b,e] 0.49[f]

[a] Y^0_{org}, the intercept value of the least-squares line, with the line constrained to a Y_{org} value of 0 at mole fraction of Br_2 = 1.0. [b] From data of Merrigan, Ellgren, and Rack, ref 8. [c] Not corrected for contribution of the $^{82m}Br(IT)^{82g}Br$ which occurred prior to freezing. [d] From data of Collins and Collins, ref 24. [e] Corrected for the portion of the $^{82m}Br(IT)^{82g}Br$ reaction which occurred in the solid state when the sample was frozen after 30 min in the liquid state. Data are also corrected by multiplying by the factor (90/91) so they accurately correspond to the ^{82g}Br which passed through the ^{82m}Br state. [f] From data of Iyer and Willard, ref 25; calculated from the reported organic yield data of 39.4% at mole fraction of Br_2 = 0.0372 and the theoretical point of 0% at mole fraction of Br_2 = 1.0.

The $^{82m}Br(IT)^{82g}Br$ process is a one-step transition from a nuclear state (^{82m}Br) which is 46 keV above the ground (^{82g}Br) state.[26,27] The probability of conversion in this transition is in excess of 0.996.[26,27] Thus, nearly every $^{82m}Br(IT)^{82g}Br$ event gives a ^{82g}Br atom with an inner-shell (K or L) vacancy. Most of these atoms will acquire additional charging as a result of vacancy cascades.[1,3] It is these charged bromine species which then interact chemically with their surroundings to ultimately attain stable chemical form. The measured Y^0_{org} for this transition, 0.495 ± 0.005, gives the probability that the directly affected bromine atom attains organic combination as a consequence of that atom acquiring the inner-shell vacancy in a *very* dilute solution of bromine in carbon tetrachloride. Thus

$$Y^0_{org}(82m/82g) = P^0_{org,c}(82m/82g) = 0.495 \pm 0.005 \quad (4)$$

The activation of ^{81}Br nuclei by thermal neutrons directly produces *both* ^{82m}Br and ^{82g}Br.[22,23] After the ^{82m}Br nuclei have decayed (6.1-min half-life), 90.0 ± 0.3% of the surviving ^{82g}Br (35.3-hr half-life) will have come from the isomeric transition and 10.0 ± 0.3% directly from n,γ activation.[26] The organic yield at infinite dilution may thus be expressed

$$Y^0_{org}(82g) = 0.100[Y^0_{org}(81/82g)] + 0.900[Y^0_{org}(81/82m/82g)] \quad (5)$$

The 10.0% of the final ^{82g}Br which results from the $^{81}Br(n,\gamma)^{82g}Br$ event has not experienced an isomeric transition. This 10.0% can only undergo Auger charging (from the inner-shell vacancy cascade) as a result of internal conversion occurring during the n,γ nuclear deexcitation process. Using eq 3, this may be expressed

$$Y^0_{org}(81/82g) = f_r(81/82g)P^0_{org,r} + f_c(81/82g)P^0_{org,c} \quad (6)$$

The other 90.0% of the final ^{82g}Br measured has undergone both the n,γ activation and an isomeric transition. This organic yield, $Y^0_{org}(81/82m/82g)$, becomes tractable as a result of the observation of Milman and coworkers[20] that the final distribution of ^{82g}Br is not dependent on the chemical form into which ^{82m}Br was stabilized after the n,γ activation. This is also true for bromine–carbon tetrachloride solutions.[21,28] The quantity $Y^0_{org}(81/82m/82g)$ becomes equivalent to $Y^0_{org}(82m/82g)$. Making the appropriate substitutions in eq 5, the $Y^0_{org}(82g)$ is given by

$$Y^0_{org}(82g) = 0.100[f_r(81/82g)P^0_{org,r} + f_c(81/82g)P^0_{org,c}] + 0.900(0.495) = 0.438 \pm 0.005 \quad (7)$$

Within the limits of experimental error, we have the surprising result that the internal conversion contribution from the $^{82m}Br(IT)^{82g}Br$ transformation *alone* accounts for essentially *all* of the measured ^{82g}Br organic yield (*i.e.*, 0.438 ± 0.005 = (0.900 ± 0.003) × (0.495 ± 0.005) = 0.445 ± 0.005). Thus the first term of eq 7, corresponding to the $^{81}Br(n,\gamma)^{82g}Br$ transformation is zero, within the range of experimental uncertainty. Since neither component of this term can be negative, both components must be zero. We know from pure isomeric transition events that $P^0_{org,c}$ is not equal to zero, hence $f_c(81/82g)$ must be zero. This means that there is little or no internal conversion accompanying the $^{81}Br(n,\gamma)^{82g}Br$ transformation. Furthermore, $f_r(81/82g) = 1$ and $P^0_{org,r}(81/82g)$ must be zero. We thus conclude that there is no contribution to organic yield from n,γ activation events which occur without internal conversion. In other words, there is no organic yield contribution from recoil—only events

(23) A. G. Worthington and J. Geffner in "Treatment of Experimental Data," Wiley, New York, N. Y., 1943, p 238.

(24) C. H. Collins and K. E. Collins, unpublished data.

(25) R. M. Iyer and J. E. Willard, *J. Amer. Chem. Soc.*, **87**, 2497 (1965).

(26) J. F. Emery, *J. Inorg. Nucl. Chem.*, **27**, 903 (1965).

(27) O. U. Anders, *Phys. Rev. B*, **138**, 1 (1965).

(28) K. E. Collins, S. Cena, P. A. Kapauan, and C. H. Collins, 6th International Hot Atom Chemistry Symposium, Brookhaven National Laboratory, Sept 1971.

occurring in the n,γ activations of bromine in carbon tetrachloride solutions.

Probability of Internal Conversion in an n,γ Activation. The general expression for organic yield from n,γ events, eq 3, then can be simplified, in the case of very dilute solutions, to

$$Y^0_{org} = f_c P^0_{org,c} \quad (8)$$

Substituting the observed value of 0.495 ± 0.005 for $P^0_{org,c}$ (from the pure internal conversion ^{82m}Br(IT)-^{82g}Br process), eq 8 permits an estimation of f_c for each n,γ process for which suitable organic yield measurements can be obtained. Table II lists values of f_c for the ^{79}Br(n,γ)^{80m}Br, ^{81}Br(n,γ)^{82g}Br, and ^{81}Br(n,γ)^{82m}Br transformations. The ^{79}Br(n,γ)^{80m}Br value was obtained directly from the organic yield (Table I) using eq 8. The f_c value for the ^{81}Br(n,γ)^{82m}Br process was calculated from the observed organic yield for the sum process, ^{81}Br(n,γ)^{82m} + ^{82g}Br. Of the total measured ^{82g}Br, 90.0% came from the ^{81}Br(n,γ)^{82m}Br route and 10.0% from the ^{81}Br(n,γ)^{82g}Br route,[22] which (in accord with the above discussion) gave no organic incorporation. In addition, the organic yield was increased slightly by the 6% of the ^{82m}Br(IT)^{82g}Br transition decays which occurred in the liquid state before the sample was frozen. The true value for the ^{81}Br(n,γ)-^{82m}Br transformation can be obtained by subtracting this isomeric transition contribution [(0.900)(0.06) × (0.495)] from the observed organic yield (0.226 ± 0.006) and then dividing this value by the normalizing factor [(0.900)(0.94)]. The true organic yield for the ^{81}Br(n,γ)^{82m}Br transformation, 0.235 ± 0.006, is then used to calculate the corresponding f_c value according to eq 8.

Table II: Probabilities of Internal Conversion Accompanying n,γ Activations of ^{79}Br and ^{81}Br

Nuclear transformation	f_c[a]
^{79}Br(n,γ)^{80m}Br	0.48
^{81}Br(n,γ)^{82m}Br	0.48
^{81}Br(n,γ)^{82g}Br	*Ca.* 0

[a] Calculated from eq 8; see text.

The f_c values of Table II indicate that some of the n,γ activation processes of ^{79}Br and ^{81}Br have substantial probabilities of internal conversion occurring during the deexcitation cascades. That f_c is not unity for these n,γ processes indicates that not all of the deexcitation cascades from n,γ events include an internal conversion. In addition, the differences in f_c values for the n,γ production of the nuclear isomeric state compared with the corresponding ground state (*i.e.*, ^{82m}Br compared to ^{82g}Br) is indicative of detailed differences in transitions making up the two sets of deexcitation cascades which give the two nuclear isomers.[29]

By contrast, the similarity of the f_c values for the two transformations yielding metastable states (*i.e.*, the ^{79}Br(n,γ)^{80m}Br and ^{81}Br(n,γ)^{82m}Br transformations, at 0.236 and 0.235, respectively) suggests that the actual probabilities of internal conversion may be identical in these two transformations.

The charging probability values of Table II are greater than the values obtained from the experiments of Wexler and Davies.[4] No inconsistency is indicated by this, since the earlier values represent lower limits to the actual quantities.

A conclusion of the present work is that there are *no* organic bromide products from recoil—only events occurring in bromine–carbon tetrachloride solutions. If this conclusion is valid, then there are no "hot" reactions of recoil bromine atoms in liquid carbon tetrachloride which produce carbon–bromine bonds. This is not necessarily true for solvent systems other than liquid-phase carbon tetrachloride. However, in this medium, the lack of carbon–bromine bond formation may mean that abstraction reactions (to form BrCl molecules) are the only "hot-atom" reactions of significant yield.

Our ratio of 2.1 for the organic yield from the ^{82m}Br-(IT)^{82g}Br transformation to that from the ^{79}Br(n,γ)-^{80m}Br transformation in bromine–carbon tetrachloride solution differs significantly from the corresponding ratio of 1.7 obtained by Merrigan, Nicholas, and Rack with solutions of bromine in several hexane isomers.[7] One interpretation of this difference is that recoil-only events can contribute to the organic yield in bromine–hydrocarbon solutions although they do not contribute in bromine–carbon tetrachloride solutions. The reasons for such differences in kinetically "hot" organic yields are not clear, but the relative ease of escape of the hydrogen atom from the final cage containing the bromine recoil atom or the relatively low rotational inertia of the CH_2 or CH_3 groups on the hydrocarbon molecule itself[30] might favor combination reactions of the bromine atom with a carbon atom initially bonded to a hydrogen.

Since the probability of internal conversion accompanying the deexcitation cascade from an n,γ event relates critically to the detailed energy level scheme and to the nuclear properties of the states involved in the deexcitation cascades,[2] the f_c values reported in this paper (Table II) may be of interest from both nuclear and chemical points of view. Thus, chemical procedures of the type employed here may be useful in obtaining nuclear data on the extent of internal conversion events which are not readily obtainable by current physical procedures.

(29) C. H. W. Jones, *J. Phys. Chem.*, **74**, 3347 (1970).

(30) A. G. Maddock and R. W. Wolfgang in "Nuclear Chemistry," L. Yaffe, Ed., Vol. 2, Academic Press, New York, N. Y., 1968, p 185.

Appendix

Internal conversion processes from low-energy transitions of high multipolarity tend to occur 10^{-10} sec or longer after the absorption of a neutron by a nucleus.[1,2,31,32] Thus, internal conversion events may occur well after the recoil atom has lost its kinetic energy (10^{-12} sec).[33]

Those internal conversion events, if any, which occur between 10^{-14} and 10^{-9} sec may perhaps be affected by the high kinetic energy event. The magnitude of this effect depends on the manner in which recoil displacement and recoil-produced fragmentation affect the chemical reactions which accompany the internal conversion. If the recoil displacement is sufficiently great to cause the recoil atom to leave the vicinity of the charged fragments resulting from a previous internal conversion, this atom would presumably have the same ultimate chemical fate as a recoil atom which had not undergone internal conversion, *i.e.*, the recoil kinetic energy of the atom would generally give no contribution to the organic yield. This might be the case for a very high-energy bromine recoil atom, such as that produced by the $^{81}Br(n,2n)^{80m}Br$ activation event where a recoil range of thousands of ångströms is involved.[1] However, for an n,γ activation event, the recoil range is only of the order of 10 Å.[1] With the energies of most of the Auger electrons from an internal conversion in bromine much greater than 10 eV and the range of such electrons and the distribution of secondary ionization in condensed media considerably greater than 10 Å,[13,34] the recoil range from an n,γ activation cannot carry the atom out of the zone created by Auger electron radiolysis even if the internal conversion were to take place prior to the recoil displacement of the atom. These Auger electron radiolysis products will then affect the chemical fate of an n,γ recoil atom which undergoes internal conversion, whether the time scale of the internal conversion is large or small compared with that (10^{-13} sec) for the high-energy motion of the recoil atom.

The number of reactive fragments and excited species from Auger radiolysis must be much greater than the number produced by recoil alone, since several thousands of electron volts are expended in radiolysis accompanying the Auger event,[13] compared to less than 10% of that amount as recoil energy.[1] Auger electrons are emitted with a spectrum of energies with low-energy (several tens of electron volts) electrons in abundance.[3,13] There is presumably no chemically significant angular correlation. It can thus be argued that the atom which undergoes internal conversion is, on the average, located in the dense central region of a roughly spherical radiolysis-fragmentation zone. If the recoil atom has expended most of its kinetic (recoil) energy by the time the internal conversion occurs, the density of fragments with which the initiating atom might react would be at a maximum. The recoil-produced fragments thus may have only a small effect upon the ultimate chemical fate of an n,γ recoil atom which undergoes internal conversion during the deexcitation cascade.

(31) G. H. Vineyand, *Discuss. Faraday Soc.*, **No. 31**, 7 (1961).

(32) A. J. Cole, M. D. Mia, G. E. Miller, and P. F. D. Shaw, *Radiochim. Acta*, **9**, 194 (1968).

(33) R. M. Noyes, *J. Chem. Phys.*, **22**, 1349 (1954).

(34) D. E. Lea in "Actions of Radiations on Living Cells," 2nd ed, Cambridge University Press, New York, N. Y., 1955, p 24.

Reactions of Photochemically Produced Hydrogen Atoms at Energies below 1.8 Electron Volts[1]

by Kong-yi Hong and Gilbert J. Mains*

The Departments of Chemistry, University of Detroit, Detroit, Michigan 48221 and Oklahoma State University, Stillwater, Oklahoma 74074 *(Received April 4, 1972)*

The addition of I_2 to HI–RD photolysis systems at 40° has been shown to unambiguously differentiate between products which arise by reaction of hot H atoms and those of thermal H atoms by efficiently removing the latter. Hot H atoms, formed with maximum initial energy of 1.8 eV by photolysis of HI at 253.7 nm, have been found to preferentially abstract hydrogen over deuterium from partially deuterated ethanes by a factor of 5 to 8. SiD_4, Si_2D_6, and CH_3SiD_3 were also studied and found to be much more reactive than their carbon analogs. Comparison of this research at very low total pressures, *ca.* 2 Torr, with earlier research on these systems in the hundred Torr region, showed that the ratio of the probability of moderation to reaction, k_5/k_{4a}, was pressure independent for the perdeuteriohydrocarbons and partially deuterated ethanes studied.

Introduction

The presence of translationally energetic, *i.e.*, "hot," hydrogen atoms in the photolysis of hydrogen halides was first noted by Ogg and Williams,[2] and later demonstrated in the photolysis of hydrogen iodide at 253.7 nm by Hamill *et al.*,[3a] who showed that the yield of hydrogen was significantly and systematically influenced by dilution with rare gases. In that study the products of the hot hydrogen atom reactions were chemically indistinguishable from products arising from the reactions of hydrogen atoms in thermal equilibrium. That limitation was subsequently removed by Carter, Williams, and Hamill[3b] by photolyzing deuterium iodide in the presence of protiated substrates. Since then much research effort has been expended to gain insight into the factors determining the reactivity of hot hydrogen atoms, and this work has been carefully reviewed by Vermeil.[4] This laboratory contributed a study of the flash photolysis of hydrogen iodide in the presence of C_2D_6, C_3D_8, n-C_4D_{10}, and various $C_2D_{6-n}H_n$ ethanes.[5]

Whereas the hot hydrogen atoms produced photochemically were below 4 eV in energy, the hot hydrogen atoms produced by nuclear recoil were in the 192,000-eV region. These higher energy H atoms were the subject of intensive studies by the late Wolfgang[6] and Rowland,[7] who have written comprehensive reviews. As these very high-energy hydrogen atoms degraded in energy they underwent completely new kinds of chemical reactions which complicated the interpretation on one hand but made them even more interesting on the other. Until Sturm's recent observation[8] that hot hydrogen atoms from the flash photolysis of HI could be detected by their reaction with N_2O using kinetic spectroscopy, data interpretation involved stable product analysis and the effects of gas composition, pressure, temperature, and inert gases as diagnostic variables. At the high-energy end of the spectrum the data were treated by a method developed by Estrup and Wolfgang (see ref 6) and in the low-energy region by the usual method of characterizing each reaction with a rate constant. Biordi[5] showed both methods applicable in the flash photolysis of hydrogen iodide, even though the assumptions made in deriving the equation of Estrup and Wolfgang might not have been expected to be applicable at the low energies employed by her.

It has been shown[9] that the equation of Estrup and Wolfgang can be deduced from the Boltzmann equation, and that results of this analytical solution are in satisfactory agreement with a stochastic approach.[10] The latter theoretical study is especially interesting because it showed that even small reaction probabilities can have a marked influence on the collision density distribution. Kupperman[11] has pointed out that a knowledge of *all processes*, reactive and nonreactive, is necessary to evaluate the collision density distribution function. White[12] defined the rate constant for the

(1) Taken in part from a Ph.D. Thesis of Kong-yi Hong submitted to the Graduate School at the University of Detroit.

(2) R. A. Ogg, Jr., and R. R. Williams, Jr., *J. Chem. Phys.*, **13**, 586 (1945).

(3) (a) H. A. Schwarz, R. R. Williams, and W. H. Hamill, *J. Amer. Chem. Soc.*, **74**, 6007 (1952); (b) R. J. Carter, R. R. Williams, and W. H. Hamill, *ibid.*, **77**, 6457 (1955).

(4) C. Vermeil, *Isr. J. Chem.*, **8**, 147 (1970).

(5) J. C. Biordi, Y. Rousseau, and G. J. Mains, *J. Chem. Phys.*, **49**, 2642 (1968).

(6) R. Wolfgang, *Progr. React. Kinet.*, **3**, 97 (1965).

(7) F. S. Rowland in "Molecular Beams and Reaction Kinetics," Ch. Schlier, Ed., Academic Press, New York, N. Y., 1970, p 108.

(8) R. E. Tomalesky and J. E. Sturm, *J. Chem. Phys.*, **55**, 4299 (1971).

(9) M. Baer, *ibid.*, **50**, 3116 (1969).

(10) D. M. Chapin and M. D. Kostin, *ibid.*, **46**, 2506 (1967).

(11) A. Kupperman, J. Stevenson, and P. J. O'Keefe, *Discuss. Faraday Soc.*, **44**, 46 (1967).

reaction of hot hydrogen atoms from the photolysis of HBr in terms of eq a

$$k_i = \int_0^\infty \sigma_i(v) v f(v) dv \qquad (a)$$

where v is the relative velocity of the collision, $f(v)$ is the distribution of collisions function, and σ_i is the reaction cross section. Reasonable agreement was obtained for *ratios* of k's assuming a *triangular* distribution function, $f(v)$, in spite of the fact that this function is quite far in form from that predicted.[10]

The research described here was undertaken to resolve conflicting conclusions about whether or not an isotope effect was present for hot hydrogen atoms. The data of Biordi, *et al.*,[5] suggested *either* the absence of an isotope effect for the abstraction reaction of hot hydrogen atoms with $C_2D_{6-n}H_n$ ethanes *or* a moderation effect of protiated ethane that masked the isotope effect, *i.e.*, a shift of $f(v)$ to lower energies upon protiating the ethane. The authors leaned toward the first interpretation, no isotope effect, and were reinforced in this opinion by Wolfgang's early high-energy recoil hydrogen atom experiments with CH_3F and CD_3F.[13] On the other hand, Rowland and coworkers[14] had found an isotopic preference ratio of 1.3 (H over D) in their study of recoiling T atoms with CH_2D_2. This study was extended into the much lower 2.8-eV region by Chou and Rowland,[15] again yielding data consistent with an isotope effect of 1.4 to 2.0 per bond. Therefore, the systems studied by Biordi, Rousseau, and Mains[5] by flash photolysis have been reinvestigated at low intensity using 253.7-nm radiation at 40° so that sufficient iodine, I_2, could be present to scavenge all thermalized hydrogen atoms. In performing the experiments in this way, the presence of an isotope effect could be uniquely ascertained (*vide infra*).

Experimental Section

A. Apparatus and Procedure. The reaction vessel was fabricated from 7-cm diameter quartz tubing fitted at one end with a Vycor window and at the other with a Teflon high-vacuum needle valve and a freeze tip. The vessel, $V = 400 \pm 1$ cc, was positioned reproducibly within an air-thermostated box, the temperature of which was controlled to $40 \pm 0.5°$. The lamp (Ultra-violet Products Inc., Model SL 2537) was located outside of the thermostat and the radiation was admitted through a double quartz window assembly located at one end. Actinometry measurements were performed by measuring the yields of hydrogen from HI at 100, 150, and 200 Torr to ensure complete absorption. Assuming the quantum yield of H_2 to be 1.00 under these conditions[16] the light flux incident upon the reaction vessel was 1.28×10^{18} photons/sec. High-vacuum gas handling techniques were used to transfer the gases into the reaction vessel.

B. Materials. Hydrogen iodide (Matheson Co.) was purified by bulb-to-bulb distillation and stored in a blackened Pyrex bulb closed by a Fisher and Porter Co. Teflon needle valve stopcock. In those experiments in which I_2 was initially excluded, the hydrogen iodide was distilled from a $-96.7°$ (methylene chloride slush) bath into a liquid N_2 trap thereby separating I_2 (and the H_2 also) formed by slow decomposition of HI upon storage.

Perdeuterated ethane was obtained from Merck of Canada and was found to contain 1.7% ethylene by gas chromatography and 5.0% C_2D_5H by mass spectrometry. Perdeuteriopropane was obtained from Stohler and was found to contain 16% (mol %) C_3D_7H by mass spectrometry. The perdeuteriobutane was also obtained from Merck of Canada and contained 8.7% n-C_4D_9H by mass spectrometry. These gases were used without further purification. Since trace amounts of olefin impurities were shown to be negligible in these kinds of experiments by Biordi, *et al.*,[5] no attempt was made to remove any trace olefin impurities which might be present.

Ethane-*1,1,1-d*$_3$, ethane-*1,1,2,2-d*$_4$, and ethane-d_5 were also obtained from Merck of Canada and used without further purification. The manufacturer's stated isotopic purity for these gases was 98% (atom %) for CH_3CD_3 and 99% for the other two isotopic isomers.

Perdeuteriosilane, SiD_4, was obtained from Merck of Canada and further purified by distillation from a $-160°$ bath (isopentane slush) to a $-195°$ bath (liquid nitrogen). Mass spectrometric analysis revealed 2.4 atom % isotopic impurity in the form SiD_3H. Perdeuteriodisilane and methylsilane-d_3 were prepared according to the method of Finholt, Bond, Wilzbach, and Schesinger,[17] except tetraethylene glycol ether was used instead of diethyl ether as the solvent. Mass spectrometric analysis found the Si_2D_6 to contain 2 atom % impurity, Si_2D_5H, which is presumed to originate from the small amount of isotopic impurity in the $LiAlD_4$ reactant. Similarly, CH_3SiD_3 is expected to contain 2 atom % of CH_3SiD_2H as impurity.

Helium (Matheson Co.) was purified by passing it through a molecular sieve (5A) trap immersed in liquid nitrogen. No impurity could be found by mass spectrometric analysis.

Except for the few experiments reported in Figure 1, all product analyses were performed using a C.E.C. Model 21-103C (modified) mass spectrometer and the isotopic impurities deduced either from standard mass spectral patterns of the impurity or from assumed

(12) J. White, Los Alamos Scientific Laboratory, private communication.

(13) H. Jurgleit and R. Wolfgang, *J. Amer. Chem. Soc.*, **85**, 1057 (1963).

(14) J. K. Lee, B. Musgrave, and F. S. Rowland, *J. Phys. Chem.*, **64**, 1950 (1960).

(15) C. Chou and F. S. Rowland, *ibid.*, **75**, 1283 (1971).

(16) R. Penzhorn and B. deB. Darwent, *ibid.*, **72**, 1639 (1968).

(17) A. E. Finhold, A. C. Bond, Jr., K. E. Wilzbach, and H. I. Schesinger, *J. Amer. Chem. Soc.*, **69**, 2692 (1947).

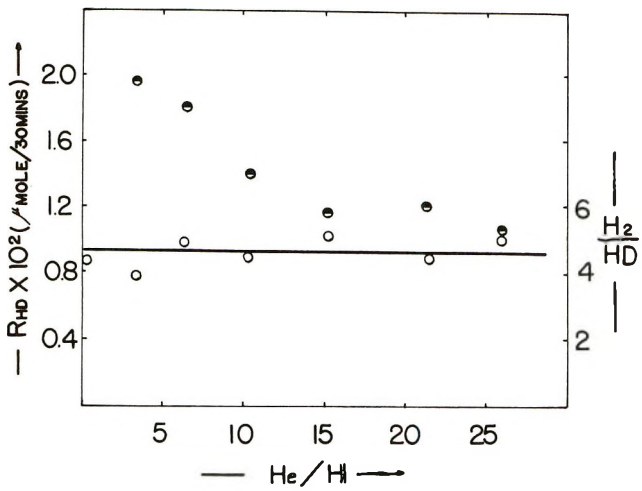

Figure 1. Rate of HD production and the ratio of H_2/HD as a function of added He moderating gas. The 253.7-nm photolysis of the He–I_2–HI–C_2D_6 system was at 40°.

mass spectral patterns deduced from the appropriate perdeuterated or protiated isomer. In general, mass spectral patterns were not available for most of the silane impurities. A few analyses were performed using the LKB Model 9000 mass spectrometer after modifying it for quantitative work, *i.e.*, precise pressure measurement in a gas reservoir, which was attached to the ionization chamber by a molecular leak.

Results

Mixtures of HI, C_2D_6, I_2, and helium were photolyzed to demonstrate the presence of hot hydrogen atoms in these systems. The amounts of HI, I_2 (1.1 Torr, in equilibrium with I_2(s) at 40°), and C_2D_6 were all held constant in the ratios I_2/HI = 2.3 and HI/C_2D_6 = 0.2. The data so obtained are presented in Figure 1, where it may be observed that the rate of HD production (half filled circles) was markedly diminished by added He whereas the ratio, H_2/HD, (open circles) was unchanged over a 26-fold variation in the He/HI ratio. It is important to note from Figure 1 that less than 1% of the incident light flux was absorbed in the reaction vessel and that the He pressure in the system had to be increased to about 2 Torr before a diminuation in the rate of production of HD was measurable.

Mixtures of HI, I_2, and the following compounds were photolyzed at 40°: C_2D_6, C_3D_8, n-C_4D_{10}, SiD_4, Si_2D_6, C_2D_5H, CHD_2CHD_2, CH_3CD_3, and CH_3SiD_3. Plots of H_2/HD *vs.* initial HI/RD ratios gave straight lines as depicted in Figures 2 and 3. Note that all perdeuterated compounds give zero intercepts (Figure 2) whereas the compounds which are partially deuterated give positive intercepts (Figure 3). Note also that the ratio of I_2 to HI was fixed at 2.3 for all of these experiments and conversions were always kept below 2%. These intercept observations are similar to those reported earlier by Fink, *et al.*,[18] for the DBr–Br_2–C_2H_6 system and Chou and Rowland[15] for the DBr–Br_2–CH_4 system. Because the

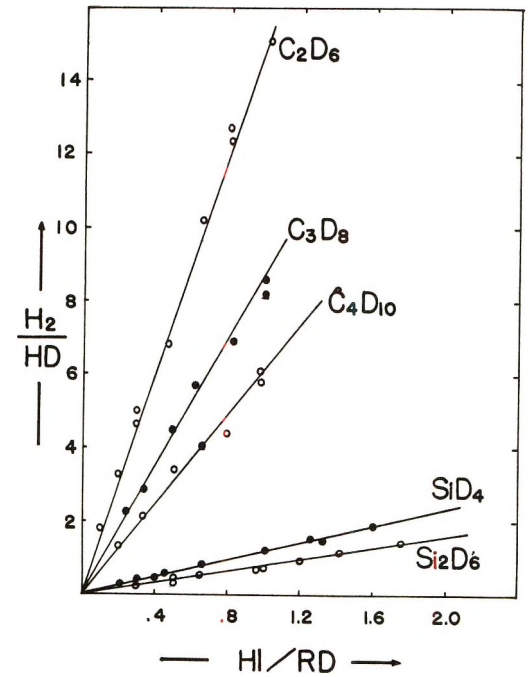

Figure 2. Initial yields of H_2/HD as a function of HI/RD in the 253.7-nm photolysis of I_2–HI–RD systems at 40°.

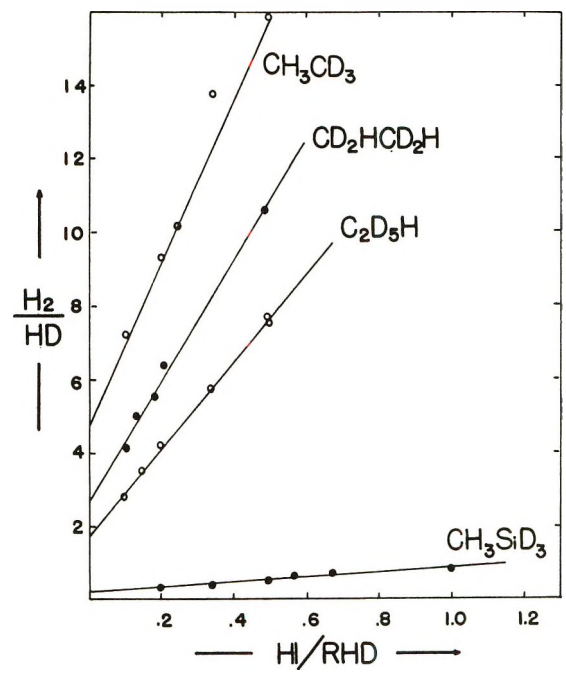

Figure 3. Initial yields of H_2/HD as a function of HI/RHD in the 253.7-nm photolysis of I_2–HI–RHD systems at 40°.

earlier experiments of Biordi, Rousseau, and Mains[5] were performed at 25°, they were repeated at 40° (using the lower intensity 253.7-nm source and a constant P_{HI} = 0.48 Torr) for comparison purposes. These data are displayed in Figure 4 where it may be ob-

(18) J. E. Nicholas, F. Bayrakcekan, and R. D. Fink, *J. Phys. Chem.*, 75, 841 (1971).

Table I: Data from the 253.7-nm Photolysis of HI + RD (or RHD) and HI + I_2 + RD (or RHD) Mixtures at 40°

Substrates	RD (or RHD) + HI: Slope = $\frac{k_2 + k_3}{k_{4a}}$	RD (or RHD) + HI: Intercept = $\frac{k_5{}^a}{k_{4a}}$	RD (or RHD) + HI + I_2: Slope = $\frac{k_2}{k_{4a}}$	RD (or RHD) + HI + I_2: Intercept = $\frac{k_{4b}}{k_{4a}}$
C_2D_6	21.4 ± 0.9	9.4 ± 0.6	15.1 ± 0.5	0
C_3D_8	9.6 ± 0.2	6.2 ± 0.1	7.7 ± 0.2	0
n-C_4D_{10}	9.2 ± 0.4	5.0 ± 0.3	5.1 ± 0.4	0
C_2D_5-H	22.0 ± 2.2	10.6 ± 1.4	11.9 ± 0.3	1.7 ± 0.1
CHD_2-CHD_2	29.1 ± 2.2	13.4 ± 1.9	16.3 ± 0.7	2.7 ± 0.2
CH_3CD_3	45.1 ± 1.2	18.1 ± 0.7	23.1 ± 2.8	4.8 ± 0.9
CH_3SiD_3	1.7 ± 0.1	0.95 ± 0.04	1.7 ± 0.1	0.21 ± 0.05
SiD_4			1.2 ± 0.2	0
Si_2D_6			0.81 ± 0.05	0

[a] In the case of RHD intercept = $(k_{4b} + k_5)/k_{4a}$.

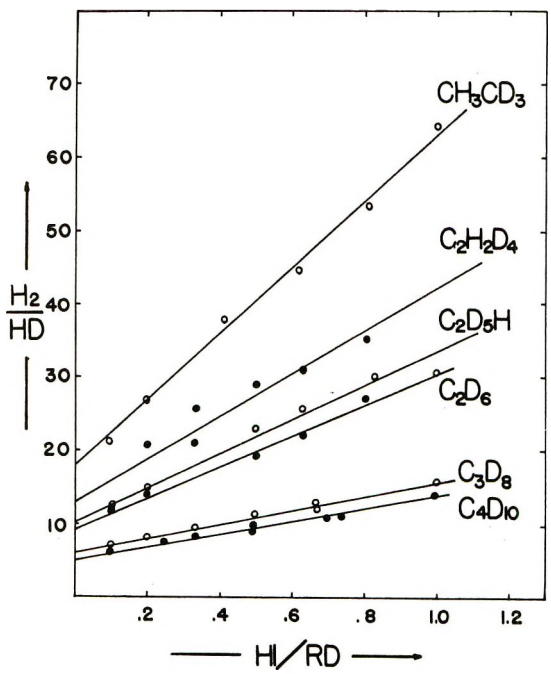

Figure 4. Initial yields of H_2/HD as a function of HI/RD (or RHD) in 273.7-nm photolysis of HI–RD (or RHD) systems at 40°.

served that straight lines and positive intercepts, comparable with those of Biordi, *et al.*,[5] were obtained. All of the slopes and intercepts are reported in Table I.

Discussion

Although there are certainly more details to be revealed by future studies, there seems to be no controversy regarding the important mechanistic steps involved in the photolysis of HI in the presence of various substrates.[2,3,5,16] A summary of the elementary processes follows.

$$HI + h\nu \longrightarrow H^* + I \quad (1)$$

$$H^* + HI \longrightarrow H_2 + I \quad (2)$$

$$H^* + HI \longrightarrow H + HI \quad (3)$$

$$H^* + RD \longrightarrow HD + R \quad (4a)$$

$$H^* + RHD \longrightarrow H_2 + RD \quad (4b)$$

$$H^* + RD \longrightarrow H + RD \quad (5)$$

$$H + HI \longrightarrow H_2 + I \quad (6)$$

$$2I + M \longrightarrow I_2 + M \quad (7)$$

$$H^* + I_2 \longrightarrow HI + I \quad (8)$$

$$H^* + I_2 \longrightarrow H + I_2 \quad (9)$$

$$H + I_2 \longrightarrow HI + I \quad (10)$$

$$H^* + M \longrightarrow H + M \quad (11)$$

The fate of the thermalized hydrogen atoms is of prime importance in the interpretation of the data. In the studies reported in Figure 4, reaction 6 is the primary means by which thermal hydrogen atoms are removed from the system. In the studies reported in Figures 2 and 3, the possibility of a competition between reaction 6 and reaction 10 exists. Hamill, *et al.*,[3a] report data for the ratio k_{10}/k_6 which extrapolates to 92 at 40°. Holmes and Rogers[19] reinvestigated the effects of He, H_2, and Ar as hot H atom moderators in the photolysis of HI at 253.7 nm and report the ratio, k_{10}/k_6, to be 12.0 ± 1 in the temperature range 50–200°, in good agreement with k_{10}/k_6 = 13.7 calculated from the equation of Penzhorn and Darwent.[16] This suggests a maximum error of 4% would result if reaction 6 is neglected in treating the data reported in Figures 2 and 3, where the ratio, I_2/HI, was held constant at 2.3. (The error would, of course, appear as excess H_2.) Therefore, we shall assume that reaction 6 is the sole fate of thermalized hydrogen atoms in I_2 *excluded* systems and that reaction 10 is the sole fate of thermalized hydrogen atoms in I_2 *included* systems. Support for these assumptions may be found on Figure 1. If reaction 6 made a significant contribution in the I_2 *included* systems the ratio, H_2/HD, would be expected

(19) J. L. Holmes and P. Rogers, *Trans. Faraday Soc.*, 64, 2368 (1968).

to increase as the steady-state concentration of thermal H atoms was increased by adding helium. Additional support for these assumptions can be found in the zero intercepts of Figure 2 and the nonzero intercepts for the perdeuterated hydrocarbons in Figure 4.

For the I_2 *excluded* systems, the rate of production of H_2 and HD can be written as follows.

$$R_{H_2} = k_2(H^*)(HI) + k_6(H)(HI) \quad (b)$$

$$R_{HD} = k_{4a}(H^*)(RD) \quad (c)$$

At the very low conversions employed in this study the concentrations of HI and RD will be assumed constant. Application of the steady-state treatment to H and H* atoms permits the ratio of eq b and c to be rewritten in the following form

$$\frac{(H_2)}{(HD)} = \frac{k_2 + k_3}{k_{4a}}\frac{(HI)}{(RD)} + \frac{k_5}{k_{4a}} \quad (d)$$

This treatment is essentially the stochastic treatment and eq d is identical in form with that derived earlier by Biordi, Rousseau, and Mains[5] except that specific rate constants appear in the equation instead of probabilities. The rate constants in eq d are expected to be functions of those variables which effect $f(v)$ in eq a and should not be confused with k_6 or k_{10} where $f(v)$ is specified solely by the temperature of the system. Equation d does indeed predict the linearity observed in Figure 4 for a wide variety of systems. Furthermore, the intercepts observed in this study at a total pressure less than 2 Torr are within experimental error the same as observed by Biordi, *et al.*,[5] at pressures which were a factor of 100 greater. However, the slopes observed in this study are 50 to 100% larger than observed previously. Since none of the reactions are intensity dependent, it is concluded that k_5/k_{4a} is independent of pressure and consistent with the interpretation that this ratio represents the relative probability of moderation to abstraction by a hot hydrogen atom in pure RD. On the other hand, the significantly larger slopes observed in this study suggests a rather large total pressure dependence on the $(k_3 + k_2)/k_{4a}$ ratio. It is tempting to attribute this pressure dependence to the thermalization process, reaction 3, which probably cannot occur in a single collision process as written. Alternately, one could attribute the larger slopes to a total pressure dependence of $f(v)$ in the region between the threshold for process 4a and that for reactions 2 and 3. Intuitively one would expect the slopes to be smaller (not larger as observed) at lower total pressures for the reactions with the lower threshold energies. One final possibility, that thermalization does not occur homogeneously at the lower pressure, cannot be ignored. If k_3 and k_5 are small relative to thermalization at the walls of the vessel, the observed trend in slopes can be understood. In the absence of surface to volume experiments further speculation is not warranted and resolution of this will have to be left to future studies. It is important to note, nonetheless, that linearity of the graphs observed over a wide range of composition and total pressure suggests that basic interpretation is correct and that while the slope $(k_2 + k_3)/k_{4a}$ may be very sensitive to pressure, the ratio k_5/k_{4a} is not.

For the I_2 *included* systems, the interpretation is greatly simplified. Equation b may be written as $R_{H_2} = k_2(H^*)(HI)$ and eq d becomes the much simpler equation

$$(H_2)/(HD) = [k_2/k_{4a}](HI)/(RD) \quad (e)$$

for perdeuterated compounds and, more interestingly

$$(H_2)/(HD) = [k_2/k_{4a}](HI)/(RHD) + k_{4b}/k_{4a} \quad (f)$$

for partially deuterated compounds. Verification of the form of eq e may be found in Figure 2. Verification of the form of eq f may be found in Figure 3. The observed slopes and intercepts are reported in Table I. Note that determination of the intercept, k_{4b}/k_{4a}, constitutes *a direct measurement of the isotope effect* for the reaction of hot hydrogen atoms.

In comparing the slopes for the I_2 *excluded* systems with those obtained in the I_2 *included* one notes that the former are always larger than the latter for the hydrocarbons. It is exceedingly tempting to assume that k_2/k_{4a} is the same in these two systems and attribute the difference to k_3. Calculation of ratios, k_5/k_3, for these systems would then be possible. This ratio, k_5/k_3, would provide insight into the factors which cause hydrocarbons to be so much more efficient at moderation than reaction and produce the very large k_5/k_{4a} intercepts observed in the I_2 *excluded* systems. However, when this is done for the partially protiated systems and compared with the perdeuterio systems the conclusion is reached that protonation of ethane *decreases* the moderation rate constant,[20] a conclusion which is inconsistent with the earlier observations of Biordi, *et al.*,[5] regarding the isotope effect. Furthermore, assuming that k_2/k_{4a} is the same in the I_2 *excluded* and I_2 *included* systems is unrealistic when one considers that $f(v)$ must be significantly different in these two systems.[21] Based upon the magnitude of the isotope effect *per bond* calculated from Table I, 8.5 ± 0.4 for C_2D_5H, 5.4 ± 0.4 for CHD_2CHD_2, and 4.8 ± 0.8 for CH_3CD_3, one is forced to the conclusion that I_2 is a much better moderator than ethane since these isotope effects are rather large and closer to what might be expected for thermal H atoms. The mechanism of moderation by I_2, of course, is not known but could possibly be related to the very much closer rotational energy levels of I_2 relative to ethane. The isotope effects reported here are not subject to variations in $f(v)$ which mislead us in interpreting our earlier work[5]

(20) Kong-yi Hong, Ph.D. Thesis, University of Detroit, 1972.

(21) C. Rebick and J. Dubrin, *J. Chem. Phys.*, **53**, 2079 (1970).

and, while somewhat higher than those observed by Rowland and Chou, *i.e.*, 1.4–2.0, confirm the existence of an isotope effect by this laboratory.

Finally, the very high reactivity of the silane compounds with hot hydrogen atoms merits discussion. It should be observed that disilane, Si_2H_6, is actually *more reactive* than HI and is the first compound to exhibit this behavior. Although SiD_4 is lower in reactivity than CH_3SiH_3, it is not uncommon for the first member of an homologous series to be anomalous. It appears that disilane is twice as reactive as CH_3SiD_3 suggesting an approximately equal reactivity per Si–D bond. While part of the difference in reactivity of ethane and silanes may be attributable to the larger cross section of the latter, the fact that the Si–D bond is considerably weaker than the corresponding C–D bond is almost certainly another important factor. In view of the observed isotope effect for C–H abstraction over C–D abstraction for hot hydrogen atoms excited initially to a maximum energy of 1.8 eV reported here, bond energy considerations are significant. The size factor certainly cancels out in the case of CH_3SiD_3 where the intercept k_{4b}/k_{4a} is slightly over 10% of the slope and about 24 times smaller than the CH_3CD_3 intercept. There seems little doubt that even for a very fast moving H atom, maximum velocity about 10^3 km/sec, the probability of abstracting a deuterium atom depends very much on the strength of the R–D bond.

Acknowledgments. We gratefully acknowledge the financial support of the University of Detroit and Oklahoma State University. Thanks are due to Drs. H. Niki, E. Nemeth, S. J., and Joan Biordi for criticism of Kong-yi Hong's thesis. Special thanks are given to Professor F. S. Rowland whose detailed and constructive criticism of the earlier version of this manuscript was extremely valuable to one of us (G. J. M.) in revision.

Reactions of Iodine with Olefins. III. Radiative Neutron Capture Induced Reactions of Iodine-128 with Gaseous Ethylene and Propylene[1]

by R. R. Pettijohn and E. P. Rack*

Department of Chemistry, University of Nebraska, Lincoln, Nebraska 68508 *(Received May 4, 1972)*

Publication costs assisted by the U. S. Atomic Energy Commission

Reactions of (n,γ) activated ^{128}I with gaseous ethylene and propylene have been studied. The total organic product yields were found to be 18 ± 1 and 24 ± 2%, respectively. In both studies $CH_3{}^{128}I$ was found to be the predominant product. Gas additive studies have shown that $CH_3{}^{128}I$ is stabilized in the order Xe > Kr > He. This trend, exactly opposite to that expected of kinetic energy moderation, is attributed to the ion–molecule reaction $I^+(^3P_0 \text{ or } ^3P_1) + C_2H_4 \rightarrow C_2H_4I^+$ as the initiating step in $CH_3{}^{128}I$ formation. Additional labeled products from ethylene are $C_2H_3{}^{128}I$ and $C_2H_5{}^{128}I$. The formation of $C_2H_3{}^{128}I$ is dependent on the presence of molecular iodine and appears to be due to the reaction $^{128}I_2{}^+ + C_2H_4 \rightarrow C_2H_3{}^{128}I^+ + HI$. The results suggest that $C_2H_5{}^{128}I$ is formed *via* the activated monoiodoethyl radical. $CH_3C^{128}I{=}CH_2$ from propylene is believed to be produced in an analogous way to that of $C_2H_3{}^{128}I$ from ethylene.

Introduction

As a result of γ-ray recoil followed by auger electron cascades, ^{128}I atoms or ions formed from the $^{127}I(n,\gamma)^{128}I$ reaction acquire a spectrum of kinetic energies ranging from 0 to 194 eV. The most probable energy is 152 eV.[2a] It has also been shown that at least 50%[3] of the ^{128}I atoms are positively charged and at least 25% of these iodine ions are in electronically excited states.[2b]

In contrast, recoil species produced by the $^{37}Cl(n,\gamma)^{38}Cl$, $^{19}F(n,2n)^{18}F$, or $^3He(n,p)T$ nuclear reactions react as neutral atoms and in low or ground electronic states.[4-6]

(1) This research was supported through an Atomic Energy Commission Contract No. AT(11-1)-1617. This is AEC Document No. COO-1617-32.

(2) (a) M. Yoong, Y. C. Pao, and E. P. Rack, *J. Phys. Chem.*, **76**, 2685 (1972); (b) E. P. Rack and A. A. Gordus, *J. Chem. Phys.*, **34**, 1855 (1961).

(3) S. Wexler and H. Davies, *ibid.*, **20**, 1688 (1952).

(4) C. M. Wai and F. S. Rowland, *J. Amer. Chem. Soc.*, **90**, 3638 (1968).

Studies[5,7,8] of the reactions of these species with olefins have been dominated by direct hot substitution and/or high energy decomposition reaction modes. Therefore it seemed that the investigation of olefins with (n,γ)-produced iodine should provide an interesting complement to these studies.

A recent condensed phase study[9] has shown a definite preference for the addition of (n,γ)-activated iodine at the position of the double bond in pentenes over that found for radiolytically activated ^{131}I. However, the interpretation of experimental results in condensed phase systems from a mechanistic viewpoint is seriously hindered by the lack of suitable liquid phase scavengers and moderators and also by complications due to the solvent caging effect. In addition, interpretation of the results obtained in condensed phase I_2 + olefin reaction systems may be further complicated by thermal reactions.[10]

In the present work reactions of (n,γ)-produced ^{128}I with ethylene and propylene have been studied in the gas phase to avoid the complications of both cage effects and thermal reactions. The changes in individual yields of organic products as a function of the varying amounts of gaseous additives introduced into the reaction system makes possible the indirect determination of the manner in which ^{128}I and/or the respective product intermediate interacts with the additive.

Experimental Section

Approximately 400 samples in quartz ampoules were filled on a greaseless vacuum line and irradiated at a thermal flux of 1.1×10^{11} neutrons cm^{-2} sec^{-1} in the Omaha, Neb., VA Hospital Triga reactor. The accompanying γ-radiation flux was 3×10^{17} eV g^{-1} min^{-1}.

Each sample contained 0.10 ± 0.02 Torr of I_2 to serve as a thermal scavenger. The iodine was sublimed from a mixture of Mallinckrodt reagent grade I_2 and Baker reagent KI and CaO. The higher vapor pressure of CH_3I facilitated its use as a major source of iodine. Matheson Coleman and Bell reagent grade CH_3I was used after purification in a vacuum line employing freeze–pump–thaw cycles to remove air and stored with copper turnings under vacuum. Ethylene and propylene (Phillips research grade, 99.98%), and helium, krypton, xenon, and oxygen (Airco research grade, 99.995% minimum) were used without further purification. All samples were filled to a total pressure of 760 ± 10 Torr.

Samples were filled in a dark room to prevent photoinduced reactions, wrapped in foil, and stored in liquid nitrogen until just prior to irradiation at which time they were warmed to room temperature.

Total organic product yields were determined by breaking the irradiated bulblet in a separatory funnel containing a two-phase mixture of CCl_4 + I_2 and 0.5 *M* aqueous Na_2SO_3. The organic fraction was separated from the inorganic and 3.00 ml of each fraction was counted using a 3-in. NaI well-type crystal. Irradiation times were 2.0 min for xenon-containing samples[11] and 1.0 min for all other total organic yield determinations.

The radiogas chromatograph used in this research has been previously described in detail.[12,13] The column used was a 3-m SS coil containing 5% by weight di(2-ethylhexyl)sebacate on 50/60 mesh firebrick at 50°. Linear temperature programming from 50 to 100° was used for the propylene study. Individual product yields were determined by triplicate radiogas chromatographic runs for 5.0-, 10.0-, and 15.0-min activations, respectively. These product yields were then plotted as a linear function of irradiation time. Individual product yields were corrected for radiolytic contributions by extrapolating these plots to zero activation time.[14] These corrected relative yields were then normalized to the total absolute yield to give the absolute product yields for a particular mole fraction additive.

The data have been corrected for (a) radiative decay between counted fractions, (b) decay of eluted chromatography peaks, (c) 1.1% failure to C–I bond rupture for CH_3I,[15] and (d) radiation-induced reactions.

The ion–molecule reactions were studied using a Varian ICR-9 spectrometer.

Results and Discussion

Summarized in Table I are the observed absolute yields of the individual products formed from the reactions of (n,γ)-activated ^{128}I with ethylene and propylene. Three primary reaction channels appear to be present in the ethylene system which lead to the formation of $CH_3{}^{128}I$, $C_2H_3{}^{128}I$, and $C_2H_5{}^{128}I$. In contrast, only two dominant products, $CH_3{}^{128}I$ and $CH_3C^{128}I{=}CH_2$, were found in the ^{128}I reactions with propylene. The large yields of $CH_3{}^{128}I$ formed in both the ethylene and propylene reaction systems are undoubtedly due,

(5) T. Smail, G. Miller, and F. S. Rowland, *J. Phys. Chem.*, **74**, 3464 (1970).

(6) R. Wolfgang, *Progr. React. Kinet.*, **3**, 109 (1965).

(7) C. M. Wai and F. S. Rowland, *J. Amer. Chem. Soc.*, **91**, 1053 (1969).

(8) E. K. C. Lee and F. S. Rowland, *J. Phys. Chem.*, **74**, 439 (1970).

(9) R. L. Ayres, O. C. Gadeken, and E. P. Rack, *ibid.*, **75**, 2880 (1971).

(10) R. L. Ayres, C. J. Michejda, and E. P. Rack, *J. Amer. Chem. Soc.*, **93**, 1389 (1971).

(11) All xenon-containing samples were irradiated for 2.0 min and then allowed to decay for 30 min after immediate extraction to allow for ^{137}Xe (3.9-min half-life) to decay. These samples were also counted with the single channel's lower window set at 0.4 MeV to discriminate the lower energy emitting Xe isotopes.

(12) R. L. Ayres, Ph.D. Dissertation, University of Nebraska, 1971.

(13) Progress Report No. 6 (No. COO-1617-29), Feb 15, 1972.

(14) This was a necessary correction due to the extended irradiation times needed as a result of a 60-min trip between irradiation facilities and the radiogas chromatograph. Corrections were on the order of 1–3%.

(15) A. A. Gordus and C. Hsiung, *J. Chem. Phys.*, **36**, 954 (1962).

Table I: Yields of ^{128}I-labeled Products from $^{127}I(n,\gamma)^{128}I$-Induced Reactions with Ethylene and Propylene without Additive Present

Product	Ethylene, %	Propylene, %
CH_3I	10.0	18.7
C_2H_3I	4.0	0.3[c]
C_2H_5I	4.0	0.1[c]
$CH_3CI:CH_2$	...	4.0
$CH_2:CICH_3$	...	0.5[c]
$CH_2:CHCH_2I$[a]	...	0.5[c]
$CH_3CH_2CH_2I$[a]		
Total organic yield[b]	18.0 ± 1.0	24.1 ± 2.0

[a] Unresolved radiogas chromatography peaks. [b] All total organic yield samples contained 0.1 Torr I_2 and 4.0 Torr CH_3I. [c] Owing to the small yields of these products, no attempt has been made to discuss their origin.

in part, to the same reaction mechanism. In addition, the product $CH_3C^{128}I{=}CH_2$ appears to be the propylene analog to $C_2H_3{}^{128}I$ formed from ethylene.

Prior to the investigation of the effects of additives on these individual product yields, it was necessary to determine the influence of several representative additives on the contribution of radiolysis to the observed yields.

Radiation damage studies for both krypton and xenon additives in the ethylene system were made. This was accomplished by irradiating identical samples for varying lengths of time (0.5 to 15.0 min). The increase in organic yield was found to be linear with respect to time. The difference between the extrapolated organic yield at time zero and the usual irradiation time of 1.0 min (2.0 min for xenon) was then taken to be the radiation damage at the particular mole fraction additive studied. A plot of mole fraction additive (Kr or Xe) *vs.* per cent organic yield due to radiation damage showed the same linear dependence as did that of Rack and Gordus.[2b] Extrapolations to unit mole fraction of additive were 0.9% for krypton and 6.8% for xenon. The correction for radiation-induced reactions was made by subtracting a quantity equal to the product of the mole fraction of the additive and the extrapolated values above.

Formation of $C_2H_5{}^{128}I$ from Ethylene. It is evident from the rare gas additive plots of helium, krypton, and xenon shown in Figures 1, 2, and 3 that the yield of $C_2H_5{}^{128}I$ decreases with increasing mole fraction additive. The fact that the yield extrapolates to zero at unit mole fraction suggests that the observed 4% yield of this product is due entirely to hot iodine reactions.

Benson, *et al.*, have established that $ICH_2\dot{C}H_2$ is unstable with respect to decomposition to $I + C_2H_4$ by 6 ± 1 kcal.[16,17] However, experimental results of our oxygen additive study suggest that this radical intermediate is involved in the formation of $C_2H_5{}^{128}I$. Evidence for this is shown in Figure 4; the addition of a small amount of oxygen substantially quenches the formation of this product. To our knowledge no previous report has been made concerning the formation of C_2H_5I from the iodoethyl radical intermediate. The high internal energy and/or electronic excitation imparted to this radical by the recoiling ^{128}I could account for the difference in reactivity of this radical intermediate in our systems. It is therefore hypothesized that the intermediate in $C_2H_5{}^{128}I$ formation is the internally excited iodoethyl radical formed as a result of energetic iodine atom attack at the double bond of ethylene.

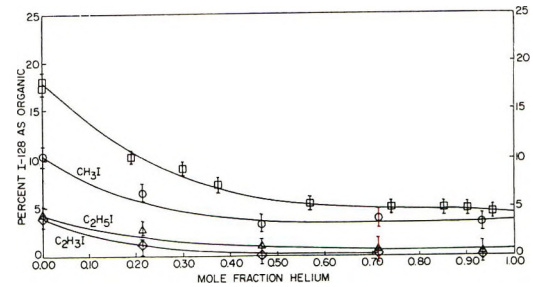

Figure 1. Effect of helium additive on the per cent ^{128}I formed as organic activity due to ^{128}I reactions with C_2H_4: total organic yield, □; absolute yields: CH_3I, ○; C_2H_5I, △; C_2H_3I, ◇.

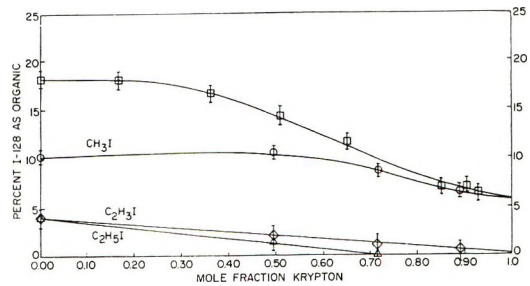

Figure 2. Effect of krypton additive on the per cent ^{128}I formed as organic activity due to ^{128}I reactions with C_2H_4: total organic yield, □; absolute yields: CH_3I, ○; C_2H_3I, ◇; C_2H_3I, △.

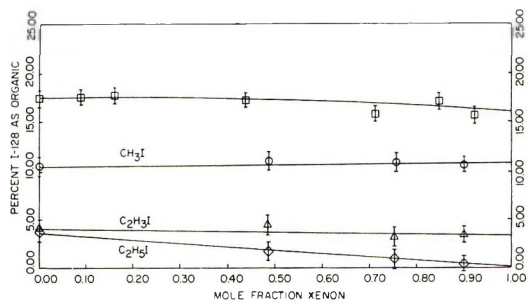

Figure 3. Effect of xenon additive on the per cent ^{128}I formed as organic activity due to ^{128}I reactions with C_2H_4: total organic yield, □; absolute yields: CH_3I, ○; C_2H_3I, △; C_2H_5I, ◇.

(16) S. W. Benson, D. M. Golden, and K. W. Egger, *J. Chem. Phys.*, 42, 4265 (1965).

(17) S. W. Benson and J. H. Buss, *ibid.*, 29, 546 (1958).

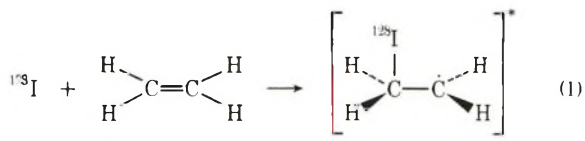

(1)

If the radical is born in a nonexcited state it can only abstract a proton from CH_3I. However, it may possess enough internal energy to abstract a proton from C_2H_4.

$$[^{128}ICH_2\dot{C}H_2]^* + C_2H_4 \longrightarrow C_2H_5{}^{128}I + \cdot C_2H_3 \quad (2)$$

The absence of the product diiodoethane from the scavenging reaction shown in (3) is most likely due to the instability of this product with respect to decomposition to the olefin and I_2.[18]

$$^{128}ICH_2\dot{C}H_2 + I_2 \rightleftharpoons C_2H_4{}^{128}I_2 + I\cdot \quad (3)$$

It is interesting to note that the saturated analog of $C_2H_5{}^{128}I$ (4.0%) from the ethylene system was found to be a relatively minor product in the propylene system ($\leq$0.5%). The hydrogen abstraction from C_3H_6 by the $C_3H_6{}^{128}I$ radical to form $C_3H_7{}^{128}I$ should be extremely efficient due to the presence of the weakly bonded allylic protons. In view of this the yield of $C_3H_7{}^{128}I$ should be $\geq$4%. This discrepancy is not presently understood.

Ion–Molecule Reactions. When a series of samples were analyzed without I_2 present, the yield of $C_2H_3{}^{128}I$ decreased from 4% (with 0.1 mm of I_2) to $\leq$0.3%. In addition, the yield of $CH_3{}^{128}I$ decreased from 10 to 8% (the $C_2H_5{}^{128}I$ yield remained unchanged). By reducing the radical scavenging efficiency of the system it was expected that the respective yields should increase instead of decrease. It appears that the entire 4% of $C_2H_3{}^{128}I$ as well as 2% of the $CH_3{}^{128}I$ are due to the presence of I_2 in the reaction system. The effect of rare gas additives on the yield of $C_2H_3{}^{128}I$, causing it to extrapolate to zero at unit mole fraction additive, as shown in Figures 1 and 2, would normally be interpreted as showing that this product was formed *via* an iodine reacting species possessing excess kinetic energy. However, the effect of the presence of I_2 and the failure of xenon additive to depress the yield of this product (Figure 3) is indicative of an alternant reaction mode.

An ion-cyclotron resonance mass spectrometer was used to study possible stable ion–molecule reaction intermediates. Pulsed double resonance has confirmed that reaction 4 takes place at thermal energies while $^{127}I^+$ in the $^3P_2$ electronic ground state does not form the m/e 155 charge complex. A small peak (ap-

$$^{127}I_2{}^+ + C_2H_4 \longrightarrow \underset{m/e\ 155}{C_2H_4I^+} + I \quad (4)$$

proximately 1/20 the intensity of m/e 155) was observed at m/e 142. The peak is no doubt due to CH_3I^+. Owing to its weak signal, no double resonance experiment was attempted to determine its origin.

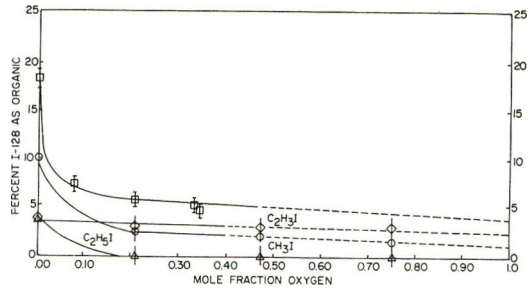

Figure 4. Effect of oxygen additive on the per cent ^{128}I formed as organic activity due to ^{128}I reactions with C_2H_4: total organic yield, □; absolute yields: CH_3I, ○; C_2H_3I, ◇; C_2H_5I, △.

It is important to recall that at least 50% of the ^{128}I atoms are positively charged. In this environment of charged iodine species reaction 5 should be highly probable since it is exoergic by 1.65 eV when I^+ is in the $^3P_2$ ground state and higher in the excited states. The proposed mechanism is initiated by form-

$$I^+(^3P_2, {}^3P_0, {}^3P_1, \text{ or } {}^1D_2) + I_2 \longrightarrow I_2{}^+ + I \quad (5)$$

ation of labeled $I_2{}^+$ by reaction 6.

$$^{128}I^+ + I_2 \longrightarrow {}^{128}I_2{}^+ + I \quad (6)$$

Labeled $^{128}I_2{}^+$ then reacts with C_2H_4 *via* a transition state to form the relatively stable charge complex as in

$$^{128}I_2{}^+ + C_2H_4 \longrightarrow (C_2H_4{}^{128}I_2{}^+)^\dagger \longrightarrow C_2H_4{}^{128}I^+ + I \quad (7)$$

The formation of $C_2H_3{}^{128}I$ could be explained by the possible elimination of HI or HI^+ from the transition state by reaction 8 rather than the unlikely elimination of a proton from $C_2H_4{}^{128}I^+$.

$$(C_2H_4{}^{128}I_2{}^+)^\dagger \longrightarrow HI(HI^+) + C_2H_3{}^{128}I^+(C_2H_3{}^{128}I) \quad (8)$$

If $C_2H_4I^+$ is the precursor to CH_3I by a bimolecular reaction as in

$$C_2H_4{}^{128}I^+ + C_2H_4 \longrightarrow CH_3{}^{128}I + C_3H_5{}^+ \quad (9)$$

then the small ion current of m/e 142 (CH_3I^+) could be attributed to the low pressure of C_2H_4 ($1–10 \times 10^{-6}$ Torr) that must be used in these ion-cyclotron resonance experiments. This of course results in a low probability for a favorable collision during the short analysis time ($\sim 10^{-3}$ sec).

It is therefore suggested that the 2% CH_3I dependent on the presence of I_2 is due to the formation of $C_2H_4I^+$ charge complex followed by the bimolecular disproportionation reaction 9. In addition, it is believed that the entirely I_2-dependent C_2H_3I yield is formed by the elimination reaction 8 prior to the formation of $C_2H_4I^+$.

The 4% yield of $CH_2C^{128}I{=}CH_2$ from propylene would appear to be of hot iodine origin due to its

(18) E. W. R. Steacie, "Atomic and Free Radical Reactions," 2nd ed, Reinhold, New York, N. Y., 1954.

extrapolation to zero at unit mole fraction as shown in Figures 6 and 7. However, it is more likely formed by an ion–molecule reaction analogous to that of $C_2H_3{}^{128}I$.

In focussing attention to the large amount of $CH_3{}^{128}I$ found in these experiments it is necessary to consider the possible contributions to the $CH_3{}^{128}I$ yield from reaction pathways not including C_2H_4. The following three mechanisms are of this type

(a) $CH_3{}^{127}I + {}^1n_0 \longrightarrow CH_3{}^{128}I + \gamma$ (1 or more)

(b) $^{128}I + I_2 \longrightarrow {}^{128}I_2 + I$

$^{128}I_2 + (\cdot CH_3)^* \longrightarrow CH_3{}^{128}I + I$

(c) $(^{128}I)^*$ recoil $+ CH_3I \longrightarrow CH_3{}^{128}I + I$

The contribution from case a, failure to bond rupture, has been previously studied.[15] It was found that 1.1% of all recoil ^{128}I produced from CH_3I remains as labeled $CH_3{}^{128}I$. Both organic yields and product distributions have been corrected for failure to bond rupture.

To investigate the next two cases a series of samples containing no ethylene were filled and analyzed. These organic yields (Table II) are negligible when compared to the absolute yield of 10% at zero mole fraction additive. If the CH_3I organic yield is due to case c, then the values in Table II are the upper limit of contribution from that pathway since the incorporation of C_2H_4 into the system would provide competitive reactions for the recoil iodine. The conclusion is that the methyl iodide must be formed by reaction with ethylene.

Table II: Per Cent ^{128}I Stabilized in Organic Combination without Ethylene Present

Additive	Per cent ^{128}I as organic[a]
Helium	1.1
Krypton	1.7
Xenon	1.9

[a] These samples contained 0.1 Torr of I_2, 50.0 Torr of CH_3I, and 710.0 Torr of additive.

In comparing and contrasting the $CH_3{}^{128}I$ curves of helium additive (Figure 1) with that of krypton additive (Figure 2) we find that they both extrapolate to approximately 5% within experimental error. This would ordinarily be indicative of 10% − 5% = 5% due to hot iodine reactions. However, the shapes of the curves are such that for a given mole fraction, the helium additive is reducing the amount of $CH_3{}^{128}I$ more than that by krypton. With xenon additive (Figure 3) the $CH_3{}^{128}I$ yield is not only higher at unit mole fraction additive but is higher for all mole fractions. Clearly this is not the effect that we would expect for moderation of hot iodine species. See Figure 5 showing a composite of the $CH_3{}^{128}I$ curves

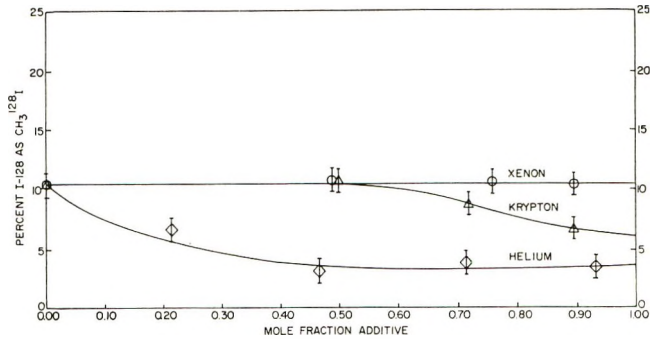

Figure 5. Composite plot from Figures 1, 2, and 3 showing the effect of rare gas additives helium, krypton, and xenon on the formation of $CH_3{}^{128}I$ from C_2H_4.

from Figures 1, 2, and 3. In fact this is entirely the opposite effect one would expect for kinetic energy moderation of hot iodine.[19] Such an effect has not previously been reported.

To summarize, the $CH_3{}^{128}I$ product yield appears to be stabilized by rare gas additives in the sequence Xe > Kr > He. Physical properties that follow this trend are an increase in ionization potential and a decrease in mass.

An increase in ionization potential should not account for the observed trend since the ionization potentials of the rare gases are higher than that of the $CH_3{}^{128}I$ intermediate, precluding the possibility of charge-transfer reactions.

The decrease in mass may account for the observed trend if $CH_3{}^{128}I$ is formed *via* an ion–molecule mechanism. Such reactions are often observed to possess an E^{-n} dependence of reaction cross section due to the kinetic energy E of the energetic ion; $n = 1$ is often found.[20] Such a dependence would be extremely sensitive to the average energy of a reactive I^+ ion. For the rare gas additive reactive system the average I^+ ion's kinetic energy would be lowest for Xe with a correspondingly higher reaction cross section for ion–molecule reactions than would be present with other additives.

There is no direct evidence to support the suggestion that $C_2H_4{}^{128}I^+$ is the precurser to $CH_3{}^{128}I$ formation as in reaction 9. However, there is strong experimental evidence that $CH_3{}^{128}I$ is formed by some ion–molecule reaction instead of hot interaction, and that C_2H_4 is related to its formation. The fact that $C_2H_4{}^{128}I^+$ has been found to be readily formed in ion experiments and may likely be the precursor should provide a sufficient basis to pursue the following discussion

(19) Assuming a "hard-sphere" collision the kinetic theory shows that the energy degradation factor $\Delta E/E = 4Mm/(M + m)^2$ is the fraction of energy lost per collision by the recoiling species. The energy lost is greatest when $M \simeq m$, where M and m are the masses of the colliding entities. Thus, in the iodine system the most efficient kinetic energy moderator should be xenon.

(20) L. Friedman, *Advan. Chem. Ser.*, No. 58, 99 (1966).

concerning its possible formation in these recoil iodine systems.

An additional icr study showed that the ion–molecule reaction

$$CF_3I^+ + C_2H_4 \longrightarrow C_2H_4I^+ + \cdot CF_3 \qquad (10)$$

takes place. It is necessary to recall that I_2^+ has also been confirmed to form this same charge complex while I^+ in its $^3P_2$ ground state does not. In considering the differences between the reactive species I_2^+ and CF_3I^+ and that of unreactive $I^+(^3P_2)$ it seems reasonable to deduce that $I^+(^3P_2)$ has the wrong electronic configuration to form the complex $C_2H_4I^+$. However, I^+ ions are present in the recoiling reaction system also in the excited $^3P_0$, $^3P_1$, and $^1D_2$ electronic states.[2b,21] It may be that one or more of these states are able to enter into a successful collision complex to form the $C_2H_4I^+$ intermediate.

Further evidence in support of this theory is the sharp decrease in yield of $CH_3{}^{128}I$ upon addition of O_2 (Figure 4). The paramagnetism of O_2 enhances spin–orbit interaction in the excited specie and makes possible singlet–triplet transitions.[22] A previous study by Rack and Gordus[21] has shown that the addition of O_2 had no effect on the quenching of $I^+(^1D_2)$ as did Xe. If $I^+(^1D_2)$ state was the initial reactive ion in $CH_3{}^{128}I$ formation, then (a) it would not have been quenched by addition of O_2 (Figure 4); and (b) the addition of xenon (Figure 3) should have sharply lowered the yield. Thus, I^+ in the $^1D_2$ state is not the reactive species. Excited triplet states have also been shown to be quenched by O_2.[23,24] It is likely then that ion–molecule reaction 11 is the initiating step in the $CH_3{}^{128}I$ mechanism.

$$^{128}I^+ (^3P_0 \text{ or } ^3P_1) + C_2H_4 \longrightarrow C_2H_4{}^{128}I^+ \qquad (11)$$

The $CH_3{}^{128}I$ product yield in the propylene system is almost certainly due in part to the same mechanism as that present in the ethylene system. The relative yields are again reversed as compared to what would be expected in a hot atom reaction. That is, the $CH_3{}^{128}I$ yield is greater with krypton additive than that of helium at all mole fraction additive concentrations as shown in Figures 6 and 7. The increase in yield of $CH_3{}^{128}I$ in the propylene system compared to that of ethylene can be explained by the availability of an additional reaction channel with propylene for the formation of $CH_3{}^{128}I$ as shown in

$$^{128}I + CH_3CH{=}CH_2 \longrightarrow CH_3{}^{128}I + \cdot CH{=}CH_2 \qquad (12)$$

Previous researchers[2b,25] have investigated the reactions of (n,γ)-activated ^{128}I with saturated hydrocarbons. An interesting phenomena is found in going from single carbon methane to multicarbon molecules. The organic yield drastically decreases (see Table III). This effect has been explained by consideration of the

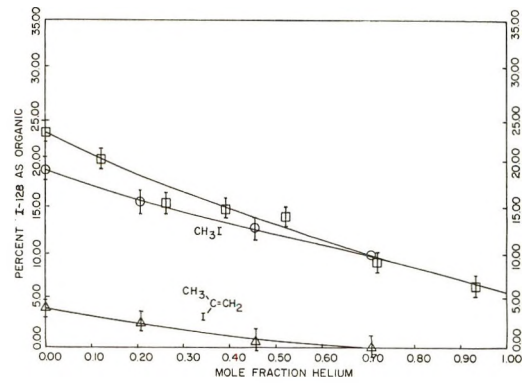

Figure 6. Effect of helium additive on the per cent ^{128}I formed as organic activity due to ^{128}I reactions with C_3H_6: total organic yield, □; absolute yields: CH_3I, ○; $CH_3CI{=}CH_2$, △.

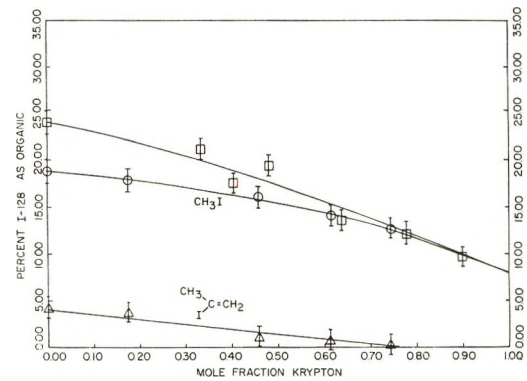

Figure 7. Effect of krypton additive on the per cent ^{128}I formed as organic activity due to ^{128}I reactions with C_3H_6: total organic yield, □; absolute yields: CH_3I, ○; $CH_3CI{=}CH_2$, △.

ionization potentials of the following excited states of I^+[2b,21]

$I(^2P_{1/2}) \longrightarrow I^+(^3P_2)$	10.45 eV
$I^+(^3P_0)$	11.25 eV
$I^+(^3P_1)$	11.33 eV
$I^+(^1D_2)$	12.16 eV

The following exoergic charge-transfer reactions 13 and 14 can take place for C_2H_6 (IP = 11.65 eV)[26] or C_3H_8 (IP = 11.08)[26] but are endoergic for CH_4 due to its higher ionization potential (IP = 12.99)[26]

$$I^+(^1D_2) + C_2H_6 \longrightarrow I + C_2H_6{}^+ \qquad (13)$$

$$I^+(^3P_0, ^3P_1, ^1D_2) + C_3H_8 \longrightarrow I + C_2H_6{}^+ \qquad (14)$$

(21) E. P. Rack and A. A. Gordus, *J. Chem. Phys.*, **36**, 287 (1962).
(22) A. Terenin, *Acta Physicochim. URSS*, **18**, 210 (1943); *Chem. Abstr.*, **38**, 5149 (1944).
(23) R. Livingston and U. S. Rao, *J. Phys. Chem.*, **63**, 794 (1959).
(24) B. Stevens, *Chem. Rev.*, **57**, 439 (1957).
(25) A. A. Gordus and J. E. Willard, *J. Amer. Chem. Soc.*, **79**, 4609 (1957).
(26) K. Watanabe, *J. Chem. Phys.*, **26**, 542 (1957).

Table III: Previous Gas Phase Alkane Studies Using $^{127}I(n,\gamma)^{128}I$-Induced Recoil Iodine

Species studied	Total organic yield with no additive, %	Components	Ionization potential, eV
CH_4[a]	54	CH_3I	12.99
		18% from hot ^{128}I	
		25% from $I^+(^1D_2)$	
		11% from excited iodine atoms or ions in the $^3P_2$, $^3P_1$, $^3P_0$ states	
C_2H_6[b]	3	Not given	11.65
C_3H_8[b]	4	Not given	11.08

[a] Reference 2b. [b] Reference 25.

Neutralization of I^+ is thought to make it less reactive in these low ionization potential systems since ion–molecule reaction modes are no longer available.

However in our current study of ethylene and propylene reactions, high total organic yields of 18 and 24%, respectively, were obtained. A consideration of the low ionization potentials for ethylene (10.52 eV)[26] and propylene (9.73 eV)[26] indicates that the charge-transfer process should also be present in these systems. It was therefore concluded that (1) a new reaction pathway for organic stabilization is present in alkenes; (2) this pathway would most likely be due to iodine ions or radicals attacking the electron-rich double bond; and (3) if it is due to iodine ions, then the reaction rate for the organic product must be faster than that for the charge-transfer deactivation reactions described.

Acknowledgments. We are indebted to Dr. M. L. Gross for his help with the running and interpretation of the ion-cyclotron resonance spectra. We would also like to express our appreciation to Dr. R. L. Ayres for examining this manuscript and offering valuable suggestions.

Paramagnetic Resonance Study of Liquids during Photolysis. XIV. Pyridine, Pyrazine, Pyrimidine, and Pyridazine[1,2]

by Henry Zeldes* and Ralph Livingston

Chemistry Division, Oak Ridge National Laboratory, Oak Ridge, Tennessee 37830 *(Received May 8, 1972)*

Publication costs assisted by the Oak Ridge National Laboratory

Electron paramagnetic resonance measurements of solutions of the radical 1-hydropyridine and of the cation radicals of 1,4-dihydropyrazine, 1,3-dihydropyrimidine, and 1,2-dihydropyridazine have been made. The radicals were made by the reaction of photolytically generated hydroxyisopropyl radical (electron donor) with pyridine, pyrazine, pyrimidine, and pyridazine. Selective deuteration of the cation radical of dihydropyridazine made possible the assignment of the coupling for the hydrogen atoms attached to nitrogens. All couplings and their signs with the exception of the sign of one weakly coupled pair of protons of the hydropyridine radical were assigned from experimental data and MO theory. Values of spin polarization parameters were determined and are discussed. Consistent values of Q^H_{NH} and Q^H_{CH} were found, but not of $Q^N_{N(C_2H)}$ and Q^N_{CN}.

We have been studying electron paramagnetic resonance (epr) spectra of simple short-lived free radicals made by the photolysis of liquids with ultraviolet light. This work has been extended to include heterocyclic compounds.[2,3] This paper reports a study of heterocyclic radicals made by reduction of pyridine, pyrazine, pyrimidine, and pyridazine (Figure 1) in solutions most of which are primarily aqueous. In each case the radical is the one which would result from electron capture followed by protonation of every nitrogen atom. The radicals were produced in solutions near room temperature by the reaction of the parent compounds with $(CH_3)_2\dot{C}OH$ which is known to be a good electron donor.[3–6] The donor radical was made[7] by the

(1) Research sponsored by the U. S. Atomic Energy Commission under contract with Union Carbide Corporation.

(2) Part XIII: J. K. Dohrmann and R. Livingston, *J. Amer. Chem. Soc.*, **93**, 5363 (1971).

(3) J. K. Dohrmann, R. Livingston, and H. Zeldes, *ibid.*, **93**, 3343 (1971).

FIRST CLASS
PERMIT No. 1411-R
WASHINGTON, D. C.

BUSINESS REPLY MAIL
No Postage Stamp Necessary if Mailed in the United States

— POSTAGE WILL BE PAID BY —

AMERICAN CHEMICAL SOCIETY
1155 Sixteenth Street, N.W.
Washington, D.C. 20036

ATTN: J. MEDINA

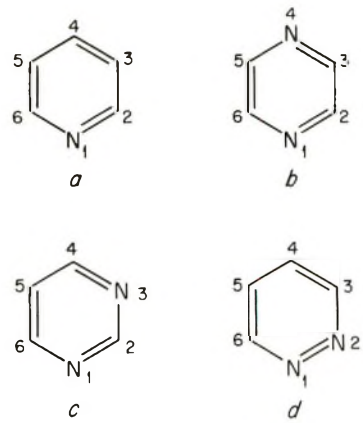

Figure 1. Structural formulas of nitrogen heterocyclic compounds: (a) pyridine, (b) pyrazine, (c) pyrimidine, (d) pyridazine. Radicals described in the text have hydrogen atoms attached to the nitrogen atoms. The radical derived from pyridine is neutral; the others have one unit of positive charge.

reaction of photolytically excited acetone with isopropyl alcohol.

$$(CH_3)_2CO^* + (CH_3)_2CHOH \longrightarrow 2(CH_3)_2\dot{C}OH \quad (1)$$

Radicals of nitrogen heterocyclic compounds have been the subject of many investigations by epr.[8] These provide improved relationships between the hyperfine couplings and π-electron spin density. In contrast to most of these studies, the radicals described here have a hydrogen atom attached to every ring atom allowing an estimate of π-electron spin density ρ^{π}_i at *every* ring atom position i through the well known McConnell-type relationship[9]

$$a_i^{H} = Q^{H}_{XH}\rho^{\pi}_i \quad (2)$$

where a_i^{H} is the hydrogen coupling at ring position i and X is C or N depending upon whether carbon or nitrogen is the atom at ring position i. Values of the spin polarization parameters Q^{H}_{NH} and Q^{H}_{CH} are determined using only the hydrogen couplings of the four radicals, relation 2, and the requirement that the sum of spin density on all atoms of a radical is unity; the distribution of spin density is not needed. Although MO calculations were made, they are used only to help in assigning signs and positions for the hydrogen couplings. Since spin densities can be deduced for every ring position without the usual uncertainties of MO calculations, these radicals are especially valuable for studying nitrogen couplings. The nitrogen couplings are expected to be given by a relation similar to the one developed by Karplus and Fraenkel[10] for ^{13}C couplings. With this model the coupling depends upon π-electron spin density on adjacent atoms as well as on nitrogen itself.

Experimental Section

The epr spectrometer operated at about 9.5 GHz and used 100-kHz field modulation. The experimental arrangement and method of calculating g values have already been described.[11] The solutions were freed of dissolved oxygen by purging with gaseous helium and were photolyzed near room temperature as they slowly flowed through a flat silica cell positioned inside the microwave cavity of the spectrometer. Temperatures are given for the solutions shortly after leaving the cavity. The uv source was a high-pressure mercury arc, Philips Type SP500W. All chemicals were used as purchased. The pyridine (Analytical Reagent) was from Mallinckrodt. The pyrazine, pyrimidine, and pyridazine were from Pfaltz and Bauer. Acetone and isopropyl alcohol were also present in all solutions in order to form $(CH_3)_2\dot{C}OH$ upon photolysis.

Two computer programs, which are still undergoing minor refinements, were used in analyzing the data. The hyperfine energies are calculated to second-order perturbation theory. One program finds the best values of couplings and of g from the measured resonance fields of lines using a least-squares criterion. This program may also be used to obtain an ordered printout of magnetic fields of lines together with their strengths and nuclear magnetic quantum numbers where the appropriate microwave frequency and all parameters defining the spin Hamiltonian are supplied. The second program simulates spectra. A Lorentzian derivative line shape with the same width for each line of a spectrum was used for this work where the tail of a line extends to 15 peak-to-peak derivative widths.

The general procedure followed was first to make a high-resolution recording of the spectrum and then to make accurate measurements of all or of most of the resolved lines. The previously recorded spectrum made it easily possible to identify lines as they were measured. The field was adjusted manually when it was near the center of a line until the center was found as judged from the recorder. Then the frequency of the proton nmr field probe and the spectrometer frequency were read with an electronic counter (Hewlett–Packard Model 5245L). A small field-offset correction was made

(4) A. L. Buley and R. O. C. Norman, *Proc. Chem. Soc.*, (*London*), 225 (1964).

(5) R. O. Norman and R. J. Pritchett, *J. Chem. Soc. B*, 378 (1967).

(6) H. Zeldes and R. Livingston, *J. Phys. Chem.*, **74**, 3336 (1970).

(7) H. Zeldes and R. Livingston, *J. Chem. Phys.*, **45**, 1946 (1966).

(8) See the following and references therein: (a) E. W. Stone and A. H. Maki, *ibid.*, **39**, 1635 (1963); (b) B. L. Barton and G. K. Fraenkel, *ibid.*, **41**, 1455 (1964); (c) J. C. M. Henning, *ibid.*, **44**, 2139 (1966); (d) C. L. Talcott and R. J. Myers, *Mol. Phys.*, **12**, 549 (1967); (e) T. Kubota, K. Nishikida, H. Miyazaki, K. Iwatani, and Y. Oishi, *J. Amer. Chem. Soc.*, **90**, 5080 (1968); (f) A. R. Buick, T. J. Kemp, G. T. Neal, and T. J. Stone, *J. Chem. Soc. A*, 1609 (1969); (g) M. D. Sevilla, *J. Phys. Chem.*, **74**, 805 (1970); (h) H. Taniguchi, *ibid.*, **74**, 3143 (1970).

(9) (a) H. M. McConnell, *J. Chem. Phys.*, **24**, 632, 764 (1956); (b) J. R. Bolton, "Radical Ions," E. T. Kaiser and L. Kevan, Ed., Interscience, New York, N. Y., 1968, Chapter 1.

(10) M. Karplus and G. K. Fraenkel, *J. Chem. Phys.*, **35**, 1312 (1961).

(11) (a) R. Livingston and H. Zeldes, *ibid.*, **44**, 1245 (1966); (b) *ibid.*, **47**, 4173 (1967).

Table I: Experimental Results

Radical[a]	Solvent	g	Hyperfine coupling, G				
Hydropyridine	2-Propanol[b]	2.00290	$a_1^N = 5.88$	$[a_1^H] = -3.39$	$[a_2^H] = -5.88$	$[a_3^H] = \pm 0.98$	$[a_4^H] = -11.61$
	Acetone[c]	2.00294	$a_1^N = 5.88$	$[a_1^H] = -3.28$	$[a_2^H] = -5.94$	$[a_3^H] = \pm 1.00$	$[a_4^H] = -11.63$
	Water[d]	2.00296	$a_1^N = 5.89$	$[a_1^H] = -3.45$	$[a_2^H] = -5.89$	$[a_3^H] = \pm 0.91$	$[a_4^H] = -11.55$
Dihydropyrazine$^+$	Water[e]	2.00325	$a_1^N = 7.47$	$a_1^H = -8.07$	$a_2^H = -3.17$		
Dihydropyrimidine$^+$	Water[f]	2.00289	$a_1^N = 1.34$	$[a_1^H] = -2.49$	$[a_2^H] = 0.35$	$[a_4^H] = -13.08$	$[a_5^H] = 2.42$
Dihydropyridazine$^+$	Water[g]	2.00325	$a_1^N = 7.81$	$a_1^H = -6.53$	$[a_3^H] = -0.92$	$[a_4^H] = -5.80$	

[a] See Figure 1 for structural formulas of parent compounds. The symbols a_i^X for couplings which could not be assigned to positions in the radicals by experimental data alone are placed in brackets. See text for the assignment of these positions and also for the assignment of signs. [b] Pyridine (94 ml) and 65 ml of acetone per liter of isopropyl alcohol solution at 35°. [c] Pyridine (69 ml) and 94 ml of isopropyl alcohol per liter of acetone solution at 37°. [d] Pyridine (38 ml), 180 ml of acetone, and 180 ml of isopropyl alcohol per liter of aqueous solution at 32°. [e] Pyrazine (2 g), 50 ml of acetone, 50 ml of isopropyl alcohol, and 2 ml of 1 *N* HCl per liter of aqueous solution at 32°. [f] Pyrimidine (1.8 g), 97 ml of acetone, 97 ml of isopropyl alcohol, and 8 ml of 1 *N* HCl per liter of aqueous solution at 33°. [g] Pyridazine (2.6 ml), 111 ml of acetone, 111 ml of isopropyl alcohol, and 207 ml of 1 *N* HCl per liter of aqueous solution at 32°.

for the field probe. The resonance fields were normalized to a single microwave frequency. It was possible to calculate g and the hyperfine couplings by the method of least squares after a spectrum closely resembling the experimental spectrum was found by simulation with trial parameters. The computer program requires as input the positions of measured lines in the spectrum of ordered lines. The g values determined this way have estimated error limits of ± 0.00004 due mainly to the irreproducibility of the off-set correction for the field probe. The hyperfine couplings have error limits of ± 0.02 G unless indicated otherwise.

Results and Discussion

Pyridine. The radicals made by the reduction of pyridine were formed by the photolysis of solutions of pyridine containing acetone and isopropyl alcohol (see footnotes in Table I for the compositions of solutions). Measurements were made in three media: acetone-rich, isopropyl alcohol-rich, and water-rich solutions. In working with pyridine it was necessary to remove the sample cell every few hours to clean out a yellow paramagnetic deposit formed by photolysis. The rate formation of the deposit was lower at lower concentrations of pyridine, but the concentration was kept high enough to hold the concentration of the donor radical $(CH_3)_2\dot{C}OH$ just below a detectable level. In the isopropyl alcohol solution and in the water solution, a well-resolved 60-line spectrum was seen. A 108-line spectrum was expected for this radical, but the number was reduced to 60 because of the accidental equality in the absolute values of the couplings of the nitrogen atom a_1^N and of a pair of equivalent hydrogen atoms a_2^H. The subscript on a_i^X gives the ring position of atom X as defined by Figure 1. The parameters for these two solutions were evaluated with the assumption that a_1^N and a_2^H are numerically equal. There is probably error on this account for these two couplings, but the error is small compared to the peak-to-peak derivative line width of roughly 0.1 G.

In the acetone solution additional partially resolved splittings were seen reflecting the inequality of the absolute values of a_1^N and a_2^H. Figure 2 shows a little more than half of (a) the experimental spectrum and of (b) the final simulated spectrum for an acetone solution of pyridine and isopropyl alcohol. Measurements were made of 56 lines, some of which were not well resolved. After a least-squares calculation to determine values for g and the couplings, the back-calculated fields agreed with measured values within 0.025 G. However, the simulation using those parameters was poor in that it did not show the smallest, partially resolved splittings. The parameters had errors due to the use of data from partially resolved lines. The values of some of the couplings were then changed slightly to obtain an improved simulation and, it is believed, greater accuracy. This was done with the help of the printout of lines and their associated nuclear magnetic quantum numbers. For small couplings the rate of change of a computed line position when a coupling value is changed is given by the corresponding magnetic quantum number. The magnetic quantum numbers made it possible in this case to determine quantitatively how to change parameters in such a way as to obtain a better simulation as judged both by the appearance of the simulation and the measurements. The value of $|a_4^H|$ was decreased by 0.03 G, $|a_2^H|$ increased by 0.03 G, and $|a_1^N|$ decreased by 0.01 G. The parameters determined this way for the acetone solution as well as the parameters for the other solutions are shown in Table I. The simulation in Figure 2 was made with a peak-to-peak width of 0.062 G.

Pyrazine. The radical derived from pyrazine was measured in an aqueous solution which was slightly acidified. The spectrum is not shown, as it had been

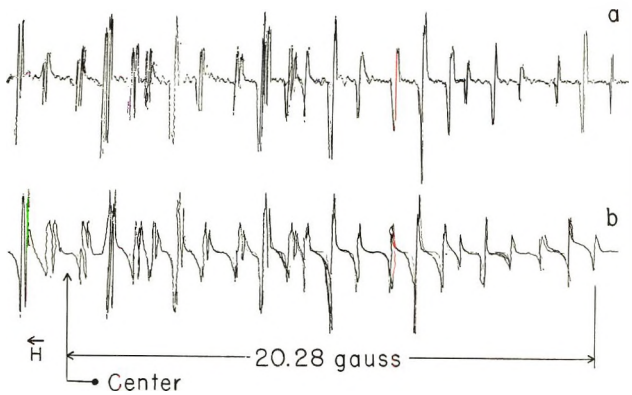

Figure 2. Observed (a) and simulated (b) spectrum of radical derived from pyridine in a solution containing 69 ml of pyridine and 94 ml of isopropyl alcohol per liter of acetone solution at 37°. The simulated lines do not appear to be accurately at the observed line positions, partly because the experimental field display is somewhat nonlinear and mainly because the length of the simulation in inches was inadvertently set too small.

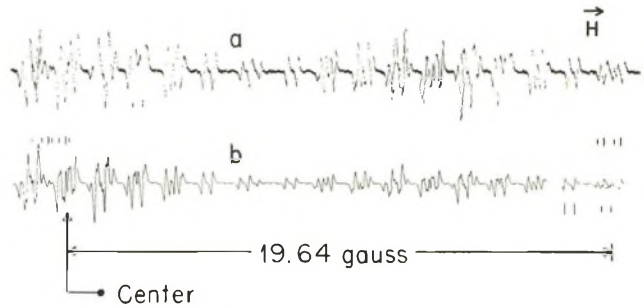

Figure 3. Observed (a) and simulated (b) spectra of the radical derived from pyrimidine and of $(CH_3)_2\dot{C}OH$. The stick lines below the simulation locate the four highest field lines of the radical derived from pyrimidine while those above locate lines of $(CH_3)_2\dot{C}OH$ which fall in the illustrated region of field. The heights of stick lines are the same as peak-to-peak heights of the derivative lines of the simulation. The solution contains 1.8 g of pyrimidine, 97 ml of acetone, 97 ml of isopropyl alcohol, and 8 ml of 1 *N* HCl per liter of aqueous solution at 33°.

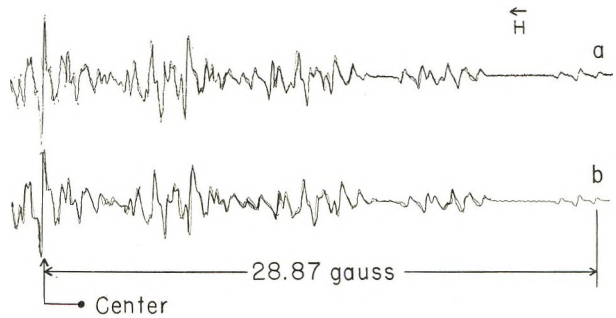

Figure 4. Observed (a) and simulated (b) spectrum of radical derived from pyridazine. The solution contains 2.6 ml of pyridazine, 111 ml of acetone, 111 ml of isopropyl alcohol, and 207 ml of 1 *N* HCl per liter of aqueous solution at 32°.

studied previously.[8b,12] In the present work there was a very strong spectrum of seemingly 69 well-resolved lines, all of which were measured. In analyzing the spectrum it became evident that there are 75 lines, 6 of which are accidentally in coincidence with other lines. After a least-squares calculation, most of the back-calculated line positions agreed with measurements within 0.01 G. The observed line width was about 0.1 G.

The absolute values of the hyperfine couplings found in this work (Table I) for an aqueous solution are $a_1^N = 7.47$ G, $a_1^H = 8.07$ G, and $a_2^H = 3.17$ G. These may be compared with corresponding values in the literature: 7.60, 8.30, and 3.26 G for a 50% H_2SO_4–H_2O solution;[12] 7.40, 7.94, and 3.13 G for an *N*,*N*-dimethylformamide (DMF) solution containing 10 drops of 70% perchloric acid per 25 ml of DMF;[8b] and 7.47, 7.93, and 3.16 G in 95% ethanol containing about 2 ml of concentrated HCl per 8 ml of ethanol.[8b]

Pyrimidine. The radical derived from pyrimidine was studied in an acidified, aqueous solution. The observed spectrum is shown in Figure 3a. This study was done with a limited quantity of pyrimidine; not enough was present to eliminate lines of the donor radical. Measurements were made of 55 lines of the cation radical of dihydropyrimidine and 7 lines of $(CH_3)_2\dot{C}OH$. Parameters of both radicals were then found by a least-squares calculation. Although the back-calculated line positions agreed with the measurements in most cases to about 0.01 G, a simulation with those parameters did not show the small, partially resolved splitting observed for many pairs of lines. This was due to the use of data from partially resolved lines. There were not enough resolved lines to determine all the parameters, since proton couplings 1 and 5 are nearly equal. The least-squares fit with unresolved lines gave very good approximate values for proton couplings 1 and 2 and final values for the remaining parameters. The simulation was then improved by increasing $|a_1^H|$ by 0.007 G and by decreasing $|a_5^H|$ by 0.014 G. The simulation with the final values for g and the couplings and using a peak-to-peak line width of 0.066 G is shown in Figure 3b. The stick lines above the simulation locate lines of $(CH_3)_2\dot{C}OH$ present in the illustrated region, and the stick lines below the simulation locate the four highest field lines of the cation radical of dihydropyrimidine.

Pyridazine. The radical derived from pyridazine was also studied in an acidified, aqueous solution. The observed spectrum is shown in Figure 4a. The line width was considerably greater than it was for the other radicals. Measurements were made of 66 lines, not all of which were well resolved. The better resolved lines were weighted more heavily in calculating

(12) J. R. Bolton, A. Carrington, and J. dos Santos-Veiga, *Mol. Phys.*, 5, 465 (1962).

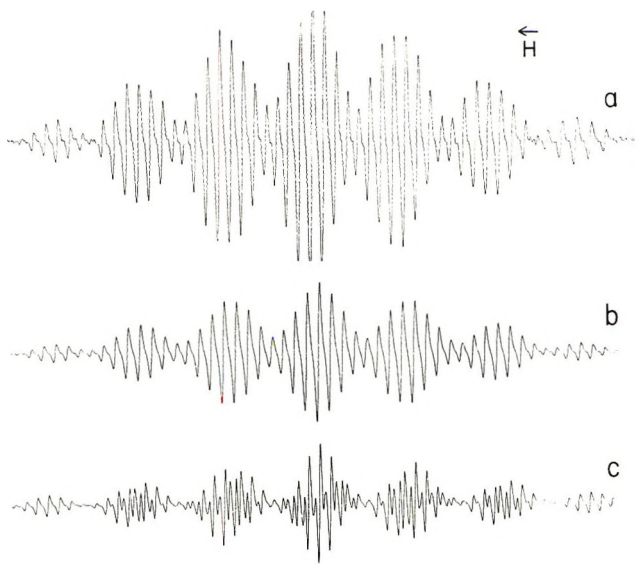

Figure 5. Observed (a) and simulated (b and c) spectra of radical derived from pyridazine in a solution containing 2.7 ml of pyridazine, 112 ml of acetone, 112 ml of isopropyl alcohol, and 17 ml of concentrated HCl per liter of D_2O solution at 29°. The simulations are with couplings determined in a similar solution containing H_2O instead of D_2O. For simulation b it is assumed that the two H atoms of the radical having $|a^H| = 6.53$ G are replaced by two D atoms. For simulation c it is assumed that the two H atoms of the radical having $|a^H| = 5.80$ G are replaced by two D atoms.

the parameters. The back-calculated line positions agreed with measurements to about 0.01 G for the well-resolved lines. The simulation shown in Figure 4b was made with the parameters found by the least-squares calculation and using a peak-to-peak line width of 0.19 G.

In order to assign hydrogen couplings to ring positions for the radical derived from pyridazine, it was necessary to also study the radical in a similar solution in which most of the H_2O was replaced by D_2O. The problem was to determine which of the two larger hydrogen splittings (see Table I) 6.53 or 5.80 G is for the hydrogen atoms bonded to nitrogens. These are expected to be the only exchangeable hydrogens. Figure 5 shows a, the observed spectrum using D_2O, and two simulations b and c. For b it was assumed that the two H atoms with splittings of 6.53 G were replaced by two D atoms, and for c it was assumed that the two H atoms with splittings of 5.80 G were replaced by D atoms. The g value and couplings used in each simulation were values determined by the measurements in H_2O solution. A line width of 0.19 G was used, which is the same as was used for the H_2O solution. It is clear from the figure that the correct choice is b. Measurements of some of the outermost lines also confirmed this, although there seemed to be a very small change in couplings in the two different media.

Assignment and Signs of Couplings. There is ambiguity in the assignment of couplings for all radicals except the cation radical of dihydropyrazine. This ambiguity was removed by making approximate calculations of spin density and by accepting the validity of the McConnell eq 2. Calculations of spin density were made using the Hückel method and also the McLachlan procedure[13] for introducing configuration interaction. Hückel parameters were used which Barton and Fraenkel[8b] had found to give good over-all agreement with splittings for cations of pyrazine, phenazine, and quinoxaline. These parameters are $h_N = 1.5$, $k_{CN} = 1.0$, and $\delta h_N = 0.3$. The Coulomb-integral parameter for the nitrogen atom h_N is defined by $\alpha_N = \alpha_C + h_N\beta$, where α_X is the Coulomb integral for atom X, and β is the resonance integral for an aromatic carbon–carbon bond. The carbon–nitrogen resonance-integral parameter k_{CN} is defined by $\beta_{CN} = k_{CN}\beta$ where β_{CN} is the carbon–nitrogen resonance integral. The auxiliary inductive parameter δ modifies the Coulomb integral $\alpha_{C'}$ for a carbon atom bonded to a nitrogen atom and is defined by $\alpha_{C'} = \alpha_C + \delta h_N\beta$. The McLachlan calculation was made with the same values of h_N, k_{CN}, and δ and with the value 1.2 for the McLachlan parameter λ. The calculated spin densities are shown in Table II. A comparison of the ordering of the calculated absolute values of spin density in Table II with the experimental couplings for hydrogen of Table I is the basis for assigning ring positions for

Table II: Calculated and Experimental Spin Densities

Radical	Position	Hückel calculation[a]	McLachlan calculation[b]	—Experimental— Choice A[c]	Choice B[d]
Hydropyridine[e]	1	0.235	0.231	0.116	0.127
	2,6	0.226	0.288	0.242	0.204
	3,5	0.015	−0.095	−0.038	0.032
	4	0.283	0.382	0.475	0.401
Dihydropyrazine$^+$	1,4	0.232	0.263	0.272	0.298
	2,3,5,6	0.134	0.118	0.114	0.101
Dihydropyrimidine$^+$	1,3	0.121	0.090	0.084	0.092
	2	0.000	−0.041	−0.012	−0.012
	4,6	0.379	0.497	0.465	0.456
	5	0.000	−0.133	−0.086	−0.084
Dihydropyridazine$^+$	1,2	0.259	0.314	0.220	0.241
	3,6	0.103	0.055	0.038	0.036
	4,5	0.137	0.131	0.242	0.224

[a] Hückel MO calculation with $h_N = 1.5$, $k_{CN} = 1.0$, $\delta h_N = 0.3$. [b] McLachlan MO calculation with $\lambda = 1.2$ and parameters used in the Hückel MO calculation. [c] Calculated from experimental H couplings in aqueous solution and the McConnell relation using $Q^H_{NH} = -29.7$; and $Q^H_{CH} = -24.32$, -27.75, -28.11, and -24.01 respectively for hydropyridine, dihydropyrazine$^+$, dihydropyrimidine$^+$, and dihydropyridazine$^+$. [d] Calculated from experimental H couplings in aqueous solution and the McConnell relation using $Q^H_{NH} = -27.1$; and $Q^H_{CH} = -28.81$, -31.34, -28.67, and -25.96 respectively for hydropyridine, dihydropyrazine$^+$, and dihydropyrimidine$^+$, and dihydropyridazine$^+$. [e] The couplings in water solution are used.

(13) A. D. McLachlan, *Mol. Phys.*, 3, 233 (1960).

hydrogen couplings. There is no ambiguity for the nitrogen couplings. The experimental spin densities of Table II will be discussed later.

The signs of the couplings of Table I may be assigned using McConnell's relation 2, the signs of the computed spin densities (Table II), and the signs of the Q values as given in the literature. The value for Q^{H}_{CH} is well known[14] to depend upon the charge on the carbon atom and also hybridization. The value -27.0 G is suitable[9b] for neutral hydrocarbon free radicals at positions where two carbon atoms and a hydrogen atom are bonded to the trigonal carbon atom of interest. In analyzing epr data for methyl-substituted dihydropyrazine cations and related radicals, Barton and Fraenkel[8b] used the value -23.7 G which is the value calculated for a CHC_2 fragment.[10] Using this value, Barton and Fraenkel determined that $Q^{H}_{NH} = -33.7$ G for the methyl-substituted dihydropyrazine cations and related radicals. In line width studies of the radical cation of dihydropyrazine, Barton and Fraenkel[15] were able to determine that the nitrogen coupling a_N is positive, that the proton coupling a^{H}_{NH} of the protons bonded to the nitrogen atoms is negative, and that Q^{H}_{NH} is negative.

Noting that Q^{H}_{CH} and Q^{H}_{NH} are negative, it was possible to use the approximate values for spin density (McLachlan values of Table II) to assign signs of couplings in most instances. For the cation radical of dihydropyrimidine, Hückel calculations give a node at carbons 2 and 5. However, the McLachlan calculation gives small amounts of negative spin density at these locations, and accordingly it is assumed that a_2^{H} and a_5^{H} are positive. The sign of the coupling for the 3,5 positions of the hydropyridine radical is considered unknown; Hückel and McLachlan calculations give small amounts of spin density but with opposite signs. Table I summarizes the experimental findings and assignments of signs and positions for the couplings.

NH- and CH-Hydrogen Couplings. An independent determination of Q^{H}_{NH} and Q^{H}_{CH} can be made from the hydrogen couplings of Table I, McConnell's relation 2, and the equation for the conservation of spin density for a radical

$$\sum_i \rho^{\pi}_i = 1 \qquad (3)$$

where the summation is over all atoms of the π-electron system. It is only assumed that eq 2 and 3 are valid, that the Q's are constant for the four radicals studied, and that couplings and their signs are assigned properly. Equations 2 and 3 are used to derive for a given radical

$$\left(\sum_i a^{H}_{N_iH}\right)/Q^{H}_{NH} + \left(\sum_i a^{H}_{C_iH}\right)/Q^{H}_{CH} = 1 \qquad (4)$$

A plot of the sum of the couplings of hydrogen atoms attached to nitrogen *vs.* the sum of those attached to carbon for each radical should give a straight line and the intercepts on the nitrogen and carbon axes respectively are Q^{H}_{NH} and Q^{H}_{CH}. This plot is shown in Figure 6 for the four radicals. Points 1A and 1B are for the two choices of sign for a_3^{H} ($= a_5^{H}$) for the hydropyridine radical (Table I). Choice A is for the positive sign. The two straight lines result from least-squares calculations for choice A and for choice B. The results in units of gauss for the two ways respectively are $Q^{H}_{NH} = -29.7 \pm 4.3$, $Q^{H}_{CH} = -26.1 \pm 1.9$; and $Q^{H}_{NH} = -27.1 \pm 2.1$, $Q^{H}_{CH} = -28.6 \pm 1.3$. It is clear from the figure as well as the standard errors that choice B is just slightly better. It is not enough better to permit one to decide which is correct. These are reasonable Q values. If Barton and Fraenkel[8b] had used the value -28.6 (our value for choice B) for Q^{H}_{CH}, their value of Q^{H}_{NH} would have been -28.2. Although these Q values are reasonable, the standard errors are certainly large compared to the experimental errors showing that these Q values vary somewhat from one radical to another. Nonetheless, they are believed to provide much better estimates of spin density than the theoretical estimates.

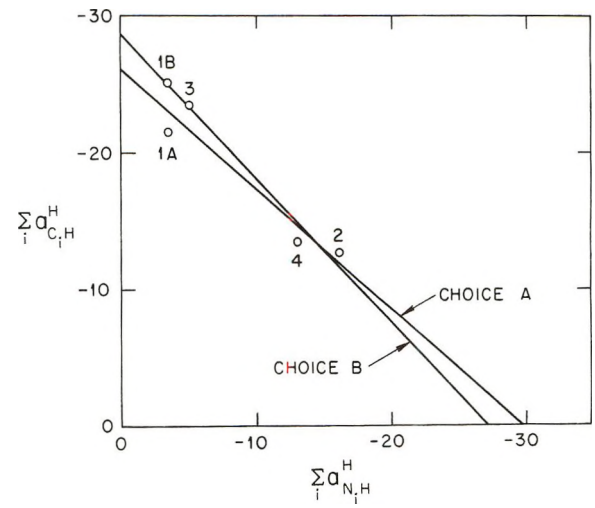

Figure 6. Plot of the sum of the couplings of all H atoms bonded to C *vs.* the sum of the couplings of all H atoms bonded to N for (1A) the hydropyridine radical taking the sign of a^{H}_3 positive, (1B) the hydropyridine radical taking the sign of a^{H}_3 negative, (2) the cation radical of dihydropyrazine, (3) the cation radical of dihydropyrimidine, and (4) the cation radical of dihydropyridazine. The straight line labeled choice A is for a least-squares calculation using points 1A, 2, 3, and 4; that labeled choice B is with points 1B, 2, 3, and 4. The intercepts on the axes of ordinates and abscissas respectively give the calculated values of Q^{H}_{CH} and Q^{H}_{NH}.

The values of Q^{H}_{CH} determined above were changed slightly for each radical studied in order to obtain Q values for which eq 3 would be satisfied for each radical. For each radical the value of Q^{H}_{NH} determined

(14) See ref 8b and 9b and references therein.

(15) B. L. Barton and G. K. Fraenkel, *J. Chem. Phys.*, **41**, 695 (1964).

by the least-squares calculation was retained. Then a different value of Q^{H}_{CH} was calculated for each radical by use of eq 4. The values thus calculated are given in footnotes *c* and *d* of Table II. Using these Q values and the hydrogen couplings, "experimental" spin densities were calculated for the four radicals for both choices A and B. These are shown in Table II.

Nitrogen Couplings. The coupling for nitrogen should be described by a relation similar to that developed by Karplus and Fraenkel[10] for ^{13}C couplings. A term of the form $Q^{N}_{CN}\rho^{\pi}_{C_i}$ is present for each carbon i bonded to the nitrogen atom. This represents the contribution to the nitrogen coupling of π-electron spin density $\rho^{\pi}_{C_i}$ on a contiguous carbon. There are many determinations of Q^{N}_{CN} in the literature[8] mostly from data on anion radicals. Many of the determinations depend upon the reliability of molecular orbital calculations of spin density in one or more positions. Values of Q^{N}_{CN} ranging from 9.1 to -6.66 G have been reported. Two determinations which do not depend upon molecular orbital calculations for spin densities seem especially reliable. One[8d] is the value -1.7 G which was determined from the coupling constants for the radical anions of pyridine, pyrazine, and pyrimidine. The other[8b] is the value 2.62 G which was found for the cation radical of dihydropyrazine and its methyl-substituted derivatives. Barton and Fraenkel[8b] suggest that Q^{N}_{CN} is quite sensitive to structural factors and possibly also to the charge distribution.

Our results for the hydropyridine radical, and the cation radicals of dihydropyrazine and dihydropyrimidine, were also expected to provide reliable Q values describing the nitrogen coupling provided the Q values are constant for all three radicals. The Karplus–Fraenkel[10] relation for these three radicals takes the form

$$a^{N} = Q^{N}_{N(C_2H)}\rho^{\pi}_{N} + Q^{N}_{CN}\sum_{adj}\rho^{\pi}_{C_i} \qquad (5)$$

where the summation is over the carbon atoms bonded to the nitrogen atom, where

$$Q^{N}_{N(C_2H)} = S^{N} + 2Q^{N}_{NC} + Q^{N}_{NH} \qquad (6)$$

and ρ^{π}_{N} is π-electron spin density on the nitrogen atom. The term S^{N} gives the contribution which results from polarization of the 1s electrons of nitrogen, and Q^{N}_{NC} and Q^{N}_{NH} give the contributions which result from polarizations of the N–C and N–H bonds. From eq 2 for a hydrogen atom bonded to nitrogen and eq 5, one can write

$$\frac{a^{N}}{a^{H}_{NH}} = \frac{Q^{N}_{N(C_2H)}}{Q^{H}_{NH}} + \frac{Q^{N}_{CN}}{Q^{H}_{NH}}R \qquad (7)$$

where

$$R = \left(\sum_{adj}\rho^{\pi}_{C_i}\right)/\rho^{\pi}_{N} \qquad (8)$$

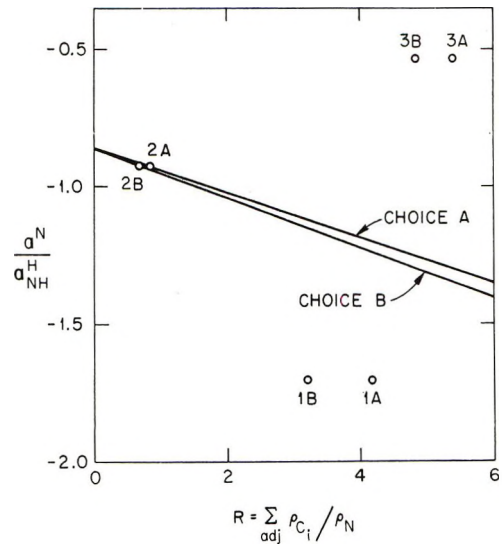

Figure 7. Plot of a^{N}/a^{H}_{NH} *vs.* R, the ratio of the sum of spin density on carbons adjacent to the nitrogen atom to the spin density on the nitrogen atom, for (1) the hydropyridine radical, (2) the cation radical of dihydropyrazine, and (3) the cation radical of dihydropyrimidine for choices A and B. Choice A is for the positive sign for the coupling a_3^{H} of the hydropyridine radical; choice B is for the negative sign. The straight lines are drawn using criteria described in the text.

If a^{N}/a^{H}_{NH} for each radical is plotted against "experimental" R, the ratio of the sum of experimental spin density on contiguous carbons to that on the nitrogen atom, there should result a straight line with slope Q^{N}_{CN}/Q^{H}_{NH} and intercept $Q^{N}_{N(C_2H)}/Q^{H}_{NH}$. Since Q^{H}_{NH} is known, this would determine Q^{N}_{CN} and $Q^{N}_{N(C_2H)}$. This plot for choices A and B is shown in Figure 7. Values of experimental R and of a^{N}/a^{H}_{NH} are in Table III. Clearly a straight line can not reasonably be passed through these points for either choice; $Q^{N}_{N(C_2H)}$ or Q^{N}_{CN} or both are not at all constant for these radicals.

Moreover, using results of Barton and Fraenkel,[8b] it can be shown that the values of $Q^{N}_{N(C_2H)}$ and Q^{N}_{CN} for both the hydropyridine radical and the cation radical of

Table III: Nitrogen and NH–Proton Couplings and Derived[a] Values of Q^{N}_{CN}

Radical	Choice	a^{N}, G	a^{H}_{NH}, G	a^{N}/a^{H}_{NH}	R^{b}	Q^{N}_{CN}
Hydropyridine[c]	A	5.89	−3.45	−1.707	4.17	6.06
	B	5.89	−3.45	−1.707	3.21	7.12
Dihydro-pyrazine^{+}	A	7.47	−8.07	−0.925	0.84	2.44
	B	7.47	−8.07	−0.925	0.68	2.44
Dihydro-pyrimidine^{+}	A	1.34	−2.49	−0.537	5.40	−1.75
	B	1.34	−2.49	−0.537	4.83	−1.83

[a] For choice A use $Q^{H}_{NH} = -29.7$ and $Q^{N}_{N(C_2H)} = 25.41$; for choice B use $Q^{H}_{NH} = -27.1$ and $Q^{N}_{N(C_2H)} = 23.41$. See text for discussion. [b] $R = (\Sigma_{adj}\rho_{C_i})/\rho_{N}$. [c] The couplings in water solution are used.

dihydropyrimidine are not the same as for the cation radical of dihydropyrazine. Values of Q for the latter radical were derived from the work of Barton and Fraenkel[8b] on the cation radicals of dihydropyrazine and its methyl-substituted derivatives. They determined that for these radicals $Q^{N}_{N(C_2H)}$ is given accurately by $Q^{N}_{N(C_2H)} = -0.7674Q^{H}_{NH} + 2.6164$. This expression was then used to derive values of $Q^{N}_{N(C_2H)}$ appropriate for choices A and B using our values of Q^{H}_{NH}. These are given in footnote *a* of Table III. Using eq 7 one can now calculate Q^{N}_{CN}. The straight lines for choices A and B drawn in Figure 7 are predicted by these Q values for the cation radical of dihydropyrazine, and would be expected to pass through the data points for radicals having the same Q values. The data points for both the hydropyridine radical and the radical cation of dihydropyrimidine are far from these lines.

If it is assumed that $Q^{N}_{N(C_2H)}$ is a good constant, then one can compute a value for Q^{N}_{CN} for each of the three radicals described by eq 5. This is done just as it was done for the radical cation of dihydropyrazine using the values of $Q^{N}_{N(C_2H)}$ given in footnote *a* of Table III. These values are given in Table III. As expected, the values of Q^{N}_{CN} vary greatly from radical to radical. It is interesting that R is relatively large for both the hydropyridine radical and the radical cation of dihydropyrimidine, and that these radicals have the extreme values found for a^{N}/a^{H}_{NH}. Since R is large, the ratio a^{N}/a^{H}_{NH} should be sensitive to the value of Q^{N}_{CN}. This suggests that it may indeed be mainly Q^{N}_{CN} which varies from radical to radical. Further work will be required to determine whether the values of Q^{N}_{CN} in Table III are correct or whether $Q^{N}_{N(C_2H)}$ is also not a good constant for these radicals. This finding is in contrast to that of Talcott and Myers[8d] who found that Q^{N}_{CN} is a good constant for the anion forms of the same radicals.

Values of g. The g values (Table I) for the N-heterocyclic radicals reported here are larger than typical values for aromatic hydrocarbon radicals. For instance, values for the cation and anion radicals of anthracene are 2.002565 and 2.002709, respectively,[16] and the value for the anion radical of benzene is 2.002850,[16] whereas the smallest value reported here is 2.00289 for the cation radical of dihydropyrimidine. It may be significant that both the g value and the spin density on nitorgens are higher for the cation radicals of dihydropyridazine and dihydropyrazine than for the hydropyridine radical and the cation radical of dihydropyrimidine.

(16) B. G. Segal, M. Kaplan, and G. K. Fraenkel, *J. Chem. Phys.*, 43, 4191 (1965).

Photochemistry of Phenylcyclobutane

by P. Autard

Department of Chemistry, The University of Texas at Austin, Austin, Texas 78712[1] *(Received May 15, 1972)*

Publication costs assisted by The University of Texas at Austin

The photochemistry of phenylcyclobutane has been investigated in the gas phase. On excitation in the 0–0 band, the following quantum yields were obtained: fluorescence, 0.28; formation of styrene, 0.24; formation of ethylene, 0.43; formation of *cis*-1-phenyl-2-methylcyclopropane, 0.018; formation of *trans*-1-phenyl-2-methylcyclopropane, 0.023. Fluorescence and product formation, quenching experiments, and the fact that they do not give an unambiguous answer as to the nature of the state from which phenylcyclobutane dissociation occurs are discussed.

Introduction

Unlike that of phenylalkylcyclopropanes,[2-9] the photochemistry of phenylcyclobutane has received no attention. The only important primary process in the direct photolysis of cyclobutane[10] is fragmentation or cycloreversion to ethylene. The other two significant products of photolysis, hydrogen and acetylene, are probably formed by secondary decomposition of the excited ethylene

(1) All correspondence should be addressed to Professor W. Albert Noyes, Jr., Department of Chemistry, The University of Texas at Austin, Austin, Texas 78712.

(2) (a) G. S. Hammond, P. Wyatt, C. D. Deboer, and N. J. Turro, *J. Amer. Chem. Soc.*, 86, 2532 (1964); (b) A. C. Cookson, M. J. Nye, and G. Subrahmanyam, *Proc. Chem. Soc.*, 144 (1964).

$$H_2C{-}CH_2 \xrightarrow{h\nu} 2CH_2{=}CH_2^* \xrightarrow{M} 2CH_2{=}CH_2$$
$$H_2C{-}CH_2 \qquad\qquad CH_2{=}CH_2^* \longrightarrow CH{\equiv}CH + H_2$$

Walsh's main paper on cyclopropane[11] mentions the possibility of four-center unsaturation analogous to the three-center unsaturation of cyclopropane but does not discuss the possible conjugation of cyclobutane with the phenyl group in phenylcyclobutane. Early extended Hückel calculations by Hoffmann[12] indicated no special conjugative ability for the cyclobutane ring. Experimental work has not revealed any striking indication of conjugative power by a cyclobutane ring but there is some evidence which suggests that it is not negligible.[13]

The absorption spectrum of phenylcyclobutane in solution in hexane is shown in Figure 1. Three features of this spectrum give a measure of the interaction of the cyclobutane ring with the benzene ring: position, intensity, and internal distribution of intensity. A large interaction moves the absorption of the monosubstituted benzene to longer wavelengths, intensifies the spectrum, and changes the internal intensity distribution away from that of benzene.

The strong bands in the benzene spectrum are at $0 + 520$ cm^{-1} (called $A + B$), $0 + 520 + 930$ ($A + B + C$), $0 + 520 + 2 \times 930$ ($A + B + 2C$), etc.... In the monosubstituted benzene, these bands still appear and in addition there occur 0–0 (A) and 0–930 ($A + C$) bands, etc. The ratio of the intensity of $A + C$ to $A + B$ increases with an increasing interaction between the substituent and the ring. If we compare the absorption spectrum of phenylcyclobutane to those of phenylcyclopropane, phenylcyclopentane, and phenylcyclohexane obtained by Robertson, Music, and Matsen[14] in the same solvent, we see that the intensity, the 0–0 band frequency, and the ratio $(A + C)/(A + B)$ for phenylcyclobutane are intermediate between those of phenylcyclopropane and phenylcyclopentane. Moreover, the drop of 402 cm^{-1} in the frequency of the 0–0 band from phenylcyclohexane (37,590 cm^{-1}, 266.0 nm) where the cyclohexyl group is essentially aliphatic in character to phenylcyclobutane (37,188 cm^{-1}, 268.9 nm) is too large to be due only the effect of increasing molecular weight of the substituent and indicates that there is enough ring strain in the cyclobutyl group to generate some π orbital character in the bond functions. Further evidence of ring strain is given by the higher $(A + C)$ to $(A + B)$ intensity ratio for phenylcyclobutane than for phenylcyclohexane.

The molecular orbitals of cyclobutane have been discussed by several workers[15] and most explicitly by Salem and Wright,[16] and Hoffmann and Davidson,[17] who followed the procedure originally outlined by Walsh for cyclopropane.[11] They all agree that the highest occupied orbitals of cyclobutane are a degenerate e_u set with a b_{1g} level not far below. The choice of e_u orbitals is not unique and one set is given below.

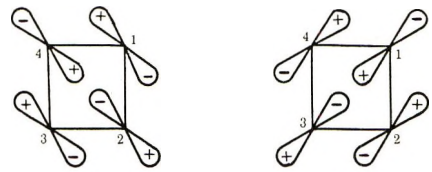

Interaction between the cyclobutane and the benzene ring in the bisected conformation of phenylcyclobutane is accompanied by electron transfer out of orbital e_u (I); this decreases 2–4 antibonding and this in turn should allow C-2 and C-4 to approach each other, resulting in a molecular distortion shown in B. Interaction between the cyclobutane and the benzene ring in the coplanar conformation of phenylcyclobutane is accompanied by electron transfer out of orbital e_u(II),

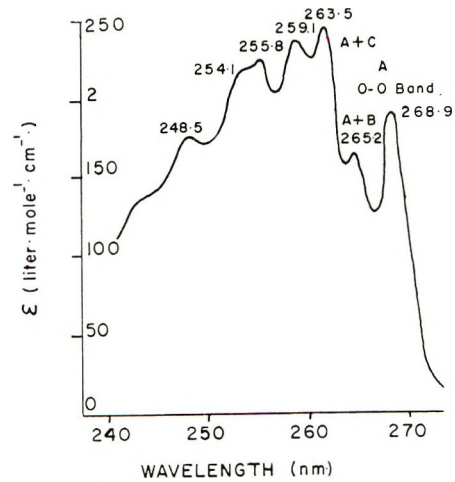

Figure 1. Absorption spectrum of phenylcyclobutane in solution in hexane.

(3) H. Kristinsson and G. W. Griffin, *J. Amer. Chem. Soc.*, **88**, 378 (1966).

(4) H. Kristinsson and G. W. Griffin, *Tetrahedron Lett.*, 3259 (1966).

(5) P. H. Mazzocchi, R. S. Lustig, and G. W. Green, *J. Amer. Chem. Soc.*, **92**, 2168 (1970).

(6) D. B. Richardson, L. R. Durrett, J. M. Martin, Jr., W. E. Putman, S. C. Slaymaker, and I. Dvoretzky, *ibid.*, **87**, 2763 (1965).

(7) E. W. Valyocsik and P. Segal, *J. Org. Chem.*, **36**, 66 (1971).

(8) J. K. Foote, Ph.D. thesis, The University of California, Riverside, Calif., 1966.

(9) K. Salisbury, *Chem. Commun.*, 934 (1971).

(10) R. D. Doepker and P. Ausloos, *J. Chem. Phys.*, **43**, 3814 (1965).

(11) A. D. Walsh, *Trans. Faraday Soc.*, **45**, 179 (1949).

(12) R. Hoffmann, *Tetrahedron Lett.*, 3819 (1965).

(13) (a) J. J. Wren, *J. Chem. Soc.*, 2208 (1956); (b) E. G. Creschova, Yu N. Panchenko, N. I. Valilyev, M. G. Kuzmin, Uy S. Shabarov, and R. Ya Levina, *Opt. Spektrosk.*, **8**, 371 (1960).

(14) W. W. Robertson, J. F. Music, and F. A. Matsen, *J. Amer. Chem. Soc.*, **72**, 5260 (1950).

(15) (a) Z. Maksic, L. Klasinc, M. Randic, *Theor. Chim. Acta*, **4**, 273 (1966); (b) T. Yonezawa, K. Shimizu, and H. Kato, *Bull. Chem. Soc. Jap.*, **40**, 456 (1967).

(16) (a) L. Salem and J. S. Wright, *J. Amer. Chem. Soc.*, **91**, 5947 (1969); (b) L. Salem, *Chem. Brit.*, **5**, 449 (1969); (c) J. S. Wright and L. Salem, *Chem. Commun.*, 1370 (1969).

(17) R. Hoffmann and R. B. Davidson, *J. Amer. Chem. Soc.*, **93**, 5699 (1971).

this decreases 1–3 antibonding, with consequent distortion shown in C.

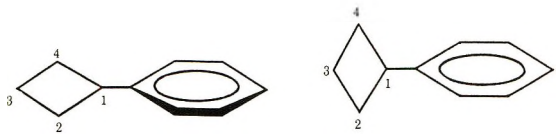

B C

Would the distance of C1–C3 determine the nature of the products of an electrocyclic concerted reaction of phenylcyclobutane, *i.e.*, be "small enough" in the conformation C to allow isomerization to phenylmethylcyclopropane but too large in the conformation B which would thus undergo cycloreversion to styrene and ethylene? Additional and precise structural determinations are needed to investigate that matter further. The present work was undertaken to elucidate the photochemical primary process in phenylcyclobutane vapor in the spectral region of 250 ± 20 nm.

Results and Discussion

Photolysis Products and Fluorescence. On irradiation of phenylcyclobutane in the gas phase (4.5 Torr, 40°), four products were formed. These were identified as ethylene (I), styrene (II), *cis*- and *trans*-1-methyl-2-phenylcyclopropane (III and IV). Table I

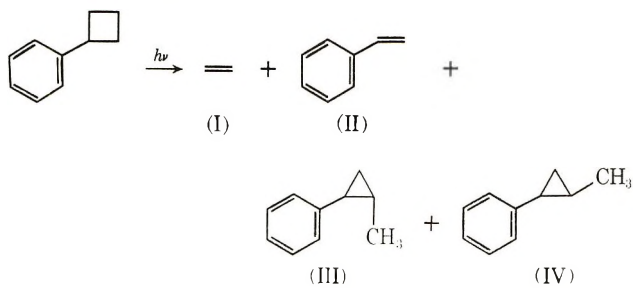

shows the measured quantum yields of formation of these products on irradiation near the 0–0 band (266 nm) and at shorter wavelengths. The observed yield of styrene is smaller than the yield of ethylene, probably because of polymerization of styrene. Polymer formation was evident on the front window of the cell. Predominance of dissociation over isomerization is interpreted as the result of predominance of the bisected conformation over the coplanar conformation in terms of the hypothesis already mentioned about conformation and nature of the photolysis products.

Table I: Variation of Quantum Yields with Wavelength in Phenylcyclobutane[a]

λ, nm	Φ_I		Φ_{II}	Φ_{III}	Φ_{IV}
248 ± 0.8	0.27	0.22	0.20	0.007	0.007
254 ± 0.8	0.36	0.31	0.22	0.011	0.012
266 ± 0.8	0.44	0.42	0.24	0.018	0.023

[a] Temperature, 40°; pressure, 4.5 Torr; lamp, 1000-W Hg–Xe; monochromator slits: entrance, 1 mm; exit, 1 mm.

The decrease in quantum yield of products with decreasing wavelength does not parallel the decrease in the fluorescence quantum yield Q_f of phenylcyclobutane with decreasing wavelength. This decrease may be due to a valence isomerization of phenylcyclobutane to a benzvalene type of intermediate which would rapidly revert to the starting material and thereby result in a decrease of all the other photochemical processes. Nevertheless, the dissociation reaction is less quenched than fluoresence since it may result from vibrational energy transfer from the benzene ring to the cyclobutane ring and since phenylcyclobutane has more vibrational energy at shorter wavelengths.

Q_f for phenylcyclobutane at 40° was measured over a range of wavelengths. The expected decrease in Q_f with decreasing wavelength is noted. The value of Q_f is taken to be 0.28 ± 0.07 for 4.5 Torr at 40°, excited at 266 ± 0.4 nm. It is based on 0.18 for benzene vapor at 20 Torr, 253 nm, and 25°.[18] Measurement of the absorption and fluorescence of phenylcyclobutane in solution showed that the spectra were nearly identical with those of toluene. On these grounds, the singlet radiative lifetime ($1/k_2$, k_2 being the Einstein coefficient for spontaneous emission) may be taken as 177 nsec.[19] The mean lifetime $\tau = 1/k_2 + \Sigma k_n$, where Σk_n is the sum of all the probabilities per unit time which are competitive with fluorescence, is $0.28 \times 177 \times 10^{-9} = 4.97 \times 10^{-8}$ sec.

Collisions with Added Gases: Effect on the Fluorescence. Collisions with n-Butane Molecules. Figure 2 shows that, at 248 and 254 nm, the fluorescence of phenylcyclobutane increases in the presence of *n*-bu-

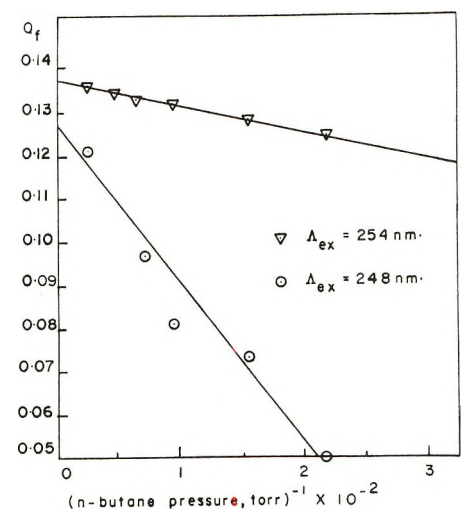

Figure 2. Effect of *n*-butane pressure on phenylcyclobutane fluorescence: T = 40°; phenylcyclobutane pressure = 4.5 Torr.

(18) W. A. Noyes, Jr., D. Harter, and W. A. Mulac, *J. Chem. Phys.*, **44**, 2100 (1966).

(19) I. B. Berlman, "Handbook of Fluorescence Spectra of Aromatic Molecules," Academic Press, New York, N. Y., 1971, p 114.

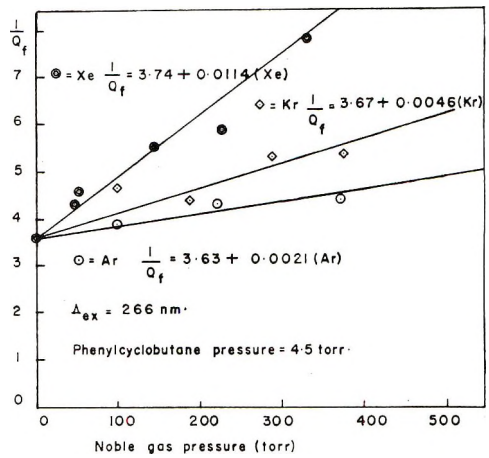

Figure 3. Quenching of phenylcyclobutane fluorescence by noble gases; $T = 40°$.

tane. This is interpreted as due to the quenching of the processes in competition with fluorescence at wavelengths shorter than the 0–0 band. At 266 ± 0.4 nm, a very small quenching of phenylcyclobutane fluorescence by *n*-butane (effective cross section $\simeq 0.06 \times 10^{-16}$ cm^2) was observed. This has been explained by Noyes and Harter.[20] Absorption by molecules in vibrational levels of the ground state greater than the zeroth level would lead to formation of excited singlet state molecules with less than the mean vibrational energy; vibrational relaxation might lead to "warming" rather than "cooling" the excited molecules.

Collisions with Noble Gases. The results of Figure 3 show that the fluorescence of phenylcyclobutane is nearly unaffected by argon but is quenched by krypton and xenon. In view of the known effect of noble atoms on electronic relaxation processes,[21] it is suggested that this quenching is due to the collision-induced intersystem crossover

$$^1PCB_0 + N \longrightarrow {}^3PCB + N \qquad k_3[^1PCB_0][N]$$

The transition may be thought as arising from the following processes. A collision complex is first formed as the result of weak exchange interactions; then spin–orbit interaction (almost exclusively from the noble gas) enhances the breakdown of spin-conservation. The slopes of Q_f^{-1} *vs.* noble gas pressure, the corresponding k_3 values, and the cross sections for the individual gases are given in Table II.

Collisions with Oxygen Molecules. The results of Figure 4 clearly show that the fluorescence of phenylcyclobutane is quenched by oxygen. However, our data offer no evidence on the nature of the final states of the aromatic molecule and of the oxygen after collision. The minimum energy transfer for the process

$$^1PCB + O_2(^3\Sigma_g) = {}^3PCB + O_2(^1\Delta_g^-)$$

is at least 22.6 kcal/mol required for the excitation of $(^3\Sigma_g^-)O_2$ into its lowest excited singlet state $(^1\Delta_g)O_2$.

Table II: Rate Constants for Rare Gas Fluorescent Quenching in Phenylcyclobutane[a]

Gas	Slope, Torr^{-1}	k_3, l. mol^{-1} sec^{-1} × 10^{-8}	σ^2, cm^2 × 10^{16}
Ar	0.00214	2.00	0.0227
Kr	0.004668	4.37	0.0643
Xe	0.01148	10.76	0.178

[a] For comparison, effective cross sections for quenching for other molecules given in this article may be stated (all in cm^2 × 10^{16}): (a) *n*-butane, 0.06; (b) oxygen, 14; (c) 1,3-pentadiene, 3.06.)

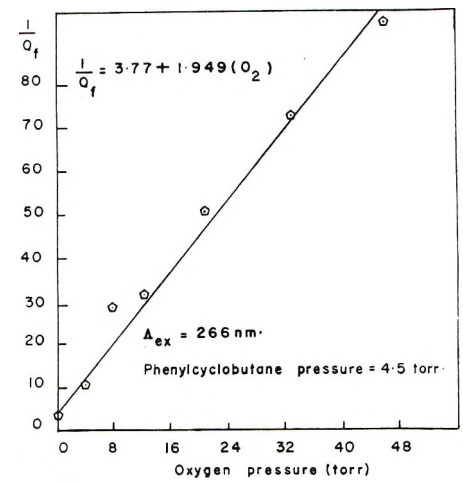

Figure 4. Quenching of phenylcyclobutane fluorescence by oxygen; $T = 40°$.

The minimum energy transfer necessary for the process

$$^1PCB_0 + O_2(^3\Sigma_g^-) = {}^3PCB + O_2(^1\Sigma_g^-)$$

is 37.8 kcal/mol. These conditions are both met by phenylcyclobutane. Another energy transfer is also possible, *viz.*

$$^1PCB_0 + O_2(^3\Sigma_g^-) = PCB + O_2(^3\Sigma_u^+)$$

The reaction

$$^1PCB + O_2(^3\Sigma_g^-) \longrightarrow {}^3PCB + O_2(^3\Sigma_g^-)$$

can also be proposed, as in the work of Lee, Schmidt, Shortridge, and Haninger.[22]

(20) W. A. Noyes, Jr., and D. A. Harter, *J. Amer. Chem. Soc.*, **91**, 7585 (1969).

(21) The first work on this subject seems to have been performed by M. R. Wright, R. F. Frosch, and G. W. Robinson, *J. Chem. Phys.*, **33**, 934 (1960). Other work has elaborated the method: T. Medinger and F. Wilkinson, *Trans. Faraday Soc.*, **61**, 620 (1965); A. R. Horrocks, T. Medinger, and F. Wilkinson, *Chem. Commun.*, 452 (1965); T. Medinger and F. Wilkinson, *Trans. Faraday Soc.*, **62**, 1785 (1966); A. R. Horrocks, A. Kearwell, K. Tickle, and F. Wilkinson, *ibid.*, **62**, 3393 (1966). See also C. S. Burton and W. A. Noyes, Jr., *J. Chem. Phys.*, **49**, 1712 (1968). J. G. Calvert and J. N. Pitts, Jr., "Photochemistry," Wiley, New York, N. Y., 1966, p 304, have given a summary of this method.

(22) E. K. C. Lee, M. W. Schmidt, R. G. Shortridge, Jr., and G. A. Haninger, Jr., *J. Phys. Chem.*, **73**, 1805 (1969).

Mulliken[23] gives strong evidence for a weak-contact charge-transfer complex between aromatic molecules and oxygen; the importance of the ionization potential in determining the oxygen quenching rate constant of the aromatic excited singlet state[24] tends to support the idea that the above reactions could occur *via* a contact charge-transfer complex mechanism.

Peroxide formation is also possible but that matter was not thoroughly investigated. We will just write

$$^1\text{PCB} + O_2(^3\Sigma_g^-) = ? \qquad k_4[^1\text{PCB}][O_2]$$

With this step, and application of the steady-state assumption

$$Q_f^{-1} = 1 + \frac{\Sigma k_n}{k_2} + \frac{k_4}{k_2}[O_2]$$

From Figure 4, the slope was found to be 1.949 Torr^{-1} and $k_4 = 1.83 \times 10^{11}$ l. mol^{-1} sec^{-1}. From gas kinetic theory, the quenching cross section was calculated to be 14 Å^2. The phenylcyclobutane fluorescence is quenched essentially on every collision with an oxygen molecule.

Collisions with trans-Piperylene Molecules. *trans*-Piperylene (1,3-pentadiene) was first suggested as a means of destroying triplet states of molecules without simultaneously destroying the singlet states.[25] It was later shown that *trans*-piperylene is an efficient quencher of triplet states (as low as 60 kcal) but that it also quenches the singlet states of many molecules.

Inclusion of the step $^1\text{PCB} + \text{PD} = \text{PCB} + \text{PD}$ $k_5[^1\text{PCB}][\text{PD}]$ and application of the steady state assumption results in

$$Q_f^{-1} = 1 + \frac{\Sigma k_n}{k_2} + \frac{k_5}{k_2}[\text{PD}]$$

where PD is a molecule of *trans*-1,3-pentadiene.

From Figure 5, the slope was determined to be 0.238 Torr^{-1} and $k_5 = 2.33 \times 10^{10}$ l. mol^{-1} sec^{-1}. Noyes and Harter,[20] by measuring the fluorescence quenching of the xylenes by piperylene, obtained a main value of 1.4×10^{10} l. mol^{-1} sec^{-1} for the singlet quenching rate constant by piperylene; the same order of magnitude is thus obtained. The collisional cross section was calculated to be 3.06 Å^2.

Temperature Quenching of Fluorescence. The data show that as the temperature is increased, the fluorescent yield decreases.

$$Q_f^{-1} - 1 = \frac{\Sigma k_n}{k_2}$$

Plots of ln $[Q_f^{-1} - 1]$ *vs.* $1/T$ (Figure 6) are not linear as would be the case if Σk_n were equal to $k_0 e^{-E/RT}$, *i.e.*, if only one process having an activation energy E were competing with fluorescence. Before any single process can be claimed to be responsible for temperature quenching, additional and more precise experiments will be necessary.

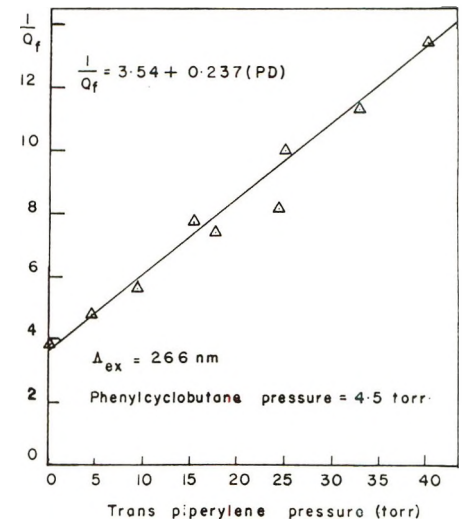

Figure 5. Quenching of phenylcyclobutane fluorescence by *trans*-piperylene; $T = 40°$.

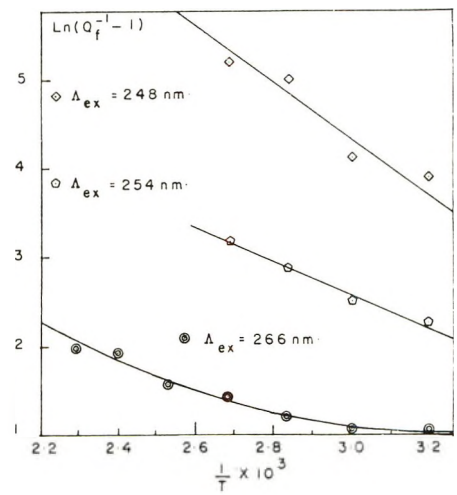

Figure 6. Effect of temperature on phenycyclobutane fluorescence.

Quenching of Product Formation by Added Gases. The formation of ethylene was not quenched by butane; if a vibrationally excited intermediate is important en route to the products, its lifetime must be less than 2×10^{-9} sec, which is the time between collisions at the pressure of butane added.

The ethylene formation quenching efficiency of *cis*-2-butene was found to be too small to be consistent with a triplet quenching[26] (Figure 7) unless ethylene formation is extremely fast (too fast to be quenched by even 100 Torr of the quenchers), after a possible intersystem crossing from the singlet phenylcyclobutane to

(23) H. Tsubomura and R. S. Mulliken, *J. Amer. Chem. Soc.*, **82**, 5966 (1960).

(24) T. Brewer, *ibid.*, **93**, 775 (1971).

(25) A. A. Lamola and G. S. Hammond, *J. Chem. Phys.*, **43**, 2129 (1965).

(26) R. B. Cundall, F. J. Fletcher, and D. G. Milne, *Trans. Faraday Soc.*, **60**, 1146 (1960).

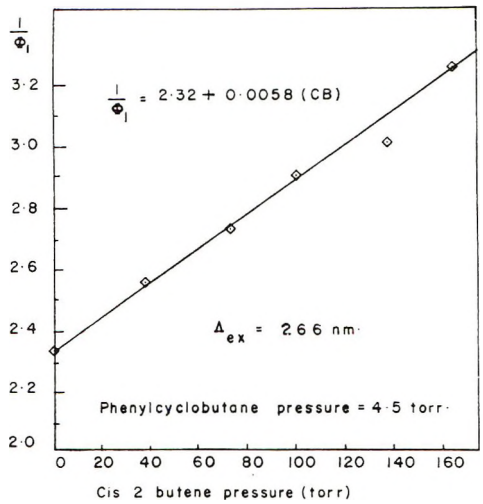

Figure 7. Quenching of phenylcyclobutane dissociation by *cis*-2-butene; $T = 40°$.

the benzenoid triplet. It must be emphasized that differentiating between a singlet and a triplet state reaction and either from a ground-state reaction may be very difficult.

trans-Piperylene has been found to quench phenylcyclobutane fluorescence strongly and thus the phenylcyclobutane singlet state. Ethylene formation is also strongly quenched by *trans*-piperylene ($1/\Phi_I = 2.50 + 0.184$(PD) where (PD) is pressure in Torr). The ratio R = slope/intercept has been found equal to 0.079 Torr^{-1} for Φ_I^{-1} *vs.* [PD] and to 0.066 Torr^{-1} for Q_f^{-1} *vs.* [PD]. These two values can be considered as equal within experimental error. The process leading to ethylene formation must be very fast. *trans*-Piperylene quenches the singlet state and thus the very fast ethylene formation. Thus it is impossible to draw any conclusions about the nature of the state which gives products.

Conclusion

Chemical methods of triplet quenching depend upon the fact that triplets are usually much longer lived than the corresponding singlets and not upon an intrinsic property of the spin state. In the case of the very fast dissociation of phenylcyclobutane ($k > 10^8$ sec^{-1}), quenching methods do not give an unambiguous answer as to the nature of the state (singlet, triplet, or vibrational ground state) from which dissociation occurs. Another unsolved question of the photochemistry of phenylcyclobutane is the mechanism of products formation. It might occur through a concerted scission of the cyclobutane ring either as a $[{}_\sigma 2_s + {}_\sigma 2_a]$ cycloreversion or as a diradical mechanism. The photochemistry of *cis*-2,3-dideuteriophenylcyclobutane and the infrared analysis of the dideuterioethylene produced[27] could give an answer to that question.

Experimental Section

Materials. Phenylcyclobutane was prepared according to the procedure of Shabarov, Donskaya, and Levina.[28] The action of phenylmagnesium bromide on cyclobutane gives 1-phenylcyclobutan-1-ol. This was reduced with sodium in liquid ammonia to phenylcyclobutane. The product was identified by its nmr spectrum consistent with the phenylcyclobutane structure, five aromatic hydrogens at 2.9 ppm, one benzylic hydrogen, centered at 6.9 ppm. Six aliphatic hydrogens as a broad multiplet between 7.6 and 8.3 ppm were indicated. The infrared spectrum, which was similar to that reported for this compound,[29] also supported this assignment, although identification of arylcyclopropanes and arylcyclobutanes from their infrared spectra in the region of deformation vibrations of the small ring is extremely difficult because the absorption bands of the phenyl group are in the same region. The phenylcyclobutane was separated and purified, by a 6.1-m long, 0.62-cm diameter, 20% FFAP (Free Fatty Acid Phthalate) on Chromosorb P (45/60) column, to better than 99.95% before use and the major impurity was believed to be 3-phenylcyclobutene.

cis- and *trans*-1-phenylbut-2-ene (95% pure) from Aldrich Chemical Co. were purified by preparative gas chromatography on the FFAP on a modified Carbowax–Carbowax 20M–2-nitroterephthalate column.

n-Butane (Philips pure grade) was distilled bulb to bulb between −80° (Dry Ice + acetone) and −160° (isopentane + liquid nitrogen) and only the middle part was retained.

trans-Penta-1,3-diene (piperylene) from Aldrich Chemical Co. (containing 2% of the cis isomer), acetone, tetrahydrofuran, *tert*-butylbenzene, oxygen, argon, krypton, xenon, ethane (Matheson Spectroquality), benzene, toluene, and *cis*-2-butene (Philips research grade) were used after bulb to bulb distillation. All organic compounds were thoroughly degassed at −160°.

Apparatus. This is similar to an arrangement already described[30] but with some differences. The light source for photolyses was a Hanovia 1-kW mercury–xenon super pressure lamp, while a 1-kW xenon lamp was used for the fluoresence measurements. A Bausch and Lomb grating monochromator, with a linear dispersion of 1.6 mm nm^{-1} was used. The monochromator slits were 1 mm (entrance) and 0.5 mm (exit) in fluorescence experiments and 1 mm (entrance) and 1 mm (exit) in photolysis experiments. The photolysis cell was 20 cm long, 4.5 cm in diameter with the side window 6 cm from the front window, and 4.5 cm in diameter and of a total volume (including access tubing)

(27) A. B. Callear and R. J. Cvetanovic, *J. Chem. Phys.*, 24, 873 (1956).

(28) S. Shabarov, N. A. Donskaya, and R. Ya Levina, *Zh. Obsch. Khim.*, 33, 3434 (1963).

(29) N. A. Donskaya, V. K. Potapov, S. Shabarov, and R. Ya Levina, *J. Org. Chem. USSR*, 1, 1835 (1965).

(30) M. Comtet, *J. Amer. Chem. Soc.*, 92, 5309 (1970).

of 305 cm^3. The cross section of the beam, modulated by a series of circular holes in black plates, was 14 cm^2 in photolysis experiments and 0.2 cm^2 in fluorescence experiments.

The cell, storage reservoir for phenycyclobutane, and the connecting valves (Hoke 413 A) were housed in an asbestos oven. The oven had two Supracil windows, one of which was incorporated into an adjustable wall of the oven (designed so that cells of various sizes could be used). The oven was heated electrically and good heat distribution was achieved by the use of a small fan. The valves inside the oven were reached through small windows with a special tool, and in this way the valves could be operated with little effect on the oven temperature control.

The RCA 935 phototube was attached to the rear window of the cell and calibrated by comparison of its response to light intensity to the production of hydrogen from hydrogen iodide. At 40°, for a pressure of hydrogen iodide between 10 and 40 Torr, the quantum yield for H_2 formation at wavelengths 248, 254, and 266 nm is equal to 1.[31] The actinometry was performed at total absorption of the light incident on the cell. Analysis for hydrogen was made by removing the gas noncondensable at −196° with a Toepler pump, measuring its amount, and checking its identity and purity on a residual gas analyzer (Consolidated Electrodynamics, Type 21-64). Corrections for changes in sensitivity of the phototube with wavelength were made by using the manufacturer's figures, found satisfactory after check by use of the sodium salicylate plate method.

An IP 28 photomultiplier tube (operated at 900 V) mounted inside the oven was used for fluorescence detection. The system was standardized by using toluene (Q_f(266 nm) = 0.30 ± 0.07 for toluene at 40° relative to Q_f(253.7 nm) = 0.18 for benzene).[18] (See Burton and Noyes.[21])

The fluorescence spectrum of phenylcyclobutane (excited at 266 nm) was measured on an Aminco-Bowman spectrophotofluorimeter. Absorption spectra were measured on a Cary Model 14 spectrophotometer.

Procedure. The cell was always filled with phenylcyclobutane at a temperature of 35° and the oven then warmed to 40 ± 1° for photolysis. The other gases were condensed into the cell and sufficient time for mixing was allowed (up to 12 hr at the highest pressures) before the reaction was started. The intensities of the incident and transmitted light were continuously monitored and reflection corrections were made according to the formula of Hunt and Hill.[32]

After photolysis, phenylcyclobutane and possible condensable products were condensed (1.5 hr) into a small Pyrex tube and a known amount of *tert*-butylbenzene in tetrahydrofuran was added as an internal standard. Analysis was carried out on a Perkin-Elmer gas chromatograph using a 50-ft × 0.02-in *m*-bis(*m*-phenoxyphenoxy)benzene–Apiezon L (MBMA) column. The recorder was fitted with a disk integrator.

Possible noncondensable products were removed with a Toepler pump, pumped into a calibrated volume, and then expanded into a bulb connected to the gold lead of a residual gas analyzer (Consolidated Electrodynamics, Type 21-64), calibrated for hydrogen and ethylene.

Photolysis Products. The only products detected were ethylene (I), styrene (II), *cis*- and *trans*-1-phenyl-2-methylcyclopropane (III and IV) as well as polymer. The retention times of (II), (III), and (IV) were compared, by dual injections, with those of authentic samples of styrene, *cis*- and *trans*-1-phenyl-2-methylcyclopropane (prepared by the method of Simmons and Smith[33] from a mixture of *cis*- and *trans*-1-phenylprop-2-ene separated and purified by the 6.1-m long, 0.62-cm diameter, 20% FFAP on Chromosorb P (45/60) column). The column used was the MBMA capillary column already described and was able to separate the isomers from phenylcyclobutane. However, three MBMA columns in series and at 150° were necessary to show the absence of *cis*- and *trans*-1-phenyl-2-butene and to distinguish them from *cis*- and *trans*-1-phenyl-2-methylcyclopropane. Ethylene was analyzed on the residual gas analyzer as already described for hydrogen in the actinometry.

Acknowledgment. I thank the National Science Foundation and the Robert A. Welch Foundation for financial support and acknowledge the guidance or criticisms of Professor W. Albert Noyes, Jr., and Dr. K. Salisbury. The material presented was taken from a thesis submitted in 1972 by P. Autard to the University of Texas at Austin for the degree of Master of Arts in Chemistry.

(31) R. M. Martin and J. E. Willard, *J. Chem. Phys.*, 40, 2999 (1964).

(32) R. E. Hunt and T. L. Hill, *ibid.*, 15, 111 (1947).

(33) H. E. Simmons and R. D. Smith, *J. Amer. Chem. Soc.*, 81, 4256 (1959).

Photochemistry of Phenylimidazoles

by J. Hennessy and A. C. Testa*

Department of Chemistry, St. John's University, Jamaica, New York 11432 *(Received June 5, 1972)*

The photochemical formation of 9,10-phenanthroimidazole from 4,5-diphenylimidazole and 2-phenyl-9,10-phenanthroimidazole from 2,4,5-triphenylimidazole have been studied with 313-nm excitation in different solvents. Noteworthy is the observation that no dihydrophenanthrene intermediate could be detected and that the photocyclization proceeds in air-saturated as well as in degassed solutions. The quantum yields for the formation of 9,10-phenanthroimidazole are generally an order of magnitude larger in air-saturated than in degassed solutions. The process proceeds through the singlet state and the quantum yield for the cyclization reaction in degassed acetonitrile solutions for 4,5-diphenylimidazole and 2,4,5-triphenylimidazole is $0.91 \pm 0.1 \times 10^{-3}$ and $0.57 \pm 0.07 \times 10^{-3}$, respectively. The luminescence spectra and quantum yields for 4,5-diphenylimidazole and its photoproduct have also been measured.

Introduction

The photocyclization of stilbene and its analogs to phenanthrene type molecules has been a subject of continuing interest.[1-4] The formation of the yellow colored 4a,4b-dihydrophenanthrene intermediate has been demonstrated in the photocyclization of *cis*-stilbene and its analogs to phenanthrenes, and the formation of hydrogen peroxide has been shown to arise from the reaction between oxygen and dihydrophenanthrene. In a degassed solution the yellow color disappears and the system reverts back to *cis*-stilbene.[5] Although it has been shown that the cyclization of *cis*-stilbene proceeds *via* the π,π^* singlet state,[6] the mechanism by which the dihydrophenanthrene intermediate is converted to the corresponding phenanthrene continues to be a source of controversy. Recently, Srinivasan and Hsu[7] suggested a free-radical process which leads to either 9,10-dihydrophenanthrene or directly to the corresponding phenanthrene, depending upon whether the termination step involves a gain or loss of a hydrogen atom. In fact, they report that the 313-nm irradiation of a degassed solution of α-phenylcinnamic acid in methanol leads directly to the 9-phenanthroic acid in the absence of any oxidizer.

In view of the continuing interest in photocyclizations and the unresolved problem concerning dihydrophenanthrene we have investigated the photochemistry of 4,5-diphenyl- and 2,4,5-triphenylimidazole at 313 nm in four different solvents, in air-saturated and degassed solutions. In addition to measuring the photochemical quantum yields, the luminescence spectra and quantum yields have also been measured.

Experimental Section

Materials. 4,5-Diphenyl- and 2,4,5-triphenylimidazole were obtained from Aldrich Chemical Co. and recrystallized prior to use. The former was recrystallized as white needles (mp 232–233°) from benzene and the latter was recrystallized from dilute ethanol as a white powder (mp 273–274°). Zone-refined benzophenone from J. Hinton was used as a triplet sensitizer and *cis*-1,3-pentadiene from Chemical Samples Co. as a triplet quencher. Spectrograde acetonitrile, EPA, and hexane were used as received from Matheson Coleman and Bell.

9,10-Phenanthroimidazole was prepared by refluxing 9,10-diaminophenanthrene with an equivalent amount of formic acid in xylene, and the white product obtained in low yield was recrystallized from dilute ethanol water solutions. The uv spectrum and the melting point (303–304°) agree satisfactorily with the literature.[8]

Apparatus. Small scale photolyses were performed in 1-cm quartz spectrophotometric cells, connected by a graded seal to a vacuum system (10^{-4} mm), and sealed off after degassing. Excitations at 285 and 313 nm were isolated from an Osram HBO 100W/2 high-pressured mercury lamp with 10-nm half-bandwidth interference filters. The ferrioxalate actinometer[9] was used to measure light intensities, which were typically 1.4×10^{15} quanta/sec. Large-scale photolyses were performed at concentrations of approximately 10^{-3} M,

(1) K. A. Muszkat and A. Fischer, *J. Chem. Soc. B*, 662 (1967).

(2) F. R. Stermitz in "Organic Photochemistry," Vol. I, O. L. Chapman, Ed., Marcel Dekker, New York, N. Y., 1967, p 247.

(3) M. Scholz, F. Dietz, and M. Mühlstadt, *Z. Chem.*, **7**, 329 (1967).

(4) A. V. Blackburn and C. J. Timmons, *Quart. Rev., Chem. Soc.*, **23**, 482 (1969).

(5) W. M. Moore, D. D. Morgan, and F. R. Stermitz, *J. Amer. Chem. Soc.*, **85**, 829 (1963).

(6) F. B. Mallory, C. S. Wood, and J. T. Gordon, *ibid.*, **86**, 3094 (1964).

(7) R. Srinivasan and J. N. C. Hsu, *ibid.*, **93**, 2816 (1971). There are two dihydrophenanthrenes which can occur during the degassed photocyclization of stilbene and its analogs, *i.e.*, 4a,4b-dihydrophenanthrene and 9,10-dihydrophenanthrene. The former is produced with stilbene while the latter has been observed in certain stilbenes containing one or more electron-withdrawing substituents on the central double bond.

(8) R. Epsztein, *Mem. Serv. Chim. Etat. (Paris)*, **36**, 353 (1951).

(9) C. H. Hatchard and C. A. Parker, *Proc. Roy. Soc., Ser. A*, **235**, 518 (1956).

using a 450-W Hanovia medium-pressure lamp and a Pyrex sleeve to limit the incident wavelength region to values greater than 280 nm. Nitrogen gas was continuously bubbled through the solution during the large-scale runs.

Analytical Procedures. The disappearance of 4,5-diphenyl- and 2,4,5-triphenylimidazole was followed quantitatively at 254 and 262 nm, respectively, with a Beckman DU spectrophotometer. The following molar extinction coefficients were used at 254 nm: 9.0×10^3 for the diphenylimidazole and 77×10^3 for 9,10-phenanthroimidazole, and at 262 nm: 8.0×10^3 for triphenylimidazole and 56×10^3 for 2-phenyl-9,10-phenanthroimidazole. Uv spectra were recorded with a Bausch and Lomb Model 505 spectrophotometer. Flourescence and phosphorescence spectra were obtained with an apparatus described elsewhere,[10,11] and were not corrected for the variation of sensitivity of the photomultiplier–monochromator combination with wavelength.

The photoproduct was separated by thin layer chromatography (Eastman Kodak or Brinkman Instruments thin layer plates with fluorescent indicator) using three different solvent systems: ethyl acetate, acetone, and 90% hexane–10% ethanol. The photoproduct from the 4,5-diphenylimidazole photolysis was obtained, following large scale photolysis, by flash evaporation and identified by the usual spectroscopic methods and by comparison with an authentic sample of 9,10-phenanthroimidazole. Fractional sublimation was found to be a convenient method for the separation of phenanthroimidazole from the diphenylimidazole.

Results

Our initial interest in the photoexcitation of 4,5-diphenylimidazole (DPI) arose from the observation that its fluorescence in 0.1 *M* NaOH decreased with time. Figure 1 illustrates the change of fluorescence intensity occurring with 285-nm excitation. Large scale photolyses were used to determine that the photochemistry of DPI leads to 9,10-phenanthroimidazole (PI) and similarly that 2,4,5-triphenylimidazole (TPI) leads to 2-phenyl-9,10-phenanthroimidazole (PPI), *i.e.*

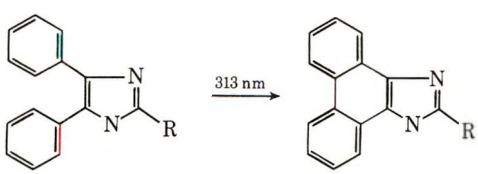

(DPI, TPI) (PI, PPI)
R = H, C_6H_5

Identification of the photoproduct was made by using uv, ir, and thin layer chromatography and by comparison with an authentic sample. It was observed that in 0.1 *M* NaOH a side reaction occurs which complicates the photochemistry; consequently, quantitative photolyses were performed in its absence. The photocyclization

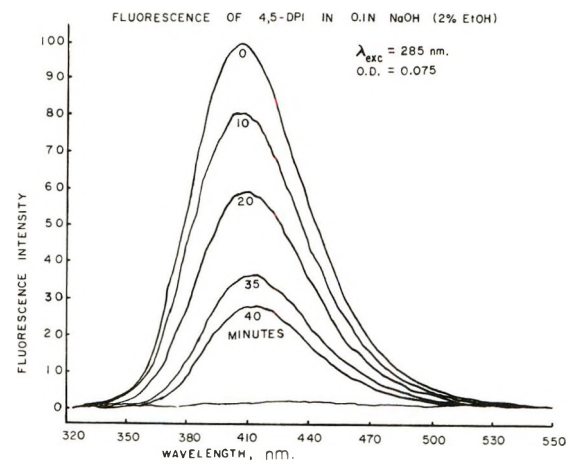

Figure 1. Time dependence of the fluorescence of 4,5-diphenylimidazole in 0.1 *M* NaOH (2% ethanol) excited at 285 nm.

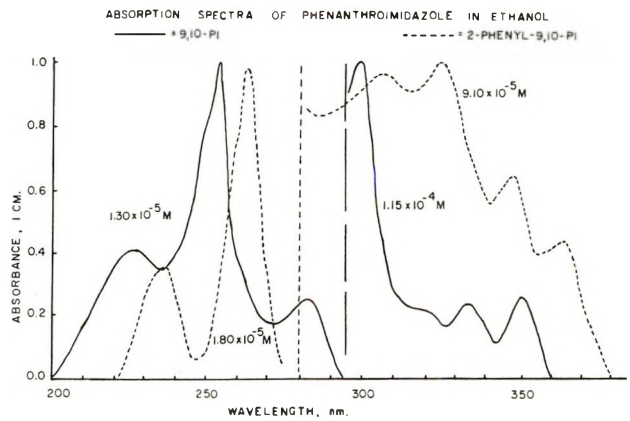

Figure 2. Absorption spectrum of 9,10-phenanthro- and 2-phenyl-9,10-phenanthroimidazole in ethanol, resulting from the photochemistry of 4,5-diphenyl- and 2,4,5-triphenylimidazole, respectively.

of DPI in solvents such as ethanol, 97% hexane–3% ethanol, 70% water–30% ethanol, and acetonitrile proceeds without any detectable side reaction.

The photochemical formation of PI from DPI and PPI from TPI is very well suited for a spectrophotometric determination of the quantum yields, since i most solvents the photochemistry proceeds ver cleanly, *i.e.*, DPI → PI and TPI → PPI. In each o the two systems studied, the product formed does not undergo further photochemistry. During the photochemistry of DPI the appearance of the photoproduct PI is manifested by five well-defined peaks in the uv spectrum which agree with the following reported absorption peaks and molar extinction coefficients of 9,10-phenanthroimidazole: 254 (7.7×10^3), 282 (1.1×10^3), 300 (8.8×10^3), 324 (sh), 334 (1.5×10^3), and 351 nm (2.0×10^3).[8] The absorption spectrum of the ob-

(10) A. Weisstuch and A. C. Testa, *J. Phys. Chem.*, 72, 1982 (1968).

(11) M. O'Sullivan and A. C. Testa, *J. Amer. Chem. Soc.*, 92, 258 (1970).

served photoproducts, PI and PPI, are presented in Figure 2.

The quantum yield results in air-saturated and degassed solutions for the photocyclization of DPI with 313-nm excitation are presented in Table I. It is evident that in all cases the quantum yield is very small, but significantly larger in the air-saturated runs. Stegemeyer[12] has reported a value of $\Phi = 0.07$ for the photochemical formation of phenanthrene from *cis*-stilbene in aerated hexane at 25°. Of particular interest in the present investigation is the result that the yellow dihydrophenanthrene intermediate was never observed during the photolysis of DPI, and that the presence of air is not necessary for the formation of 9,10-phenanthroimidazole.

Table I: Photochemical Quantum Yields for the Formation of 9,10-Phenanthroimidazole from 4,5-Diphenylimidazole[a]

Solvent	I_a, quanta/sec	Photolysis time, min	$\Phi_{deg} \times 10^3$	$\Phi_{air} \times 10^3$
Acetonitrile	1.60×10^{15}	100–300	0.91 ± 0.1	4.3 ± 0.2
70% water–30% ethanol	1.32×10^{15}	200–800	0.47 ± 0.05	4.7 ± 0.9
Ethanol	1.30×10^{15}	100	0.46	2.0
97% hexane–3% ethanol	1.40×10^{15}	75–200	0.30	6.9

[a] λ_{exc} 313 nm; concentration $7–8 \times 10^{-5}$ *M*.

In the aerated photolysis of TPI the sum of the concentration of the cyclized product and unreacted TPI was considerably less than the initial TPI concentration indicating that some additional photoreaction occurs in the presence of oxygen. Investigations performed by Dufraisse[13] and White[14] indicate that TPI forms a peroxide upon uv irradiation in aerated solution. Consequently, quantum yields for this molecule were determined only in degassed solutions, where the reaction proceeds without side effects. A summary of the results are given in Table II. It is seen that the quantum yields for TPI are $\sim 10^{-3}$ in each of the three solvent systems studied. This photocyclization occurs in degassed solutions without any evidence of the dihydrophenanthrene intermediate as was the case with DPI photochemistry. An unexpected result was that the photochemistry of TPI in degassed diethyl ether does not lead to the phenanthroimidazole, while DPI under the same conditions does.

It has been demonstrated that the photocyclization of *cis*-stilbene proceeds *via* its lowest excited singlet state, and in general this has been true in analogs of stilbenes.[1-4] In the present study we attempted to deduce the nature of the reactive state by using *cis*-piperylene as a triplet quencher and benzophenone as a

Table II: Photochemical Quantum Yields for the Formation of 2-Phenyl-9,10-phenanthroimidazole from 2,4,5-Triphenylimidazole in Degassed Solutions[a]

Solvent	I_a, quanta/sec	Photolysis time, min	$\Phi \times 10^3$
Acetonitrile	1.20×10^{15}	100	0.57 ± 0.07
Ethanol	1.10×10^{15}	65–200	2.2 ± 0.2
99.5% hexane–0.5% ethanol	1.40×10^{15}	120	2.2 ± 0.3

[a] λ_{exc} 313 nm; concentration $3–4 \times 10^{-5}$ *M*.

triplet sensitizer. A degassed solution of 7.8×10^{-5} *M* DPI in 97% hexane–3% ethanol with 0.2 *M* *cis*-piperylene irradiated at 313 nm for 1020 min did not lead to any significant change in the quantum yield for the formation of PI. In addition, the fluorescence of DPI was unaffected by the presence of added *cis*-piperylene. PI was not formed in degassed acetonitrile solutions when DPI was sensitized by triplet energy transfer from benzophenone (E_T = 69.0 kcal/mol). The excited singlet state energy of DPI was estimated to be 87 kcal/mol from the mirror image plots of its absorption and fluorescence spectrum, and the triplet state energy, estimated from its phosphorescence spectrum in EPA at 77°K, is 67 kcal/mol. The approximate one order of magnitude increase in the quantum yield for air-saturated solutions relative to degassed solutions tends to rule out a triplet mechanism. In view of the above results it appears that the photocyclodehydrogenation of DPI proceeds from the lowest excited π,π^* singlet state. It is somewhat more difficult to elucidate the photoreactive state in TPI photochemistry because of enhanced and undetermined photochemistry in the presence of 0.2 *M* *cis*-piperylene; however, the similarity of the process with DPI and the increased quantum yields in air-saturated solutions suggest a singlet state reaction.

In this photochemical investigation the fluorescence and phosphorescence spectra of 9,10-phenanthroimidazole are reported for the first time. The fluorescence yield in ethanol, relative to a value of 0.09 for *d,l*-tryptophan,[15] was determined to be 0.35 and its phosphorescence yield in EPA at 77°K was estimated to be 0.08 relative to a value of 0.90 for benzophenone.[16] The fluorescence yield of DPI in ethanol was determined to be 0.09, while in 0.1 *M* NaOH, $\Phi_F = 0.68$. This significant increase of fluorescence in a basic

(12) H. Stegemeyer, *Z. Naturforsch.*, **176**, 153 (1962).

(13) C. Dufraisse, A. Etienne, and J. Martel, *C. R. Acad. Sci.*, **244**, 970 (1957).

(14) A. White and M. Harding, *Photochem. Photobiol.*, **4**, 1129 (1965).

(15) V. G. Shore and A. B. Pardee, *Arch. Biochem. Biophys.*, **60**, 100 (1956).

(16) N. J. Turro, "Molecular Photochemistry," W. A. Benjamin, New York, N. Y., 1965, p 75.

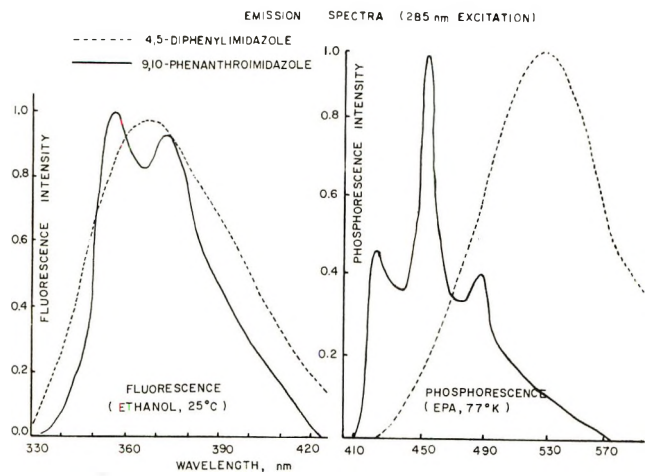

Figure 3. Fluorescence and phosphorescence spectra of 4,5-diphenylimidazole and 9,10-phenanthroimidazole obtained with 285-nm excitation.

medium is due to the formation of the anion.[17] The phosphorescence yield of DPI in EPA was determined to be 0.02 relative to benzophenone. The fluorescence and phosphorescence spectra of 4,5-diphenylimidazole and its photoproduct, 9,10-phenanthroimidazole, are presented in Figure 3. Noteworthy is the observation that there is increased structure in the fluorescence and phosphorescence spectrum of PI relative to DPI, which may be related to the restricted motion of the phenyl rings in forming the photoproduct.

Discussion

The photocyclization of stilbene and its analogs to phenanthrene type compounds is generally accepted to occur *via* a dihydrophenanthrene intermediate, which is air oxidized to the phenanthrene.[1] In the present investigation we have been unable to observe any evidence for the dihydrophenanthrene intermediate during the degassed photolyses of DPI and TPI; consequently, it appears that the formation of the phenanthroimidazoles can occur directly from the phenylimidazoles without any oxidizer.

The formation of PI from DPI is enhanced by a factor of 20, relative to degassed runs, when photolyzed in air-saturated hexane–ethanol solutions; however, it is very unlikely that sufficient dissolved molecular oxygen exists in degassed solutions, at the concentrations needed for the amount of phenanthroimidazole formed. When degassed samples of DPI and TPI were opened to the atmosphere after photolysis no additional phenanthrene was formed. Moore, *et al.*,[5] Mallory, *et al.*,[6] and Fisher[1] postulate that oxygen is required to oxidize the 4a,4b-dihydrophenanthrene intermediate, formed by irradiation, to the corresponding phenanthrene. Moore, *et al.*,[5] have reported that 0.92 mol of oxygen are consumed for each mole of phenanthrene formed. This type of oxidation does not appear to be operative in the photocyclization of DPI.

Srinivasan and Hsu[7] recently demonstrated solvent effects on the photocyclization of stilbene as an indication of a free-radical mechanism, which appears to be a factor in the photochemistry of DPI and TPI. Although we are unable to account for the loss of hydrogen atoms in forming the phenanthrene compounds, a hydrogen abstraction involving the solvent, followed by cyclization and aromatization, as suggested by Srinivasan and Hsu,[7] could lead to formation of a species, which either loses a hydrogen atom to produce the phenanthroimidazole or undergoes a hydrogen abstraction process to form 9,10-dihydrophenanthroimidazole, *i.e.*

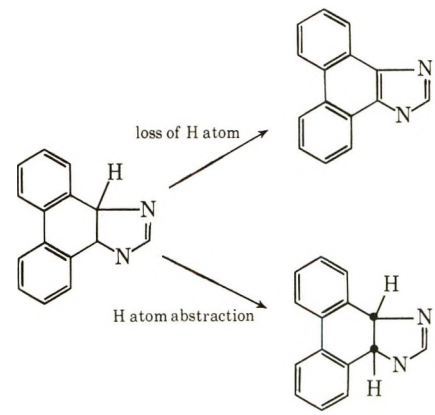

The absence of the dihydrophenanthrene intermediate during the degassed photolysis of DPI and TPI in this investigation suggests that the process involving loss of an H atom predominates. A more definitive mechanism, however, for the loss of hydrogen atoms during the photochemistry of phenylimidazoles and other analogs of stilbene still needs to be elucidated.

(17) H. Walbe and R. Isensee, *J. Org. Chem.*, 26, 2789 (1961), report pK_a = 12.80 for the loss of the proton attached to the pyrrole nitrogen.

On the Mechanisms of Photobleaching of Trapped Electrons in Ethylene Glycol–Water Glass

by Harald B. Steen* and Johan Moan[1]

Norsk Hydro's Institute for Cancer Research, Montebello, Oslo 3, Norway *(Received June 13, 1972)*

Publication costs assisted by the Norsk Hydro's Institute for Cancer Research

The mechanisms of excitation and photobleaching of radiation-induced trapped electrons, e_t^-, have been investigated by studying the effect of electron scavengers on the photobleaching of e_t^- in equivolume ethylene glycol–water glass. OD at λ_{max} (*i.e.*, at 585 nm) was measured during X irradiation and subsequent exposure to monochromatic light of various wavelengths λ_b. The photobleaching quantum yield, ϕ, decreases by a factor of about 15 between 366 and 546 nm, while above 546 nm it is constant. The presence of NO_3^- enhances ϕ significantly. This effect decreases with increasing λ_b. e_t^- appears to exhibit a number of excited levels, some of which are below the ionization potential E_i. Thus, the lowest excited level seems to be at about 1.8 eV whereas $E_i = (2.4 \pm 0.2)$ eV. The results are in accordance with the assumption that the photoactivation of e_t^- occurs *via* excited states of e_t^- located above E_i, whereas the direct transition of e_t^- to the conduction band seems to be insignificant. The excited states of e_t^-, both below and above E_i, may react with the solvent glass, *i.e.*, with ethylene glycol, as well as with solute molecules.

Introduction

The solvated electron e_s^- is characterized by a strong optical absorption usually covering the entire visible region of the spectrum. However, the nature of the optical transitions involved is not fully understood. Thus, it is not known whether the excitation of e_s^- occurs to bound or quasi-bound excited levels or directly to the state of a free electron, *i.e.*, to a conduction band, or both. The transient nature of e_s^- makes detailed studies of its optical properties difficult. Hence, considerable effort has been concentrated on electrons trapped in the rigid glasses formed by various polar liquids at low temperature. Except for their stability these trapped electrons e_t^- appear to be essentially similar to e_s^-.[2]

A number of investigations have shown that when glasses containing e_t^- are exposed to visible light, the electrons disappear and, furthermore, that this photobleaching may be accompanied by photoconductivity, indicating that the absorption of light may bring e_t^- into the state of a free, mobile electron e_m^-.[2] Eisele and Kevan[3] found that for γ-irradiated 10 *M* NaOH at 77 K the wavelength dependence of the photoconductivity matches the absorption spectrum of e_t^-. They concluded that, in contrast to the predictions of most current theories, e_t^- has no excited bound states. However, they were not able to decide whether the formation of e_m^- occurs directly from the ground state of e_t^- or by ionization of a quasi-bound excited state, *i.e.*, excited states above E_i.

In the present work we have tried to elucidate further the nature of the excited states of e_t^- and the mechanism of the photoactivation. It appears that in the present glass e_t^- has at least one bound excited level, *i.e.*, an excited level which is below E_i. Furthermore, the results support the hypothesis that the photoinduced transition of e_t^- to e_m^- occurs *via* quasi-bound excited states of e_t^-. The excited states of e_t^-, both below and above E_i, may react with the solvent as well as with solute molecules.

Theoretical Considerations

Photobleaching Kinetics. Since it is easily overlooked that the kinetics of the photoinduced decay of e_t^- depend critically on the concentration of e_t^-, $[e_t^-]$, we derive here the exact formula.

Consider the case that all e_t^- in a sample have uniform trap depth, *i.e.*, that all occupied traps are identical, and consequently have the same probability, ϕ, to disappear upon absorption of a photon of wavelength λ_b. The number of e_t^- disappearing per unit time and volume is then

$$\frac{d}{dt}[e_t^-] = -I\phi a = -I\phi(1 - 10^{-\epsilon_b l[e_t^-]}) = -I\phi(1 - 10^{-OD_b}) \quad (1)$$

where I is the quantum intensity of the bleaching light, a the fraction of this light which is absorbed in the sample, l the optical path length in the sample, ϵ_b the extinction coefficient at λ_b, and t the bleaching time. Integration of eq 1 gives

(1) Fellow of The Norwegian Research Council.

(2) Several reviews of this subject have been published. See, for example, A. Ekstrom, *Radiat. Res. Rev.*, 2, 381 (1970); F. S. Dainton, *Ber. Bunsenges. Phys. Chem.*, 75, 608 (1971).

(3) I. Eisele and L. Kevan, *J. Chem. Phys.*, 53, 1867 (1970).

$$OD_b + \frac{1}{\ln 10} \ln (1 - 10^{-OD_b}) =$$

$$OD_b^0 + \frac{1}{\ln 10} (1 - 10^{-OD_b^0}) - I\phi\epsilon_b lt \quad (2)$$

where OD_b^0 is OD_b at $t = 0$.

The decay of OD_b, as calculated from eq 2, is shown in Figure 1. It can be seen that it is reasonably exponential only when a small fraction of the incident light is absorbed, say for $OD_b < 0.2$. For large values of OD_b the decay will obviously approach a linear time dependence (see eq 1). Thus, for $OD_b > 1$ this is a good approximation. For intermediate values of OD_b, which is perhaps the region which is most commonly utilized, the decay kinetics have no simple analytical form at all.

Photoactivation Models. We shall consider two mechanisms for the photoactivation of e_t^- which are both shown schematically in Figure 2. For both cases we assume that all e_t^- have the same trap depth and consequently the same ionization potential, *i.e.*, the same energy difference between e_m^- and the ground state of e_t^-.

The upper diagram of this figure represents what we shall call "the direct activation" model, namely, the hypothesis that by absorption of a photon e_t^- is transferred directly to a free mobile electron e_m^-, *i.e.*, a direct transition from the ground state to the conduction band. e_m^- may be retrapped in competition with reaction with the molecules of the solvent glass itself and with a scavenging solute S. We assume that the original formation of e_t^-, *e.g.*, by ionizing radiation, occurs *via* the formation of e_m^-. The following symbols are used: [S] = scavenger concentration, $G(e_t^-)$ = yield of e_t^-, ϕ = photobleaching quantum yield, $[S]_{1/2}$ = the value of [S] necessary to halve $G(e_t^-)$, $[S]_\phi$ = the value of [S] necessary to double ϕ, k_t = probability per second that e_m^- will become trapped, k_s = probability per second and per unit concentration of S that e_m^- will react with S, k_r = probability per second that e_m^- will react with the solvent glass including recombination with positive holes. Subscript 0 denotes that S = 0.

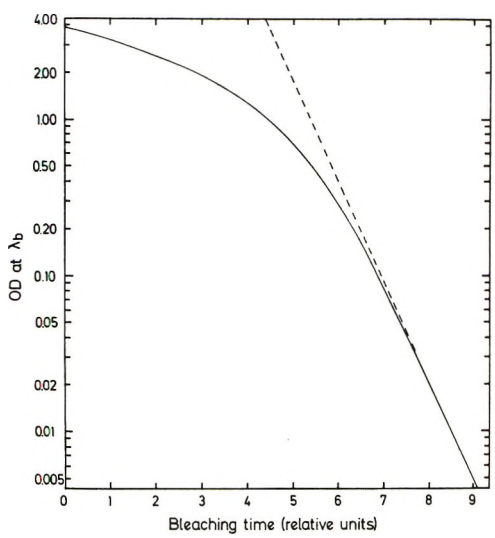

Figure 1. OD decay kinetics during photobleaching with constant light intensity as calculated from eq 2.

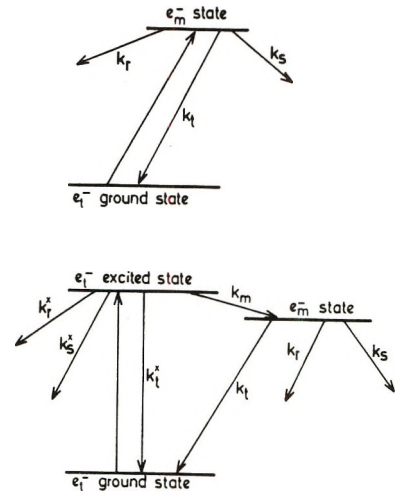

Figure 2. Schematic representation of the two models of photoactivation considered here. The upper diagram represents the assumption that by absorption of a photon e_t^- is transformed directly to a free electron e_m^- whereas in the lower model it is assumed that e_m^- is formed by ionization of an excited state of e_t^-.

We assume that the reactivity of e_m^- is independent of its mode of formation, *i.e.*, that k_s, k_r, and k_t are independent of whether e_m^- results from X-ray-induced ionization or from photoactivation of e_t^- and independent of the energy of the photon which causes the photoactivation. Physically this is to say that electrons released either by ionization or photoactivation are essentially unreactive until they reach the state e_m^- which is conceivably the thermalized free electron. The experimental support for this assumption is discussed below.

Assuming that k_s is independent of [S], one obtains the expression for homogeneous scavenging kinetics

$$G_0(e_t^-)/G^-(e_t^-) = 1 + k_s[S]/(k_t + k_r) \quad (3)$$

Measurements of the scavenging kinetics of e_m^- [4] indicate that although eq 3 is not valid for large [S], it is a reasonable approximation as long as $G_0(e_t^-)/G(e_t^-)$ is relatively small, say ≤ 2. Accepting this, we have

$$[S]_{1/2} = (k_t + k_r)/k_s \quad (4)$$

$$\phi = (k_r + k_s[S])/(k_t + k_r + k_s[S]) \quad (5)$$

$$\phi_0 = k_r/(k_t + k_r) \quad (6)$$

(4) H. B. Steen, O. Kaalhus, and M. Kongshaug, *J. Phys. Chem.*, **75**, 1941 (1971).

and hence

$$\phi/\phi_0 = \left(1 + \frac{k_s}{k_r}[S]\right)\Big/\left(1 + \frac{k_s}{k_t + k_r}[S]\right) \quad (7)$$

Putting $\phi/\phi_0 = 2$ in eq 7, we find

$$[S]_\phi = \frac{k_r}{k_s}\frac{k_t + k_r}{k_t - k_r} \quad (8)$$

The present experiments show that for all λ_b $\phi_0 \ll 1$. According to eq 6 this implies that $k_r \ll k_t$. Hence

$$[S]_\phi \approx k_r/k_s \quad (9)$$

By combining this with eq 4 and 6, we find

$$[S]_\phi/[S]_{1/2} \approx k_r/(k_t + k_r) = \phi_0 \quad (10)$$

Hence, the direct activation model implies that to the extent that the above assumptions hold true, ϕ_0, ϕ, and $[S]_\phi$ should be independent of λ_b up to a certain value of λ_b corresponding to the ionization potential of e_t^-, E_i. For wavelengths above this, ϕ should drop sharply to zero provided there are no bound, *reactive*, excited levels of e_t^-. It also follows that the relative amounts of the radicals formed by the reaction of e_m^- with the scavenger and the solvent glass, respectively, should be independent of λ_b.

The "indirect activation" model, shown in the lower diagram of Figure 2, implies that the photoactivation occurs *via* an excited state e_t^{-*}. The deexcitation of e_t^{-*} to the ground state occurs in competition with reaction of e_t^{-*} with the solvent glass and with the scavenger. If the excitation energy is above the ionization potential, e_t^{-*} is analogous to a quasi-bound or superexcited state of e_t^- and may be autoionized to form e_m^-. e_m^- may react as described above. In analogy with the preionization of molecules the probability that the excited states of e_t^- above E_i will ionize, *i.e.*, for the transition $e_t^{-*} \rightarrow e_m^-$ to occur, is likely to increase markedly with the excitation energy. And since the formation of e_m^- gives the electron a greatly increased chance to react with the scavenger as well as with solvent molecules and positive holes, the efficiency of the scavenger as well as ϕ_0 should increase significantly with the photon energy. That is, ϕ_0 is expected to decrease and $[S]_\phi$ is expected to increase with increasing λ_b up to the wavelength corresponding to E_i. For larger wavelengths bleaching may still occur as a result of a reaction of the bound excited states of e_t^- with scavenger molecules, solvent, and positive holes.

Experimental Section

OD Measurements. Samples were prepared from an equivolume mixture of ethylene glycol (Chromatoquality from Matheson Coleman and Bell) and doubly distilled water, EG–H_2O. $NaNO_3$ was Merck analytical grade.

Samples (50 μl) were contained in perspex cups, 1 mm deep and 8 mm in diameter, which were situated in a $<10^{-5}$-mm vacuum and thermoregulated to within ±1°. The optical density within a narrow (~1 nm) wavelength band was measured continuously during X irradiation and the subsequent photobleaching. The apparatus has been described elsewhere.[5]

One sample at a time was X irradiated until the OD at λ_{max} (585 nm) reached 0.2.

The dose rate of the 50-kV X irradiation was about 120 krads/min. The irradiation time varied from 15 to 100 sec depending on the solute concentration. The bleaching exposure was started about 30 sec after X irradiation. The source of the bleaching light was a 200-W, high-pressure Hg lamp which was fitted to a Bausch & Lomb high-intensity monochromator. The light was focused on the sample by a quartz lens and the bleaching time was controlled by a shutter. The wavelengths employed for the photobleaching were those of the most prominent lines in the spectrum of the lamp, thus limiting the effective band width to a few nm. Cut-off filters were used to eliminate stray light. The intensity of the bleaching light ranged from 4 to 15 mW/cm² and the resulting half-life of e_t^- during bleaching varied between 5 and 80 sec depending on wavelength.

Esr Measurements. Solid spheres of sample solution were made from drops falling into liquid N_2. A sample consisted of two such spheres in a Pyrex tube of 3-mm inner diameter which was sealed off under high vacuum. The samples were irradiated with 220-kV X-rays for 30 min with a dose rate of about 3 krads/min. One end of the tube was shielded during the X irradiation and the spheres were transferred to this end for esr measurement and photobleaching. The tubes were kept in liquid N_2 throughout the entire experiment.

The esr spectrometer was an X-band type with transmission cavity and 110-kHz field modulation.

Results

OD Decay Kinetics. In Figure 3 is reproduced the recorder tracing from a typical experiment showing OD at λ_{max} during X irradiation and subsequent photobleaching. $G(e_t^-)$ can be determined from the initial slope of that part of the tracing which is recorded during X irradiation. When plotted on a semilogarithmic scale, as shown in Figure 4, it appears that the decay of OD at 77 K can be decomposed into two exponential components of approximately the same size, whereas at 113 K the fastest of these components has vanished almost completely. At 120 K the decay is strictly exponential so that only the slowest component remains. These results are in accordance with observations of the effect of photobleaching on the optical

(5) H. B. Steen, O. I. Sorensen, and J. Aa. Holteng, *Int. J. Radiat. Phys. Chem.*, **4**, 75 (1972).

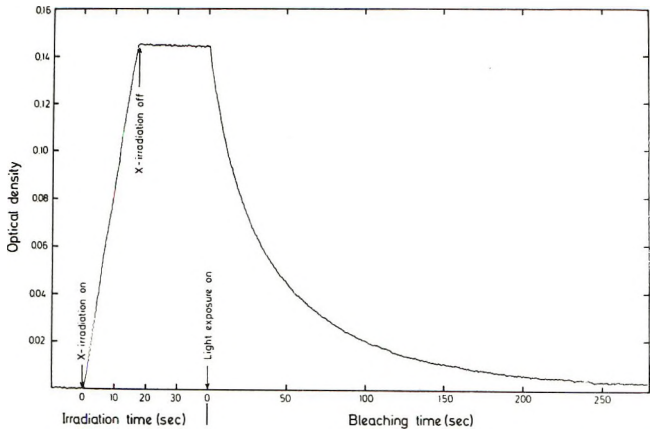

Figure 3. Recorder tracing of OD at 585 nm as obtained during X irradiation and subsequent photobleaching at 546 nm, T = 77 K.

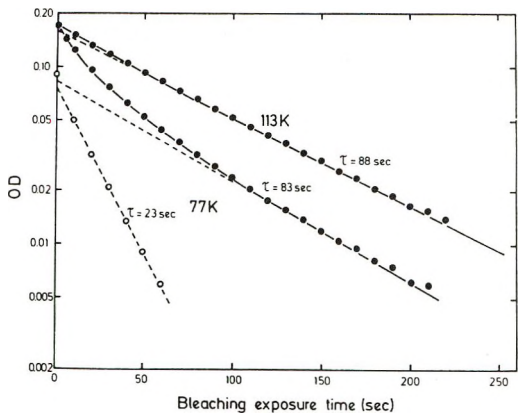

Figure 4. Semilogarithmic plot of the decay of OD at 585 nm during photobleaching at 546 nm as observed at 77 and 113 K.

absorption spectrum of e_t^-.[6] Thus, by exposing X-irradiated EG–H_2O glass to monochromatic light of various wavelengths above and below λ_{max}, we have found that the spectrum of e_t^- at 77 K can be decomposed into two broad structureless components of approximately the same size, both covering the entire region from below 350 nm to above 700 nm. One of these components, *i.e.*, the one most prominent at shorter wavelengths, is closely similar to the spectrum observed at 120 K and above. The shape of this spectrum at 120 K cannot be altered much by photobleaching or by further thermal annealing. Hence, it appears that at this temperature all e_t^- have approximately the same absorption spectrum and consequently a fairly uniform trap depth. According to the decay curves of Figure 4 this appears to be a very good approximation also at 113 K. The reason that the trap depth appears to be nearly uniform at these temperatures is probably that the viscosity of the glass is low enough to allow complete dielectric relaxation of all traps.

In agreement with several others,[2] we find that the rate of the photoinduced decay of OD is proportional to the light intensity, demonstrating that the photobleaching in the present case is a single-photon process.

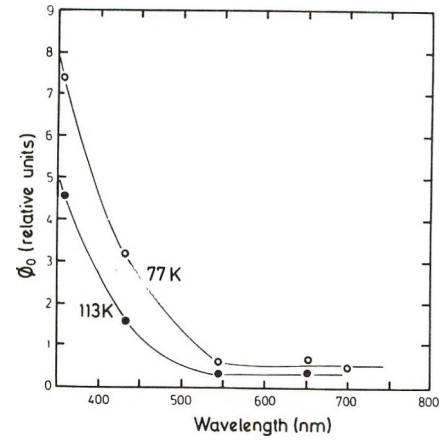

Figure 5. Wavelength dependence of the quantum yield of photobleaching in the absence of scavenger at 77 and 113 K.

Quantum Yields of Photobleaching. Figure 5 shows the wavelength dependence of ϕ_0 at 77 and 113 K. ϕ_0 has been taken to be inversely proportional to the half-life, $\tau_{1/2}$ of OD at λ_{max} during the photobleaching. At 113 K where the absorption spectrum appears to consist primarily of only one component and where the decay of e_t^- consequently is approximately exponential, this is obviously a good approximation. The ϕ_0 given for 77 K, however, should be regarded as an intermediate of the bleaching quantum yields associated with the two decay components observed at this temperature. In the calculation of these yields we have assumed that the optical absorption is due exclusively to e_t^-. At 366 nm, however, there may be a contribution to the absorption from other radiation-induced species. If this is so, the values of ϕ_0 at 366 nm given in Figure 5 are too low. It can be seen from Figure 5 that ϕ_0 decreases strongly with increasing λ_b up to about λ_b 540 nm, while above this wavelength it becomes approximately constant. The wavelength dependence of ϕ_0 shown in Figure 5 is qualitatively similar to that reported by Bernas, *et al.*,[7] for e_t^- in γ-irradiated ethanol glass.

The absolute value of ϕ_0 at λ_b 436 nm and T = 113 K is $\phi_0 = 0.012 \pm 0.006$. This value also applies to the slow component observed at 77 K, whereas the fast component has a ϕ_0 which is roughly three times larger. The absolute value of ϕ_0 has been calculated on the assumption that ϵ at λ_{max} is $1.5 \times 10^4\ M^{-1}\ cm^{-1}$. The wide error limits given, *i.e.*, $\pm 50\%$, are mainly due to the uncertainty of this value and to the fact that we do not know the degree of homogeneity of the intensity of the bleaching light on the sample. The reproducibility of ϕ_0 is within $\pm 10\%$.

(6) H. B. Steen, to be submitted for publication.

(7) A. Bernas, D. Grand, and C. Chachaty, *Chem. Commun.*, 1667 (1970).

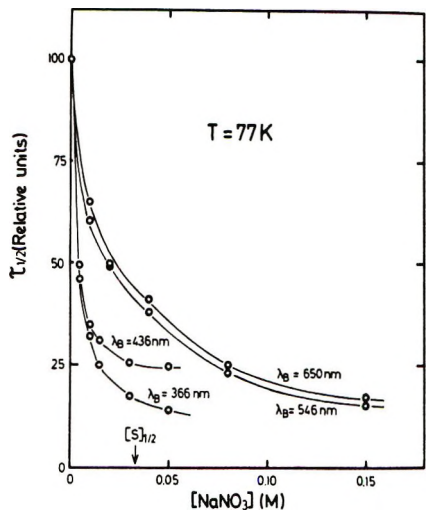

Figure 6. Effect of $NaNO_3$ on the half-life of OD at 585 nm during photobleaching at various wavelengths as observed at 77 K.

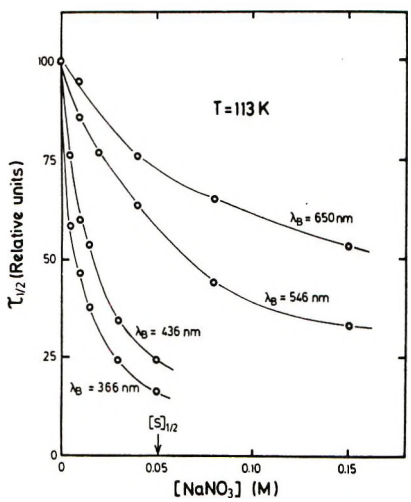

Figure 7. Effect of $NaNO_3$ on the half-life of OD at 585 nm during photobleaching at various wavelengths as observed at 113 K.

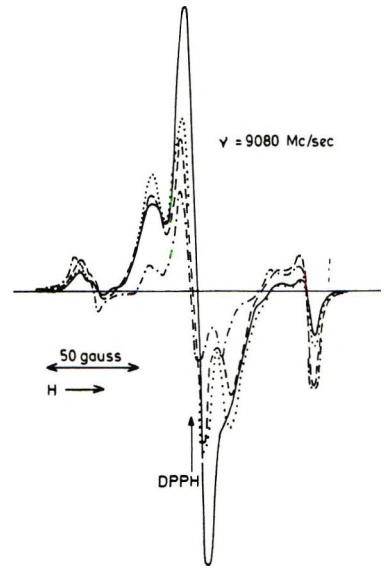

Figure 8. Esr spectra of X-irradiated samples with 0.01 *M* $NaNO_3$ before and after photobleaching: (——) before bleaching; (· · · · · ·): after exposure to light at 575 nm; (– – –) after exposure to light at 366 nm; (–·–·–·) unbleached sample containing 0.2 *M* $NaNO_3$ which is sufficient to capture virtually all electrons prior to trapping.

According to the theoretical models outlined above it seems reasonable to assume that the wavelength region for which ϕ_0 is constant corresponds to photon energies below E_i. Hence we find $E_i = (2.4 \pm 0.2)$ eV. This result may be compared to the value of 2.3 eV obtained for ethanol by Bernas, *et al.*[7]

Scavenger Effects. Figure 6 depicts how $\tau_{1/2}$ of OD at λ_{max} during photobleaching at various wavelengths depends on the concentration of an electron scavenger, *i.e.*, $NaNO_3$, at 77 K. Figure 7 shows similar data as obtained at 113 K. It is evident from these results that the presence of an electron scavenger reduces $\tau_{1/2}$ considerably and, furthermore, that the effect of the scavenger decreases strongly when λ_b increases. Qualitatively similar results have been obtained for other electron scavengers. As noted above, $\tau_{1/2}$ measured at 77 K should be considered to be associated with an intermediate of the ϕ values of the two absorption components.

The values of $[S]_\phi$ determined from the results of Figures 6 and 7 are given in Table I together with those of $[S]_{1/2}$.

Table I

	$[S]_\phi$, *M*				
T, K	λ_b 366 nm	λ_b 436 nm	λ_b 546 nm	λ_b 650 nm	$[S]_{1/2}$, *M*
77	0.004	0.006	0.019	0.024	0.033
113	0.008	0.017	0.066	0.18	0.051

Esr Spectra. Figure 8 shows the esr spectra of X-irradiated EG–H_2O glass containing $NaNO_3$ before and after photobleaching at two different wavelengths. As discussed elsewhere[8] the central singlet is due to e_t^-. This singlet is superimposed on a triplet which in the unbleached samples represents approximately the same number of radicals as the singlet. The triplet appears to be due to ethyl radicals which are probably associated with the holes left by the electrons or with the products of the reaction of these holes with ethylene glycol. The peaks at the outer ends of the spectra represent the NO_2 radical resulting from the reaction of electrons with NO_3^-.[9] The rest of the signal from

(8) H. B. Steen, *Photochem. Photobiol.*, 9, 479 (1969).
(9) T. Henriksen, *Radiat. Res.*, 38, 231 (1969).

the radicals associated with the scavenger is hidden in the main spectrum, as indicated by the spectrum observed in the presence of a large concentration of $NaNO_3$ when supposedly all e_m^- have reacted with NO_3^-. The NO_2 radicals seen in the spectrum of the unbleached sample arise from the capture of e_m^- prior to trapping.

From Figure 8 it can be seen that photobleaching at λ_b 366 nm eliminates the e_t^- singlet and produces a significant rise in the number of NO_2 radicals as well as ethyl radicals. A corresponding bleaching at λ_0 575 nm, however, causes no noticeable rise in the number of NO_2 radicals, whereas the increase of the ethyl radical triplet is somewhat larger than in the previous case. These results seem to demonstrate that the photon energy corresponding to 575 nm is not sufficient to transfer e_t^- to e_m^-. Hence, in agreement with the above results, this photon energy and the corresponding excited level appears to be below the ionization potential of e_t^-.

A more detailed account of the esr measurements will be published.

Discussion

It is commonly assumed that λ_{max} of the absorption spectrum of e_t^- represents the excitation energy of the lowest excited level of e_t^-. Thus, the absorption at longer wavelengths has been attributed to electrons in more shallow traps with a lower excitation energy. The present results, however, seem to demonstrate that at 113 K and above all e_t^- have approximately the same absorption spectrum and consequently a uniform trap depth. The absorption spectrum at this temperature extends up to about 700 nm, indicating that the lowest excited level is about 1.8 eV above the ground state. On the other hand, the ionization potential E_i of e_t^- as inferred from the wavelength dependence of ϕ_0 (Figure 5) is at 2.4 eV. We therefore conclude that the lowest excited state of e_t^- in the present glass is a bound state. Considering that there seems to be no appreciable broadening of the spectrum due to variation in trap depth, the structureless appearance of the spectrum indicates that e_t^- exhibits a number of excited levels with energies from about 1.8 eV to far above the ionization potential.

The observation that photobleaching occurs also for photon energies well below E_i demonstrates that the bound excited states of e_t^- are reactive. The fact that ϕ_0 is constant for wavelengths above 540 nm (Figure 5) seems to rule out the possibility that the photobleaching at longer wavelengths can be explained in terms of a variation of trap depths. Thus, if this was the case, ϕ_0 should continue to decrease with increasing λ_b above 540 nm. This is supported also by the esr spectra which indicate that photoactivation of e_t^- at 575 nm does not lead to formation of e_m^-.

In the two theoretical models for photoactivation outlined above it was assumed that all e_t^- are identical. Our results show that this is definitely not the case at 77 K, whereas at 113 K it appears to be a good approximation. Hence, when discussing the results on a quantitative basis we shall concentrate on the data obtained at 113 K.

According to the direct activation model ϕ_0 as well as $[S]_\phi$ should not vary appreciably with λ_b for photon energies above E_i. The basis for this assumption is that the relative probabilities for trapping and reaction of e_m^- with solvent and solute do not depend significantly on the initial energy of e_m^-. According to eq 4 this assumption implies that $[S]_{1/2}$ should also be independent of the mode of formation of e_m^-. The latter expectation is experimentally supported by our finding that $[S]_{1/2}$ as observed for electrons produced by X irradiation is approximately the same as that obtained with uv-induced photoionization. In fact, the values of $[S]_{1/2}$ observed with X irradiation is 10 to 40% larger than those found with photoionization, the difference depending on the electron scavenger studied. This difference, however, can be quantitatively accounted for by the fact that with X-rays a fraction of the electrons are formed in spurs containing more than one electron. Hence, it appears that the relative reactivities of e_m^- are approximately independent of the initial energy of the electron.

In contrast to the predictions of the direct activation model the experimental data (Figures 5–7 and Table I) show that both ϕ_0 and $[S]_\phi$ vary strongly with λ_b for photon energies above E_i and furthermore that they vary in the opposite direction. Thus, the ratio $[S]_\phi/\phi_0$, which according to eq 10 should be independent of λ_b, changes by a factor of about 120 between 366 and 546 nm.

On the other hand, the strong wavelength dependence of both ϕ_0 and $[S]_\phi$ for photon energies above E_i is in accordance with the predictions of the indirect activation model. We therefore conclude that the photoactivation seems to occur predominantly *via* excited levels of e_t^-, whereas the direct transition from e_t^- to the conduction band e_m^- appears to be insignificant.

Even for photon energies below E_i the presence of $NaNO_3$ enhances the rate of photobleaching although the effect is much less pronounced than for higher photon energies. This result indicates that the bound excited states of e_t^- may react with solute molecules when present in sufficiently high concentrations. The observation that $[S]_\phi$ continues to increase with λ_b, also for photon energies below E_i, shows that the probability of the reaction of e_t^{-*} with scavenger relative to that of deexcitation increases with the excitation energy. This observation also seems to support the conclusion that there is more than one bound excited level.

Conclusion

We conclude the following.

(1) e_t^-, as observed in the present glass, appears to exhibit a number of excited levels, some of which are well below the ionization potential.

(2) Photobleaching of e_t^- by a direct transition to the conduction band does not seem to be significant.

(3) Thus, the data appear to be in accordance with the assumption that the formation of e_m^- resulting from photoactivation of e_t^- occurs by ionization of excited levels of e_t^- which are above the ionization potential, *i.e.*, by a process comparable to autoionization of superexcited molecules. The probability of autoionization relative to that of deexcitation increases rapidly with the excitation energy.

(4) The excited states of e_t^- both below and above the ionization potential may react with the solvent glass, *i.e.*, with ethylene glycol, as well as with an electron scavenging solute. These reactions, however, are fairly slow as compared to deexcitation of e_t^{-*} to its ground state.

Kinetic Studies of the Catalytic Activity of Alkaline Earth Oxides in 2-Propanol Decomposition

by E. F. McCaffrey, T. A. Micka, and R. A. Ross*

Department of Chemistry, Lakehead University, Thunder Bay, Ontario, Canada *(Received July 11, 1972)*

The catalytic decomposition of 2-propanol over the metal oxides of group IIa, excepting radium oxide, has been investigated from 230 to 350° using 3.12 to 15.62 mm partial pressure alcohol. The apparent activation energies for dehydrogenation varied from 19 kcal mol^{-1} for beryllium oxide to 45 kcal mol^{-1} for calcium oxide. The apparent activation energies for dehydration were always greater than those for dehydrogenation on the corresponding oxide and varied from 38 kcal mol^{-1} for beryllium oxide to 54 kcal mol^{-1} for calcium and strontium oxides. The rate-controlling step in both dehydrogenation and dehydration reactions was concluded to be either adsorption of 2-propanol or reaction of the adsorbed alcohol. The selectivity for dehydrogenation increased with increasing mobility of surface oxygen as measured in ^{18}O exchange experiments while the ionicity of the surface oxygen is believed to play a decisive role in influencing the catalytic activity of the oxides.

Introduction

A recent study of the catalytic decomposition of 2-propanol on manganese(II) oxide[1] showed that the reaction was more complex than had been recognized.[2] The expected dehydrogenation and dehydration reactions were interlinked in a fairly complex manner while condensation products were also detected. These observations indicated a need to obtain further kinetic and analytical data on the decomposition over a wide range of metal oxide catalysts since the reaction is often used as a model in studies of catalyst activity variations.[2]

This communication describes a kinetic study of the decomposition of the alcohol on the oxides of the metals of group IIa in the periodic classification, excluding only radium. Careful attention has been given to the identification of the products of catalysis and to specifying important structural and surface parameters of the catalysts.

In previous relevant studies involving alkaline earth oxides, decomposition kinetics were examined on magnesium oxide[3] to evaluate the influence of preparation temperature on its catalytic activity and also on calcium, strontium, and barium oxides as a series[4] when it was concluded that the oxide activity in catalysis increased with an increase in the atomic weight of the metal.

Experimental Section

Full details of the apparatus and methods of analysis have been reported.[1] Surface areas were determined by low-temperature krypton adsorption (BET, −196°; σ = 21.5 Å^2; Table I).

(1) D. G. Klissurski, E. F. McCaffrey, and R. A. Ross, *Can. J. Chem.*, **49**, 3778 (1971).

(2) O. V. Krylov, "Catalysis by Nonmetals," Academic Press, New York, N. Y., 1970.

(3) W. F. N. M. de Vleeschauwer, "Physical and Chemical Aspects of Adsorbents and Catalysts," B. Linsen, Ed., Academic Press, London, 1970.

(4) O. V. Krylov, S. Z. Roginsky, and E. A. Fokina, *Izv. Akad. Nauk SSSR, Otd. Khim. Nauk*, **6**, 1668 (1956).

Table I: Experimental Reaction Rates and Apparent Activation Energies for the Dehydrogenation (r_1, E_1) and Dehydration (r_2, E_2) of 2-Propanol (9.37 mm) at 300 ml min^{-1} (NTP) on Group IIa Oxides

Catalyst	Temp range, °C	r_1, (mol m^2 sec^{-1}) × 10^{10} (300°)	r_2, (mol m^2 sec^{-1}) × 10^{10} (300°)	E_1, kcal mol^{-1} ± 1	E_2, kcal mol^{-1} ± 1	Surface area, m^2 g^{-1}	Selectivity, $r_1/(r_1 + r_2)$
BeO	350–230	229.0	331.0	19	38	3.3	0.41
MgO	350–270	94.0	8.5	29	47	9.5	0.92
CaO	350–290	126.0	10.2	45	54	1.6	0.93
SrO	350–270	21.7	0.2	22	54	1.3	0.99
BaO	350–280	479.0	4.2	37	48	0.4	0.99

Materials. (*a*) *Oxides.* Beryllium oxide (99.90% w/w, Alfa Inorganics Inc.) was heated at 600° for 10 hr in air and magnesium oxide was prepared from the basic carbonate (99.90% w/w, British Drug Houses Ltd.) by heating at 900° for 12 hr in air. Calcium oxide (99.90% w/w, British Drug Houses Ltd.) was heated at 700° for 10 hr in air prior to use. Strontium oxide (99.98% w/w, Research Organics/Inorganics Inc.) and barium oxide (99.90% w/w, Alfa Inorganics Inc.) were heated to 600° for 10 hr in dry nitrogen (60 ml min^{-1} (NTP)). The bulk structure of each oxide was confirmed by X-ray powder photography.[5]

(*b*) *Reagents.* 2-Propanol and acetone were Spectroquality reagents and their ultraviolet absorption characteristics, Unicam SP 800A, were the same as those given on their accompanying certificates. Nitrogen (Canadian Liquid Air Ltd.) was 99.99% pure.

Results

The particle size of the 1 g of the oxide catalysts used in the experiments was kept below 0.05 mm. The absence of internal and external diffusion was demonstrated by the usual tests.[1,6]

All samples were brought to the highest temperature of the experiment in an atmosphere of 2-propanol (300 ml min^{-1} (NTP); partial pressure, 9.37 mm) and kept under these conditions for 12 hr to establish the steady activity levels used in the rate calculations. At the end of each catalytic experiment the reaction temperature was raised to the highest value used in the course of the runs, when it was observed that no measurable change had taken place in the original values of the reaction rates. Before removal from the reactor, catalysts were cooled to room temperature in flowing nitrogen (60 ml min^{-1} (NTP)). Subsequently, X-ray powder diffraction patterns[5] and surface areas were determined. These areas were used in the specific reaction rate calculations. All catalysts were stable under the conditions of the experiments.

The Effect of 2-Propanol Partial Pressure on the Reaction Rates. In these experiments the partial pressure of 2-propanol was varied between 3.12 and 15.62 mm at 300 ml min^{-1} (NTP). Several runs were carried out with each catalyst to determine the steady dehydrogenation and dehydration reaction rates at three fixed temperatures within the range shown (Table II) and subsequently the reaction orders were obtained from logarithmic plots.[1] There was a tendency for the reaction order with respect to 2-propanol to increase slightly for both dehydrogenation and dehydration with increase in reaction temperature and with decrease in alcohol pressure.

Table II: The effect of 2-Propanol Partial Pressure (3.12–15.62 mm) on the Reaction Rates

Catalyst	Temp range, °C	Reaction order with respect to 2-propanol: Dehydrogenation	Dehydration
BeO	300–270	0.30–0.20	0.20–0.20
MgO	350–290	0.40–0.20	0.10–0.00
CaO	350–290	0.10–0.10	0.10–0.00
SrO	350–270	0.50–0.40	0.00–0.00
BaO	350–280	0.40–0.30	0.10–0.00

The reaction rate data fitted Langmuir plots in a similar manner to that shown for manganese(II) oxide.[1] The values of the heats of adsorption of 2-propanol calculated[7] from the Langmuir plots for adsorption leading to dehydrogenation varied from 14 ± 1 kcal mol^{-1} with magnesium oxide to 20 ± 1 kcal mol^{-1} with barium oxide. The heat of adsorption on magnesium oxide was 19 ± 1 kcal mol^{-1} for adsorption leading to dehydration. No other heats of adsorption for the dehydration reaction could be calculated with accuracy due to small changes in reaction order (Table II).

Magnesium oxide was the only catalyst which gave accurately measurable amounts of 4-methyl-1,3-pentadiene (maximum level 1.00% v/v of the reaction products) and mesityl oxide (maximum level 0.20% v/v of the reaction products) over the entire range of 2-propanol partial pressures used. The reaction order for both of these products was −0.50 with respect to 2-propanol partial pressure at 350°.

The Effect of the Partial Pressure of the Reaction Products on the Reaction Rates. Both the dehydrogenation

(5) American Society for Testing Materials; Card Index, 1967.

(6) E. F. McCaffrey, D. G. Klissurski, and R. A. Ross, *J. Catal.*, in press.

(7) J-E. Germain, J. Bigourd, J-P. Beaufils, B. Gras, and L. Ponsalle, *Bull. Soc. Chim. Fr.*, 1777 (1961).

and dehydration reactions were found to be zero order with respect to hydrogen when the total hydrogen partial pressure was varied from 1 to 20 mm over beryllium oxide at 350°. Propylene, 1 to 20 mm total partial pressure, did not affect either the rate of dehydration or the rate of dehydrogenation over beryllium oxide at 350°.

The effect of 0.40 to 4.80 mm total partial pressure of acetone on the rates of reaction of 9.37 mm of 2-propanol over beryllium oxide was examined at 319 and 273°. For dehydrogenation the reaction order with respect to acetone was 0.40 and 0.30 at 319 and 273°, respectively. The rate of dehydration at these temperatures was only slightly affected by acetone pressure and the reaction order for dehydration was taken as zero with respect to the partial pressure of this component.

On beryllium oxide the reaction order for dehydration with respect to water vapor between 0.90 and 3.00 mm total partial pressure was −0.30 at 319° while the rate of dehydrogenation was not affected.

Over barium oxide the reaction order for dehydrogenation and dehydration was −0.60 and −0.10, respectively, with respect to acetone at 350°. For the dehydration reaction on barium oxide the order with respect to added water vapor was −0.30 and −0.20 at 350 and 300°, respectively. The dehydrogenation reaction had reaction orders of −0.30 and −0.20 with respect to added water vapor at 350 and 300°. These effects were not examined on the other three oxide catalysts.

The Effect of Temperature on the Reaction Products. Both dehydrogenation and dehydration reactions occurred on all oxides at all temperatures. Table I shows the reaction rates at 300° for both dehydrogenation, r_1, and dehydration, r_2, along with the catalyst selectivities for dehydrogenation and the apparent activation energies for dehydrogenation, E_1, and dehydration, E_2. The rate constants for the Arrhenius plots, Figures 1 and 2, were calculated as shown previously[6] and the apparent activation energies, Table I, were obtained from these plots.

The primary products of the decomposition were acetone and propylene. Three secondary products, propane, 4-methyl-1,3-pentadiene, and mesityl oxide were detected. Isopropyl ether was not detected in the reaction products from any of the catalysts.

At 350° and 3.12 mm 2-propanol partial pressure, 4-methyl-1,3-pentadiene composed 1.00% v/v of the reaction products from both magnesium and calcium oxides. This component was not detected in the products of catalysis from beryllium oxide and it was present only in trace amounts (<0.01% v/v) in the products from strontium and barium oxides under these conditions.

At 350° with 3.12 mm 2-propanol partial pressure, mesityl oxide was detected in the reaction products from magnesium, calcium, strontium, and barium oxides in the respective amounts of 0.20, <0.01, 0.15, and 0.05% v/v. The product was not detected from beryllium oxide catalysts. Propane was detected at a maximum concentration of 5% v/v only in the products of catalysis from barium oxide under the conditions specified in Table I.

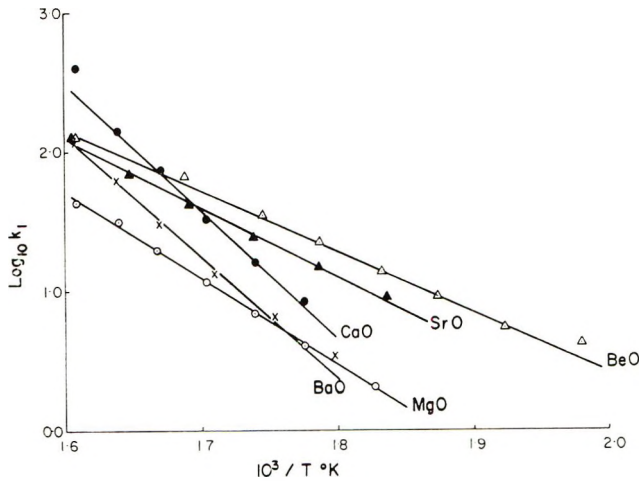

Figure 1. Arrhenius plots for dehydrogenation over the group IIa oxides: △, (log k_1) + 8, beryllium oxide; ○, (log k_1) + 8, magnesium oxide; ●, (log k_1) + 8, calcium oxide; ▲, (log k_1) + 8, strontium oxide; ×, (log k_1) + 8, barium oxide.

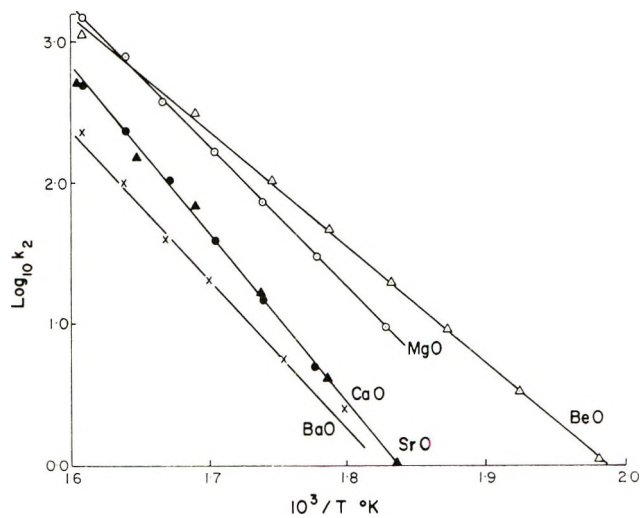

Figure 2. Arrhenius plots for dehydration over the group IIa oxides: △, (log k_2) + 8, beryllium oxide; ○, (log k_2) + 10, magnesium oxide; ●, (log k_2) + 9, calcium oxide; ▲, (log k_2) + 10, strontium oxide; ×, (log k_2) + 9, barium oxide.

Discussion

A number of possible rate equations have been derived[8] for the dehydrogenation of 2-propanol over zinc oxide. If the reaction of adsorbed alcohol is assumed to be rate controlling,[8] then

(8) Y. Dechatre, and S. J. Teichner, *Bull. Soc. Chim. Fr.*, 2804 (1967).

$$\text{rate} = \frac{k^1 N K_1 p_{alc}}{1 + K_1 p_{alc} + K_3 p_{ac}} \quad (1)$$

where K_1 and K_3 are the equilibrium constants for the adsorption of alcohol and acetone, respectively, k^1 is the rate constant for reaction of adsorbed alcohol, N is the total number of adsorption sites, and p_{alc} and p_{ac} are the partial pressures of 2-propanol and acetone, respectively. The equation is similar to that used previously[1,9] and a similar equation can be derived on the assumption that adsorption of alcohol is the rate-controlling step.[8]

For small partial pressure of acetone, $(1 + K_1 p_{alc}) \gg K_3 p_{ac}$ and the equation may be written in a Langmuir form[8]

$$\text{rate} = \frac{kKp}{1 + Kp} \quad (2)$$

Langmuir transformation plots for the reactions over magnesium oxide in the absence of added acetone are shown in Figure 3 and since these results were all obtained at 2-propanol conversions of <10% the assumption made to derive eq 2 can be justified for these experiments.

If acetone and 2-propanol are both strongly adsorbed and have similar partial pressures, then $1 \ll K_1 p_{alc} + K_3 p_{ac}$ and eq 1 becomes

$$\text{rate} = \frac{k^1 N K_1 p_{alc}}{K_1 p_{alc} + K_3 p_{ac}} \quad (3)$$

which may be transformed to

$$\frac{1}{\text{rate}} = \frac{1}{k^1 N} + \frac{K_3 p_{ac}}{k^1 N K_1 p_{alc}} \quad (4)$$

Hence a plot of 1/rate against p_{ac}/p_{alc} should give a straight line. Figure 4 shows this plot for dehydrogenation in the presence of added acetone, from 0.40 to 4.80 mm total acetone pressure, over beryllium oxide at 319°.

It may be concluded that reaction rate is extremely sensitive to changes in acetone partial pressure and that either adsorption of 2-propanol or decomposition of the adsorbed alcohol is rate controlling in dehydrogenation. The possibility that the slow step is acetone desorption is most unlikely since the reaction rate would then show a dependence on hydrogen partial pressure[8] which was not observed.

Replacing p_{ac} with p_w, partial pressure of water vapor, in (1) to (4) gives the dehydration rate equations from which the transformation plots shown in Figures 3 and 4 are obtained. Similar deductions to those for dehydrogenation may be made regarding the possible rate-controlling steps involved in dehydration since the propylene partial pressure did not affect this reaction rate.

Table I shows that the apparent activation energies for dehydration on each oxide, E_2, were greater than

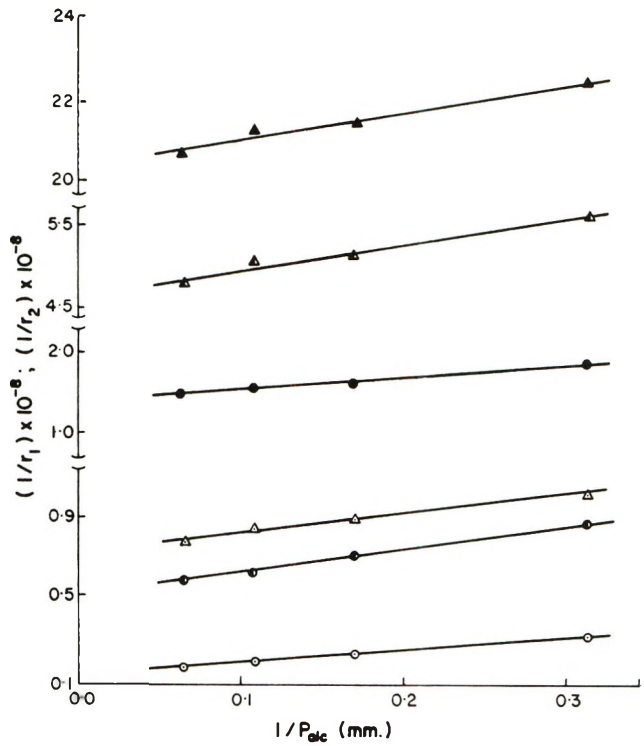

Figure 3. Langmuir transformations of the rates of dehydrogenation, r_1, and dehydration, r_2, over magnesium oxide at 349, 314, and 291°: ⊙, ◐, and ● dehydrogenation at 349, 314, and 291°, respectively; △, ◭, and ▲ dehydration at 349, 314, and 291; respectively.

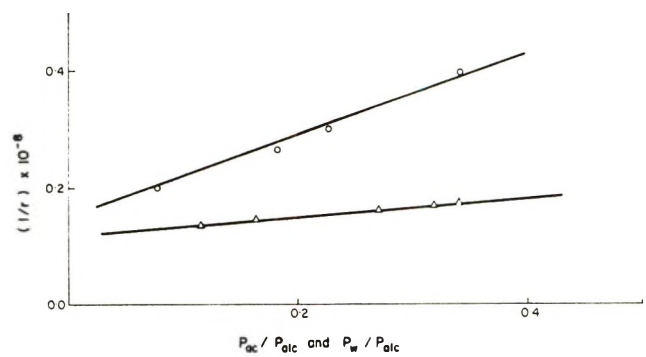

Figure 4. Transformation plots of 2-propanol dehydrogenation (⊙) and dehydration (△) equations for beryllium oxide catalyst at 319° in the presence of added acetone, dehydrogenation, and added water vapor, dehydration.

those for dehydrogenation. It was noted also that the values of the preexponential factor for dehydration were greater than those for dehydrogenation on any individual catalyst. A similar result was reported earlier[2,10] and has been interpreted as indicating that the intermediate complex formed in dehydration has more degrees of rotational freedom than that formed in dehydrogenation, which may indicate that single-

(9) O. V. Krylov, *Russ. J. Phys. Chem.*, **39**, 1554 (1965).

(10) O. V. Krylov and E. A. Fokina, *Russ. J. Phys. Chem.*, **40**, 1135 (1966).

point adsorption is involved in dehydration while a two-point adsorption complex occurs in dehydrogenation.[10]

Although no trend was observed in either the rates of reaction or the apparent activation energies, Table I, the selectivity toward dehydrogenation at 300° increased from 0.41 for beryllium oxide to 0.99 for barium oxide, the most ionic oxide in the group.[11] However,

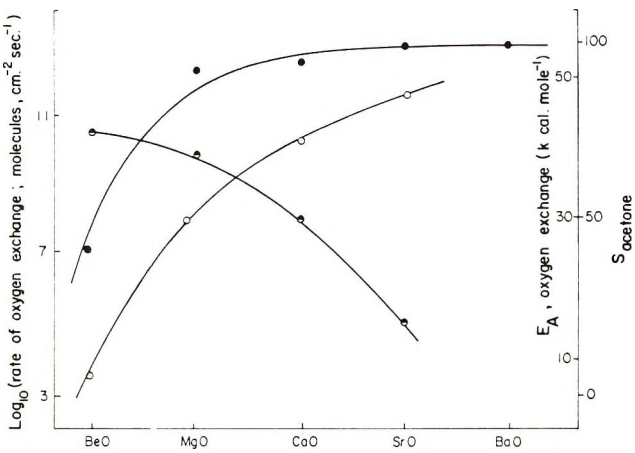

Figure 5. The relationships between the rates and activation energies of the isotopic exchange of oxygen on the surface of the group IIa metal oxides and their selectivities, S, in the catalytic dehydrogenation of 2-propanol: ●, $S_{acetone}$; ◓, activation energy for oxygen exchange;[12] ○, rate of oxygen exchange ((300°).

it is not possible to separate the possible influences of the metal–oxygen bond length, the width of the forbidden zone, the electronegativity, or the work function for this oxide series since all these properties change in a parallel fashion through the group.[2]

A composite plot of the rates of oxygen exchange[12] at 300°, the apparent activation energies for oxygen exchange,[12] and the selectivity for dehydrogenation of 2-propanol over the group IIa metal oxides is shown in Figure 5. The selectivity for dehydrogenation increases with increasing mobility of the surface oxygen as measured both by the rates and the apparent activation energies of oxygen exchange. A similar observation has been made for the oxides of the first transition metal series.[13]

Since the ionic character of these materials increases from beryllium to barium oxide, the tendency for surface oxygen ions to share their negative charge with adsorbed species will increase also and it has been suggested[12] that this phenomenon explains, at least in part, the increase in oxygen mobility down the group. Further, the tenacity with which the surface retains a proton will increase with this increase in ionicity.[14] Thus, if dehydration of 2-propanol is considered to proceed by a carbonium ion mechanism, it would be more difficult for (i) a proton to be donated to 2-propanol or (ii) a hydroxyl group to be abstracted from 2-propanol on barium oxide than on beryllium oxide. It seems likely that dehydrogenation involves hydrogen or proton coupling with surface oxygen ions and that dehydration involves coupling of the hydroxyl group with the surface as has been suggested earlier.[15] These conclusions are compatible with the increase in selectivity for dehydrogenation observed in the series from beryllium to barium oxide (Table I).

The rates of dehydrogenation over these catalysts are generally lower by a factor of 10 than those measured for the first transition series of metal oxides,[13] an observation which is consistent with the extra stability conferred on the group IIa oxides by filled orbitals. A similar phenomenon has been noted in studies of the dehydrogenation of cyclohexane[16] on these oxide catalysts.

(11) N. N. Greenwood, "Ionic Crystals, Lattice Defects and Nonstoichiometry," Butterworths, London, 1968.

(12) E. R. S. Winter, *J. Chem. Soc. A*, 2889 (1968).

(13) E. F. McCaffrey, D. G. Klissurski, and R. A. Ross, *Proc. Int. Congr. Catal., 5th, 1972*, in press.

(14) K. Tanaka and K. Tamaru, *Bull. Chem. Soc. Jap.*, **37**, 1862 (1964).

(15) I. Batta, S. Borcsok, F. Solymosi, and Z. G. Szabo, *Proc. Int. Congr. Catal., 3rd, 1964*, **2**, 1340 (1965).

(16) P. C. Richardson and D. R. Rossington, *J. Catal.*, **14**, 175 (1969).

An Electron Spin Resonance Study of Nitrile and Other Radicals Trapped in γ-Irradiated Single Crystals of Cyanoacetic Acid

by K. Toriyama[1] and W. C. Lin*

Department of Chemistry, University of British Columbia, Vancouver 8, B. C., Canada *(Received May 8, 1972)*

Publication costs assisted by the National Research Council of Canada

Single crystals of cyanoacetic acid were irradiated with γ rays at 77°K and studied by esr spectroscopy at various temperatures. A radical with a nitrogen coupling and a large proton coupling was found. This was interpreted as the nitrile radical, $\dot{N}CHCH_2COOH$. The g and the hyperfine coupling tensors were determined: $g_1 = 2.0021$, $g_2 = 2.0027$, $g_3 = 2.0057$, $A^{N}_1 = 37.0$ G, $A^{N}_2 = 2.9$ G, $A^{N}_3 = 6.3$ G, $A^{H}_1 = 93.7$ G, $A^{H}_2 = 89.6$ G, $A^{H}_3 = 88.0$ G. Besides the nitrile radical, an anion radical, a radical of the formula $\dot{N}CCH_2\cdot$, and a π radical, $NC\dot{C}HCOOH$, were also observed. The nitrile radical was thought to be formed from the anion radical in a postradiation process.

Introduction

Since the beginning of esr study of the radiation damage of organic crystals, carboxylic acids have been some of the most widely investigated compounds. As a result, it has been shown that the main product of radiation in this case is a radical of the type $RR'\dot{C}COOH$[2] produced by C–H bond rupture, or by hydrogen addition in the case of an unsaturated compound. Recent studies performed at lower temperatures than before have indicated that the primary products of radiation were charged species instead of neutral radicals as were observed at room temperatures.[2b] It is therefore desirable that studies be made which elucidate the relationship between the ionic primary products and the stable ultimate products and, if possible, the intermediate stages in between. For a carboxylic acid containing a CN group, the formation of a proton addition radical may be expected as well as proton elimination, and a study of the possible primary products would therefore be of great interest. In this work, single crystals of cyanoacetic acid ($NCCH_2COOH$) were subjected to γ irradiation at 77°K and studied by esr spectroscopy at various temperatures. A hydrogen addition radical considered to be $\dot{N}CHCH_2COOH$ and a radical produced by a C–H bond rupture ($NC\dot{C}HCOOH$) were indeed observed. At lower temperatures, some of their precursors were also detected and studied to some extent. Investigation of the behavior of the radicals step-by-step provided some information on the sequence of the radical formation.

From the viewpoint of radical structure, the nitrile radical $H_2CH\cdot$ or its derivative $RHCN\cdot$ are also of interest because of the unusually large proton hyperfine coupling. These radicals were observed by Adrian, *et al.*, first in argon matrix[3] and then in cyanide-doped alkali halides,[4] and by others in frozen hydrogen cyanide and acetonitrile.[5] The present work, particularly with its study of the orientations of the coupling tensors, provides a better understanding of the structure of the radical than that hitherto attained.

Previously, Cyr and Lin[6] and Lau and Lin[7] observed similar spectra in crystals of malonamide and cyanoacetylurea and attributed them to a σ-type radical, $RC\dot{O}NH$. However, some reasons have been suggested which cast doubt upon this assignment.[8] They are: the isotropic term of the nitrogen hyperfine tensor is too small for a σ-type radical and the anisotropy of the proton coupling tensor is of the order of that of a β proton. As will be shown later, comparison of the results for these compounds with that of cyanoacetic acid suggested that the radicals previously reported should be reassigned as nitrile radicals.

Experimental Section

Cyanoacetic acid ($NCCH_2COOH$) was purified by recrystallization from ethyl alcohol. Single crystals were grown by slow evaporation at about −20°. A sketch of a typical crystal together with the coordinate system used in the experiment is shown in Figure 1. Although the crystal structure was not known, the crys-

(1) On leave from Government Industrial Research Institute, Nagoya, Hirate, Kita, Nagoya, Japan.

(2) (a) J. R. Morton, *Chem. Rev.*, **64**, 453 (1964). (b) M. Iwasaki, "MTP International Review of Science, Physical Chemistry Series," Vol. 4, C. A. McDowell, Ed., Butterworths, London, in press.

(3) F. J. Adrian, E. L. Cochran, V. A. Bowers, and B. C. Weatherley, *Phys. Rev.*, **177**, 129 (1969).

(4) F. J. Adrian, E. L. Cochran, and V. A. Bowers, *J. Chem. Phys.*, **36**, 1938 (1962).

(5) J. A. Brivati, K. D. Root, M. C. R. Symons, and D. J. A. Tinling, *J. Chem. Soc. A*, 1326 (1970).

(6) N. Cyr and W. C. Lin, *J. Chem. Phys.*, **50**, 3701 (1969).

(7) P. W. Lau and W. C. Lin, *ibid.*, **51**, 5137 (1970).

(8) P. Neta and R. W. Fessenden, *J. Phys. Chem.*, **74**, 3362 (1970).

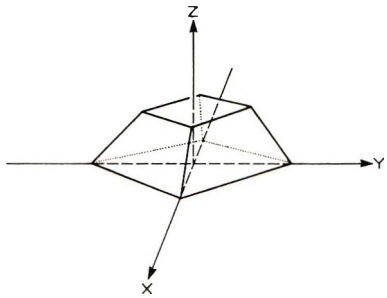

Figure 1. Sketch of a typical crystal of cyanoacetic acid and the experimental coordinate system.

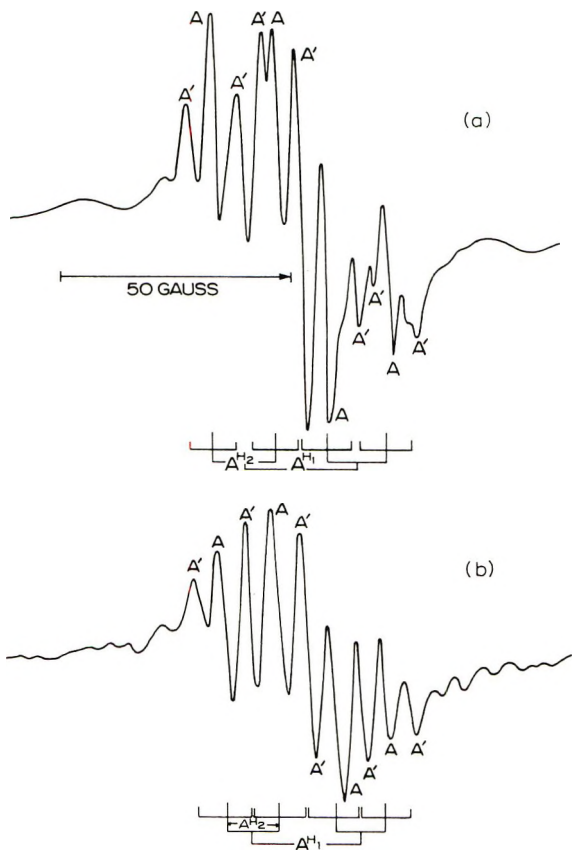

Figure 2. Esr spectra of a single crystal of cyanoacetic acid, γ-irradiated at 77°K and measured without warming. The magnetic field was applied parallel to (a) the Z axis and (b) the Y axis.

tal was found to have a monoclinic symmetry from the angular variation of the esr spectra. Since no site splitting was observed for all orientations with the magnetic field lying in the ZX and the YZ plane, the unique b axis of the monoclinic system must be parallel to either X or Y.

The crystal has a good cleavage plane which is coplanar with the XY plane. By analogy with crystal structures of cyanoacetamide[9] and other carboxylic acids,[10] this cleavage plane is likely to be one in which the molecules lie flat and are connected through intermolecular bonds. As will be shown, this assumption is in good agreement with the directions of the hyperfine tensors of all the radicals formed.

The samples were irradiated with γ rays at 77°K. The dose rate was 3.0×10^5 rads/hr, and the total dosage was 6.0×10^5 rads.

The esr spectra were recorded by a Varian Model E3 spectrometer operated at 9.2 GHz. As the marker of the magnetic field, the signal of Mn^{2+} in ZnS was used, which had been previously calibrated with a proton nmr signal.

Results

Two of the esr spectra of a single crystal of cyanoacetic acid are shown in Figure 2. The samples were irradiated at 77°K and maintained at that temperature during the recording. At this stage, two or more radical species were present, giving rise to a rather complicated spectrum, but the main feature is dominated by four lines labeled A. These four lines have equal intensities and can be interpreted as the hyperfine structure due to two β protons. The splittings are almost isotropic and are 12–13 and 21–22 G, respectively. The lines marked A′ in the same figure can be due to "spin flip" lines,[11] splittings due to two more protons, and superposition of lines due to another radical. Although a complete analysis of the two main proton coupling tensors was not made, spectrum A was attributed to an anion radical (Ia) or its protonated form (Ib)

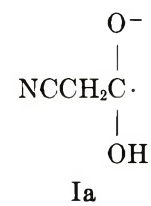

Ia

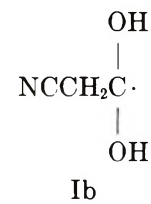

Ib

When the sample was warmed to 233°K, spectrum A disappeared, leaving a spectrum labeled C (Figure 3). At the same time, a new signal B (Figure 3) appeared concurrently with the decay of spectrum A. As shown by the stick diagram, the radical giving rise to spectrum B is understood to have one nitrogen and three protons coupling to the electron spin. The angular variations of the g value and the coupling values of a nitrogen and one of the three protons are shown in Figures 4 and 5.

(9) P. C. Chieh and J. Trotter, *J. Chem. Soc. A*, 184 (1970).

(10) J. S. Broadley, D. W. J. Cruickshank, J. D. Morrison, J. M. Robertson, and H. M. M. Shearer, *Proc. Roy. Soc., Ser. A*, **251**, 442 (1959).

(11) M. T. Rogers and L. D. Kispert, *J. Chem. Phys.*, **46**, 221 (1967).

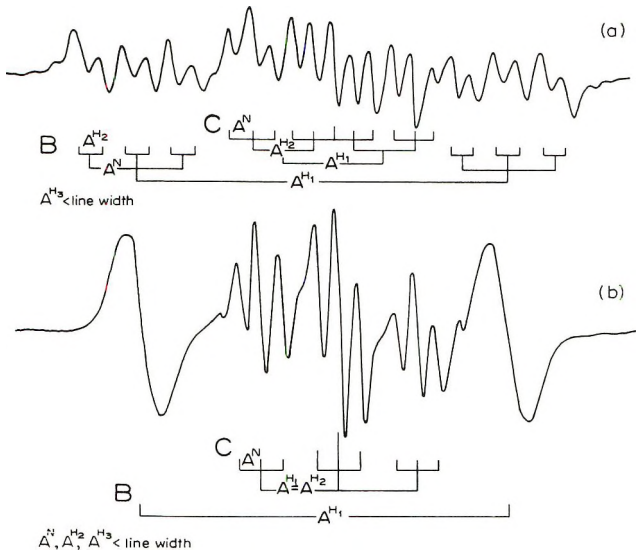

Figure 3. Esr spectra of a single crystal of cyanoacetic acid γ-irradiated at 77°K and annealed subsequently at 233°K for about 30 min. Esr measurement was made at 77°K, with the magnetic field (a) 30° from Z to X in the ZX plane and (b) parallel to Z.

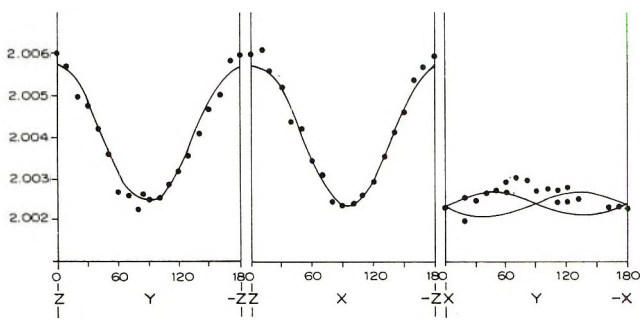

Figure 4. Angular variation of g value for radical II ($\dot{N}CHCH_2COOH$) with the magnetic field perpendicular to the X, Y, and Z axes. Solid lines are theoretical curves calculated using the principal values and principal axes listed in Table I.

The principal values and the directions of the g and the hyperfine tensors were obtained by least-squares fitting of the observed data. The results are listed in Table I and used to calculate the continuous curves shown in the figures. The magnitude of the anisotropic term of the nitrogen coupling tensor indicates that most of the spin is in a nitrogen 2p orbital. The relatively small anisotropy of the proton hyperfine tensor indicates that this proton is a β proton. From the unusually large isotropic term, this proton is expected to be in the same plane as the orbital of the unpaired electron. As a radical which satisfies all these features and is likely to be expected from the parent molecule, the nitrile radical (II) is suggested. The remaining two weakly

$$\dot{N}{=}CCH_2COOH$$
II

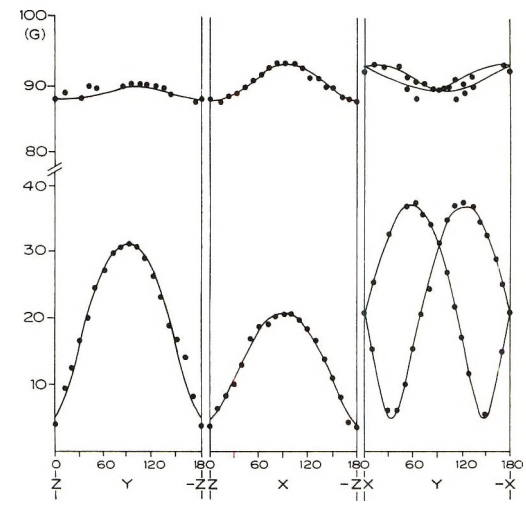

Figure 5. Angular variation of the hyperfine splitting of nitrogen and one of the three protons of radical II. Solid lines are calculated curves. The hyperfine splittings of the remaining two protons were 0–6 G in the ZX and the XY plane. In the YZ plane, the coupling values of these protons were less than the line width.

coupled protons are probably the two methylene protons. The coupling of these two protons, 0–5 G, is reasonable for γ protons.

Table I: g and Hyperfine Tensors of $\cdot NCHCH_2COOH$ (II) at 77°K[a]

		Principal values	Direction cosines with respect to X, Y, Z[b] l	m	n
g	g_1	2.0021 ± 0.0003	0.752	−0.655	−0.066
	g_2	2.0027 ± 0.0003	0.653	0.755	−0.050
	g_3	2.0057 ± 0.0003	0.083	−0.005	0.997
N	A^{N_1}	37.2 ± 0.2	0.550	0.835	0.009
	A^{N_2}	2.9 ± 2.0	0.636	−0.425	0.644
	A^{N_3}	6.3 ± 1.0	−0.542	0.349	0.765
H^1	A^{H_1}	93.7 ± 0.2	0.976	−0.217	−0.026
	A^{H_2}	89.6 ± 0.2	0.214	0.971	−0.105
	A^{H_3}	88.0 ± 0.2	0.048	0.097	0.994
H^2, H^3	A = 0–5 G				

[a] The unit of the hyperfine tensors is gauss. [b] The directions of the other radical site are given by $(l, -m, n)$ if Y axis is the unique monoclinic axis or by $(-l, m, n)$ if X is the unique b axis.

Spectrum C, left after the decay of radical I, consists of four sets of triplets. The splittings of these four sets are rather anisotropic, in marked contrast to the four lines of spectrum A. These lines C are attributed to the radical III although the spectra were too complicated to analyze completely.

$$NC\dot{C}H_2$$
III

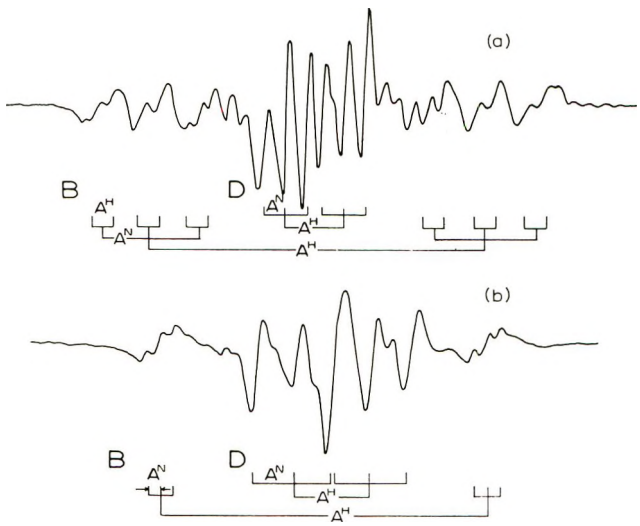

Figure 6. Esr spectra of a single crystal of cyanoacetic acid observed at 273°K following γ irradiation at 77°K. The magnetic field was applied (a) 50° from Z to X in the ZX plane, and (b) parallel to Z.

The reasons for such an assignment are (i) the dominating feature of spectrum C is due to two equivalent protons, (ii) the coupling values of the two protons, ranging from ~10 to almost 30 G, are typical of an α proton of a π radical, and (iii) further splittings of the four lines form triplets of equal intensities for most of the spectra observed. The same radical (III) was detected in the photolysis of aqueous solutions of acetonitrile with hydrogen peroxide,[12] in which case the isotropic part of the nitrogen and the proton coupling tensors were found to be 3.5 and 21 G, respectively. The triplet splittings of spectrum C range from 0 *to* 6 G, agreeing with the nitrogen coupling observed in the liquid phase.

It should be added here that signal C, the spectrum of radical III, shows a marked temperature change at around 263°K (Figure 7d). This spectral change is reversible and is interpreted as being due to the intramolecular motion around the twofold axis of the radical. The existence of signal C from the beginning is suggested on account of the following facts. First, the spectra in Figure 2 are not centrosymmetric, suggesting superposition of more than one spectrum. Second, some lines in the spectra observed immediately after irradiation (Figure 2) coincide with some of those observed after thermal annealing at 233°K (Figure 3).

By annealing further at 263°K, the lines C disappeared simultaneously with the appearance of a new spectrum D (Figure 6). The lines D could well be interpreted as a radical with one proton and one nitrogen. The g and the hyperfine tensors obtained by the same procedure as that described for radical II are listed in Table II. These values were obtained using data measured at 273°K. As the proton hyperfine tensor showed characteristic features of an α proton of a π radical, the spectrum is assigned to radical IV. Since

$$\mathrm{NC\dot{C}HCOOH}$$
IV

spectrum D appears concurrently with the decay of spectrum C, radical III is considered to be the precursor of radical IV.

Table II: g and Hyperfine Tensors of $\mathrm{NC\dot{C}HCOOH}$ (IV) at 273°K[a]

		Principal values	Direction cosines with respect to X, Y, Z[b] l	m	n
g	g_1	2.0046 ± 0.0003	0.736	−0.677	0.010
	g_2	2.0034 ± 0.0003	0.639	0.690	−0.339
	g_3	2.0023 ± 0.0003	0.223	0.256	0.941
N	A^N_1	10.6 ± 0.5	0.128	−0.025	0.992
	A^N_2	0 ± 1.0		⊥ to A_1	
	A^N_3	0 ± 1.0			
H^1	A^H_1	−30.0 ± 0.5	−0.262	0.965	0.018
	A^H_2	−20 ± 0.5	0.122	0.015	0.993
	A^H_3	−9.0 ± 0.5	0.957	0.263	−0.121

[a] The unit of the hyperfine tensors is gauss. [b] The directions of the other radical site are given by $(l, -m, n)$ if Y axis is the unique monoclinic axis or by $(-l, m, n)$ if X is the unique b axis.

Although radical IV is stable at room temperatures, radical II decays above 273°K.

The spectral changes due to the thermal annealing described above may be better illustrated by the spectra of a polycrystalline sample (Figure 7), and the sequence of change may be summarized as

$$\mathrm{NCCH_2COOH} \xrightarrow[77^\circ\mathrm{K}]{\gamma} \begin{cases} \mathrm{A} \xrightarrow{233^\circ\mathrm{K}} \mathrm{B} \xrightarrow{273^\circ\mathrm{K}} \text{decay} \\ \mathrm{C} \xrightarrow{263^\circ\mathrm{K}} \mathrm{D} \longrightarrow \text{stable at room temp} \end{cases}$$

Discussion

The Nitrile Radical. The spin densities in the 2p and the 2s orbitals of nitrogen are estimated to be 0.64 and 0.028, respectively.[3] These spin densities correspond to a p:s ratio of 24, indicating that the unpaired electron orbital is predominantly a nitrogen 2p orbital. The unusually large isotropic term of the proton hyperfine tensor, about 90 G, strongly suggests that this proton is in the plane containing the density axis of the unpaired electron orbital on nitrogen. This is further supported by the anisotropy of the proton hyperfine tensor as shown below. The isotropic term of the proton hyperfine tensor of the nitrile radical is considered to be positive and the principal axis of the maximum coupling value A^H_{max} must be in the direction of the vector N–H. From the direction cosines listed

(12) R. Livingston and H. Zeldes, *J. Magn. Resonance*, 1, 169 (1969).

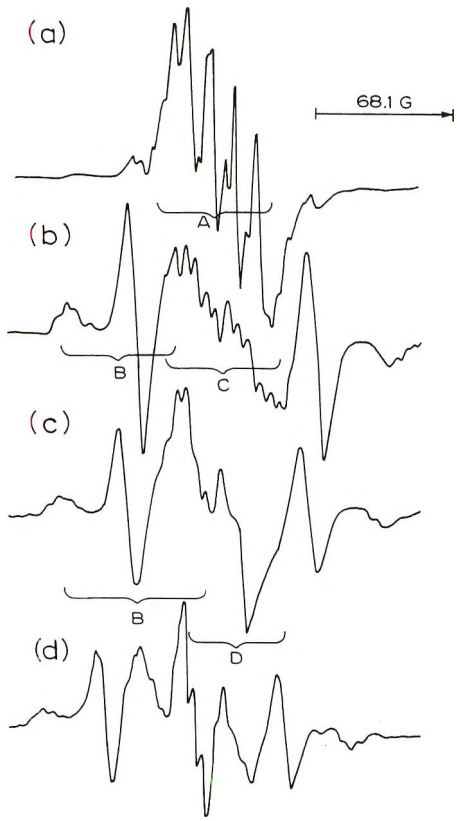

Figure 7. Esr spectrum of polycrystalline cyanoacetic acid. All spectra except (d) were recorded at 77°K, (a) immediately after γ irradiation at 77°K, (b) after subsequent annealing at 233°K, and (c) at 263°K. Spectrum d was observed at 233°K. The spectral change from (b) to (d) was reversible if the sample was maintained below 243°K.

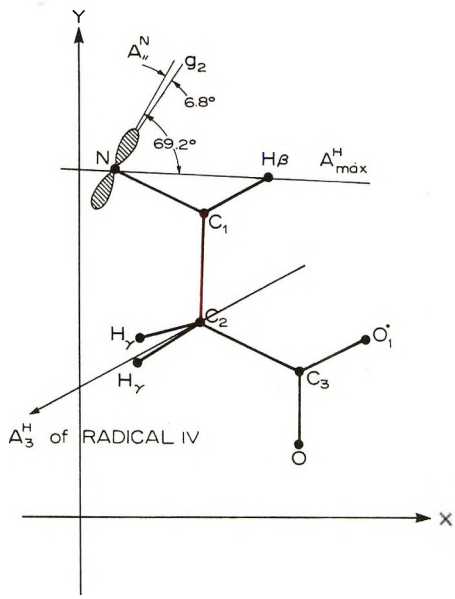

Figure 8. Radical orientation in the experimental coordinate system. Although the other conformation with the COOH group in the cis position cannot be ruled out, the trans form seems more likely from the anisotropy of the hyperfine splitting of the two methylene protons. The diagram shows only one of the two unequivalent sites.

in Table I, the unique axis of the nitrogen coupling tensor, A^{N}_1, is seen to be in the plane perpendicular to the A^{H}_3 axis and to make an angle of 69.2° with the $A_{max}{}^{H}$ (*i.e.*, A^{H}_1) axis. From this result, the structure shown in Figure 8 is derived for radical II. If 1.34 and 1.07 Å are the bond lengths of N–C and C–H, respectively, and 120° is the bond angle ∠NCH, then the angle between the vector N–H and the density axis of the nitrogen 2p orbital is calculated to be 63.7°, in good agreement with 69.2° obtained from the experiment.

The coplanarity of the unpaired electron orbital and the C–H bond also is supported by the g tensor. For a radical with a structure like that shown in Figure 8, a large positive g shift is expected in the direction perpendicular to the NCH plane, because of the strong mixing of the unpaired electron orbital with the filled σ-lone-pair orbital of nitrogen. This orbital is considered to be lower than the unpaired electron orbital but higher than the CN π-bonding orbital. On the other hand, the principal axis of the g-value nearest to the free spin g value (g_f) should be parallel to the density axis of the spin orbital. Actually, the directions of g_{max} and g_f which correspond to g_3 and g_2 in Table I are nearly perpendicular and parallel to the A^{N}_1 axis with a deviation of 3 and 6.8°, respectively.

It should be added here that the NCH plane of the nitrile radical thus estimated is in the crystalline cleavage plane which corresponds to the experimental XY plane. As will be mentioned later, this plane is also the radical plane of the π radical IV and possibly the molecular plane of the undamaged molecule.

The positions of the two methylene protons of the nitrile radical II are symmetric with respect to the NCH plane, as suggested by the 1:2:1 triplet structure of its spectra for most of the orientations with the magnetic field being in the XY plane.

Previously, Cyr and Lin[6] and Lau and Lin[7] observed spectra similar to spectrum B in crystals of X-irradiated malonamide and also cyanoacetylurea. They attributed the spectra to a σ-type radical RCONH. In the light of the present study and some work on cyanoacetamide[13] these should be reassigned, respectively, as $\dot{N}CHCH_2CONH_2$ and $\dot{N}CHCH_2CONHCONH_2$. The similarity between the hyperfine tensors and the g tensors of these radicals is shown in Table III.

It is not clear yet why the ṄCHR radical can be trapped in a crystal of malonamide which has no CN group. What should be considered is the effect of impurities such as that found in the case of succinic acid.[14] The presence of an impurity in the original sample is unlikely, since we could detect no difference in the yield of this type of radical among samples from different sources or samples recrystallized from different sol-

(13) W. C. Lin, N. Cyr, and K. Toriyama, *J. Chem. Phys.*, **56**, 6272 (1972).

(14) I. Miyagawa and K. Itoh, *Nature*, **209**, 504 (1966).

Table III: Nitrogen and Proton Hyperfine Tensors of N-Containing Radicals Observed in Various Crystals

Compound	A^N	A^H	Temp (obsd)	References
$NCCH_2COOH$	30.0	91.1		
	5.6	87.5	273°K	This
	0.2	87.5		work
$CH_2(CONH_2)_2$	35.7	84.3	Room	6
	6.9	79.6	temp	
	0.3	80.0		
$NCCH_2CONHCONH_2$	21.8	87.0	Room	7
	5.7	85.4	temp	
	7.4	84.8		
$NCCH_2CONH_2$	$A_{\|\|}$ = 27.0	84	Room temp	*a*
$NCCH_2CONH_2$	$A_{\|\|}$ = 38.0	82	77°K	*a*

[a] Unpublished, this laboratory.

vents. The other possibility is an impurity produced in the sample during irradiation. For example, acetamide is known to lose water easily forming CH_3CN by γ radiolysis in the solid state.[15] By analogy, the formation of some RCN may be expected in malonamide upon irradiation.

The Anion Radical. Esr spectra of anion radicals produced by irradiation have been observed in many carboxylic and amino acids,[2] and the spin has been found to localize on the carbon of the carboxyl group. From study of the ^{13}C hyperfine tensors,[16-18] anion radicals of this type were found to have a pyramidal structure. A smaller value of the constant B should be assumed in the "$\cos^2\theta$ rule" for β protons than was originally suggested for a planar radical.

$$A^{H\beta} = B_0 + B\cos^2\theta$$

In the above equation, B_0 and B are empirical constants with $B \gg B_0$, and θ, the dihedral angle between (i) the plane containing the C–C bond and the spin orbital axis and (ii) the plane passing through the C–C and the C–H bonds. Assuming B to be 27 G, twice the coupling for the freely rotating methyl protons of $[CH_3COOH]\cdot^-$,[17,19] and B_0 to be 0 G, the dihedral angles for the two β protons were found to be 25.5 and 48°, respectively. These values suggest that the anion radical of cyanoacetic acid has a conformation with the CN group nearly in the COOH plane, as shown in Figure 9. Similar conformations can be expected for the anion radicals trapped in glycine and succinic acid irradiated at 77°K. An anion radical with β-proton coupling values of 26 and 7–9 G was found in glycine,[20] and one with β-proton coupling values of 27 and 9 G in succinic acid.[18,20] Assuming B_0 and B to be 0 and 27 G again, the dihedral angles are calculated to be 11 and 54° for glycine and 0 and 56° for succinic acid. These values suggest a conformation of the anion radical with

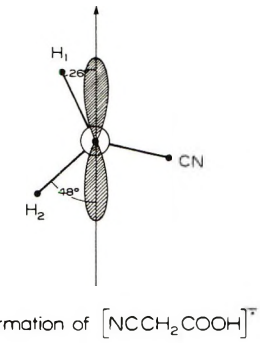

Figure 9. Conformations of the anion radical (Ia) of cyanoacetic acid (or its protonated form Ib).

the NH_3^+ group or CH_2COOH group lying in the nodal plane of the unpaired electron orbital. Although the authors of these two papers have suggested different conformations by assuming larger values for B, our assumption seems more probable because the dihedral angles obtained by us are close to the values for undamaged molecules calculated from the crystal structure data[10,21] (12 and 48° for glycine, and 19 and 41° for succinic acid). In succinic acid, the principal values and the principal axes have been obtained by endor observation.[22] The directions of the two β protons of the anion radical of succinic acid determined from the anisotropic hyperfine tensors are very close to those expected for the conformation proposed here. By analogy with these cases, the molecular geometry of the undamaged cyanoacetic acid is considered to be almost the same as the anion radical. In other words, the CN group appears to be in the same plane as the COOH.

Other Radicals. The proton hyperfine tensor of the most stable radical IV shows the characteristic features of an α proton of a π radical. Assuming 27 G for the spin polarization factor Q,[23] the spin density on the central carbon atom is estimated to be 0.73. The spin density on the nitrogen 2p orbital is evaluated to be 0.2 from the anisotropy of the nitrogen hyperfine tensor. These values show that the resonance structure $\dot{N}$=C=CHCOOH contributes to the radical structure IV to the extent of 20%.

Consideration of the orientations of the radicals IV and II gives some additional support to the assignment of spectrum C to radical III. In a previous section, al-

(15) K. Narayana Rao and A. O. Allen, *J. Phys. Chem.*, **72**, 2181 (1968).

(16) J. E. Bennett and L. H. Gale, *Trans. Faraday Soc.*, **64**, 1174 (1968).

(17) J. Sinclair and M. W. Hanna, *J. Chem. Phys.*, **50**, 2125 (1969).

(18) H. C. Box, H. G. Freund, and K. T. Lilga, *ibid.*, **42**, 1471 (1965).

(19) M. D. Sevilla, *J. Phys. Chem.*, **74**, 669 (1970).

(20) J. Sinclair, *J. Chem. Phys.*, **55**, 245 (1971).

(21) R. Marsh, *Acta Crystallogr.*, **11**, 654 (1968).

(22) J. W. Wells, *J. Chem. Phys.*, **52**, 4062 (1970).

(23) J. R. Bolton, "Radical Ions," E. T. Kaiser and L. Kevan, Ed., Interscience, New York, N. Y., 1968, p 26.

though signal C was attributed to $NC\dot{C}H_2$, the possibility of $\cdot CH_2COOH$ could not be excluded completely. From the g and the hyperfine tensors of radicals II and IV, the relative positions of the three carbon atoms of cyanoacetic acid with respect to the crystalline X, Y, Z axes can be determined as shown in Figure 8. If the radical giving rise to spectrum C is $NC\dot{C}H_2$, formed by the C–COOH bond scission, then the twofold axes of this radical should be nearly parallel to C_1–C_2. On the other hand, if spectrum C originates from $\cdot CH_2COOH$ produced by the loss of NC, then the bisector of the angle HCH is expected to be parallel to C_2–C_3. The overall spread of spectrum C was found to be largest when the magnetic field is nearly parallel to the Y axis. This indicates that the twofold axis of the $R\text{–}\dot{C}H_2$ radical is approximately parallel to Y and, since C_1–C_2 is nearly parallel to Y, the radical is considered more likely to be $NC\dot{C}H_2$.

Proposed Mechanism for Radical Formation. From the above considerations, we propose the following scheme for the radical formation

$$NCCH_2COOH \xrightarrow[77°K]{\gamma} [NCCH_2COOH]^+ + e \quad (1)$$

$$[NCCH_2COOH]^+ \longrightarrow NCCH_2\overset{\overset{O}{\|}}{C}\cdot + H^+ \quad (2)$$

$$NCCH_2\overset{\overset{O}{\|}}{C}\cdot \longrightarrow \underset{\text{III}}{NC\dot{C}H_2} + CO_2 \quad (3)$$

$$NC\dot{C}H_2 + NCCH_2COOH \longrightarrow NCCH_3 + \underset{\text{IV}}{NC\dot{C}HCOOH} \quad (4)$$

$$NCCH_2COOH + e \longrightarrow NCCH_2\overset{\overset{O^-}{|}}{\underset{\underset{OH}{|}}{C}}\cdot \quad (5)$$

Ia

$$NCCH_2\overset{\overset{O^-}{|}}{\underset{\underset{OH}{|}}{C}}\cdot + H^+ \longrightarrow NCCH_2\overset{\overset{OH}{|}}{\underset{\underset{OH}{|}}{C}}\cdot \quad (6)$$

Ib

$$NCCH_2\overset{\overset{OH}{|}}{\underset{\underset{OH}{|}}{C}}\cdot \longrightarrow \cdot N{=}CHCH_2COOH \quad (7)$$

II

Reactions 1 to 4 form the sequence following the loss of an electron. There have been only a few reports on the detection of a trapped hole in organic crystals, these being (i) potassium salts of fumaric acid,[24] (ii) L-α-alanine,[25] and (iii) some sulfur-containing amino acids.[26,27] The radical RCOO·, however, has been observed in several irradiated carboxylic acids.[27-29] It has been elucidated from the work on maleic acid,[28] succinic acid,[27] and some others that the carboxyl radical is rather unstable and readily decarboxylates on annealing or photobleaching. Since no evidence of the radical RCOO· was observed in irradiated cyanoacetic acid and radical III was found to be present immediately after irradiation, steps 1 and 3 are assumed to have been completed during the irradiation process.

As was described before, the $NCCH_2\cdot$ radical decays above 263°K, accompanied by the formation of the stable radical $NC\dot{C}HCOOH$ (IV). This can be interpreted as due to reaction 4. Hydrogen abstraction by a radical from a neighboring molecule is observed in irradiated fluoroacetamide,[30] glycine,[20] and others. In disodium succinate,[31] in contrast to this, an intramolecular hydrogen transfer (reaction 8) had been assumed to follow decarboxylation.[32]

$$^-OOCCH_2CH_2\cdot \longrightarrow {}^-OOC\dot{C}HCH_3 \quad (8)$$

The ejected electron from reaction 1 is captured by a molecule forming an anion radical (Ia). Protonation of an anion from an adjacent molecule was found in L-α-alanine by observing the hyperfine structure due to the proton thus transferred.[33] It was interpreted as quantum tunneling through the intermolecular hydrogen bond.[33c] However, no conclusive evidence has been observed in other crystals. In cyanoacetic acid, it is also not clear if the radical responsible for spec-

(24) M. Iwasaki, K. Minakata, and K. Toriyama, *J. Amer. Chem. Soc.*, **93**, 3533 (1971).

(25) E. A. Friday and I. Miyagawa, *J. Chem. Phys.*, **55**, 3589 (1971).

(26) K. Akasaka, S. Ohnishi, J. Suita, and I. Nitta, *ibid.*, **40**, 3110 (1964).

(27) H. C. Box, H. G. Freund, K. T. Lilga, and E. E. Budginski, *J. Phys. Chem.*, **74**, 40 (1970).

(28) (a) M. Iwasaki, B. Eda, and K. Toriyama, *J. Amer. Chem. Soc.*, **92**, 3211 (1970); (b) B. Eda and M. Iwasaki, *J. Chem. Phys.*, **55**, 3442 (1971).

(29) K. Toriyama and M. Iwasaki, *J. Chem. Phys.*, **55**, 2181 (1971); K. Toriyama, M. Muto, and M. Iwasaki, *ibid.*, **55**, 1885 (1971); H. C. Box, E. E. Budzinski, and W. Potter, *ibid.*, **55**, 315 (1971).

(30) M. Iwasaki and K. Toriyama, *ibid.*, **46**, 4693 (1967).

(31) B. L. Bales, R. N. Schwartz, and M. W. Hanna, *ibid.*, **51**, 1974 (1969).

(32) The formation of the decarboxylated radical $\cdot CH_2CH_2COOH$ was verified and analyzed by M. Muto and M. Iwasaki in succinic acid crystals doped with deuterated fumaric acid, HOOCCD=CDCOOH. They also found that $\cdot CH_2CH_2COOH$ changes to $CH_3\dot{C}HCOOH$ upon annealing (private communication).

(33) (a) J. W. Sinclair and M. W. Hanna, *J. Phys. Chem.*, **71**, 84 (1967); (b) A. Minegishi, Y. Shinozaki, and G. Meshitsuka, *Bull. Chem. Soc. Jap.*, **40**, 1549 (1967); (c) I. Miyagawa, N. Tamura, and J. W. Cook, *J. Chem. Phys.*, **51**, 3520 (1969).

trum A is an anion radical (Ia) or its protonated form (Ib). In any case, since the nitrile radical (II) is found to be formed at the expense of the radical giving rise to spectrum A, the nitrile radical is considered to come from the anion radical Ia through Ib as an intermediate state. Thus, steps 5 to 7 are proposed as the sequence following the capture of an ejected electron. Although another possibility, the intermolecular hydrogen transfer (reaction 9), cannot be ruled out, the

$$\begin{matrix} & OH & & \\ & | & & \\ NCCH_2C\cdot & + & NCCH_2COOH & \longrightarrow \\ & | & & \\ & OH & & \end{matrix}$$

$$NCCH_2COOH + \dot{N}CHCH_2COOH \quad (9)$$

intramolecular reaction 7 seems more probable. The reason for this is that radical Ia can take a conformation with one of its O–H protons very close to the nitrile carbon by rotation about the O_1–H bond.

The direct protonation of the negatively charged NC group to produce a nitrile radical (reaction 10) does not seem possible in the present system, because the esr spectrum of the precursor of the nitrile radical did not show large nitrogen coupling indicating that most of the unpaired spin was localized in the COOH group.

$$^{-}N\dot{C}CH_2COOH + H^{+} \longrightarrow \dot{N}CHCH_2COOH \quad (10)$$

The formation of a hydrogen addition radical in unsaturated carboxylic acid through anion radical formation has been suggested for the fumaric acid–succinic acid system,[34] in good agreement with the present result. Since cyanoacetic acid has the characteristics of both a saturated and an unsaturated carboxylic acid, both hydrogen addition and hydrogen elimination radicals are produced. From the sequences of the observed radicals, the hydrogen addition radical, $\dot{N}CHCH_2COOH$ (II), is suggested to come from the electron excess primary and the hydrogen elimination radical, $N\dot{C}CHCOOH$ (IV), from the positive ion.

Acknowledgment. The authors wish to thank the National Research Council of Canada for financial support.

(34) M. Iwasaki, M. Muto, and K. Toriyama, *J. Chem. Phys.*, **55**, 1894 (1971).

Electron Spin Resonance and Electron Nuclear Double Resonance Study of the α-Phenylbenzylidene Malononitrile Anion Radical

by Raymond Chang

Department of Chemistry, Williams College, Williamstown, Massachusetts 01267

and Robert D. Allendoerfer*

Department of Chemistry, State University of New York at Buffalo, Buffalo, New York 14214

(Received May 30, 1972)

Publication costs assisted by the Petroleum Research Fund

The previously reported esr spectrum of the α-phenylbenzylidene malononitrile anion radical has been reinterpreted with the aid of endor spectroscopy. The hyperfine coupling constants are now in good agreement with those calculated by McLachlan-HMO theory. It is inferred that the phenyl rings are canted with respect to the plane of the molecule but exchange conformations so rapidly that no effect of this asymmetric phenyl ring conformation is seen in the esr spectrum.

Introduction

Recently there has been considerable interest in assessing the relative influence of steric and electronic effects on the rate of rotation of phenyl rings. Hirota[1] found the rate of ring flipping in benzophenone ketyl was just slow enough to affect the esr line widths at low temperature in ether solution, but they were unable to see any effects for diphenyl nitroxide under similar conditions. Dalton, *et al.*,[2] also observed complete equivalence among the four ortho and among the four meta protons in the diphenylmethyl radical. The barrier to

(1) T. Takeshita and N. Hirota, *J. Chem. Phys.*, **51**, 2146 (1969).

(2) D. R. Dalton, S. A. Liebman, and H. Waldman, *Tetrahedron Lett.*, **2**, 145 (1968).

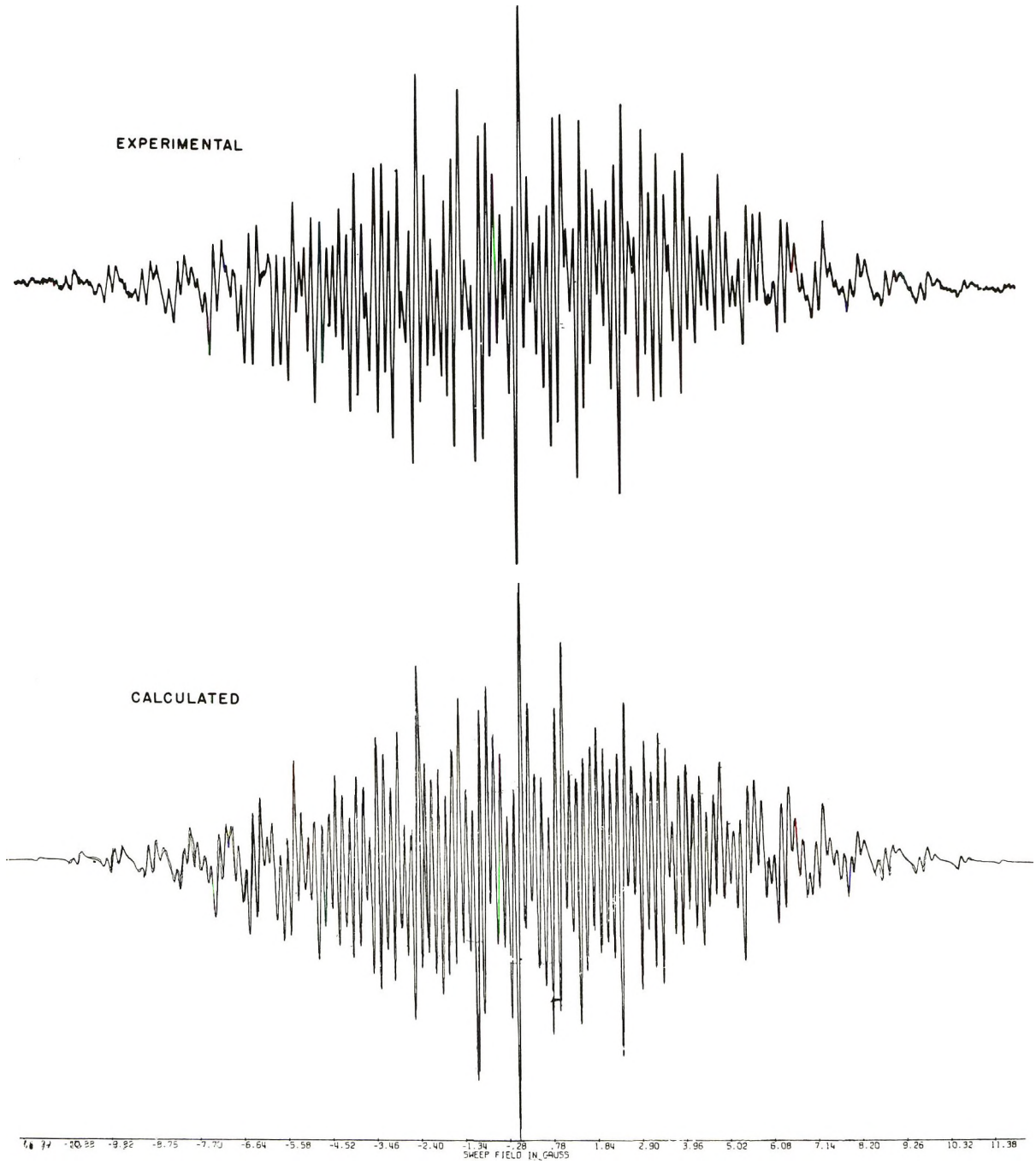

Figure 1. Experimental and computer simulated esr spectra of the α-phenylbenzylidene malononitrile radical anion.

rotation for the 1,1-diphenylethylene anion would be a valuable addition to the list since while the steric effects should be similar to diphenylmethyl, the barrier may well be higher because of increased conjugation; however, this radical is difficult to study because it polymerizes.[3] α-Phenylbenzylidene malononitrile (I) forms a stable monomer anion radical[4] with a similar electronic structure to the 1,1-diphenylethylene radical. Thus, we have chosen this radical in which to look for the effects of restricted phenyl ring rotation.

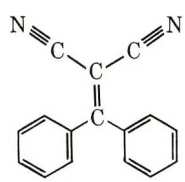

I

Experimental Section

The esr and endor spectra were obtained on a Varian V-4502 epr spectrometer which was modified as de-

(3) M. Shima, D. N. Bhettacharyya, J. Smid, and M. Szwarc, *J. Amer. Chem. Soc.*, **85**, 1306 (1963).

(4) F. J. Smentowski and G. P. Stevenson, *J. Phys. Chem.*, **74**, 2525 (1970).

scribed previously[5] to perform the high-power CW endor experiment.

α-Phenylbenzylidene malononitrile (I), Aldrich Chemical Co., Inc., was recrystallized once before use. Standard methods for preparation of anion radicals by reduction with potassium in 1,2-dimethoxyethane (DME) were used to prepare $I\cdot^-$.[6] The radical anion was also generated in a high-vacuum electrolytic cell with DME as the solvent and tetra-*n*-butylammonium perchlorate as the supporting electrolyte.

Results

Figure 1 shows the esr spectrum of $I\cdot^-$ prepared by the reduction with potassium in DME at −90° together with the computer simulation computed using a 0.10-G peak-to-peak Lorentzian line shape. The same esr spectrum was obtained when the radical was generated electrolytically. The analysis was aided by a proton endor experiment at the same temperature. This endor spectrum is shown in Figure 2. The coupling constants thus obtained are given in Table I.

Table I: Coupling Constants

Position	Exptl, G	Calcd, G
Ortho	2.49	−1.93[a]
Meta	0.99	0.69[a]
Para	2.96	−2.42[a]
Nitrogen	0.81	1.10[b]

[a] $Q_{CH}{}^{H} = -27 + 12\rho_C$. [b] $A_N = K\rho_N$, $K = 19.8 \pm 0.7$ G, ref 9.

Because of the many degenerate spins and the notoriously difficult choice between a quintet due to 2 equivalent spin 1 nuclei and that of a quintet from 4 equivalent spin $^1/_2$ nuclei, the analysis of this spectrum and the assignment of the coupling constants to molecular position is not straightforward.[7] The analysis can be made in an unambiguous way as follows. The upper half of the endor spectrum given in Figure 2 shows only three sharp lines. There is an identical set of endor lines displaced symmetrically below the free proton frequency of 14.28 MHz which establishes that the three couplings 2.96, 2.49, and 0.99 G are due to protons. This confirms the equivalence of all four ortho and all four meta protons, and proves that the ortho and meta couplings must be different. The assignment of the 2.96-G coupling to the para ring position is accomplished by noting that the 18.5-MHz line is the least intense endor line and further confirmed by the observation of a 1:2:1 triplet in the esr spectrum with this coupling constant. Thus, having established the degeneracy of each of the proton couplings, the length of the nitrogen quintet can be found by subtracting the sum of the proton couplings from the total length of the esr spectrum. That this 0.81-G coupling

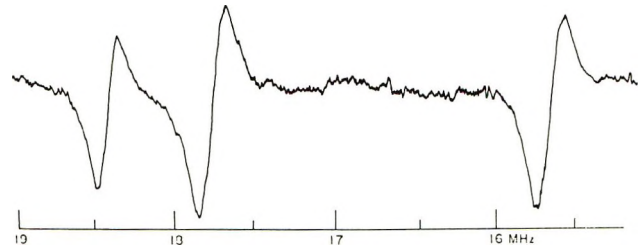

Figure 2. High-frequency half of the endor spectrum of the α-phenylbenzylidene malononitrile radical anion.

is due to nitrogen is confirmed by the presence of a 1:2:3:2:1 quintet in the esr spectrum with this coupling constant. Finally, the assignment of the 2.49- and 0.99-G quintets to the ortho and meta positions, respectively, cannot be made experimentally but can be made with considerable confidence by comparison with the splittings predicted by molecular orbital calculations as will be discussed below.

Table I also shows the results of a McLachlan-HMO calculation[8] for $I\cdot^-$. The heteroatom parameters, taken from the work of Rieger and Fraenkel,[9] were $h_N = 1.0$, $k_{CN} = 2.0$, $k_{C-CN} = 0.9$. $k_{C=C} = 1.1$ and $k_{C-Ph} = 0.9$ were used[10] and McLachlan's λ parameter[8] was taken as 1.2.

Discussion

Qualitatively, the agreement between the calculated and experimental coupling constants is quite reasonable but not nearly as good quantitatively as that for the nitriles studied by Rieger and Fraenkel.[9] There is too much spin density calculated for the cyano groups and too little for the phenyl rings so the calculation is not correctly reproducing the result of the competition for spin density between the phenyl and cyano ends of the molecule. Our calculation assumes the phenyl rings are coplanar although they are undoubtedly canted with respect to the plane of the molecule because of their mutual steric interaction. Any decrease in k_{C-Ph} to account for this effect increases the discrepancy between the calculated and experimental results. We believe this discrepancy is simply a solvent effect. The heteroatom parameters were optimized to fit nitrile anions in *N*,*N*-dimethylformamide while our solvent is DME. Typically, substituted benzene

(5) R. D. Allendoerfer and D. J. Eustace, *J. Phys. Chem.*, **75**, 2765 (1971).

(6) D. E. Paul, D. Lipkin, and S. I. Weissman, *J. Amer. Chem. Soc.*, **78**, 116 (1956).

(7) For $I\cdot^-$ prepared by reduction with potassium metal in DME at −60°, Smentowski and Stevenson[4] proposed $A_N = 2.47$ G, $A_o = A_m = 1.47$ G, and $A_p = 0.17$ G. Their assignment, while incorrect, does predict qualitatively the same esr spectrum since their coupling constants are just the differences between those in our assignment, *i.e.*, $2.49 - 0.99 \cong 1.47$ and $0.99 - 0.81 \cong 0.17$.

(8) A. D. McLachlan, *Mol. Phys.*, **3**, 233 (1960).

(9) P. H. Rieger and G. K. Fraenkel, *J. Chem. Phys.*, **37**, 2795 (1962).

(10) A. Streitwieser, "Molecular Orbital Theory for Organic Chemists," Wiley, New York, N. Y., 1961.

anions have larger hyperfine couplings for the substituent in lower dielectric constant solvents just the opposite of what we find here. For example, the nitrogen coupling for the sodium salt of nitrobenzene in DME is 11.1 G[11] while in hexamethylphosphoramide it is 8.43 G.[12] This generalization, however, neglects variations in spin density within the substituent. The valence bond approach of Schug, Brown, and Karplus to the calculation of hyperfine couplings[13] provides a straightforward explanation of the direction of our solvent effect. These ions can be viewed as a mixture of two extreme types valence bond structures: a set of delocalized spin structures and a set of delocalized charge structures as shown in Schemes I and II.

Scheme I: Delocalized Spin

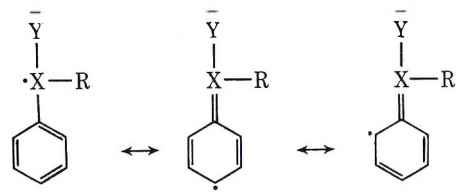

Scheme II: Delocalized Negative Charge

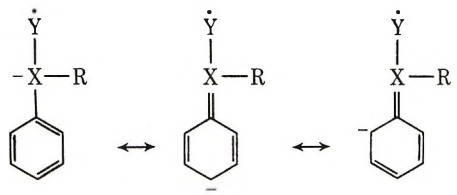

Low dielectric constant solvents which give rise to tight ion pairs will obviously favor the delocalized spin set at the expense of the delocalized charge set, so for nitrobenzene where X is nitrogen and Y oxygen, relatively larger nitrogen hyperfine couplings are expected in lower dielectric constant solvents just as is observed experimentally. For nitriles, however, X is carbon and Y is nitrogen so smaller nitrogen couplings are expected. Thus, the shift in spin density toward phenyl and negative charge density toward cyano observed above on going from a theoretical model for a molecule in DMF to the experimental spin density distribution in DME is just what this solvent effect model predicts.

Finally, the lack of observation of any difference between the ortho and meta ring coupling constants deserves some comment. The line widths in the endor spectrum are 200 kHz peak-to-peak so differences in coupling constants as small as 50 mG should have been easily observable. Apparently, the phenyl rings in $I\cdot^-$, diphenylmethyl, and diphenyl nitroxide are sufficiently twisted from planarity by steric forces that little barrier remains to prevent rapid exchange of the two ortho and meta positions, thus making the coupling constants appear equivalent. The 4.3-kcal barrier to rotation found by Hirota[1] for benzophenone ketyl is thus anomalous and must represent some specific solvent effect related to the ketyl portion of that molecule. Tetraphenylethylene, which is even more sterically crowded than the diphenyl systems, has also recently been observed to have nonequivalent ortho and meta couplings.[14] Since the rate of ring flipping is sufficiently slow to observe narrow line esr spectra, the barrier to rotation must be higher here due to the entropy requirements of the cooperative movements necessary to flip all four rings at once.

Acknowledgment. R. C. acknowledges funds made available as part of a grant to Williams College by the Alfred P. Sloan Foundation for preliminary esr work. Acknowledgment is also made to the donors of the Petroleum Research Fund, administered by the American Chemical Society, for support of the magnetic resonance equipment through a grant to R. A.

(11) J. H. Sharp and M. C. R. Symons, "Ions and Ion Pairs in Organic Reactions," M. Szwarc, Ed., Wiley-Interscience, New York, N. Y., 1972, p 216.

(12) G. R. Stevenson and L. Echegoyen, *J. Phys. Chem.*, **76**, 1439 (1972).

(13) J. C. Schug, T. H. Brown, and M. Karplus, *J. Chem. Phys.*, **37**, 330 (1962).

(14) B. J. Tabner, *J. Chem. Soc. A*, 2487 (1969).

Spectroscopic Studies of Zeolite Synthesis

by B. D. McNicol,* G. T. Pott, and K. R. Loos

Koninklijke/Shell-Laboratory, Amsterdam, The Netherlands *(Received May 30, 1972)*

Publication costs assisted by Shell Research N.V.

The synthesis of zeolites Linde A and faujasite has been studied using phosphorescence spectroscopy and laser–Raman spectroscopy. The phosphorescence of tracer amounts of Fe^{3+} was used to monitor changes in the framework of the solid gel phase during induction and crystallization periods. The liquid and solid gel phases were studied using the Raman spectra of silicate and aluminate tetrahedral anionic species and tetramethylammonium cationic species as probes. The results obtained were indicative of a zeolite crystallization in the solid gel phase *via* condensation between hydroxylated Si–Al tetrahedra.

Previous studies of zeolite crystal growth using chemical analysis, X-ray diffraction, and electron microscopy have given rise to two main proposals for the mechanism of formation of zeolite crystals from aluminosilicate gels.[1,2] On the one hand there exists a school of thought that zeolite crystallization occurs by dissolution of the amorphous gel to produce active aluminosilicate anionic species in solution. These species then grow by consumption of the gel to form the nuclei and ultimate crystals.[1] The second mechanism, first put forward by Breck and Flanigen,[2] proposes that the crystal nuclei are formed in the solid phase of the gel and that formation of these nuclei and ultimate crystal growth occurs by depolymerization of the gel by the OH^- ions in the medium.

The investigation of zeolite crystal growth has suffered from the lack of suitable physical techniques for the study of the complicated gel system, and as a result hypotheses regarding the mechanism have had to rely on chemical analysis of solid and liquid phases, X-ray diffraction, and, to a lesser extent, electron microscopy. These techniques are not very sensitive in the detection of trace concentrations of crystalline material.

We have studied the crystal growth of some zeolites (Linde A, in particular) using phosphorescence spectroscopy to study the solid phase, and laser–Raman spectroscopy to study both the liquid and the solid phase during the induction and crystallization periods of zeolite crystal growth.

The phosphorescence technique has recently been applied to the study of transition metal coordination in oxides and zeolites.[3] These studies showed that Fe^{3+} impurity ions in zeolite crystals occupy tetrahedrally coordinated Al^{3+} framework sites. Such a coordination for Fe^{3+} gives rise to a phosphorescence and excitation spectrum characteristic for zeolites (Figure 1). Addition of trace amounts of Fe^{3+} to the gel then permits the study of the build-up of any zeolite-like framework during the induction and crystallization periods. This technique has the advantage over X-ray diffraction and other spectroscopic techniques that it is able to detect tetrahedrally coordinated Fe^{3+} in the parts per million range.

Silicate, aluminate, and aluminosilicate anionic species existing in solution in significant concentrations can be studied by Raman spectroscopy and thus the liquid phase can be monitored during the reaction for changes in concentration of such species. In addition, laser–Raman spectroscopy has proved to be a useful probe for the detection of large cations such as $(CH_3)_4N^+$ occluded in zeolite cavities.[4] Thus by monitoring a gel system containing $(CH_3)_4N^+$ we can follow any changes which may occur in the surroundings of the $(CH_3)_4N^+$ ions.

Experimental Section

A. Phosphorescence. The aluminosilicate gel for a Linde A synthesis was made by adding a solution of Fe^{3+}-doped silicic acid in NaOH to a solution of $Al(OH)_3$ in NaOH. The gel of composition $6Na_2O \cdot Al_2O_3 \cdot 1.7SiO_2 \cdot 370H_2O$, 0.01 wt % Fe^{3+} was heated to 100° and small samples of gel were extracted at different time intervals during the synthesis. The gel samples were placed in 3-mm internal diameter quartz tubes and quenched in liquid nitrogen ready for measurement. No pretreatment of gel such as filtering or drying was required. Spectra were measured using the phosphorescence spectrometer described previously.[5]

B. Laser–Raman Spectroscopy. Spectra were obtained of the centrifuged liquid phase and dried solid phase of gels designed to give Linde A or faujasite as ultimate product. Measurements were made using a

(1) See, for example, S. P. Zhdanov, *Advan. Chem. Ser.*, **No. 101**, 20 (1971); G. T. Kerr, *J. Phys. Chem.*, **70**, 1047 (1966); J. Ciric, *J. Colloid Interface Sci.*, **28**, 315 (1968).

(2) D. W. Breck and E. M. Flanigen, presented at the 137th National Meeting of the American Chemical Society, Cleveland, Ohio, April 1960.

(3) G. T. Pott and B. D. McNicol, *Chem. Phys. Lett.*, **12**, 62 (1971); B. D. McNicol and G. T. Pott, *J. Catal.*, **25**, 223 (1972).

(4) K. R. Loos and J. F. Cole, unpublished results.

(5) G. T. Pott and B. D. McNicol, *J. Chem. Phys.*, **56**, 5246 (1972).

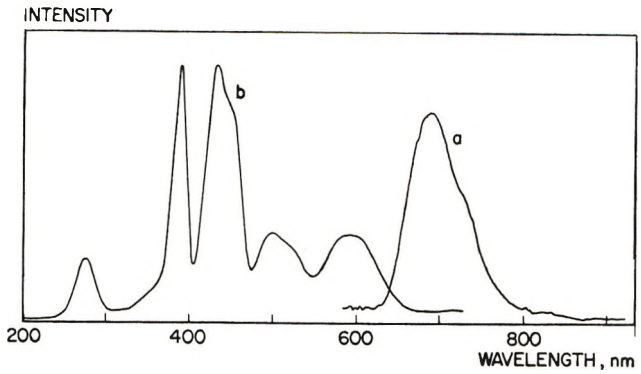

Figure 1. Phosphorescence (a) and excitation (b) spectra of Fe^{3+}-doped zeolite gel.

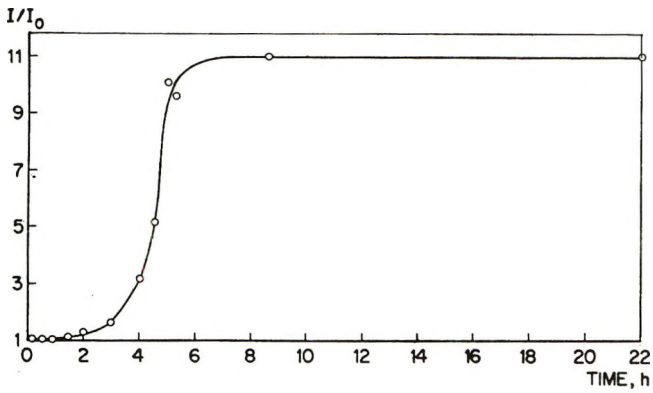

Figure 2. Relative intensity of Fe^{3+} phosphorescence of gel as a function of time.

Spex Ramalog spectrometer equipped with a Coherent Radiation Model 52 argon ion laser.

Results

A. Phosphorescence. The results of a typical experiment, a Linde A synthesis, are shown in Figure 2. Similar results were obtained in the synthesis of other zeolites such as faujasite, gmelinite, and P.

The phosphorescence data can be summarized as follows: (1) immediately upon the formation of the gel a weak signal similar to that shown in Figure 1 was observed; (2) the phosphorescence intensity (Figure 2) rises only slightly during the induction period of synthesis and then rapidly increases until finally the fully crystallized phase has a constant phosphorescence intensity; (3) the wavelength and band shape of the excitation and emission spectrum of the final crystals are essentially identical with the spectrum of the initial gel; (4) experiments on Fe^{3+}-doped neutral aluminosilicate gels showed that Fe^{3+} centers in such systems do not phosphoresce; (5) the liquid phase of the gel, separated by centrifugation, did not give a Fe^{3+} phosphorescence signal at any time during crystallization.

These results indicate that immediately upon gel formation tetrahedrally coordinated zeolite framework sites exist which are similar to the $Fe^{3+}(Al^{3+})$ sites in the final crystal. These gel sites exist exclusively in the solid phase. The initial period of time during which the Fe^{3+} signal rises only slightly in intensity corresponds to the well-known induction period,[6] while the steeply rising part parallels the appearance of a diffraction pattern on X-ray powder photographs. This part of the kinetic curve indicates macroscopic crystallization. Crystals grown in this way were smaller than 5 μ.

B. Laser–Raman Spectroscopy. Characteristic bands in the liquid phase due to $Al(OH)_4^-$ at 618 cm^{-1} and $SiO_2(OH)_2^{2-}$ at 772 and 915 cm^{-1} were observed during both Linde A and faujasite syntheses. Throughout the induction period, and even after crystallization had set in, the concentration of these species remained essentially constant within the error of the technique (15%). Furthermore, no evidence of the existence of an anionic aluminosilicate species was noted. These observations indicate that no significant net dissolution of the solid phase of the gel occurs throughout the synthesis.

In another experiment Raman spectra were obtained of a Linde A system in which 60% of the sodium ions were replaced by $(CH_3)_4N^+$ ions. In the liquid phase a spectrum identical with that of $(CH_3)_4N^+$ in aqueous basic solution was observed with a strong N–C symmetric stretching mode at 752 cm^{-1}. Throughout both the induction and crystallization periods the signal did not change in shape, position, or intensity. During the induction period the centrifuged, washed (to pH 9), and dried solid phase showed a weak band at 754 cm^{-1}. Upon the onset of observable crystallization the 754-cm^{-1} band decreased in intensity and a concomitant increase of a new band at 769 cm^{-1} was observed. The growth in intensity of this signal paralleled the increase in Fe^{3+} phosphorescence after the induction period. This band at 769 cm^{-1} was similar to that found for $(CH_3)_4N^+$ ions occluded in sodalite[4] and is therefore believed to be due to $(CH_3)_4N^+$ ions occluded within the zeolitic cages of the Linde A crystals.

Discussion

The Raman and phosphorescence results do not show any observable changes occurring in the liquid phase but do show significant alteration in the solid phase, which supports the view that crystal growth occurs from the solid gel phase.

Barrer and coworkers[7] have recently reported the observation of amorphous laminae precursors to zeolite crystals. The presence of a phosphorescence signal upon gel formation is consistent with the presence of such laminae. The considerably lower intensity of

(6) D. W. Breck and E. M. Flanigen, "Molecular Sieves," Society of Chemical Industry, London, 1967, p 47.

(7) R. Aiello, R. M. Barrer, and I. S. Kerr, *Advan. Chem. Ser.*, No. 101, 44 (1971).

the phosphorescence observed throughout the induction period can be due to the presence of many more terminal hydroxylated framework $Fe^{3+}(Al^{3+})$ ionic species in the gel which do not phosphoresce. The final crystals, however, having a very much higher ratio of bulk to surface framework sites would therefore have a much more intense phosphorescence signal. Similarly, the 754-cm^{-1} $(CH_3)_4N^+$ Raman band in the solid phase during the induction period is explicable as $(CH_3)_4N^+$ ions bound to the negatively charged Al framework sites of the amorphous gel. On transformation of the amorphous material to zeolite crystals the $(CH_3)_4N^+$ ions become trapped in the cages of the crystals. Summarizing, it can be said that our experiments are compatible with a zeolite crystallization mechanism occurring in the solid phase where some amorphous laminae are produced upon gel formation. During the induction period further laminar species can be formed, destroyed, and modified until the first zeolite crystals are formed, after which autocatalysis of crystal growth produces an "avalanche" of zeolite crystals.

Transmission Ellipsometry and Polarization Spectrometry of Thin Layers

by D. den Engelsen

Philips Research Laboratories, Eindhoven, Netherlands *(Received May 19, 1972)*

Publication costs assisted by Philips Research Laboratories

A theoretical description is given of the transmission ellipsometry and polarization spectrometry (dichroic spectra) of thin films deposited on a transparent substrate. It is shown that transmission ellipsometry is a sensitive method of measuring the anisotropy of the optical constants. The dichroism of films thinner than the wavelength of the light used to make the measurements depends strongly on their thickness, whereas for thick films the dichroism is almost independent of the thickness. The theory about transmission ellipsometry and dichroic spectra is illustrated by Langmuir–Blodgett layers.

Introduction

Ellipsometric and spectroscopic methods are at present widely used for studying thin films. Most applications deal with isotropic thin layers on which a vast literature exists, including several well-known handbooks.[1-3] Thus far, little attention has been paid to the transmittance and reflectance of anisotropic thin films. Anisotropy may refer to either the components of the dielectric tensor or the components of the conductivity tensor. The absence of much information or knowledge about this subject is caused by the difficulties inherent in preparing thin anisotropic layers. For instance, evaporation techniques seldom yield anisotropic systems. An exception is formed by polymer sheets containing rod-shaped dye molecules. Stretching of such sheets gives rise to a more or less well-defined orientation of the dye molecules with their long axes in the stretch direction.[4] However, nonrodlike molecules can also be oriented.[5] The dichroic spectra of these anisotropic systems can be interpreted in terms of the degree of orientation of the dye molecules.[6] Another class of essentially anisotropic layers is formed by the so-called Langmuir–Blodgett (LB) layers.[7,8] The birefringence in nonabsorbing layers of barium stearate has been measured by Langmuir and Blodgett by comparing the respective transmittances of the p (parallel) wave and s ("senkrecht") wave.[8] The anisotropy in the optical constants of both nonabsorbing and absorbing LB layers can also be determined with (reflection) ellipsometry.[9,10]

In this paper I shall present a theoretical description of the dichroic spectra of uniaxially anisotropic layers

(1) A. Vasicek, "Optics of Thin Films," North-Holland, Amsterdam, 1960.

(2) O. S. Heavens, "Optical Properties of Thin Solid Films," Butterworths, London, 1955.

(3) O. S. Heavens, "Thin Film Physics," Methuen, London, 1970, Chapter 6.

(4) (a) E. W. Thulstrup, J. Michl, and J. H. Eggers, *J. Phys. Chem.*, **74**, 3868 (1970); (b) H. Inoue, *et al.*, *Ber. Bunsenges. Phys. Chem.*, **75**, 441 (1971).

(5) This was kindly pointed out to me by the reviewer of the manuscript.

(6) Y. Tanizaki, *Bull. Chem. Soc. Jap.*, **38**, 1798 (1965).

(7) K. B. Blodgett, *J. Amer. Chem. Soc.*, **57**, 1007 (1935).

(8) K. B. Blodgett and I. Langmuir, *Phys. Rev.*, **51**, 964 (1937).

(9) D. den Engelsen, *J. Opt. Soc. Amer.*, **61**, 1460 (1971).

(10) E. P. Honig, J. H. Th. Hengst, and D. den Engelsen, *J. Colloid Interface Sci.*, in press.

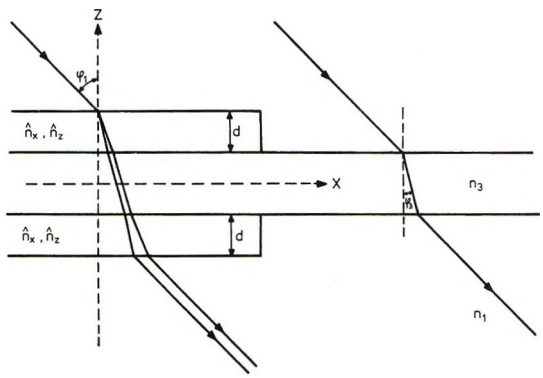

Figure 1. Anisotropic film on glass: Y axis normal to the plane of the drawing; X,Z plane is plane of incidence.

with the optic axis either in or normal to the plane of incidence. The range of film thicknesses considered varies between zero and the wavelength of the incident light. Furthermore, a description will be given of transmission ellipsometry which is a useful technique for determining the optical constants of anisotropic layers. The theoretical considerations are illustrated by some absorbing and nonabsorbing LB layers. With these layers the degree of anisotropy in the indices of absorption can easily be varied by using mixed layers of dyes and fatty acids.[9,11]

Theory

The reflectance of an anisotropic film deposited on an isotropic substrate has been described previously.[9] Again, only uniaxial anisotropy will be considered with the optic axis coinciding with one of the cartesian axes of Figure 1. First, we will deal with the case of Z axis as the optic axis. Later on, simple transformations will be given to deal with systems having their optic axis in the direction of either the X or the Y axis. Thus, the principal indices of refraction of the film with respect to the coordinate system of Figure 1 are

$$\left.\begin{aligned} \hat{n}_z &= n_z(1 - i\kappa_z) \\ \hat{n}_x = \hat{n}_y &= n_x(1 - i\kappa_x) \end{aligned}\right\} \quad (1)$$

If the film is nonabsorbing, then the indices of absorption, κ_x and κ_z, are zero. In the next section n_j ($j = x$, y, or z) will stand for both absorbing and nonabsorbing films. It will be assumed that the substrate is an isotropic transparent medium (glass, fused quartz). Figure 1 has been made in accordance with the experimental conditions, because with the Langmuir–Blodgett dipping technique both sides of the slide are equally covered by a "built-up" film. The equations derived hereafter refer to this case, but the transformation to a singly covered slide is trivial.

When a monochromatic light beam falls on the covered part of the slide, the beam passes four phase boundaries successively. Since the slides are thick enough, internal reflections within the slide need not be considered. Hence, for small beam diameters the five-phase system may be split in two three-phase systems. If t_{1p} and r_{1p} are, respectively, Fresnel's coefficients of transmission and reflection for the p wave at the air–film interface, and t_{2p} and r_{2p} are the corresponding coefficients at the film–glass interface, then the total transmission coefficient T_p becomes[1,2]

$$T_p = \left(\frac{t_{1p}^{(u)} t_{2p}^{(u)} e^{-i\beta_p^{(u)}}}{1 + r_{1p}^{(u)} r_{2p}^{(u)} e^{-2i\beta_p^{(u)}}}\right)\left(\frac{t_{2p}^{(l)} t_{1p}^{(l)} e^{-i\beta_p^{(l)}}}{1 + r_{2p}^{(l)} r_{1p}^{(l)} e^{-2i\beta_p^{(l)}}}\right) \quad (2)$$

where the superscripts (u) and (l) refer to the upper and the lower surfaces of the slide (Figure 1). The transmission coefficient T_s of the s wave is similar to eq 2 by changing subscript p's into s's. The phase differences β_p and β_s are

$$\beta_p = 2\pi d n_p \cos \varphi_p \lambda^{-1} \text{ and } \beta_s = 2\pi d n_s \cos \varphi_s \lambda^{-1} \quad (3)$$

where n is the refractive index, φ is the angle of refraction, d is the thickness of the film, and λ is the wavelength of the light under vacuum. Only in isotropic media or when using normally incident light are φ_p and φ_s equal. When the film absorbs light, then the refractive angles φ_p and φ_s are complex quantities too.[1,12] Using the equations of Snell and Fresnel, n_p, n_s, φ_p, and φ_s can be expressed in terms of the optical c onstants n_x nd n_z of the film, the angle of incidence φ_1 and the refractive index n_1 of the outer medium (air).[9,12] Thus

$$\beta_p = 2\pi d n_x X_p/(n_z\lambda) \text{ and } \beta_s = 2\pi d X_s/\lambda \quad (4)$$

where $s = n_1 \sin \varphi_1$, and $X_p = \sqrt{n_z^2 - s^2}$ and $X_s = \sqrt{n_x^2 - s^2}$. As a consequence of the preparation technique of the LB layers, the film thicknesses on both sides of the slide are equal; therefore $\beta_p^{(u)} = \beta_p^{(l)}$.

For a singly covered slide the second factor on the right-hand side of (2) becomes simply Fresnel's coefficient of transmission for the glass–air interface.

Fresnel's coefficients of reflection at the successive phase boundaries have been given before.[9] The reflection coefficients at the upper and lower interface of the slide are related by

$$r_{mk}^{(u)} = -r_{mk}^{(l)}$$

where m is 1 or 2 and k stands for p or s. We further have[9]

$$t_{1p}^{(u)} t_{2p}^{(u)} = \frac{4n_1 (\cos \varphi_1) n_z n_x X_p}{(n_x n_z \cos \varphi_1 + n_1 X_p)(n_x n_z \cos \varphi_3 + n_3 X_p)} \quad (5)$$

and

$$t_{1s}^{(u)} t_{2s}^{(u)} = \frac{4n_1 (\cos \varphi_1) X_s}{(n_1 \cos \varphi_1 + X_s)(n_3 \cos \varphi_3 + X_s)} \quad (6)$$

(11) H. Bücher, *et al.*, *Mol. Cryst.*, 2, 199 (1967).

(12) M. Born and E. Wolf, "Principles of Optics," Pergamon Press, Elmsford, N. Y., 1965.

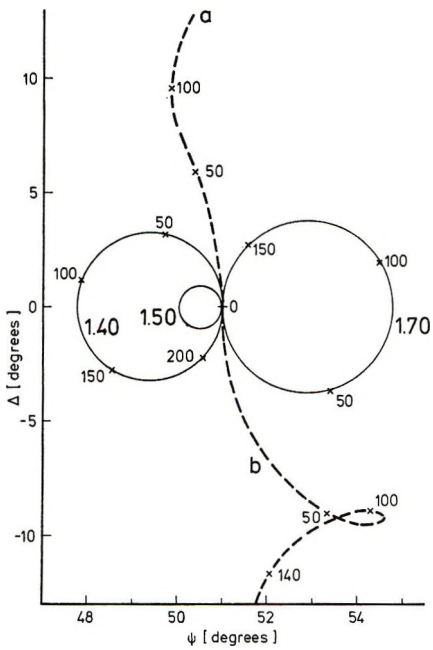

Figure 2. ψ *vs.* Δ plot of the *transmitted* wave for nonabsorbing film: $\varphi_1 = 60°$, λ 500 nm, $n_3 = 1.54$. Full lines refer to isotropic films with $n = 1.4$, 1.5, and 1.7, respectively. Curve a: $n_x = 1.5$, $n_z = 1.7$. Curve b: $n_x = 1.7$, $n_z = 1.5$. Inserted numbers indicate film thickness in nm.

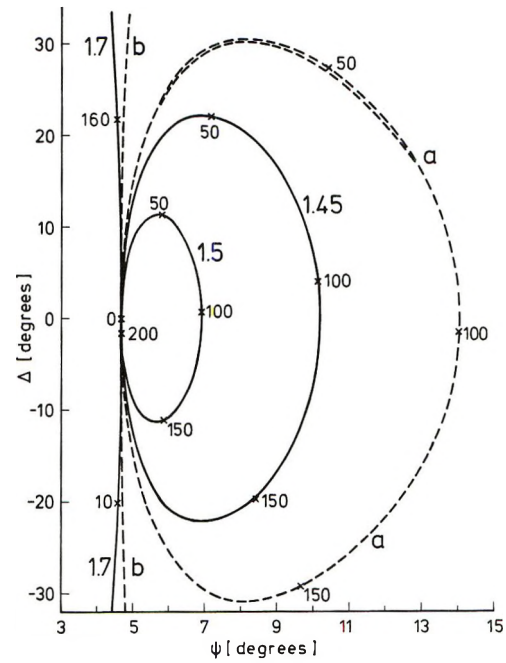

Figure 3. ψ *vs.* Δ plot of the *reflected* wave for a nonabsorbing film. Since the curve for $n = 1.4$ almost coincides with curve a, a curve for $n = 1.45$ has been drawn. Other data as in Figure 2.

As shown in Figure 1, φ_3 refers to the direction of the wave normal in the glass slide with refractive index n_3. Corresponding equations for $t_{1p}^{(1)}$ $t_{2p}^{(1)}$ and $t_{1s}^{(1)}$ $t_{2s}^{(1)}$ are readily derived from (5) and (6) by replacing n_1 and φ_1 by n_3 and φ_3. Making use of (5) and (6) the total transmission coefficient T_p, defined in eq 2, can be rewritten

$$T_p = \frac{16n_1n_3(\cos\varphi_1\cos\varphi_3)n_z^2n_x^2X_p^2e^{-2i\beta_p}}{[(n_zn_x\cos\varphi_1 + n_1X_p)\times (n_2n_x\cos\varphi_3 + n_3X_p)(1 + r_{1p}r_{2p}e^{-2i\beta_p})]^2} \quad (7)$$

T_s becomes

$$T_s = \frac{16n_1n_3(\cos\varphi_1\cos\varphi_3)X_s^2e^{-2i\beta_s}}{[(n_1\cos\varphi_1 + X_s)(n_3\cos\varphi_3 + X_s)(1 + r_{1s}r_{2s}e^{-2i\beta_s})]^2} \quad (8)$$

In analogy with reflection ellipsometry we define ψ and Δ with

$$(\tan\psi)e^{i\Delta} = \frac{T_p}{T_s} = \left[\frac{n_zn_xX_pe^{i(\beta_s-\beta_p)}(n_1\cos\varphi_1 + X_s)\times (n_3\cos\varphi_3 + X_s)(1 + r_{1s}r_{2s}e^{-2i\beta_s})}{X_s(n_xn_z\cos\varphi_1 + n_1X_p)\times (n_xn_z\cos\varphi_3 + n_3X_p)(1 + r_{1p}r_{2p}e^{-2i\beta_p})}\right]^2 \quad (9)$$

In Figures 2, 4, and 6, Δ has been plotted *vs.* ψ at various values of the film thickness d between zero and about 200 nm. For the sake of comparison the corresponding curves for the case of reflection ellipsometry have been plotted in Figures 3 and 5, using the equations of ref 9. At reflection the ellipsometric effect is induced by the upper film only, because multiple reflections of the slide are neglected.

It is shown in Figures 2 and 4 that a thin isotropic film on both sides of a transparent slide gives rise to relatively small ellipsometric effects in the transmitted wave. The reason for this is that the exponential $2i(\beta_s - \beta_p)$ in eq 9 is always zero for the isotropic case. Hence, the periodicity of the ellipsometric effect as a function of the film thickness stems solely from the ratio $(1 + r_{1s}r_{2s}e^{-2i\beta_s})/(1 + r_{1p}r_{2p}e^{-2i\beta_p})$, which is close to unity for the used limited range of values for the refractive indices of film and substrate. In the case of dielectric anisotropy in a nonabsorbing film ($n_x \neq n_z$) $2i(\beta_s - \beta_p)$ is purely imaginary, which leads to a relatively large effect in Δ only. This is shown for instance by the dashed line of Figure 2. On the other hand, anisotropy in the indices of absorption (*i.e.*, $\kappa_x \neq \kappa_z$) causes fairly large variations in ψ, as can be seen from Figure 4. Principally, this effect stems from the real part of $\exp[2i(\beta_s - \beta_p)]$. The fairly sharp angle in curve b of Figure 4 is purely accidental; insertion of other values for the optical constants of the film can yield a spiral as curve b of Figure 2. Finally, Figure 6 shows the amplification of the ellipsometric effect by increasing the refractive index of the substrate.

It can be seen from Figures 2–5 that transmission

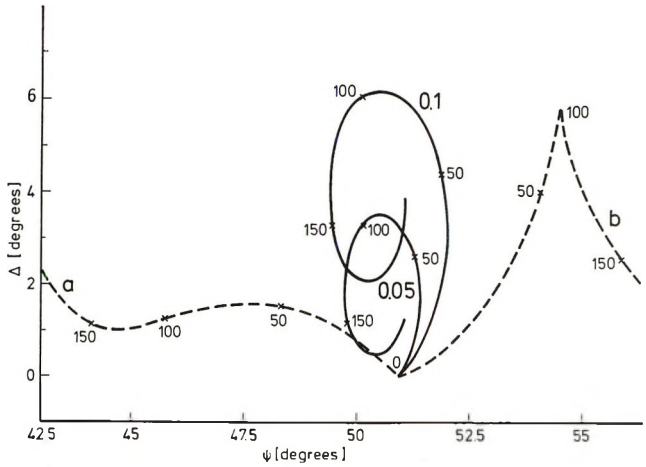

Figure 4. ψ *vs.* Δ plot of the *transmitted* wave for an absorbing film. Full lines refer to isotropic films with $\kappa = 0.05$ and 0.1, respectively. Curve a: $\kappa_x = 0$, $\kappa_z = 0.1$. Curve b: $\kappa_x = 0.1$, $\kappa_z = 0$. For all curves $n_x = n_z = 1.5$. Other data as in Figure 2.

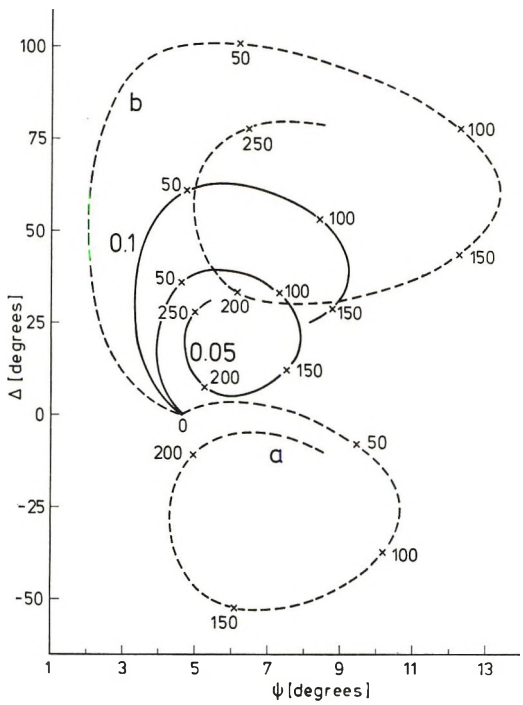

Figure 5. ψ *vs.* Δ plot of the *reflected* wave for absorbing film. Same conditions as in Figure 4.

ellipsometry is not a very practical technique for determining the optical constants of an *isotropic* film; reflection ellipsometry under the same conditions is better. In the case of anisotropy of either the dielectric or the conductivity tensor (or both), transmission ellipsometry can be very useful for determining the optical constants of the film along the principal axes. Transmission ellipsometry is indeed a very sensitive method to measure the birefringence of thin films. Comparing Figures 2 and 3, it can be seen that although curve a of the latter figure refers to a birefringent film, the asymmetry in this curve (second loop[9]) caused by anisotropy is very small.

The transmission coefficients of the beam passing through the slide at zero film thickness are

$$T_p^{(0)} = 4n_1n_3 \cos\varphi_1 \cos\varphi_3(n_3 \cos\varphi_1 + n_1 \cos\varphi_3)^{-2} \quad (10)$$

$$T_s^{(0)} = 4n_1n_3 \cos\varphi_1 \cos\varphi_3(n_1 \cos\varphi_1 + n_3 \cos\varphi_3)^{-2} \quad (11)$$

The transmitted intensity I of the light will be defined with respect to the light transmitted by a blank slide; thus

$$I_k = T_k T_k^*(T_k^{(0)})^{-2} \quad (12)$$

where k stands for p or s, and T_k^* is the complex conjugate of T_k. Finally, the optical density is defined as

$$D_k = -\log I_k \quad (13)$$

The optical density D_k of an absorbing film is not a linear function of the film thickness, because the product $r_{1k}r_{2k} \neq 0$.

By dividing eq 7 and 8 by eq 10 and 11, respectively, one obtains

$$T_k/T_k^{(0)} = \left\{(1 + r_{1k}r_{2k})/(e^{i\beta_k} + r_{1k}r_{2k}e^{-i\beta_k})\right\}^2 \quad (14)$$

A quantity that has been much used in literature[4] is the ratio between the transmittances I_p and I_s or the ratio between the optical densities D_p and D_s. The first ratio is simply

$$I_p/I_s = (\tan\Psi/\tan\bar{\Psi})^2 \quad (15)$$

where $\bar{\Psi}$ is the value of Ψ for the bare substrate. It is immediately clear from eq 15 that I_p/I_s varies as a function of the film thickness for an absorbing (anisotropic) film (see for instance Figure 4). Although no simple expressions can be derived for D_p/D_s, this ratio is a function of the film thickness too. In Figures 7, 8, and 9 D_p/D_s has been plotted *vs.* d for films with isotropic and anisotropic indices of absorption, respectively. Obviously, the ratio D_p/D_s reaches a limiting value both at $d \to \infty$ and $d \to 0$. We will first investigate the behavior of D_p/D_s for very thick films. The phase differences β_k of eq 4 are complex quantities for absorbing films, *viz.* $\beta_k = d(R_e + iI_m)$. For large d the term $r_{1k}r_{2k}\ e^{-i\beta_k} = r_{1k}r_{2k}\ e^{-idR_e}e^{dI_m}$ in the denominator of eq 14 becomes dominant. Hence

$$\lim_{d\to\infty} \frac{D_p}{D_s} = \left|\frac{n_x[\nu_p(1 + \kappa_x\kappa_z) + \mu_p(\kappa_z - \kappa_x)]}{\nu_s n_z(1 + \kappa_z^2)}\right| \quad (16)$$

where μ_p and ν_p are the real and imaginary parts of X_p, ν_s is the imaginary part of X_s, while n and κ are the real and imaginary parts of the complex refractive index (see eq 1). This limiting value of eq 16 is reached to within 1% when d satisfies the following inequality; $d > \lambda/\pi\nu_s$. Thus, irrespective of the value of κ_z, if

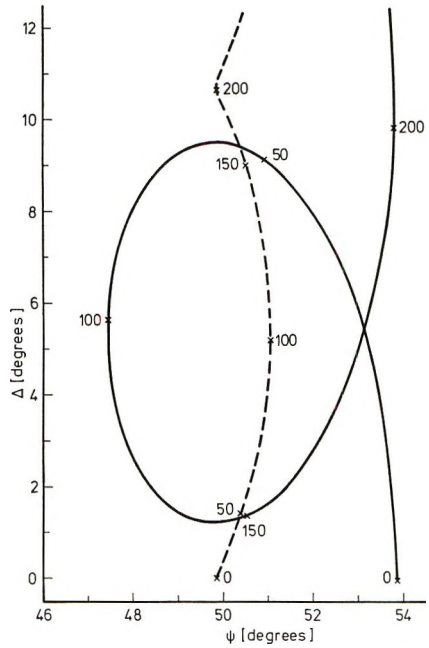

Figure 6. ψ *vs.* Δ plot of the transmitted wave for a birefringent nonabsorbing film on different substrates. Refractive index of the film: $n_x = 1.5$, $n_z = 1.6$. Full line: $n_3 = 1.8$. Dashed line: $n_3 = 1.45$. Other data as in Figure 2.

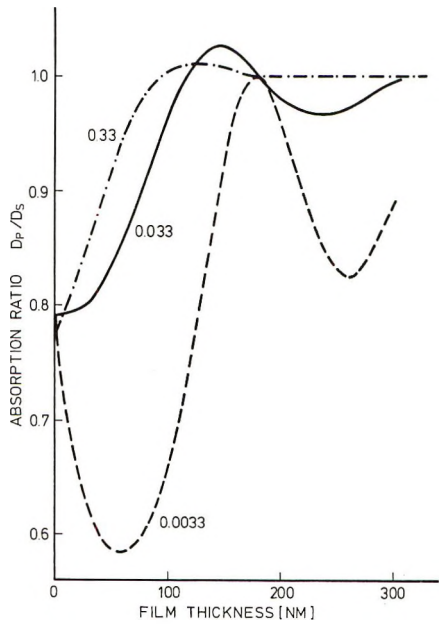

Figure 7. Dichroic ratio D_p/D_s *vs.* film thickness for $\kappa_x = \kappa_z$ and $n_x = n_z = 1.52$. $\varphi_1 = 45°$, λ 500 nm, $n_3 = 1.5$. Absorption index κ is 0.0033, 0.033, and 0.33.

$\kappa_x \leq 0.15$, then D_p/D_s is constant when $d > \lambda$. If $\kappa_x > 0.15$, then the limiting value of D_p/D_s is reached at a smaller film thickness (see Figures 7 and 8). Figure 9 shows the opposite anisotropy in the absorption index: $\kappa_x \ll \kappa_z$. Since κ_x is zero for three curves, a singularity occurs at about $d = 186$ nm (and $d = 0$), where $D_s = 0$. Such films are difficult to prepare in practice, because imperfections in the layers will give rise to κ_x values slightly different from zero. Therefore, curve a of Figure 9 is more likely.

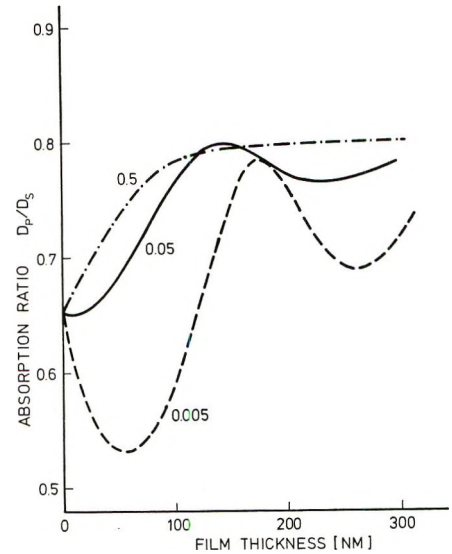

Figure 8. Dichroic ratio D_p/D_s *vs.* film thickness for $\kappa_z = 0$ and $\kappa_x = 0.005$, 0.05, and 0.5. Other data as in Figure 7.

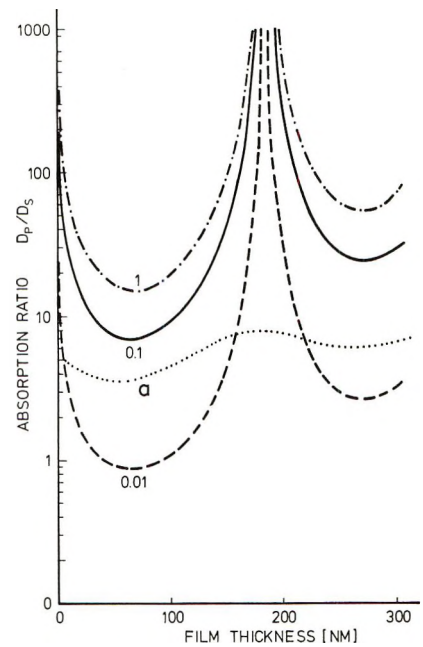

Figure 9. Semilog plot of dichroic ratio D_p/D_s *vs.* film thickness. For curve a: $\kappa_z = 0.1$, $\kappa_x = 0.003$. Other curves: $\kappa_x = 0$, $\kappa_z = 0.01$, 0.1, and 1. Other data as in Figure 7.

The limit of D_p/D_s at $d \to 0$ can also easily be calculated from eq 14 by linear expansion of the exponentials (in the case of nonabsorbing films also quadratic terms in d have to be accounted for). After some algebra we get

$$\lim_{d\to 0} \frac{D_p}{D_s} = \frac{n_1 \cos \varphi_1 + n_3 \cos \varphi_3}{n_3 \cos \varphi_1 + n_1 \cos \varphi_3} \times \left[\frac{n_x^2 \kappa_x (\cos \varphi_1 \cos \varphi_3) n_z^4 (1 + \kappa_z^2)^2 + n_z^2 \kappa_z s^2 n_1 n_3}{n_x^2 n_z^4 \kappa_x (1 + \kappa_z^2)^2}\right] \quad (17)$$

In eq 17 the real and imaginary parts of the complex refractive indices have been separated. However, the limit of eq 17 has only a theoretical meaning, since it is difficult to obtain reliable experimental optical densities at $d \simeq 0$. Moreover, the LB film preparation technique is a discontinuous process proceeding in steps of at least 5 nm (the first step may be 2.5 nm).

Concluding, we may say that the interpretation of dichroic spectra in terms of the anisotropy of the absorption index depends on the thickness of the film. If the film thickness is large compared to the wavelength of light, then usually the effect of multiple reflections of the film may be neglected. In those cases one may rely on simple geometrical considerations such as the directions of the transition moments of dyes with respect to the electric vector of the light.[13] If $d \ll \lambda$, then an extended treatment (*e.g.*, eq 14) is necessary.

Thus far we have only considered uniaxially anisotropic films with the optic axes coinciding with the Z axis of Figure 1, *i.e.*, normal to the surface. As was mentioned earlier, a vast literature exists on the dichroic spectra of stretched polymer films containing dyes. The results obtained in the previous section cannot be applied directly to these films. By stretching a polymer sheet, rod-shaped dye molecules are oriented in the direction of the stretch. If the film thickness is assumed to be large compared to molecular dimensions, then uniaxial anisotropy is likely. Hence it may be concluded that the optic axis points in the direction of stretch. Two relatively simple cases can be distinguished: the optic axis coincides with either the X or the Y axis of Figure 1. The equations derived thus far are readily modified for both these cases. First, the case of the X axis as the optic axis will be considered. In this case the following optical constants have to be distinguished: n_x and $n_z = n_y$. The expression for T_p, eq 7, is invariant under this transformation; T_s has to be changed in such a way that all n_x's are replaced by n_z's or n_y's. Corresponding to these changes the phase difference β_s (eq 4) has to be transformed. When the optic axis coincides with the Y axis, we distinguish n_y and $n_x = n_z$. The transformation of T_p (eq 7) is then simply made by setting $n_x = n_z$, while β_p becomes $2\pi d X_p/\lambda$ (compare eq 4). T_s and β_s are transformed by replacing n_x by n_y. Figure 10 shows the effect on ψ and Δ of the transmitted wave if we choose the optic axis normal to the plane of incidence (Y axis in Figure 1). To make this figure comparable to Figures 2 and 4 the same experimental conditions (magnitude of the anisotropy, angle of incidence, etc.) are taken. The ellipsometric effects of the films shown in Figure 10 are at a given thickness about a factor 3 greater than the effects depicted in Figures 2 and 4. Intermediate effects are obtained by rotating the same films through 90° about the Z axis in which case the X axis becomes the optic axis.

The dichroic spectra are also affected by a change of

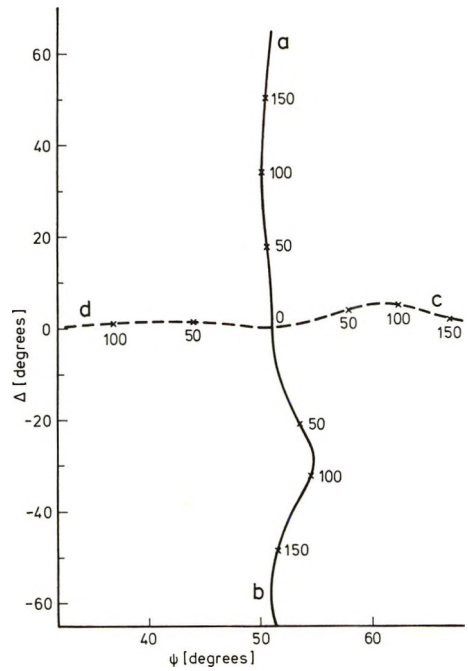

Figure 10. ψ *vs.* Δ of the transmitted wave. Y axis (normal to the plane of incidence) is the optic axis. Curve a: $n_z = n_x = 1.7$, $n_y = 1.5$, $\kappa_z = \kappa_x = \kappa_y = 0$. Curve b: $n_z = n_x = 1.5$, $n_y = 1.7$, $\kappa_z = \kappa_x = \kappa_y = 0$. Curve c: $n_z = n_x = n_y = 1.5$, $\kappa_z = \kappa_x = 0$, $\kappa_y = 0.1$. Curve d: $n_z = n_x = n_y = 1.5$, $\kappa_z = \kappa_x = 0.1$, $\kappa_y = 0$. Other data as in Figure 2.

the optic axis. However, the dichroism in these cases is qualitatively very similar to that depicted in Figures 7, 8, and 9. Since the stretched polymer films are comparable with or thicker than the wavelength of light, the multiple reflections of the film may be neglected. Only under conditions of high dilution (little dye) should these effects be taken into account.

Experimental Section

Several experiments were carried out to test the validity of eq 9 and 14. Thin films were prepared according to the scheme of Langmuir and Blodgett in an apparatus described elsewhere.[10] Nonabsorbing films of barium arachidate were prepared. These films are said to be positively uniaxial, because $n_z > n_x$.[12] Negatively uniaxial LB films do not exist as far as we know. Absorbing films were made of mixed monolayers of arachidic acid and a surface-active trimethyne cyanine dye (TMC), which has been used previously.[9] It is known that TMC forms completely mixed monolayers with arachidic acid and that the chromophoric system of the dye lies almost flat on the water surface.[9,11] Thus it is not surprising that $\kappa_z \simeq 0$ in such LB layers. Unfortunately, the opposite situation with $\kappa_x \simeq 0$ and $\kappa_z \neq 0$ could not be realized since no suitable dyes were available.

The aqueous solutions in the Langmuir trough were buffered at pH 6.6 with KH_2PO_4 and NaOH containing

(13) K. Beck, Thesis, University of Marburg, 1966, p 53.

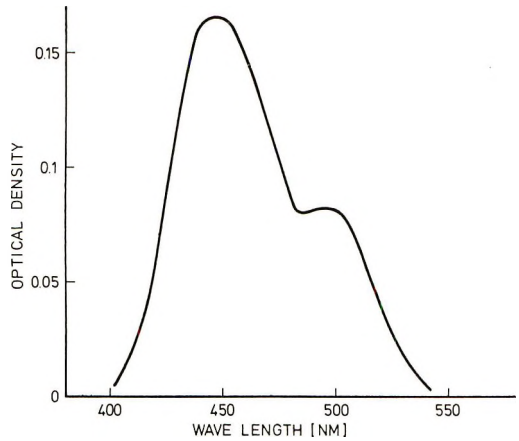

Figure 11. Absorption spectrum of 24 layers of TMC and barium arachidate (1:16) on glass; angle of incidence is 0°.

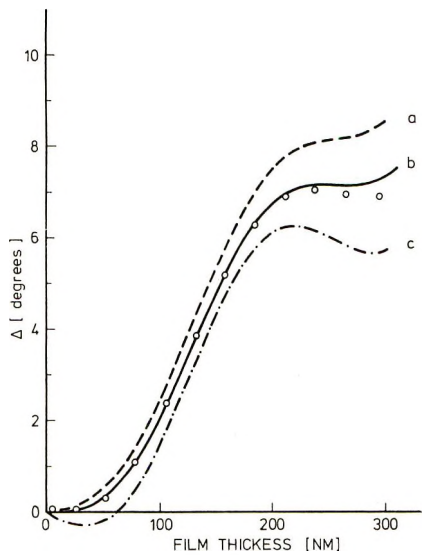

Figure 12. Plot of Δ *vs.* film thickness of barium arachidate multilayers on quartz (n_3 = 1.457 at λ 632.8 nm). Curve a: n_z = 1.580, n_x = 1.505. Curve b: n_z = 1.570, n_x = 1.505. Curve c: n_z = 1.570, n_x = 1.515.

3×10^{-4} *M* $BaCl_2$. The surface pressure and the temperature of the monolayers spread on the water surface were kept constant at 20 dyn/cm and 23.8°, respectively. The slides were made hydrophobic by treating them with $Si(CH_3)_2Cl_2$.[14]

Survey spectra were recorded with a double beam spectrophotometer (Beckman Model DK-2A).

Measurements of I_p and I_s (eq 12 and eq 9) were done at an angle of incidence of 60 ± 0.2°. The glass slides were kept in the slide lift mechanism[10] during the measurements (*in situ*), thus avoiding mechanical damage and unnecessary contamination of the LB layers. The components of our ellipsometer have been discussed before.[9] A He–Ne laser (Spectra Physics Model 120) was used as a source of light for nonabsorbing films; at other wavelengths a halogen lamp and a grating monochromator were used.

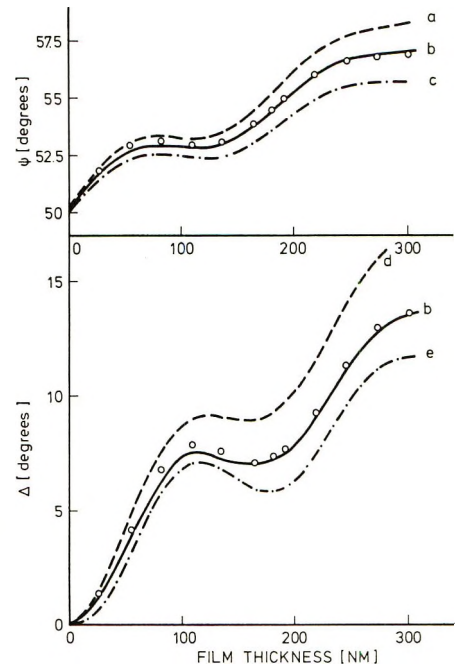

Figure 13. Plot of ψ and Δ *vs.* film thickness of TMC–barium arachidate multilayers on quartz (n_3 = 1.466 at λ 445 nm). Curve a: n_z = 1.56, n_x = 1.50, κ_z = 0, κ_x = 0.06. Curve b: n_z = 1.56, n_x = 1.50, κ_z = 0, κ_x = 0.05. Curve c: = n_z = 1.56, n_x = 1.50, κ_z = 0, κ_x = 0.04. Curve d: n_z = 1.58, n_x = 1.50, κ_z = 0, κ_x = 0.055. Curve e: n_z = 1.57, n_x = 1.52, κ_z = 0, κ_x = 0.05.

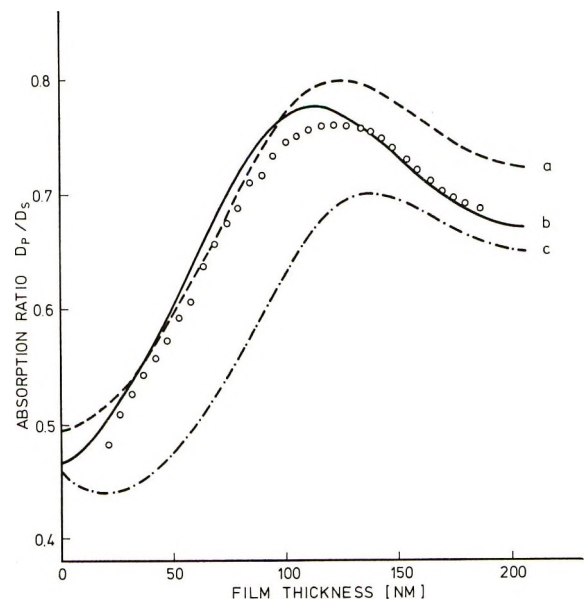

Figure 14. Plot of absorption ratio D_p/D_s *vs.* film thickness of TMC–barium arachidate layers on glass (n_3 = 1.55 at λ 445 nm). Curve a: n_z = 1.60, n_x = 1.55, κ_z = 0.001, κ_x = 0.055. Curve b: n_z = 1.55, n_x = 1.52, κ_z = 0, κ_x = 0.055. Curve c: n_z = 1.55, n_x = 1.60, κ_z = 0, κ_x = 0.06.

Figure 11 shows the absorption spectrum of 24 layers of a mixture of TMC and barium arachidate

(14) H. Bücher, *et al.*, *Z. Phys. Chem.* (*Frankfurt am Main*), 65, 152 (1969).

(1:16) on glass. The tests of the theoretical curves of Figures 4 and 8 were effected at λ 445 and 495 nm, these being the absorption maxima of the dimer and monomer, respectively, of the TMC dye. Figure 12 deals with LB layers of pure barium arachidate which is a nonabsorbing substance at 632.8 nm. The full line (curve b) almost fits the experimental data. The dashed curves a and c show that Δ depends strongly on the difference $n_z - n_x$. This demonstrates nicely the sensitivity of the method. Since the variations of ψ did not exceed 1° (compare Figure 2), we have not made a plot of the experimental ψ's. The thickness of one layer of barium arachidate prepared under the same experimental conditions was determined very accurately at 2.660 nm by (reflection) ellipsometry.[10] The experimental results of transmission ellipsometry of an absorbing anisotropic film are depicted in Figure 13. Since this film of TMC–barium arachidate (1:16) was anisotropic in both the index of refraction and the index of absorption, Δ as well as ψ were strongly affected by an increase in the film thickness. The thickness of one layer of this mixed film was assumed to be 2.74 nm.[9] The "best fit" of the optical constants with the experimental data (inserted circles) is $n_z = 1.56$, $n_x = 1.50$, $\kappa_z = 0$, and $\kappa_x = 0.052$.

In Figure 14 the dichroic ratio D_p/D_s of the same film at 445 nm has been plotted *vs.* the film thickness. The theoretical curves a and c show the sensitiveity of D_p/D_s to small changes of the optical constants of the film. Curve b almost represents the "best fit". Figure 14 alone does not give sufficient information to calculate both κ_x and κ_z and to estimate n_x and n_z. Since D_p and D_s are determined separately, κ_x can be calculated directly from the experimental values of D_s. The dichroic ratio at another wavelength (495 nm) is qualitatively the same as that shown in Figure 14.

Acknowledgments. I am indebted to Dr. E. P. Honig for many discussions and for his critical reading of the manuscript. The experiments were partly performed by Mr. E. Davelaar.

Fluorescence Spectra and Lifetimes of Sm^{3+} in $POCl_3$–$SnCl_4$

by P. Tokousbalides and J. Chrysochoos*

Department of Chemistry, University of Toledo, Toledo, Ohio 43606 *(Received July 6, 1972)*

Publication costs assisted by Owens-Illinois (Corporate Research Laboratories) Toledo, Ohio

The fluorescence efficiency of Sm^{3+} in $POCl_3$–$SnCl_4$ is markedly enhanced relative to the efficiency in aqueous solutions. Both the fluorescence efficiency and fluorescence lifetime depend very strongly on the ratio of $POCl_3$ and $SnCl_4$. Optimum results are obtained at a molar ratio of about 10:1. At both low concentrations of Sm^{3+} and low $[POCl_3]/[SnCl_4]$ ratios the fluorescence lifetimes approach a high value of 3.3 msec. At higher concentrations of Sm^{3+} considerable self-quenching is observed with a self-quenching rate constant, k_Q, of about $8 \times 10^2\ M^{-1}\ sec^{-1}$. A discussion of the above data is presented.

Introduction

The fluorescence efficiency of the rare earth ions in aqueous solutions and in various organic solvents depends on the energy difference between the lowest excited state and the highest ground state of the rare earth ion.[1,2] Furthermore, the higher the energy of the vibrational modes associated with the solvent, the lower the fluorescence efficiency of the ion.[3] A decrease in the fluorescence efficiency of Eu^{3+} in organic solvents was attributed to the radiationless deexcitation of Eu^{3+} *via* the overtones of the →C–H and –O–H groups of the solvent molecules both in the primary and secondary solvation sphere of the rare earth ion.[4,5]

The ratios of the fluorescence intensities of the rare earth ions in D_2O and in D_2O–H_2O, *i.e.*, I_D/I_{D+H}, was found to increase in proportion to the concentration of the hydroxyl group.[3,6] Similar results were observed with rare earth ions in alcohols.[7] These results indicate a nonradiative transfer from the lowest excited state of

(1) A. Heller, *J. Mol. Spectrosc.*, **28**, 208 (1968).
(2) V. L. Ermolaev and E. B. Sveshnikova, *Opt. Spektrosk.*, **28**, 98 (1970).
(3) A. Heller, *J. Amer. Chem. Soc.*, **88**, 2058 (1966).
(4) J. Chrysochoos, *Spectrosc. Lett.*, **5**, 57 (1972).
(5) J. Chrysochoos, *Chem. Phys. Lett.*, **14**, 270 (1972).
(6) J. L. Kropp and M. W. Windsor, *J. Chem. Phys.*, **45**, 761 (1966).
(7) N. A. Kazanskaya and E. B. Sveshnikova, *Opt. Spektrosk.*, **28**, 376 (1970).

the rare earth ion to the overtones of certain vibrational modes of the solvent. Such a mechanism, however, has been accepted on qualitative rather than quantitative evidence.

The energy difference between the $^4G_{5/2}$ and $^4F_{11/2}$ states of Sm^{3+} is about 7400 cm^{-1}.[8] This energy difference matches some of the low overtones of the stretching vibrational modes of such groups as →C–H, –O–H, →C–D, –O–D, etc. In solvents containing such groups, Sm^{3+} should exhibit a very weak, if any, fluorescence efficiency. This is the case. On the other hand, Sm^{3+} should exhibit a high fluorescence yield in solvents which do not contain groups with high energy vibrational modes. Such solvents include $POCl_3$ in combination with $SnCl_4$, $ZrCl_4$, $SbCl_5$, etc. The usefulness of such solvents has been confirmed in the case of Nd^{3+}.[9,10]

Experimental Section

Fluorescence spectra were measured with the Aminco Bowman spectrophotofluorimeter using an RCA-1P21 photomultiplier and a 200-W xenon–mercury lamp. Absorption spectra were taken using the Cary-14 spectrophotometer. Fluorescence lifetimes were obtained by exciting the samples with a xenon flash lamp whose flash duration was about 20 μsec. The excitation light was filtered with a UG-5, ultraviolet transmitting, glass filter. The emitted light was also filtered with a filter whose peak transmission was at 6000 Å with a half-width of about 125 Å (Optics Technology, Inc., set No. 1018; filter No. 600). Therefore, the fluorescence lifetimes measured are associated with the emission band of Sm^{3+} at 595 mμ, *i.e.*, $^4G_{5/2} \rightarrow {}^6H_{7/2}$. The rare earth ion was used in the form of Sm_2O_3 (99.9–99.99%). Ultrapure $POCl_3$ and $SnCl_4$ were used with no further purification. Samarium oxide mixed with appropriate amounts of $POCl_3$ and $SnCl_4$ dissolved slowly at 70–80° under reflux conditions and in the absence of water vapor and CO_2. The reaction was completed within 24 to 48 hr, giving rise to transparent solutions containing up to 3×10^{-1} *M* Sm^{3+}. All samples were kept in a drybox.

Results and Discussion

Typical fluorescence spectra are shown in Figure 1A. This figure also contains the fluorescence spectrum of Sm^{3+} in aqueous solutions for comparison. An enhancement in the fluorescence efficiency of Sm^{3+} in $POCl_3$–$SnCl_4$ relative to that in aqueous solutions is apparent. The ratio of the fluorescence intensities in the two systems is of the order of 10^3. A further enhancement, by about a factor of 3, is observed by lowering the temperature from +25 to −2°. Fluorescence spectra at lower temperatures were unattainable because the freezing point of the samples under consideration was about −2°. Variation in the composition of the $POCl_3$–$SnCl_4$ system has a considerable effect upon the fluorescence spectra of Sm^{3+}. Such an effect is

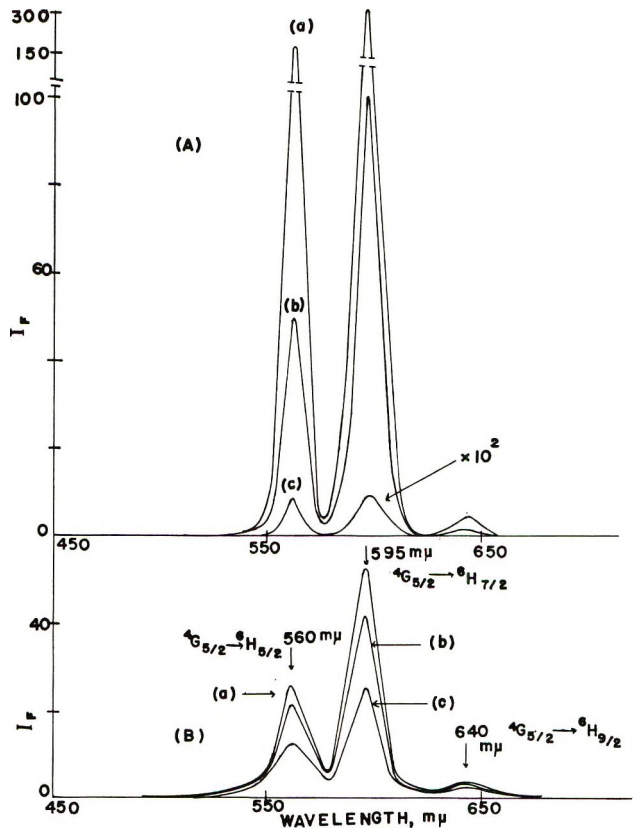

Figure 1. (A) Fluorescence spectra of 2×10^{-1} *M* Sm^{3+}, uncorrected; λ_{exc} 402 mμ: (a) Sm^{3+} in $POCl_3$–$SnCl_4$ ($[POCl_3]/[SnCl_4]$ = 10.34) at −2°; (b) Sm^{3+} in $POCl_3$–$SnCl_4$ at 25°; (c) Sm^{3+} in aqueous solution. (B) Fluorescence spectra of 4×10^{-2} *M* Sm^{3+} in $POCl_3$–$SnCl_4$; λ_{exc} 402 mμ: (a) $[POCl_3]/[SnCl_4]$ = 10.34; (b) $[POCl_3]/[SnCl_4]$ = 13.24; (c) $[POCl_3]/[SnCl_4]$ = 27.76.

shown in Figure 1B. The fluorescence efficiency of Sm^{3+} increases as the $[POCl_3]/[SnCl_4]$ decreases. However, the concentration of $SnCl_4$ has to be within certain limits to attain clear solutions. The rare earth salts are insoluble in both pure $POCl_3$ and $SnCl_4$ but they are fairly soluble in certain combinations of these two solvents. The conductivities of both pure $POCl_3$ and $SnCl_4$ are very low,[11] *i.e.*, 1.6×10^{-6} and 1×10^{-8} Ω^{-1} cm^{-1}, respectively. However, $POCl_3$ with 6% (in moles) $SnCl_4$ exhibits conductivity of about 6×10^{-5} Ω^{-1} cm^{-1}, indicating the presence of the ionized forms of both $POCl_3$ and $SnCl_4$, possibly *via*

$$2POCl_3 + SnCl_4 \longrightarrow 2POCl_2^+SnCl_6^{2-}$$

A complex, $2POCl_3 \cdot SnCl_4$, precipitates at the beginning, but it is dissolved in an excess of $POCl_3$. Therefore, it appears as if the $POCl_2^+$ ion may react with the oxide

(8) G. H. Dieke and H. M. Grosswhite, *Appl. Opt.*, 2, 675 (1963).
(9) A. Lempicki and A. Heller, *Appl. Phys. Lett.*, 9, 108 (1966).
(10) N. Blumenthal, C. B. Ellis, and D. Grafstein, *J. Chem. Phys.*, 48, 5726 (1968).
(11) F. Collier, H. Dubost, R. Kohlmuller, and G. Raoult, *C. R. Acad. Sci., Ser. C*, 267, 1065 (1968).

$$Sm_2O_3 + 6POCl_2^+ \longrightarrow 2Sm^{3+} + 4POCl_3 + P_2O_5$$

The Sm^{3+} formed is then associated with the $SnCl_6^{2-}$ ions. At low concentrations of $SnCl_4$ there is not sufficient concentration of $POCl_2^+$ to react with Sm_2O_3, whereas at high concentrations of $SnCl_4$ the complex $2POCl_3 \cdot SnCl_4$ precipitates. Therefore, the variation in $[SnCl_4]$ has to be confined within these two limits.

The effect of the $[POCl_3]/[SnCl_4]$ ratio upon the fluorescence lifetimes is shown in Figure 2A. The fluorescence lifetimes increase as the ratio decreases. This change in the $[POCl_3]/[SnCl_4]$ ratio reflects a considerable change in the concentration of $SnCl_4$ but a rather negligible change in the concentration of $POCl_3$. The dependence of the fluorescence lifetimes upon $[POCl_3]$ and $[SnCl_4]$ is shown in Figure 2B. Since it is rather unlikely that a 10% increase in $[POCl_3]$ can be associated with the variation of the fluorescence lifetimes observed, it seems more reasonable that such a variation may relate to $[SnCl_4]$. If we visualize Sm^{3+} ions surrounded by $SnCl_6^{2-}$ ions, the quenching effect of such a solvation sphere will be insignificant due to the low energy vibrational modes involved. At lower concentrations of $SnCl_4$, the primary solvation sphere may contain also $POCl_3$ molecules. Such molecules could

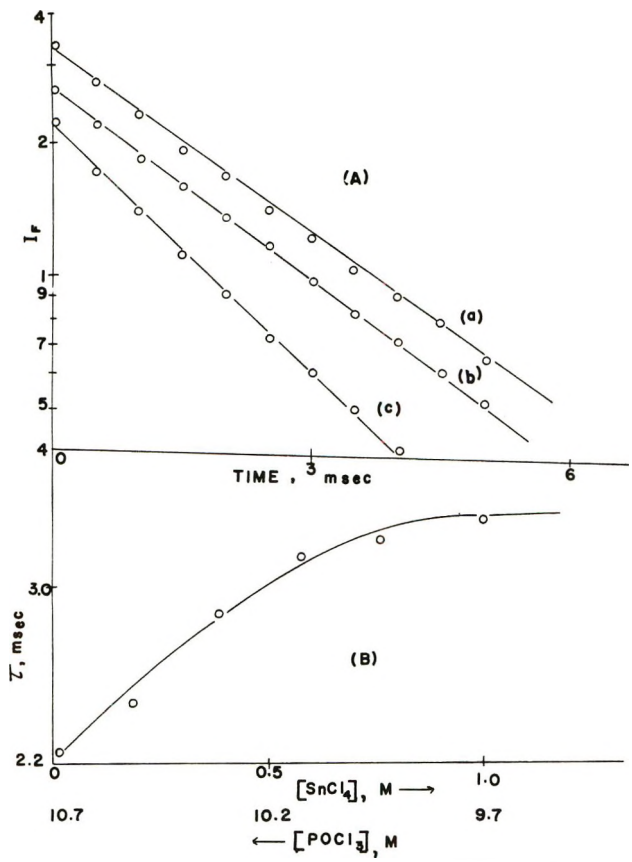

Figure 2. (A) Fluorescence decay of 4×10^{-2} M Sm^{3+} in $POCl_3$–$SnCl_4$; λ_{exc} 300–450 mμ; $\lambda_{fl} \sim$ 590–630 mμ: (a) $[POCl_3]/[SnCl_4]$ = 10.34; (b) $[POCl_3]/[SnCl_4]$ = 13.24; (c) $[POCl_3]/[SnCl_4]$ = 56.81. (B) Fluorescence lifetimes of 1×10^{-2} M Sm^{3+} as a function of $[SnCl_4]$ and $[POCl_3]$.

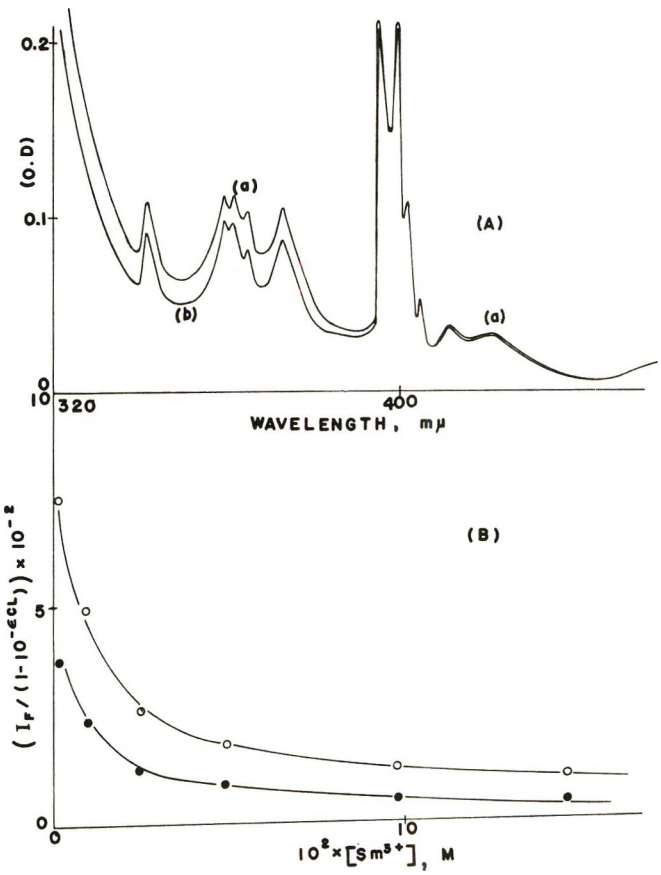

Figure 3. (A) Ultraviolet absorption spectra of 4×10^{-2} M Sm^{3+} in $POCl_3$–$SnCl_4$ *vs.* air; L = 1 cm: (a) $[POCl_3]/[SnCl_4]$ = 13.24; (b) $[POCl_3]/[SnCl_4]$ = 56.81. (B) Fluorescence intensity (normalized) of Sm^{3+} in $POCl_3$–$SnCl_4$ ($[POCl_3]/[SnCl_4]$ = 10.34); λ_{exc} 402 mμ: ○, λ_{fl} 595 mμ; ●, λ_{fl} 560 mμ.

greatly enhance the quenching effect of the solvation sphere owing to the participation of the relatively high energy stretching vibrational mode of →P=O. This will result in a marked decrease in the fluorescence lifetime. If the change in the solvation sphere is very drastic, it may be accompanied by appropriate changes in the transition probabilities. Under these conditions the change in the fluorescence lifetimes will be much more complex. In the cases examined in the present study, the absorption spectra, which furnish a direct measure of the transition probabilities, were practically identical (Figure 3A) in the spectral region which was used for the excitation, *i.e.*, 390–410 mμ. Therefore, it seems very likely that the effect of the $[POCl_3]/[SnCl_4]$ ratio upon the fluorescence lifetimes is associated with a radiationless deexcitation of Sm^{3+} *via* the vibrational modes of the solvent. If a solvation sphere is established containing only $SnCl_6^{2-}$, no further effect should be observed. This can be verified in Figure 2B. The fluorescence lifetimes increase rapidly up to 0.6 M $SnCl_4$ and then level off. An extrapolated value of τ = 2.2 msec at $[SnCl_4]$ = 0 represents the fluorescence life-

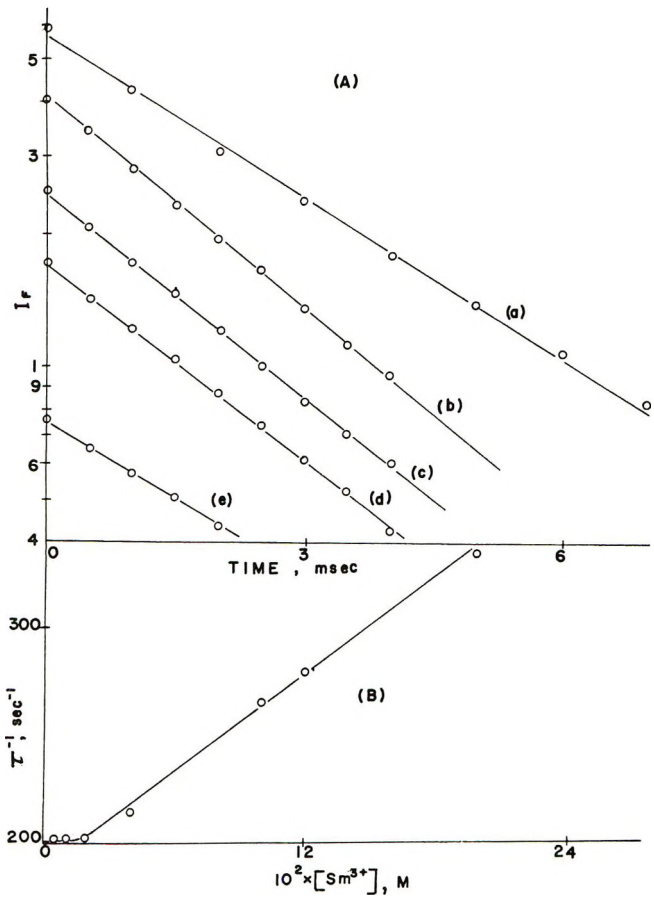

Figure 4. (A) Fluorescence decay of Sm^{3+} in $POCl_3$–$SnCl_4$ ($[POCl_3]/[SnCl_4]$ = 10.34); λ_{exc} ~300–450 mμ; λ_{fl} ~590–630 mμ: (b) 1×10^{-1} *M* Sm^{3+}; (c) 5×10^{-2} *M* Sm^{3+}; (d) 2.5×10^{-2} *M* Sm^{3+}; (e) 5×10^{-3} *M* Sm^{3+}; (a) 1×10^{-1} *M* Sm^{3+} in K_2O–SiO_2–CaO glass. (B) Variation of the reciprocal fluorescence lifetime, τ^{-1}, of Sm^{3+} in $POCl_3$–$SnCl_4$ ($[POCl_3]/[SnCl_4]$ = 10.34) as a function of $[Sm^{3+}]$.

time of Sm^{3+} in 100% $POCl_3$ provided the transition probabilities are the same.

The effect of the $[POCl_3]/[SnCl_4]$ ratio upon the fluorescence spectra and lifetimes were studied at low concentrations of Sm^{3+} to avoid self-quenching of excited Sm^{3+} ions by neighboring Sm^{3+} ions in their ground state. Such an effect is shown in Figure 3B where the fluorescence intensity, $I_F/(1 - 10^{-\epsilon CL})$, is plotted against $[Sm^{3+}]$. The effect of $[Sm^{3+}]$ upon the decay of fluorescence is similar (Figure 4A). At very low concentrations of Sm^{3+} in $POCl_3$–$SnCl_4$, the fluorescence lifetimes approach the lifetime of Sm^{3+} in the glass, *i.e.*, 3.3 msec for Sm^{3+} in $POCl_3$–$SnCl_4$ and 3.7 msec for Sm^{3+} in the glass. The fluorescence lifetimes of Sm^{3+} in CH_3OH, C_2H_5OH, C_3H_7OH, and H_2O were found to be 10.5, 10, 9.0, and <3 μsec, respectively.[7] Therefore, the fluorescence lifetimes of Sm^{3+} in $POCl_3$–$SnCl_4$ is about 1000 times larger than the lifetime of Sm^{3+} in aqueous solutions. This is in close agreement with the results presented in Figure 1A in which an enhancement of about 1000 is shown for the fluorescence efficiency of Sm^{3+} in $POCl_3$–$SnCl_4$ relative to that in aqueous solutions.

In the presence of self-quenching the spectroscopy of Sm^{3+} in $POCl_3$–$SnCl_4$ can be outlined as

$$Sm^{3+}(^6H_{5/2}) \xrightarrow[398\text{–}402\ m\mu]{h\nu} Sm^{3+}(^4F_{7/2})$$

$$Sm^{3+}(^4F_{7/2}) \rightsquigarrow Sm^{3+}(^4G_{5/2})$$

$$Sm^{3+}(^4G_{5/2}) \longrightarrow Sm^{3+}(^6H) + h\nu_{fl}; \quad k_{fl}$$

$$Sm^{3+}(^4G_{5/2}) \xrightarrow[\text{solvation sphere}]{\text{primary}} Sm^{3+}(^6H \text{ or } ^6F) + \text{heat}; \quad k_h$$

$$Sm^{3+}(^4G_{5/2}) + \text{solvent} \longrightarrow Sm^{3+}(^6H \text{ or } ^6F) + \text{heat}; \quad k_{solv}^{sec}$$

$$Sm^{3+}(^4G_{5/2}) + Sm^{3+}(^6H_{5/2}) \longrightarrow Sm^{3+}(^6H) + Sm^{3+}(^6F); \quad k_Q$$

The aforementioned mechanism lead to the following expression for the fluorescence efficiency

$$\phi_Q = k_{fl}/(k_{fl} + k_h + k_{solv}^{sec}[\text{solvent}] + k_Q[Sm^{3+}]) \quad (1)$$

or for the fluorescence lifetime

$$\tau_Q^{-1} = k_{fl} + k_h + k_{solv}^{sec}[\text{solvent}] + k_Q[Sm^{3+}] \quad (2)$$

At constant $[POCl_3]/[SnCl_4]$ ratio the only variable in eq 1 and 2 is the concentration of Sm^{3+}. Results plotted according to eq 1 are shown in Figure 3B. On the other hand, results plotted according to eq 2 are depicted in Figure 4B. At very low concentrations of Sm^{3+} self-quenching is negligible and therefore the fluorescence lifetimes approach a maximum value for a given $[POCl_3]/[SnCl_4]$ ratio. In the case considered we obtain $k_{fl} + k_h + k_{solv}^{sec}[\text{solvent}] = 3 \times 10^2$ sec^{-1}. From the slope we also obtain the rate constant for self-quenching, *i.e.*, $k_Q = 8 \times 10^2 M^{-1}$ sec^{-1}.

Values of the fluorescence lifetimes of Sm^{3+} in $POCl_3$–$SnCl_4$ at various conditions are given in Table I.

Table I: Fluorescence Lifetimes of Sm^{3+} in $POCl_3$–$SnCl_4$ (msec)

$[Sm^{3+}]$, *M*	$[POCl_3]/[SnCl_4]$ 10.34	13.24	18.08	27.76	56.81	231
5×10^{-3}	3.31	...	...	...	...	...
1×10^{-2}	3.31	3.17	3.17	2.88	2.45	2.31
2×10^{-2}	3.31	...	...	...	...	...
4×10^{-2}	3.17	3.03	3.03	2.74	2.74	...
1×10^{-1}	2.74	...	...	...	...	...
2×10^{-1}	2.31	...	...	...	...	...

Acknowledgment. This project was supported by a grant from Owens-Illinois (Corporate Research Laboratories) for which we are grateful.

d^2 and d^8 Quadrate Energy Levels Including Spin–Orbit Perturbation

by Jayarama R. Perumareddi

Department of Chemistry, Florida Atlantic University, Boca Raton, Florida 33432 *(Received June 7, 1972)*

Starting from strong-field octahedral representation, the symmetry adapted quadrate wave functions are derived in both coordinate and spin space for d^2 and d^8 electronic configurations. The corresponding energy matrices are constructed as parametrically dependent on ligand field, electron correlation, and spin–orbit interaction perturbations in the coupling scheme in which the spin–orbit perturbation is applied last. The energy diagrams displaying the splittings of the cubic energy levels by the additive axial part of the quadrate ligand field and further by the spin–orbit perturbations are obtained by considering octahedral d^8 configuration as an example. The importance of full configuration interaction on the quadrate splittings of the cubic energy levels is emphasized. Applications of our energy equations to optical spectral and magnetic studies on quadrately distorted or substituted octahedral, quadrately distorted tetrahedral, and five-coordinate square pyramidal systems, of d^2 and d^8 electronic configurations, are pointed out.

I. Introduction

The few attempts that have been made so far in interpreting the electronic spectra of quadrate (tetragonal) nickel(II) complexes made use of energy levels with no spin–orbit perturbation, and either with complete or partial neglect of configuration interaction.[1] Treatment of octahedral nickel(II) complexes with full configuration interaction and spin–orbit perturbation in the past[2] gave rise to a better understanding of their electronic structures. Inclusion of configuration interaction is very important in that it may alter the energies considerably and in some instances even affect the assignments. Spin–orbit interaction, though it acts as a minor perturbation in the case of the early members of the 3d transition series elements, can be dominant for the later members of the series. It is certainly necessary to include spin–orbit perturbation for meaningful studies on systems involving elements of 4d and 5d transition series.

The purpose of this investigation is to derive the energy levels of d^2 and d^8 electronic configurations immersed in quadrate ligand fields including spin–orbit perturbation with complete configuration interaction and interpret the electronic spectra of appropriate compounds. The present report is concerned with the development of the underlying theory. Applications of the theory to optical spectra and other experimental data will be described in future papers. The appropriate compounds of d^2 and d^8 electronic configurations that can be studied by the theory developed here are the tetragonally distorted or substituted octahedral and tetrahedral complexes and the five-coordinate square pyramidal systems. The tetragonally substituted octahedral complexes include the mono- and the trans disubstituted octahedral systems. The cis disubstituted octahedral complexes can also be treated by the same theory if it is assumed that the ligand fields of trans ligand pairs can be averaged.[3]

II. Theory

Octahedral Orientation. In the systems for which the theory is developed here, the additive axial ligand field acts as a minor perturbation relative to the major cubic ligand field so that these systems can be treated as slightly distorted cubic field complexes. In other words, we shall use the two electron cubic wave functions as the basis set which will then be decomposed properly to correspond to the symmetry adapted functions of quadrate symmetry. The decomposition of the cubic functions relative to the representations of quadrate symmetry is given in Table I.

Coupling Scheme. We utilize the coupling scheme in which the spin–orbit perturbation is applied last. If V_C, V_a, $\Sigma_{j>i}e^2/r_{ij}$, and $\Sigma_i\xi(r_i)\vec{l}_i\cdot\vec{s}_i$ denote, respectively, the perturbations due to the cubic ligand field, axial ligand field, electron correlation, and spin–orbit interaction, the sequence[4] in which these perturbations are applied is as follows

$$V_C > \sum_{j>i} e^2/r_{ij} > V_a > \sum_i \xi(r_i)\vec{l}_i\cdot\vec{s}_i$$

Wave Functions. The procedure of fabricating symmetry adapted two-electron cubic wave functions in coordinate space is well known.[5] Once these are ob-

(1) (a) See for a review of these, N. S. Hush and R. J. M. Hobbs, "Progress in Inorganic Chemistry," Vol. 10, F. A. Cotton, Ed., Interscience Publishers, New York, 1968. See also (b) C. W. Reimann, *J. Phys. Chem.*, **74**, 561 (1970); (c) R. L. Chiang and R. S. Drago, *Inorg. Chem.*, **10**, 453 (1971), and references therein.

(2) A. D. Liehr and C. J. Ballhausen, *Ann. Phys.*, **6**, 134 (1959).

(3) (a) R. Krishnamurthy, W. B. Schaap, and J. R. Perumareddi, *Inorg. Chem.*, **6**, 1338 (1967); (b) J. R. Perumareddi, *Coord. Chem. Rev.*, **4**, 73 (1969).

(4) For a review and importance of other coupling schemes possible for low-symmetry ligand fields, read (a) J. R. Perumareddi, *J. Phys. Chem.*, **71**, 3144 (1967); (b) J. R. Perumareddi and A. D. Liehr, Abstracts, Symposium on Molecular Structure and Spectroscopy, Columbus, Ohio, June 14–19, 1965; (c) J. R. Perumareddi, to be submitted for publication.

(5) See, for instance, C. J. Ballhausen, "Introduction to Ligand Field Theory," McGraw-Hill, New York, N. Y., 1962.

Table I: Decomposition of Cubic Representations Relative to Quadrate Symmetry

Cubic	Quadrate	Cubic	Quadrate
$A_{1g}{}^C$	$A_{1g}{}^Q$	$T_{1gb}{}^C$	$E_{ga}{}^Q$
$A_{2g}{}^C$	$B_{1g}{}^Q$	$T_{1gc}{}^C$	$E_{gb}{}^Q$
$E_{ga}{}^C$	$A_{1g}{}^Q$	$T_{2ga}{}^C$	$B_{2g}{}^Q$
$E_{gb}{}^C$	$B_{1g}{}^Q$	$T_{2gb}{}^C$	$E_{ga}{}^Q$
$T_{1ga}{}^C$	$A_{2g}{}^Q$	$T_{2gc}{}^C$	$E_{gb}{}^Q$

tained, they are decomposed to quadrate functions according to the Table I. The next step is to make these functions symmetry adapted including spin space. It should be noted that the spin–singlet functions are symmetry adapted both in coordinate and spin space to begin with. We need only make the spin–triplet functions spin oriented. This is done by first studying the symmetry transformation properties of spin functions. If α and β represent the one-electron spin states, their transformation properties can be obtained by the substitution of angular values into the spinor array of Goldstein[6] after the angles are determined by identifying the transformation matrix of the symmetry operation with the Eulerian matrix.[6] The two-electron spin functions properly transforming as the cubic and quadrate representations can then be constructed by examining the transformation properties of the two-electron spin "product" functions. The spin functions so constructed and their symmetry transformation properties are given in Table II which also includes the transformation properties of orbital representations. The inclusion of spin space is then achieved by appropriately combining these spin functions with the orbital functions resulting in quadrate functions which are again made to transform in exactly the same way as the symmetry transformations of quadrate representations shown in Table II. The two-electron wave functions which are symmetry adapted both in coordinate and spin space[7] derived by this procedure are given in Table III. The corresponding eight-electron wave functions can be easily obtained if needed from those listed by considering the two electrons as holes.

Energy Matrices. The various perturbations can be parametrized as usual.[4] Thus, the ligand field gives rise to a cubic Dq and axial Ds, Dt parameters, the electron correlation yields the A, B, C parameters, and the spin–orbit perturbation results in a one-electron spin–orbit coupling constant parameter ζ.

The secular determinants obtained as a function of these parameters with the use of the wave functions of Table III are given in Tables IVa to e. The cubic ligand field (Dq) is completely diagonalized, as it should be, in these energy matrices. The electron correlation (A, B, C) and the axial ligand field (Ds, Dt) are diagonal, respectively, in the cubic quantum number $\{X_j{}^C\}$ and quadrate quantum number $\{X_j{}^Q\}$.

Table II: Symmetry Transformation Properties of Quadrate Oriented Cubic Orbital and Spin Functions

Function	Representation: Cubic	Representation: Quadrate	Symmetry operation: $C_4(z)$	Symmetry operation: $C_2(y)$	Symmetry operation: $C_3(z')$
z	t_{1ua}	a_2	t_{1ua}	$-t_{1ua}$	t_{1ub}
y	t_{1ub}	e_a	t_{1uc}	t_{1ub}	t_{1uc}
x	t_{1uc}	e_b	$-t_{1ub}$	$-t_{1uc}$	t_{1ua}
xy	t_{2ga}	b_2	$-t_{2ga}$	$-t_{2ga}$	t_{2gb}
zx	t_{2gb}	e_a	$-t_{2gc}$	t_{2gb}	t_{2gc}
yz	t_{2gc}	e_b	t_{2gb}	$-t_{2gc}$	t_{2ga}
z^2	e_{ga}	a_1	e_{ga}	e_{ga}	$-\frac{1}{2}e_{ga} - \frac{\sqrt{3}}{2}e_{gb}$
$(x^2 - y^2)$	e_{gb}	b_1	$-e_{gb}$	e_{gb}	$-\frac{1}{2}e_{gb} + \frac{\sqrt{3}}{2}e_{ga}$
$(\alpha\beta - \beta\alpha)/\sqrt{2}$	a_1	a_1	a_1	a_1	a_1
$(\alpha\beta + \beta\alpha)/\sqrt{2}$	t_{1a}	a_2	t_{1a}	$-t_{1a}$	t_{1b}
$i(\alpha\alpha + \beta\beta)/\sqrt{2}$	t_{1b}	e_a	t_{1c}	t_{1b}	t_{1c}
$-(\alpha\alpha - \beta\beta)/\sqrt{2}$	t_{1c}	e_b	$-t_{1b}$	$-t_{1c}$	t_{1a}

The spin–orbit interaction (ζ), of course, is diagonal only in the double group quadrate quantum number $\{\Gamma_j{}^Q\}$. It should be noted that in the limit of zero spin–orbit and axial ligand field perturbations, these energy matrices become identical with the cubic d^2 energy matrices of Tanabe and Sugano[8] within phases. The correctness of our quadrate energy matrices had been checked by directly calculating all the matrix elements from the corresponding energy matrices of the other coupling schemes possible and the unitary transformation matrices connecting these coupling schemes with the coupling scheme used in this report.

The quadrate energy matrices of d^8 configuration are obtained simply by changing the sign of Dt, Ds, and ζ. The constant additive energy term in the diagonal elements, $27A - 42B + 21C$, only shifts the d^8 energies but does not affect the energy differences. With the appropriate sign for ζ, the energy equations listed here are applicable to quadrately distorted or substituted octahedral d^8 and quadrately distorted tetrahedral d^8

(6) H. Goldstein, "Classical Mechanics," Addison-Wesley, Cambridge, Mass., 1951.

(7) The symmetry adapted wave functions with and without spin space, respectively, are given the Bethe's Γ_i (i = 1 to 5) and Mulliken's X_j ($X_j{}^C$ = A_1, A_2, E, T_1, T_2 and $X_j{}^Q$ = A_1, A_2, B_1, B_2, and E) classifications. It should be noted that although the energy levels in the diagrams have superscripts Q and C to denote, respectively, the quadrate symmetry designation and cubic parentage, these superscripts have been omitted in the main text for convenience. Similarly quadrate levels have been written variously with and without a g subscript in this report. Strictly speaking, if the complex is noncentrosymmetric (*e.g.*, C_{4v}), the quadrate levels should not have the g subscript. The g subscript should be retained for the quadrate representations of a centrosymmetric complex (*e.g.*, D_{4h}).

(8) (a) Y. Tanabe and S. Sugano, *J. Phys. Soc. Jap.*, 9, 753 (1954); (b) see also S. Sugano, Y. Tanabe, and H. Kamimura, "Multiplets of Transition-Metal Ions in Crystals," Academic Press, New York, N. Y., 1970.

Table III: Two-Electron Spin-Adapted Quadrate Wave Functions

$[\Psi_0 = (\alpha\beta + \beta\alpha)/\sqrt{2},\ \Psi_1 = i(\alpha\alpha + \beta\beta)/\sqrt{2},\ \Psi_{-1} = -(\alpha\alpha - \beta\beta)/\sqrt{2}]$

Γ_1 Representation

$$|\ 1\rangle = {}^3A_{2g}[{}^3T_{1g}(t_{2g}{}^2)] = |(zx)(yz)|\Psi_0$$

$$|\ 2\rangle = {}^3E_g[{}^3T_{1g}(t_{2g}{}^2)] = \frac{1}{\sqrt{2}}[|(yz)(xy)|\Psi_1 + |(xy)(zx)|\Psi_{-1}]$$

$$|\ 3\rangle = {}^3E_g[{}^3T_{2g}(t_{2g}e_g)] = \frac{1}{\sqrt{2}}\left\{\left[-\frac{1}{2}|(zx)(z^2)| - \frac{\sqrt{3}}{2}|(zx)(x^2 - y^2)|\right]\Psi_1 - \left[-\frac{1}{2}|(yz)(z^2)| + \frac{\sqrt{3}}{2}|(yz)(x^2 - y^2)|\right]\Psi_{-1}\right\}$$

$$|\ 4\rangle = {}^3A_{2g}[{}^3T_{1g}(t_{2g}e_g)] = |(xy)(x^2 - y^2)|\Psi_0$$

$$|\ 5\rangle = {}^3E_g[{}^3T_{1g}(t_{2g}e_g)] = \frac{1}{\sqrt{2}}\left\{\left[-\frac{1}{2}|(zx)(x^2 - y^2)| + \frac{\sqrt{3}}{2}|(zx)(z^2)|\right]\Psi_1 + \left[-\frac{1}{2}|(yz)(x^2 - y^2)| - \frac{\sqrt{3}}{2}|(yz)(z^2)|\right]\Psi_{-1}\right\}$$

$$|\ 6\rangle = {}^1A_{1g}[{}^1A_{1g}(t_{2g}{}^2)] = \frac{1}{\sqrt{3}}[|(xy)(xy)| + |(zx)(zx)| + |(yz)(yz)|](\alpha\beta - \beta\alpha)/\sqrt{2}$$

$$|\ 7\rangle = {}^1A_{1g}[{}^1E_g(t_{2g}{}^2)] = \frac{1}{\sqrt{6}}[-2|(xy)(xy)| + |(zx)(zx)| + |(yz)(yz)|](\alpha\beta - \beta\alpha)/\sqrt{2}$$

$$|\ 8\rangle = {}^1A_{1g}[{}^1A_{1g}(e_g{}^2)] = \frac{1}{\sqrt{2}}[|(z^2)(z^2)| + |(x^2 - y^2)(x^2 - y^2)|](\alpha\beta - \beta\alpha)/\sqrt{2}$$

$$|\ 9\rangle = {}^1A_{1g}[{}^1E_g(e_g{}^2)] = \frac{1}{\sqrt{2}}[|(z^2)(z^2)| - |(x^2 - y^2)(x^2 - y^2)|](\alpha\beta - \beta\alpha)/\sqrt{2}$$

Γ_2 Representation

$$|\ 1\rangle = {}^3E_g[{}^3T_{1g}(t_{2g}{}^2)] = \frac{1}{\sqrt{2}}[|(yz)(xy)|\Psi_{-1} - |(xy)(zx)|\Psi_1]$$

$$|\ 2\rangle = {}^3E_g[{}^3T_{2g}(t_{2g}e_g)] = \frac{1}{\sqrt{2}}\left\{\left[-\frac{1}{2}|(zx)(z^2)| - \frac{\sqrt{3}}{2}|(zx)(x^2 - y^2)|\right]\Psi_{-1} + \left[-\frac{1}{2}|(yz)(z^2)| + \frac{\sqrt{3}}{2}|(yz)(x^2 - y^2)|\right]\Psi_1\right\}$$

$$|\ 3\rangle = {}^3E_g[{}^3T_{1g}(t_{2g}e_g)] = \frac{1}{\sqrt{2}}\left\{\left[-\frac{1}{2}|(zx)(x^2 - y^2)| + \frac{\sqrt{3}}{2}|(zx)(z^2)|\right]\Psi_{-1} - \left[-\frac{1}{2}|(yz)(x^2 - y^2)| - \frac{\sqrt{3}}{2}|(yz)(z^2)|\right]\Psi_1\right\}$$

$$|\ 4\rangle = {}^1A_{2g}[{}^1T_{1g}(t_{2g}e_g)] = |(xy)(x^2 - y^2)|(\alpha\beta - \beta\alpha)/\sqrt{2}$$

Γ_3 Representation

$$|\ 1\rangle = {}^3E_g[{}^3T_{1g}(t_{2g}{}^2)] = \frac{1}{\sqrt{2}}[|(yz)(xy)|\Psi_1 - |(xy)(zx)|\Psi_{-1}]$$

$$|\ 2\rangle = {}^3B_{2g}[{}^3T_{2g}(t_{2g}e_g)] = |(xy)(z^2)|\Psi_0$$

$$|\ 3\rangle = {}^3E_g[{}^3T_{2g}(t_{2g}e_g)] = \frac{1}{\sqrt{2}}\left\{\left[-\frac{1}{2}|(zx)(z^2)| - \frac{\sqrt{3}}{2}|(zx)(x^2 - y^2)|\right]\Psi_1 + \left[-\frac{1}{2}|(yz)(z^2)| + \frac{\sqrt{3}}{2}|(yz)(x^2 - y^2)|\right]\Psi_{-1}\right\}$$

$$|\ 4\rangle = {}^3E_g[{}^3T_{1g}(t_{2g}e_g)] = \frac{1}{\sqrt{2}}\left\{\left[-\frac{1}{2}|(zx)(x^2 - y^2)| + \frac{\sqrt{3}}{2}|(zx)(z^2)|\right]\Psi_1 - \left[-\frac{1}{2}|(yz)(x^2 - y^2)| - \frac{\sqrt{3}}{2}|(yz)(z^2)|\right]\Psi_{-1}\right\}$$

$$|\ 5\rangle = {}^1B_{1g}[{}^1E_g(t_{2g}{}^2)] = \frac{1}{\sqrt{2}}[|(zx)(zx)| - |(yz)(yz)|](\alpha\beta - \beta\alpha)/\sqrt{2}$$

$$|\ 6\rangle = {}^1B_{1g}[{}^1E_g(e_g{}^2)] = -\frac{1}{\sqrt{2}}[|(z^2)(x^2 - y^2)| + |(x^2 - y^2)(z^2)|](\alpha\beta - \beta\alpha)/\sqrt{2}$$

Table III (*Continued*)

Γ_4 Representation

$$|1\rangle = {}^3E_g[{}^3T_{1g}(t_{2g}^2)] = \frac{1}{\sqrt{2}}[|(yz)(xy)|\Psi_{-1} + |(xy)(zx)|\Psi_1]$$

$$|2\rangle = {}^3E_g[{}^3T_{2g}(t_{2g}e_g)] = \frac{1}{\sqrt{2}}\left\{\left[-\frac{1}{2}|(zx)(z^2)| - \frac{\sqrt{3}}{2}|(zx)(x^2 - y^2)|\right]\Psi_{-1} - \left[-\frac{1}{2}|(yz)(z^2)| + \frac{\sqrt{3}}{2}|(yz)(x^2 - y^2)|\right]\Psi_1\right\}$$

$$|3\rangle = {}^3E_g[{}^3T_{1g}(t_{2g}e_g)] = \frac{1}{\sqrt{2}}\left\{\left[-\frac{1}{2}|(zx)(x^2 - y^2)| + \frac{\sqrt{3}}{2}|(zx)(z^2)|\right]\Psi_{-1} + \left[-\frac{1}{2}|(yz)(x^2 - y^2)| - \frac{\sqrt{3}}{2}|(yz)(z^2)|\right]\Psi_1\right\}$$

$$|4\rangle = {}^3B_{1g}[{}^3A_{2g}(e_g^2)] = |(z^2)(x^2 - y^2)|\Psi_0$$

$$|5\rangle = {}^1B_{2g}[{}^1T_{2g}(t_{2g}^2)] = \frac{1}{\sqrt{2}}[|(zx)(yz)| + |(yz)(zx)|](\alpha\beta - \beta\alpha)/\sqrt{2}$$

$$|6\rangle = {}^1B_{2g}[{}^1T_{2g}(t_{2g}e_g)] = |(xy)(z^2)|(\alpha\beta - \beta\alpha)/\sqrt{2}$$

$\Gamma_{5a,b}$ Representation

$$|1\rangle = {}^3A_{2g}[{}^3T_{1g}(t_{2g}^2)] = |(zx)(yz)|\Psi_{-1}, - |(zx)(yz)|\Psi_1$$

$$|2\rangle = {}^3E_g[{}^3T_{1g}(t_{2g}^2)] = |(xy)(zx)|\Psi_0, - |(yz)(xy)|\Psi_0$$

$$|3\rangle = {}^3B_{2g}[{}^3T_{2g}(t_{2g}e_g)] = |(xy)(z^2)|\Psi_{-1}, |(xy)(z^2)|\Psi_1$$

$$|4\rangle = {}^3E_g[{}^3T_{2g}(t_{2g}e_g)] = -\left[-\frac{1}{2}|(yz)(z^2)| + \frac{\sqrt{3}}{2}|(yz)(x^2 - y^2)|\right]\Psi_0, - \left[-\frac{1}{2}|(zx)(z^2)| - \frac{\sqrt{3}}{2}|(zx)(x^2 - y^2)|\right]\Psi_0$$

$$|5\rangle = {}^3A_{2g}[{}^3T_{1g}(t_{2g}e_g)] = |(xy)(x^2 - y^2)|\Psi_{-1}, - |(xy)(x^2 - y^2)|\Psi_1$$

$$|6\rangle = {}^3E_g[{}^3T_{1g}(t_{2g}e_g)] = \left[-\frac{1}{2}|(yz)(x^2 - y^2)| - \frac{\sqrt{3}}{2}|(yz)(z^2)|\right]\Psi_0, \left[\frac{1}{2}|(zx)(x^2 - y^2)| - \frac{\sqrt{3}}{2}|(zx)(z^2)|\right]\Psi_0$$

$$|7\rangle = {}^3B_{1g}[{}^3A_{2g}(e_g^2)] = |(z^2)(x^2 - y^2)|\Psi_1, - |(z^2)(x^2 - y^2)|\Psi_{-1}$$

$$|8\rangle = {}^1E_g[{}^1T_{2g}(t_{2g}^2)] = \frac{1}{\sqrt{2}}[|(yz)(xy)| + |(xy)(yz)|](\alpha\beta - \beta\alpha)/\sqrt{2}, \frac{1}{\sqrt{2}}[|(xy)(zx)| + |(zx)(xy)|](\alpha\beta - \beta\alpha)/\sqrt{2}$$

$$|9\rangle = {}^1E_g[{}^1T_{1g}(t_{2g}e_g)] = \left[-\frac{1}{2}|(zx)(x^2 - y^2)| + \frac{\sqrt{3}}{2}|(zx)(z^2)|\right](\alpha\beta - \beta\alpha)/\sqrt{2}, \left[-\frac{1}{2}|(yz)(x^2 - y^2)| - \frac{\sqrt{3}}{2}|(yz)(z^2)|\right](\alpha\beta - \beta\alpha)/\sqrt{2}$$

$$|10\rangle = {}^1E_g[{}^1T_{2g}(t_{2g}e_g)] = \left[-\frac{1}{2}|(zx)(z^2)| - \frac{\sqrt{3}}{2}|(zx)(x^2 - y^2)|\right](\alpha\beta - \beta\alpha)/\sqrt{2}, \left[-\frac{1}{2}|(yz)(z^2)| + \frac{\sqrt{3}}{2}|(yz)(x^2 - y^2)|\right](\alpha\beta - \beta\alpha)/\sqrt{2}$$

systems and by changing the sign of Dq, they will be applicable to quadrately distorted or substituted octahedral d^8 and quadrately distorted tetrahedral d^2 systems. Similarly the d^2 energy matrices and the d^8 energy matrices obtained by changing the sign of ζ, Dq, Dt, and Ds can also be utilized in studying the electronic structures of the corresponding five-coordinate square pyramidal systems once the Dt and Ds are considered as symmetry parameters.[9]

Energy Diagrams. The splitting of cubic levels by the additive axial ligand field perturbation of quadrate symmetry in the limit of zero spin–orbit interaction[10] is shown in Figure 1 by considering octahedral d^8 configuration as an example. A B value of 800 cm^{-1} is chosen in this diagram to represent a series of octahedral

(9) (a) K. G. Caulton, *Inorg. Chem.*, **7**, 392 (1968); (b) see also J. R. Perumareddi, *J. Phys. Chem.*, **71**, 3155 (1967).

(10) In the limit of zero spin–orbit interaction, with the exception of ^3E_g, ^1E_g which are 3 × 3 matrices and $^1A_{1g}$ which is a 4 × 4 matrix, all other levels are either single ($^3B_{1g}$, $^3B_{2g}$, $^1A_{2g}$) or at the most 2 × 2 matrices ($^3A_{2g}$, $^1B_{1g}$, $^1B_{2g}$). The solutions of 2 × 2 secular determinants yield the energy equations: $^3A_{2g} = (-3Dq - Ds - 3Dt - {}^1/_2B) \pm {}^1/_2[(10Dq - 6Ds + 10Dt + 9B)^2 + 144B^2]^{1/2}$, $^1B_{1g} = (2Dq + Ds - {}^1/_2Dt + {}^1/_2B + 2C) \pm {}^1/_2[(20Dq - 2Ds + 15Dt - B)^2 + 48B^2]^{1/2}$, and $^1B_{2g} = (-3Dq + Ds - {}^1/_2Dt + {}^1/_2B + 2C) \pm {}^1/_2[(10Dq - 2Ds + 15Dt - B)^2 + 48B^2]^{1/2}$.

Table IVa: Quadrate Energy Matrices of d^2 Electronic Configuration, Γ_1 Representation

Γ_1	$^3A_{2g}[^3T_{1g}(t_{2g}^2)]$	$^3E_g[^3T_{1g}(t_{2g}^2)]$	$^3E_g[^3T_{2g}(t_{2g}e_g)]$	$^3A_{2g}[^3T_{1g}(t_{2g}e_g)]$	$^3E_g[^3T_{1g}(t_{2g}e_g)]$	$^1A_{1g}[^1A_{1g}(t_{2g}^2)]$	$^1A_{1g}[^1E_g(t_{2g}^2)]$	$^1A_{1g}[^1A_{1g}(e_g^2)]$	$^1A_{1g}[^1E_g(e_g^2)]$
$^3A_{2g}[^3T_{1g}(t_{2g}^2)]$	$-8Dq + 2Ds - 8Dt + A - 5B$	$\frac{\sqrt{2}}{2}\zeta$	$-\frac{\sqrt{6}}{2}\zeta$	$-6B$	$\frac{\sqrt{2}}{2}\zeta$	$-i\frac{\sqrt{6}}{3}\zeta$	$-i\frac{\sqrt{3}}{3}\zeta$	0	0
$^3E_g[^3T_{1g}(t_{2g}^2)]$		$-8Dq - Ds - 3Dt + A - 5B + \frac{1}{2}\zeta$	$\frac{\sqrt{3}}{2}\zeta$	$\frac{\sqrt{2}}{2}\zeta$	$-6B + \frac{1}{2}\zeta$	$-i\frac{2\sqrt{3}}{3}\zeta$	$i\frac{\sqrt{6}}{6}\zeta$	0	0
$^3E_g[^3T_{2g}(t_{2g}e_g)]$			$2Dq - \frac{7}{4}Dt + A - 8B + \frac{1}{4}\zeta$	$-\frac{\sqrt{6}}{4}\zeta$	$-\frac{\sqrt{3}}{4}(4Ds + 5Dt) + \frac{\sqrt{3}}{4}\zeta$	0	0	0	$-i\frac{\sqrt{6}}{2}\zeta$
$^3A_{2g}[^3T_{1g}(t_{2g}e_g)]$				$2Dq - 4Ds + 2Dt + A + 4B$	$-\frac{\sqrt{2}}{4}\zeta$	$i\frac{\sqrt{6}}{3}\zeta$	$-i\frac{2\sqrt{3}}{3}\zeta$	$i\zeta$	$-i\zeta$
$^3E_g[^3T_{1g}(t_{2g}e_g)]$					$2Dq + 2Ds + \frac{3}{4}Dt + A + 4B - \frac{1}{4}\zeta$	$i\frac{2\sqrt{3}}{3}\zeta$	$i\frac{\sqrt{6}}{3}\zeta$	$i\sqrt{2}\zeta$	$i\frac{\sqrt{2}}{2}\zeta$
$^1A_{1g}[^1A_{1g}(t_{2g}^2)]$						$-8Dq - \frac{14}{3}Dt + A + 10B + 5C$	$\frac{2\sqrt{2}}{3}(3Ds - 5Dt)$	$\sqrt{6}(2B + C)$	0
$^1A_{1g}[^1E_g(t_{2g}^2)]$							$-8Dq - 2Ds - \frac{4}{3}Dt + A + B + 2C$	0	$-2\sqrt{3}B$
$^1A_{1g}[^1A_{1g}(e_g^2)]$								$12Dq + 7Dt + A + 8B + 4C$	$4Ds + 5Dt$
$^1A_{1g}[^1E_g(e_g^2)]$									$12Dq + 7Dt + A + 2C$

Table IVb: Quadrate Energy Matrices of d^2 Electronic Configuration, Γ_2 Representation

Γ_2	$^3E_g[^3T_{1g}(t_{2g}^2)]$	$^3E_g[^3T_{2g}(t_{2g}e_g)]$	$^3E_g[^3T_{1g}(t_{2g}e_g)]$	$^1A_{2g}[^1T_{1g}(t_{2g}e_g)]$
$^3E_g[^3T_{1g}(t_{2g}^2)]$	$-8Dq - Ds - 3Dt + A - 5B + \frac{1}{2}\zeta$	$\frac{\sqrt{3}}{2}\zeta$	$-6B + \frac{1}{2}\zeta$	$-\frac{i\sqrt{2}}{2}\zeta$
$^3E_g[^3T_{2g}(t_{2g}e_g)]$		$2Dq - \frac{7}{4}Dt + A - 8B + \frac{1}{4}\zeta$	$-\frac{\sqrt{3}}{4}(4Ds + 5Dt) + \frac{\sqrt{3}}{4}\zeta$	$-\frac{i\sqrt{6}}{4}\zeta$
$^3E_g[^3T_{1g}(t_{2g}e_g)]$			$2Dq + 2Ds + \frac{3}{4}Dt + A + 4B - \frac{1}{4}\zeta$	$-\frac{i\sqrt{2}}{4}\zeta$
$^1A_{2g}[^1T_{1g}(t_{2g}e_g)]$				$2Dq - 4Ds + 2Dt + A + 4B + 2C$

Table IVc: Quadrate Energy Matrices of d^2 Electronic Configuration, Γ_3 Representation

Γ_3	$^3E_g[^3T_{1g}(t_{2g}^2)]$	$^3B_{2g}[^3T_{2g}(t_{2g}e_g)]$	$^3E_g[^3T_{2g}(t_{2g}e_g)]$	$^3E_g[^3T_{1g}(t_{2g}e_g)]$	$^1B_{1g}[^1E_g(t_{2g}^2)]$	$^1B_{1g}[^1E_g(e_g^2)]$
$^3E_g[^3T_{1g}(t_{2g}^2)]$	$-8Dq - Ds - 3Dt + A - 5B - \frac{1}{2}\zeta$	$\frac{\sqrt{6}}{2}\zeta$	$-\frac{\sqrt{3}}{2}\zeta$	$-6B - \frac{1}{2}\zeta$	$\frac{i\sqrt{2}}{2}\zeta$	0
$^3B_{2g}[^3T_{2g}(t_{2g}e_g)]$		$2Dq + 7Dt + A - 8B$	$-\frac{\sqrt{2}}{4}\zeta$	$\frac{\sqrt{6}}{4}\zeta$	0	$-i\zeta$
$^3E_g[^3T_{2g}(t_{2g}e_g)]$			$2Dq - \frac{7}{4}Dt + A - 8B - \frac{1}{4}\zeta$	$-\frac{\sqrt{3}}{4}(4Ds + Dt) - \frac{\sqrt{3}}{4}\zeta$	0	$\frac{i\sqrt{2}}{2}\zeta$
$^3E_g[^3T_{1g}(t_{2g}e_g)]$				$2Dq + 2Ds + \frac{3}{4}Dt + A + 4B + \frac{1}{4}\zeta$	$i\sqrt{2}\zeta$	$\frac{i\sqrt{6}}{2}\zeta$
$^1B_{1g}[^1E_g(t_{2g}^2)]$					$-8Dq + 2Ds - 8Dt + A + B + 2C$	$-2\sqrt{3}B$
$^1B_{1g}[^1E_g(e_g^2)]$						$12Dq + 7Dt + A + 2C$

Ni(II) complexes and the theoretical ratio of 4 for C to B is used. Employing fixed values of Dt and κ,[11] the Ds/Dt ratio, the energy levels are plotted as a function of Dq which is varied from 0 to 4000 cm^{-1}. At $Dq = 0$, the levels correspond to those of cylindrical symmetry. It should be noted that for $Dq \sim <125$ cm^{-1}, the $^3E[^3T_{2g}]$ level becomes the ground state.[12] The further splitting of these levels by the additional

Table IVd: Quadrate Energy Matrices of d^2 Electronic Configuration, Γ_4 Representation

Γ_4	$^3E_g[^3T_{1g}(t_{2g}^2)]$	$^3E_g[^3T_{2g}(t_{2g}e_g)]$	$^3E_g[^3T_{1g}(t_{2g}e_g)]$	$^3B_{1g}[^3A_{2g}(e_g^2)]$	$^1B_{2g}[^1T_{2g}(t_{2g}^2)]$	$^1B_{2g}[^1T_{2g}(t_{2g}e_g)]$
$^3E_g[^3T_{1g}(t_{2g}^2)]$	$-8Dq - Ds - 3Dt + A - 5B - \frac{1}{2}\zeta$	$-\frac{\sqrt{3}}{2}\zeta$	$-6B - \frac{1}{2}\zeta$	0	$\frac{i\sqrt{2}}{2}\zeta$	$-\frac{i\sqrt{6}}{2}\zeta$
$^3E_g[^3T_{2g}(t_{2g}e_g)]$		$2Dq - \frac{7}{4}Dt + A - 8B - \frac{1}{4}\zeta$	$-\frac{\sqrt{3}}{4}(4Ds + 5Dt) - \frac{\sqrt{3}}{4}\zeta$	$\sqrt{2}\zeta$	$\frac{i\sqrt{6}}{2}\zeta$	$-\frac{i\sqrt{2}}{4}\zeta$
$^3E_g[^3T_{1g}(t_{2g}e_g)]$			$2Dq + 2Ds + \frac{3}{4}Dt + A + 4B + \frac{1}{4}\zeta$	0	$-\frac{i\sqrt{2}}{2}\zeta$	$\frac{i\sqrt{6}}{4}\zeta$
$^3B_{1g}[^3A_{2g}(e_g^2)]$				$12Dq + 7Dt + A - 8B$	0	$i\zeta$
$^1B_{2g}[^1T_{2g}(t_{2g}^2)]$					$-8Dq + 2Ds - 8Dt + A + B + 2C$	$2\sqrt{3}B$
$^1B_{2g}[^1T_{2g}(t_{2g}e_g)]$						$2Dq + 7Dt + A + 2C$

spin–orbit perturbation (Liehr–Ballhausen diagram) is displayed in Figure 2[13] where once again the energy levels have been plotted for the same set of parameters but with a value of -550 cm^{-1} for the one-electron spin–orbit coupling constant parameter,[14] ζ.

Similar to quadrate d^3 systems,[3,4a] it has been noted before[1,4b,c] (*cf.* also Tables IVc and IVd or Table IVe) that in the case of quadrate d^8 complexes also[15] the difference in energy between the B_2 component of the first cubic band, $^3T_{2g}$, and the B_1 ground state is 10 Dq including configuration interaction. Because of this conclusion, energy diagrams constructed by fixing a value of Dq appropriate to a parent octahedral complex and varying Dt will be convenient in studying the spectral properties of a series of mono and trans disubstituted derivatives of that octahedral complex.[3,9b] Such an energy diagram is shown in Figure 3 for a Dq value of 1075 cm^{-1} which is that of a hexaammine complex. In this diagram, the Dt is varied from $+2000$ to -2000 cm^{-1} and a κ value of 3 is employed. At zero Dt, the levels are those of octahedral symmetry. The energy levels on the positive and negative sides of Dt are applicable to substituted complexes in which the substituting ligands are of weaker and stronger ligand field strength, respectively, than the ligand of the parent octahedral system. The two halves of the diagram with positive and negative Dt also correspond to tetragonally elongated and compressed octahedral systems, respectively. At the extreme end of positive Dt, the sudden change in the trajectory of energy levels is due to change in the ground state[12] from $^3B_1[^3A_{2g}]$ to $^3E[^3T_{2g}]$.

(11) The choice of both Ds and Dt positive for the one-electron parameters corresponds to a pure tetragonal axial compression of the initially cubic system or to a substitution by ligands of stronger ligand field strength along the fourfold axis of the resulting tetragonal system. The choice of both Ds and Dt negative corresponds to a pure axial elongation or to a substitution by ligands of weaker ligand field strength along the fourfold axis. The five-coordinate square pyramidal and the four-coordinate square planar systems can be considered as the semilimiting and limiting cases of the latter choice. The choice of mixed signed magnitudes, *i.e.*, Ds and Dt of opposite signs, corresponds to more complex situations of variable covalency effects. For more discussion on this, see ref 4c.

(12) The change in ground state from $^3B_1[^3A_{2g}]$ to $^3E[^3T_{2g}]$ can take place if $^{35}/_4\,Dt + CI < -10Dq$ where CI is the energy of configuration interaction by which the $^3E[^3T_{2g}]$ level is lowered as compared to its energy in the first-order estimated from the diagonal elements only (see either Table IVd or IVe). If $4Ds + 5Dt + CI < -10Dq - 12B$, where CI is the energy due to configuration interaction by which the $^3A_2[^3T_{1g}(t_{2g}^5e_g^3)]$ level is lowered as compared to its energy without configuration interaction, then the $^3A_2[^3T_{1g}(t_{2g}^5e_g^3)]$ level becomes the ground state (see either Tables IVa and IVd or Table IVe). This situation is identical with the quadrate case of octahedral d^3 (*cf.* ref 9b, 15, 16).

(13) The superscripts on the energy labels in the figure refer to the percentage content of that eigenvector component of the eigenfunction. The various symbols have the following meaning: § = 75 ± 2.5%, ‡ = 70 ± 2.5%, ‡‡ = 65 ± 2.5%, $ = 60 ± 2.5%, ¢ = 55 ± 2.5%, ₱ = 50 ± 2.5%, ¥ = 45 ± 2.5%, # = 40 ± 2.5%, ₦ = 35 ± 2.5%, Ð = 30 ± 2.5%, Ŧ = 25 ± 2.5%, and ₩ = 20 ± 2.5%. No superscript implies greater than 75%.

(14) Although the free ion ζ value of nickel(II) is -666 cm^{-1} [A. D. Liehr, *J. Phys. Chem.*, **67**, 1314 (1963)], the available optical and magnetic studies of nickel(II) complexes show that it is usually reduced to around -550 cm^{-1} in the complexes.

(15) The similarity of d^8 and d^3 configurations in octahedral ligand fields in the limit of zero spin–orbit interaction [see for instance, J. R. Perumareddi, *Z. Naturforsch. B*, 22, 908 (1967)] extends to quadrate ligand fields also. The quadrate splittings of the (spin) triplet octahedral levels of d^8 are identical with those of the (spin) quartet octahedral levels of d^3. Thus, the quadrate splittings of the three spin-allowed cubic bands in the case of octahedral d^8 are given by $^3T_{2g}(^3B_{2g} - {}^3E_g) = -{}^{35}/_4Dt$, $^3T_{1g}(^3A_{2g} - {}^3E_g) = 6Ds - {}^5/_4Dt$, and $^3T_{1g}(^3A_{2g} - {}^3E_g) = -3Ds + 5Dt$ (*cf.* either Tables IVa and IVc or Table IVe).

Table IVe: Quadrate Energy Matrices of d^2 Electronic Configuration, Γ_5 Representation

Γ_5	$^3A_{2g}[^3T_{1g}(t_{2g}^2)]$	$^3E_g[^3T_{1g}(t_{2g}^2)]$	$^3B_{2g}[^3T_{2g}(t_{2g}e_g)]$	$^3E_g[^3T_{2g}(t_{2g}e_g)]$	$^3A_{2g}[^3T_{1g}(t_{2g}e_g)]$	$^3E_g[^3T_{1g}(t_{2g}e_g)]$	$^3B_{1g}[^3A_{2g}(e_g^2)]$	$^1E_g[^1T_{2g}(t_{2g}^2)]$	$^1E_g[^1T_{1g}(t_{2g}e_g)]$	$^1E_g[^1T_{2g}(t_{2g}e_g)]$
$^3A_{2g}[^3T_{1g}(t_{2g}^2)]$	$-8Dq + 2Ds - 8Dt + A - 5B$	$-\frac{1}{2}\zeta$	0	$\frac{\sqrt{3}}{2}\zeta$	$-6B$	$-\frac{1}{2}\zeta$	0	$\frac{i}{2}\zeta$	$\frac{i}{2}\zeta$	$-\frac{i\sqrt{3}}{2}\zeta$
$^3E_g[^3T_{1g}(t_{2g}^2)]$		$-8Dq - Ds - 3Dt + A - 5B$	$\frac{\sqrt{3}}{2}\zeta$	0	$-\frac{1}{2}\zeta$	$-6B$	0	$\frac{i}{2}\zeta$	$-\frac{i}{2}\zeta$	$-\frac{i\sqrt{3}}{2}\zeta$
$^3B_{2g}[^3T_{2g}(t_{2g}e_g)]$			$2Dq + 7Dt + A - 8B$	$-\frac{1}{4}\zeta$	0	$\frac{\sqrt{3}}{4}\zeta$	$-\zeta$	$-\frac{i\sqrt{3}}{2}\zeta$	$-\frac{i\sqrt{3}}{4}\zeta$	$\frac{i}{4}\zeta$
$^3E_g[^3T_{2g}(t_{2g}e_g)]$				$2Dq - \frac{7}{4}Dt + A - 8B$	$\frac{\sqrt{3}}{4}\zeta$	$-\frac{\sqrt{3}}{4}(4Ds + 5Dt)$	$-\zeta$	$-\frac{i\sqrt{3}}{2}\zeta$	$\frac{i\sqrt{3}}{4}\zeta$	$\frac{i}{4}\zeta$
$^3A_{2g}[^3T_{1g}(t_{2g}e_g)]$					$2Dq - 4Ds + 2Dt + A + 4B$	$\frac{1}{4}\zeta$	0	$-\frac{i}{2}\zeta$	$\frac{i}{4}\zeta$	$\frac{i\sqrt{3}}{4}\zeta$
$^3E_g[^3T_{1g}(t_{2g}e_g)]$						$2Dq + 2Ds + \frac{3}{4}Dt + A + 4B$	0	$-\frac{i}{2}\zeta$	$-\frac{i}{4}\zeta$	$\frac{i\sqrt{3}}{4}\zeta$
$^3B_{1g}[^3A_{2g}(e_g^2)]$							$12Dq + 7Dt + A - 8B$	0	0	$i\zeta$
$^1E_g[^1T_{2g}(t_{2g}^2)]$								$-8Dq - Ds - 3Dt + A + B + 2C$	0	$2\sqrt{3}B$
$^1E_g[^1T_{1g}(t_{2g}e_g)]$									$2Dq + 2Ds + \frac{3}{4}Dt + A + +4B + 2C$	$-\frac{\sqrt{3}}{4}(4Ds + 5Dt)$
$^1E_g[^1T_{2g}(t_{2g}e_g)]$										$2Dq - \frac{7}{4}Dt$ $A + 2C$

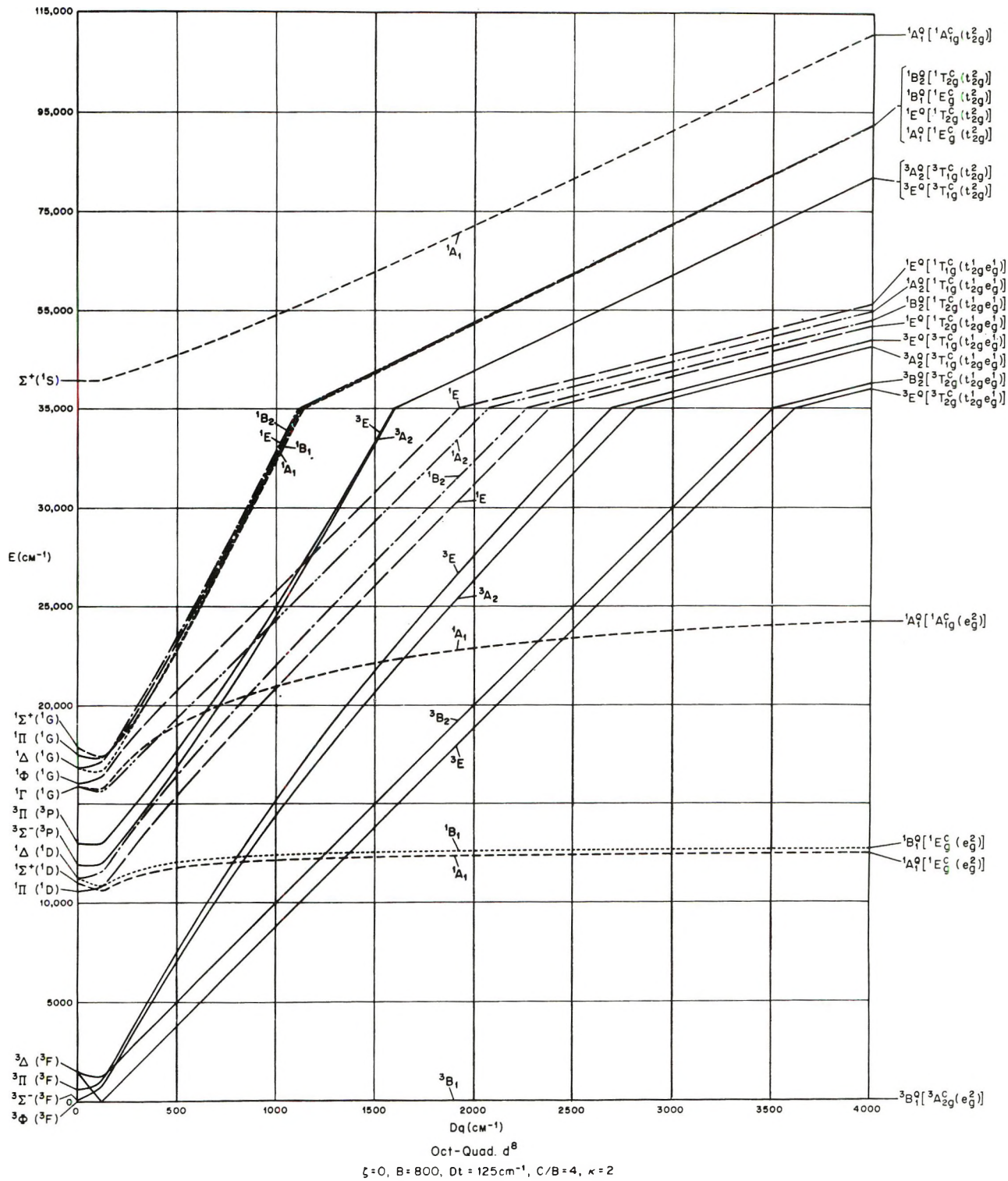

Figure 1. Quadrate splittings of octahedral d^8 energy levels in the limit of zero spin–orbit interaction: $\zeta = 0$, $B = 800$ cm^{-1}, $C/B = 4$, $Dt = 125$ cm^{-1}, $\kappa = 2$.

It is interesting to note that the cubic ^1E level arising from the ground state configuration $t_{2g}^6e_g^2$ does not split in going to quadrate symmetry in the first order, *i.e.*, considering only the diagonal elements. Thus, the energy of both $^1A_1$ and $^1B_1$ quadrate levels of $^1E(e_g^2)$ is given by $12Dq + 7Dt + 2C$ (*cf.* Tables IVa and IVe). It is the configuration interaction that can lift the otherwise degeneracy of this cubic level.[16] The dramatic effect of configuraton interaction in splitting the $^1E(e_g^2)$ cubic level can be seen in Figure 3. The

(16) This situation is exactly similar again to quadrate d^3 systems where also all the cubic (spin) doublets of ground state t_{2g}^3 configuration (^2E_g, $^2T_{1g}$, and $^2T_{2g}$) are split only by configuration interaction in quadrate ligand fields just as the ^2E_g and $^2T_{1g}$ levels themselves are in the parent octahedral ligand fields (*cf.* ref 9b).

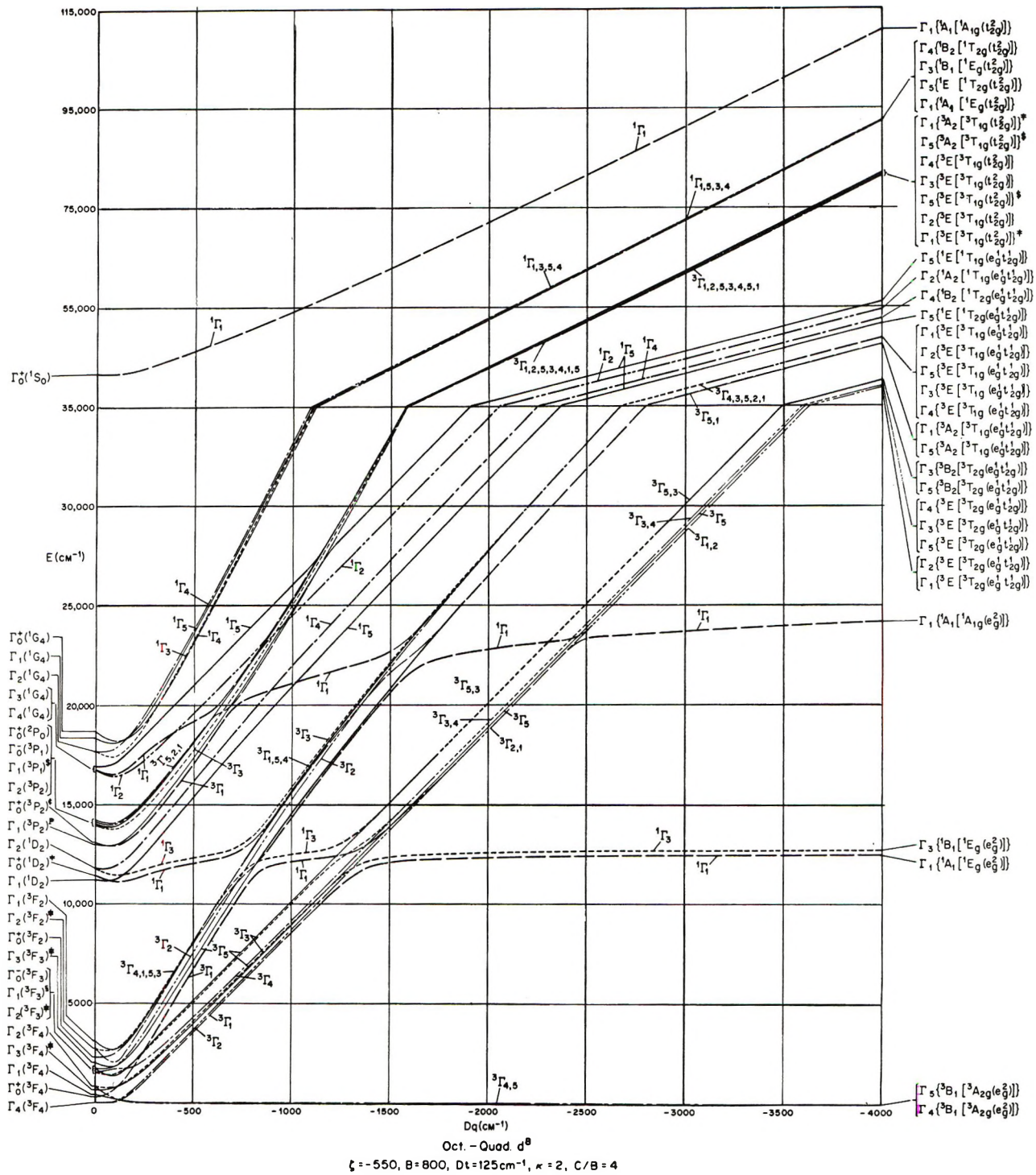

Figure 2. Quadrate splittings of octahedral d^8 energy levels including spin–orbit interaction: $\zeta = -550$ cm^{-1}, $B = 800$ cm^{-1}, $C/B = 4$, $Dt = 125$ cm^{-1}, $\kappa = 2$.

splitting of this level at Dt values appropriate to substituted ammine derivatives ($\sim$350 cm^{-1}) can be as much as $\sim$1500 cm^{-1} and more when spin–orbit coupling is included.[17]

III. Summary

In order to bring out the full significance of complete configuration interaction into focus and for a definitive study of spectral and magnetic properties of quadrate complex compounds of d^2 and d^8 electronic configurations, we have derived the complete energy matrices including spin–orbit perturbation. The symmetry adapted wave functions utilized in the construction of energy matrices have been obtained first in coordinate

(17) J. Merriam and J. R. Perumareddi, to be submitted for publication.

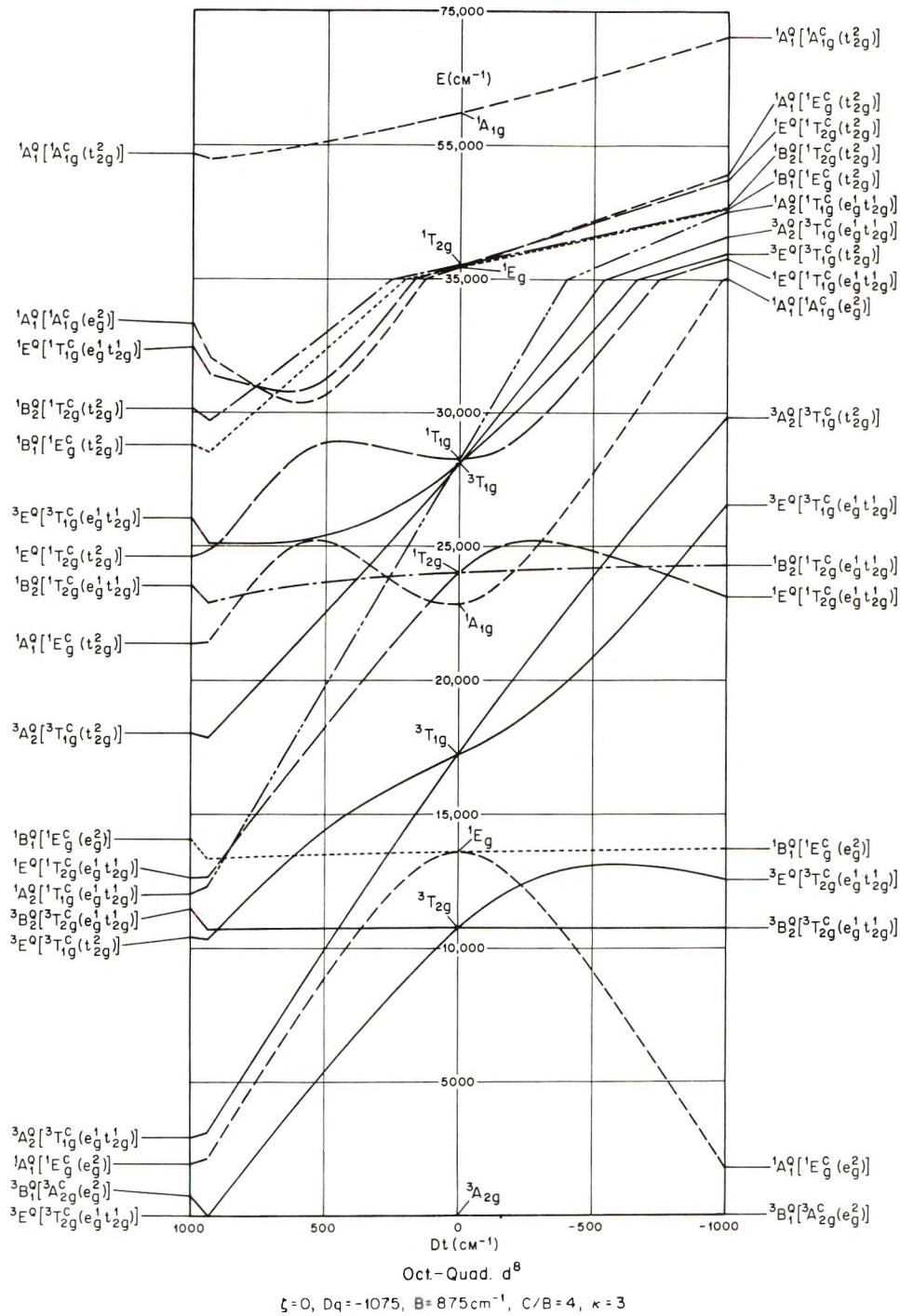

Figure 3. Effect of varying Dt on the quadrate splittings of octahedral d^8 energy levels in the limit of zero spin–orbit interaction: $Dq = 1075$ cm^{-1}, $\zeta = 0$, $B = 875$ cm^{-1}, $C/B = 4$, $\kappa = 3$.

space in strong-field octahedral orientation and then spin oriented so that the quadrate ligand field can be treated as an additive axial ligand field to major cubic ligand field perturbation. The correctness of our secular determinants has been checked by independently calculating all the matrix elements from the energy matrices of other coupling schemes possible for low-symmetry ligand fields and the unitary transformation matrices connecting those coupling schemes with the one used here. Quadrate energy diagrams have been constructed for octahedral d^8 configuration by varying Dq and Dt parameters of the ligand field. These diagrams and similar diagrams that can be obtained for tetrahedral d^8, octahedral and tetrahedral d^2, and for five-coordinate square pyramidal systems of d^2 and d^8 will be utilized in the interpretation of the spectral and other properties of appropriate compounds in subsequent communications.

A Thermodynamic Consistency Test for Adsorption of Liquids and Vapors on Solids

by A. L. Myers* and S. Sircar

School of Chemical Engineering, University of Pennsylvania, Philadelphia, Pennsylvania 19104
(Received June 28, 1971)

Publication costs assisted by the National Science Foundation

A thermodynamic consistency test is derived for adsorption of liquids and their vapors on solid adsorbents. The test relates adsorption from any pair of unsaturated vapors to adsorption from their liquid mixture. The test is satisfied by experimental data for the adsorption of six pairs of vapors on silica gel at 30°.

Adsorption equilibria are usually analyzed in terms of the thermodynamics of adsorption. However, adsorption thermodynamics contain certain variables such as surface tension and surface area that are sometimes ambiguous, particularly under the conditions to be discussed. The following derivation of a thermodynamic consistency test for adsorption of liquids and vapors on solid adsorbents is carried out in the more familiar language of solution thermodynamics.[1] This is permissible because the adsorbent, which is assumed to be a crystalline solid, has a fixed surface area and pore volume. If the surface area were to change during the experiment, as it might for adsorption on liquid droplets, then bulk solution thermodynamics would fail because it does not allow for changes in the degree of dispersion of the adsorbent.

The system is shown schematically in Figure 1. There are two adsorbates (no. 1 and 2) and a solid adsorbent (A) which is nonvolatile. The adsorbent might be silica gel, activated carbon, zeolite, etc. The gas phase is a mixture of component no. 1 and 2. The condensed phase is the solid adsorbent plus the adsorbed gases. Whether the gas is adsorbed in pores or in parallel layers, whether the gas is adsorbed or absorbed is immaterial as long as the process is reversible. The number of moles of each adsorbate in the condensed phase (n_1' and n_2') is measured by conventional gravimetric or volumetric adsorption experiments.

The system is immersed in a temperature bath at T but the pressure is variable. Under these conditions the Gibbs equation for the condensed phase is[2]

$$n_1'\mathrm{d}\mu_1' + n_2'\mathrm{d}\mu_2' + n_\mathrm{A}\mathrm{d}\mu_\mathrm{A} = V'\mathrm{d}P \qquad (1)$$

The prime denotes the condensed phase. The $V'\mathrm{d}P$ term may be ignored because $\Delta U' \gg \Delta(PV')$ for the condensed phase in which V' is small and the pressure is subatmospheric. At equilibrium

$$\mu_1' = \mu_1 \qquad (2)$$

$$\mu_2' = \mu_2 \qquad (3)$$

where μ_1 and μ_2 are the values of the chemical potentials in the gas phase. μ_A is the chemical potential of the adsorbent. At the low pressure of interest

$$\mathrm{d}\mu_i = RT\ \mathrm{d}\ln(Py_i) \qquad (4)$$

for both gases, where y_i is the mole fraction of component i in the equilibrium gas phase. Combining eq 1–4

$$-\frac{n_\mathrm{A}\mathrm{d}\mu_\mathrm{A}}{RT} = n_1'\mathrm{d}\ln(Py_1) + n_2'\mathrm{d}\ln(Py_2) \qquad (5)$$

Equation 5 is integrated over a closed path in three steps shown in Figure 2. Step 1 is the adsorption of pure vapor of component no. 2 for which

$$-\frac{n_\mathrm{A}\Delta\mu_\mathrm{A}}{RT} = \int_{P=0}^{P_2^s}\frac{n_2'}{P}\mathrm{d}P \qquad (6)$$

and step 3 is the desorption of component no. 1 for which

$$-\frac{n_\mathrm{A}\Delta\mu_\mathrm{A}}{RT} = -\int_{P=0}^{P_1^s}\frac{n_1'}{P}\mathrm{d}P \qquad (7)$$

For step 2 the adsorbent is immersed in a liquid mixture of component no. 1 and 2 which is in equilibrium with its saturated vapor (see Figure 3). Therefore the partial pressure in the gas is equal to the fugacity in the bulk liquid[2]

$$P^s y_i = P_i^s \gamma_i x_i \qquad (8)$$

x_i is the mole fraction of component i in the liquid mixture. The activity coefficients in the bulk liquid (γ_1, γ_2) are related according to the isothermal Gibbs–Duhem equation[2]

$$x_1\mathrm{d}\ln\gamma_1 + x_2\mathrm{d}\ln\gamma_2 = 0 \qquad (9)$$

Combination of eq 5, 8, and 9 gives

(1) T. L. Hill, *J. Chem. Phys.*, **18**, 246 (1950).

(2) K. Denbigh, "The Principles of Chemical Equilibrium," Cambridge University Press, New York, N. Y., 1966, pp 272, 284.

$$-\frac{n_A d\mu_A}{RT} = \frac{[n_1' - (n_1' + n_2')x_1]}{x_2} d \ln (\gamma_1 x_1) \quad (10)$$

The quantity in the numerator is the familiar surface excess[3] for adsorption from liquid solutions

$$n_1^e \equiv n_1' - (n_1' + n_2')x_1 \quad (11)$$

Integration of eq 10 for step 2 in Figure 1 gives

$$-\frac{n_A \Delta\mu_A}{RT} = \int_{x_1=0}^{1} \frac{n_1^e}{x_2} d \ln (\gamma_1 x_1) \quad (12)$$

Adding eq 6, 7, and 12 for the closed path in Figure 1 we get

$$\int_{P=0}^{P_2^s} \frac{n_2'}{P} dP - \int_{P=0}^{P_1^s} \frac{n_1'}{P} dP + \int_{x_1=0}^{1} \frac{n_1^e}{\gamma_1 x_1 x_2} d(\gamma_1 x_1) = 0 \quad (13)$$

This thermodynamic consistency test relates adsorption from a pair of unsaturated vapors (the first two integrals) to adsorption from their liquid mixture (the last integral). However, eq 13 is not applicable to the special case where adsorbate vapor condenses on the solid in the form of liquid droplets, because cooperative forces in the adsorbate are stronger than solid–vapor adsorptive forces and therefore neither solution thermodynamics nor adsorption thermodynamics applies.

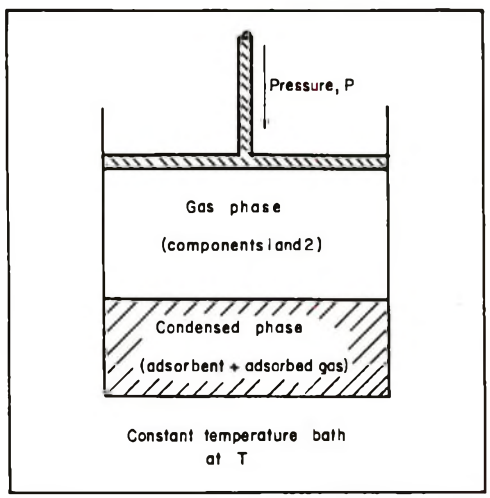

Figure 1. Thermodynamic system at subsaturation conditions.

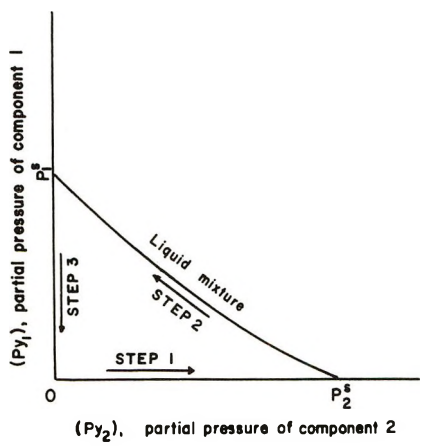

Figure 2. Integration path for thermodynamic consistency test.

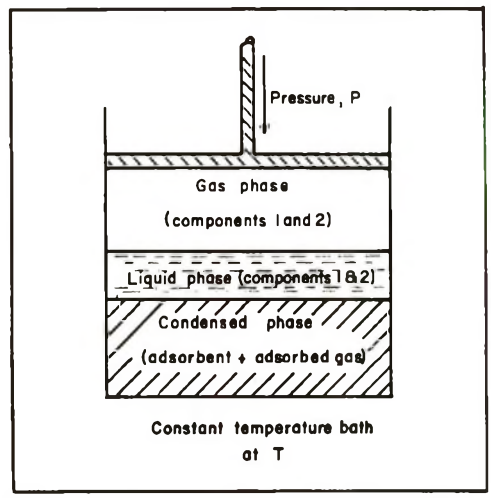

Figure 3. Thermodynamic system at condition of saturation.

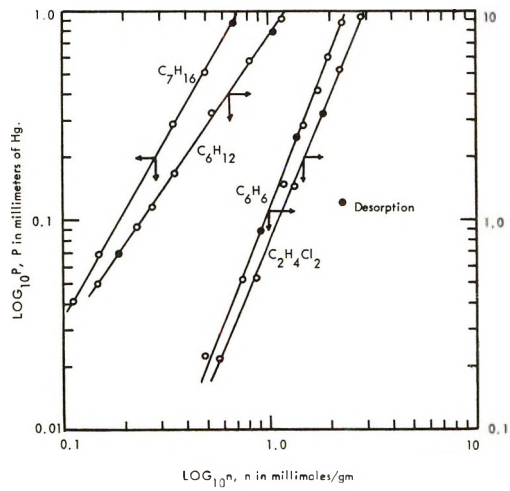

Figure 4. Adsorption of 1,2-dichloroethane, benzene, cyclohexane, and *n*-heptane on silica gel at 30°.

Experimental Section

In order to test eq 13, isotherms of benzene, cyclo-

Table I: Integration of Vapor Isotherm for Adsorption on Silica Gel at 30°

Vapor	$\int_0^{P^s} \frac{n'}{P} dP$, mmol/g
Benzene	14.5
Cyclohexane	7.9
n-Heptane	7.9
1,2-Dichloroethane	15.5

(3) S. Sircar and A. L. Myers, *J. Phys. Chem.*, **74**, 2828 (1970).

Table II: Thermodynamic Consistency Test for Pairs of Vapors Adsorbed on Silica Gel at 30°

Pair (1)	Pair (2)	mmol/g $\int_0^{P_2^s} \frac{n_2'}{P} dP$	mmol/g $-\int_0^{P_1^s} \frac{n_1'}{P} dP$	mmol/g $\int_{x_1=0}^{1} \frac{n_1^e}{x_2} d \ln (\gamma_1 x_1)$	|Sum|
Benzene	Cyclohexane	7.9	−14.5	7.2 ± 0.7	0.6
Benzene	*n*-Heptane	7.9	−14.5	7.2 ± 0.7	0.6
Benzene	1,2-Dichloroethane	15.5	−14.5	−1.1 ± 0.1	0.1
n-Heptane	Cyclohexane	7.9	−7.9	0	0
n-Heptane	1,2-Dichloroethane	15.5	−7.9	−8.3 ± 0.8	0.7
Cyclohexane	1,2-Dichloroethane	15.5	−7.9	−7.9 ± 0.7	0.3

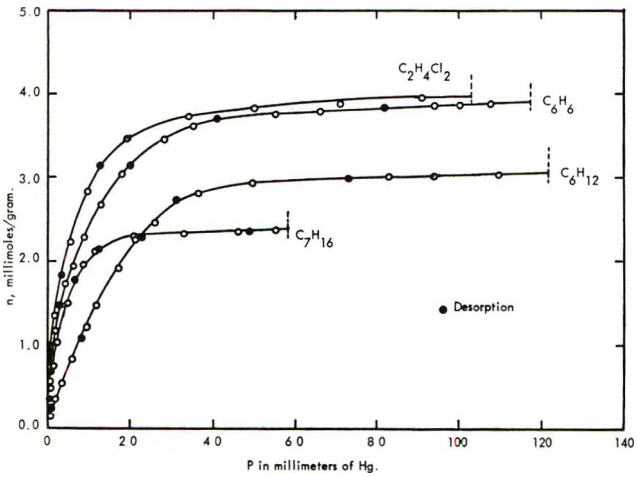

Figure 5. Adsorption of 1,2-dichloroethane, benzene, cyclohexane, and *n*-heptane on silica gel at 30°.

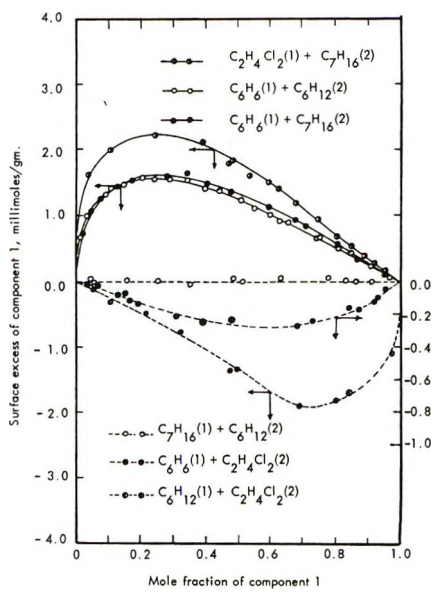

Figure 6. Surface excess isotherms of binary liquid mixtures on silica gel at 30°.

hexane, *n*-heptane, and 1,2-dichloroethane vapors adsorbed on silica gel were measured gravimetrically at 30°. These isotherms are shown in Figures 4 (low pressure) and 5 (high pressure). The values of the integrals for the vapor isotherms are given in Table I.

Surface excess isotherms for adsorption from liquid pairs on the same gel (Davison PA400, specific surface area based upon capacity at saturation = 660 m^2/g) were also measured at 30°;[4] these are shown in Figure 6. The integrals for the surface excess isotherms are recorded in Table II. Activity coefficients in the bulk liquid solutions were obtained from vapor–liquid equilibrium and heat of mixing measurements.[5-10]

The consistency test, eq 13, requires that the sum of the integrals in Table II be zero. The instrumental error in the integral for the surface excess is about 10%, estimated using uncertainties of ±0.0001 in refractive index (used for measurement of composition) and ±0.01° in temperature. This error is given in Table II. The measured composition of the solution has an uncertainty of only ±1% but this error is magnified by the measurement of small differences in composition due to adsorption. The error in the measurement of vapor adsorption is negligible by comparison.

Table II shows that the systems studied obey the thermodynamic consistency test within the precision of the experiment.

Equation 13 may be used in conjunction with the vapor isotherms to predict, at a glance, adsorption from liquid mixtures. According to eq 13, component no. 1 is preferentially adsorbed from the liquid ($n_1^e > 0$) if $n_1' > n_2'$ at corresponding values of reduced pressure (P/P^s). The larger the difference ($n_1' - n_2'$), the greater the value of n_1^e. Therefore, according to Figure 5, we expect dichloroethane to be somewhat more strongly adsorbed from the liquid relative to benzene and strongly adsorbed relative to heptane and cyclohexane. We expect benzene to be strongly adsorbed relative to cyclohexane and heptane. The adsorbent

(4) S. Sircar, Doctoral Dissertation, University of Pennsylvania, 1970.

(5) G. Scatchard, S. E. Wood, and J. M. Mochel, *J. Phys. Chem.*, **43**, 119 (1939).

(6) I. Brown and A. H. Ewald, *Aust. J. Res. Nat. Bur. Stand.*, **24**, 33 (1940).

(7) H. S. Myers, *Petrol. Refiner*, **36**, 178 (1957).

(8) J. J. Kipling and D. A. Tester, *J. Chem. Soc.*, 4123 (1952).

(9) C. R. Fordyce and D. R. Simonson, *Ind. Eng. Chem.*, **41**, 104 (1949).

(10) K. Amaya and R. Fujishiro, *Bull. Chem. Soc. Jap.*, **31**, 90 (1958).

should be neutral with respect to adsorption from liquid mixtures of cyclohexane and heptane because the isotherms cross one another; preferential adsorption of heptane at low pressure is cancelled by preferential adsorption of cyclohexane at high pressure. All of these qualitative predictions are verified by the experimental data shown in Figure 6.

Acknowledgment. Financial support by the National Science Foundation is gratefully acknowledged.

Analogy between Adsorption from Liquids and Adsorption from Vapors

by A. L. Myers* and S. Sircar

School of Chemical Engineering, University of Pennsylvania, Philadelphia, Pennsylvania 19104
(Received May 16, 1972)

Publication costs assisted by the National Science Foundation

The relation between adsorption from liquids and adsorption from unsaturated vapors is derived. The surface excess for adsorption from liquids can be calculated from equilibrium data on adsorption of the unsaturated gases. Equations for the surface excess are derived from simple type I and type II models of gas adsorption.

Theories of adsorption from liquids are made difficult by the chemical heterogeneity and structural irregularity of the solid surface as well as the fact that at least two components are involved in competitive adsorption at the solid surface.[1] The simplest case is the interaction of a dense fluid mixture with a solid surface.

Lack of specific information about the composition and structure of the surface also complicates theories of adsorption from single gases. Several theories that ignore the detailed structure of the surface have been proposed, *viz:* Langmuir,[2] Brunauer, Emmett, and Teller (BET),[3] Steele and Halsey,[4] Frenkel–Halsey–Hill slab theory,[5] etc. Although these and other theories are useful to a degree for fitting observed data, they contain constants that cannot be independently measured.

Thus there is no fully adequate theory of adsorption from gases, nor is there a satisfactory theory of adsorption from liquids. However, the two phenomena are related: adsorption from liquids can be fully explained in terms of adsorption from their unsaturated vapors. The object of this work is to study the analogy between adsorption from liquids and adsorption from unsaturated vapors.

Theory

Equilibria for adsorption from a binary mixture must obey the following thermodynamic consistency test[6]

$$\int_{P=0}^{P_2^s} \frac{n_2'}{P}dP - \int_{P=0}^{P_1^s} \frac{n_1'}{P}dP + \int_{x_1=0}^{1} \frac{n_1^e}{\gamma_1 x_1 x_2}d(\gamma_1 x_1) = 0 \quad (1)$$

The first two integrals refer to the pure, unsaturated vapor adsorption isotherms and the last integral refers to the isotherm for adsorption from the liquid mixture. n_1^e is the surface excess of component no. 1; the activity coefficients (γ_1,γ_2) and mole fractions (x_1,x_2) are those in the equilibrium bulk liquid.

Define the integral for adsorption of a pure vapor by

$$\frac{\phi_i^s}{RT} \equiv -\int_{P=0}^{P_i^s} \frac{n_i'}{P}dP \quad (2)$$

where ϕ_i^s is called the free energy of immersion of the ith adsorbate. This terminology is appropriate because ϕ_i^s is related to the heat of immersion of the adsorbent in the liquid by a Gibbs–Helmholtz type of equation.[7] With this definition eq 1 becomes

(1) A. C. Zettlemoyer and F. J. Micale, *Croat. Chem. Acta*, **42**, 247 (1970).

(2) I. Langmuir, *J. Amer. Chem. Soc.*, **40**, 1361 (1918).

(3) S. Brunauer, P. H. Emmett, and E. Teller, *ibid.*, **60**, 309 (1938).

(4) W. A. Steele and G. D. Halsey, Jr., *J. Chem. Phys.*, **22**, 979 (1954).

(5) D. M. Young and A. D. Crowell, "Physical Adsorption of Gases," Butterworths, London, 1962, p 167.

(6) A. L. Myers and S. Sircar, *J. Phys. Chem.*, **76**, 3412 (1972).

(7) S. Sircar, J. Novosad, and A. L. Myers, *Ind. Eng. Chem., Fundam.*, **11**, 249 (1972).

$$\int_{x_1=0}^{1} \frac{n_1^e}{\gamma_1 x_1 x_2} d(\gamma_1 x_1) = -\frac{(\phi_1^s - \phi_2^s)}{RT} \quad (3)$$

According to eq 3 there is no difference between adsorption from saturated vapors and the corresponding liquids; the thermodynamic properties (in this case, free energy) of the pure adsorbates are identical.

The surface excess for adsorption from a binary liquid mixture (n_1^e) is given by[8]

$$n_1^e = n'(x_1' - x_1) = n^0(x_1^0 - x_1) \quad (4)$$

n' is the total number of moles of adsorbate in the adsorbed phase and x_1' is the mole fraction of component 1 in the adsorbed phase. x_1^0 and x_1 are the mole fraction of component 1 in the bulk liquid before and after contact with the adsorbent, respectively. The second expression, $n^0(x_1^0 - x_1)$, is used to make experimental measurements of adsorption from liquids.[8] n_1^e may also be obtained from experimental data on the *unsaturated* vapor mixture by determining the limiting value of the quantity $n'(x_1' - x_1)$ at saturation pressure

$$n_1^e = \lim_{P \to P^s} [n'(x_1' - x_1)] \quad (5)$$

Both n' and x_1' are a function of pressure. At any equilibrium point, let the mole fraction of component 1 in the unsaturated vapor be y_1; then x_1 is the mole fraction in the liquid that would be in equilibrium with vapor of composition y_1 at saturation. Thus $x_1 = x_1(y_1)$ is the liquid–vapor equilibrium which is measured independently of the adsorption experiment.

Both n' and $(x_1' - x_1)$ have finite values at saturation for adsorption on a microporous adsorbent. However, n' tends to infinity and x_1' approaches x_1 as P approaches P^s if the adsorption takes place on a nonmicroporous adsorbent (see, for example, Figure 1); the product $n'(x_1' - x_1)$ has the form $\infty \times 0$ but the limit (n_1^e) is finite. Thus the limit in eq 5 is finite whether the adsorbent is microporous or nonmicroporous.

Application of Eq 5 to Experimental Data

Equation 5 applies to adsorption on any highly dispersed (or microporous) adsorbent with a large surface area (*e.g.*, 1 m²/g or more). Consider, for example, the experimental data of Arnold[9] for the adsorption of mixtures of nitrogen and oxygen vapor on titanium dioxide (surface area 13.8 m²/g) at 78.2°K. Figure 1 shows Arnold's data for a vapor mixture containing 49.8 mol % nitrogen. The surface excess of nitrogen for adsorption from the saturated vapor, $n'(x_1' - x_1)$ was calculated from these data and is plotted in Figure 2. For this vapor composition the equilibrium liquid contains 15.4 mol % nitrogen at saturation (P = 296 mm). The limit in eq 5 is n_1^e = 70 μmol/g and is found most conveniently at $(1/n') = 0$ on a plot of $n'(x_1' - x_1)$ *vs.* $(1/n')$. The complete isotherm for the liquid mixture, shown in Figure 3, was obtained by repetition

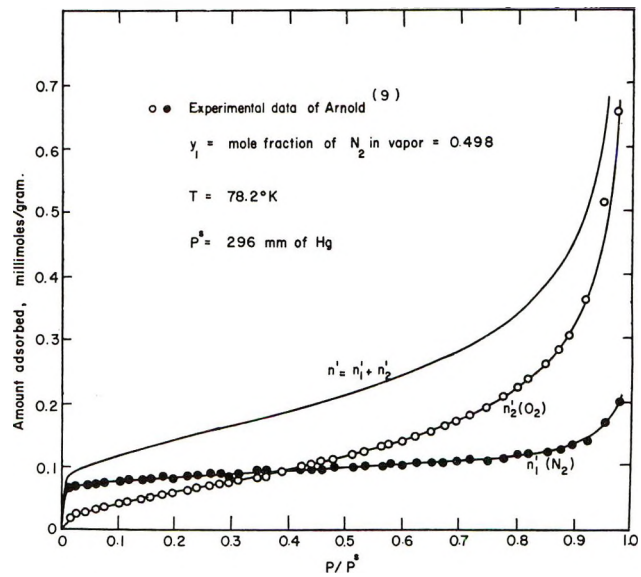

Figure 1. Adsorption from gas mixture of nitrogen and oxygen on TiO_2 at 78.2°K.

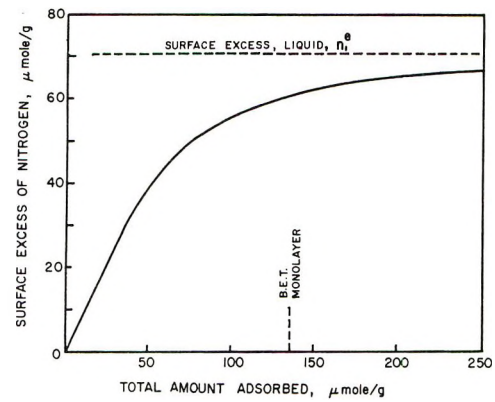

Figure 2. Surface excess of nitrogen adsorbed on TiO_2 from vapor mixture of 50.2 % oxygen and 49.8 % nitrogen at 78.2°K.

of the preceding calculation at the other vapor compositions studied by Arnold.[9]

There are two interesting features of Figure 2. First, the surface excess adsorbed from the vapor approaches the surface excess for adsorption from the liquid smoothly and asymptotically, in spite of the fact that the individual isotherms (Figure 1) intersect: nitrogen is preferentially adsorbed at low coverage but oxygen is preferentially adsorbed at high coverage. Second, the surface excess at BET monolayer coverage is 85% of the value for adsorption from the liquid solution. This suggests that the monolayer theory of adsorption from liquids,[8] for which the entire contribution to the surface excess comes in the first molecular layer, is reasonable as a first approximation.

(8) J. J. Kipling, "Adsorption from Solutions of Non-Electrolytes," Academic Press, New York, N. Y., 1965, pp 28, 40.

(9) J. R. Arnold, *J. Amer. Chem. Soc.*, **71**, 104 (1949).

Table I: Surface Excess Quantities and Their Limits at Saturation

Quantity	Langmuir model	BET model
n_i^0	$\frac{m_i c_i P}{(1 + c_i P)}$	$\frac{m_i C_i (P/P_i^s)}{[1 - P/P_i^s][1 + (C_i - 1)(P/P_i^s)]}$
$\int_{P=0}^{P} \frac{n_i^0}{P} dP$	$m_i \ln (1 + c_i P)$	$m_i \ln \left(\frac{(1 + (C_i - 1)(P/P_i^s))}{(1 - P/P_i^s)} \right)$
P_1^0	$P\left(y_1 + y_2 \frac{c_2}{c_1} \right)$	$\frac{P\left[y_1 + y_2 \frac{P_1^s C_2}{P_2^s C_1} \right]}{1 + \frac{P y_2}{P_2^s}\left(\frac{C_2}{C_1} - 1 \right)}$
$x_1' - x_1$	$\frac{y_1}{\left(y_1 + \frac{C_2}{C_1} y_2 \right)} - x_1$	$\frac{y_1\left[1 - \left\{ 1 - \frac{C_2}{C_1} \right\} \frac{P}{P_2^s} y_2 \right]}{y_1 + \frac{P_1^s C_2}{P_2^s C_1} y_2} - x_1$
$\lim_{P \to P^s} (x_1' - x_1)$	$\frac{x_1 x_2 (c_1 P_1^s - c_2 P_2^s)}{c_1 P_1^s x_1 + c_2 P_2^s x_2}$	0
$n_1' + n_2'$	$\frac{m_1 P (c_1 y_1 + c_2 y_2)}{1 + c_1 y_1 P + c_2 y_2 P}$	$\frac{m_1 C_1 P_1^0 / P_1^s}{\left(1 + (C_1 - 1)\frac{P_1^0}{P_1^s} \right)\left(1 - \frac{P y_1}{P_1^s} - \frac{P y_2}{P_2^s} \right)}$
$\lim_{P \to P^s} (n_1' + n_2')$	$\frac{m_1 (c_1 P_1^s x_1 + c_2 P_2^s x_2)}{1 + c_1 P_1^s x_1 + c_2 P_2^s x_2}$	∞
$n_1^e = \lim_{P \to P^s} n'(x_1' - x_1)$	$\frac{m_1 x_1 x_2 (c_1 P_1^s - c_2 P_2^s)}{1 + c_1 P_1^s x_1 + c_2 P_2^s x_2}$	$\frac{m_1 x_1 x_2 (1 - C_2/C_1)}{x_1 + (C_2/C_1) x_2}$

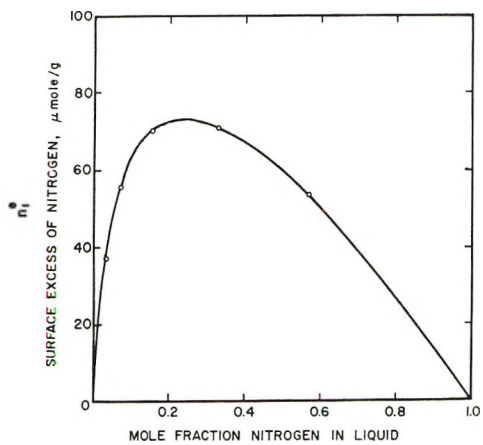

Figure 3. Surface excess of nitrogen adsorbed on TiO_2 from liquid solution of oxygen and nitrogen at 78.2°K.

Derivation of Equations for Adsorption from Liquids

Analytic expressions for adsorption from liquids (n_1^e) can be derived from equations for adsorption from pure gases using eq 5. Here we shall derive equations for n_1^e based upon the Langmuir[2] and BET[3] equations of gas adsorption. These gas isotherms are chosen because they are the simplest examples of the two extremes mentioned previously: the amount adsorbed at saturation pressure (P^s) is finite for the Langmuir model but tends to infinity for the BET model.

The Langmuir and BET equations for adsorption of pure gases are given in Table I. The mixed-gas isotherms are based upon the assumption that the adsorbed phase and the bulk liquid phase obey Raoult's law; for the bulk liquid[10]

$$P^s y_1 = P_1^s x_1 \tag{6}$$

$$P^s y_2 = P_2^s x_2 \tag{7}$$

and for the adsorbed phase[11]

$$P y_1 = P_1^0 x_1' \tag{8}$$

$$P y_2 = P_2^0 x_2' \tag{9}$$

P_i^0 is the sorbate vapor pressure of the pure ith component. The values of P_1^0 and P_2^0 are measured at equal values of spreading pressure[11] so that

$$\int_{P=0}^{P_1^0} \frac{n_1^0}{P} dP = \int_{P=0}^{P_2^0} \frac{n_2^0}{P} dP \tag{10}$$

The total amount adsorbed (n') from an ideal adsorbed solution is[11]

$$\frac{1}{n'} = \frac{x_1'}{n_1^0} + \frac{x_2'}{n_2^0} \tag{11}$$

(10) K. Denbigh, "The Principles of Chemical Equilibrium," Cambridge University Press, London, 1966, p 250.

(11) A. L. Myers and J. M. Prausnitz, *AIChE J.*, 11, 121 (1965).

It is assumed that the amount adsorbed at monolayer coverage is the same for both adsorbates

$$m_1 = m_2 \tag{12}$$

Since $(x_1' + x_2') = 1$, we obtain from eq 8 and 9

$$\frac{Py_1}{P_1^0} + \frac{Py_2}{P_2^0} = 1 \tag{13}$$

Elimination of P_2^0 between eq 10 and 13 gives an equation for P_1^0 as a function of pressure (P) and vapor composition (y_1); the result is shown in Table I.

The composition of the adsorbed phase (x_1'), the number of moles in the adsorbed phase (n'), and the surface excess are calculated from eq 6–13. The equations for these quantities and their limiting values at saturation are given in Table I. The variables must be expressed in terms of P and y_1 before taking the limit $P \rightarrow P^s$ at constant y_1.

Both n' and $(x_1' - x_1)$ are finite at saturation according to the Langmuir model and therefore there is no difficulty in calculating the surface excess using eq 5. For the BET model, on the other hand, n' approaches infinity and $(x_1' - x_1)$ approaches zero at saturation. This is the expected behavior for a type II isotherm. The surface excess at saturation for the BET model is derived by means of L'Hôpital's rule

$$n_1^e = \lim_{P \rightarrow P^s} \frac{(x_1' - x_1)}{1/n'} = \frac{\lim_{P \rightarrow P^s} \frac{d}{dP}(x_1' - x_1)}{\lim_{P \rightarrow P^s} \frac{d}{dP}(1/n')} \tag{14}$$

The result is given in Table I.

A comparison of the equations for surface excess in Table I shows that both are of the form

$$n_1^e = \frac{m_1 x_1 x_2 (1 - K)}{x_1 + K x_2} \tag{15}$$

where

$$K = C_2/C_1 \quad \text{(BET model)} \tag{16}$$

and

$$K = \frac{1 + c_2 P_2^s}{1 + c_1 P_1^s} \quad \text{(Langmuir model)} \tag{17}$$

For the Langmuir model the free energy of immersion (see eq 2 and Table I) is

$$\phi_i^s/RT = -m_i \ln (1 + c_i P_i^s) \tag{18}$$

Equations 15, 17, and 18 for the Langmuir model satisfy the thermodynamic consistency test, eq 3. For the BET model, the right-hand side of eq 3 is of the form $(\infty - \infty)$ because the free energy of immersion approaches infinity at saturation. This incorrect limiting behavior for the free energy of immersion is one of the flaws of the BET theory.[12] However it can be shown that the limit of the *difference* in free energies of immersion is finite so that the BET model does satisfy eq 3.

Equation 15 is identical with the result obtained from the monolayer cell model of adsorption from ideal, binary liquid solutions[13] and is considered the basic equation describing adsorption from liquids.[14] However, it has never been derived before from models for adsorption of gases; eq 16 and 17 are new. The agreement of the derivation with accepted theories of adsorption from liquids confirms the validity of our basic equations (3 and 5).

At first sight it is unclear why the BET model (a type II isotherm) and the Langmuir model (a type I isotherm) should give the same equation (15) for adsorption from liquids. The BET model does allow for multilayer formation but the properties of the second and higher layers are assumed to be the same as that of the bulk liquid. Therefore the surface excess of any component must be concentrated in the first layer and, at least with respect to the surface excess, the BET model is a disguised monolayer model. It would be interesting to derive expressions for the surface excess using more realistic models of multilayer adsorption.

Equations 15 and 16 may be tested using the BET constants (C_i, m_i) found by Arnold;[9] these are given in Table II. Equation 15 used with the average value of m (0.136 mmol/g) underestimates the experimental values shown in Figure 3 by a factor of about 2. The reason for this poor agreement is that the BET equation, which fits Arnold's data reasonably well in the region of high surface coverage, does not fit the low-coverage data where the adsorbent has a strong preference for nitrogen.

Table II: Constants of BET Equation for Adsorption of Nitrogen and Oxygen on Anatase at 78.2°K[9]

Gas	C	m, mmol/g
N_2	143	0.141
O_2	72	0.131

Summary

This work shows how adsorption from liquids is related to adsorption isotherms for the unsaturated vapors. Here we have restricted ourselves to simple but representative models of gas adsorption in order to illustrate the method but the theory can be applied to more realistic models of adsorption. Another interesting possibility is to predict adsorption from liquids in terms of the experimental isotherms for adsorption

(12) T. L. Hill, "An Introduction to Statistical Mechanics," Addison-Wesley, Reading, Mass., 1960, p 135.

(13) S. Sircar and A. L. Myers, *J. Phys. Chem.*, **74**, 2828 (1970).

(14) D. H. Everett, *Trans. Faraday Soc.*, **60**, 1803 (1964).

from pure vapors, without recourse to any particular model of adsorption.

Acknowledgment. Financial support by the National Science Foundation is gratefully acknowledged.

Appendix. Notation

c = constant in Langmuir equation (see Table I)
C = constant in BET equation (see Table I)
K = constant, eq 16 and 17
m = number of moles adsorbed at monolayer surface coverage per gram of adsorbent
n_i^0 = number of moles of pure ith component adsorbed per gram of adsorbent
n_i' = number of moles of ith component adsorbed from mixture per gram of adsorbent
n' = total number of moles adsorbed from mixture per gram of adsorbent
n_i^e = surface excess of ith component adsorbed from liquid per gram of adsorbent
n^0 = total number of moles in bulk liquid per gram of adsorbent (before contact with adsorbent)
P = pressure
P_i^0 = vapor pressure of sorbate of ith component
P^s = vapor pressure of bulk liquid
R = gas constant
T = absolute temperature
x_i = mole fraction of ith component in bulk liquid phase
x_i' = mole fraction of ith component in adsorbed phase
y_i = mole fraction of ith component in vapor phase
x_i^0 = mole fraction of ith component in bulk liquid phase (before contact with adsorbent)
γ_i = activity coefficient of ith component in bulk liquid phase
ϕ_i^e = free energy of immersion of adsorbent in ith liquid, eq 2

A New Procedure for Calculating the Four Diffusion Coefficients for Ternary Systems from Gouy Optical Data. Application to Data for the System KBr–HBr–H_2O at 25°[1,2]

by Arnold Revzin[3]

Department of Chemistry and The Institute for Enzyme Research, University of Wisconsin, Madison, Wisconsin 53706 *(Received April 17, 1972)*

A new method is presented for calculating the four diffusion coefficients, D_{ij}, for ternary systems from Gouy optical data. In this approach, the very accurately measurable reduced height-area ratios, $\mathfrak{D}_A$, are first fit directly to the precisely known values of the solute refractive index fractions, α_1, using the method of least squares. Then the experimentally measured reduced fringe deviations, Ω, are fit to the corresponding reduced fringe numbers, $f(\zeta)$, by a least-squares procedure using the theoretical expression for Ω *vs.* $f(\zeta)$. This calculation procedure, which is a theoretical improvement over previously used methods, was applied to new data for the system KBr–HBr–H_2O at 25°. The new method gives values for D_{ij} for this particular system which are slightly better than those computed using the older "area" method. Gosting's approximate theory for predicting D_{ij} in electrolyte systems gives values for the diffusion coefficients which agree semiquantitatively with the measured D_{ij}, indicating that the interaction between solutes in this system is due mainly to the electric field created by the rapid diffusion of H^+ ion relative to Br^- ion. The Onsager reciprocal relation was tested and found to hold within experimental error.

Introduction[4]

Calculation of the four diffusion coefficients,[5] D_{ij}, for ternary liquid systems from Gouy optical data presents a very interesting problem in the treatment of experimental results. A difficulty arises because it is not feasible to derive closed-form analytical expressions for the D_{ij} in terms of measured quantities. However, the theoretical equations relating the D_{ij} to experimental parameters do contain certain recurring *combinations* of the D_{ij}, which can be determined from the data. It is then possible to derive expressions for each of the four D_{ij} in terms of any four such "convenient combina-

(1) This investigation was supported, in part, by research Grant No. AM-05177-02 from NIAMD, National Institutes of Health. The author was the recipient of predoctoral fellowships from the Wisconsin Alumni Research Foundation and from the National Institutes of Health.

(2) Portions of this work were submitted to the Graduate School of the University of Wisconsin in partial fulfillment of the requirements for the Ph.D. degree.

(3) Present address: Institute of Molecular Biology, University of Oregon, Eugene, Oregon 97403.

tions;" various calculation procedures have been used,[6-12] with the different methods involving different "convenient quantities" from which the D_{ij} are computed. Each of these methods was developed to improve on those used previously and even the recent procedure of Dunn and Hatfield[12] appears to give somewhat more accurate D_{ij} values than do the older methods developed by Gosting, *et al.*[6-11] The Dunn and Hatfield method, however, does not use the experimental data in the most direct manner, so a new computation procedure has been derived and is presented here. The new approach is theoretically an improvement over previous methods, and so should yield the most accurate D_{ij} values to date for the types of data currently extracted from Gouy diffusion experiments.

New diffusion data are reported for the three-component system KBr–HBr–H_2O, and the D_{ij} values obtained using the new method are compared with those computed by other procedures. The experimental results are discussed in terms of Gosting's approximate theory for predicting values of D_{ij} in electrolyte systems.[13] The ternary system studied is one of a series of systems for which data are now being compiled as part of a program to study the influence of hydrogen ion transport on the diffusion of other electrolytes.

Brief Summary of Calculation Procedures Now in Use

A method which has found wide use was developed in 1960 by Fujita and Gosting.[10] In this procedure, two of the four necessary combinations of D_{ij} are determined from data for the reduced height–area ratio,[7] $\mathcal{D}_A$. Of the various quantities which can be derived from Gouy fringe photographs, $\mathcal{D}_A$ can be determined with the greatest accuracy. If several experiments are performed on the same system, with the mean concentration of each solute held constant from experiment to experiment but with different solute refractive index fractions, α_1, then the values of $1/\sqrt{\mathcal{D}_A}$ are linearly related[8] to α_1.

$$1/\sqrt{\mathcal{D}_A} = I_A + S_A\alpha_1 \qquad (1)$$

Here, I_A and S_A are expressions containing the D_{ij} and the (known) refractive index increments, R_i. The method involves determination of I_A and S_A by fitting the $1/\sqrt{\mathcal{D}_A}$ values to α_1 using the method of least squares. Two other D_{ij} combinations are obtained from the fringe deviation graphs,[14] consisting of the reduced fringe deviations, Ω_j, plotted against the corresponding reduced fringe numbers, $f(\zeta_j)$. Fujita and Gosting[10] showed that the ratio $Q/\sqrt{\mathcal{D}_A}$, where Q is the area under the fringe deviation graph, is a quadratic function of α_1. Two of the coefficients in this quadratic expression are used along with I_A and S_A in the calculation of the D_{ij} by this "area" method.

Dunn and Hatfield[12] have pointed out that the "area" method uses graphs of reduced fringe deviations which are drawn by hand through the experimental points. They observed that it is not very probable that two different workers will draw exactly the same curves, nor is it certain that these curves will be the "best" curves through the data points. To avoid such problems, Dunn and Hatfield have presented a computation method in which they fit the fringe deviation data by the least-squares method [using the theoretical relation between Ω and $f(\zeta)$] while *simultaneously* fitting the data for $1/\sqrt{\mathcal{D}_A}$ through use of the quantity[8] Γ_n (where n denotes the particular diffusion experiment). For the system to which their method has been applied,[15] it appears to yield somewhat more accurate D_{ij} values than do other procedures, as judged by comparing the experimentally deduced fringe deviation graphs with those calculated from the theoretical equation using the derived D_{ij} values. However, the Dunn and Hatfield approach does not directly fit the $1/\sqrt{\mathcal{D}_A}$ values to α_1, but involves an iterative procedure for determining Γ_n and the D_{ij}. This means that the fitting of the reduced height–area ratios may be influenced by the fitting of the fringe deviation data. This is undesirable because the $1/\sqrt{\mathcal{D}_A}$ values can be determined with much higher accuracy than can the values of Ω. Thus, a new calculation procedure has been derived in which the very accurate $1/\sqrt{\mathcal{D}_A}$ *vs.* α_1 data are fit independently of the fringe deviation results, after which the Ω *vs.* $f(\zeta)$ data are fit to their theoretical expression.

New Method

For the four diffusion experiments which are ordinarily[16] performed at given mean solute concentrations, $\bar{p}_1$ and $\bar{p}_2$ (but with different values of α_1), there are five curves to fit [one plot of $1/\sqrt{\mathcal{D}_A}$ *vs.* α_1 plus four Ω *vs.* $f(\zeta)$ graphs]. In this new method, as in most of the previous methods (excepting that of Dunn and Hatfield[12]), I_A and S_A are determined using the method of least squares to best fit the data for $1/\sqrt{\mathcal{D}_A}$ *vs.* α_1 according to eq 1. This choice is made because the $\mathcal{D}_A$

(4) In this paper, the symbols have the meanings used in related publications (*cf.*, ref 6–11).

(5) L. J. Gosting, *Advan. Protein Chem.*, 11, 429 (1956). This review article includes the flow equations in which the D_{ij} appear. The symbol D_{ij} is used to denote the set of four diffusion coefficients, D_{11}, D_{12}, D_{21}, D_{22}. For convenience the reference frame for D_{ij} will be omitted unless it is necessary to specify it.

(6) R. L. Baldwin, P. J. Dunlop, and L. J. Gosting, *J. Amer. Chem. Soc.*, **77**, 5235 (1955).

(7) P. J. Dunlop and L. J. Gosting, *ibid.*, **77**, 5238 (1955).

(8) H. Fujita and L. J. Gosting, *ibid.*, **78**, 1099 (1956).

(9) P. J. Dunlop, *J. Phys. Chem.*, **61**, 994 (1957).

(10) H. Fujita and L. J. Gosting, *ibid.*, **64**, 1256 (1960).

(11) H. Kim, *ibid.*, **70**, 562 (1966).

(12) R. L. Dunn and J. D. Hatfield, *ibid.*, **69**, 4361 (1965).

(13) See p 535 of ref 5.

(14) D. F. Akeley and L. J. Gosting, *J. Amer. Chem. Soc.*, **75**, 5685 (1953).

(15) O. W. Edwards, R. L. Dunn, J. D. Hatfield, E. O. Huffman, and K. L. Elmore, *J. Phys. Chem.*, **70**, 217 (1966).

(16) See p 542 of ref 5.

and α_1 values are known to a high degree of accuracy, while the uncertainties in other measured quantities are considerably higher. There remain two parameters[17] with which to fit the fringe deviation data; these are chosen to be p and $\sqrt{\sigma_+}$, quantities which are functions only of the D_{ij} and which are defined by eq 30 and 31 of ref 8, along with the definition,[10] $p = \sqrt{\sigma_-}/\sqrt{\sigma_+}$.

The theoretical equation for the reduced fringe deviations is found by combining eq 5, A6, A7, and A8 of ref 10 to give

$$\Omega_j = \exp\{-\zeta_j^2\} - \frac{(1-\Gamma_-)\sqrt{\sigma_+}\exp\{-\sqrt{\sigma_+}^2 y_j^2\} + \Gamma_-\sqrt{\sigma_-}\exp\{-\sqrt{\sigma_-}^2 y_j^2\}}{(1-\Gamma_-)\sqrt{\sigma_+} + \Gamma_-\sqrt{\sigma_-}} \quad (2)$$

where the quantities y_j and ζ_j are related by eq A5 of ref 10. By using eq 4 and 15 of ref 10, one can derive

$$\Omega_j = \exp\{-\zeta_j^2\} - \frac{\{[p\sqrt{\sigma_+} - (I_A + S_A\alpha_1)]\exp\{-\sqrt{\sigma_+}^2 y_j^2\} + p[(I_A + S_A\alpha_1) - \sqrt{\sigma_+}]\exp\{-p^2\sqrt{\sigma_+}^2 y_j^2\}\}}{(I_A + S_A\alpha_1)(p-1)} \quad (3)$$

For the experiment numbered i, with $\alpha_1 = \alpha_1^i$, one defines

$$w^i = I_A + S_A\alpha_1^i \quad (4)$$

and then eq 3 becomes

$$\Omega_j^i = \exp\{-\zeta_j^2\} - \frac{\{(p\sqrt{\sigma_+} - w^i)\exp\{-\sqrt{\sigma_+}^2 y_j^2\} + p(w^i - \sqrt{\sigma_+})\exp\{-p^2\sqrt{\sigma_+}^2 y_j^2\}\}}{w^i(p-1)} \quad (5)$$

One then defines "residual equations"[18]

$$\Delta_j^i = \Omega_j^i - \Omega_{jE}^i \quad (6)$$

where Ω_j^i is the calculated value (using eq 5) of the reduced fringe deviation for each value of the reduced fringe number, $f(\zeta_j)^i$, corresponding to fringe number j in experiment i, and Ω_{jE}^i is the observed value averaged for all times in a given experiment. To fit the fringe deviation data by the method of least squares, one minimizes, with respect to p and $\sqrt{\sigma_+}$, the function ϕ, where[19]

$$\phi = \sum_i\sum_j (\Delta_j^i)^2 \quad (7)$$

Here, one summation is over the i experiments while the other summation is over the j fringes measured in each experiment. Minimization of ϕ leads to the simultaneous equations

$$\frac{\partial\phi}{\partial p} = 0 \qquad \frac{\partial\phi}{\partial\sqrt{\sigma_+}} = 0 \quad (8)$$

which must be solved for p and $\sqrt{\sigma_+}$. Due to the complicated way in which p and $\sqrt{\sigma_+}$ appear in ϕ, eq 8 cannot be solved in closed form, and thus some iterative method must be used to extract the values of p and $\sqrt{\sigma_+}$. The Gauss method[18,20] for the general least-squares problem was chosen because it is a convenient and easily understood procedure.

The Gauss method requires approximate starting values, p_0 and $(\sqrt{\sigma_+})_0$, such that

$$p = p_0 + \Delta p; \qquad \sqrt{\sigma_+} = (\sqrt{\sigma_+})_0 + \Delta\sqrt{\sigma_+} \quad (9)$$

where Δp and $\Delta\sqrt{\sigma_+}$ are the correction terms. Then, the function Ω_j^i may be approximated by

$$\Omega_j^i \simeq (\Omega_j^i)_0 + \left(\frac{\partial\Omega_j^i}{\partial p}\right)_0\Delta p + \left(\frac{\partial\Omega_j^i}{\partial\sqrt{\sigma_+}}\right)_0\Delta\sqrt{\sigma_+} \quad (10)$$

where $(\Omega_j^i)_0$ means $(\Omega_j^i)_{p=p_0,\sqrt{\sigma_+}=(\sqrt{\sigma_+})_0}$, etc. An equation of form (10) can be written for each fringe measured in each experiment. The quantities Ω^k and Ω^l, where $k \neq l$, differ in that they have different values for $w(w^k \neq w^l)$, but both Ω^k and Ω^l are functions of p and $\sqrt{\sigma_+}$. Inserting eq 10 into eq 6 gives for the residuals

$$\Delta_j^i = \left(\frac{\partial\Omega_j^i}{\partial p}\right)_0\Delta p + \left(\frac{\partial\Omega_j^i}{\partial\sqrt{\sigma_+}}\right)_0\Delta\sqrt{\sigma_+} + (\Omega_j^i)_0 - \Omega_{jE}^i \quad (11)$$

From the residual equations one can immediately write the "normal" equations,[18] from which Δp and $\Delta\sqrt{\sigma_+}$ are determined.

$$\Delta p\sum\left(\frac{\partial\Omega}{\partial p}\right)_0^2 + \Delta\sqrt{\sigma_+}\sum\left(\frac{\partial\Omega}{\partial p}\right)_0\left(\frac{\partial\Omega}{\partial\sqrt{\sigma_+}}\right)_0 = \sum(\Omega_E - \Omega_0)\left(\frac{\partial\Omega}{\partial p}\right)_0 \quad (12)$$

$$\Delta p\sum\left(\frac{\partial\Omega}{\partial p}\right)_0\left(\frac{\partial\Omega}{\partial\sqrt{\sigma_+}}\right)_0 + \Delta\sqrt{\sigma_+}\sum\left(\frac{\partial\Omega}{\partial\sqrt{\sigma_+}}\right)_0^2 = \sum(\Omega_E - \Omega_0)\left(\frac{\partial\Omega}{\partial\sqrt{\sigma_+}}\right)_0$$

The summations are over all fringes from all experiments (subscript j and superscript i have been dropped

(17) If two quantities, I_A and S_A, are derived from data for the reduced height–area ratios, it is then permissible to determine *two, and only two*, more quantities from other data. If, for example, three more quantities were determined, the result would be five equations having four unknowns (the D_{ij}) and the solution would not be unique.

(18) J. B. Scarborough, "Numerical Mathematical Analysis," Johns Hopkins Press, Baltimore, Md., 1930.

(19) For clarity in the presentation of this method, ϕ is defined with the assumption of equal weighting for all points of all graphs of Ω *vs.* $f(\zeta)$. Extension to the case of nonequally weighted points is straightforward. In ordinary applications, uncertainties in the reduced fringe deviations should be about the same for all points, so equal weighting will probably be used.

(20) R. H. Moore and R. K. Zeigler, "The Solution of the General Least-Squares Problem with Special Reference to High-Speed Computers," Los Alamos Scientific Laboratory (LA-2367), March 4, 1960; available from the Clearinghouse for Federal Scientific and Technical Information, Springfield, Va. 22151.

for convenience). This simple set of equations is easily solved for Δp and $\Delta\sqrt{\sigma_+}$. Equations for the derivatives of Ω are given in Appendix I. The values of Δp and $\Delta\sqrt{\sigma_+}$, when combined with starting values p_0 and $(\sqrt{\sigma_+})_0$ using eq 9, give the quantities p and $\sqrt{\sigma_+}$ which minimize the value of ϕ, subject to the approximation of eq 10. To get an improved approximation to the "best" fit of the fringe deviation data, the current values of p and $\sqrt{\sigma_+}$ are used as the new starting values, p_0' and $(\sqrt{\sigma_+})_0'$

$$\begin{aligned} p_0' &= p_0 + \Delta p \\ (\sqrt{\sigma_+})_0' &= (\sqrt{\sigma_+})_0 + \Delta\sqrt{\sigma_+} \end{aligned} \tag{13}$$

and the process is repeated giving new values for Δp and $\Delta\sqrt{\sigma_+}$. Iteration is continued until Δp and $\Delta\sqrt{\sigma_+}$ are judged to be sufficiently small. The values of p and $\sqrt{\sigma_+}$ when the iteration is ceased are the parameters which give the best fit of the fringe deviation graphs (under the procedure used here, in which I_A and S_A are determined from data for $1/\sqrt{\mathfrak{D}_A}$ *vs.* α_1). In Appendix II are given equations with which the D_{ij} may be calculated from the values of I_A, S_A, p, and $\sqrt{\sigma_+}$.

This calculation procedure, like that of Dunn and Hatfield,[12] eliminates subjective errors in drawing the fringe deviation graphs. The new method should, in theory, have an advantage over that of Dunn and Hatfield in that two parameters, I_A and S_A, are evaluated directly from the most accurate data, while in the Dunn and Hatfield approach the fit of the $1/\sqrt{\mathfrak{D}_A}$ data may be affected by the fitting of the fringe deviation data (especially for more than two experiments at given $\bar{\rho}_1$ and $\bar{\rho}_2$).

Diffusion Results for the System KBr–HBr–H_2O

A. Apparatus. All diffusion measurements were performed on a new optical diffusiometer recently constructed at the Institute for Enzyme Research. Detailed description of the apparatus and general methods of its use can be found elsewhere.[21-28] The quartz diffusion cell was of the usual Tiselius type, the value of the cell dimension, a, along the optic axis being 2.4938 cm. The optical lever arm, b, was 308.91 cm.

Illumination was provided by a GE H-100A4 mercury vapor lamp fitted with a Kodak Wratten filter 77A. The wavelength of the emitted light, λ, was taken to be 5460.7 Å (in air). All photographs of interference fringes were taken on Kodak Type III G spectroscopic glass plates and were measured with a photoelectric null indicator mounted on a Gaertner Model M2001RS toolmaker's microscope.[29-31]

During each experiment the temperature of the water bath was read at 10-min intervals, using a previously calibrated mercury-in-glass thermometer. The Bayley Model 123 temperature regulator kept the temperature constant to ±0.005° of the average value for each experiment. The maximum deviation of the mean temperature from 25° for any experiment was ±0.017°. Conversion to 25.000° was made by using a series form of the Stokes–Einstein relation.[32]

The density of each solution was measured in triplicate with single-stem pycnometers, each holding about 28 ml of solution. The percentage deviation from the average of the three densities measured for each solution was 0.0005% or less.

B. Preparation of Solutions. The water used to prepare all solutions was obtained from a Barnstead water purification system which circulated water through an organic removal cartridge, a mixed bed Bantam demineralizer, and a submicron filter. Ordinary distilled water was used to fill the system initially and the water was recirculated until the resistance of water from the high-purity tap was at least 12–14 megohm-cm. The purified water was saturated with air and stored in a Pyrex glass bottle.

The HBr was Baker Analyzed Reagent grade (47–49%). It was twice distilled at a rate of about 4 ml/min, and each time the first 100 ml of material passing over was discarded. The procedure was based on that of Bonner, *et al.*,[33] for the preparation of constant-boiling HBr, but no CO_2 atmosphere was used, nor was there any attempt made to achieve the constant-boiling solution. A stock solution of about 0.175 *M* was prepared by diluting the concentrated distillate with "Barnstead-distilled" water. The stock solution was stored in a Pyrex bottle which was painted black to prevent light from having any effect on the HBr. The HBr concentration of the stock solution was determined both before and after the diffusion experiments by gravimetric precipitation with $AgNO_3$, and was found to be 0.1748 ± 0.0003 *M*. A binary diffusion experiment for the system HBr–H_2O at $\bar{C}$ = 0.1 *M*, ΔC = 0.1 *M*, gave a fringe deviation graph with an area, Q, of less than 1.5×10^{-4} unit, so the HBr was deemed to be adequately pure.[34]

(21) L. J. Gosting, H. Kim, C. A. Landsness, M. A. Loewenstein, G. Reinfelds, and A. Revzin, submitted for publication.

(22) A. Revzin, Ph.D. Thesis, University of Wisconsin, 1969.

(23) G. Reinfelds-Michel, Ph.D. Thesis, University of Wisconsin, 1970.

(24) L. J. Gosting, E. M. Hanson, G. Kegeles, and M. S. Morris, *Rev. Sci. Instrum.*, **20**, 209 (1949).

(25) L. J. Gosting and M. S. Morris, *J. Amer. Chem. Soc.*, **71**, 1998 (1949).

(26) L. J. Gosting, *ibid.*, **72**, 4418 (1950).

(27) P. J. Dunlop and L. J. Gosting, *ibid.*, **75**, 5073 (1953).

(28) L. A. Woolf, D. G. Miller, and L. J. Gosting, *ibid.*, **84**, 317 (1962).

(29) R. P. Wendt, *J. Phys. Chem.*, **66**, 1279 (1962).

(30) R. P. Wendt, Ph.D. Thesis, University of Wisconsin, 1961.

(31) J. G. Albright, Ph.D. Thesis, University of Wisconsin, 1963.

(32) J. G. Albright and L. J. Gosting, *J. Phys. Chem.*, **64**, 1537 (1960).

(33) W. D. Bonner, L. G. Bonner, and F. J. Gurney, *J. Amer. Chem. Soc.*, **55**, 1406 (1933).

(34) See p 502 of ref 5.

The KBr was Matheson Coleman and Bell ACS reagent grade. It was purified by recrystallization from Barnstead-distilled water, then was fused in a platinum dish before storage.

All solutions were prepared by weight using the values of 1.00698, 2.75, and 8.4 g/cm³ for the densities of HBr stock solution, KBr, and the metal weights, respectively, in calculating the air-buoyancy corrections. The weighings could be performed to ±0.0002 g and the concentrations were known with an accuracy of about 0.002%. (The absolute HBr concentration was, of course, known only to the accuracy of the gravimetric analysis, but the amounts of stock solution used in each diffusion experiment were weighed to 0.002%, so that the concentration difference between the upper and lower solutions was known to this order of accuracy.)

In order to prepare each solution to a predetermined concentration, preliminary density measurements were made on two accurately weighed solutions, one of which had concentrations of both solutes somewhat higher than the desired mean concentrations for the ternary system, the other having concentrations of both solutes somewhat lower than the desired mean concentrations. From these density data, preliminary values of H_1 and H_2 (see eq 14) were calculated, which permitted preparation of new solutions to the desired mean concentrations. The starting solutions for each experiment were prepared so that $\bar{\rho}_1$ and $\bar{\rho}_2$ were within ±0.01% of the desired mean concentrations, $\bar{\rho}_1$ = 0.029753 g/cm³ (0.25 *M*), $\bar{\rho}_2$ = 0.008092 g/cm³ (0.10 *M*).

C. Diffusion Experiments. Detailed descriptions of experimental procedure can be found elsewhere.[5,24-28] Here, only a brief outline and relevant data will be given.

The cell (and also the pycnometers) were filled using syringes with Teflon syringe needles to avoid contamination of the acidic solutions with metal ions from the stainless steel syringe needles ordinarily used. The diffusion cell was allowed to stand in the water bath for at least 1 hr to reach temperature equilibrium. Then sets of seven photographs were taken to determine the reference corrections[26] δ and δ'. The initial boundary was formed by siphoning through a platinum capillary for 50 min at a rate of 2 ml/min. During the latter part of siphoning a set of seven photographs was taken to determine the fractional part[24] of J, the total number of fringes. The integral part of J was determined by counting the Gouy fringes as far as possible, then extrapolating to the position of the undeviated slit image.[24] In all experiments, diffusion was allowed to proceed for 1 hr, and nine Gouy fringe patterns were photographed. Lengths of the fringe patterns ranged between 0.7 and 1.7 cm. Each photograph was timed from the moment that siphoning was stopped; this time, t', was read from a Precision Scientific Co. electric timer. In general, positions of fringe minima were read for Gouy patterns, while fringe maxima were read for δ, δ', and fringe fraction photographs, and also for Gouy reference patterns.

Calculations

A. Density and Refractive Index Derivatives. Because both solute concentrations were always close to those for the composition being studied, the density, $d(\rho_1, \rho_2)$, and refractive index, $n(\rho_1, \rho_2)$, may be written

$$d(\rho_1,\rho_2) = d(\bar{\rho}_1,\bar{\rho}_2) + H_1(\rho_1 - \bar{\rho}_1) + H_2(\rho_2 - \bar{\rho}_2) \quad (14)$$

$$n(\rho_1,\rho_2) = n(\bar{\rho}_1,\bar{\rho}_2) + R_1(\rho_1 - \bar{\rho}_1) + R_2(\rho_2 - \bar{\rho}_2) \quad (15)$$

Here, the H_i are the density[35] derivatives and the R_i are the refractive index[14] derivatives. The quantities $d(\bar{\rho}_1,\bar{\rho}_2)$ and $n(\bar{\rho}_1,\bar{\rho}_2)$ are the density and the refractive index, respectively, of a ternary solution in which the solute concentrations are $\rho_1 = \bar{\rho}_1$ and $\rho_2 = \bar{\rho}_2$. Values of $d(\bar{\rho}_1,\bar{\rho}_2)$, H_1, and H_2 were computed by the method of least squares from density and concentration data. The average deviation of the experimentally observed densities from those determined by the plane surface described by eq 14 was found to be ±0.00015%.

The refractive index derivatives were computed by the method of least squares using the equation[36]

$$\frac{\lambda J}{a(\Delta\rho_1 + \Delta\rho_2)} = \frac{[\Delta\rho_1(R_1 - R_2)]}{(\Delta\rho_1 + \Delta\rho_2)} + R_2 \quad (16)$$

where Δ refers to differences between the upper and lower solutions. The solute fraction, α_1, was calculated from the relationship

$$\alpha_1 = \frac{R_1\Delta\rho_1}{R_1\Delta\rho_1 + R_2\Delta\rho_2} \quad (17)$$

Partial specific volumes, $\bar{v}_i$, were obtained from the quantities $d(\bar{\rho}_1,\bar{\rho}_2)$, H_1, and H_2, using the equations[37]

$$\bar{v}_i = \frac{1 - H_i}{d - (H_1\rho_1 + H_2\rho_2)} \quad (i = 1,2) \quad (18)$$

$$d = \rho_0 + \rho_1 + \rho_2 \quad (19)$$

$$1 = \rho_0\bar{v}_0 + \rho_1\bar{v}_1 + \rho_2\bar{v}_2 \quad (20)$$

where d is the solution density in g/cm³, ρ_i is the concentration in g/cm³ of component i, and the subscripts 0, 1, 2 refer to water, KBr, and HBr, respectively.

B. Values for $(D_{ij})_V$. Calculations were made with both the "area" method[10] and the new "least-squares" method. The first part of the computation, in which values of $\mathfrak{D}_A$ and Ω_j are determined, is the same for both calculation procedures.

A computer program kindly supplied by Professor Dunlop was used for some of the calculations.[38] For

(35) P. J. Dunlop and L. J. Gosting, *J. Phys. Chem.*, **63**, 86 (1959).

(36) I. J. O'Donnell and L. J. Gosting, "The Structure of Electrolytic Solutions," W. J. Hamer, Ed., Wiley, New York, N. Y., 1959, p 165.

(37) G. Reinfelds and L. J. Gosting, *J. Phys. Chem.*, **68**, 2464 (1964).

(38) All computer calculations were performed at the University of Wisconsin Computer Center.

each experiment, the measured fringe displacements, Y_j, for fringes numbered j = 0,1,2,3,4,5,6,10,15, 20,...45 were fed into Part I of the program from which were obtained values for the ratio[14] $Y_j/e^{-\zeta_j^2}$. Graphs of $Y_j/e^{-\zeta_j^2}$ *vs.* $Z_j^{2/3}$ were plotted and extrapolated[10,14,39] to obtain values of the quantity C_t for each Gouy fringe photograph. These quantities were inserted into Part II of the computer program, which calculated the preliminary values, $\mathfrak{D}_A'$, of the reduced height–area ratio, where

$$\mathfrak{D}_A' = (J\lambda b)^2/(4\pi C_t^2 t') \quad (21)$$

The $\mathfrak{D}_A'$ values were then fit to $1/t'$ by the method of least squares, according to[40]

$$\mathfrak{D}_A' = \mathfrak{D}_A(1 + \Delta t/t') \quad (22)$$

The correction, Δt, for the imperfect starting boundary, ranged between 11 and 13 sec. Values of $\mathfrak{D}_A$ determined from the intercept at infinite time ($1/t' = 0$) were used in further calculations.

The computer program also provides values of the reduced fringe deviation, Ω_j, (averaged over the several photographs) for each fringe measured. From these results the time-independent fringe deviation graphs were constructed.

$(D_{ij})_V$ *Using the "Area" Method.*[10] The area, Q_E, of each fringe deviation graph was evaluated by means of Simpson's one-third rule for numerical integration. No base line correction was applied. Part III of the Dunlop computer program gives the values of $(D_{ij})_V$ from data for $\mathfrak{D}_A$, $\Delta\rho_i$, J, and Q_E. The "area" method calculation (and also the "least-squares" approach) requires data from at least two diffusion experiments with the desired values of $\bar{\rho}_1$ and $\bar{\rho}_2$, but at different values of α_1. In this work, data were obtained from four experiments, at values of α_1 of approximately 0, 0.27, 0.60, and 1.0 to provide checks on the internal consistency of the data and to increase the accuracy of the results.

$(D_{ij})_V$ *Using the New "Least-Squares" Method.* A new computer program was written for the Univac 1108 computer. Starting values, p_0 and $(\sqrt{\sigma_+})_0$ were determined from the $(D_{ij})_V$ found using the "area" method. The values of $\mathfrak{D}_A$ and α_1, and also for Ω and $f(\zeta)$ were fed into the computer. The program first evaluates I_A and S_A for use in further calculations. Values of y which correspond to the particular $f(\zeta)$, p_0, and $(\sqrt{\sigma_+})_0$ involved are determined using the Newton–Raphson method (see Appendix I). All values of Ω for all experiments were equally weighted.[19]

The program generates correction terms Δp and $\Delta\sqrt{\sigma_+}$, after which the calculation is repeated using the modified starting values p_0' and $(\sqrt{\sigma_+})_0'$ (eq 13). Iteration was ceased when both ratios $\Delta p/p$ and $\Delta\sqrt{\sigma_+}/\sqrt{\sigma_+}$ were less than 10^{-6}, at which time values of the $(D_{ij})_V$ were calculated using the equations defined in Appendix II.

C. Test of the Onsager Reciprocal Relation (ORR). The procedure for calculating values of $(L_{ij})_0$ was similar to that of Dunlop and Gosting.[35] The measured $(D_{ij})_V$, which correspond to volume-fixed flows,[41] J_V, having the units g cm^{-2} sec^{-1}, were converted to $(D_{ij})_0$, corresponding to solvent-fixed flows, J_0, in units of mol cm^{-2} sec^{-1}, using eq 2 of ref 35. Conversion from molarity to molality units was easily performed using the measured solution densities. The necessary osmotic and activity data for the binary systems KBr–H_2O and HBr–H_2O were obtained from Tables 1, 2, 9, and 11 of Appendix 8.10 in the book of Robinson and Stokes.[42] The Harned coefficients,[43,44] α_{12} and α_{21}, were derived from the work of Lietzke and Stoughton,[44] who found that at a total molal ionic strength of 0.41 (not too different from the ionic strength of 0.355 used in this work), both HBr and KBr obey Harned's rule with $\beta_{12} = \beta_{21} = 0$. Values for α_{12} and α_{21} were also derived by combining data in Table 9, Appendix 8.10 of ref 42, and in Table (14-2-1A), Appendix A, ref 43. The activity coefficient derivatives, $[\partial \log \gamma_{1(0)}/\partial m]$ and $[\partial \log \gamma_{2(0)}/\partial m]$, were evaluated by measuring slopes on large plots of $\log \gamma_{1(0)}$ and $\log \gamma_{2(0)}$ *vs.* m.

Results

Table I summarizes the initial diffusion data for the ternary system. The densities, d_l and d_u, are the values for the lower and upper initial solutions, respectively; these solutions had the solute concentrations reported in lines 4, 5, 7, and 8. The quantities J are the total number of fringes determined experimentally. Values of $\Delta\rho_1$ and $\Delta\rho_2$, along with results for R_1 and R_2 (Table II) were used in eq 16 to compute J_{calcd} (Table I, line 13). The average deviation of J from J_{calcd} is $\pm 0.014\%$ which indicates satisfactory accuracy in the determination of J and in the preparation of solutions.

In Table II are given the values of I_A and S_A, which were computed according to eq 1 using the method of least squares. These results for I_A and S_A, when inserted into eq 1, give the values of $(\mathfrak{D}_A)_{calcd}$ (Table I, line 16). The average agreement of $\mathfrak{D}_A$ and $(\mathfrak{D}_A)_{calcd}$ is $\pm 0.088\%$, which is quite adequate, though this is a slightly larger discrepancy than has been obtained in some other ternary systems.[28,37] The larger uncertainty may be primarily due to the fact that for this fast diffusing system the largest t' was 3600 sec, so that the

(39) L. J. Gosting and H. Fujita, *J. Amer. Chem. Soc.*, **79**, 1359 (1957).

(40) L. G. Longsworth, *ibid.*, **69**, 2510 (1947).

(41) J. G. Kirkwood, R. L. Baldwin, P. J. Dunlop, L. J. Gosting, and G. Kegeles, *J. Chem. Phys.*, **33**, 1505 (1960).

(42) R. A. Robinson and R. H. Stokes, "Electrolyte Solutions," 2nd ed, Butterworths, London, 1959.

(43) H. S. Harned and B. B. Owen, "The Physical Chemistry of Electrolytic Solutions," 3rd ed, Reinhold, New York, N. Y., 1958.

(44) M. H. Lietzke and R. W. Stoughton, *J. Phys. Chem.*, **67**, 2573 (1963).

Table I: Initial Diffusion Data for the System KBr–HBr–H_2O at 25°[a,b]

1		Expt no. 1	2	3	4
2	$\bar{\rho}_1$	0.0297535	0.029753	0.029753	0.029756
3	$\bar{\rho}_2$	0.008092	0.008092	0.008092	0.008092
4	ρ_{1l}	0.0297545	0.0310884	0.032753	0.034756
5	ρ_{2l}	0.0121384	0.010803	0.009592	0.008092
6	d_l	1.026439	1.026470	1.026815	1.027211
7	ρ_{1u}	0.0297526	0.0284176	0.026753	0.024756
8	ρ_{2u}	0.004046	0.005381	0.006592	0.008092
9	d_u	1.020924	1.020890	1.020542	1.020158
10	$\Delta\rho_1$	0.000002	0.002671	0.006000	0.010000
11	$\Delta\rho_2$	0.008092	0.005422	0.003000	0.000000
12	J	56.49	52.03	52.80	53.07
13	J_{calcd}	56.496	52.026	52.79	53.08
14	α_1	0.00019	0.27251	0.60330	1.00000
15	$\mathfrak{D}_A \times 10^5$	3.30025	2.78874	2.32135	1.90056
16	$(\mathfrak{D}_A)_{calcd} \times 10^5$	3.29607	2.79260	2.32220	1.89959
17	$Q_E \times 10^4$	190.2	175.2	115.9	6.3
18	$Q_{calcd} \times 10^4$	190.5	174.3	116.8	6.0

[a] Units: concentrations, ρ_i, g/cm³; densities, d, g/cm³; reduced height–area ratios, $\mathfrak{D}_A$, cm²/sec. [b] 1 = KBr, 2 = HBr, $\bar{C}_1 = 0.25\ M$, $\bar{C}_2 = 0.10\ M$.

Table II: Refractive Index Derivatives, Partial Specific Volumes, and Density Data for the System KBr–HBr–H_2O at 25°[a,b]

1	$\bar{\rho}_1$	0.029753	7	R_2	0.15285
2	$\bar{\rho}_2$	0.008092	8	$\bar{v}_0$	1.002824
3	$d(\bar{\rho}_1,\bar{\rho}_2)$	1.023681	9	$\bar{v}_1$	0.29562
4	H_1	0.70521	10	$\bar{v}_2$	0.31946
5	H_2	0.68144	11	I_A	174.17
6	R_1	0.11623	12	S_A	55.27

[a] Units: concentrations, $\bar{\rho}_i$, g/cm³; density, $d(\bar{\rho}_1,\bar{\rho}_2)$, g/cm³; density derivatives, H_i, correspond to d and ρ_i in g/cm³; refractive index derivatives, R_i, cm³/g; partial specific volumes, $\bar{v}_i$, cm³/g. [b] 0 = H_2O, 1 = KBr, 2 = HBr, $\bar{C}_1 = 0.25\ M$, $\bar{C}_2 = 0.10\ M$.

extrapolation of $\mathfrak{D}_A'$ *vs.* $1/t'$ to infinite time[40] may be subject to greater errors than is the case for experiments where t' values are considerably larger.

The measured areas under the fringe deviation graphs, Q_E, are given in line 17 of Table I, while line 18 shows values of Q computed from the derived values of $(D_{ij})_V$.

Table II contains the refractive index derivatives, partial specific volumes, and density data for this ternary system. The gravitational stability of the column of diffusing liquid in each experiment was tested by means of the simplified criteria derived by Reinfelds and Gosting[37] (eq 42 and 43 of ref 37, for a class III system). For each experiment, $\Delta\rho_1$ and $\Delta\rho_2$ were both greater than or equal to zero, and in every case the appropriate conditions for gravitational stability were fulfilled.

Values of the diffusion coefficients are displayed in Table III. Included here are results for $(D_{ij})_V$ computed by the "area" method[10] and by the new "least-squares" method. The uncertainities reported were computed by repeating the calculations with each measured Q_E or Ω_E value changed by 2×10^{-4} unit, which is the estimated uncertainty in the experimental values for these quantities. In column 3 are listed values of $(D_{ij})_V$ calculated from Gosting's approximate theory[13] for predicting diffusion coefficients in electrolyte systems. Also given in Table III are values for two quantities which may be used to compare the accuracy of the $(D_{ij})_V$ computed by the two calculation procedures. The quantity $(\Omega - \Omega_E)_{av}$ is equal to the sum (for all fringes measured) of the magnitudes of the differences between measured values of $\Omega(= \Omega_E)$ and values computed from the appropriate $(D_{ij})_V$ values, divided by the total number of fringes measured. The quantity $(Q - Q_E)_{av}$ equals the sum of the magnitudes of the differences between measured and calculated Q values, divided by the number of experiments, in this case four.

Table IV contains data for testing the Onsager reciprocal relation, while Table V presents the results of the calculations. In column 1 of Table V are given results for the $(L_{ij})_0$ computed using values for the Harned constants deduced from the data of Lietzke and Stoughton,[44] while column 2 gives results using Harned constants deduced from a more approximate computation using data in ref 42 and 43. For further comparisons, in column 3 are presented $(L_{ij})_0$ values derived using the activity data of Lietzke and Stoughton,[44] but with $(D_{ij})_V$ results at the limit of the estimated uncertainties given in Table III.

Discussion

A. Calculation Methods. Convergence of the Gauss

Table III: Diffusion Coefficients for the System KBr–HBr–H_2O at 25°[a,b]

Method	1 Area	2 Least squares	3 Gosting theory[c]
$(D_{11})_V \times 10^5$	1.8530 ∓ 0.016	1.8531 ∓ 0.016	1.922
$(D_{12})_V \times 10^5$	−2.1976 ∓ 0.027	−2.1947 ∓ 0.027	−1.980
$(D_{21})_V \times 10^5$	0.0528 ± 0.018	0.0528 ± 0.018	0.046
$(D_{22})_V \times 10^5$	5.7536 ± 0.030	5.7504 ± 0.030	6.752
p	0.573573	0.573732	
$\sqrt{\sigma_+} \times 10^{-3}$	0.230450	0.230450	
$(\Omega - \Omega_E)_{av} \times 10^4$	1.663	1.648	
$(Q - Q_E)_{av} \times 10^4$	0.615	0.569	

[a] Units: diffusion coefficients, $(D_{ij})_V$, cm²/sec, corresponding to volume-fixed flows, with flow equations expressed in terms of grams of the components. [b] 1 = KBr, 2 = HBr, $\bar{C}_1 = 0.25\ M$, $\bar{C}_2 = 0.10\ M$. [c] Values of the limiting equivalent conductivities of H^+, K^+, and Br^- ions, needed for calculations using Gosting's theory, were taken from Appendix 6.1 of ref 42.

Table IV: Data for Testing the Onsager Reciprocal Relation for the System KBr–HBr–H_2O at 25°[a-c]

1	$\bar{C}_1$	0.2500	8	$\bar{V}_2$	25.848
2	$\bar{C}_2$	0.1000	9	$\bar{V}_0$	18.070
3	$\bar{C}_0$	54.708	10	d log $\gamma_{1(0)}$/dm	−0.130
4	m_1	0.25360	11	d log $\gamma_{2(0)}$/dm	+0.0205
5	m_2	0.10143	12	Φ	−0.077
6	m_{total}	0.35503	13	β_{12}	0
7	$\bar{V}_1$	35.181	14	β_{21}	0

[a] Nomenclature corresponds to that in ref 35. [b] 0 = H_2O, 1 = KBr, 2 = HBr, $M_0 = 18.016$, $M_1 = 119.01$, $M_2 = 80.92$. [c] Units: concentrations, $\bar{C}_i$, M; concentrations, m, molality; partial specific volumes $\bar{V}_i$, cm³/mol.

Table V: Summary of Tests of the Onsager Reciprocal Relation for the System KBr–HBr–H_2O at 25°[a,b]

		1[c]	2[c]	3[c]
1	α_{12}	−0.048	−0.064	−0.048
2	α_{21}	+0.106	+0.090	+0.106
3	Γ_{11}	−0.1310	−0.1310	−0.1310
4	$\Gamma_{12} = \Gamma_{21}$	−0.083	−0.067	−0.083
5	Γ_{22}	0.0230	0.0230	0.0230
6	μ_{11}/RT	6.3097	6.3100	6.3097
7	μ_{12}/RT	2.5167	2.5916	2.5167
8	μ_{21}/RT	2.5376	2.6130	2.5376
9	μ_{22}/RT	13.0140	13.0145	13.0140
10	$(D_{11})_0 \times 10^5$	1.8701	1.8701	1.8542
11	$(D_{12})_0 \times 10^5$	−1.4679	−1.4679	−1.4880
12	$(D_{21})_0 \times 10^5$	0.0844	0.0844	0.1109
13	$(D_{22})_0 \times 10^5$	5.7601	5.7601	5.7929
14	$(L_{11})_0 \times RT \times 10^9$	3.706	3.739	3.685
15	$(L_{22})_0 \times RT \times 10^9$	4.771	4.795	4.790
16	$(L_{12})_0 \times RT \times 10^9$	−1.845	−1.873	−1.856
17	$(L_{21})_0 \times RT \times 10^9$	−1.785	−1.852	−1.750
18	$\%\Delta_{exp}$[d]	3.3	1.1	5.9

[a] Units: diffusion coefficients, $(D_{ij})_0$, cm²/sec, corresponding to amounts of solute expressed in moles, in flow equations written with flows relative to a solvent-fixed reference frame; Onsager coefficients, $(L_{ij})_0$, are for flow equations expressed in moles of the components. [b] Nomenclature corresponds to that in ref 35. 1 = KBr, 2 = HBr, $\bar{C}_1 = 0.25\ M$, $\bar{C}_2 = 0.10\ M$. [c] Calculations in column 1 were made using the best activity and diffusion data, those in column 2 using the best D_{ij} and the more approximate activity data, those in column 3 using the best activity data but D_{ij} at the estimated limit of error corresponding to the upper sign in Table III. [d] Calculated using the equation: $\%\Delta_{exp} = 100 \times \{(L_{12} - L_{21})/[(L_{12} + L_{21})/2]\}_{exp}$.

method iteration was rapid for the starting values of p_0 and $(\sqrt{\sigma_+})_0$ taken from the "area" method results. For the particular system studied here, only two iterations were needed before the $\Delta p/p$ and $\Delta\sqrt{\sigma_+}/\sqrt{\sigma_+}$ ratios were both less than the specified cut-off value, 10^{-6}. The figure 10^{-6} was chosen on the basis of tests of the method using p_0 and $(\sqrt{\sigma_+})_0$ values which were purposely in error. These tests showed rapid convergence to a point where the ratios were about 10^{-6}, while further convergence was much slower. For some starting values, the ratios converged to about 10^{-6}, then diverged slightly as iteration was continued. This is believed due to uncertainty in the value of J, the total number of fringes. Errors in J will be reflected in the values of $f(\zeta)$. Even for the case where the uncertainty in J is taken to be 0.01 fringe, one is justified in using only five decimal places in the value of $f(\zeta)$.[25,45,46] This limits, in turn, the accuracy with which the values of y can be computed, and this may account for the fact that the ratios $\Delta p/p$ and $\Delta\sqrt{\sigma_+}/\sqrt{\sigma_+}$ do not continue to decrease with further iteration.

From Table III it is evident that for this system, the values of the D_{ij} as calculated by the "area" and "least-squares" methods agree well within the estimated experimental error.[47] Furthermore, the average values of $(\Omega - \Omega_E)$ and of $(Q - Q_E)$ are not significantly different for the two calculation procedures. The observed values for $(\Omega - \Omega_E)_{av}$ and $(Q - Q_E)_{av}$ are

(45) G. Kegeles and L. J. Gosting, *J. Amer. Chem. Soc.*, **69**, 2516 (1947).

(46) L. J. Gosting and L. Onsager, *ibid.*, **74**, 6066 (1952).

(47) The characteristics of the Dunn and Hatfield method[12] are such that if the "area" and the new "least-squares" methods give very similar results, then the Dunn and Hatfield method will not give significantly different values for the D_{ij}. Thus, it was not necessary to perform the calculations for this particular system using the Dunn and Hatfield approach.

slightly smaller for the new method (as expected) though the values for the two methods agree to considerably better than the estimated uncertainties ($\pm 2 \times 10^{-4}$) in these quantities.

The new "least-squares" method has been presented as a logical culmination to the series of computation procedures which have been developed by Gosting and his coworkers.[6-11] Although for the particular system used here, the "area" and the "least-squares" methods give very nearly the same results, nevertheless the new calculation procedure is a theoretical improvement for the types of data currently used, and it should prove valuable for other systems to be studied in the future.

B. Test of the ORR. Line 18 of Table V shows the percentage deviation from equality of the values for $(L_{12})_0$ and $(L_{21})_0$. Using what is judged to be the best diffusion data ("least squares") and the best activity data (column 1), a disagreement of 3.3% was found, similar to results found for systems tested previously.[28,35] This figure is not affected by use of D_{ij} values from the "area" method.

The most direct way to test whether this 3.3% discrepancy is within expected errors is to recalculate $(L_{12})_0$ and $(L_{21})_0$ using activity data and values for D_{ij} which are estimated to be at the limits of experimental errors. The results of such calculations are given in columns 2 and 3 of Table V. Use of the "best" diffusion data, along with what is felt to be more approximate activity data is seen to *improve* the agreement in the $(L_{12})_0$ and $(L_{21})_0$ results by 2.2% (column 2). This presumably fortuitous result emphasizes the need for accurate values for all data used in testing the ORR. The results given in column 3 show that errors in the D_{ij} values can affect the agreement between $(L_{12})_0$ and $(L_{21})_0$ by $\pm 2.6\%$ (depending on whether the error limits for D_{ij} correspond to the upper or lower sign in the uncertainities given in Table III). For this system, then, the total estimated error in the ORR calculations, $\%\Delta_{est}$, is about 4.8%, arising about equally from uncertainties in activity data (2.2%) and in D_{ij} values (2.6%). It is seen that $\%\Delta_{est}$ is larger than the 3.3% observed difference between the Onsager cross coefficients, and therefore the ORR is verified within experimental error.

C. $(D_{ij})_V$ Values. The results given in Table III are in qualitative agreement with what one might expect from elementary physical chemical principles. Thus, the main diffusion coefficient for HBr ($D_{22} = 5.75 \times 10^{-5}$ cm²/sec) is much larger than the value of the binary diffusion coefficient of 0.1 *M* HBr in water,[48] $D_{HBr} = 3.15 \times 10^{-5}$ cm²/sec. The KBr which is present in the ternary solution acts as a "swamping electrolyte" and reduces the drag on the (more mobile) H^+ ion due to Br^- ion, thereby increasing the HBr diffusion coefficient relative to that in the two-component HBr–H_2O system. The main diffusion coefficient for KBr (D_{11}) is very nearly equal to its binary value of 1.87×10^{-5} cm²/sec in 0.25 *M* solution.[48] This behavior is in agreement with the idea that the addition of another electrolyte will have little effect on the diffusion of KBr since the K^+ and Br^- ions have very nearly the same mobility. The very large, negative value of the cross-term diffusion coefficient D_{12} is expected from the concept of the "diffusion potential."[13] The tendency of H^+ ion to move ahead of the less mobile Br^- ion creates an electric potential gradient, which, in turn, induces a movement of K^+ ion in a direction opposite to that in which the H^+ ion is moving. In this case, the effect is so large that the cross coefficient for KBr is of the same magnitude as the main diffusion coefficient for KBr. Finally, the similar mobilities of K^+ and Br^- ions imply that the KBr will create only a small "diffusion potential" so that the cross coefficient for HBr, D_{21}, should be small, as is observed.

Gosting[13] has presented an elementary theory which may be used to estimate D_{ij} values for systems of electrolytes. In this approach the main assumption is that the cross-term diffusion coefficients arise only through the "diffusion potential." Comparison of the measured D_{ij} values with those computed from the Gosting theory shows excellent qualitative agreement, both in sign and magnitude.

The system KBr–HBr–H_2O was chosen for investigation as part of a wider program to study diffusion in three and four-component systems containing KBr, HBr, Bu_4NBr, and H_2O. The project is aimed at studying the influence of hydrogen ion transport on the diffusion of other electrolytes. The transport of H^+ ion can be modified through use of the "water-structuring" agent Bu_4NBr.[49] The fact that diffusion results in the KBr–HBr–H_2O system can be semiquantitatively understood in terms of the simple electrostatic concepts discussed above will be of great help in interpreting the results from the four-component studies.

Acknowledgments. The author wishes to express his appreciation to Professor L. J. Gosting for his assistance and encouragement during this work. The manuscript was written after his untimely death, and it is poorer for lack of his critical comments. Thanks are also due to Professor H. Kim for extensive discussions about the overall diffusion study, and to Dr. M. Loewenstein for reading the manuscript.

Appendix I

Equations for the Derivatives Used in the Gauss Method for Fitting the Theoretical Equation for Ω vs. $f(\zeta)$ to the Experimental Data. Subscript j and superscript i are

(48) R. H. Stokes, *J. Amer. Chem. Soc.*, **72**, 2243 (1950). The diffusion coefficient for HBr in 0.1 *M* aqueous solution was confirmed by A. Revzin as part of an experiment to test the purity of the HBr.

(49) H. Kim, work in progress.

dropped for convenience. By differentiation of eq 5, one finds

$$\frac{\partial\Omega}{\partial p} = \frac{1}{w(p-1)^2}[(p\sqrt{\sigma_+} - w)\exp\{-\sqrt{\sigma_+}^2y^2\} + p(w - \sqrt{\sigma_+})\exp\{-p^2\sqrt{\sigma_+}^2y^2\}] - \frac{1}{w(p-1)} \times \left[\sqrt{\sigma_+}\exp\{-\sqrt{\sigma_+}^2y^2\} + (p\sqrt{\sigma_+} - w) \times \left(-2\sqrt{\sigma_+}^2y\frac{\partial y}{\partial p}\right)\exp\{-\sqrt{\sigma_+}^2y^2\} + (w - \sqrt{\sigma_+}) \times \exp\{-p^2\sqrt{\sigma_+}^2y^2\} + p(w - \sqrt{\sigma_+}) \times \left(-2p\sqrt{\sigma_+}^2y^2 - 2p^2\sqrt{\sigma_+}^2y\frac{\partial y}{\partial p}\right)\exp\{-p^2\sqrt{\sigma_+}^2y^2\}\right] \quad \text{(I-1)}$$

$$\frac{\partial\Omega}{\partial\sqrt{\sigma_+}} = -\frac{1}{w(p-1)}\left[p\exp\{-\sqrt{\sigma_+}^2y^2\} + (p\sqrt{\sigma_+} - w)\left(-2\sqrt{\sigma_+}y^2 - 2\sqrt{\sigma_+}^2y\frac{\partial y}{\partial\sqrt{\sigma_+}}\right) \times \exp\{-\sqrt{\sigma_+}^2y^2\} - p\exp\{-p^2\sqrt{\sigma_+}^2y^2\} + p(w - \sqrt{\sigma_+})\left(-2p^2\sqrt{\sigma_+}y^2 - 2p^2\sqrt{\sigma_+}^2y \times \frac{\partial y}{\partial\sqrt{\sigma_+}}\right)\exp(-p^2\sqrt{\sigma_+}^2y^2)\right] \quad \text{(I-2)}$$

Values for y, $\partial y/\partial p$, and $\partial y/\partial\sqrt{\sigma_+}$ are found from eq I-3 below, which was derived by combining eq 4, 5, 15, and A5 of ref 10 to give

$$f(\zeta) = \frac{(w - p\sqrt{\sigma_+})}{\sqrt{\sigma_+}(1-p)}f(\sqrt{\sigma_+}y) + \frac{(\sqrt{\sigma_+} - w)}{\sqrt{\sigma_+}(1-p)}f(p\sqrt{\sigma_+}y) \quad \text{(I-3)}$$

where

$$f(u) = \frac{2}{\sqrt{\pi}}\left(\int_0^u e^{-B^2}dB - ue^{-u^2}\right)$$

Implicit differentiation of eq I-3 yields the desired derivatives, $\partial y/\partial p$ and $\partial y/\partial\sqrt{\sigma_+}$ (since $\partial f(\zeta)/\partial p = 0$ and $\partial f(\zeta)/\partial\sqrt{\sigma_+} = 0$ in this differentiation).

$$\frac{\partial y}{\partial p} = \frac{\left\{\frac{(\sqrt{\sigma_+} - w)}{(1-p)}[f(\sqrt{\sigma_+}y) - f(p\sqrt{\sigma_+}y)] - \frac{4}{\sqrt{\pi}}(\sqrt{\sigma_+} - w)p^2\sqrt{\sigma_+}^3y^3\exp\{-p^2\sqrt{\sigma_+}^2y^2\}\right\}}{\frac{4}{\sqrt{\pi}}\sqrt{\sigma_+}^3y^2[(w - p\sqrt{\sigma_+})\exp\{-\sqrt{\sigma_+}^2y^2\} + - p^3(\sqrt{\sigma_+} - w)\exp\{-p^2\sqrt{\sigma_+}^2y^2\}]} \quad \text{(I-4)}$$

$$\frac{\partial y}{\partial\sqrt{\sigma_+}} = \frac{\left\{\frac{w}{\sqrt{\sigma_+}^2}[f(\sqrt{\sigma_+}y) - f(p\sqrt{\sigma_+}y)] - \frac{4}{\sqrt{\pi}} \times \sqrt{\sigma_+}y^3[(w - p\sqrt{\sigma_+})\exp\{-\sqrt{\sigma_+}^2y^2\} + p^3(\sqrt{\sigma_+} - w)\exp\{-p^2\sqrt{\sigma_+}^2y^2\}]\right\}}{\frac{4}{\sqrt{\pi}}\sqrt{\sigma_+}^2y^2[(w - p\sqrt{\sigma_+})\exp\{-\sqrt{\sigma_+}^2y^2\} + p^3(\sqrt{\sigma_+} - w)\exp\{-p^2\sqrt{\sigma_+}^2y^2\}]} \quad \text{(I-5)}$$

Finally, one must determine the value of y for the particular $f(\zeta)$, w, p_0, and $(\sqrt{\sigma_+})_0$ under consideration. This value is readily obtained from eq I-3 by using the Newton–Raphson method[18] to find the value of y which satisfies

$$F(y) = \frac{[w - p_0(\sqrt{\sigma_+})_0]}{(\sqrt{\sigma_+})_0(1-p_0)}f[(\sqrt{\sigma_+})_0y] + \frac{[(\sqrt{\sigma_+})_0 - w]}{(\sqrt{\sigma_+})_0(1-p_0)}f[p_0(\sqrt{\sigma_+})_0y] - f(\zeta) = 0 \quad \text{(I-3')}$$

The Newton–Raphson method involves assuming an initial value for y ($y = y_0$), then solving for a correction

$$h = \frac{-F(y_0)}{[\partial F(y_0)/\partial y]} \quad \text{(I-6)}$$

The process is repeated using $(y_0 + h)$ as the starting value, and the iteration is continued until satisfactory convergence is obtained. The derivative of $F(y)$ with respect to y is

$$\frac{dF(y)}{dy} = \frac{[w - p_0(\sqrt{\sigma_+})_0]}{(\sqrt{\sigma_+})_0(1-p_0)}\left[\frac{4}{\sqrt{\pi}}(\sqrt{\sigma_+})_0^3y^2 \times \exp\{-(\sqrt{\sigma_+})_0^2y^2\}\right] + \frac{[(\sqrt{\sigma_+})_0 - w]}{(\sqrt{\sigma_+})_0(1-p_0)} \times \left[\frac{4}{\sqrt{\pi}}p_0^3(\sqrt{\sigma_+})_0^3y^2\exp\{-p_0^2(\sqrt{\sigma_+})_0^2y^2\}\right] \quad \text{(I-7)}$$

Good starting values for y are obtained from the equation

$$y_0 = \frac{\zeta\sqrt{\mathfrak{D}_A}}{1 + \frac{2\zeta}{\sqrt{\pi}}\frac{\partial\Omega}{\partial f(\zeta)}} \quad \text{(I-8)}$$

which is derived by combining eq 34 and 37 of ref 14 with eq 9 of ref 8. Values of $d\Omega/df(\zeta)$ are adequately approximated by the relation

$$\frac{\partial\Omega_j}{\partial f(\zeta_j)} \simeq \frac{\Omega_{j+1} - \Omega_{j-1}}{f(\zeta_{j+1}) - f(\zeta_{j-1})} \quad \text{(I-9)}$$

The equations in this appendix, then, are sufficient for calculation of the derivatives, $\partial\Omega/\partial p$ and $\partial\Omega/\partial\sqrt{\sigma_+}$, for use in the "normal" equations (see eq 12).

Appendix II

Computation of the D_{ij} from Values of I_A, S_A, p, and $\sqrt{\sigma_+}$. Straightforward algebraic manipulations of eq 30, 31, 57, 58, and 64 of ref 8 along with the definition of $p = \sqrt{\sigma_-}/\sqrt{\sigma_+}$ give the following results

$$\frac{R_1}{R_2}D_{12} = \frac{(I_A - p\sqrt{\sigma_+})(I_A - \sqrt{\sigma_+})(p+1)}{S_A\sqrt{\sigma_+}^3p^2} \quad \text{(II-1)}$$

$$D_{11} = \frac{R_1}{R_2}D_{12} + \frac{I_A(p+1) - p\sqrt{\sigma_+}}{\sqrt{\sigma_+}^3p^2} \quad \text{(II-2)}$$

$$D_{22} = \frac{(1+p^2)}{\sqrt{\sigma_+}^2p^2} - D_{11} \quad \text{(II-3)}$$

$$\frac{R_2}{R_1}D_{21} = D_{22} - \frac{(I_A + S_A)(p+1) - p\sqrt{\sigma_+}}{\sqrt{\sigma_+}^3p^2} \quad \text{(II-4)}$$

Effect of Charge in the Sedimentation Equilibrium of Polymerizing Protein Systems

by G. J. Howlett, P. D. Jeffrey, and L. W. Nichol*

Department of Physical Biochemistry, John Curtin School of Medical Research, Australian National University, Canberra, A.C.T., 2601, Australia *(Received May 8, 1972)*

Equations are developed which describe the distribution at sedimentation equilibrium of a chemically reacting system involving polymeric species bearing net charges. The development is in terms of species defined as electrically neutral in the manner proposed by Casassa and Eisenberg. The differential equations cannot be directly integrated, since the molecular weights and partial specific volumes of the redefined species (as well as the solution density) are functions of total concentration. Expressions for these dependencies are developed from equilibrium dialysis considerations and are used in a numerical integration procedure employing the predictor–corrector method. The results show that when charge is conserved on polymerization, analysis of the distribution for both ideal and nonideal systems is possible in terms of equations derived for nonelectrolytes and, moreover, that nonsuperposition effects in plots of apparent weight-average molecular weight *vs.* total concentration cannot arise as a sole consequence of charge effects. The possibility that a volume change occurs on reaction, leading to nonsuperposition, is also considered. Brief comment is made on the sedimentation equilibrium of systems where charge is not conserved on polymerization and it is shown, for selected models, that the variation of the apparent equilibrium constant with radial distance is small.

Introduction

The elucidation of polymerizing protein systems often involves studies performed at pH values away from the isoelectric point and thus, in relation to sedimentation equilibrium experiments, involves the interpretation of results pertaining to macromolecular species bearing net charges. Frequently, the results are interpreted on the basis of equations formally derived for nonelectrolytes.[1,2] Adams[3] has provided some justification for this approach by examining the problem in terms of the definition of an electrically neutral macromolecular component proposed by Casassa and Eisenberg.[4-6] Adams[3] considered the possibility that the activity coefficients of the monomeric and polymeric species were functions of total concentration; but neglected the concentration dependence of the solution density and of the molecular weights and partial specific volumes of the redefined species. Moreover, cases were not considered where a volume change accompanied polymerization[7] or where charge was not conserved on polymerization.[8] The purpose of this work is to examine these points and by numerical integration procedures to estimate their effect on sedimentation equilibrium distributions.

Theory

Consider a three component system comprising water (component 1), a polymerizing and ionizing

(1) E. T. Adams, Jr., and D. L. Filmer, *Biochemistry*, **5**, 2971 (1966).

(2) G. J. Howlett, P. D. Jeffrey, and L. W. Nichol, *J. Phys. Chem.*, **76**, 777 (1972).

(3) E. T. Adams, Jr., *Biochemistry*, **4**, 1646 (1965).

(4) E. F. Casassa and H. Eisenberg, *J. Phys. Chem.*, **64**, 753 (1960).

(5) E. F. Casassa and H. Eisenberg, *ibid.*, **65**, 427 (1961).

(6) E. F. Casassa and H. Eisenberg, *Advan. Protein Chem.*, **19**, 287 (1964).

(7) G. J. Howlett, P. D. Jeffrey, and L. W. Nichol, *J. Phys. Chem.*, **74**, 3607 (1970).

(8) A. J. Sophianopoulos and K. E. Van Holde, *J. Biol. Chem.*, **239**, 2516 (1964).

macromolecule (component 2), and a supporting uni-univalent electrolyte, BX (component 3). The polymerization reaction is represented by $n\mathrm{A} \rightleftharpoons \mathrm{C}$, where n (>1) is the degree of polymerization. Initially, cases are considered where charge is conserved on polymerization, viz., $q = np$ where p and q are the net charges borne by A and C, respectively.

The activity of the monomeric species, a_A, may be expressed as[9]

$$\ln a_A = \ln (W_A/M_A) + \ln Y_A + \nu_{2B} \ln (W_B/M_B) + \nu_{2X} \ln (W_X/M_X) \quad (1)$$

where M denotes the molecular weight of a particular species, W the weight of the species per kilogram of solvent, and Y_A is related to the mean ionic activity coefficient on the same scale.[9] The ν_{2j}'s (j = B or X) are the numbers of moles of diffusible species that are included per mole of monomer in the formulation of component 2 as an electrically neutral component. The choice of values of ν_{2j} made in this work is that suggested by Casassa and Eisenberg,[4-6] who visualized an equilibrium dialysis experiment involving the three components and showed that equating the inner and outer salt concentrations led to the effective elimination of the following partial derivatives

$$\left(\frac{\partial \ln a_2^*}{\partial W_3}\right)_{P,T,W_2^*} = \left(\frac{\partial \ln a_3}{\partial W_2^*}\right)_{P,T,W_3} = 0 \quad (2)$$

All quantities consistent with the definition are marked by asterisks. The chemical potential of component 2 per mole, μ_2^*, may be written as

$$\mu_2^* = \mu_2^{0*} + RT \ln a_2^* \quad (3)$$

where μ_2^{0*} is the reference chemical potential. It follows from eq 2 and 3 that μ_2^* is independent of the weight molality of component 3 and that at equilibrium

$$n\left(\frac{\partial \mu_A^*}{\partial W_3}\right)_{P,T,W_2^*} = \left(\frac{\partial \mu_C^*}{\partial W_3}\right)_{P,T,W_2^*} = 0 \quad (4)$$

Thus, at constant temperature, μ_A^* is a function only of W_A^*, W_C^*, and pressure, P.

$$\frac{d\mu_A^*}{dr} = \left(\frac{\partial \mu_A^*}{\partial W_A^*}\right)_{P,W_C^*} \frac{dW_A^*}{dr} + \left(\frac{\partial \mu_A^*}{\partial W_C^*}\right)_{W_A^*,P} \frac{dW_C^*}{dr} + \left(\frac{\partial \mu_A^*}{\partial P}\right)_{W_A^*,W_C^*} \frac{dP}{dr} \quad (5)$$

Substitution in eq 5 of $dP/dr = r\omega^2\rho$, $(\partial\mu_A^*/\partial P) = \bar{v}_A^* M_A^*$ and the sedimentation equilibrium condition[10] $(\partial\mu_A^*/\partial r)_T = r\omega^2 M_A^*$ yields

$$M_A^* r\omega^2(1 - \bar{v}_A^*\rho) = \left(\frac{\partial \mu_A^*}{\partial W_A^*}\right)_{P,W_C^*} \frac{dW_A^*}{dr} + \left(\frac{\partial \mu_A^*}{\partial W_C^*}\right)_{W_A^*,P} \frac{dW_C^*}{dr} \quad (6)$$

where r is the radial distance, ω the angular velocity, and $\bar{v}_A^*$ the partial weight molal volume.

An expression for the right-hand side of eq 6 is available as follows. First, eq 3 is rewritten on a weight molal scale for species A such that $a_A^* = \gamma_A^* W_A^*$, where γ_A^* is the activity coefficient on the same scale. Second, ln γ_A^* is written as a power series in W_2^* $(= W_A^* + W_C^*)$ and truncated after the first term, so that

$$\gamma_A^* = e^{B_A^* M_A^* W_2^*} \quad (7)$$

where B_A^* is a constant expressing nonideality. Third, the resultant expression for μ_A^* is partially differentiated with respect to W_A^* and (separately) W_C^*. It follows that

$$\frac{d \ln W_A^*}{d(r^2)} + B_A^* \frac{dM_A^* W_2^*}{d(r^2)} = L_A^* M_A^* \quad (8a)$$

where

$$L_A^* = (1 - \bar{v}_A^*\rho)\omega^2/2RT \quad (8b)$$

An entirely analogous procedure (defining $\gamma_C^* = e^{B_C^* M_C^* W_2^*}$) may be used to obtain an expression for $L_C^* M_C^*$, which may be added to eq 8a to give

$$\frac{dW_A^*}{d(r^2)} + \frac{dW_C^*}{d(r^2)} = L_A^* M_A^* W_A^* + L_C^* M_C^* W_C^* - \frac{dM_A^* W_2^*}{d(r^2)}(B_A^* W_A^* + nB_C^* W_C^*) \quad (9)$$

The condition $M_C^* = nM_A^*$, used in the formulation of eq 9, applies only for the cases under discussion where charge is conserved on polymerization. Rearrangement of eq 9 by division throughout by W_2^* yields

$$\frac{d \ln W_2^*}{d(r^2)} = \frac{L_A^* M_A^* W_A^* + L_C^* M_C^* W_C^* - W_2^*(B_A^* W_A^* + nB_C^* W_C^*)dM_A^*/d(r^2)}{W_2^*(1 + B_A^* M_A^* W_A^* + B_C^* M_C^* W_C^*)} \quad (10)$$

In what follows it is assumed that $B_A^* = B_C^* = B^*$. Braswell[11] has provided some justification for this assumption on the basis of the Debye–Hückel theory when charge is conserved. The molal volume change for the reaction may be defined as

$$\Delta V^* = M_C^* \bar{v}_C^* - nM_A^* \bar{v}_A^* \quad (11)$$

and an apparent weight-average molecular weight as[2]

$$M_w^*(r)_{app} = \frac{1}{L_A^*} \frac{d \ln W_2^*}{d(r^2)} \quad (12)$$

Combination of eq 10, 11, and 12 gives

(9) G. Scatchard, *J. Amer. Chem. Soc.*, **68**, 2315 (1946).

(10) H. Fujita in "Mathematical Theory of Sedimentation Analysis," Academic Press, New York, N. Y., 1962.

(11) E. Braswell, *J. Phys. Chem.*, **72**, 2477 (1968).

$$M_W^*(r)_{app} = \frac{\dfrac{M_A^*W_A^* + M_C^*W_C^*}{W_2^*} - \dfrac{\Delta V^*\rho W_C^*}{(1 - \bar{v}_A^*\rho)W_2^*} - \dfrac{\dfrac{B^*(W_A^* + nW_C^*)}{L_A^*}\dfrac{dM_A^*}{d(r^2)}}{(1 + B^*M_A^*W_A^* + B^*M_C^*W_C^*)} \quad (13)$$

The last term in the numerator of eq 13 arises by virtue of the definitions of the activity coefficients in terms of M_A^* and M_C^*, which will be shown later to be functions of total concentration and hence of r. Omission of this term, which is negligible in practice, leads to the formal identification of eq 13 with eq 16 of Howlett, *et al.*,[2] which was derived for a nonelectrolyte on the basis of a weight per unit volume scale. Moreover, the treatment is then consistent with eq 36d of Adams[3] for cases where $\Delta V^* = 0$.

Equation 13 embodies a description of the nonsuperposition effect which may be seen as follows. An equilibrium constant on the weight molal scale may be defined as

$$X^* = W_C^*\gamma_C^*/(W_A^*\gamma_A^*)^n = W_C^*/(W_A^*)^n \quad (14)$$

since $e^{B^*M_C^*W_2^*}/e^{B^*nM_A^*W_2^*} = 1$ when $M_C^* = nM_A^*$. Let the weight-fraction of the redefined polymeric species be $\alpha^* = W_C^*/W_2^*$. It follows that $W_A^* = (1 - \alpha^*)W_2^*$ and from eq 14

$$\alpha^*/(1 - \alpha^*)^n = X^*(W_2^*)^{n-1} \quad (15)$$

Equation 13 may also be written in terms of α^* to give

$$M_W^*(r)_{app} = M_A^* + [M_C^* - M_A^* - \Delta V^*\rho/(1 - \bar{v}_A^*\rho)]\alpha^* \quad (16)$$

where it has been assumed, for simplicity, that $B^* = 0$. The effect of nonsuperposition occurs when different values of $M_W^*(r)_{app}$ pertain, *at the same value of* W_2^*, when derived from experiments conducted with various values of initial concentration and/or angular velocity. Provided M_A^*, M_C^*, $\bar{v}_A^*$, and ρ are pressure independent, it follows from eq 15 and 16 that the effect will not arise if $X^*(r)$ is identical at the same W_2^* in the different experiments. However, when $\Delta V^* \neq 0$ the values of $X^*(r)$ (and hence $\alpha^*(r)$) will not be identical when comparisons are made at the same W_2^*, since $(\partial \ln X^*/\partial P) = -\Delta V^*/RT$, and nonsuperposition will be observed. From eq 11, the statement $\Delta V^* \neq 0$ implies that $\bar{v}_A^* \neq \bar{v}_C^*$ for the case of charge conservation ($M_C^* = nM_A^*$).

It is possible to compute numerical examples on the basis of eq 8, which with $B^* = 0$ may be written for both species as

$$\frac{d \ln W_i^*}{d(r^2)} = L_i^*M_i^* \ (i = A \text{ or } C) \quad (17)$$

The application of eq 17 in an integration procedure requires consideration of the product, $L_i^*M_i^*$, which proves to be a function of total concentration, thereby preventing direct integration.

Without loss of generality, the situation is considered where the monomer bears a net charge of $+p$ and the polymer of $+q$: the gegenions B and X are taken as positive and negative, respectively. Equilibrum dialysis of this system results in the activities of the diffusible ions, B and X, being equal on either side of the membrane and this together with the requirement of electroneutrality yields

$$m_B(m_Ap + m_Cq + m_B) = m_3^2 \quad (18)$$

$$m_X(m_X - m_Ap - m_Cq) = m_3^2 \quad (19)$$

where the symbol m denotes molality and the subscript 3 refers to the solution outside the membrane. It is implied in eq 18 and 19 that the mean ionic activity coefficients of the electrolyte inside and outside the membrane are equal (the ideal Donnan equilibrium[3]). Equation 18 may be solved for m_B and the square root of the discriminant expanded to yield as a first approximation

$$m_B = -\left(\frac{m_Ap + m_Cq}{2}\right) + \left[m_3 + \frac{(m_Ap + m_Cq)^2}{8m_3}\right] \quad (20)$$

or

$$\frac{m_3 - m_B}{m_Ap + m_Cq} = \left[1 - \frac{(m_Ap + m_Cq)}{4m_3}\right]\Big/2 \quad (21)$$

Equation 21 corresponds to the definition of the membrane distribution parameter as used by Eisenberg and Casassa[12] in their treatment of a single ionizing component. The number of moles of B to be included per mole of A is termed $\nu_{A,B}^*$ and in accordance with the chosen definition is

$$\nu_{A,B}^* = \frac{-(m_3 - m_B)p}{m_Ap + m_Cq} = -p\left[1 - \frac{(m_Ap + m_Cq)}{4m_3}\right]\Big/2 \quad (22)$$

Similarly

$$\nu_{A,X}^* = p\left[1 + \frac{(m_Ap + m_Cq)}{4m_3}\right]\Big/2 \quad (23)$$

$$\nu_{C,B}^* = -q\left[1 - \frac{(m_Ap + m_Cq)}{4m_3}\right]\Big/2 \quad (24)$$

$$\nu_{C,X}^* = q\left[1 + \frac{(m_Ap + m_Cq)}{4m_3}\right]\Big/2 \quad (25)$$

It is noted that $\nu_{C,B}^*/\nu_{A,B}^* = \nu_{C,X}^*/\nu_{A,X}^* = q/p$. From these relations it is clear that the $\nu_{i,j}^*$ depends on the composition of the mixture which in the case of a

(12) H. Eisenberg and E. F. Casassa, *J. Polymer Sci.*, **47**, 29 (1960).

polymerizing system varies with total concentration. It is however possible to calculate M_A^* and M_C^* at particular concentrations using eq 22–25 and

$$M_A^* = M_A + \nu_{A,B}^* M_B + \nu_{A,X}^* M_X \quad (26)$$

$$M_C^* = M_C + \nu_{C,B}^* M_B + \nu_{C,X}^* M_X \quad (27)$$

It could also be noted that eq 22–27 are consistent with the requirement that $M_C^* = nM_A^*$ when $q = np$. In utilizing eq 22–25 to calculate the $\nu_{i,j}^*$ referring to sedimentation equilibrium, it has been assumed that the equilibrium dialysis condition pertains even after solute redistribution, an assumption assessed by Casassa and Eisenberg[4,6] as reasonable for experiments of usual design where the protein and other solute gradients are not excessive.

It remains to discuss L_i^* or more explicitly the term $(1 - \bar{v}_i^*\rho)$. The appropriate apparent specific volume is given by[5]

$$\phi^* = (\phi + \bar{v}_3\xi)/(1 + \xi) \quad (28a)$$

where ϕ is the apparent specific volume determined by density measurements on undialyzed solutions, $\bar{v}_3$ is the partial specific volume of the salt in the three component system, and

$$\xi = \sum \nu_{2i}^* M_i/M_2 - \sum \nu_{2i} M_i/M_2 \quad (28b)$$

ν_{2i}^* has already been defined and ν_{2i} has the same significance as in eq 1 but with a value chosen appropriate to the determination of ϕ. The apparent specific volumes, ϕ and ϕ^*, are weight molal quantities if weight molal concentrations are used to evaluate them. Although $\bar{v}^* = \phi^* + W_2^*(d\phi^*/dW_2^*)$, it is assumed in what follows that the concentration-dependence term is zero and that the same relations apply to A and C, separately. Thus

$$\bar{v}_i^* = (\phi_i + \bar{v}_3\xi_i)/(1 + \xi_i) \quad (i = A \text{ or } C) \quad (29)$$

where ϕ_i is also regarded as concentration independent. The solution density in the $(1 - \bar{v}_i^*\rho)$ term should be evaluated at the same concentration as $\bar{v}_i^*$ and M_i^*. This is achieved by using the following relation

$$\rho = \frac{W_A^* + W_C^* + 1000 + W_3}{W_A^*\bar{v}_A^* + W_C^*\bar{v}_C^* + (1000 + W_3)/\rho_3} \quad (30)$$

where ρ_3 is the density of a solution of weight-molal concentration W_3. The combined use of eq 22–27 and 28b–30 permits the calculation of $L_i^*M_i^*$ at a particular concentration for use in the numerical integration of eq 17.

Attention is now directed to situations where charge is not conserved on polymerization, $q \neq np$ and $M_C^* \neq nM_A^*$. Equations 22–27 and 28b–30 apply and may be used to calculate $L_i^*M_i^*$ at a series of total concentrations, which suggests that eq 17, based on eq 4, may again be employed in a numerical integration aimed at simulating an approximate sedimentation equilibrium distribution. Since the prime purpose of this work is to examine the effects of charge, it is desirable to eliminate the possible additional effect of an intrinsic volume change on reaction, which has been considered in detail previously.[2,7] Thus, in the following computations ϕ_A is set equal to ϕ_C which leads, for the case of charge conservation, to $\bar{v}_A^* = \bar{v}_C^*$ (eq 22–25, 28b, and 29) and $\Delta V^* = 0$ (eq 11). In contrast, when charge is not conserved, $\bar{v}_A^* \neq \bar{v}_C^*$, even when $\phi_A = \phi_C$, because of the difference in ξ_A and ξ_C.

Results and Discussion

The numerical integration of eq 17 was performed using the predictor–corrector method[13] in the following way. Consider first the simulation of an experiment conducted at selected values of ω and T with a system for which values are assigned to p, q, M_A, M_C (and hence n), M_B, M_X, W_3, $\bar{v}_3$, $\phi_A = \phi_C$, $W_2^*(r_m)$, and $X^*(r_m)$, r_m referring to the meniscus. The latter two quantities define $W_A^*(r_m)$ and $W_C^*(r_m)$, which may be used to obtain first estimates of $m_A(r_m)$ and $m_C(r_m)$ by respective division by M_A and M_C. Equations 22–27 were used to obtain corresponding first estimates of $\nu_{i,j}^*(r_m)$ and $M_i^*(r_m)$, the latter being employed as before, to obtain second estimates of the $m_i(r_m)$. The process was repeated until values of $m_i(r_m)$ converged. The final values of $\nu_{i,j}^*$ were employed in eq 28b–30 to obtain the value of $(1 - \bar{v}_i^*\rho)$ at the meniscus. For this purpose, $\nu_{A,X}$ was equated with p (with $\nu_{A,B} = 0$) and, similarly, $\nu_{C,X}$ was set equal to q (with $\nu_{C,B} = 0$). This set of calculations provides a value of $L_i^*M_i^*$ at the meniscus, which may be used as the starting point in the application of the predictor–corrector method in integrating eq 17. The complete distribution was generated by successively refining values of M_i^*, W_i^*, $\bar{v}_i^*$, and ρ at each increment of r^2 examined. It was then possible utilizing eq 14 to find X^* as a function of r.

Column 1 of Table I shows the results of such calculations performed for an example where $q = np$ and $M_C^* = nM_A^*$ (charge conserved), the values of the parameters being selected to resemble those describing the dimerizing lysozyme system.[8,14] It is clear that X^* is a constant, which is consistent with eq 17 written in the form

$$d \ln[W_C^*/(W_A^*)^n]/d(r^2) = L_C^*M_C^* - nL_A^*M_A^* = 0 \quad (31)$$

As noted previously, the constancy of $X^*(r)$ directly implies that values of $M_W^*(r)_{app}$, defined by eq 12, must be identical in different experiments when comparisons are made at the same value of W_2^*. Thus, the effect of nonsuperposition cannot arise in the sedimentation

(13) D. D. McCraken and W. S. Dorn in "Numerical Methods and Fortran Programming," Wiley, New York, N. Y., 1964, p 330.

(14) R. C. Deonier and J. W. Williams, *Biochemistry*, 9, 4260 (1970).

equilibrium of ideal systems as a consequence of charge effects when charge is conserved during the reaction and the experiments are conducted according to the design suggested by Casassa and Eisenberg.[6] The effect may, of course, arise when charge is conserved, if $\phi_A \neq \phi_C(\bar{v}_A^* \neq \bar{v}_C^*, \Delta V^* \neq 0)$.[2,7] Although $X^*(r)$ is a constant in column 1 of Table I, the values of $\bar{v}_A^* = \bar{v}_C^*$, $M_C^* = nM_A^*$, and ρ, nevertheless, varied with W_2^* (and hence r) in accordance with eq 22–30. The variations were slight, being 0.001% for $\bar{v}_A^*$, 0.003% for M_C^*, and 0.13% for ρ, over the range of r reported in Table I. This observation supports the neglect of the term in eq 13 involving $dM_A^*/d(r^2)$, and indicates that in cases where B^* is also small that nonsuperposition effects will be negligible as a consequence of charge even when nonideal systems are examined ($q = np$).

Table I: Variation of the Apparent Weight Molal Equilibrium Constant, X^*, as a Function of Radial Distance, r, in Sedimentation Equilibrium Experiments[a]

	$X^*(r)$		
r, cm	1	2	3
6.7000	0.03000	0.03000	0.03000
6.7223	0.03000	0.03001	0.03003
6.7816	0.03000	0.03002	0.03011
6.8403	0.03000	0.03003	0.03020
6.8986	0.03000	0.03004	0.03028
6.9563	0.03000	0.03006	0.03036
6.9849	0.03000	0.03007	0.03041
7.0136	0.03000	0.03008	0.03045

[a] All calculations were performed employing the following values of the required parameters: $M_A = 14{,}400$; $n = 2$; $M_B = 23$; $M_X = 35.5$; $\phi_A = \phi_C = 0.726$; $\bar{v}_3 = 0.46$; $W_3 = 0.15$; $W_2^*(r_m) = 4.5$; $X^*(r_m) = 0.03$; $p = 6$. Columns 1, 2, and 3 refer to calculations performed with different values of $q = 12$, 10, and 0, respectively.

Column 2 of Table I shows a systematic variation of the apparent $X^*(r)$ with r, for a case involving lack of charge conservation on dimerization. These variations are in accord with eq 31, since for this case $L_C^*M_C^* - nL_A^*M_A^* \neq 0$. The effect is small, and even when an extreme model is considered, involving the loss of all charges on dimerization (column 3), the variation in $X^*(r)$, while larger, is only ~1%.[15] The system with $q = 0$ was also used to calculate a distribution with $W_2^*(r_m)$ increased from 4.5 (Table I) to 8.0, thereby simulating an experiment with a different initial loading concentration. Equation 12 was used to obtain $M_W^*(r)_{app}$ values from the two simulated distributions, which permitted comparisons to be made at the same values of W_2^*. The effect of nonsuperposition was observed, but the maximum discrepancy was only 0.2%.

In several respects the findings in this study are reassuring to the worker involved in the interpretation of sedimentation equilibrium results obtained with ionizing and polymerizing macromolecular solutes. In cases where charge is conserved on polymerization, it is reasonable to utilize equations derived for nonelectrolytes in the analysis of sedimentation equilibrium distributions. This follows from the close similarity of eq 13 with analogous expressions for the apparent weight-average molecular weight, previously derived.[2,3] Moreover, provided the nonideality coefficient, B^*, is not large and charge is conserved, any observed nonsuperposition in plots of $M_W^*(r)_{app}$ *vs.* W_2^* must be attributed not to a charge effect, but *either* to an intrinsic volume change on reaction ($\phi_A \neq \phi_C$) *or* to one or more of the variety of other causes previously cited.[2] The discussion of lack of charge conservation has been restricted to ideal systems for simplicity. Nevertheless, even when $B_C^* = B_A^* = 0$, X^* was found to vary with r (Table I). The important point, however, is that the related nonsuperposition effect observed with the models selected is very small. It seems to us unlikely that any marked nonsuperposition observed in practice could be attributed solely to a lack of charge conservation.

(15) The procedure permits examination of the effect of changing other variables and in this connection one of our reviewers suggested that the behavior of a system described by a larger association constant would be of interest. Accordingly, the calculations referred to in column 3 of Table I were repeated employing a value of $X^*(r_m) = 0.3$, with the result that the apparent $X^*(r)$ again only varied by ~1% over the range of r reported.

Persistent Electrical Polarization in Polyelectrolyte Membranes[1,2]

by Charles Linder and Irving F. Miller*

Polytechnic Institute of Brooklyn, Brooklyn, New York 11201 *(Received February 23, 1972)*

Measurements of persistent electrical polarization as a function of composition, temperature, applied field, molecular weight of the polarizing component, and time were made on a series of membranes containing sodium polystyrenesulfonate in matrices of poly(vinyl alcohol), polyacrylamide, and polyvinylpyrrolidone. The results indicate that the process depends mainly on interactions between components, rather than the intrinsic nature of the components themselves. A model for the process has been developed in which the electret formation and stabilization mechanism involves an ion displacement in the direction of the applied field *via* a positive feedback between the local field and its reactive field component. The model is compatible with experimental data and explains observed saturation effects and the effects of such variables as membrane composition and polarizing temperature, as well as the fact that persistent polarization is compatible with electrical conductivity.

Introduction

The phenomenon of persistent electrical polarization in materials has been of interest for many years. The phenomenon was first conceived as an electrical analog of a magnet by Heaviside[3] in 1885 and was first experimentally demonstrated by Eguchi[4] in 1922 in studies involving carnauba wax. It has been postulated that such polarization phenomena underlie many biological processes such as nerve conduction,[5,6] sight,[7] and auditory processes.[8] In addition, the phenomenon has been used in many commercial devices such as microphones, electrophotography, electrometers, etc.[9-11]

In spite of the fact that persistent electrical polarization phenomena seem to appear in such a wide variety of places, these phenomena are not too well understood. Since most of the early experimental studies were made with carnauba wax, most of the theoretical work has gone into a phenomenological description of the nature of the process in carnauba wax and the dynamics of its decay.[9,12,13] As a result of this, most workers in the field still consider the phenomenon to take place essentially in dielectrics of a parallel plate condenser system.[14]

Based on our present understanding, two different types of phenomena can be distinguished. When polarization is established by charging electrodes, and when the sign of the charge on the surface of the material is the same as the charge on the adjacent electrode, the material is referred to as a homocharged electret. When the charge on the surface is opposite to the charge on the adjacent electrode, the material is referred to as a heterocharged electret.[4,13] Since the rates of formation and decay of homocharged electrets and heterocharged electrets are quite different, it is possible to distinguish between them in the same material.

Studies of homocharged electrets[15-17] indicate that they are formed essentially by absorption of charges by dielectric breakdown of the gas in the space between electrode and dielectric. This process, then, is essentially a contamination process and has not been considered in the present report. On the other hand, heterocharged electrets have been shown to involve volume polarization[18] and have been shown to decay by mechanisms of dielectric relaxation.[7,14] In most cases it is not known whether such heterocharge formation is due to dipole orientation, ion displacement, electron trapping, or some combination of these. Most studies of heterocharged electrets have involved electrical insulators, and workers have postulated their formation

(1) Based on a thesis submitted by Charles Linder in partial fulfillment of the requirements for the Ph.D. degree, Polytechnic Institute of Brooklyn.

(2) The authors gratefully acknowledge partial support for this work from the National Institutes of Health, under Grant No. GM-12013.

(3) O. Heaviside, "Electrical Papers," Vol. 1, Macmillan, New York, N. Y., 1892, p 488.

(4) M. Eguchi, *Jap. J. Phys.*, **1**, 10 (1922).

(5) L. Y. Wei, *Bull. Math. Biophys.*, **31**, 39 (1969).

(6) D. Wobschall, *J. Theor. Biol.*, **21**, 439 (1968).

(7) H. C. Berg, *Biophys. J.*, **8**, 1051 (1968).

(8) E. C. Hughes, Department of Surgery, University of Southern California, private communication.

(9) V. M. Fridkin and I. S. Zheludev, "Photoelectrets and the Electrophotographic Process," Consultants Bureau, New York, N. Y., 1960.

(10) V. A. J. Carbaub, *Electrochem. Technol.*, **6**, 3 (1968).

(11) H. R. Anderson, E. A. Bartkus, and J. A. Reynolds, *IBM J. Res. Develop.*, **15**, 140 (1971).

(12) M. M. Perlman and J. L. Mennier, *J. Appl. Phys.*, **36**, 420 (1965).

(13) F. Gutmann, *Rev. Mod. Phys.*, **20**, 457 (1948).

(14) B. Gross, "Charge Storage in Solid Dielectrics," Elsevier, Amsterdam, 1964.

(15) J. R. Beeler, J. D. Stranathan, and G. G. Wiseman, *J. Chem. Phys.*, **32**, 442 (1960).

(16) R. A. Draughn and A. Catlin, "Electrets," M. Perlman and L. M. Baxt, Ed., Electrochemical Society, New York, N. Y., 1967, p 93.

(17) M. M. Perlman and C. W. Reedyk, ref 16, p 86.

(18) B. Gross and R. J. DeMoraes, *J. Chem. Phys.*, **37**, 710 (1962).

to involve electron trapping[19] in some cases, or ion displacement of ionic impurities in other cases involving insulating plastics.[20,21] In one case, large amounts of persistent heterocharged polarization has been observed in a polyelectrolyte–polyethylene membrane[22] which was a good electrical semiconductor.

In most cases, previous work has involved phenomenological descriptions of the process and qualitative speculation on microscopic models to characterize such heterocharged electret formation. It is the purpose of this report to describe work undertaken to develop a quantitative molecular model for heterocharged electrets.

Experimental Section

Polyelectrolyte membranes were prepared with sodium polystyrenesulfonate (PSSNa) and a polar polymer matrix. The polar polymers used were poly(vinyl alcohol) (PVA), polyacrylamide (PAC), and polyvinylpyrrolidone (PVP). The structure of these materials is shown in Figure 1. The PSSNa, a linear polymer of varying molecular weight, was obtained from Dow Chemical with a 30% impurity of sodium bromide. The material was purified by washing several times in a 90% methanol–water solution, dialyzing it five times against distilled water, and then titrating with carbonate-free 0.01 *N* NaOH to pH 7. PVP was obtained from General Aniline and Film Corp. with the designation K90. PAC was obtained from American Cyanamid Co. with the designation PAM 100, and PVA was obtained from Du Pont, with the designation 72-60 (99–100% hydrolyzed and of intermediate viscosity). All polymers were purified by five dialysis washings against distilled water to remove impurities and then dried *in vacuo* for 24 hr at 50°.

Since all ingredients were water soluble, membranes were prepared by first preparing aqueous solutions of the various ingredients with deionized distilled water and mixing them in the proportion necessary to obtain the desired membrane composition. The membranes were then either cast on a plate of polystyrene or poured into a polystyrene petri dish. The water was then allowed to evaporate in a dust-free environment to form the membrane. The membranes were then preconditioned for 24 hr under vacuum at 60° to drive off most of the water. Although infrared spectra of these membranes indicated no characteristic water peaks, it is likely that some residual water of hydration remained in these membranes. However, since the presence of small amounts of water of hydration probably enhances the effects investigated, no attempt was made to completely dry the membranes.

The electrets were formed and characterized in a temperature-controlled vacuum oven, as shown in Figure 2. The oven, a cylindrical chamber of naval bronze, was able to maintain a controlled temperature to within ±0.2° in the range of 35–98°. The chamber

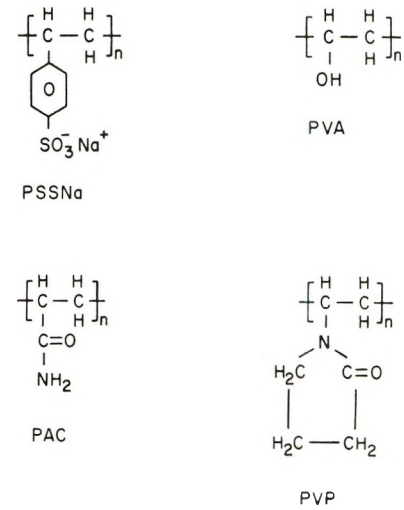

Figure 1. Molecular structure of polymers used.

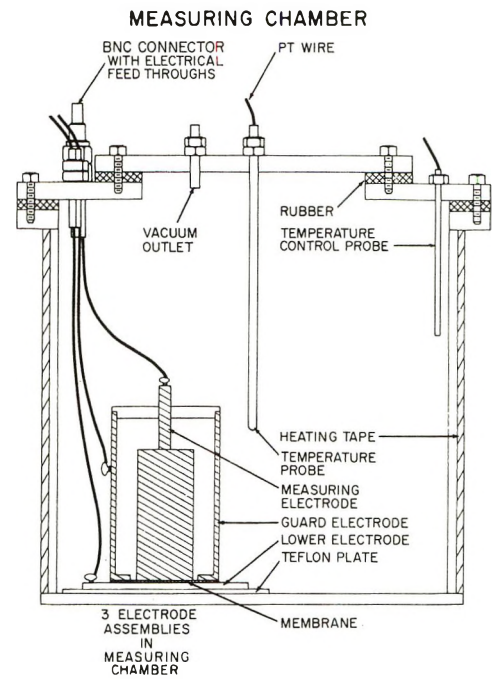

Figure 2. Diagram of polarizing cell.

was designed to hold three membranes at a time between electrodes, all of which were also machined of naval bronze. The weight of the electrodes was used to ensure intimate contact with uniform and constant pressure between the electrodes and membranes. All electrode surfaces were coated with Aquadag (an aqueous carbon suspension from the Anderson Colloids Co.) to reduce corrosion of the electrodes and subsequent membrane contamination.

In an experiment, a membrane was placed between

(19) R. Gerson and J. H. Rohrbaugh, *J. Chem. Phys.*, **23**, 238 (1955).
(20) M. L. Miller, *J. Polym. Sci., Part A-2*, **4**, 685 (1966).
(21) D. K. Donald, ref 16, p 90.
(22) Z. Urban and R. Wallace, *J. Electrochem. Soc.*, **115**, 518 (1968).

the electrodes, the chamber was closed, and a vacuum was established by use of a Welsh Duoseal vacuum pump. The chamber was brought to the desired charging temperature (above ambient conditions), and the material was polarized by placing a 22.5-V battery in series with the membrane–electrode system for an arbitrary time (usually 90 min). During the charging cycle and, subsequently, during the stabilization and discharging cycle the current flowing across the membrane (ranging from about 10^{-10} to 10^{-8} A) was monitored with a Model 610C Keithley electrometer. After a fixed time of charging, the system was cooled to room temperature at about 5°/min, using a fan and Dry Ice under the chamber while maintaining the charging field intact. As in the formation cycle, the membrane current and temperature were recorded throughout.

At room temperature the voltage was removed, and a discharge current was measured with the electrometer. The discharge current, consisting of free capacitor charge and dielectric absorption not frozen in, decayed exponentially by about three orders of magnitude over the 90 min in which the decay current was monitored.

To measure the amount of charge frozen in, the membrane was reheated to 10° above the temperature of polarization at the rate of 2°/min. The depolarization current was measured during the heating process and for an additional time required for the current to decay at least 1.5 orders of magnitude from its peak value at the elevated temperature. The measured current integrated over the time of measurement was taken as the amount of frozen polarization or electret formed per unit volume of the membrane. In all depolarization measurements the currents flowed in the opposite direction from the charging currents, thus indicating heterocharge formation with no sign of homocharge.

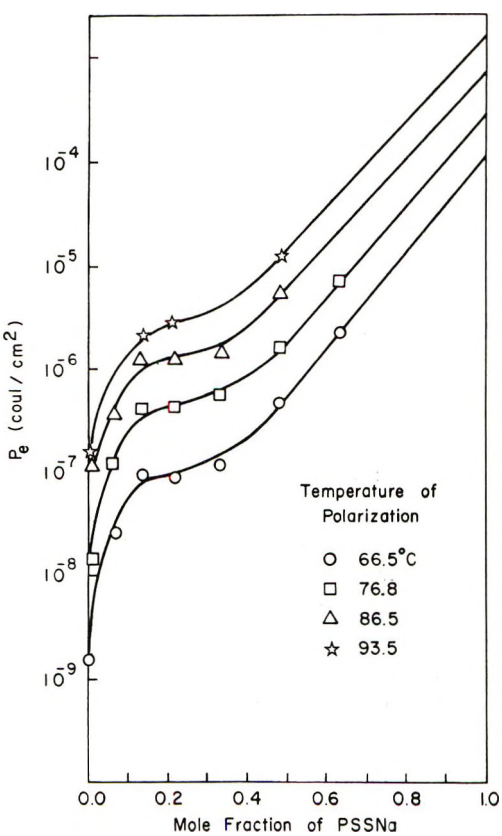

Figure 3. Polarization *vs.* mole fraction of PSSNa in PVA.

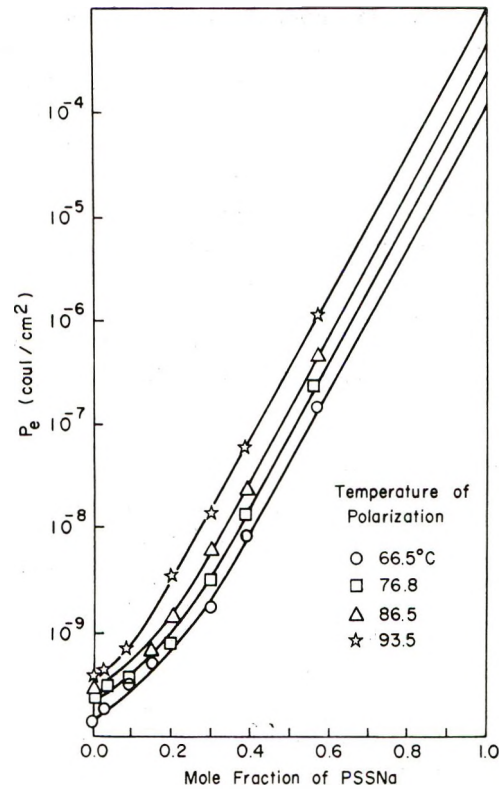

Figure 4. Polarization *vs.* mole fraction of PSSNa in PAC.

Results

Polarization characteristics of the membranes were studied as a function of such variables as membrane composition, molecular weight of the PSSNa, water content, membrane thickness, applied field, and time. The characteristics observed are reported below.

Polarization as a Function of Composition. Figures 3, 4, and 5 present data taken at four different temperatures of persistent polarization in coulombs per square centimeter as a function of the mole fraction of PSSNa in matrices of PVA, PAC, and PVP, respectively. The data presented were obtained on membranes approximately 0.005 cm thick under a potential of 22.5 V maintained for a period of 1.5 hr and represent an average of three separate measurements, with a reproducibility of ±10%. The effect of a variation of these other variables will be discussed below. A number of observations can be made from a comparison of these three figures.

In all three cases a dramatic change in the nature of charge storage seems to occur at a mole fraction of PSSNa in the neighborhood of 0.3–0.4. The reason for

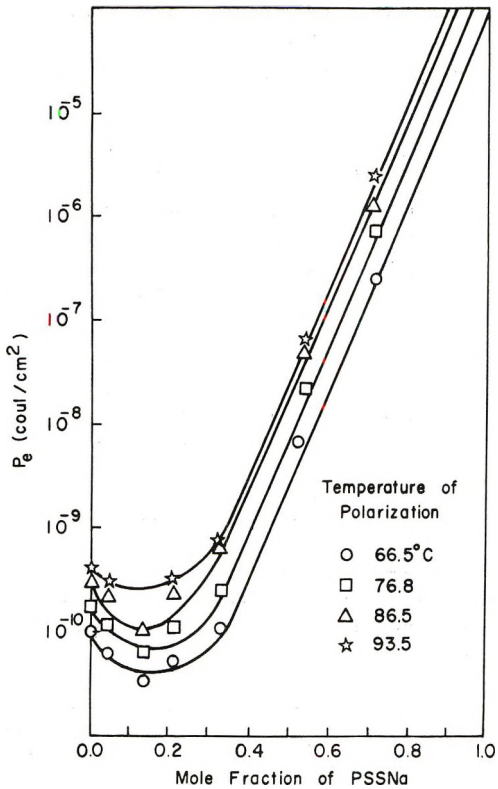

Figure 5. Polarization *vs.* mole fraction of PSSNa in PVP.

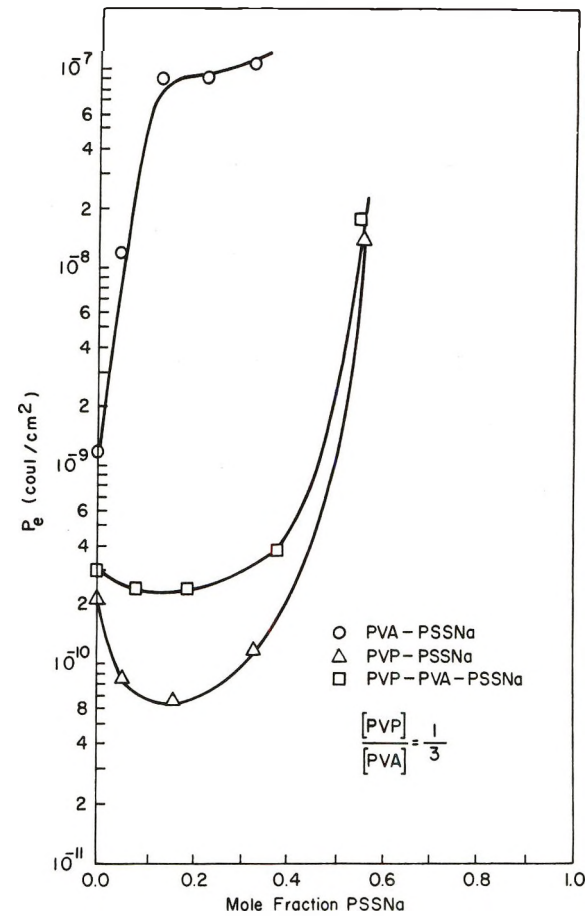

Figure 6. Polarization *vs.* mole fraction of PSSNa in matrices of PVA and PVP. Charging field is 4.5 kV/cm at 70° for 1.5 hr.

this apparent change is probably due to the fact that as the mole fraction of PSSNa increases, the primary molecular process changes from one involving PSSNa–matrix interaction to one involving PSSNa–PSSNa interaction. This will be discussed in more detail below. A comparison of the three figures indicates that the PVA matrix membrane stores the most charge, the PVP matrix membrane stores the least charge, and the PAC matrix membrane is intermediate.

It is clear from the figures that the nature of the matrix has a profound effect on the membrane's charge storage capacity. The addition of PSSNa to PVA increases the charge storage capacity of the membrane by several orders of magnitude. On the other hand, the addition of PSSNa to PVP in small amounts decreases the charge storage capacity of the membrane below that obtained for pure PVP. This difference in behavior is more clearly shown on Figure 6, in which the charge storage capacity for 0.005-cm thick membranes under 22.5 V and 1.5 hr was measured for polarization at 70°. The figure presents data for a PVA–PSSNa membrane, a PVP–PSSNa membrane, and a third membrane in which the matrix contained both PVP and PVA in a ratio of one part of PVP to three parts of PVA (by moles). From this figure it is evident that the PVP–PSSNa interaction is substantially stronger than the PVA–PSSNa interaction. In spite of the fact that the three component membrane contains substantially more PVA than PVP, the membrane behaves much more like a PVP–PSSNa membrane than a PVA–PSSNa membrane. It might also be noted that as the mole fraction of PSSNa increases, all membranes approach a common behavior. The reason for this is that PSSNa–PSSNa interactions become predominant.

Polarization as a Function of Applied Field. Figure 7 presents polarization results as a function of field intensity (volts per centimeter) for three membranes containing PVA (0, 20, and 75% PSSNa) at 70° and one membrane consisting of 33% PSSNa in PAC, with charging for a period of 90 min. The data presented for each membrane were obtained using three different membrane thicknesses, ranging from about 2×10^{-3} cm thick to about 1.5×10^{-2} cm thick. The results for the PVA membranes indicate that a saturation phenomenon occurs with the additional interesting result that those systems which saturate at a higher level of polarization also reach their saturation level at lower levels of applied field. At a given level of polarizing field the amount of polarization is essentially proportional to the number of polarizable groups available (as determined by the membrane volume). In the case of the PAC membrane, no saturation was observed, probably because the fields used were not strong enough.

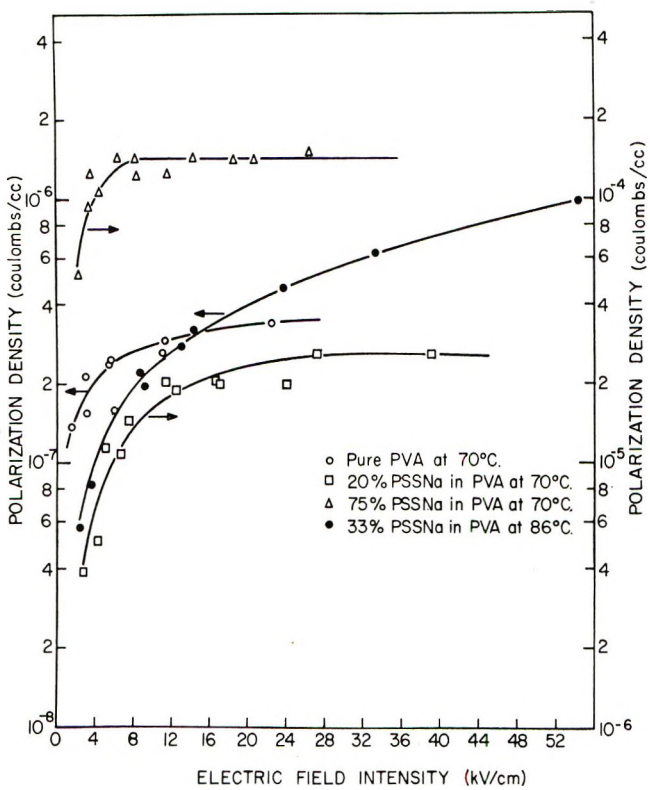

Figure 7. Polarization density *vs.* applied field for three membranes containing PVA at 70° and one membrane containing PAC at 86°.

Polarization as a Function of Molecular Weight of PSSNa. Table I presents data obtained at 70° and a polarizing field of 5 kV/cm on two formulations of PSSNa in PVA. One formulation contains 6.4 mol % PSSNa and the other contains 20 mol % PSSNa. In these formulations the number-average molecular weight of the PSSNa used varied from 194 (sodium *p*-toluenesulfonate) to 1×10^7. The amount of polarization occurring can be seen to increase up to a molecular weight of about 4×10^5 and then gradually to decrease. These results can be explained on the basis of the local density of PSSNa units in the membrane as the molecular weight changes. (The greater the molecular weight, the greater the local density.) It might be noted that at molecular weights greater than 4×10^5 the measured membrane density decreases slowly. This density decrease probably results in a reduction of interaction between adjacent PSSNa units and as a result, the degree of polarization decreases slightly.

Polarization as a Function of Time. Table II presents data on the degree of polarization for three different PSSNa–PVA membranes at 69° and a polarizing field of 4 kV/cm as a function of time. Table III presents similar results obtained with a membrane containing 25% PSSNa in different matrices where polarization was carried out at 86° in a field of approximately 8 kV/cm. As a general observation it might be noted

Table I: Variation of Polarization with Molecular Weight of PSSNa in PVA[a]

Mole fraction of PSSNa	Thickness, cm × 10^{-3}	Density, g/cm³	Molecular weight of PSSNa	P_e, (C/cm²) × 10^7
0.064	4.5	1.20	1.94×10^2	4.21
	4.5	0.98	4×10^4	9.55
	4.2	1.00	4×10^5	16.2
	4.3	1.08	3.8×10^6	13.0
	4.8	0.90	1.0×10^7	12.0
0.20	4.2	1.20	4×10^4	60.5
	4.6	1.21	4×10^5	370
	4.3	1.10	3.8×10^6	295
	4.2	1.00	1.0×10^7	210

[a] Polarization at 70° and 22.5 V.

Table II: Persistent Polarization *vs.* Time of Application of 22 V across PSSNa–PVA Membranes 0.056 mm Thick at 69°

Time, min	P_e, C/cm² × 10^8 75% PSSNa	50% PSSNa	20% PSSNa
15	7.56	5.78	2.70
60	9.20	6.0	3.0
90	11.0	6.18	3.16
180	11.5	6.35	3.36

Table III: Persistent Polarization *vs.* Time of Application of 44 V across Membranes Containing 0.25 Mole Fraction PSSNa in Different Matrices at 86°

Time, min	P_e, C/cm² × 10^9 PVA (0.049 mm)[a]	PAC (0.057 mm)[a]	PVP (0.059 mm)[a]
15	823		
30	946	0.26	0.20
60		0.55	0.26
90	986	0.79	0.28
180	1000	1.45	0.48

[a] The thickness of the membrane is indicated in parentheses.

that those systems which polarize to a much greater degree also seem to reach saturation much more rapidly.

Polarization vs. Conduction. As was mentioned earlier, it has been assumed for many years that persistent polarization and electrical conduction are incompatible in the same system. In all our experiments this was found not to be the case. In fact, in these experiments it was found that systems which polarize to a greater degree also conducted to a greater degree, and the stability of these electrets did not decrease with increasing conductivity. Typical membrane conductivity data obtained for PSSNa in PVA are shown in Figure 8. A comparison of Figure 8 with Figure 3 indicates that, indeed, both processes seem to follow similar trends.

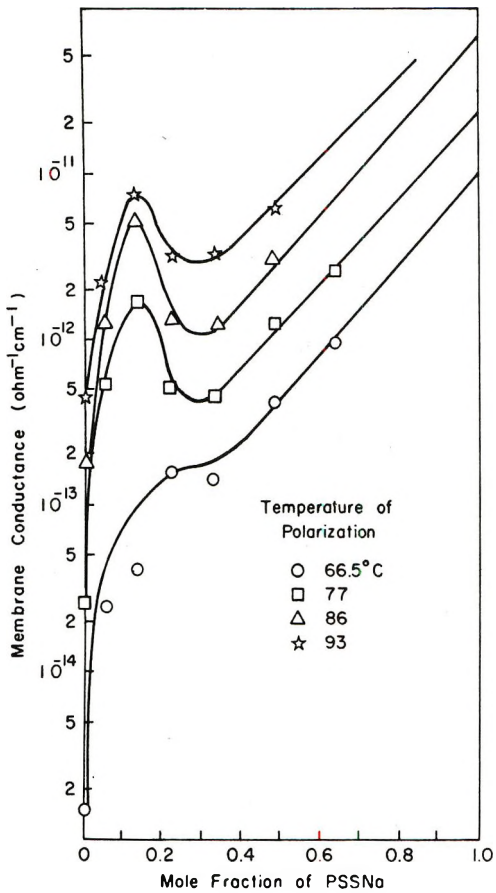

Figure 8. Membrane conductance *vs.* mole fraction PSSNa in PVA.

The implication of these results lies in the fact that the polarization process takes place by a mechanism which is not antagonistic toward the dissipative processes involved in electronic conduction.

Theory

Taken as a whole, the results presented above can be used to develop a molecular model for persistent polarization which is compatible with all the observations, along the following lines. The static dielectric polarization of polar and ionic materials in a condensed phase may be characterized as having a component that follows the applied field, called the instantaneous polarization, $\bar{P}_i$, and another component, out-of-phase with the applied field, which represents persistent polarization, $\bar{P}_e$. The instantaneous polarization, $\bar{P}_i$, is proportional to the applied electric field and disappears when the field is removed. A relationship between the total polarization, $\bar{P}_t$, and the applied electric field, $\bar{E}$, is given by[23]

$$\bar{P}_t = \frac{(\epsilon - 1)}{4\pi}\bar{E} + \bar{P}_e \qquad (1)$$

where ϵ is the static dielectric constant. In highly polarizing systems, ϵ is usually quite large so that, in the absence of the out-of-phase persistent polarization component, $\bar{P}_e$, eq 1 can be written as

$$\epsilon \approx \frac{4\pi\bar{P}_t}{\bar{E}} \qquad (2)$$

The dielectric constant, ϵ, thus characterizes the size of the applied field necessary to give a certain polarization.

Since the external field is also responsible for producing the persistent polarization component, $\bar{P}_e$, one can, by analogy, define an apparent local dielectric constant, ϵ_e, by

$$\epsilon_e = \frac{4\pi\bar{P}_e}{\bar{E}} \qquad (3)$$

In the case of a PSSNa membrane, ϵ_e is a measure of the effect that the local fields, as a function of the applied field, have on the sodium sulfonate dipole with respect to any displacement of the sodium ion, and its consequent reaction with the local environment.

In determining the local field intensity responsible for persistent polarization (electret formation) let us assume that the polarizing group (PSSNa) is in a spherical shell which represents the local environment and whose dielectric constant is ϵ_e. From classical electrostatics,[23] the electric field arising in the sphere of a local environment and polarizing dipole is given by reference to

$$\bar{E}_l = \frac{3\epsilon_e}{2\epsilon_e + \epsilon_{e_2}}\bar{E} \qquad (4)$$

where $\bar{E}_l$ is the local field in the absence of persistent polarization. In the presence of persistent polarization, $\bar{P}_e$, the actual local field, $\bar{E}_i$, is given by

$$\bar{E}_i = \bar{E}_l + \frac{4\pi}{3}\bar{P}_e \qquad (5)$$

Combining eq 3, 4, and 5 one obtains

$$\bar{E}_i = \frac{\epsilon_e(9 + 2\epsilon_e + \epsilon_{e_2})}{3(2\epsilon_e + \epsilon_{e_2})}\bar{E} \qquad (6)$$

which represents the local field at a PSSNa polarizable group when it interacts with other species (matrix molecules) in the environment. In the case where the PSSNa group is likely to be surrounded by the same configuration everywhere in the sample, $\epsilon_e = \epsilon_{e_2}$ and eq 6 reduces to

$$\bar{E}_i = \left(\frac{\epsilon_e}{3} + 1\right)\bar{E} \qquad (7)$$

Let us now consider what happens when an external electric field is applied to a system which can support persistent electrical polarization. Suppose that, ini-

(23) C. J. F. Böttcher, "Theory of Electrical Polarization," Elsevier, Amsterdam, 1952.

tially, the mobile sodium ions are in an equilibrium position associated with a local sulfonate group. When an external field is applied, the mobile sodium ion will be displaced by the field and approach a new site in which the forces acting upon it are in balance. As the ion approaches its new equilibrium position, persistent polarization, $\bar{P}_e$, begins to appear, and the local field intensity increases according to eq 5. The process, therefore, is accelerated by a mechanism which is essentially positive-feedback in nature. That is, a small local field establishes a small degree of persistent polarization which, in turn, increases the local field intensity, which then increases local polarization and so on. The stability of the system of displaced ions, matrix, and electrodes is increased by lowering the temperature and, when the electrodes are removed, the new state remains in metastable equilibrium with the original configuration and will eventually decay to the original configuration in the presence of external disturbances.

Thus, both the initial formation and the stability of the electrets formed depend on the local environments of the polarizing PSSNa units. Clearly, only those PSSNa units that have a proper environment to support the positive-feedback mechanism described above can participate in forming electrets. The saturation phenomena observed during the experimental studies are now readily explainable. The fact that those systems which support the greatest degree of persistent polarization are precisely those systems which come to the saturation level most rapidly (both as a function of time and as a function of external applied field) is a direct consequence of the positive-feedback mechanism in which the local field intensity increases as the degree of persistent polarization increases.

The effects of local membrane morphology are clearly present in the proposed model in terms of the participation of adjacent species to the polarizing groups through their local dielectric constants, ϵ_{e_2}. The apparent change in mechanism for persistent electrical polarization as the mole fraction of PSSNa increases is explainable in terms of the changing probability of finding a polarizable PSSNa group in the presence of a local matrix molecule environment, as opposed to the probability of finding such a PSSNa molecule in the presence of an environment of other PSSNa molecules.

The observation that persistent polarization and electronic conductance seem to go hand in hand is also consistent with this model. An increase in electronic conductance is an indication of an increased mobility of electrons in the membrane. Since ion mobility is the essential first step in ion displacement and stabilization, it should not be incompatible with an increase in electronic conductance.

Molecular Considerations. In the unperturbed state of the membrane a sodium ion may be considered as vibrating about an equilibrium position in the potential well of the sulfonate dipole. If the sodium ion is displaced to an adjacent site in the local environment by the application of an external electric field, the criterion for whether or not the combination of the new site and the sodium ion will remain after the applied field is removed is that the combination of the new site and the sodium ion must produce a potential well of sufficient depth at a temperature below that of polarization. Before the external field is applied, the potential well depth containing the sodium ion is characterized by the energy of a sodium sulfonate interaction, μ_s (in units of kT). The depth of the unoccupied well to which the sodium ion will be displaced is zero, as the well is only produced when the ion is present. Upon displacement of the sodium ion, the well in the field direction has a depth of at least μ_s (assuming an electret structure is formed), and the original well now has a depth of zero. The situation is that of a distortable double well system where the application of a field produces occupancy of the wells lying in the direction of the field and where the combination of environmental distortion and the lowering of the temperature before removal of the field produces the electret state.

The work required to separate the sodium ion from the sulfonate group is a function of the environment in which the dipole finds itself, as shown by

$$\mu_s = \frac{e^2}{4\pi\epsilon_s r k T} \tag{8}$$

where e is 1.6×10^{-19} C, r is the distance of charge separation in meters, and ϵ_s is the self-polarization dielectric constant of the environment. To determine μ_s for the various species studied herein, namely PSSNa, PVA, PAC, and PVP, measurements of ϵ_s for these species were made by extrapolating to time = 0 the ϵ_e values measured for different polarization times over 5-min intervals for a range of 5–20 min at 10 V and 66°. In the case of PSSNa, the measurements were made on a 94% PSSNa–PVA membrane because pure PSSNa is too brittle to work with. If the literature value of $r \approx 1.94 \times 10^{-10}$ m for the PSSNa dipole *in vacuo*[24] is assumed, then μ_s values for the different environments possible can be calculated. The results are presented in Table IV. The results presented in this table clearly indicate that electret formation is easiest in a PSSNa environment and becomes progressively more difficult as the environment shifts from PSSNa to PVA, PAC, or PVP in keeping with the observations.

The magnitude of persistent polarization observed can be taken as the volume density of induced dipoles. Since the only way to measure this polarization is by electrostatic induction of charges on the electrodes of a parallel plate condenser system, the only component of

(24) "Tables of Interatomic Distances and Configurations in Molecules and Ions," *Chem. Soc., Spec. Publ.*, No. 11, M196 (1958).

Table IV: Relative Potential Energy Barrier to Electret Formation (Eq 8)

Environment	ϵ_s	μ_s, units of kT at $T = 69°$
PSSNa	148	1.73
PVA	102	2.46
PAC	40	6.40
PVP	17	15.0

$\bar{P}_e$ that is observable is that component parallel to $\bar{E}$. Thus, $\bar{P}_e$ can be written as

$$\bar{P}_e = \frac{Ner}{V} \tag{9}$$

where N is the number of sodium sulfonate groups forming electret structures, e is the charge of a sodium or sulfonate ion, V is the volume, and r is the average displacement of the sodium ion parallel to the applied field, after the field is removed. The value of N is some fraction of the total number of PSSNa monomer units present. This fraction is made up of simply those units which have the proper environment for electret formation and, if the membrane is assumed homogeneous, this fraction is a function of the mole fraction of PSSNa in the membrane. If the relationship between N and N_a (the total number of PSSNa monomer units present) is known, then r can be calculated from eq 9. The nature of the function depends, of course, on the detailed nature of the typical electret forming unit, which is unknown. However, an attempt was made to estimate the value of r based on some reasonable models for the typical electret forming unit for the system studied. These models were developed from the shape of the experimental curves of polarization *vs.* mole fraction of PSSNa for the three matrices as shown in Figures 3, 4, and 5. The results of these calculations are given below.

PSSNa–PVA Membranes. In the case of all three matrices (PVA, PAC, and PVP) the mechanism of electret formation seems to change when one goes from mole fractions of PSSNa below about 0.33 to mole fractions of PSSNa above 0.33. The reason for this changeover is that, at low concentrations of PSSNa, the typical electret forming unit is in an environment of matrix groups; at high concentrations of PSSNa the typical electret forming unit is in an environment of PSSNa groups. In the case of the PVA matrix, at mole fractions of PSSNa below about 0.33, N, the number of PSSNa units participating in electret formation, was found to vary with mole fraction according to

$$N = N_a X_b^3 X_a \tag{10}$$

where N_a is the total number of PSSNa monomer units, X_a is the mole fraction of PSSNa, and X_b is the mole fraction of PVA ($X_b = 1 - X_a$). At higher concentrations of PSSNa ($X_a > 0.33$), N was found to vary with X_a according to

$$N = N_a X_a^5 \tag{11}$$

Equations 10 and 11 imply that the probability of finding a particular molecular configuration is a function only of the mole fraction of the particular components present. The use of only X_a in the probability function assumes that the PSSNa units are randomly distributed, which is only an approximation in polymeric materials. A polymer chain is of finite dimensions even when completely entangled by a matrix polymer, so that at low concentrations there are areas in the membrane that contain only the matrix. The approximation gets better as the number of PSSNa polymer chains increases to the point where the chains themselves are entangling and as the molecular weight decreases. Thus, the probability of having PSSNa units adjacent to each other should be higher than that calculated using X_a, so that the actual number of PSSNa units undergoing electret formation *via* PSSNa–PSSNa interactions will be higher than the calculated value. Another assumption that occurs in using a probability function solely of X_a is that if a sodium sulfonate group is surrounded by a suitable environment, it is automatically in the proper spatial arrangement to form measurable electrets. Two approximations are involved in this assumption. One is that if two PSSNa units are adjacent to each other, they are oriented so that electret formation may occur. The second is that while the PSSNa units may be properly oriented with respect to each other, the ensemble must have a component parallel to the applied field. The first approximation is not a bad one as the electrostatic interactions between the sodium sulfonate dipoles allow for several associated structures where the most stable one (the negative sulfonate ion associating with the positive sodium ion of the other dipole in a head-to-tail arrangement along the dipole moment of both dipoles) is the optimum arrangement for electret formation. The error due to the second approximation decreases the number of possible PSSNa units involved in electret formation more than that calculated using only X_a. This decrease is opposite to the effect that the approximation of complete spatial randomness of PSSNa monomer units has, such that they would, to some extent, cancel each other.

The implications of eq 10 and 11 with regard to a molecular model for the typical electret structure are as follows. At low concentrations of PSSNa the typical electret-forming structure apparently consists of one PSSNa molecule and three PVA molecules. In this configuration, the charge separation of the PSSNa group is probably stabilized by hydrogen bonding to the three surrounding PVA groups. At higher PSSNa concentrations, where the typical electret structure in-

Table V: The Theoretical Values of the Number of PSSNa Units and the Displacement Distance of Their Na^+ Ions Involved in Electret Formation in PVA–PSSNa Membranes (66° and 22.5 V)

$\bar{P}_e$, C/cm² × 10⁸	X_a, mole fraction of PSSNa	N_a/A,[a] total moles of PSSNa × 10⁵	$V \times 10^5$, cm³	N/N_{satd}	N_1/A,[b] mol	N_2/A,[b] mol	r_1,[c] Å	r_2,[c] Å
2.55	0.059	8.59	7.75	0.43	4.25×10^{-6}	6.0×10^{-11}	0.98	
9.47	0.130	17.0	7.75	0.55	1.46×10^{-5}	5.95×10^{-9}	0.87	
8.87	0.218	13.8	4.71	0.63	1.44×10^{-5}	6.65×10^{-8}	0.54	
11.8	0.328	17.7	4.86	0.68	1.75×10^{-5}	6.35×10^{-7}	0.57	
48.0	0.480	28.0	6.23	0.50	1.89×10^{-5}	7.10×10^{-6}		6.15
230	0.630	34.2	6.54	0.50	1.09×10^{-5}	3.40×10^{-5}		6.65

[a] A = Avogadro's number. [b] N_1 and N_2 are the number of PSSNa units involved in electret formation calculated from eq 10 and 11, respectively. [c] r_1 and r_2 are the distances of Na^+ ion displacement calculated with eq 10 and 11, respectively.

volves interactions between adjacent PSSNa groups, eq 11 implies that the typical electret-forming structure involves five such PSSNa groups, in a stable configuration that also tends to insulate the electret group from the surrounding PVA, a slightly poorer electret forming structure than the PSSNa, as is evidenced from Table IV.

The values of r from eq 9, 10, and 11 were determined for the experiment illustrated as the lowest curve in Figure 3, representing electret formation in a PVA–PSSNa membrane at 66° and an externally applied field of 22.5 V. The results of this calculation are presented in Table V. Since these conditions would not lead to saturation for all the membranes tested, eq 10 and 11 had to be modified slightly to account for the fact that not all configurations capable of forming electrets would actually do so. The appropriate coefficient representing the approach to saturation for the various membranes are also presented in the table. In the table, r_1 represents the distance calculated from eq 9, where N is given by eq 10; r_2 represents the distance calculated when the value of N in eq 9 is given by eq 11. For values of X_a below 0.33, the average value of r is 0.74 ± 0.08 Å. Above $X_a = 0.33$ the average value of r is 6.4 ± 0.25 Å. These values of ion displacement are in the range of what one should expect if the proposed ion displacement model for electret formation is correct. It might be noted that r is considerably larger for the case where the chief mechanism involves PSSNa–PSSNa interactions than it does when the mechanism involves chiefly PSSNa–PVA interactions. This is reasonable since the PVA monomer unit is smaller in size than a PSSNa unit and might be expected to be closer to the polarizing unit.

A linear superposition of eq 9, 10, and 11, along with the average values of r for the range in which it is valid should give a single equation valid over the entire range of X_a. Such a superposition leads to

$$\bar{P}_e = \frac{m_a}{V}[4.04 \times 10^{-6}X_a(1 - X_a)^3 + 4.25 \times 10^{-5}X_a^5] \quad (12)$$

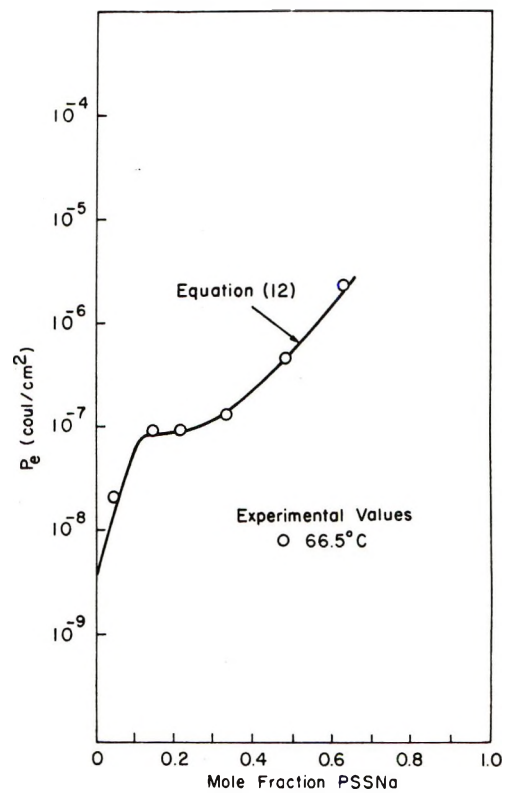

Figure 9. Polarization *vs.* mole fraction of PSSNa in PVA at 66.5° and 22.5 V. Measured values are compared to values predicted by eq 12.

where $\bar{P}_e$ is polarization in coulombs per square centimeter, V is membrane volume under the electrodes in cubic centimeters, and m_a is the number of moles of PSSNa present. In Figure 9, this equation, representing variation of total persistent polarization as a function of mole fraction of PSSNa at 66.5° and an external field of 22.5 V, is plotted along with the measured values of polarization and the equation is found to fit the experimental data extremely well.

As the temperature of electret formation increases above 66°, the total amount of polarization was also found to increase. The question arises as to whether the polarization increase is accounted for by an increase

in the displacement of the sodium ion from its initial site, or rather by an increase in the number of PSSNa units involved. From eq 8, it may be seen that an increase in temperature should lower the potential energy barrier to ion displacement and thus should increase the number of electrets formed. At the same time, however, a temperature increase also increases randomization and the rate in which the sodium ion would return to its initial site. The measured amounts of persistent polarization as a function of temperature and mole fraction of PSSNa in PVA are shown in Table VI. It must be noted from this table that, as the temperature increases from 66 to 93°, the measured amounts of polarization for all membrane formulations increase by about a factor of 25. From Table V it must also be noted that in all cases a substantially larger fraction than $^1/_{25}$ of the available PSSNa groups participate in electret formation (for all cases, the fraction involves approximately one in ten). Thus, while an increase in temperature perhaps does increase the number of PSSNa units contributing to the electret phenomenon, this increase in number can only be a partial explanation for the temperature variation of polarization.

Table VI: Persistent Polarization as a Function of Temperature and Mole Fraction of PSSNa in PVA (at 22.5 V for 1.5 hr)

T, °C	X_a 0.06	0.13	0.22	0.33	0.48	0.63
	P_e, C/cm² × 10⁸					
66	2.55	9.47	8.87	11.8	48.0	230
76.5	12.9	42.4	46.7	56.3	162	700
86.5	34.0	125	116	151	597	...
93	61.0	232	249	295	120	...

Another possible explanation for the large increase in persistent polarization with temperature is that increasing temperature increases the number of possible environmental configurations in which a PSSNa unit may find itself. If such were the case, then the general shape of the $\bar{P}_e$ *vs.* X_a isotherm would change with temperature. However, it does not.

It thus appears likely that the observed polarization increase with temperature is due to the further displacement of the sodium ion from its first jump site to another one further down the field. If one assumes that at the higher temperatures all the membranes are at saturation, then the variation of r with temperature can be calculated from the data in Table VI by use of eq 9, 10, and 11. The results of these calculations are shown in Table VII. These results indeed bear out the contention that the average displacement of the sodium ions increases with increasing temperature. In the PSSNa–PVA system the glass transition temperature is in the range of 76–86°. As the temperature increases from 65 to 93°, the amount of chain movement in response to the thermal energy present increases significantly. Membrane conductance was also found to increase significantly as the temperature was increased. From these considerations then significant increases in ion displacement with temperature are to be expected, and the results presented in Table VII are very reasonable.

Table VII: The Variation of Ion Displacement with the Temperature of Polarization for PSSNa–PVA Membranes[a]

T, °C	X_a 0.06	0.13	0.22	0.33	0.48	0.63
	r, Å					
65	0.98	0.87	0.54	0.57	6.15	6.65
76.5	2.42	2.33	1.75	1.61	14.5	14.1
86.5	6.43	7.03	4.35	4.32	53.5	
93	11.5	12.8	9.33	8.44	107.0	

[a] Membranes of different PSSNa mole fractions.

PSSNa–PVP Membranes. In the same manner as with the PVA system, equations equivalent to eq 10 and 11 can be derived for the PVP matrix system from an analysis of the shape of the lowest PSSNa–PVP curve in Figure 5. For mole fractions of PSSNa greater than 0.33 the appropriate equation is now

$$N = N_a X_a^{10} \tag{13}$$

For mole fractions of PSSNa below 0.33 it was not possible to obtain a single function. However, in the range $X_a < 0.14$ the appropriate equation is

$$N = N_b X_b^3 \tag{14}$$

where N_b is the total number of PVP monomer units and X_b its mole fraction. In the range $0.14 < X_a < 0.33$ the appropriate equation is

$$N = N_a X_a \tag{15}$$

The significance of these equations must be determined from an analysis of what they mean on a molecular level. The inhibiting effect of PVP–PSSNa interactions on electret formation manifests itself by a minimum in the $\bar{P}_e$ *vs.* X_a curves at low PSSNa concentrations and a rapid increase in polarization above a mole fraction of PSSNa of 0.33. At mole fractions of PSSNa greater than 0.33, the basic electret forming units of PSSNa monomers must be well insulated from any contact with the strongly inhibiting PVP. Equation 13 implies that any two interacting PSSNa groups must be insulated from their surroundings by at least eight other PSSNa groups if a local PVP molecule is not to prevent electret formation. In other words, a pair of interacting PSSNa groups must be insulated in a PVP-free region several shells deep.

Table VIII: The Theoretical Values of the Number of PSSNa Units in Moles and the Displacement Distances of Their Na^+ Ions Involved in Electret Formation in PVP–PSSNa Membranes (66° and 22.5 V)

P_e, C/cm² × 10^{10}	X_a, mole fraction of PSSNa	$N_a/A \times 10^4$,[a] total moles of PSSNa	$V \times 10^2$, cm³	N/N_{satd}[b]	N/A, mol	r,[c] Å
1.03	0.33	2.35	7.6		3.55×10^{-9}	4.56
65.5	0.52	3.71	9.1		5.30×10^{-7}	4.52
2360	0.71	2.79	6.4	0.50	9.04×10^{-6}	2.46

[a] A = Avogadro's number. [b] N is calculated from eq 13. [c] r is calculated from eq 9.

At mole fractions of PSSNa below 0.14 the measured amounts of persistent polarization can be attributed exclusively to the polarization of PVP reacting in a configuration involving three PVP units. At these concentrations the PSSNa is so tightly bound to the PVP that it cannot participate in electret formation at all. In the range of mole fractions of PSSNa between 0.14 and 0.33 the presence of the PSSNa begins to make itself felt.

Equations 9 and 13 were used to estimate r, the average amount of sodium ion displacement for PSSNa–PVP electret membranes above a mole fraction of PSSNa of 0.33. The results of these calculations are shown in Table VIII. The average value for sodium ion displacement under these conditions is seen to be $r = 3.85 \pm 0.92$ Å, a reasonable number. An estimate for the value of r for mole fractions of PSSNa below 0.33 was not possible because it was not possible to determine the saturation level of polarization in these systems.

PSSNa–PAC Membranes. The behavior of the PSSNa–PAC system turned out to be intermediate between the PSSNa–PVA system and the PSSNa–PVP system. For a mole fraction of PSSNa greater than 0.33, the appropriate equation for N to be used in eq 9 is

$$N = N_a X_a^7 \qquad (16)$$

The exponent on X_a indicates that the typical electret-forming unit consists of seven PSSNa units. Thus, interacting PSSNa monomer units must be insulated from their surroundings to a slightly greater degree than in the PVA system but not nearly as much as in the PVP system. Below a mole fraction of PSSNa of 0.33 the appropriate equation is identical with eq 10, indicating that PAC does not bind PSSNa to the point where it cannot participate in electret formation at all at these low mole fractions, as in the case of the PVP system. In fact, at these low mole fractions, PAC behaves very much the same way as PVA. The results of the calculation of r, the average displacement of sodium ion in the PAC matrix system, are presented in Table IX. For $X_a > 0.33$, the average value of r turned out to be $r = 2.90 \pm 0.44$ Å, a reasonable value. Again, it was not possible to determine r for values of X_a below 0.33 because polarization saturation for such membranes could not be achieved.

Conclusions

A model for persistent electrical polarization in polymer membranes has been developed in which the electret formation and stabilization mechanism involves an ion displacement in the direction of the applied field *via* a positive feedback between the local field and its reactive field component. The model has been used to explain experimental data involving persistent polarization in membranes consisting of PSSNa in matrices of PVA, PAC, and PVP at various mole fractions. Observed saturation effects have also been explained by the model.

The experimental observations that the chief variables in electret formation involve those variables affecting the interaction of components on a microscopic level rather than the intrinsic nature of the components themselves, are completely in keeping with the proposed ion displacement model.

This work has potentially highly significant implications in biological processes. One such area of application is in nerve excitation. In the currently most widely held view of how nerve cells conduct[25] the nerve cell membrane in the resting state is impermeable to sodium ion and slightly permeable to potassium ion. When a nerve impulse approaches, the permeability of the membrane to sodium changes drastically and sodium is allowed to pass across the nerve membrane. In this view, the membrane permeability to ions is a function only of the membrane potential and can change over several orders of magnitude when the membrane potential is changed. In the view of Tasaki and coworkers[26] in the resting state, the nerve membrane, containing fixed negatively charged sites, also contains divalent cationic counterions (mostly Ca^{2+} and Mg^{2+}). In the process of excitation, in this view, the membrane undergoes rapid reversible transition between two stable configurations which have different physiological properties. In the excited state, in fact, the counter-

(25) A. L. Hodgkin and A. F. Huxley, *J. Physiol.*, **116**, 449, 473, 497 (1952); **117**, 500 (1952).

(26) I. Singer and I. Tasaki in "Biological Membranes," D. Chapman, Ed., Academic Press, New York, N. Y., 1968, Chapter 8.

Table IX: The Theoretical Values of the Number of PSSNa Units in Moles and the Displacement of the Na^+ Ion Involved in Electret Formation in PAC–PSSNa Membranes (66° and 22.5 V)

P_e, C/cm² × 10^9	X_a, mole fraction of PSSNa	$N_a/A \times 10^4$,[a] total moles of PSSNa	$V \times 10^2$, cm³	N/N_{satd}[b]	N/A, mol	r,[c] Å
1.90	0.30	2.12	6.82		4.83×10^{-8}	3.56
8.56	0.39	2.80	7.75		3.84×10^{-7}	2.44
16.0	0.57	3.90	8.66	0.94	7.60×10^{-6}	2.70

[a] A = Avogadro's number. [b] N is calculated from eq 16. [c] r is calculated from eq 9.

ions are chiefly univalent (Na^+ and K^+). More recently[27-29] a number of workers have suggested that the two stable states involve dipole orientation. The ion displacement model for persistent polarization is an extremely attractive one for use in the nerve excitation problem. In this model the amount of persistent polarization possible is clearly a very strong function of the nature of the displaceable ion. The observation that the nerve membrane permeability changes occurring at excitation are a function only of membrane potential is also compatible with the ion displacement model in terms of the effect that such external potentials would have on the microscopic environment of mobile ions. Work on the application of this ion displacement model for persistent electrical polarization in polymer membranes to the problem of nerve membrane conduction is continuing.

(27) L. Y. Wei, *Bull. Math. Biophys.*, 31, 39 (1969).
(28) D. Wobschall, *J. Theor. Biol.*, 21, 439 (1968).
(29) B. B. Hamel and I. Zimmerman, *Biophys. J.*, 10, 1029 (1970).

A Theory for the Dependence of pH on Polyelectrolyte Concentration

by Hiroshi Maeda*

Department of Chemistry, Faculty of Science, Nagoya University, Nagoya, Japan

and Fumio Oosawa

Institute of Molecular Biology and Department of Physics, Faculty of Science, Nagoya University, Nagoya, Japan *(Received April 4, 1972)*

A thermodynamic theory is presented on the dependence of pH of polyelectrolyte solutions on the polymer concentration. This theory is based on both the additivity of the osmotic pressure or the counter ion activity in polyelectrolytes containing low-molecular weight salts and the invariability of the osmotic coefficient or the counter ion activity coefficient with respect to the polymer concentration in salt-free solutions. In salt-free solutions, pH is shown to change in proportion to the logarithm of the polymer concentration. This proportionality holds even when the salts are contained, if the change of the polymer concentration is caused by the removal or the addition of the solvent. In the presence of excess salts, pH becomes independent of the polymer concentration. These results agree well with available experimental data. The theory also gives a procedure for obtaining the osmotic coefficient from the observed relation between the pH and the polymer concentration. Interpretation of the theoretical result is made in terms of the Donnan equilibrium between small ions free in the solvent and those bound on the polymer.

Introduction

In a solution of binary monovalent electrolytes, pH is expected to change in proportion to the square root of the total electrolyte concentration, so long as the Debye–Hückel theory is valid. All interactions between small ions in such a solution are essentially equivalent and may be said to be symmetric. On the contrary, ionic interactions in a polyelectrolyte solution contribute to its thermodynamic properties in different manners. The interaction of polyions with small ions plays a central role, whereas that between polyions is of secondary importance and that between small ions is of

minor importance. This asymmetry of interactions is one of the characteristic features of polyelectrolyte solutions. Owing to this asymmetry, we can not expect that the effect of the polymer concentration on dissociation properties is of the same nature as that caused by the addition of simple salt.

It has been shown that pH of polyelectrolyte solutions decreases in proportion to the logarithm of added salt concentration.[1-3] This peculiar dependence has been explained to arise either from the screening effect of added salt on the interaction between charged sites in a polyion,[1,2] or from the additivity of the counter ion activity.[3] In either case, the logarithmic dependence can be regarded as a manifestation of the most fundamental property of polyelectrolytes.

On the other hand, little has been worked out on the effect of the polymer concentration on pH. No satisfactory procedure has been developed to take into account this effect. In the theory based on a cell model, the effect is taken into account only in terms of the change of the free volume of a polyion. It is not clear, however, whether the polyion–polyion interaction can be sufficiently incorporated in this way. Another approach in terms of the cluster integral involves a great difficulty to evaluate the clusters containing two or more polyions which have many interaction sites.

A purpose of this paper is to present a simple thermodynamic theory on the dependence of pH on the polymer concentration. This approach has an advantage that it suffers little from the troubles mentioned above. The theoretical treatment is based on two experimentally established properties of polyelectrolytes.[4-8] They are the invariability of the osmotic coefficient or the activity coefficient of counter ions in salt-free solutions with respect to the polymer concentration, and the additivity for the osmotic pressure and the counter ion activity.

A simple picture on the interaction of polyions and counter ions is given for understanding of the present result in combination with the previous result on the effect of added salts.[3]

The present result can be used to obtain the osmotic coefficient of salt-free polyelectrolyte solutions from the relation between pH and the polymer concentration.

Theory

Thermodynamic Relations. Let us consider a polyelectrolyte solution containing four components: solvent (w), *e.g.*, H_2O; polyacid (p); alkali (a), *e.g.*, NaOH; and simple salt (s), *e.g.*, NaCl. Let us denote the number of moles of water as n_w and the molalities of solutes as m's with corresponding suffices. Here counter ions from alkali and those from simple salt are assumed to be of the same species. Since we consider the change under constant temperature and pressure, these two variables are not involved explicitly in the present treatment.

The Gibbs free energy of the solution (G) can be written as follows.

$$G = (n_w M_w/10^3)[(10^3/M_w)\mu_w + m_p\mu_p + m_s\mu_s + \alpha x m_p\mu_a] \quad (1)$$

Here M_w represents the molecular weight of water and μ's chemical potentials of components. The degree of neutralization α is defined as $m_a/m_p x$, where x denotes the number of dissociable sites on a polyion. The following relation comes from the differentiation of G with respect to m_p and α.

$$m_p x(\partial\mu_a/\partial m_p)_{m_s,\alpha} = (\partial\mu_p/\partial\alpha)_{m_p,m_s} + \alpha x(\partial\mu_a/\partial\alpha)_{m_p,m_s} \quad (2)$$

From the Gibbs–Duhem relation

$$\partial\mu_p/\partial\alpha + \alpha x(\partial\mu_a/\partial\alpha) = (-1/m_p)[(10^3/M_w)(\partial\mu_w/\partial\alpha) + m_s(\partial\mu_s/\partial\alpha)] \quad (3)$$

Substitution of eq 3 into eq 2 gives

$$\partial\mu_a/\partial m_p = -(1/m_p^2 x)[(10^3/M_w)(\partial\mu_w/\partial\alpha) + m_s(\partial\mu_s/\partial\alpha)] \quad (4)$$

In terms of chemical potentials of ionic species, eq 4 can be rewritten as follows.

$$-(\partial\mu_H/\partial m_p)_{m_s,\alpha} = -(\partial\mu_+/\partial m_p)_{m_s,\alpha} - (\partial\mu_w/\partial m_p)_{m_s,\alpha} - (10^3/m_p^2 x M_w)(\partial\mu_w/\partial\alpha)_{m_p,m_s} - (m_s/m_p^2 x)[(\partial\mu_+/\partial\alpha)_{m_p,m_s} + (\partial\mu_-/\partial\alpha)_{m_p,m_s}] \quad (5)$$

Here μ_+, μ_-, and μ_H represent the chemical potentials of counter ions, coions, and hydrogen ions, respectively.

Dependence of pH on Polymer Concentration. It is necessary to introduce explicit expressions for chemical potentials in order to derive the dependence of pH on polymer concentration from eq 5. We assume the additivities for the osmotic pressure and the counter ion activity. According to these additivities chemical potentials of water and of salt and counter ions in a polyelectrolyte solution containing a low-molecular weight salt can be written in the following way.

$$\mu_w = \mu_w^0 - RT(M_w/10^3)(\phi_p\alpha x m_p + 2\phi_s m_s) \quad (6)$$

Here the contribution from polyions is ignored compared with those from small ions. The quantities ϕ_p

(1) A. Katchalsky and S. Lifson, *J. Polym. Sci.*, **11**, 409 (1953).
(2) G. S. Manning and B. H. Zimm, *J. Chem. Phys.*, **43**, 4250 (1965).
(3) F. Oosawa, *Biopolymers*, **6**, 135 (1968).
(4) R. A. Mock and C. A. Marshall, *J. Polym. Sci.*, **13**, 263 (1954).
(5) M. Nagasawa, M. Izumi, and I. Kagawa, *ibid.*, **37**, 375 (1959).
(6) Z. Alexandrowicz, *ibid.*, **43**, 325,337 (1960); **56**, 115 (1962).
(7) A. M. Liquori, F. Ascoli, C. Botre, V. Crescenzi, and A. Mele, *ibid.*, **40**, 169 (1959).
(8) G. Torrence, S. Amdur, and J. A. Marinsky, *J. Phys. Chem.*, **75**, 2144 (1971).

and ϕ_s denote the osmotic coefficient of the salt-free polyelectrolyte solution and that of the simple salt solution.

$$\mu_s = \mu_s^0 + RT \ln (\gamma_+^p \alpha x m_p + \gamma_+^s m_s)(\gamma_- m_s) \quad (7\text{-}1)$$

and

$$\mu_+ = \mu_+^0 + RT \ln (\gamma_+^p \alpha x m_p + \gamma_+^s m_s) \quad (7\text{-}2)$$

Here γ_+^p and γ_+^s are the activity coefficients of counter ions in the salt-free polyelectrolyte solution and of counter ions in the simple salt solution. Further γ_- denotes the activity coefficient of coions in the polyelectrolyte–simple salt mixture, and is considered to be very close to that in the simple salt solution. Substitution of eq 6 and 7 into eq 5 yields

$$\partial \text{ pH}/\partial \log m_p = -[\gamma_+^p \alpha x m_p + m_s \gamma_+^p (1 + \partial \ln \gamma_+^p / \partial \ln \alpha)]/(\gamma_+^p \alpha x m_p + \gamma_+^s m_s) + \partial(\alpha\phi_p)/\partial\alpha \quad (8)$$

In the transformation from eq 5 to eq 8, we assumed the invariability of γ_+^p with respect to m_p. Moreover, the second term in eq 5, $\partial\mu_w/\partial m_p$, is always negligible owing to a factor, $M_w/10^3$, involved and the third term $\partial\mu/\partial\alpha$ is very small according to the assumed additivities. Equation 8 is a fundamental equation which gives a relation between pH and polymer concentration. According to this equation we will examine the behavior of pH under various conditions.

(*1*) *When Added Salt is Absent* ($m_s = 0$). Under this condition, eq 8 is reduced to

$$\partial \text{ pH}/\partial \log m_p = -1 + \partial(\alpha\phi_p)/\partial\alpha \quad (9)$$

This can be also derived directly from eq 5. Since the rhs of this equation is approximately independent of m_p, this equation clearly demonstrates that pH decreases in proportion to log m_p. Moreover, from this equation we can relate the slope of the pH *vs.* log m_p relation with the osmotic coefficient in the following way.

$$\phi_p = (1/\alpha)\int_0^\alpha (1 + \partial \text{ pH}/\partial \log m_p)\mathrm{d}\alpha \quad (10)$$

By using this equation, we can evaluate the osmotic coefficient from the slope at various degrees of neutralization. If ϕ_p is not sensitive to α, we have approximately the following instead of eq 10

$$\phi_p = 1 + \partial \text{ pH}/\partial \log m_p \quad (11)$$

Then we can obtain ϕ_p directly from the slope. The value of ϕ_p obtained from eq 11 is always smaller than that evaluated by eq 10. It should be stressed that the results obtained here, eq 9–11, are entirely free from the assumption of the additivities, since no added salt is present.

(*2*) *When Salt is Present in Excess* ($m_s \gg xm_p$). Under this condition the counter ion activity becomes almost independent of the polymer concentration, and eq 8 is reduced to

$$\partial \text{ pH}/\partial \log m_p = \partial\alpha(\phi_p - \gamma_+^p/\gamma_+^s)/\partial\alpha \quad (12)$$

To a good approximation, the quantity $(\phi_p - \gamma_+^p/\gamma_+^s)$ is very much smaller than unity for any value of α. Therefore from eq 12, pH does not depend appreciably on the polymer concentration under the condition of excess salt.

(*3*) *Intermediate Region.* On addition of small amount of salts to a salt-free polyelectrolyte solution, a deviation from the linearity characterizing the dependence of pH on polymer concentration in the case of no added salt becomes significant at low polymer concentration, although at high polymer concentration pH still decreases in proportion to log m_p with the same slope. On increasing salt concentration further, a region develops at low polymer concentration where pH does not depend essentially on polymer concentration. Finally at the limit of excess salt, this region grows to such an extent that pH remains constant over a wide range of the polymer concentration. Thus the effect of added salt is to bring a deviation from the linearity observed in the case of no added salt.

An Alternate Approach. We have analyzed the change of pH due to polymer concentration at a constant salt concentration. The results presented in the preceding section are clear-cut under two limiting conditions: of no added salt and of excess salt. On the other hand, the behavior under an intermediate condition has been found to be rather complex and can not be expressed in a simple manner. However, we can have a simple expression valid for any value of the ratio m_s/xm_p, if we follow an alternate approach previously developed.[9]

In this approach, we regard the change of polymer concentration as caused by the removal or the addition of water. Therefore the concentration of salt, if coexisting, is also changed by this process. The change of pH due to dilution is given as follows.

$$(\partial\mu_H/\partial n_w)_{n_p,n_s,\alpha} = -(\partial\mu_w/\partial n_w)_{n_p,n_s} + (\partial\mu_+/\partial n_w)_{n_p,n_s,\alpha} \quad (13)$$

Substitution of eq 6 and 7 into eq 13 yields

$$(\partial \text{ pH}/\partial \log m_p)^* = -(\partial \text{ pH}/\partial \log n_w)_{n_p,n_s,\alpha} = -1 + \partial(\alpha\phi_p)/\partial\alpha \quad (14)$$

Here the term $\partial \ln \gamma_+^p/\partial \ln n_w$ can be ignored as before since $\mathrm{d} \ln n_w = -\mathrm{d} \ln m_p$ for the process under consideration. The variation of γ_+^s with salt concentration is also neglected. The asterisk on the derivative $\partial \text{ pH}/\partial \log m_p$ is used here to distinguish it from the usual one that appeared in the preceding section. Equation 14 shows that the linear relation is

(9) F. Oosawa, *Biopolymers*, 6, 145 (1968).

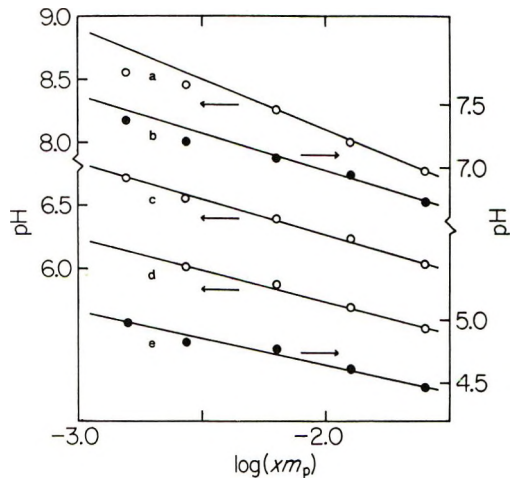

Figure 1. Dependence of pH on polymer concentration in salt-free solutions of poly(methacrylic acid). Circles indicate experimental data taken from the work of Oth and Doty.[10] Degrees of neutralization are (a) 0.75, (b) 0.50, (c) 0.35, (d) 0.20, and (e) 0.08. Polymer concentration is expressed in monomolal. Ordinate on left side refers to open circles and that on right side to filled circles.

satisfied between pH and log m_p at any salt concentration, so long as the change of m_p is caused by the procedure adopted here. Moreover, the slope becomes independent of the ratio $m_s/m_p x$ and identical with that observed in the case of no added salt (eq 9). The dependence of pH on the polymer concentration at a constant salt concentration can be also derived as follows.

Accompanying the change of pH expressed in eq 14, salt concentration is also changed by d ln m_s = −d ln n_w. At a constant polymer concentration the change of pH due to a change in m_s can be written as follows.[3]

$$(\partial \text{ pH}/\partial \log m_s)_{m_p,\alpha} = [m_s\gamma_+^{p}(1 + \partial \ln \gamma_+^{p}/\partial \ln \alpha) - m_s\gamma_+^{s}]/(\gamma_+^{p}\alpha x m_p + \gamma^{s}{}_+ m_s) \quad (15)$$

By means of eq 14 and 15 we can obtain eq 8, if the following relation is applied.

$$(\partial \text{ pH}/\partial \log m_p)_{m_s,\alpha} = (\partial \text{ pH}/\partial \log m_p)^* - (\partial \text{ pH}/\partial \log m_s)_{m_p,\alpha}$$

Application to Experimental Data

In Figure 1 the titration data of poly(methacrylic acid) (PMA), taken from the work of Oth and Doty,[10] are given. As expected in the present theory, linear relations are found between pH and log m_p. Only at the highest degree of neutralization investigated (α = 0.75) small deviation from the linearity is observed for a low-concentration range. It may be due to concentration dependence of osmotic coefficient. Equation 10 can not be used to evaluate the osmotic coefficients because extrapolation of the obtained slope to zero degree of neutralization is difficult on account of a conformational transition to a more compact form (the "a" state).[11] The osmotic coefficients can be tentatively obtained if we assume that the term $\alpha\partial\phi_p/\partial\alpha$ can be ignored as compared with ϕ_p. However, the result thus obtained showed that the term $\alpha\partial\phi_p/\partial\alpha$ had a comparable magnitude with ϕ_p. Hence the validity of the assumption was violated.

Discussion

Let us examine the assumptions used in the present investigation. An assumption employed throughout is the invariability of the osmotic coefficient or the activity coefficient with respect to the polymer concentration. Though this has been introduced as an experimentally established relation, it has been also predicted from a theory[12] and interpreted as a consequence of the asymmetry of interionic interactions in polyelectrolyte solutions.

In addition to this assumption, the additivities are further assumed to analyze salt-containing solutions. The additivity of osmotic pressure, eq 6, has been proven to have a general validity in the case of an infinitely long and thin rod-like polyion.[13−15] To derive the additivity for the counter ion activity from this additivity, it is necessary to assume that the activity coefficient of coions is practically unaffected by the presence of polyions.[13,16] It should be noted, therefore, that the approximate identity of activity coefficients of coions in salt solutions and in polyelectrolyte solutions composes a part of the additivity for the counter ion activity.

Two assumptions assumed here independently, the invariability and the additivity, have a close connection with each other. For example, in theoretical derivation of the latter, the former is an indispensable condition in a theory,[16] or in another theory,[13] it is implicitly satisfied as a consequence of the employed rod model.[12]

In order to clarify essential features involved in eq 8, we analyze this equation from the standpoint of the cell theory. The cell theory of solutions inevitably leads to the conclusion that γ_+^{p} and ϕ_p are equivalent.[13,16] Further we approximate that γ_+^{s} is unity. By means of these approximations, we can reduce eq 8 into a concise form.

$$d\mu_H = (RT/a_+)(1 - \partial\alpha\phi_p/\partial\alpha)(\gamma_+^{p}\alpha x dm_p) \quad (16)$$

(10) A. Oth and P. Doty, *J. Phys. Chem.*, **56**, 43 (1952).

(11) (a) R. Arnold and J. Th. G. Overbeek, *Recl. Trav. Chim. Pays-Bas*, **69**, 192 (1950); (b) J. C. Leyte and M. Mandel, *J. Polym. Sci., Part A-2*, 1879 (1964); (c) M. Mandel, J. C. Leyte, and M. G. Stadhouder, *J. Phys. Chem.*, **71**, 603 (1967).

(12) S. Lifson and A. Katchalsky, *J. Polym. Sci.*, **13**, 43 (1954).

(13) F. Oosawa, *J. Polym. Sci., Part A-1*, 1501 (1963).

(14) G. S. Manning, *J. Chem. Phys.*, **43**, 4260 (1965).

(15) G. S. Manning, *ibid.*, **51**, 924 (1969).

(16) A. Katchalsky and Z. Alexandrowicz, *J. Polym. Sci., Part A-1*, 2093 (1963).

Here a_+ denotes the activity of counter ions, *i.e.*, $a_+ = \gamma_+^{p}\alpha x m_p + m_s$. To the same extent of approximation, eq 15, which is demonstrating the effect of added salt on pH, is reduced to

$$d\mu_H = (RT/a_+)(1 - \partial\gamma_+^{p}\alpha/\partial\alpha)(dm_s) \quad (17)$$

The only difference between eq 16 and 17 resides in the last factors involved in them. These factors, however, can be identified with the change of counter ion activity in respective circumstances. Hence, the effect of the polymer concentration on pH is no more than that caused by a corresponding change in the counter ion activity. Generally, accompanying this change in the counter ion activity, the concentration of counter ions near the surface of a polyion c_+' also changes. In terms of the Donnan equilibria for counter ions and hydrogen ions we have

$$da_H/a_H = da_+/a_+ - dc_+'/c_+' \quad (18)$$

since the concentration of hydrogen ions near the surface of a polyion is determined solely by the degree of neutralization and hence unchanged on the addition of salt or polymer under a constant degree of neutralization. Therefore we can reasonably interpret eq 16 and 17 on the basis of the Donnan equilibria, if the distribution of counter ions be given as

$$dc_+'/da_+ = (c_+'/a_+)(\partial\alpha\phi_p/\partial\alpha) \quad (19)$$

Clearly, ϕ_p or γ_+^{p} is proportional to the number of free counter ions and $\partial(\alpha\phi_p)/\partial\alpha$ is the increase of free counter ions due to the increase of the degree of neutralization. In the case of ideal counter ion condensation, $\partial(\alpha\phi_p)/\partial\alpha = 0$ and therefore $dc_+' = 0$. In general $\partial(\alpha\phi_p)/\partial\alpha$ has a small positive value.

A general expression for the change of pH can be also derived, valid under the present approximation, if we combine eq 16 and 17.

$$d\mu_H = (RT/a_+)(1 - \partial\alpha\phi_p/\partial\alpha)(\gamma_+^{p}\alpha x dm_p + dm_s) = RT(1 - \partial\alpha\phi_p/\partial\alpha)d\ln a_+ \quad (20)$$

It should be remarked that the change in the counter ion activity due to the change of polymer concentration comes from a change of a free volume at a constant number of counter ions, whereas added salts directly change the number of counter ions at a constant free volume.

Next we consider the case that the invariability of activity coefficient or osmotic coefficient is no longer valid. In this case we have the following result for the effect of polymer concentration instead of eq 16.

$$d\mu_H = (RT/a_+)[\alpha x d(\gamma_+^{p}m_p) - (\partial\alpha\phi_p/\partial\alpha)\alpha x\gamma_+^{p}dm_p] \quad (21)$$

The change in the counter ion activity is given as $\alpha x d(\gamma_+^{p}m_p)$ rather than $\alpha x\gamma_+^{p}dm_p$. Rewriting eq 21 into an expression similar to eq 18 we have

$$da_H/a_H = da_+/a_+ - (\partial\alpha\phi_p/\partial\alpha)(\alpha x\gamma_+^{p}dm_p/a_+) \quad (22)$$

The Donnan distribution of counter ions in this case should be

$$dc_+'/da_+ = (c_+'/a_+)(\partial\alpha\phi_p/\partial\alpha)[\gamma_+^{p}\,\partial m_p/\partial(\gamma_+^{p}m_p)] \quad (23)$$

if eq 22 is compared with eq 18.

The Donnan distribution of counter ions will be thus altered if γ_+^{p} is dependent on m_p. However, in the case of ideal counter ion condensation, the concentration of counter ions near the surface of a polyion remains constant and hence the following relation holds irrespective of the dependence of γ_+^{p} on the polymer concentration.

$$d\mu_H = RT\ d\ln a^+ \quad (24)$$

It is pertinent to give a brief discussion about the work of Alexandrowicz and Katchalsky.[17] They analyzed thermodynamic properties of rod-like polyelectrolyte solutions based on the cell theory. One of their results concerning the dependence of pH on concentrations of polymer and salt, eq 41 in ref 17a, involves a term containing a rather complicated parameter β in addition to a term representing the effect due to the counter ion activity. However, it was not clearly examined whether this term behaved in a similar manner as the other term or it could be approximated to be negligible. If we compare the term representing the effect due to the counter ion activity with our result, eq 20, their result differs in the respect that the proportionality factor between pH and log a_+ is always unity whereas it is given by $1 - \partial\alpha\phi_p/\partial\alpha$ in our result.

A brief comment should be added about a usual procedure to extrapolate experimental data to zero polymer concentration in the case of the potentiometric titration. The purpose of this procedure is to obtain the titration behavior of a polyion immersed in a salt solution of an infinite volume. To predict such a behavior is clearly beyond the validity of the present analysis, because it is based on the additivities which are valid only for a finite polymer concentration. If the rhs of eq 12 is zero, the pH converges to a certain value when the polymer concentration is decreased at a constant salt concentration. However, this limiting value of pH can not necessarily be correlated to that which will be expected in the limit that m_p really approaches zero. In the case of no added salt, the presence of a limiting value of pH is also experimentally assured. However, there should be a critical polymer concentration below which the assumption of infinitely long rod becomes invalid. For such an extremely dilute concentration range, counter ion condensation no

(17) (a) Z. Alexandrowicz and A. Katchalsky, *J. Polym. Sci., Part A-1*, 3231 (1963); (b) A. Katchalsky, Z. Alexandrowicz, and O. Kedem, "Chemical Physics of Ionic Solutions," B. E. Conway and R. G. Barradas, Ed., Wiley, New York, N. Y., 1966, p 295.

longer occurs and ϕ_p or γ_+^p increases to unity as the polymer concentration decreases.

Appendix

It is pertinent to describe an alternative procedure to treat the dependence of pH on polymer concentration in the case of no added salt.

Let us consider a salt-free polyelectrolyte solution as a two-component system, water and polymer salt (ps), rather than a three-component system employed in the main part of this paper.

From the Gibbs–Duhem relation

$$-(\mathrm{d} \ln \gamma_\pm/\mathrm{d}\, m_{ps}) = (1 - \phi_p)/m_{ps} \quad \text{(A-1)}$$

Here $\gamma_\pm$ denotes the mean activity coefficient of polymer component ps. Comparing this equation with eq 9, which we can derive if the following relation can be verified

$$-(\mathrm{d} \ln \gamma_\pm/\mathrm{d}\, m_{ps}) = (1/RT)(\partial\mu_H/\partial m_p)_\alpha + (1/m_p)(\partial\phi_p/\partial \ln \alpha) \quad \text{(A-2)}$$

The chemical potentials of both polymer components, employed in the main part and in this Appendix, are interrelated with each other in terms of their definitions.

$$\mu_{ps} = \mu_{p,\alpha} + \alpha x\mu_+ = \mu_{p,\alpha} + \alpha x\mu_H + \alpha x(\mu_+ - \mu_H) = \mu_p + \alpha x(\mu_+ - \mu_H) \quad \text{(A-3)}$$

where $\mu_{p,\alpha}$ denotes the chemical potential of polyion. Generally μ_{ps} can be written as follows.

$$\mu_{ps} = \mu_{ps}^0 + RT \ln [(\alpha x)^{\alpha x}(\gamma_\pm m_{ps})^{1+\alpha x}] \quad \text{(A-4)}$$

Using eq A-4 we differentiate both sides of eq A-3 with respect to $m_p = m_{ps}$.

$$RT(1 + \alpha x)(\mathrm{d} \ln \gamma_\pm/\mathrm{d}m_{ps} + 1/m_{ps}) = (\partial\mu_p/\partial m_p)_\alpha - \alpha x(\partial\mu_H/\partial m_p)_\alpha + \alpha xRT(1/m_p + \partial \ln \gamma_+^p/\partial m_p) \quad \text{(A-5)}$$

Neglecting the derivative of γ_+^p as before and approximating $(1+\alpha x)$ to αx

$$-(\mathrm{d} \ln \gamma_\pm/\mathrm{d}\, m_{ps}) = (1/RT)(\partial\mu_H/\partial m_p)_\alpha - (1/\alpha xRT)(\partial\mu_p/\partial m_p)_\alpha \quad \text{(A-6)}$$

From the Gibbs–Duhem relation

$$(\partial\mu_p/\partial m_p)_\alpha = -\alpha x(\partial\mu_a/\partial m_p)_\alpha - (10^3/M_w m_p)(\partial\mu_w/\partial m_p)_\alpha \quad \text{(A-7)}$$

Setting $m_s = 0$ in eq 4, we obtain

$$(\partial\mu_a/\partial m_p)_\alpha = -(10^3/m_p^2\alpha x M_w)(\partial\mu_w/\partial\alpha)_{m_p} \quad \text{(A-8)}$$

Substitution of eq A-8 into eq A-7 yields

$$(\partial\mu_p/\partial m_p)_\alpha = -(RT\alpha x/m_p)(\partial\phi_p/\partial \ln \alpha) \quad \text{(A-9)}$$

We have arrived at eq A-2 by means of the introduction of eq A-9 into the rhs of eq A-6.

Another procedure to prove eq A-2 in terms of the nonideal term in a potentiometric equation, ΔpK, will be presented below. Analyzing a potentiometric equation, we can show that

$$2.3\Delta pK = \ln(\gamma_\pm/\gamma_+^p) + \partial \ln(\gamma_\pm/\gamma_+^p)/\partial \ln \alpha \quad \text{(A-10)}$$

Here ΔpK is defined as $pH - pK_0 - \log(\alpha/1 - \alpha)$ as usual. From this definition of ΔpK

$$(1/RT)(\partial\mu_H/\partial m_p)_\alpha = -2.3(\partial\Delta pK/\partial m_p)_\alpha \quad \text{(A-11)}$$

Substitution of eq A-10 into eq A-11 gives

$$(1/RT)(\partial\mu_H/\partial m_p)_\alpha = -(\partial \ln \gamma_\pm/\partial m_p)_\alpha - \partial^2 \ln \gamma_\pm/\partial m_p\partial \ln \alpha \quad \text{(A-12)}$$

Here we again make use of the invariability of γ_+^p with respect to m_p. Rewriting the second term of this equation in terms of ϕ_p with the aid of eq A-1, we can derive eq A-2, if the dependence of ϕ_p on m_p is ignored as before.

The recent work of Torrence, *et al.*, should be mentioned here since they presented a different expression for ΔpK.[8] According to them, the presented relation was

$$2.3\Delta pK = \ln \gamma_\pm$$

Clearly this relation can not serve in place of eq A-10 for the derivation of eq A-2. Hence the mean activity coefficient employed by them should be interpreted as having a somewhat different meaning from usual one assigned to $\gamma_\pm$.

Apparent Molal Volumes of Polyelectrolytes in Aqueous Solutions

by C. Tondre and R. Zana*

CNRS, Centre de Recherches sur les Macromolécules, Strasbourg, France *(Received May 12, 1972)*

Using a precision densimeter, the densities of a series of carefully prepared and purified aqueous solutions of polyelectrolytes of accurately known concentrations have been determined. The following polyelectrolytes have been investigated: poly(methacrylic acid) (PMA) samples of various molecular weights, carboxymethylcelluloses of various substitution degrees (acid form and tetramethylammonium (TMA) salt), poly(acrylic acid) (PAA), poly(maleic acid–methyl vinyl ether), polyphosphate, poly(ethylenesulfonic acid), and poly(styrenesulfonic acid). Measurements of densities have also been performed on the alkali metal and TMA salts of the last five polyelectrolytes. The densities have been used for the calculation of the apparent molal volumes Φ_{CP}. In the concentration range investigated the plots $\Phi_{CP} = f(\text{concentration})$ have been found to be linear and the values of Φ_{CP} have been extrapolated to zero concentration to give the Φ_{CP}^0's. For PAA and PMA, Φ_{CP}^0 shows practically no dependence on the polymer molecular weight. The Φ_{CP}^0's have been found to be nonadditive, in contradistinction to what is observed with simple electrolytes. This result gives an additional experimental evidence to the so-called counterion "site binding." The volume changes associated with this process have been determined for various counterions and found to present large differences, according to the nature of both the polyion and the counterion. Finally for polycarboxylic acids simple assumptions have permitted the determination of the contribution of electrostriction to the apparent molal volume of the polyion at infinite dilution and of the fraction of bound counterions with total dehydration.

I. Introduction

The apparent molal volumes at infinite dilution (Φ_2^0) of simple electrolytes in aqueous solutions have been the subject of extensive studies, recently reviewed by Millero.[1] The Φ_2^0 values of a large number of electrolytes are now known with great accuracy. For instance, two series[2,3] of independent determinations of the Φ_2^0's for the alkali chlorides showed differences of only a few hundredths of cm³/mol. Such accurate results have demonstrated the additivity of the Φ_2^0's. On the other hand, the values of the ionic apparent molal volumes at infinite dilution have been used to obtain informations on the interaction between ions and the surrounding water molecules.[1] It would be interesting to obtain the same kind of informations with polyelectrolytes. Unfortunately the situation is much less favorable than for simple electrolytes as indicated by the paucity of the apparent molal volume data found in the literature[4-8] and by the large discrepancies which exist between the results of the various workers. For instance values as different as 33 and 37 cm³/mol have been reported for the Φ_2^0 of sodium polyacrylate.[4,7] Also Ise and Okubo[4] results for poly(ethylenesulfonic acid) and for poly(styrenesulfonic acid) are incompatible as will be shown below. Moreover, these workers reported that the additivity also applies to the Φ_2^0 of polyelectrolytes in contradiction with the present ideas[9] on counterion–polyion interactions. The above facts alone would have been sufficient to motivate new and more accurate determinations of the apparent molal volumes of polyelectrolytes. Our interest however also arose from the state of our current studies of the excess ultrasonic absorption observed in polyelectrolyte solutions.[10,11] We have shown that this excess absorption is due to the "specific" or "site" binding of counterions by polyions. Ultrasonic absorption measurements should then be capable of providing informations on the kinetics of site binding processes, particularly the values of the rate constants. However, preliminary measurements[10] have shown that counterion site binding is a multistep process, chracterized by a large number of unknown quantities (rate constants, volume changes, concentrations of the species). As will be shown in the Discussion, the measurement of the apparent molal volumes of polyelectrolytes permits the evaluation of the total volume change associated with the site binding of the counterion and thus helps greatly the thorough analysis of the ultrasonic absorption data.

(1) F. Millero, *Chem. Rev.*, **71**, 147 (1971).

(2) F. Vaslow, *J. Phys. Chem.*, **70**, 2286 (1966).

(3) F. Millero and W. Drost-Hansen, *J. Chem. Eng. Data*, **13**, 330 (1968).

(4) N. Ise and T. Okubo, *J. Amer. Chem. Soc.*, **90**, 4527 (1968); *Macromolecules*, **2**, 401 (1969).

(5) B. Conway, J. Desnoyers, and A. Smith, *Phil. Mag.*, **256**, 359 (1964); J. Lawrence and B. Conway, *J. Phys. Chem.*, **75**, 2353, 2362 (1971).

(6) M. Rinaudo and C. Pierre, *C. R. Acad. Sci.*, **269**, 1280 (1969).

(7) P. Roy-Chowdhury, *J. Appl. Polym. Sci.*, **12**, 751 (1968); **14**, 2937 (1970); *J. Polym. Sci., Part A-2*, **7**, 1451 (1969).

(8) S. Friedman, A. Caillé, and H. Daoust, *Macromolecules*, **3**, 700 (1970).

(9) G. Manning, *J. Chem. Phys.*, **51**, 924 (1969).

(10) C. Tondre and R. Zana, Abstracts, IUPAC Symposium on Macromolecules, Vol. I, Leiden, 1970, p 387; *J. Phys. Chem.*, **75**, 3367 (1971).

(11) R. Zana, C. Tondre, M. Milas, and M. Rinaudo, *J. Chim. Phys.*, **68**, 1258 (1971).

II. Experimental Section

a. Density Measurements. The density of the solution was measured by means of a digital precision densimeter DMA 02 designed by Stabinger, Leopold, and Kratky.[12] The density is determined from the measurement of the resonant frequency of a mechanical oscillator filled with the solution. The oscillator is a U-glass tubing placed within a temperature controlled metal block. The electronic part provides an excitation of the oscillator and allows a precise measurement of the oscillator frequency within a short time T (typically 2 min). An ultrathermostat attached to the instrument controls the temperature at 25 ± 0.002°. The measurements are performed once the sample solution has reached a constant temperature. The time T read on the apparatus is the time required for a number N of oscillations. The apparatus is calibrated by measuring the values T_0 and T_1 for water and air whose densities d_0 and d_1 are known. The apparatus constant A and the difference between the density d of the solution and that of water (taken as 0.997044 g/cm³) are then obtained from

$$A = (T_0^2 - T_1^2)/(d_0 - d_1) \quad (1)$$

$$d - d_0 = (T^2 - T_0^2)/A \quad (2)$$

The apparent molal volume Φ_{CP} of a polyelectrolyte CP solution with a concentration c (in mole of monomer per liter) was obtained from the density d of the solution according to

$$\Phi_{CP} = \frac{M_M}{d_0} - 10^3 \frac{d - d_0}{d_0 c} \quad (3)$$

where M_M is the molecular weight of the monomeric unit of the polyelectrolyte under study.

The results were corrected for atmospheric pressure changes when such changes occurred during the measurements.[13] The precision of the density measurements was about 1 to 2 × 10^{-5} g/cm³. The overall accuracy of the apparatus was checked by measuring the apparent molal volumes of a series of alkali chlorides as a function of concentration. Extrapolation to zero concentration yielded the following values of the apparent molal volumes at infinite dilution: 16.88, 16.62, 26.66, 31.73 and 39.1 cm³/mol for LiCl, NaCl, KCl, RbCl, and CsCl, respectively. These values are in good agreement (±0.2 cm³/mol) with those previously reported.[1-3] For the polyelectrolyte solutions the accuracy on the apparent molal volumes is likely to be not as good since, as will be seen below, other causes of error are introduced in the making of the polyacid and polysalt solutions. The duplication of some experiments led us to estimate the accuracy on Φ_{CP} as ±0.5 cm³/mol or ±1% depending on whichever the larger.

b. Materials. Measurements of density have been performed on the following polyelectrolytes: poly(acrylic acid) (PAA), poly(methacrylic acid) (PMA) with various molecular weights, carboxymethylcellulose (CMC) with various substitution degrees, alternate copolymer of maleic acid and methyl vinyl ether (MA–MVE), poly(ethylenesulfonic acid) (PESA), poly(styrenesulfonic acid) (PSSA), and polyphosphate (PP). The origin of the CMC, MA–MVE, PESA, PSSA, and PP samples has been previously given.[10] PAA was purchased from K and K Laboratories (Calif.) as a 25% aqueous solution free of ionic impurities and was found to have a molecular weight of 120,000. PMA was prepared in our laboratory by a bulk polymerization of the purified monomer under uv irradiation. The resulting polymer was fractionnated using methanol as solvent and benzene as precipitant. The fractions were purified as described below and the molecular weights determined by means of viscosity.[14]

c. Purification and Preparation Procedures. The major sources of discrepancies among the values of the apparent molal volumes reported by various workers are likely to be found (1) in the purity of the samples, (2) in the accuracy on the values of the concentrations of the polyacid stock solutions and, (3) in the preparation of solutions of polysalts of accurately known concentrations and free of ionic impurities.

These three points will be now examined in detail.

1. Purification of the Polyelectrolytes. Several of the products used in this work as well as in previous studies[4,5,8] were of commercial origins and may have contained sizable amounts of ionic and nonionic impurities. The classical method of polymer purification, *i.e.*, dissolution and precipitation, being inoperant for ionic impurities, the following procedure was adopted. Aqueous solutions of the raw materials were first extensively dialyzed against distilled water in order to remove most impurities of low molecular weights. A further purification was achieved by passing the polyelectrolyte solutions through anion and cation exchange resins and filtering them. These purified polyelectrolyte solutions, in the acid form, had concentrations between 0.2 and 0.4 equiv/l. They were used as stock solutions and stored below 5° to avoid a bacterial contamination which was found to occur at room temperature with polycarboxylic acid solutions.

2. Determination of the Concentration of the Polyacid Stock Solutions. Two methods were used for the polycarboxylic acids (PAA, PMA, CMC, and MA–MVE): potentiometric titration and dry content measurement. The determinations were performed on a weighted sample of the stock solution (about 5 ml), the density of which had been measured thus yielding the value of the

(12) H. Stabinger, H. Leopold, and O. Kratky, "Digital Densimeter DMA 02," Institute for Physical Chemistry, University of Graz, Austria.

(13) J. Francois, R. Clement, and E. Franta, *C. R. Acad. Sci., Ser. C*, 273, 1577 (1971).

(14) A. Katchalsky and H. Eisenberg, *J. Polym. Sci.*, 6, 145 (1951).

volume of the sample with great accuracy, at 25°. The two results usually agreed to better than 0.7% and the average value of the concentration was used in the following.

Accurate values of the dry contents of PSSA, PESA, and PP solutions could not be obtained as these compounds were found to retain water even under vacuum and at temperatures where decomposition occurs. However the very sharp change of pH corresponding to the neutralization of PESA and PSSA permitted an accurate determination of their concentration. For PP a special procedure was necessary.[10]

Attempts to obtain the concentration of alkali metal and tetramethylammonium (TMA) salts of the polyelectrolytes from dry content measurements have been unsuccessful as all these salts have been found to retain water.

3. Preparation of Solutions of Polysalts with Known Concentration. The following procedure has been adopted for all of the polyelectrolytes but the PP salts. A known volume (5.009 ± 0.005 cm³) of metal hydroxide solution whose concentration is known to within 1‰ is introduced into a 25-ml volumetric flask with a calibrated pipet. Then is added a mass of the polyacid stock solution (of known density and concentration) calculated as to neutralize the hydroxide and leaves a small amount of free polyacid (1 to 2‰). Finally water is added to reach a final volume of 25 ml at 25°. An excess of polyacid was used as both calculations and experiments showed that for heavy alkali metals (essentially Rb and Cs) free hydroxide introduces a substantial error on Φ_{CP}. On the contrary a slight excess of polyacid has practically no influence on the result.

In this procedure the concentration of the polysalt is readily obtained from that of the hydroxide and from the ratio of the volumes of the hydroxide and of the volumetric flask. Moreover, this procedure avoids both evaporation and formation of carbonate which occur in the potentiometric preparation of polysalts if special precautions are not taken. The presence of carbonate in the metal hydroxides used to prepare the polysalts is thought to have been one of the major sources of disagreement between the various workers. In this work the hydroxides were thoroughly decarbonated by passing them through an anion exchange resin. The operation was performed under nitrogen. The stock solution of metal hydroxide was titrated and stored under nitrogen. The titration curves determined before and after the ion exchange showed that the carbonate had been completely removed.

The above method of preparation of polysalts could not be used for the polyphosphate salts as depolymerization occurs when PP is in the acid form. Therefore a KPP solution was prepared and passed through a cation exchange resin previously neutralized by the chosen metal hydroxide. The concentration of the

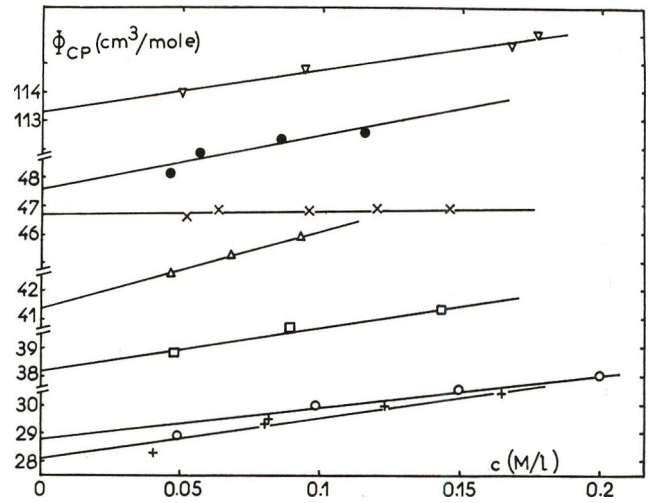

Figure 1. Variation of Φ_{CP} with c for polyacrylic acid (×) and for its Na(○), Li(+), K(□), Rb(△), Cs(●), and TMA(▽) salts.

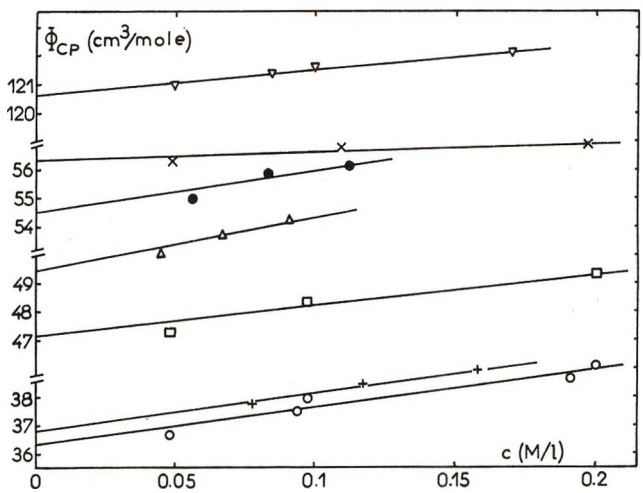

Figure 2. Variation of Φ_{CP} with c for MA–MVE in the acid form (×) and for its Na(○), Li(+), K(□), Rb(△), Cs(●), and TMA(▽) salts.

PP salts were then determined potentiometrically as previously reported.[10] This procedure resulted in a lesser accuracy (about 1%).

The water used throughout this work was first deionized by means of a mixed-bed ion exchange resin and then distilled.

III. Results

Figures 1–4 show the apparent molal volumes as a function of concentration (in mole of monomer per liter) for PAA, MA–MVE, PESA, and PSSA and for the alkali metal and TMA salts of these polyacids. The results relative to samples of PMA with molecular weights M_w ranging from 44,000 to 370,000 are given in Figure 5. Figure 6 is plotted relative to the acid forms and the TMA salts of CMC with substitution degrees (SD) 0.98, 1.3, 2.1, and 2.65. For most of the polyelectrolytes studied in this work the concentrations in-

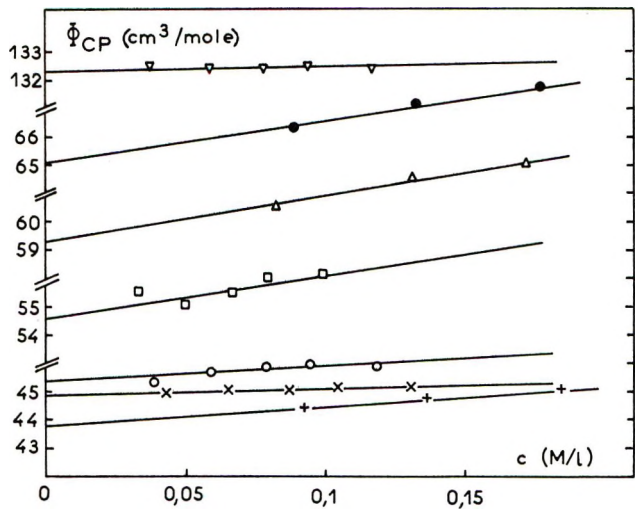

Figure 3. Variation of Φ_{CP} with c for PESA(×) and for its Li(+), Na(○), K(□), Rb(△), Cs(●), and TMA(▽) salts.

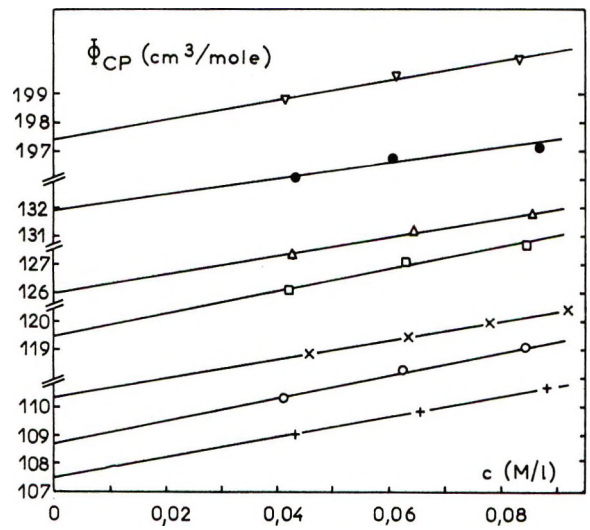

Figure 4. Variation of Φ_{CP} with c for PSSA(×) and for its Li(+), Na(○), K(□), Rb(△), Cs(●), and TMA(▽) salts.

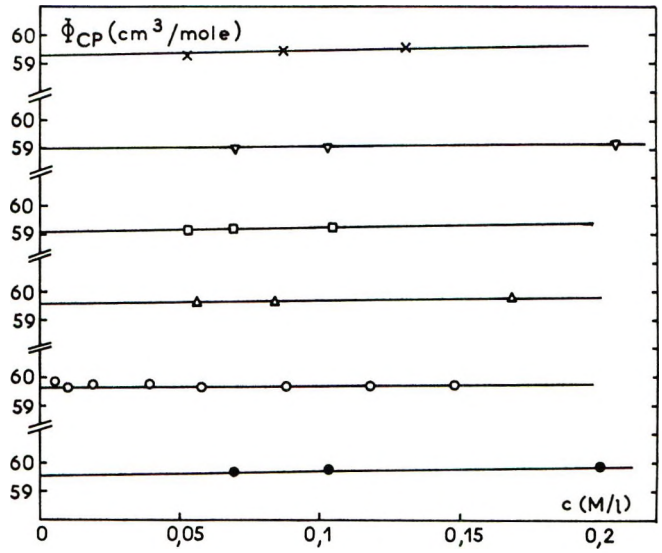

Figure 5. Variation of Φ_{CP} with c for poly(methacrylic acid) samples of molecular weights 44,000(●), 76,000(○), 97,500(△), 184,000(□), 275,000(▽), and 370,000(×).

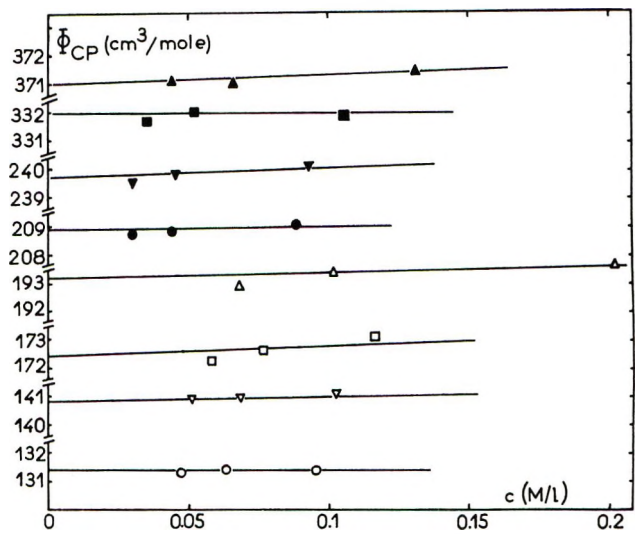

Figure 6. Variation of Φ_{CP} with c for carboxymethylcellulose samples with substitution degrees 0.98(○,●), 1.3(▽,▼), 2.1(□,■), and 2.65(△,▲). The symbols ○, ▽, □, and △ refer to the acid form of the CMC's while ●, ▼, ■, and ▲ are relative to the TMA salts.

vestigated ranged from 0.04 to 0.25 N. In this limited range all of the plots $\Phi_{CP} = f(c)$ were found to be linear, and, as c was increased, Φ_{CP} either remained constant (see CMC's, TMA-CMC's, PMA's, PAA, TMA-APES, and MA-MVE) or increased linearly. Similar linear increases of Φ_{CP} with c have been previously reported by Conway, *et al.*,[5] and Ise and Okubo[4] for various polyelectrolytes. Such a behavior has been interpreted in terms of an overlapping of the hydration shells of the polyions as c increases. This results in a lesser electrostrictive effect per polyion and therefore, in a positive slope for the plots $\Phi_{CP} = f(c)$. These linear plots led us to a tentative estimate of the apparent molal volumes at zero concentration (Φ_{CP}^0) from the extrapolation of Φ_{CP} to zero concentration. The values of Φ_{CP}^0 obtained from the results on Figures 1–6 and also from our results on PP which were not shown are given in Tables I–III together with the values of Φ_{CP}^0 reported by other workers. The comparison of these results shows points of excellent agreement (PSSA, PAA, PMA), of fair agreement (NaPP, PAA, and PSSA salts), and of strong disagreement (PESA and PESA salts). The latter case requires special consideration because the two sets of data are clearly incompatible. The difference between the Φ_{CP}^0 values for PSSA and PESA represents the apparent molal volume of a phenyl ring minus two H atoms. This volume is found to be 125 cm^3/mol in Ise and Okubo work while our results yield the value 65 cm^3/mol. On the other hand this volume can be eval-

Table I: Apparent Molal Volumes of Polyelectrolytes

	PAA			PESA		PSSA		PP	
	MA–MVE	This work	Other results	This work	Other results	This work	Other results	This work	Other results
Acid form	56.3	46.7	46.7[a] 47.8[b]	44.9	−13.2[b]	110.3	110[b]		
Li salt	36.8	28.1	33[b]	43.8		107.5	110[b]	17.6	
Na salt	36.3	28.8	37[a] 33[b]	45:4	−10.6[b]	108.7	108.2[b]	18.8	22[c]
K salt	47.1	38.2	43[b]	54.6		119.5	121[b]	28.4	
Rb salt	49.5	41.4		59.3		126		30.3	
Cs salt	54.5	47.6		65.1		131.9			
TMA salt	120.6	113.3	118[b]	132.3		197.4	213[b]	100.1	

[a] From ref 7. [b] From ref 4. [c] From ref 5.

Table II: Poly(methacrylic Acid), Effect of the Molecular Weight

M_w	44,000	76,000	87,000	185,000	270,000	370,000	680,000[a]
Φ_{CP}^0, cm³/mol	59.4	59.6	59.6	59.1	59.0	59.3	60.0

[a] From ref 7, $c > 0.1$ M.

uated in two different ways, (1) from an ultrasonic vibration potential study of monocarboxylic acids[15] and (2) from the Φ_{CP}^0 values for CH_3PhSO_3Na[1] and CH_3SO_3Na (obtained by extrapolating the data of Corkill, *et al.*[16]). Given the approximations involved in these calculations the average value 58 cm³/mol compares well with that obtained in this work and shows that Ise and Okubo data[4] for PESA and PESA salts cannot be taken into consideration.

Table III: Carboxymethylcellulose, Effect of the Substitution Degree

	SD				
	0.98	1.3	2.1	2.65	2.5[a]
CMC acid form Φ_{CP}^0	131.4	140.8	172.4	193.2	190.5
TMA CMC Φ_P^0, cm³/mol[b]	208.9	239.7	332.0	371	
	126.4	130.2	155.2	147.9	
ΔV^0, cm³/mol[c]	10.3	17.6	28.5	59.7	
ΔV^0/SD, cm³/equiv	10.5	13.5	13.6	22.5	

[a] From ref 6. [b] $\Phi_P^0 = \Phi_{TMA-CMC}^0 - \Phi_{TMA}^0 SD$. [c] $\Delta V^0 = \Phi_{H-CMC}^0 - \Phi_P^0 - \bar{V}_H^0 SD$.

Figure 7 shows that for PMA Φ_{CP}^0 does not depend on M_w. This result is discussed in the next paragraph.

On the other hand, Figure 8 shows a linear increase of Φ_{CP}^0 with SD for CMC's in the acid form. For CMC–TMA's Φ_{CP}^0 also increase linearly with SD up to SD = 2.1. Above this value there is a departure from linearity which is explained in part IVd of this paper. It is noteworthy that the two curves $\Phi_{CP}^0 = f(SD)$ relative to CMC's in the acid form and CMC–TMA's extrapolate at SD = 0 to the same value, $(\Phi_{CP}^0)_{SD=0}$ = 95 cm³/mol. This result which represents the apparent molal volume of the cellulose monomer appears as a rather original one when it is pointed out that cellulose is insoluble in water.

IV. Discussion

As said in the Introduction the results reported in the literature show strong discrepancies. In particular, contradictory results have been reported for the effect (1) of the polyelectrolyte molecular weight M_w and (2) of the concentration c, at $c < 0.05$ N on the value of Φ_{CP} for polycarboxylic acids. These two points will be examined first as they condition in part the rest of the discussion. The separation of the Φ_{CP}^0's of polyelectrolytes into those of their ionic components (polyion P and counterion C) will be then examined. It will be shown that, as expected from ultrasonic[10,11] and dilatometric[17,18] studies, the additivity does not hold for the apparent molal volumes of polyelectrolytes because part of the counterions are bound by the polyions. Finally a method for the evaluation of the contribution of electrostriction to the apparent molal volumes of polyions will be presented and applied to polycarboxylic ions.

a. Effect of the Polyelectrolyte Molecular Weight. Highly charged polyelectrolytes can be approximated by charged cylinders.[5,9] This model predicts that for sufficiently long polymer chains, *i.e.*, when M_w is large enough, the Φ_{CP}^0 per monomer becomes independent of

(15) R. Zana and E. Yeager, *J. Chim. Phys.*, 65, 467 (1968).

(16) J. Corkill, J. Goodman, and T. Walker, *Trans. Faraday Soc.*, 63, 768 (1967).

(17) Y. Po Leung and U. Strauss, *J. Amer. Chem. Soc.*, 87, 1476 (1965).

(18) A. Begala and U. Strauss, *J. Phys. Chem.*, 76, 254 (1972).

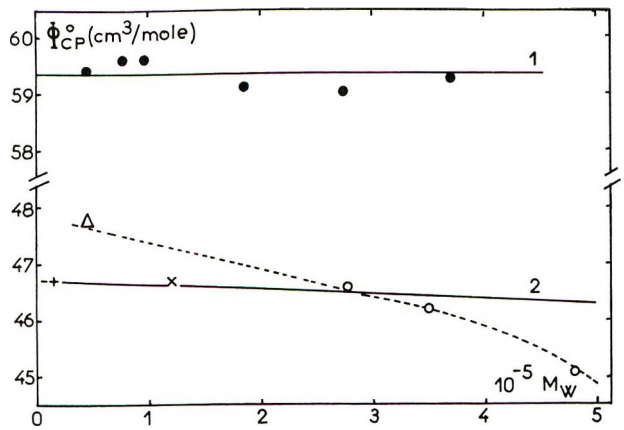

Figure 7. Effect of the polyelectrolyte molecular weight on the value of Φ_{CP}° for PMA (curve 1) and PAA (curve 2). The results on curve 2 have been taken from ref 4(Δ), ref 7(+), ref 8(○), and this work (×). (- - - -) curve is given in ref 8.

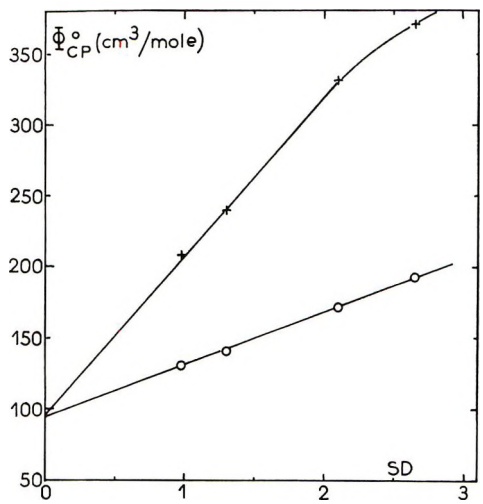

Figure 8. Effect of the substitution degree on the Φ_{CP}° for CMC's in the acid form(○) and for TMA-CMC's(+).

M_w. This conclusion has been verified for NaPP[5] and polyethyleneimine-HBr.[5]

The situation is more complicated for weakly charged polyelectrolytes, *i.e.*, for polycarboxylic acids, whose conformation is close to that of a coil with a radius of gyration R_G slightly larger than in the uncharged state. However, Tanford[19] has shown that the intrinsic volume of the polymer chain represents less than 1% of the volume of the sphere of radius R_G, the rest being solvent. Moreover the hydration shell is then mainly the result of short-range forces since the polymer chain bears only a small charge. Thus, the amount of water within the polymer coil appears sufficient to ensure a complete hydration of each part of the polymer chain, independently of the others parts of the chain in the immediate vicinity. One should therefore expect Φ_{CP}^{0} to be independent of M_w when M_w is large enough. This prediction has been verified for uncharged polyethyleneimine.[6] Also, for PMA, the results of Roy-Chowdhury[7] together with those obtained in this work show no effect of M_w on Φ_{CP}^{0} in the range 44,000–680,000 (see Table II and Figure 7). On the contrary, Friedman, *et al.*,[8] observed for PAA a decrease of Φ_{CP}^{0} for increasing M_w. However it can be seen on Figure 7 that if the results reported by these workers (four PAA samples) are plotted on the same graph than the result of Roy-Chowdhury[7] (PAA 14,000) and that obtained in this work (PAA 120,000), a straight line with a very small negative slope can be drawn which goes very close to four of the six experimental points. Two results are left out, one which has been taken from Ise and Okubo work,[4] whose results have been found systematically too large (see above and in ref 5), the other is from the Friedman, *et al.*, study.[8] In terms of concentration the departure of this last result from the straight line (curve 2 on Figure 7) corresponds to a 3% error on the concentration. The small negative slope of curve 2 may be explained by the reported use of catalyst in the preparation of these PAA samples.[4,7,8] This catalyst remains bound to the polymer by a covalent bond and is impossible to eliminate. As usually each macromolecule binds one catalyst molecule the relative effect of the catalyst on Φ_{CP}^{0} should decrease as M_w increases. It is noteworthy that the PMA samples of curve 1 on Figure 7 were catalyst free and showed no dependence on M_w. From the above it can be safely concluded that M_w has no influence on Φ_{CP}^{0} at least for M_w sufficiently large, *i.e.*, above 5000 to 10,000.

For lower values of M_w, a dependence of Φ_{CP}^{0} on M_w should appear, as indicated by a comparison of the Φ_{CP}^{0} values for the monomer alone (Φ_{CM}^{0}) and for the same monomer included into a polymer. These values, given in Tables IVa and IVb, show that polymerization results in a sizable decrease of apparent molal volume and suggest a possible use of apparent molal volume measurements for the determination of M_w for oligomers. The results in Table IVa are relative to weak polyelectrolytes and nonpolyelectrolytes. They show that the ratio $\Delta V_{MP}/M_M$ (where $\Delta V_{MP} = \Phi_{CM}^{0} - \Phi_{CP}^{0}$ and M_M is the molecular weight of the monomer) is independent of M_M, within experimental accuracy.

Table IVb is relative to strong polyelectrolytes. Φ_M^{0} and Φ_P^{0} represent respectively the apparent molal volumes of the monomeric ion alone and included in the polyion. The values of Φ_P^{0} and Φ_M^{0} have been evaluated as indicated in the footnote in Table IVb, and in part c of the Discussion. In this case $\Delta V_{MP}/M_M$ decreases for increasing M_M. This result is examined in part IVd.

b. Effect of Concentration on the Partial Molal Volume of Polycarboxylic Acids. For concentrations

(19) C. Tanford, "Physical Chemistry of Macromolecules," Wiley New York, N. Y., 1961, p 178.

Table IV: Comparison among Monomers and Polymers

a. Weak Polyelectrolytes

Monomer	Acrylic acid	Methacrylic acid	Acrylamide	Methacrylamide
Φ_{CM}^0	61.7[a]	78.6[a]	65.5[a]	81[a]
Polymer	PAA	PMA	Polyacrylamide	Polymethacrylamide
Φ_{CP}^0	46.7[b]	59.4[b]	50.9[a]	62.5[a]
M_M	72.06	86.08	71.1	85.1
$\Delta V_{MP} = \Phi_{CM}^0 - \Phi_{CP}^0$	15	19.2	14.6	19.5
$\Delta V_{MP}/M_M$	0.209	0.223	0.205	0.226

b. Strong Polyelectrolyte

Monomer	Acrylic ion	Vinylsulfonic ion	Styrenesulfonic ion
Φ_M^0	51.5[c]	74[c]	133[c]
Polyion	PAA^-	$PESA^-$	$PSSA^-$
Φ_P^0	29.1[d]	48.1[d]	113.2[d]
$\Delta V_{MP} = \Phi_M^0 - \Phi_P^0$	22.4	25.9	19.8
M	71.06	107	181
$\Delta V_{MP}/M$	0.315	0.241	0.11

[a] From ref 7. [b] This work. [c] From the combination of results in ref 1, 7, and 16 and with the assumption that the removal of two H atoms in order to create a double bond C=C brings about a decrease of apparent molal volume of 6.5 cm^3/mol. This assumption is based on the comparison of the apparent molal volumes data from ref 7 and from E. King, *J. Phys. Chem.*, **73,** 1220 (1969); W. Hargraves, *et al.*, *ibid.*, **73,** 3249 (1969); and International Critical Tables, Vol. 3, McGraw-Hill, New York, N. Y., 1928. [d] This work, as explained in part IVc.

above 0.1 N the results reported for PAA[4,7,8] and PMA[5,7] agree with those obtained in this work for PAA, PMA, CMC, and MA–MVE (see Figures 1, 2, 5, and 6) in showing no dependence of Φ_{CP} on c. This behavior is probably the result of the very low state of charge of these polymers at concentration above 0.1 N.

On the contrary, conflicting results are found at concentrations below 0.1 M. Some workers[5,7] observed that the apparent molal volume of PMA is increased by several cm^3/mol at concentrations below 0.1 N. On the other hand, all PMA samples studied in this work showed no concentration effect in the range 0.05–0.15 N (see Figure 5). Moreover, measurements performed in the range 5.10^{-3}–10^{-1} N on the PMA sample 76,000 failed to reveal any concentration dependence of Φ_{CP}. This last result is quite similar to that reported by other workers[7,8] for PAA. The purity of the samples is likely to be the source of the conflicting results found for PMA because the samples used in previous studies were not as thoroughly purified as in this work. In any case, it must be pointed out that no simple explanation can be given for such a large increase of Φ_{CP} at low concentrations if it were to exist. The results of Wall[20] have been presented in the Friedman, *et al.*,[8] paper as giving support to such an effect. However both dilatometric[17,18] and refractometric[21] studies have shown these results to be incorrect, *i.e.*, the apparent molal volume decreases with increasing ionization, as it should be from the resulting increased electrostriction of the polyion.

c. *Separation of the Φ_{CP}^0 of Polysalts into Those of Their Ionic Components. Experimental Evidence of Counterion Site Binding.* For simple electrolytes the apparent molal volume of a salt at infinite dilution is equal to the sum of those of its ionic components. For polysalts this additivity should not hold as part of the counterion must remain bound to the polyion, even at infinite dilution.[9] Our Φ_{CP}^0 data can be used as follows to give support to this theoretical prediction. Writing the additivity of the apparent molal volumes at infinite dilution for polysalt solutions leads to

$$\Phi_{CP}^0 = \Phi_P^0 + \Phi_C^0 \quad (4)$$

where Φ_C^0 is the counterion apparent molal volume at zero concentration. As the Φ_C^0's values are known,[1,22] eq 4 can be used to calculate the values of Φ_P^0. The results, given in Table V, show that for a given polyion the value of Φ_P^0 depends on the nature of the counterion. This dependence reveals that part of the counterions must be bound to the polyion, and that this binding is accompanied by a positive volume change associated to the release of electrostricted water molecules. This result confirms the conclusions of dilatomeric[17,18] and ultrasonic absorption[10,11] studies. Equation 4 however is verified when $C^+ = TMA^+$ as it has been shown that a negligible volume change is associated with the site binding of this large ion.[10,11,17] Then it can easily be demonstrated that if in a solution of the polysalt CP a fraction β_{CP} of counterion C is bound to the polyion P, the volume change ΔV_{CP}^0 for the binding reaction 5 is given by eq 6.

$$C^+ + P^- \longrightarrow CP \quad (5)$$

$$\Delta V_{CP}^0 = \delta V_{CP}/\beta_{CP} = [(\Phi_P^0)_C - (\Phi_P^0)_{TMA}]/\beta_{CP} \quad (6)$$

In this equation $(\Phi_P^0)_C$ and $(\Phi_P^0)_{TMA}$ represent the apparent molal volumes of the polyion as obtained from eq 4 applied to the counterions C^+ and TMA^+. In what follows the apparent molal volume of the polyion Φ_P^0 is taken as $(\Phi_P^0)_{TMA}$.

Both β_{CP} and ΔV_{CP}^0 are of great interest to the workers involved in the study of polyelectrolytes. In particular these two quantities are needed for the complete analysis of ultrasonic absorption data.[10,11] Thus, the Φ_{CP}^0 values for polysalts allow us to obtain δV_{CP} which gives us a relationship between β_{CP} and ΔV_{CP}^0.

(20) F. Wall and S. Gill, *J. Phys. Chem.*, **58,** 740 (1954).

(21) A. Ikegami, *J. Polym. Sci., Part A-2,* 907 (1964); *Biopolymers,* **6,** 431 (1968).

(22) R. Zana and E. Yeager, *J. Phys. Chem.*, **71,** 521, 4241 (1967).

Table V[a]

C	Φ_C^0	MA-MVE		PAA		PESA		PSSA		PP	
		$(\Phi_P^0)_C$	$\delta\bar{V}_{PC}$	$(\Phi_P^0)_C$	$\delta\bar{V}_{PC}$	$(\Phi_P^0)_C$	$\delta\bar{V}_{PC}$	$(\Phi_P^0)_C$	$\delta\bar{V}_{PC}$	$(\Phi_P^0)_C$	$\delta\bar{V}_{PC}$
H^+	−5.4	61.7	25.3	52.1	23	50.3	2.2	115.7	2.5		
Li^+	−6.3	43.1	6.7	34.4	5.3	50.1	2.0	113.8	0.6	23.9	8.0
Na^+	−6.6	42.9	6.5	35.4	6.3	52	3.9	115.3	2.1	25.4	9.5
K^+	3.6	43.5	7.0	34.6	5.5	51	2.9	115.9	2.7	24.8	8.9
Rb^+	8.7	40.8	4.4	32.7	3.6	50.6	2.5	117.3	4.1	21.6	5.7
Cs^+	15.9	38.5	2.1	31.6	2.5	49.1	1.0	115.9	2.7		
TMA^+	84.2	36.4	0	29.1	0	48.1	0	113.2	0	15.9	0

[a] $(\Phi_P^0)_C$ = apparent molal volumes of polyion P^- obtained from eq 4 using the values of Φ_{CP}^0 of Table I.

An approximate method of calculation of β_{CP} is given in the next paragraph.

In Table V are also given the values of δV_{CP} for a series of polysalts. These values show considerable changes according to the nature of both the polyion and the counterion. This behavior has been interpreted in terms of a model where bound cations form either an ion pair or some kind of a chelate with polyion charged sites, according to the respective values of the counterion radius and the actual distance between charged sites.[11] The δV_{CP} values in Table V are in fair agreement with those found by means of dilatometry.[17,18] In those experiments, however, the ratio (metal ion)/site was always below 0.4, while in ours this ratio equals 1.

d. Evaluation of the Contribution of Electrostriction to the Φ_P^0's of Polycarboxylates. For polycarboxylic acids the ionization is small and the fraction of bound protons is close to 1 at concentrations above 0.1 *N*. Therefore $\delta V_{HP} \neq \Delta V_{HP}^0$, where ΔV_{HP}^0 represents the molar volume change for the reaction

$$-CO_2^- + H^+ \longrightarrow -CO_2H \qquad (7)$$

One can write

$$\Delta V_{HP}^0 = \Delta V_H^0 + \Delta V_P^0 \qquad (8)$$

where ΔV_H^0 and ΔV_P^0 are the volume changes due to the release of electrostricted water molecules by H^+ and P^-. Thus ΔV_P^0 represents the contribution of electrostriction to the apparent molal volume of the polyion $(\Phi_P^0)_{TMA}$. On the other hand ΔV_H^0 is to a very good approximation equal to 5.4 cm³/mol.[1,22] If we assume that the hydrophobic contributions to the apparent molal volume of a polyelectrolyte in the fully ionized and in the near uncharged states are equal, then eq 8 permits the calculation of ΔV_P^0, using the ΔV_{HP}^0 values of Table V. The results of these calculations are given in Table VI. For the CMC's the plot $\Delta V_P^0 = f(SD)$ shows a plateau for SD values between 1.3 and 2.1. This behavior is likely to be the result of the way in which the OH groups are substituted on the cellulose monomer. It is known[23] that at SD below 2 the substituted OH groups are mainly those in position 2 and 6 on the sugar ring. The ionized carboxyl groups even though on the same sugar ring are then far enough apart to act almost independently on the surrounding water molecules and thus to cause only a small electrostriction. It is only for SD > 2 that a sizable proportion of monomers are carboxymethylated in positions 3 and 6. The corresponding $-CO_2^-$ groups are then close enough to each other as to bring larger electrostrictive effects, comparable with those measured for PAA, PMA, and MA–MVE. This explains the departure from linearity which can be seen in Figure 8 for the result relative to TMA–CMC SD 2.65.

Table VI: Electrostriction of Polyions

Polyion	ΔV_P/mol of CO_2^-	Polyion	ΔV_P/mol of CO_2^-
PAA^-	17.6	CMC DS 1.3	8.1
PMA^-	22.1[a]	DS 2.1	8.2
$MA\text{–}MVE^{2-}$	19.9	DS 2.65	17.1
CMC DS 0.98	5.1		

[a] Calculated as explained in part IVd, and using the data Φ_{H-PMA}^0 = 59.6 cm³/mol (see Figure 5) and $\Phi_{TMA-PMA}^0$ = 121.7 cm³/mol obtained for the PMA sample 76,000.

For strong polyacids the above method of evaluating ΔV_P^0 cannot be used as ionization of strong polyacids is almost complete. This evaluation can be done in another way, as will be reported later.

Considerations on the electrostriction of polyions provide an explanation for the results of Table IVb. The volume change ΔV_{MP} is related to the electrostriction per monomer. This quantity is larger for the monomer within the polymer chain than for the monomer alone as the proximity of the charged sites on the polymer chain results in an increased electrostriction per monomer. On the other hand the three polyions in Table IVb are polyvinylic polyelectrolytes. One can then expect the electrostriction per monomer to in-

(23) I. Croon and C. Purves, "Encyclopedia of Polymer Science and Technology," Vol. 3, Wiley-Interscience, New York, N. Y., 1965, p 532.

crease as the distance l between one charged site and the polymer chain is decreased.[10] This dependence results in the observed variation of $\Delta V_{MP}/M_M$ with M_M because an increase of l is associated with the increase of M_M for the three polyions of Table IVb.

The above values of ΔV_P^0 may be used to evaluate the binding coefficients β_{CP} of the various counterions, in the assumption that complete dehydration of both the counterion C and the polyion site occurs upon binding. The values of β_{CP} thus obtained will represent a lower bound for the fraction of bound counterions as it is evident that the binding is not accompanied by a complete dehydration as assumed in the following calculation. From eq 6 and 8, applied to the polysalt CP one obtains

$$\beta_{CP} = \frac{\delta V_{CP}}{\Delta V_C^0 + \Delta V_P^0} \qquad (9)$$

The volume change ΔV_C^0 due to the release of the counterion hydration water can be estimated from the counterion apparent molal volume at infinite dilution.[1,22] Table VII gives the calculated values of β_{CP} for the alkali metal salts of PAA and MA–MVE. As expected from above these values are smaller than the fractions of bound counterions which may be calculated from Manning's theory.[9]

Table VII: Lower Bound for the Fraction of Bound Counterions

	Polyion	
Salt	PAA	MA–MVE
Li	0.21	0.24
Na	0.22	0.21
K	0.22	0.25
Rb	0.15	0.16
Cs	0.11	0.08

Conclusion

The apparent molal volumes of carefully prepared and purified polyelectrolytes have been determined. The results show that for polycarboxylic acids the apparent molal volumes are, within the experimental accuracy, independent of the polymer molecular weight, for $M_w > 15{,}000$ and of the polymer concentration in the range 5.10^{-3}–0.15 N. For most of the other polyacids and polysalts Φ_{CP} has been found to increase linearly with polymer concentration. The apparent molal volumes at infinite dilution Φ_{CP}^0 have then been used for the evaluation of (1) the volume change associated to the site binding of counterions by polyions, (2) the contribution of electrostriction to the apparent molal volumes of polyions, and (3) the fractions of bound alkali metal counterions.

Acknowledgment. The authors are pleased to acknowledge Dr. J. François for allowing the use of the digital densimeter.

Reduction of Methylene Blue on Illuminated Titanium Dioxide in Methanolic and Aqueous Solutions

by Hiroshi Yoneyama,* Yoshinori Toyoguchi, and Hideo Tamura

Department of Applied Chemistry, Faculty of Engineering, Osaka University, Yamadakami, Suita, Osaka, Japan
(Received January 20, 1972)

Reduction of methylene blue to leuco-methylene blue on illuminated rutile crystals in methanolic and aqueous solutions containing hydrogen chloride was investigated colorimetrically and electrochemically. A fairly good correlation was observed between the reduction rate determined by the electrochemical analysis, based on the local cell process, and that determined by the colorimetric analysis. Methylene blue was reduced more rapidly in the methanolic than in the aqueous solution owing to the difference in the oxidation of the solvent. The overall reduction is proposed as follows: $M^+ + CH_3OH + H^+ \rightarrow MH_3^{2+} + CH_2O$ in the methanol solution, and $M^+ + H_2O + H^+ \rightarrow MH^{2+} + {}^1/_2O_2$ in the aqueous solution, where M is methylene blue.

Introduction

It was stated in a review by Clark[1] that the catalytic activity of a semiconductor is controlled by an electronic interaction between the semiconductor and a reactant. Recently, an electrochemical measurement on an illuminated ZnO catalyst[2,3] was applied to the oxidation of formic acid

$$HCOOH + O_2 \longrightarrow CO_2 + H_2O_2$$

and an individual reaction step involving holes in the valence band and electrons in the conduction band was elucidated by measuring the polarization as well as the surface capacitance. On the other hand, electrochemical analysis based on the local cell process was recently performed[4,5] for elucidating the hydrogenation reaction of quinone, vinyl acetate, and allyl alcohol on platinum in acid aqueous solutions. However, no attempt has been made to estimate a reaction rate on semiconductor catalysts by electrochemical methods.

In this paper, a correlation of an electrochemical analysis with a colorimetric analysis is examined for a catalytic reduction of methylene blue to leuco-methylene blue on illuminated TiO_2[6] in aqueous and methanolic solutions. It is demonstrated that the reduction of methylene blue proceeds at the same rate as that of the oxidation of the solvent. As a result, the electrochemical analysis based on the local cell process is found to be useful for estimating a rate of the catalytic reduction of methylene blue and for elucidating factors controlling the rate of the reduction.

Experimental Techniques

Titanium Dioxide Catalyst. Two kinds of commercial single crystals of rutile with different donor densities were used in this study. A face perpendicular to the *c* axis was chosen as the surface of the catalyst.

The main source of the donor is possibly connected with vacant sites of oxygen, for the samples increased their electrical resistance[7] if they were annealed in the air, for example, at 600° for 3 hr. To estimate the donor density, the differential capacitance of the TiO_2 electrode was measured at 1 kHz in methanolic 0.1 *N* HCl by using a bridge described in another paper.[8] The results are shown in Figure 1. The donor density N_D was estimated from the slope of the line[9,10] by using an equation shown in the figure, in which the dielectric constant of rutile was assumed to be 173.[10] The measurements of the differential capacitance were made within the potential range between 0 and 4 V *vs.* sce for obtaining good reproducibility. When the measurements were made in the potential above 4 V, plots of $1/C^2$ *vs.* V were nonlinear and hystereses were observed in these plots, where C and V are the capacitance per unit surface area and the electrode potential, respectively. It was already clarified[10] that these phenomena are due to rapid drifts of the ionized impurities along the *c* axis.[10] The high values of the capacitance for the highly doped sample are due to either the depletion layer of the space charge formed in the surface of the electrode or to the Helmholtz double layer, or both. However, this is not a serious problem, since it is only important in this study whether the donor density of the catalyst is qualitatively high or low.

(1) A. Clark, "Theory of Adsorption and Catalysis," Academic Press, New York, N. Y., 1970, Chapter 15.

(2) S. R. Morrison and T. Freund, *J. Chem. Phys.*, **47**, 1543 (1967).

(3) S. R. Morrison and T. Freund, *Electrochim. Acta*, **13**, 1343 (1968).

(4) C. Wagner, *ibid.*, **15**, 987 (1970).

(5) Z. Takehara, *ibid.*, **15**, 999 (1970).

(6) A. V. Pamfilov, Ya. S. Mazurkevich, and E. P. Pakhomova, *Kinet. Catal. (USSR)*, **10**, 915 (1969).

(7) D. C. Cronemeyer, *Phys. Rev.*, **87**, 876 (1952).

(8) H. Yoneyama and H. Tamura, *Bull. Chem. Soc. Jap.*, **45**, 3048 (1972).

(9) J. F. Dewald, *Bell System Tech. J.*, **39**, 615 (1959).

(10) P. J. Boddy, *J. Electrochem. Soc.*, **115**, 199 (1968).

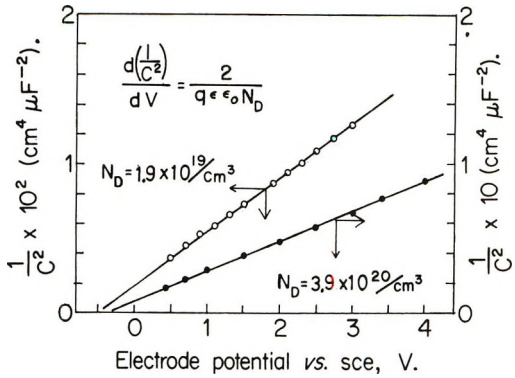

Figure 1. $1/C^2$ *vs.* V plot for two kinds of catalysts in methanolic 0.1 N HCl.

The TiO_2 electrode was prepared by the following procedures. Indium was electroplated on one side of a thin slice of the TiO_2 crystal (6 × 6 × 2.5 mm) as an ohmic contact.[11] The crystal was first fixed in a glass tube with epoxy resin and then coated with silicone rubber cement in such a way that the other side of the slice was contacted by the electrolyte. Before measurements, the crystal face was dipped in concentrated nitric acid for 1 min and then washed thoroughly with de-ionized water.

Solutions. The solutions used in this study were methanol, water, and a methanol–water mixture containing 6.25 M methanol, with 0.1 N HCl, respectively. Methylene blue was dissolved into these solutions so as to give 10^{-5} mol/l.

Light Source. The crystal was illuminated by monochromatic light of 390 nm, which corresponds to the energy gap of TiO_2, obtained from a 500-W xenon arc lamp by using a Shimazu Model QB-50 monochromator. The intensity of the light was detected electrochemically[2] by using the TiO_2 catalysts as the test electrodes in an electrolytic cell with a quartz window and was adjusted by changing the width of a slit of the monochromator so as to give an anodic photocurrent of 2.05 μA/cm^2 at 2.0 V against the sce. In the case of the colorimetric experiments, the electrolytic cell was replaced with a glass container after the light intensity was adjusted.

Colorimetric Analysis. The TiO_2 crystal was set in an upper part of a Bausch and Lomb spectrophotometer cell with silicone rubber cement. The cell was filled with 6 cc of the sample solution and then sealed with a rubber stopper. These procedures were done in a glove box under nitrogen atmosphere free from oxygen. Afterwards, the Bausch and Lomb cell was held in a glass container through which the catalyst was illuminated. Change in the methylene blue content was detected photometrically, by using a 610-nm light.

Electrochemical Measurements. After oxygen-free nitrogen gas was bubbled through the cell for ~30 min, polarization curves were measured. The reference electrode was an sce, and the measurements were made under a stationary state. The potential was recorded by a Takeda Riken Co. electrometer, Model TR-8641, and the current by a Takeda Riken Co. picoammeter, Model TR-8651.

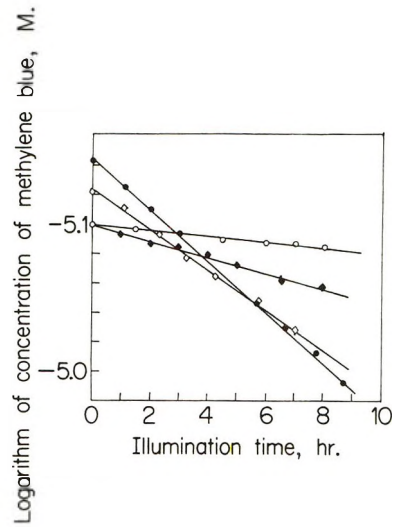

Figure 2. Change of methylene blue concentration in various 0.1 N HCl solutions with illumination time. Solvent: —●—, —◇—, methanol; —◆—, mixture of methanol and water (6.25 M methanol); —○—, water. N_D of catalyst: —○—, —●—, —◆—, low N_D; —◇—, high N_D.

Results and Discussion

Colorimetric Analysis. As Figure 2 shows, the concentration of methylene blue was decreased by the illumination. The reduction seems to be first order in the concentration of methylene blue. The third column of Table I shows the rate constants of the reduction under the various conditions. The reduction rates shown in the fourth column were obtained as products of the quantity of methylene blue in the cell ((6/1000) × 10^{-5} mol), the rate constant in the third column, and the quantity of electricity consumed in the reduction (2 F/mol of methylene blue). Methylene blue was reduced more rapidly in the methanolic solution and on the catalyst of the lower donor density.

Table I: Reduction Rate of Methylene Blue Determined by Colorimetric Analysis

Nominal N_D of catalyst × 10^{-18}, cm^{-3}	Solvent	Rate constant k × 10^{-3}, hr^{-1}	Reduction rate,[a] nA cm^{-2}
19	CH_3OH	40	360
19	$CH_3OH + H_2O$[b]	13	110
19	H_2O	4.5	40
390	CH_3OH	31	280

[a] Surface area of the catalysts was 0.36 cm^2. [b] 6.25 M CH_3OH.

(11) A. Fujishima, K. Honda, and S. Kikuchi, *Kogyo Kagaku Zasshi*, 72, 108 (1969).

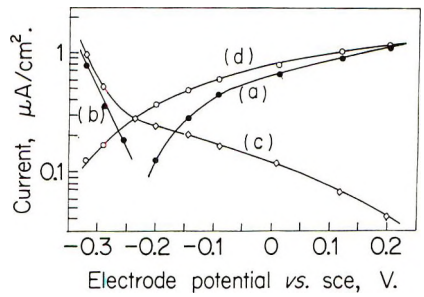

Figure 3. Polarization curves of a TiO_2 electrode of low N_D in 0.1 N HCl–methanol solution: a, measured anodic curve under illumination; b, measured cathodic curve under illumination; c, measured cathodic curve in the dark; d, real anodic curve under illumination.

Methylene blue was hardly reduced by the 610-nm light which was used for analysis. Also, methylene blue scarcely absorbs the light of 390 nm used for experiment. For these reasons, the possibility that the reduction proceeds *via* the photoexcitation of methylene blue is almost negligible.

Oxidation of Solvent. The anodic current in both methanolic and also water solutions increased greatly in proportion to the light intensity. It follows from this observation that holes in the valence band, which are the minority carriers, participate in the anodic process. The anodic process in aqueous solutions involves the decomposition of water and is expressed as[11]

$$H_2O + 2p \longrightarrow {}^1/_2O_2 + 2H^+$$

The anodic photocurrent increased by adding methanol to 0.1 N aqueous HCl at a fixed light intensity. After prolonged polarization of the TiO_2 electrode at 2.0 V in methanolic solution, the carbonyl group was detected in the solution by color identification tests,[12] *i.e.*, the Tollen's reagent test and the mercuric chloride test. Therefore, the following "current doubling" which was already found on ZnO[13] and CdS[14] electrodes must occur also on the TiO_2 electrode

$$CH_3OH + p \longrightarrow CH_3O\cdot + H^+$$
$$CH_3O\cdot \longrightarrow CH_2O + H^+ + e$$

Analysis Based on the Local Cell Process. Figure 3 shows the polarization curves of the TiO_2 electrode of the low N_D in the methanolic solution without methylene blue. The apparent anodic polarization curve (a) and the cathodic one (b) were obtained under illumination, and the cathodic curve (c) was obtained in the dark. An exponential increase of the current with the cathodic polarization was observed both for curves (b and c) for potentials less noble than −0.25 V. This suggests that electrons, which are the majority carriers, are concerned with the cathodic process. The current increase in the potential region less noble than −0.25 V must be brought about by proton discharge superposed on a residual current which is noticeable in the potential range between −0.2 and +0.2 V for the curve c. The nature of the residual current could not be elucidated at present. The decrease of the cathodic current (c) by illumination must be due to participation of an anodic photocurrent (d), since the electron density in the surface of the electrode can hardly be changed by the illumination. The real anodic photocurrent (d) in the potential region of curve a was obtained as the sum of the current in curve a and the absolute value of the current in curve c.

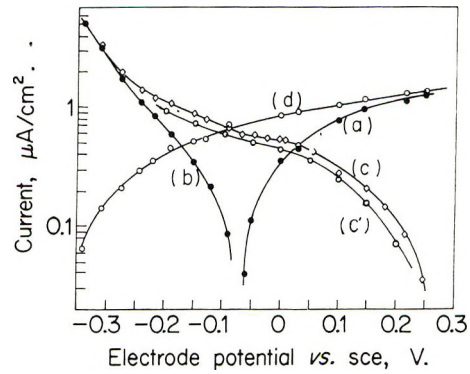

Figure 4. Polarization curves of the same TiO_2 electrode as in Figure 3 in 0.1 N HCl–methanol solution containing 10^{-5} M methylene blue. Notations are the same as in Figure 3; c′, a curve due to the reduction of methylene blue.

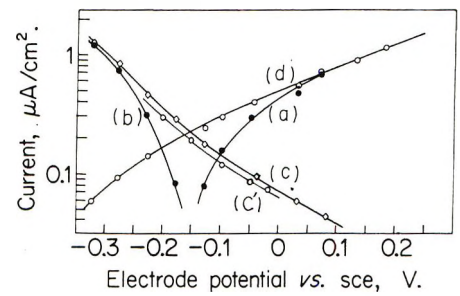

Figure 5. Polarization curves of the same TiO_2 electrode as in Figure 3 in 0.1 N HCl–methanol–water solution (6.25 M methanol) containing 10^{-5} M methylene blue.

Figure 4 shows similar polarization curves of the same electrode in methanolic solution containing 10^{-5} mol/l. of methylene blue. Good reproducibility of the current–potential curves was obtained. It can be noticed that curves d in Figures 3 and 4 really coincide with each other. This suggests that the anodic process consists entirely of the oxidation of the solvent. It is also noticed from comparison of curves c in the two figures that the anodic current is increased greatly by the addition of methylene blue. The increase of the cathodic current in the dark by adding methylene blue should be ascribed to the current reducing methylene

(12) E. Funakubo, "Yūki Kagōbutsu Kakuninhō," Vol. 1, Yokendo, Tokyo, 1967, p 193; Vol. 2, p 73.

(13) W. P. Gomes, T. Freund, and S. R. Morrison, *J. Electrochem. Soc.*, 115, 818 (1968).

(14) H. Gerischer, *Surface Sci.*, 18, 97 (1969).

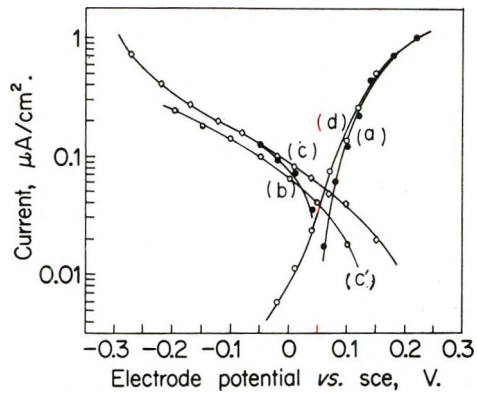

Figure 6. Polarization curves of the same TiO_2 electrode as in Figure 3 in 0.1 N HCl–aqueous solution containing 10^{-5} M methylene blue.

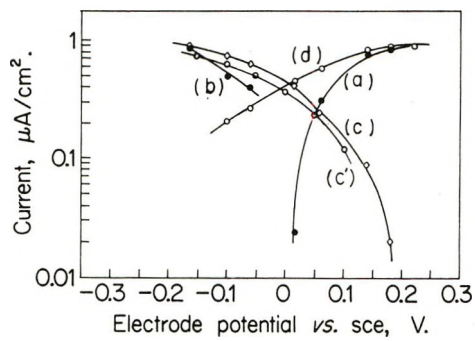

Figure 7. Polarization curves of the TiO_2 electrode of high N_D in 0.1 N HCl–methanol solution containing 10^{-5} M methylene blue. Notations are the same as in Figure 4.

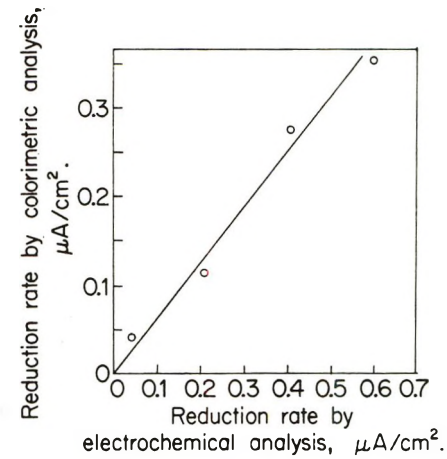

Figure 8. Correlation of reduction rates of methylene blue determined by electrochemical analysis with those determined by colorimetric analysis.

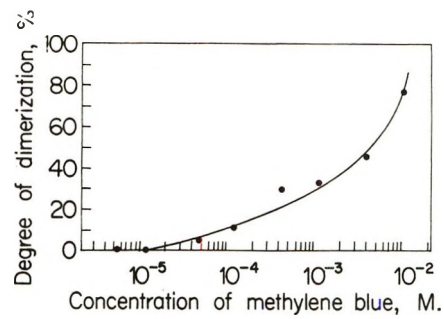

Figure 9. Degree of dimerization of methylene blue in 0.1 N HCl–methanol solution as a function of concentration of methylene blue.

blue to leuco-methylene blue. The curve c′ in Figure 4 shows this increment. It is found from the above discussion that the real rates of the oxidation of the solvent and of the reduction of methylene blue are given by the curves d and c′, respectively. Since the catalyst can be maintained at electrical neutrality at the intersecting point of curves d and c′, the catalytic reduction of methylene blue must proceed at a rate given by the current value at the intersecting point.

Similar polarization curves for methanol–water and water solvents are shown in Figures 5 and 6, respectively, using the same TiO_2. It is found from comparison of the respective curves d and c′ among Figures 4 through 6 that rates both of oxidation of the solvent and of reduction of methylene blue were decreased by changing the solvent from methanol to water and that the current at the interesecting point was decreased as a matter of course by this change of the solvent.

Figure 7 shows the similar polarization curves of the high N_D TiO_2 electrode in methanolic solution. Both Figures 4 and 7, which were obtained in the same solution but on catalysts of different N_D, indicate that the currents c′ and d at the interesting point are controlled by the diffusion rate of methylene blue to the surface of the catalyst and by the number of holes reaching the surface from the interior. It is noticeable that the curves c′ in Figures 4 and 7 almost coincide with each other, while the curves d in these two figures do not. Therefore, it turns out that the difference in the number of holes at the surface possibly brings about the difference in the rate of catalytic reduction of methylene blue in the methanolic solution.

The electrode potential at which curves c′ and d intersect is possibly more noble than the flat-band potential for all experimental conditions in Figures 4 through 7, because a flat-band potential of about −0.3 V was obtained in both methanolic and aqueous solutions containing methylene blue. When the electrode is polarized at a potential more noble than the flat-band potential, the depth of the depletion layer of the space charge is deep for the low N_D, and the field due to the space charge layer can effectively cause holes to drift to the surface. The difference in the number of holes at the surface would arise in such a way if the electrode were illuminated by light having the band gap energy. Such an interpretation would be supported by Gärtner's theoretical analysis[15] of the photocurrent of the minority carrier.

(15) W. W. Gärtner, *Phys. Rev.*, **116**, 84 (1959).

Figure 8 shows the current values at the intersecting points of curves c′ and d in Figures 4 through 7 as a function of the colorimetrically determined reduction rate shown in the fourth column in Table I. A fairly good correlation was observed, although the current values determined by the latter method were about 60% of the values by the former. The difference in the current may be ascribed to the difference in the intensity of the light on the surface of the catalyst, for the glass container and the Bausch and Lomb cell imaginably scatter and absorb the light of 390 nm more than the quartz window.

Methylene blue in aqueous solutions is not dimerized when its concentration is of the order of 10^{-5} *M*. A similar result was obtained in the methanolic HCl solution by an electromotive force measurement,[16] which is shown in Figure 9. Therefore, from the results obtained by the analysis of the local cell process, the reduction of methylene blue can be shown as

$$M^+ + CH_3OH + H^+ \longrightarrow MH_3^{2+} + CH_2O$$

in acid methanol solution, and

$$M^+ + H_2O + H^+ \longrightarrow MH_3^{2+} + {}^1/_2O_2$$

in acid aqueous solution, where M represents the uncharged center of the methylene blue molecule.

Morrison described in his recent review[17] some advantages in the application of electrochemical measurements to studies of electronic interaction between a semiconductor and a molecule: (1) the flow of electrons and holes to the surface can be followed directly; (2) the measurements and controls of the surface potential can be easily done; (3) a variety of substances can be chosen for studies of the electronic interaction. In connection with these advantages, it was found that the electrochemical analysis gave information on the factors controlling the reaction rate rather easily, as had been shown in various studies of electrode reactions.

(16) K. J. Vetter and J. Bardeleben, *Z. Elektrochem.*, **61**, 135 (1957).

(17) S. R. Morrison, "Progress in Surface Science," Vol. 1, S. G Davison, Ed., Pergamon Press, Oxford, 1971, p 107.

The Helix–Coil Transition of Poly-γ-benzyl-L-glutamate in the Solvent System, 1,3-Dichlorotetrafluoroacetone–Water

by G. E. Gajnos* and F. E. Karasz

Polymer Science and Engineering, University of Massachusetts, Amherst, Massachusetts 01002 *(Received March 22, 1972)*

Publication costs assisted by the National Science Foundation

The random coil to helix conformational transition of poly-γ-benzyl-L-glutamate in 1,3-dichlorotetrafluoroacetone–water mixtures was studied as a function of solvent composition, using optical rotation measurements. The polypeptide was soluble in solvent compositions containing between 3.8 and 10.7 wt % water. Within this range, a maximum in the transition temperature was found, at 47.2° and about 8.3 wt % water. This phenomenon can be attributed to the formation of a *gem*-diol of 1,3-dichlorotetrafluoroacetone with an optimum intermolecular hydrogen bonding capability. On either side of the maximum, the transition temperature was found to decrease because of dilution of this species with, respectively, 1,3-dichlorotetrafluoroacetone and water. The thermodynamics of and role of hydrogen bonding in this transition are discussed.

Introduction

The random coil to helix conformational transition of poly-γ-benzyl-L-glutamate (PBG) in binary solvent mixtures containing a strong acid, for example, dichloroacetic acid (DCA) or trifluoroacetic acid (TFA), and a second, "inert" organic solvent has been extensively studied.[1-4] In such mixtures the acid component favors the disruption of the intramolecularly bonded helical conformation, while the other component, for example, chloroform or 1,2-dichloroethane (DCE), is regarded as indifferent to the presence of hydrogen bonds.

Among alternative solvent systems in which a con-

* Department of Chemistry, Western New England College, Springfield, Mass. 01119.

(1) T. Norisuye, M. Matsuoka, A. Teramoto, and H. Fujita, *Polym. J.*, **1**, 691 (1970).

(2) G. Giacometti, A. Turolla, and A. S. Verdini, *J. Amer. Chem. Soc.*, **93**, 3092 (1971).

(3) J. Steigman, A. S. Verdini, C. Montagner, and L. Strasorier, *ibid.*, **91**, 1829 (1969).

formational transition may be observed, some attention has been focused on halogenated ketones and their hydrated derivatives. Middleton investigated several such solvent systems for proteins and polypeptides,[5] while Longworth observed a solvent-induced conformational transition for PBG in mixtures of the monohydrate of 1,3-dichlorotetrafluoroacetone with chloroform.[6] More recently, Roche and coworkers studied the conformation of poly-γ-methyl-L-glutamate in a number of halogenated alcohols, finding that the compounds of greatest hydrogen bonding capability disrupted the ordered conformation of this polypeptide.[7,8] Although thus qualitatively similar in effect to DCA or TFA, these compounds are in fact very weak acids with pK_a's around 6–7.[8] All the studies reported above were carried out at ambient temperatures.

In the present investigation we have made a systematic study of the conformational transition of PBG in the 1,3-dichlorotetrafluoroacetone (DCTFA)–water system over a range of solvent compositions and temperatures. The purpose of this study was to determine the precise relation of solvent structure and composition to intermolecular hydrogen bonding capability. In addition, estimates of the transition enthalpy and cooperativity were of interest.

Experimental Section

A sample of PBG (Pilot Chemicals, Inc., Lot G-145, $\bar{M}_v$ 300,000) was used as received. DCTFA (Hynes Chemical Research Corp., Lot H-115) was distilled at atmospheric pressure (45.3°) under dry nitrogen and stored at 0°. The water was doubly distilled. It was found that the PBG was soluble in solvent mixtures containing between 3.8 and 10.7 wt % water, and all experiments reported were thus performed within this composition range.

The optical rotation of PBG solutions in different solvent compositions was measured as a function of temperature at 589 nm using a Perkin-Elmer Model 141 polarimeter and a 10-cm jacketed micro-cell. All solutions were handled under a dry nitrogen atmosphere and filtered before insertion in the cell. The PBG concentration of most solutions studied was 0.2% w/v; in a few cases, however, the concentration was varied from 0.1 to 0.7% w/v. No effect on the specific rotation and hence on the transition temperature was observed.

Results

Typical specific rotation *vs.* temperature curves obtained are shown in Figure 1. Sigmoidal curves characteristic of the thermally induced conformational transition of a polypeptide were observed for all solvent compositions in the range available. The change from negative to positive [α] values with increasing temperature,[4] taken in conjunction with existing data

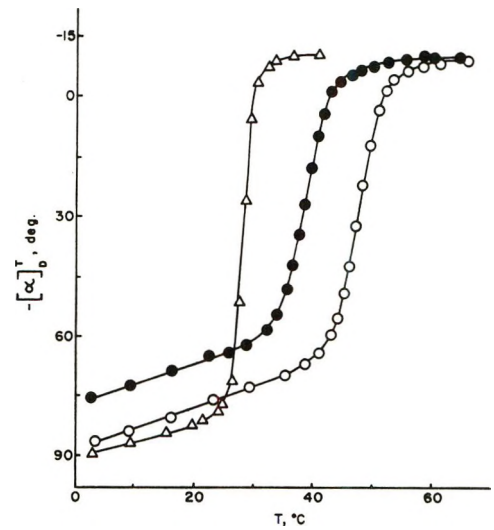

Figure 1. Typical specific rotation (589 nm) *vs.* temperature for 0.2% PBG in DCTFA–H_2O mixtures: △, 4.68 wt % H_2O; ●, 8.26 wt % H_2O; ○, 10.12 wt % H_2O.

for PBG, in particular those in related fluoroalcohol solvents,[6] establishes that a coil to helix, or so-called "inverse" thermal transition was observed. The specific optical rotation at 589 nm of the helical conformation, around +10°, corresponds approximately to that found for this conformation in other solvents,[9] but as was already observed by Longworth, the coiled conformation displays a considerably greater negative [α], (−70° to −90°) in halogenated ketones[6] than is observed in the strong acid solvents (*e.g.*, −15° for PBG in DCA). There is one point in the solvent composition–temperature plane studied here at which a quantitative comparison with existing optical rotation data can be made: at a composition of 91.7 wt % DCTFA–8.3 wt % H_2O and at 25° Longworth found $[\alpha]_{589}$ to be −71.6°; our value was −74°.

Transition temperatures (T_c) were determined from [α] *vs.* T data in the normal manner; the fractional helical content (f_H) was assumed to vary linearly with [α] and the temperature corresponding to $f_H = 0.5$ thus obtained.[10] The value of [α] for the coiled conformation is seen to vary considerably with temperature (Figure 1) and thus a slight degree of arbitrariness with respect to the determination of f_H is present; we have taken the value of $[\alpha]_{589}$ at which the sig-

(4) For earlier references, see G. D. Fasman in "Poly-α-amino Acids," G. D. Fasman, Ed., Marcel Dekker, Inc., New York, N. Y., 1967.

(5) W. J. Middleton and R. V. Lindsey, Jr., *J. Amer. Chem. Soc.*, **86**, 4948 (1964).

(6) R. Longworth, *Nature (London)*, **203**, 295 (1964).

(7) D. Balasubramanian and R. S. Roche, *Polym. Prepr., Amer. Chem. Soc. Div. Polym. Chem.*, **11**, 127, 132 (1970).

(8) D. Balasubramanian and R. S. Roche, IUPAC International Symposium on Macromolecules, Paper IIC30, Leiden, 1970.

(9) E. R. Blout, P. Doty, and J. T. Yang, *J. Amer. Chem. Soc.*, **79**, 749 (1957).

(10) J. Applequist, *J. Chem. Phys.*, **38**, 934 (1963).

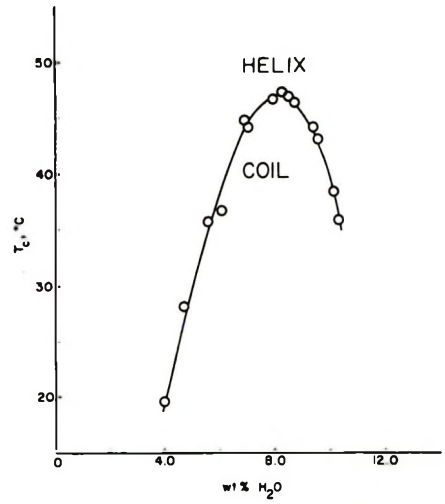

Figure 2. Transition temperatures of PBG in DCTFA–H_2O mixtures as function of solvent composition.

moidal portion of the curve meets the linear section as representing the point $f_H = 0$ in the calculation. Because of the relatively large overall change in $[\alpha]$ in the transition, and the high $d[\alpha]/dT$, any error in this assignment can not reasonably affect T_c by more than a few tenths of a degree.

Figure 2 is a phase diagram showing the observed transition temperature as a function of solvent composition. A maximum is seen to occur at about 47.2° with a solvent composition of 91.74 wt % DCTFA–8.26 wt % H_2O. The phase boundary curve (locus of points at which $f_H = 0.5$) separates regions in which the polypeptide assumes ordered or disordered conformations as indicated.

Because of the nature of the phase diagram, an isothermal measurement of $[\alpha]$ as a function of solvent composition at any temperature below 47.2° will display two transitions. Thus, in an isothermal solvent titration experiment the addition of water to a solution of PBG in 97% DCTFA will induce first a helix to coil transition followed by the reverse conformational change upon further addition of water. This effect is demonstrated in Figure 3, in which we observe also that at 45° the width of the transition zone is such as to prevent the complete formation of the coiled conformation in the solvent-induced transition. At lower temperatures this is not the case, as is indicated by the flat minimum in the 40° isotherm.

The explanation for this overall phenomenon is the following. The solvent composition at the maximum in T_c corresponds to an equimolar mixture of DCTFA and water, *i.e.*, to the composition of the *gem*-diol, 1,3-dichloro-1,1,3,3-tetrafluoropropan-2,2-diol (DCTFPD). Nonequimolar compositions thus contain excess DCTFA or H_2O, respectively, and such compositions may therefore be regarded as binary mixtures of the *gem*-diol DCTFPD with either the ketone or the water. Both of the latter compounds assume the role

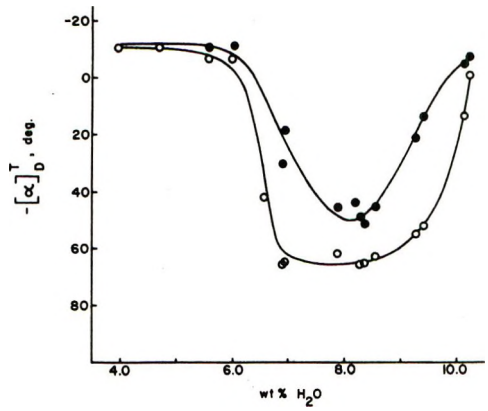

Figure 3. Isothermal specific rotation (589 nm) curves as function of solvent composition: ●, 45°; ○, 40°.

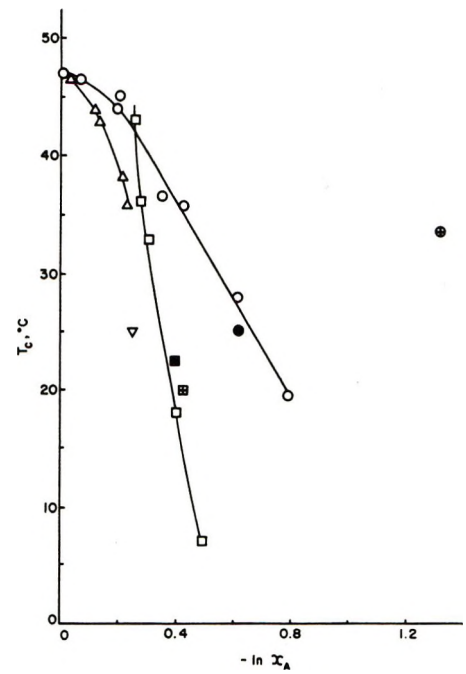

Figure 4. Transition temperatures as function of mole fraction of active solvent, A, in binary solvent pairs (active solvent given first): △, DCTFPD–H_2O (this work); ○, DCTFPD–DCTFA (this work); ●, DCTFPD–$CHCl_3$ (ref 6); □, DCA–DCE (ref 11); ▽, DCA–H_2O (ref 3): ■, DCA–$CHCl_3$ (ref 9); ⊕, TFA–$CDCl_3$ (ref 12); ⊞, DCA–tetrabromoethane (ref 12).

of inert solvent and therefore depress the transition temperature, T_c. Their effect, therefore, is entirely analogous to the effect of DCE in lowering the thermal transition temperature of PBG in DCA.[11] Thus, the data in Figure 2 have been replotted in terms of T_c *vs.* log x_A, where x_A is the solvent composition expressed in terms of mole fraction of the diol in the DCTFPD–water or DCTFPD-DCTFA mixtures (Figure 4). Such a plot stems from a consideration of the simplest thermodynamic model for the transition in a binary

(11) F. E. Karasz and J. M. O'Reilly, *Biopolymers*, 5, 27 (1967).

active–inert solvent system.[11] If water and DCTFA were completely inert diluents, we would expect the two branches to superimpose; this is clearly not the case. The deviation is due to the fact that water, because of its own hydrogen bonding capability, acts as a competitor for the intermolecular bonding between the diol and the polypeptide. This competition effectively weakens the helix-disrupting capability of the *gem*-diol, as is indicated by the fact that the water branch of the melting point depression curve falls to the left of the DCTFA branch in Figure 4.

This situation is developed in a wider context with the inclusion in Figure 4 of available T_c *vs.* solvent composition data for several other binary mixtures, in each case plotted in terms of x_A, mole fraction of the active species, *i.e.*, the species capable of forming intermolecular hydrogen bonds. Such a plot indicates directly the relative strength of the active species in inducing a helix to coil transition in PBG by preferential binding. Thus, we see that trifluoroacetic acid is, as expected, by far the strongest species in this context.[12] Unfortunately, T_c measurements as a function of composition do not appear to be available for TFA and thus we cannot comment on the binding enthalpy, which can be deduced from the slope $\partial \ln x_A/\partial T$. It is seen from Figure 4 that the *gem*-diol under consideration in this study, DCTFPD, is capable of inducing the transition in PBG at ambient temperatures more readily than the strong acid DCA. The single point from the data of Longworth for the diol in which $CHCl_3$ was used as the inert species fits well on the DCTFA branch of the DCTFPD curve, thus supporting our view that the ketone itself may be regarded as an inert diluent in this system. Clearly, additional data would be desirable with regard to this point. We next consider the DCA melting point curve. Data for solvents which may be reasonably regarded as inert are shown. These are DCE,[11] $CHCl_3$,[9] and 1,1,2,2-tetrabromoethane,[13] and the data for all three diluents are satisfactorily collinear. The single point available for the system DCA–H_2O[3] lies to the left of the DCA–organic solvent line; this again appears to fit in with the view expressed above that water must in this context be regarded as a competitive rather than truly inert species.

In the above discussion it has been implied that the activity coefficients of the active species in the mixtures, while not necessarily unity, are independent of the inert species. That this is not necessarily the case when the latter are of relatively high molecular weight has been shown earlier.[11] In general, any solvent–solvent interaction could be considered in terms of changes in relative activity coefficients.

Finally, we wish to comment on the thermodynamic aspects of the studies carried out. The van't Hoff heat, ΔH_{VH}, can be calculated from f_H *vs.* T data using the result[10]

$$\left(\frac{\partial f_H}{\partial(1/T)}\right)_{f_H=0.5} = -\frac{\Delta H_{VH}}{4R}$$

in the usual manner. It was found that ΔH_{VH} varied with T_c and hence with solvent composition, decreasing from about 200 kcal/mol to about 80 kcal/mol as the weight percentage of water in the DCTFA–H_2O mixtures increased from 3.8 to 10.7%. Thus, ΔH_{VH} first decreases with increasing T_c, as has been found to be the case for the PBG–DCA–DCE system,[14] an observation which can be accounted for in terms of decreasing peptide–DCA interaction. Beyond the maximum in T_c, 47.2° in the present system, ΔH_{VH} is approximately constant. This can be related to a possible change in cooperativity as a function of solvent composition when parallel values for the calorimetric heats of transition become available.[10]

From T_c *vs.* ln x_A data presented in Figure 4, we can calculate the transition enthalpy according to

$$\frac{\partial \ln x_A}{\partial(1/T)} = -\frac{\Delta H_c}{R}$$

where ΔH_c is the "composition" enthalpy, defined in terms of moles of bound solvent,[11] in this case the diol. The relation of ΔH_c to the calorimetric enthalpy ΔH, which is calculated on a peptide residue mole basis, depends on the peptide–solvent stoichiometry. However, it can be shown that ΔH_c is an upper limit for ΔH. Using the data of the "inert," DCTFA branch of the T_c *vs.* ln x_A curve, Figure 4, we find that at 30°, ΔH_c is about 4000 cal/mol. The corresponding upper limit to the Zimm–Bragg cooperativity parameter σ,[15] which is equal to $(\Delta H/\Delta H_{VH})^2$, is thus about 4×10^{-4}. This is within the range of σ found for the PBG transition in other solvent systems and leads to the conclusion that at least from the point of view of cooperativity the helix to coil transition mechanism in the *gem*-diol–inert solvent mixtures studied here is essentially the same as in solvent systems containing strong acids.

Conclusion

The present study shows clearly the considerable potency of DCTFPD as a disrupting agent for the PBG helix. In this respect it is roughly comparable to DCA at ambient temperatures. The maximum in the plot of the transition temperature as a function of solvent composition, while unusual, is readily explicable; we would predict that, in principle, other halogenated ketone–water solvent systems could show the same effect with PBG or with any other polypeptide whose ordered conformation is relatively stable. (For *weak* ordered conformations, the thermally induced

(12) D. I. Marlborough, K. G. Orrell, and H. N. Rydon, *Chem. Commun.*, 518 (1965).

(13) J. Y. Cassim and E. W. Taylor, *Biophys. J.*, **5**, 553 (1965).

(14) F. E. Karasz and J. M. O'Reilly, *Biopolymers*, **4**, 1015 (1966).

(15) B. H. Zimm and J. K. Bragg, *J. Chem. Phys.*, **31**, 526 (1959).

transition would be of the "normal" helix-to-coil variety, and hence increasing inert diluent concentration would *increase* T_c.) Whether such a maximum can actually be observed within the accessible temperature and solute solubility range, however, would depend on the thermodynamic parameters for the particular system under investigation.

In terms of the overall transition parameters, ΔH_{VH} and σ, also, the present system appears to be quite similar to the PBG–DCA system. The stoichiometry of the peptide-active solvent binding reaction which is, of course, a key factor in determining the transition temperature and indeed the direction of the thermal transition, unfortunately, cannot yet be assessed from the available data. It would be reasonable to assume that the different potential binding sites in the *gem*-diol and the strong carboxylic acid would be reflected here.

Acknowledgment. The work reported above was supported by the National Science Foundation, Grant GB 8080 (F. E. K.).

Aggregation of Salts of Thianthrene Radical Cations

by M. de Sorgo, B. Wasserman, and M. Szwarc*

SUNY Polymer Research Center, College of Forestry at Syracuse University, Syracuse, New York 13210
(Received May 4, 1972)

Publication costs assisted by the National Science Foundation

A partial association of the paramagnetic perchlorate salt of thianthrene radical cation ($T\cdot^+$, ClO_4^-) into a diamagnetic dimer takes place in propionitrile and in trifluoroacetic anhydride containing 10% trifluoroacetic acid, but not in 10^{-3} M solution in trifluoroacetic acid. Quantitative association occurs trifluoroacetic anhydride. The optical spectra of the monomer ($T\cdot^+$ or $T\cdot^+$, ClO_4^-) and of the dimer ($T\cdot^+$, $ClO_4^-)_2$ are reported. In propionitrile the equilibrium of association seems to be given by the equation, $2T\cdot^+ + 2ClO_4^- \rightleftarrows (T\cdot^+, ClO_4^-)_2$; *i.e.*, ion pairs $T\cdot^+$, ClO_4^- are dissociated in propionitrile but the dimer is not. The equilibrium constants and the relevant ΔH and ΔS are reported. The equilibrium of association in $(CF_3CO)_2O$ + 10% CF_3COOH probably is described by the equation $2(T\cdot^+, ClO_4^-) \rightleftarrows (T\cdot^+, ClO_4^-)_2$.

Investigations of the spectra and chemical behavior of thianthrene radical cation, $T\cdot^+$, led to some conflicting

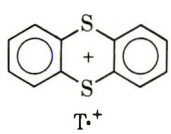

$T\cdot^+$

results[1-3] (see *e.g.*, ref 2a). The system seems to be complex and indeed Lucken[1] reported that the spectra of solutions of $T\cdot^+$ vary with dilution, temperature, and the nature of the solvent. His attempts to follow quantitatively these changes were unsuccessful.

In the course of our studies of various electron-transfer processes we reinvestigated the optical and esr spectra of thianthrene perchlorate, $T\cdot^+$, ClO_4^-, in propionitrile and less extensively in trifluoroacetic acid and trifluoroacetic anhydride. The results clarify, at least to some extent, the puzzling features of this system and might be helpful in future investigations.

Lucken suggested[1] that thianthrene radical cations may dimerize, and the spectrum of the dimer may substantially differ from that of the monomer. Our observations confirm this idea. At room temperature the dilute propionitrile solutions of $T\cdot^+$, ClO_4^- are paramagnetic, their esr spectra give the previously reported quintuplet, and the visible spectrum, shown in Figure 1, has a single peak at λ_{max} 543 nm (ϵ 1.2 × 10^4). However, at higher concentrations and at lower temperatures the spectrum broadens and eventually the spectrum shown in Figure 2 is produced. This spectrum is characterized by two bands λ_{max} 470 (ϵ 0.35 × 10^4) and 594 nm (ϵ 0.56 × 10^4) and the extinction coefficient at 543 nm (λ_{max} in dilute solution) is 0.31 × 10^4. Furthermore, the concentrated solution is diamagnetic at low temperature. The ratios of the intensities of the two bands, corrected for the absorption

(1) E. A. C. Lucken, *J. Chem. Soc.*, 4963 (1962).

(2) (a) H. J. Shine and L. Piette, *J. Amer. Chem. Soc.*, **84**, 4798 (1962); (b) Y. Murata and H. J. Shine, *J. Org. Chem.*, **34**, 3368 (1969).

(3) Y. Sato, M. Kinoshita, M. Sano, and H. Akamatu, *Bull. Chem. Soc. Jap.*, **40**, 2539 (1967); **42**, 548 (1969).

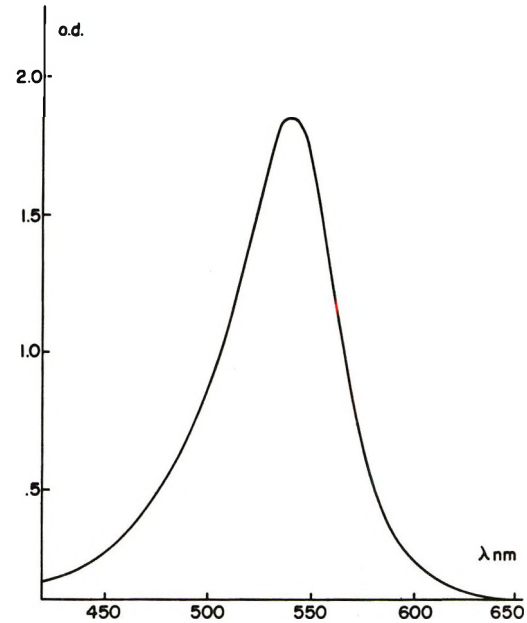

Figure 1. Visible spectrum of thianthrinium perchlorate (monomeric radical cation) in propionitrile at 21° ($[T\cdot^+,ClO_4^-] = 1.5 \times 10^{-4}\ M$).

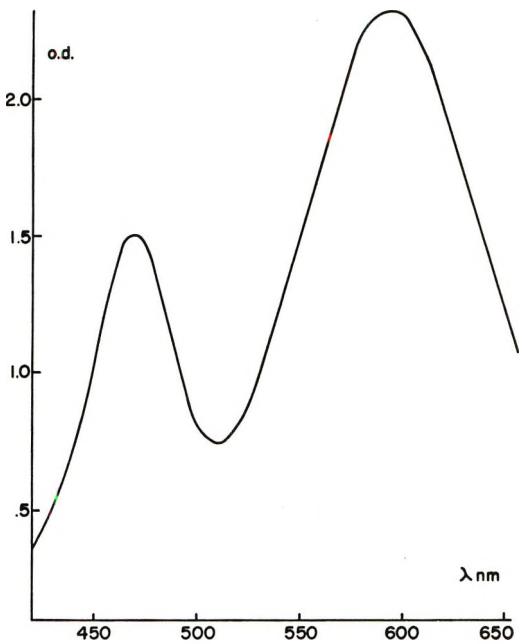

Figure 2. Visible spectrum of thianthrinium perchlorate aggregate (the diamagnetic species) in propionitrile at −80° (total salt concentration $\sim 4.9 \times 10^{-3}\ M$).

due to the paramagnetic species, are independent of concentration. Hence, it is plausible to assume that these two bands arise from one species only.

The changes in the optical and esr spectra are reversible. Cooling and warming the solution or diluting it and then concentrating restores the properties of the original solution. Moreover, the normalized optical spectra obtained at different concentrations show two isosbestic points at about 490 and 570 nm, respectively.[4] These results indicate that we deal here with only two distinct species in equilibrium with each other, and thus we reconfirm the conclusion that the two bands at 470 and 494 nm, respectively, belong to one species.

We attribute the spectrum shown in Figure 1 to the paramagnetic, monomeric thianthrene radical cation, $T\cdot^+$, whereas the spectrum shown in Figure 2 seems to be due to a diamagnetic aggregate. The extinction coefficients of the paramagnetic species at 470 and 594 nm are 0.25×10^4 and 0.15×10^4, respectively. Hence, all the data needed to determine the composition of the solution by spectrophotometric methods are available. The composition was calculated from the ratios of optical densities at 543 and 594 nm. The results are summarized in Table I and were supplemented by esr analysis, calculating the concentrations of paramagnetic species from the overmodulated esr signal.

Plots of log $[T\cdot^+]$ *vs.* log [diamagnetic species] at various constant temperatures are shown in Figure 3. A series of parallel straight lines with slope 4 fit reasonably well the experimental points obtained at the lowest temperature, although substantial deviations are seen at −20 and 0°. This surprising result could be interpreted as evidence for tetramerization of $T\cdot^+$ salts in propionitrile, *viz.*

$$4T\cdot^+, ClO_4^- \rightleftharpoons (T\cdot^+, ClO_4^-)_4$$

paramagnetic diamagnetic

However, an alternative interpretation is possible. Dielectric constant of propionitrile is relatively high, ~28 at 20° and still higher at lower temperatures. The

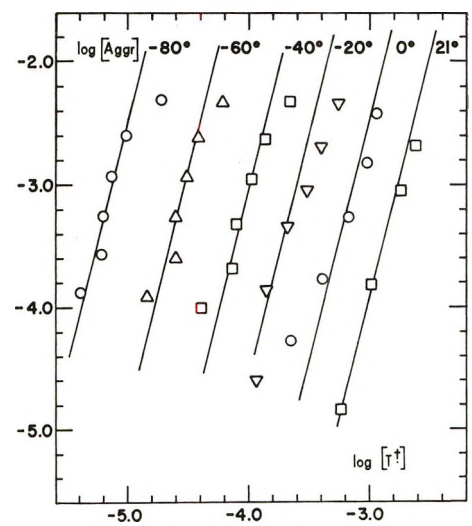

Figure 3. Plot of log $[T\cdot^+]$ *vs.* log [diamagnetic species]. At 21° the data were obtained spectrophotometrically, at other temperatures by esr determination.

(4) Similar changes in the optical spectra of acetonitrile solutions $T\cdot^+$ and the appearance of two isosbestic points were noted by H. J. Shine (private communication).

Table I: Equilibrium Concentrations of the Paramagnetic $T\cdot^+$ and Its Diamagnetic Aggregate in Propionitrile as Functions of Dilution and Temperature[a]

T, °C		Concentrations					
21	[$T\cdot^+$]	22.7	16.9	10.2	5.45	2.65	1.38
	[Aggr.]	26.1	7.0	1.49	0.14	0.02	
					$K = 1 \times 10^8\ M^{-3}$		
0	[$T\cdot^+$]	10.1	9.2	6.4	3.9	2.1	1.1
	[Aggr.]	37.9	14.7	5.3	1.7	0.5	0.25
					$K = 2.6 \times 10^9\ M^{-3}$		
−20	[$T\cdot^+$]	5.2	3.8	2.9	2.0	1.4	0.76
	[Aggr.]	43.6	20.1	8.9	3.56	1.31	0.62
					$K = 2.2 \times 10^{11}\ M^{-3}$		
−40	[$T\cdot^+$]	2.1	1.28	1.00	0.78	0.69	0.39
	[Aggr.]	46.7	22.5	10.7	4.81	1.98	0.99
					$K = 1.0 \times 10^{13}\ M^{-3}$		
−60	[$T\cdot^+$]	0.58	0.37	0.30	0.25	0.24	0.14
	[Aggr.]	48.2	23.5	11.4	5.34	2.43	1.24
					$K = 4 \times 10^{14}\ M^{-3}$		
−80	[$T\cdot^+$]	0.18	0.09	0.07	0.06	0.06	0.04
	[Aggr.]	48.6	23.8	11.6	5.53	2.61	1.34
					$K = 3 \times 10^{17}\ M^{-3}$		

[a] All the concentrations given in $10^{-4}\ M$ units; Aggr. is counted as 2 equivalents.

equilibrium between the paramagnetic and diamagnetic species could, therefore, be described by the equation

$$2T\cdot^+ + 2ClO_4^- \rightleftharpoons \underset{\text{diamagnetic}}{(T\cdot^+, ClO_4^-)_2}$$

implying that under our experimental conditions the thianthrene perchlorate is virtually dissociated into free ions, whereas the diamagnetic dimer is associated with two ClO_4^-, forming perhaps a sandwich-like structure. This simple relation is probably valid at the lowest temperatures, since the ion pair dissociation is then favored. At higher temperatures some association of $T\cdot^+$ and ClO_4^- ions may take place leading to deviations reflected in Figure 3.

To verify the above ideas we investigated in a semi-quantitative fashion the conductance of thianthrene perchlorate in propionitrile at room temperature. The results led to $\Lambda = 130$ and 160 cm²/ohm equiv at the total concentration of the salt of 25×10^{-4} and $6 \times 10^{-4}\ M$, respectively (Λ's were calculated on the basis of the *total* salt concentration). This indicates a high degree of dissociation of the salt in the investigated concentration range. We may add that the conductance of H_3O^+, ClO_4^- (a wet perchloric acid) in propionitrile is similar, the respective Λ_0 being about 200 cm²/ohm equiv.

The results given in Table I lead to the approximate equilibrium constants of the "tetramerization" which are listed in the table. The respective van't Hoff plot is shown in Figure 4 and leads to the values of $\Delta H = -23$ kcal/mol and $\Delta S = -42$ eu.

It is interesting to compare the above ΔH and ΔS values with those found for the association of free ions of alkali salts into ion pairs in tetrahydrofuran.

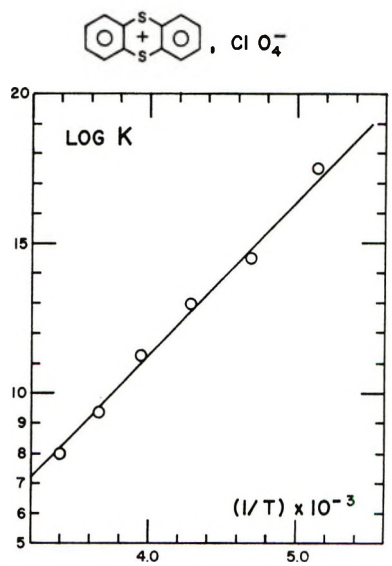

Figure 4. Van't Hoff plot of log K *vs.* $1/T$.

ΔH and ΔS of such associations are often *positive*, indicating that desolvation of the ions takes place on their pairing. Apparently, propionitrile is not a strongly solvating agent; the dissociation of ion pairs is facilitated by its relatively high dielectric constant and not by a powerful solvation of the free ions.

Further evidence for the ionic type of aggregation is provided by the following observations. The spectrum of $1 \times 10^{-3}\ M$ solution of $T\cdot^+$, ClO_4^- in trifluoroacetic acid revealed only one peak with λ_{max} at 540 nm; apparently the concentration of the aggregate was negligible at that concentration. The spectrum was broader at the salt concentration of $3 \times 10^{-2}\ M$, and a shoulder at about 610 nm was clearly discerned, imply-

ing an increase in the proportion of the aggregate. Interestingly, the spectrum of $T\cdot^+$, ClO_4^- in trifluoroacetic anhydride containing 10% trifluoroacetic acid showed the two peaks characteristic of the aggregate at salt concentration as low as 5×10^{-4} M and even at a concentration of 1×10^{-4} M the spectrum clearly reveals the presence of an appreciable fraction of the aggregates.

The dielectric constant of trifluoroacetic acid[5] is only 8.9 at 0°, and it increases at lower temperatures. This value is substantially lower than that reported for propionitrile[6] (about 28). Nevertheless, it seems that the aggregation is much less pronounced in trifluoroacetic acid than in propionitrile. Probably the former solvent strongly interacts with the ions and this either favors the dissociation of ion pairs into free ions or modifies the character of ion pairs from tight ones into loose ones (the respective anion might be $(CF_3\cdot COO)_2H^-$).

Apparently trifluoroacetic anhydride is a poorer solvating agent and its dielectric constant[5] is only 2.7. These properties account for the high degree of aggregation in the anhydride. It is also probable that the equilibrium in this solvent is given by the equation

$$2(T\cdot^+, ClO_4^-) \rightleftharpoons (T\cdot^+, ClO_4^-)_2$$

i.e., the aggregation is described as a dimerization and not tetramerization, because $T\cdot^+$, ClO_4^- ion pairs are not expected to dissociate in this medium.

Finally, it is known that some radical cations combine with the parent compound into dimers,[7] *e.g.*, $(naphthalene)_2\cdot^+$. We investigated, therefore, the effect of addition of neutral thianthrene to the solution of $T\cdot^+$, ClO_4^- in propionitrile. Such an addition did not change the spectrum implying that the equilibrium

$$T\cdot^+ + T \rightleftharpoons (T_2)\cdot^+$$

lies far to the left.

In conclusion, we showed the importance of ionic aggregation in the investigated system and hope that these findings might help in clarifying some peculiarities of this complex system.[8]

Experimental Section

Thianthrinium perchlorate was prepared by reacting equimolar amounts of thianthrene and $HClO_4$ in acetic anhydride.[2b] The resulting salt was precipitated and washed by CCl_4 and dried under high vacuum. Propionitrile was dried by refluxing it over P_2O_5, redistilled onto Na_2CO_3, and finally distilled onto $MgClO_4$. It was then deaerated and distilled into a sealed container on a high-vacuum line. Before being used for preparation of a solution, the solvent was dried again with molecular sieves, 4×, for 2 days.

The stock solution (4.8×10^{-3} M) of thianthrinium perchlorate was prepared on a high-vacuum line and the other solutions were then prepared by dilution technique, all the operations being performed again on a high-vacuum line.

Acknowledgment. We wish to thank the National Science Foundation and the Petroleum Research Fund, administered by the American Chemical Society, for the financial support of this investigation.

(5) F. E. Harris and C. T. O'Konski, *J. Amer. Chem. Soc.*, **76**, 4317 (1954).

(6) J. M. Tedder, *J. Chem. Soc.*, 2646 (1954). Interestingly the dielectric constant of acetic anhydride is reported to be 21 and that of acetic acid only 6. Perhaps these results should be checked.

(7) I. C. Lewis and L. S. Singer, *J. Chem. Phys.*, **43**, 2712 (1965).

(8) NOTE ADDED IN PROOF. During a recent meeting on organosulfur compounds which took place in Sweden in the fall of 1972, O. Hammerich and V. D. Parker reported dimerization of $T\cdot^+$ observed at −60° in a mixture of trifluoroacetic acid, its anhydride, and CH_2Cl_2.

Ion–Solvent Interactions. Effect on Ionic Aggregation in the System Sodium Tetra-*n*-butylaluminate–Cyclohexane–Tetrahydrofuran

by J. H. Muller and M. C. Day*

Department of Chemistry, Louisiana State University, Baton Rouge, Louisiana 70803 *(Received July 26, 1971)*

Ion–solvent interactions have been studied in cyclohexane solutions of sodium tetra-*n*-butylaluminate ($NaAlBu_4$) as a function of added tetrahydrofuran (THF) using differential vapor pressure analysis. Departure from ideality, as determined by means of the differential vapor pressure method, is attributed to an aggregation process. The apparent degree of aggregation varies from ion pairs at a concentration of approximately 0.0025 *M* to an aggregation number of 6 at a concentration of the order of 2 *M*. Addition of THF to the salt solutions is found to lower the apparent molecular weight of the solute relative to that of the corresponding solvated aggregate. The magnitude of this effect is found to increase with both an increase in the ratio of THF:$NaAlBu_4$ and with an increase in $NaAlBu_4$ concentration. This is attributed to a loss of aggregate stability in both instances.

Introduction

There has historically been an interest in ionic solution models with the aggregate proposal of Fuoss and Kraus[1] still among the more important, but this model has often been attacked, even by Kraus.[2] A new element was introduced with the proposal by Winstein[3] of two types of ion pairs, and the observation of these has been reported by numerous experimenters.[4–8] This requires the consideration of specific ion–solvent interactions and, although solvent effects have long been recognized,[9] only recently has it been possible to observe specific solvation and relate it to ion pair type.[10–15]

In the research program of this group, the $NaAl(alkyl)_4$ salts have been used to study specific solvation effects. These compounds are particularly useful because of the ability of many of them to show the unique property of solubility in saturated hydrocarbon solvents. This then permits the addition of controlled amounts of a complexing agent and the observation of specific solvation. Based on infrared studies by Olander[16] and the interpretation of far-infrared data reported on solutions of sodium tetra-*n*-butylaluminate ($NaAlBu_4$) in cyclohexane, tetrahydrofuran(THF), and cyclohexane–THF mixtures by Tsatsas and Risen,[17] a model has been proposed by Olander[16] for $NaAlBu_4$ in these solvents which depends on aggregation of $NaAlBu_4$ in cyclohexane.

Herein we wish to report molecular weight studies of $NaAlBu_4$ in cyclohexane as a function of salt concentration and the effects of small ratios of THF:$NaAlBu_4$ on the degree of salt aggregation.

Experimental Section

The preparation of $NaAlBu_4$ and the solvents has previously been reported.[11]

The molecular weight determinations were made with an osmometer[18] constructed in such a manner that the system could be studied in an inert atmosphere. The thermistors were Sargent No. S-81620 with a 1500 ohm resistance at 25°. The cell was charged in a nitrogen drybox and then placed in a constant-temperature bath where measurements were made at 25 ± 0.05°. After temperature equilibration, droplets of the appropriate solutions were added to the respective thermistors by means of mounted droppers that had previously been charged in the drybox. A drop of the pure solvent was placed on the reference thermistor and a drop of the appropriate solution was placed on

(1) R. M. Fuoss and C. A. Kraus, *J. Amer. Chem. Soc.*, **55**, 21, 476, 1019, 2387 (1933).

(2) L. Kenausis, E. Evers, and C. A. Kraus, *Proc. Nat. Acad. Sci. U. S.*, **48**, 121 (1962).

(3) S. Winstein, *et al.*, *J. Amer. Chem. Soc.*, **76**, 2597 (1954); **80**, 169 (1958).

(4) T. R. Griffiths and M. C. R. Symons, *Mol. Phys.*, **3**, 90 (1960).

(5) T. E. Hogen-Esch and J. Smid, *J. Amer. Chem. Soc.*, **88**, 307 (1966).

(6) J. P. Oliver and C. A. Wilkie, *ibid.*, **89**, 163 (1967).

(7) E. S. Gore and H. S. Gutowsky, *J. Phys. Chem.*, **73**, 2515 (1969).

(8) M. Szwarc, *Accounts Chem. Res.*, **2**, 87 (1969), and references therein.

(9) C. A. Kraus, *J. Chem. Educ.*, **35**, 324 (1958).

(10) E. Schaschel and M. C. Day, *J. Amer. Chem. Soc.*, **90**, 503 (1968).

(11) E. G. Höhn, J. A. Olander, and M. C. Day, *J. Phys. Chem.*, **73**, 3880 (1969).

(12) J. L. Wuepper and A. I. Popov, *J. Amer. Chem. Soc.*, **92**, 1493 (1970).

(13) W. F. Edgell, J. Lyford, R. Wright, W. R. Risen, and A. Watts, *ibid.*, **92**, 2240 (1970).

(14) L. L. Chan, K. H. Wong, and J. Smid, *ibid.*, **92**, 1955 (1970).

(15) N. Hirota, *ibid.*, **90**, 3603 (1968).

(16) J. A. Olander and M. C. Day, *ibid.*, **93**, 3384 (1971).

(17) A. J. Tsatsas and W. M. Risen, *ibid.*, **92**, 1789 (1970).

(18) A. Wilson, L. Bini, and R. Hofstader, *Anal. Chem.*, **33**, 135 (1961).

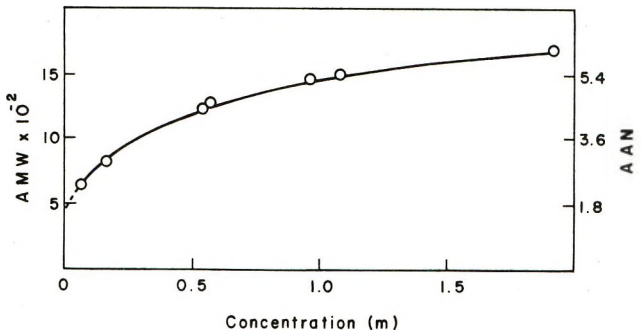

Figure 1. Average molecular weights and aggregation numbers of $NaAlBu_4$ in cyclohexane as a function of the molal $NaAlBu_4$ concentration.

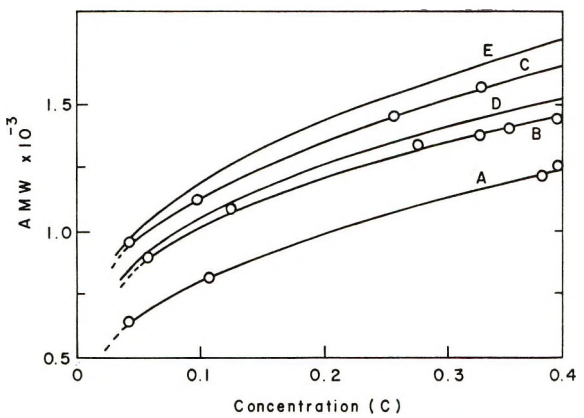

Figure 2. Effect of the addition of THF on the concentration dependence of the average molecular weight of $NaAlBu_4 \cdot x$THF in cyclohexane: (A) $NaAlBu_4$, (B) $NaAlBu_4 \cdot$THF, (C) $NaAlBu_4 \cdot 2$THF, (D) $NaAlBu_4 \cdot$THF (theoretical), (E) $NaAlBu_4 \cdot 2$THF (theoretical).

the other thermistor. The resistance differences were measured with a Müller temperature bridge, Leeds and Northrup Co., No. 8067.

A concentration dependence of biphenyl in cyclohexane was used as a standard. Thus it is assumed that, as a reasonable approximation, $NaAlBu_4$ behaves as a molecular solute in cyclohexane.

Results and Discussion

In Figure 1, the average molecular weights and the aggregation numbers of $NaAlBu_4$ in cyclohexane are given as a function of molal salt concentration. It can be seen that the degree of aggregation shows an initial rise and then tends to approach an aggregation number of approximately six. In order to make an extrapolation to lower concentrations, based on the observed shape of the curve, it is assumed that in the range where aggregation occurs the curve in Figure 1 can be expressed by

$$\bar{M} = k\sqrt[n]{C}$$

where $\bar{M}$ is the average molecular weight, k and n are constants, and C is the molar concentration. A plot of log $\bar{M}$ *vs.* log C gives a straight line, and extrapolation indicates that simple ion pairs are predominant at a molar concentration in the range of 0.0025. It should be pointed out that this expression is empirical and no specific interpretation of the constants is intended. It serves only as a means for more convenient extrapolation to obtain an estimate of the region where pairing is expected. The experimental point of lowest concentration is at 0.045 M. Thus a factor of approximately 20 exists between the last experimental point and the region of interest. Consequently, the value of 0.0025 M for the concentration where ion pairs are predominant cannot be considered to be quantitatively correct.

In Figure 2, the effects of the addition of 1:1 and 2:1 mole ratios of THF:salt are shown. It has previously been determined that for a 1:1 THF:$NaAlBu_4$ ratio essentially all of the THF is complexed with the sodium ion,[11] and it is possible to determine the degree of complexation by the second THF molecule from the studies by Olander.[16] In curve A of Figure 2, a portion of the curve in Figure 1 is reproduced but with the concentration expressed in molarity. Curves B and C represent the measured average molecular weights for the 1:1 and 2:1 mole ratios of THF:$NaAlBu_4$, respectively. Curve D represents the corresponding expected values for the 1:1 THF:$NaAlBu_4$ complex assuming 100% complexation of the aggregates existing in pure cyclohexane, and curve E represents the corresponding values corrected for dissociation of the 2:1 complex

$$2\text{THF}\cdot M^+X^- \rightleftharpoons \text{THF}\cdot M^+X^- + \text{THF}$$

using the data of Olander.[16] Thus, at any given concentration

$$\text{AMW(D)} = \frac{\text{FW}(NaAlBu_4) + \text{FW(THF)}}{\text{FW}(NaAlBu_4)}\,\bar{M}(\text{A})$$

and

$$\text{AMW(E)} = \left[\frac{\text{FW}(NaAlBu_4) + 2\text{FW(THF)}}{\text{FW}(NaAlBu_4)}\,\bar{M}(\text{A})\right]\frac{1}{1+\alpha}$$

where α represents the fraction of free solvent.

It is to be noted that the average molecular weights of the complexes are less than those of the reference curves, and the deviation becomes more pronounced with an increase in concentration of both salt and THF. We can therefore conclude that although aggregation occurs in cyclohexane with an increase in salt concentration, the stability of the aggregates decreases with an increase in both salt concentration and THF concentration. By extension of the latter trend, it might be expected that in salt solutions where complete solvation of the cation exists, only ion pairing will occur. That is, a cation in which all coordination sites are occupied by the complexing solvent cannot form contact

ion pairs, and the resultant effectively large cation might not be able to form stable aggregates larger than pairs, a conclusion supported by the observations of Kubas and Shriver of the molecular weight of sodium tetraphenylborate in THF.[19]

Although the values reported here cannot be considered to be quantitative because of the difficulties of working with aluminum alkyls as well as the presence of some ion–ion, ion dipole, etc., interactions,[20] these should be relatively small. For the latter of these, this is indicated by the low ionic conductances observed in these systems.[21] The results are in agreement with previous studies of this system,[16] and it is thus proposed that the general trends are correct.

Acknowledgment. Support of this work by National Science Foundation Grant No. GP 11427 is gratefully acknowledged.

(19) G. J. Kubas and D. F. Shriver, *J. Amer. Chem. Soc.*, **92**, 1949 (1970).

(20) H. S. Harned and B. B. Owen, "The Physical Chemistry of Electrolytic Solutions," 3rd ed, Reinhold, New York, N. Y., 1958, p 460.

(21) C. N. Hammonds and M. C. Day, *J. Phys. Chem.*, **73**, 1151 (1969).

Heats of Mixing Aqueous Electrolytes. IX. The Reciprocal Salt Pair Mg^{2+}, $Na^+||Cl^-$, Br^- [1]

by P. J. Reilly and R. H. Wood*

Department of Chemistry, University of Delaware, Newark, Delaware 19711 *(Received May 8, 1972)*

The heats of mixing aqueous solutions of all combinations of the reciprocal salt pair Mg^{2+}, $Na^+||Cl^-$, Br^- have been measured at 25°. In one set of experiments the initial solutions had the same molal ionic strength (I = 1, 3, or 6). In another set of experiments the initial solutions had the same number of equivalents per kilogram of solvent (E = 1, 3, or 6). For charge-asymmetric mixtures the magnitude of constant E mixings is less than that of the constant I mixings. Young's cross-square rule holds quite accurately for both constant I and constant E mixings even at the highest concentrations. The results indicate that predictions of the properties of multicomponent charge-asymmetric mixtures based on constant E mixings may be very useful and equations for these predictions are derived.

Introduction

Previous measurements on heats of mixing aqueous electrolytes[2-5] have shown that Young's cross-square rule.[2,3] is obeyed quite accurately for charge-symmetric mixtures (mixtures of salts of the same charge type). The present measurements were undertaken in order to test this rule at very high concentrations for a reciprocal salt pair containing salts of different charge type. Previous measurements on charge-asymmetric mixtures[6] indicated that a concentration scale based on equivalents per kilogram of solvent (E) might be more useful than the molal ionic strength (I). For this reason, measurements were made on the heats of mixing all of the possible combinations in the reciprocal salt pair Mg^{2+}, $2Na^+||2Cl^-$, $2Br^-$. The experiments were performed both at constant molal ionic strength and at constant equivalents per kilogram of solvent. The reaction at constant ionic strength is given by

$$(y_A n_W, I, 0) + (y_B n_W, 0, I) \longrightarrow (n_W, y_A I, y_B I) \quad (1)$$

where a solution is characterized by amount of water, ionic strength of salt A, and ionic strength of salt B. The change in enthalpy for this process ($\Delta_m H$) is represented by the equation

$$\Delta_m H/n_W M_W = y_A y_B I^2 (RTh_0^I + (y_B - y_A) RTh_1^I + \ldots \quad (2)$$

where y_A is the ionic strength fraction of salt A, y_B is

(1) Presented in part at the 158th National Meeting of the American Chemical Society, New York, N. Y., Sept 1969.

(2) T. F. Young, Y. C. Wu, and A. A. Krawetz, *Discuss. Faraday Soc.*, **24**, 27, 77, 80 (1957).

(3) Y. C. Wu, M. B. Smith, and T. F. Young, *J. Phys. Chem.*, **69**, 1868, 1873 (1965).

(4) R. H. Wood and R. W. Smith, *ibid.*, **69**, 2974 (1965).

(5) R. H. Wood and H. L. Anderson, *ibid.*, **70**, 992 (1966).

(6) R. H. Wood and M. Ghamkhar, *ibid.*, **73**, 3959 (1969).

the ionic strength fraction of salt B, I is the molal ionic strength ($I = {}^1/_2\Sigma_i m_i Z_i^2$), $\Delta_m H$ is the change in enthalpy (in calories), and $n_W M_W$ is the weight of water (in kg). The quantity RTh_0^I is the measure of the magnitude of the heat of mixing at $y = 0.5$, and the quantity RTh_1^I is the measure of the skew in the heat of mixing. Note that nomenclature has been changed from previous publications in this series so that the quantity of solvent on the left hand side of the equation is given explicitly and the coefficients h_0 and h_1 have a superscript I to indicate that the mixing process is at constant ionic strength.

A mixing at constant equivalents per kilogram of solvent (E) is given by the equation

$$(y_A' n_W, E, 0) + (y_B' n_W, 0, E) \longrightarrow (n_W, y_A' E, y_B E) \quad (3)$$

where E is the concentration in equivalents per kilogram of solvent ($E = {}^1/_2\Sigma_i m_i |Z_i|$); y_A' and y_B' are the equivalent fractions of salts A and B, respectively, in the final mixture. The change in enthalpy in this process is given by the equation

$$\Delta_m H / n_W M_W = y_A' y_B' E^2 (RTh_0^E + (y_B - y_A) RTh_1^E) \quad (4)$$

When two electrolytes of the same charge type are mixed, the constant I mixing is also a constant E mixing so that the two processes are the same. The difference between the two for a charge-asymmetric mixture is best illustrated by an example. At a constant ionic strength, $I = 1$, a 1 m solution of sodium chloride is mixed with a 0.3 m solution of magnesium chloride. The chloride ion concentration in the two solutions is not the same. However, for a mixing at constant $E = 1$, a 1 m solution of sodium chloride is mixed with a 0.5 m solution of magnesium chloride. The concentration of chloride ion in both the initial and final solution is 1 m. The change in the interaction of a cation, say magnesium, with the chloride ion in the course of the two mixings is most easily seen by considering the environment of the magnesium ion. At constant E the magnesium ion sees the same concentration of chloride ions around it before and after mixing.[7] The change in the interaction of the magnesium ion with these chloride ions will be due solely to the change in the activities of the chloride and magnesium ions. To a first approximation (neglecting the change in activity with ionic strength), the oppositely charged interactions will cancel in this mixing. Because at constant ionic strength the chloride ion concentration changes, these interactions do not cancel to the first approximation. This kind of reasoning led Wood and Ghamkhar[6] to suggest that at high concentrations for charge-asymmetric mixtures, the E concentration scale would be more useful. For example, it would be expected that the heat of mixing at constant E would be less than the heat of mixing at constant I. The present measurements show that this is indeed the case for the Mg^{2+}, Na^+ || Cl^-, Br^- reciprocal salt pair.

Experimental Section

Solutions. The solutions were prepared from reagent grade chemicals, which were used as received. The manufacturer's analysis indicated that the impurities present in these salts were all well below 0.05%. Stock solutions were prepared and analyzed by a potentiometric titration with silver nitrate using a silver chloride indicator electrode. Care was taken to adjust the concentration of the solutions to within 0.1% of the nominal values.

Calorimetry. The heat of mixing solutions with ionic strength or equivalent strength of 1 or 3 were measured with an LKB flow microcalorimeter. This calorimeter is a commercial model[8] based on the design of Monk and Wadsö.[9] Peristaltic pumps are used to inject the two liquids into a flow cell. The heat flow out of the cell into a constant temperature heat sink is measured by a thermopile after a steady state has been reached. Calibration is by an electrical heater in the flow cell. The flow rates of the two peristaltic pumps were measured by weighing the amount of water pumped in a known amount of time. Tests showed that the flow rate varied by as much as 1% during the course of the day. For this reason, flow rates were measured at least twice a day. The ionic strength (or equivalent) fraction of the final solution was calculated from the volume flow rates of the pumps and the density of the initial solutions. Electrical calibration was performed immediately after each experiment and the results reported here are the average of several experiments. Some difficulty was experienced with gas bubbles which were easily trapped in the calorimeter. It was found that gas bubble formation was eliminated by degassing the flow cell with a concentrated soap solution and then continually pumping degassed solutions through the flow cell. The results indicated an overall accuracy of about 1% for high heats and ± 0.5 in RTH_0 at I or $E = 1$.

The results at an ionic or equivalent strength of 6 were obtained with a LKB batch microcalorimeter.[10] This instrument is based on the design of Wadsö.[11] The calorimeter consists of a gold cell divided into 4- and 2-ml compartments. After thermal equilibration the calorimeter is tipped, this mixes the solutions in the two compartments and the heat flow from the cell into a constant temperature block is measured by a set of thermopiles. The cells were rinsed and dried with a

(7) This is strictly true only if the amount of ion pairing in the solution is small.

(8) LKB—Produkter AB, Fack, 161 25 Bromma 1, Sweden, Model 10700-1.

(9) P. Monk and I. Wadsö, *Acta Chem. Scand.*, 22, 1842 (1968).

(10) LKB—Produkter AB, Model 10700-2.

(11) I. Wadsö, *Acta Chem. Scand.*, 22, 927 (1968).

Table I: Excess Enthalpy of Mixing as a Function of y at Ionic and Equivalent Strengths of 6

	$I = 6$		$E = 6$	
		$\Delta_m H/[y_A(1 - y_A)I^2 n_W M_W]$[c]		$\Delta_m H/[y_A'(1 - y_A')E^2 n_W M_W]$[c]
Salt pair	y_A[a]	cal kg mol^{-2}	y_A[a]	cal kg mol^{-2}
$MgCl_2$–NaCl	0.686	69.49	0.665	16.96
	0.613	66.35	0.596	14.66
	0.408	59.07	0.590	14.32
	0.342	56.21	0.392	9.58
			0.359	8.86
			0.328	8.32
$MgBr_2$–NaBr	0.668	71.65	0.682	7.39
	0.608	68.71	0.665	6.88
	0.432	63.21	0.612	5.05
	0.364	61.13	0.406	−0.18
			0.357	−0.83
NaBr–NaCl[b]	0.654	3.70		
	0.581	3.67		
	0.392	3.73		
	0.355	3.85		
$MgBr_2$–$MgCl_2$	0.653	2.01	0.658	3.65
	0.585	2.04	0.591	3.70
	0.398	2.05	0.388	3.89
	0.329	2.10	0.332	3.92
$MgBr_2$–NaCl	0.676	59.41	0.671	1.87
	0.599	56.33	0.591	0.40
	0.415	49.15	0.405	−3.03
	0.353	47.52	0.347	−3.82
NaBr–$MgCl_2$	0.635	75.99	0.655	19.87
	0.571	77.72	0.616	20.70
	0.368	85.94	0.392	27.11
	0.310	88.51	0.335	28.78

[a] By definition y_A is the molal ionic strength (or equivalent) fraction of the salt with the higher formula weight. [b] For this mixture I and E are the same. [c] Units are given for $\Delta_m H/[y_A(1 - y_A)I^2 n_W M_W]$ and RTh_0 using the convention that the units of $I = (1/2)\Sigma_i m_i Z_i^2$ and $E = 1/2\Sigma_i m_i |Z_i|$ are mol kg^{-1}. Thus, if $\Delta_m H$ is in calories, $n_W M_W$ in kg, and I in mol/kg, eq 2 and 4 come out right.

stream of dry nitrogen. Solutions were transfered by weight into the cell using a syringe. A 12-min experimental period assured that all of the heat had flowed out of the calorimeter. The heat of reaction was proportional to the integral of the thermocouple signal during the 12-min experimental period. A base line correction was made by subtracting the area under a 12-min rating period immediately after the experimental period. The experiment was followed immediately by a blank heat of mixing determination and then an electrical calibration. Our results indicate that an accuracy of ±0.3% at high heats and ±0.05 in RTh_0 at low heats was achieved. In addition, the calorimeter was tested by measuring the heat of dilution of 12 m urea.[12] The results agreed with Gucker and Pickard's results[13] to within 0.5%.

Results and Discussion

The results of the mixing experiments at I and E = 6 are given in Table I. Equation 2 can be rearranged into a form suitable for plotting as follows

$$\Delta_m H/[y_A(1 - y_A)I^2 n_W M_W] = RTh_0^I + (1 - 2y_A)RTh_1^I + \ldots \quad (5)$$

where y_B has been replaced by $1 - y_A$. When the left-hand side of eq 5 is plotted *vs.* $(1 - 2y_A)$ the slope of the line equals RTh_1^I and the intercept at $1 - 2y_A = 0$ is RTh_0^I. When the data in Table I are plotted by this method, the graph is not a straight line, indicating that the further terms in eq 2 are necessary. However, the data differed from a straight line by less than 0.5 cal kg mol^{-2} in RTh_0^I so that the deviations are small. A smooth curve was drawn through the data and the intercept of this curve at $1 - 2y_A = 0$ is the value given for RTh_0^I in Table II. The slope of the best straight line through the points is given as RTh_1^I in Table II. The results at constant E = 6 were treated in a similar manner and the results are given in Table II. Again

(12) A. L. Levine, Ph.D. Thesis, University of Delaware, June 1971.

(13) F. T. Gucker, Jr., and H. B. Pickard, *J. Amer. Chem. Soc.*, **62**, 1464 (1940).

Table II: Enthalpy of Mixing at Constant Ionic and Equivalent Strengths

Salt pair	$I = 1$ y_A[a]	$I = 1$ RTh_0^I cal kg mol^{-2}	$I = 3$ y_A	$I = 3$ RTh_0^I cal kg mol^{-2}	$I = 6$ $RTh_0^I(y = 0.5)$ cal kg mol^{-2}	$I = 6$ RTh_1^I cal kg mol^{-2}
A. Constant Molal Ionic Strength (I)						
$MgCl_2$–NaCl	0.510	171.8, 172.5[d]	0.518	114.1, 113.6[d]	62.1	−18.1
$MgBr_2$–NaBr	0.511	168.2	0.519	118.2	65.1	−15.9
NaBr–NaCl	0.506	3.7, 3.2[e]	0.505	4.5, 4.3[f]	3.71	0.2
$MgBr_2$–$MgCl_2$	0.506	1.8	0.506	1.9, 1.8[g]	2.05	0.1
$\Sigma\square$[b]		345.1		238.2	132.6	
$MgBr_2$–NaCl	0.509	172.4	0.515	107.3	52.2	−17.9
NaBr–$MgCl_2$	0.488	174.1	0.477	127.4, 127.4[f]	80.4	18.6
$\Sigma\times$[c]		346.5		234.7	132.6	
$\Sigma\times - \Sigma\square$		1.4		−3.5	0.0	

Salt pair	$E = 1$ y'_A[h]	$E = 1$ RTh_0^E cal kg mol^{-2}	$E = 3$ y_A'	$E = 3$ RTh_0^E cal kg mol^{-2}	$E = 6$ $RTh_0^E(y = 0.5)$ cal kg mol^{-2}	$E = 6$ RTh_1^E cal kg mol^{-2}
B. Constant Equivalents per Kilogram of Water (E)						
$MgCl_2$–NaCl	0.510	105.1	0.515	53.9	12.0	−12.3
$MgBr_2$–NaBr	0.509	92.4	0.515	46.4	1.9	−12.0
NaBr–NaCl	0.506	−3.7	0.505	4.5	3.71	0.2
$MgBr_2$–$MgCl_2$	0.506	3.9	0.504	4.6	3.77	0.4
$\Sigma\square$[i]		205.1		109.4	21.4	
$MgBr_2$–NaCl	0.508	108.5	0.510	46.5	−1.4	−8.8
NaBr–$MgCl_2$	0.489	97.6	0.481	62.3	23.9	14.1
$\Sigma\times$[j]		206.1		108.8	22.5	
$\Sigma\times - \Sigma\square$		1.0		−0.6	1.1	

[a] By definition y_A equals the ionic strength fraction of the salt with the higher formula weight. [b] Calculated from eq 6. This is the weighted sum around the square. [c] Calculated from eq 6. This is the sum of the cross terms. [d] Results of R. H. Wood, J. D. Patton, and M. Ghamkhar, *J. Phys. Chem.*, **73**, 346 (1969). [e] Results of Y. C. Wu, M. B. Smith, and T. F. Young, *ibid.*, **69**, 1868 (1965). [f] Unpublished results of N. Bhatt and M. Ghamkhar, University of Delaware. [g] Results of R. H. Wood and H. L. Anderson, *J. Phys. Chem.*, **70**, 992 (1966). [h] Equivalent fraction of salt with highest formula weight. [i] This is the sum around the square, see eq 7. [j] This is the sum of the cross mixings; see eq 7.

small but significant deviations from a straight line plot were observed.

Compared to the charge-symmetric mixtures that have been measured, the results at I and $E = 6$ have very large skew terms (RTh_1). This is to be expected at least for constant I mixes from the analyses of the terms contributing to RTh_1^I.[14,15] For charge-symmetric mixtures at constant I, the only terms contributing to skew (RTh_1^I) are triplet interactions with all ions bearing the same charge. However, for charge-asymmetric mixtures all triplets contribute to the skew. Since triplet interactions become relatively more important as the concentration increases,[14,15] it is expected that RTh_1^I should be important for the $I = 6$ measurements.

Table II gives the results of measurements at constant I and $E = 1$ and 3. These results were taken with the flow calorimeter at a value of y or y' approximately equal to 0.5. The actual value of y at which the measurements were made is given in the table. The values of RTh_0 are calculated from eq 1 and 3 neglecting the contribution of RTh_1. A simple calculation shows that if the contributions of RTh_1 are about the same as they are in the I and $E = 6$ mixings, then the neglect of RTh_1 causes a negligible error, for the y values given in Table II. Six of the values in Table II have been checked using values from the literature or measurements with a separate calorimeter[4] on different solutions performed in this laboratory. The duplicate values given in Table II show satisfactory agreement with the present measurements.

Wood and Ghamkhar[6] have suggested that for a charge-asymmetric mixture the mixing at constant E would, to a first approximation, cancel the oppositely charged pairwise interactions in a common ion mixture. If this is true, the heat of mixing at constant E ought to be normally smaller than the heat of mixing at constant I. A comparison of the common ion mix-

(14) H. L. Friedman, "Ionic Solution Theory," Interscience, New York, N. Y., 1962, p 231.

(15) P. J. Reilly and R. H. Wood, *J. Phys. Chem.*, **73**, 4292 (1969).

tures in Table II shows that the charge-asymmetric mixtures are indeed much smaller at constant E than at constant I (the first two rows in Table IIA and B). The charge-symmetric mixtures (the third and fourth rows in Table IIA and B) show very similar heats of mixing. For the sodium bromide–sodium chloride mixture, the heat of mixing is exactly the same because the process is exactly the same. For the magnesium bromide–magnesium chloride mixture, the results differ only because the definition of the two concentration scales is not identical.

All of the mixings in a reciprocal salt pair can be represented by the diagram

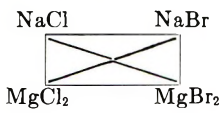

where the common ion mixtures are represented by the sides of the square, and the mixings without a common ion are represented by the cross terms. Young and coworkers[2,3] suggested that the sum of the terms around the square($\Sigma\square$) was equal to the sum of the two cross terms ($\Sigma\times$) and this is now known as Young's rule. Numerous measurements have shown that this rule usually gives quite accurate predictions for excess free energies,[16-19] heats,[2-5] and volumes.[20-22] Reilly and Wood[15] showed that for charge-asymmetric mixtures a weighted cross-square rule should be more accurate. For the present reciprocal salt pair, the weighted cross-square rule is

$$RTh_0^I(\mathrm{MgBr_2}\text{–}\mathrm{NaCl}) + RTh_0^I(\mathrm{NaBr}\text{–}\mathrm{MgCl_2}) = RTh_0^I(\mathrm{MgCl_2}\text{–}\mathrm{NaCl}) + RTh_0^I(\mathrm{MgBr_2}\text{–}\mathrm{NaBr}) + (^4/_5)RTh_0^I(\mathrm{NaBr}\text{–}\mathrm{NaCl}) + (^6/_5)RTh_0^I(\mathrm{MgBr_2}\text{–}\mathrm{MgCl_2}) \quad (6)$$

The results in Table IIA show that this equation is obeyed well within the experimental error, even at a molal ionic strength of 6.

The low values of the constant E mixings compared with the constant I mixings prompted us to explore the conditions under which a cross-square rule for constant E mixings should hold. This involved a new derivation of the general equations for the prediction of a multicomponent mixture from common-ion mixings given by Reilly and Wood. In the new derivation constant E mixes were used instead of constant I mixings and the influence of the changes in ionic strength on the interactions between the ions was neglected.[23] With this approximation, the results turn out to be identical with those derived for charge-symmetric mixtures. The details of the changes necessary to perform this derivation are given in Appendix A. The resulting equations can be used to show that within the approximations inherent in the derivation, the unweighted cross-square rule

$$RTh_0^E(\mathrm{MgBr_2}\text{–}\mathrm{NaCl}) + RTh_0^E(\mathrm{NaBr}\text{–}\mathrm{MgCl_2}) = RTh_0^E(\mathrm{MgCl_2}\text{–}\mathrm{NaCl}) + RTh_0^E(\mathrm{MgBr_2}\text{–}\mathrm{NaBr}) + RTh_0^E(\mathrm{NaBr}\text{–}\mathrm{NaCl}) + RTh_0^E(\mathrm{MgBr_2}\text{–}\mathrm{MgCl_2}) \quad (7)$$

should hold just as it does for charge-symmetric mixtures. According to the theory, the interaction between pairs of ions and triplets (except triplets containing ions all of the same charge) do not contribute to deviations from the cross-square rule.

The experimental results in Table IIB show that the cross-square rule at constant E holds very accurately. It is within experimental error at $E = 1$ and 3 and just slightly beyond the expected experimental error at $E = 6$. This result indicates that the equations in Appendix A for the prediction of multicomponent mixtures based on constant E mixings may be very useful. In particular, the fact that constant E mixes containing a common ion are generally smaller than constant I mixes indicates that if RTh_0 terms are unknown the equation at constant E will give more accurate results because the neglected RTh_0 terms will be smaller. Since this equation depends on the neglect of changes in ionic strength it would be expected to be a poor approximation at low concentrations (perhaps below 0.1 m or so). More results will be needed for charge-asymmetric mixtures at high concentrations before the relative merits of the equations at constant I and constant E can be determined.

Acknowledgment. The support of the Office of Saline Water, U. S. Department of the Interior, is gratefully acknowledged.

Appendix A

The derivation of an equation based on constant I mixtures has been given by Reilly and Wood.[15] The

(16) Y. C. Wu, R. M. Rush, and G. Scatchard, *J. Phys. Chem.*, **72**, 4048 (1968); **73**, 2047, 4434 (1969).

(17) A. K. Covington, T. H. Lilley, and R. A. Robinson, *ibid.*, **72**, 2759 (1968).

(18) R. A. Robinson, A. K. Covington, and C. P. Bezboruah, *J. Chem. Thermodyn.*, **2**, 431 (1970).

(19) R. F. Platford, *ibid.*, **3**, 319 (1971).

(20) H. E. Wirth, R. Lindstrom, and J. Johnson, *J. Phys. Chem.*, **67**, 2339 (1963).

(21) H. E. Wirth and W. L. Mills, *J. Chem. Eng. Data*, **13**, 102 (1968).

(22) H. E. Wirth and A. LoSurdo, *ibid.*, **13**, 226 (1968).

(23) There is some evidence (besides the present results) that this may not be too serious an approximation. The following observations are consistent with the idea that at moderate to high concentrations (above $I = 0.1$ or so) changes in ionic strength do not greatly affect the activity coefficients of the ions. (1) Statistical mechanical calculations (P. N. Vorontsov-Veliaminov, A. M. Eliashevich, J. C. Rasaiah, and H. L. Freedman, *J. Chem. Phys.*, **52**, 1013 (1970), J. C. Rasaiah, D. N. Card, and J. P. Valleau, *ibid.*, **56**, 248 (1972)) show that the energy difference between a system of charged spheres and the uncharged system is roughly constant except at very low concentrations. Thus the energy of charging the particles does not vary strongly as the concentration changes in the more concentrated region. (2) The values of RTh_0 for mixing many 1–1 electrolytes vary slowly with concentration at moderate concentrations (see ref 4). One of the things these coefficients depend on is the activities of the ions in the solution. (3) The concept of ionic strength is neglected quite successfully for fused salts.

Table III: Transformation Scheme

Symbol and definition in constant I equation	Replacement in constant E equation
$I = (1/2)\Sigma_i m_i Z_i^2$ = molal ionic strength	$E = 1/2\Sigma_i m_i\|Z_i\|$ = total concentration in equiv per kg of solvent
m_x = molality ion x	$E_x = m_x\|Z\|$ = equiv of x per kg of solvent
Z_k^M = charge on cation k	1
Z_1^X = charge on anion 1	-1
$g_{M_kM_1X_m} = g_0^I$ for constant I mixing of M_kX_m with M_1X_m	$g_{MN}^X = g_0^E$ for constant E mixing of MX with NX
B^{nmo} = cluster integral for n ions of type 1, m ions of type 2, o ions of type 3	$\frac{B^{nmo}}{Z_1^n Z_2^m Z_3^o}$ = cluster integral reduced by the product of the charges on all of the ions in the cluster
G^{ex} = Total excess free energy per kg of solvent	G^{ex}/n_wM_w = total excess free energy per kg of solvent. The weight of solvent is explicit for clarity
$G^0_{M_1X_m}$ = excess free energy per kg of solvent of a solution of pure M_1X_M at ionic strength I	G^0_{MX}/n_wM_w = excess free energy per kg solvent of a solution of pure MX at equivalent concentration E
y_X = ionic strength fraction of X	y_X' = equivalent fraction of X

derivation for constant E mixtures follows the same path except that all of the mixings refer to constant E mixings. The transformation scheme (Table III) converts the equations for constant I into ones for constant E.

The common ion mixing shown by Table I of ref 15 becomes the mixing of a solution of MX containing y kg water and E equivalents per kg water of both ions 1 (M) and 3 (X) with a solution of NX containing $(1 - y)$ kg of water and E equivalents per kilogram of water of both ions 2 (N) and 3 (X). The $\Delta_m C^{002}$ etc. are calculated in the same way and lead to the analog of eq 3 and 4 of ref 15 for the contributions of cluster integrals to a two salt common ion mixing.

$$g = \left(-\frac{B^{200}}{|Z_1^2|} - \frac{B^{020}}{|Z_2^2|} + \frac{B^{110}}{|Z_1Z_2|}\right) + E\left(-\frac{B^{201}}{|Z_1^2Z_3|} - \frac{B^{021}}{|Z_2^2Z_3|} + \frac{B^{111}}{|Z_1Z_2Z_3|}\right) \quad \text{(A-1)}$$

Similarly the equation for the excess free energy of a multicomponent mixture (eq 6 of ref 15) becomes

$$G^{ex}/n_wM_w = \Sigma_{M,X}y_My_X(G_{MX}^0/n_wM_w) + RTE^2\Sigma_{M<N,X}y_My_Ny_Xg_{MN}^X + RTE^2\Sigma_{X<Y,N}y_Xy_Yy_Ng_{XY}^N \quad \text{(A-2)}$$

where the sum with M < N means that each g term is taken only once; *i.e.*, either g_{MN}^X or g_{NM}^X is included but not both.

The proof of eq A-2 again involves showing that the cluster integrals included in the prediction eq A-2 are identical with the actual change in cluster integrals in the real mixing process. The predicted change in cluster integrals is obtained by substituting eq A-1 into eq A-2. The actual change in cluster integrals is calculated from the changes in the concentrations of the ions during the mixing. In this process, the changes in the cluster integrals with ionic strength are neglected. The procedure follows ref 6 and the result is that all pair and triplet interactions are correctly taken into account except for triplets containing ions of the same charge. This is just what is found when the constant I equation is applied to a charge-symmetric mixture. In fact, the constant I and constant E equations are equivalent for charge-symmetric mixtures.[5]

Bistrifluoromethyl Peroxide. II. Kinetics of the Decomposition to Carbonyl Fluoride and Trifluoromethyl Hypofluorite

by R. Craig Kennedy* and Joseph B. Levy

Department of Chemistry, The George Washington University, Washington, D. C. 20006
(Received April 10, 1972)

Publication costs assisted by the Air Force Office of Scientific Research, Office of Aerospace Research

The kinetics of the forward and reverse reactions for the equilibrium $CF_3OOCF_3 \rightleftarrows CF_3OF + COF_2$ have been measured in the temperature range 480–580°K. The results are interpreted in terms of the mechanism $CF_3OOCF_3 \rightleftarrows 2CF_3O$ (k_1, k_2); $CF_3O \rightleftarrows CF_2O + F$ (k_3, k_4); $CF_3O + F \rightleftarrows CF_3OF$ (k_5, k_6). Activation energies of 46.2 and 45.0 kcal mol^{-1} have been found for steps 1 and 6 leading to bond dissociation energies, evaluated at 298°K, of 46.7 ± 0.8 and 44.5 ± 0.8 kcal mol^{-1}, respectively, for the central oxygen–oxygen bond in bistrifluoromethyl peroxide and the oxygen–fluorine bond in trifluoromethyl hypofluorite. General rate expressions have been determined, by a consideration of kinetic and thermodynamic data, for all six rate constants.

Introduction

We have recently[1] reported measurements of the equilibrium constant, K, for the reaction $CF_3OOCF_3 \rightleftarrows CF_3OF + COF_2$, over the temperature range 500–600°K. The results gave $K = 10^{8.1} \exp -23{,}800/RT$ atm and led to a bond dissociation energy, $D_{CF_3O-OCF_3}$, of 40.6 ± 5 kcal mol^{-1}. The system was shown to be free of side products and hence, from the starting composition and the total pressure at any temperature, the composition at that temperature can be calculated. It was thus clear that the kinetics of the reactions in both directions could be studied by a manometric method and we report such a study here. The results lead to a value for the bond dissociation energy, $D_{CF_3O-OCF_3}$ of 46.7 ± 0.8 kcal mol^{-1} and to a proposed reaction mechanism.

Results

The velocities at which bistrifluoromethyl perioxide or a mixture of trifluoromethyl hypofluorite and carbonyl fluoride are transformed into the equilibrium mixtures are such that for pressures in the range 1–900 Torr it proved possible to make rate measurements manometrically from 204 to 350°. It is clear that whether one studies the peroxide decomposition (here referred to as the forward reaction) or the hypofluorite–carbonyl fluoride association the kinetics will reflect the effect of the opposing reactions as soon as some degree of reaction has occurred. Accordingly a good deal of attention has been paid to measurements of initial reaction rates. Measurements have been made for the forward reaction with the peroxide alone, or with added carbonyl fluoride or trifluoromethyl hypofluorite, and for the reverse reaction with varying ratios of carbonyl fluoride to trifluoromethyl hypofluorite. A few experiments have also been carried out with added inert gases to show the absence of total pressure effects and in a vessel of high surface area concentration to show that the reaction is homogeneous.

The experimental results are collected in Tables I–III.[2] The data in Tables I and II refer to initial rates of the forward reaction, *i.e.*, the decomposition of the peroxide; the data in Table III refer to the reverse reaction, *i.e.*, the formation of the peroxide from carbonyl fluoride and trifluoromethyl hypofluorite.

Forward Reaction. Bistrifluoromethyl Peroxide Alone and with Inert Gases. It proved convenient to examine the reaction over a rather wide range of pressures in the temperature range 211–304° and the results are collected in Table I. The general behavior of the data is that, for the highest two temperatures, the initial velocities are first order in bistrifluoromethyl peroxide over the entire range of pressure studied, *i.e.*, the quantity $10^5V_0/P_0$ is constant. For the range 221–260° first-order behavior is shown by the data for the lower end of the pressure range. Thus for 221° the quantity $10^5V_0/P_0$ is constant within experimental error for pressures below 41 Torr; at 238° the upper limit is about 120 Torr, etc. For pressures above these limits, the kinetics approach half-order behavior. This can be seen by examining data in the last column, $10^5V_0/(P_0)^{1/2}$. Thus the highest four pressures for 221° give fairly constant values in this column while the first-order constants vary from 0.13×10^{-5} to 0.35×10^{-1} sec^{-5}. The behavior is shown in Figure 1 where the log V_0–log P_0 plots show clearly a change in slope. The line drawn with a slope of 1.0 passes

(1) J. B. Levy and R. C. Kennedy, *J. Amer. Chem. Soc.*, 94, 3302 (1972).

(2) The accuracy of the initial rate measurements was ±5%. The rate constants within the first-order and half-order regimes, *i.e.*, where the particular rate constant showed no systematic trend with pressure, all have average deviations that fall within this error limit, with the exception of the data at 250°. These were all obtained with the tubular reactor for which greater scatter of the data was observed.

Table I: First-Order and Half-Order Rate Constants from Initial Velocities in the Pyrolysis of Bistrifluoromethyl Peroxide

Temp, °C	Initial peroxide pressure, P_0, Torr	$10^5 V_0$, Torr sec^{-1}	$10^5 V_0/P_0$, sec^{-1}	$10^5 V_0/(P_0)^{1/2}$, Torr$^{1/2}$ sec^{-1}
211	200[a]	17.5	0.087	1.24
	101.0	10.1	0.10	1.00
	39.5	7.10	0.18	1.10
	20.0	4.05	0.20	0.87
	10.0	2.60	0.26	0.83
221	921[a]	108	0.13	3.66
	860[a]	108	0.12	3.44
	172	43.0	0.25	3.27
	98.5	34.4	0.35	3.48
	41.0	20.4	0.49	3.20
	20.0	10.4	0.52	2.32
	15.5	7.45	0.48	1.91
	10.5	5.35	0.51	1.67
	10.0	4.90	0.49	1.56
	5.5	3.00	0.55	1.25
238	831[a]	630	0.76	21.9
	441[a]	495	1.12	23.6
	285	333	1.17	19.7
	200	262	1.31	18.6
	60	123	2.05	16.0
	50	120	2.40	17.0
	50[b]	120	2.40	17.0
	50[c]	120	2.40	17.0
	20	51.2	2.56	11.4
	10	25.5	2.55	8.0
250	362[a]	1340	3.70	70.0
	200[a]	1020	5.10	73.0
	80[a]	512	6.40	57.5
	52	400	7.95	56.5
	20[a]	178	8.90	39.7
	10[a]	79.0	7.90	25.0
260	827[a]	5550	6.74	193
	617	4920	7.98	200
	410[c]	4000	9.75	195
	310	3350	10.8	189
	100	1670	16.7	167
	100[a]	1640	16.4	164
	48.6	820	16.7	146
	10.0	170	17.0	53.8
288	120	19900	166	1820
	100[a]	16500	165	1650
	54.0	7950	162	1460
	25.0	4000	159	800
	17.0	2850	163	680
	10.0[a]	1640	164	519
	5.30	840	158	363
	4.06	655	163	328
304	59.0	30000	507	3890
	52.0	27000	520	3750
	4.80	2490	520	1140

[a] Experiments performed in aluminum tubular reactor, $A:V$ = 8.3. All others performed in aluminum cylindrical reactor, $A:V$ = 0.51 (see Experimental Section). [b] Nitrogen (450 Torr) added. [c] Carbon tetrafluoride (450 Torr) added.

through the data at the lower pressures while the data at the higher pressures fall near the line drawn with a slope of 0.5. The pressures at which the slopes change increase with increasing pressure, so that, as discussed above, for the pressures examined here, the first-order region is clearly defined from 221° up and is, in fact, the only regime described by our data above 260°.

Table II: Initial Rates of Decomposition of Bistrifluoromethyl Peroxide in the Presence of Added Carbonyl Fluoride and Trifluoromethyl Hypofluorite at 260°

CF_3OOCF_3, Torr	CF_3OF, Torr	COF_2, Torr	Initial velocity, V_0, Torr sec^{-1}	$V_0/(CF_3OOCF_3)_0$, sec^{-1}
100	0	0	0.0165	0.000165
100	50	0	0.163	0.000163
100	0	10	0.0113	0.000113
100	0	50	0.00900	0.0000900
100	0	200	0.00210	0.0000210

Table III: Kinetic Data for the CF_3OF–COF_2 Reaction from Initial Velocities

Temp, °C	Initial reactant pressures, Torr: CF_3OF	COF_2	Inert gas	$[V_0/(CF_3OF_0)] \times 10^6$ sec^{-1}
200	40	10		3.55
	40	40		5.82
	40	80		6.65
	40	160		6.72
249	20	80		79.5
	40	160		93.0
	60	240		95.0
260	10	10		68
	10	30		111
	10	60		134
	10	90		158
	40	160		230
	40	160	300 N_2	230
	40	160	300 O_2	230
	40	240		235
281	20	80		890
	40	160		1220
	80	320		1310

Experiments in an aluminum tubular reactor in which the surface area concentration was 16 times that in the aluminum cylindrical reactor are also shown in Table I from 211 to 260°. The results support the conclusion that heterogeneous contributions to the rate are negligible. Also shown in Table I are experiments at 238° in which substantial amounts of nitrogen and carbon tetrafluoride were added to the system without affecting the rate. This supports the conclusion that the data shown in Table I are independent of total pressure. It may be expected[3] that this would be true for the present pressure regime for a molecule of the complexity of bistrifluoromethyl peroxide.

The first-order rate constants determined in the above manner are plotted as the Arrhenius function in

(3) S. W. Benson, "Thermochemical Kinetics," Wiley, New York, N. Y., 1968.

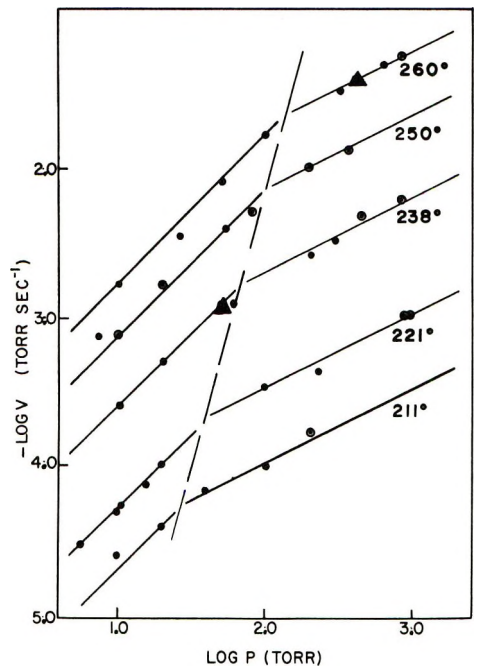

Figure 1. Log V–log P plots for the pyrolysis of bistrifluoromethyl peroxide: ●, cylindrical reactor; ▲, cylindrical reactor (inert gas added); ⊙, tubular reactor.

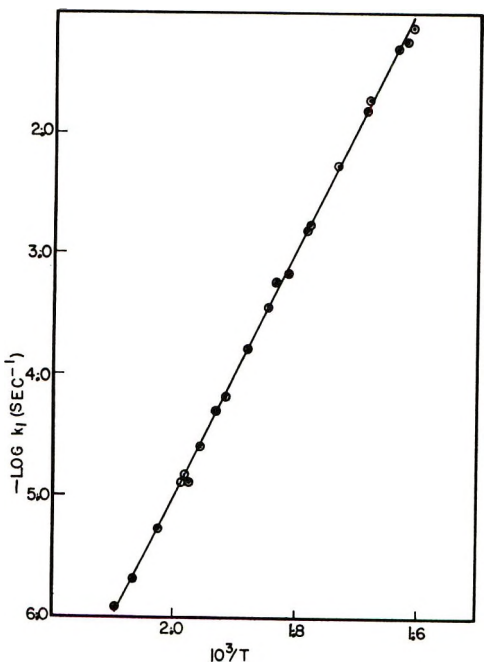

Figure 2. Arrhenius plot for the pyrolysis of bistrifluoromethyl peroxide.

Figure 2. The rate constant is designated as k_1 and has the value[4,5]

$$k_1 = 10^{15.2 \pm 0.1}10^{-46,200 \pm 330/4.57T}\ \text{sec}^{-1}$$

Forward Reaction. Bistrifluoromethyl Peroxide with Products Added. The data for the effect of the reaction products on the initial rate of decomposition of the peroxide are shown in Table II. Clearly carbonyl

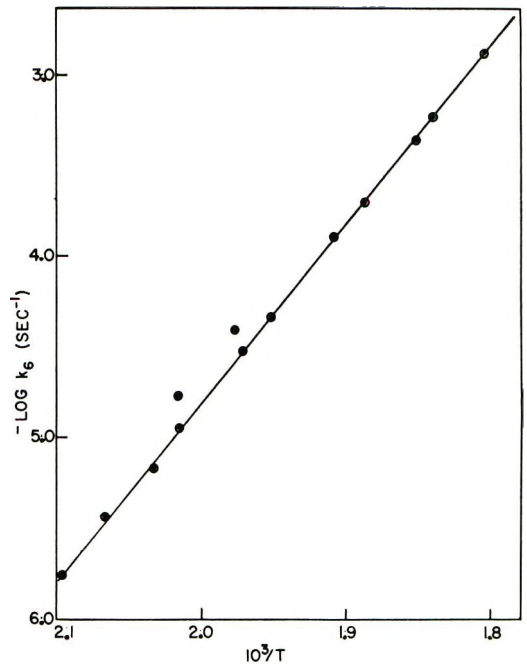

Figure 3. Arrhenius plot for the decomposition of trifluoromethyl hypofluorite with excess carbonyl fluoride: ○, present work; ●, ref 9.

fluoride inhibits the reaction powerfully while trifluoromethyl hypofluorite is without significant effect. These data furnish a very important clue to the reaction mechanism, since they require that carbonyl fluoride plays a different role than trifluoromethyl hypofluorite in the reaction.

Reverse Reaction. In Table III are shown data for the reverse reaction. The general pattern of these data is that, for a given pressure of trifluoromethyl hypofluorite, the initial velocity increased with increasing carbonyl fluoride pressure but reached a limiting plateau value at some critical carbonyl fluoride pressure. The limiting velocities have been treated on the assumption of first-order kinetics in trifluoromethyl hypofluorite and support this assignment. The addition of inert gases in rather substantial amounts has, as shown by the data at 260°, no effect on the velocity so that it is clear that the reaction is in the first-order region. Measurements of this sort were made from 204 to 282° and are plotted in Figure 3 as the Arrhenius function. The rate constant is designated, for reasons that will become clear below, as k_6.

$$k_6 = 10^{14.9 \pm 0.3}10^{-45,000 \pm 300/4.57T}\ \text{sec}^{-1}$$

Discussion

Reaction Mechanism. The most reasonable opening step in the pyrolysis of bistrifluoromethyl peroxide is

(4) Treatment of data for Arrhenius plots in the present paper is by the method of averages.[5]

(5) H. W. Salzberg, J. I. Morrow, S. R. Cohen, and M. E. Green, "Physical Chemistry, A Modern Laboratory Course," Academic Press, New York, N. Y., 1909, pp 6–40.

certainly cleavage of the central oxygen–oxygen bond. This follows not only by analogy with dialkyl peroxides, but also from the fact that the pyrolysis of bistrifluoromethyl peroxide in the presence of hexafluoropropene results in low molecular weight polymers with trifluoromethoxyl end groups.[6] The steps that follow are indicated clearly by the effects of carbonyl fluoride on both the pyrolysis of the peroxide and that of trifluoromethyl hypofluorite. The mechanism[7-9] that appears to be required by the present results is

$$CF_3OOCF_3 \underset{k_2}{\overset{k_1}{\rightleftharpoons}} 2CF_3O$$

$$CF_3O \underset{4}{\overset{3}{\rightleftharpoons}} COF_2 + F$$

$$CF_3O + F \underset{6}{\overset{5}{\rightleftharpoons}} CF_3O$$

The inert gas experiments indicate that steps 1 and 6 are in the first-order region (hence that steps 2 and 5 are in the second-order region). Step 3 is also written as a first-order reaction and this point will be considered below.

Kinetic Analysis of the Reaction. Even though the results presented above refer to initial rate studies starting from either end of the reaction, it is convenient to derive a general rate expression for the reaction first and then to consider it for the limiting cases of initial conditions.

The velocity of the forward reaction, *i.e.*, $-d(CF_3OOCF_3)/dt$, at any time, is denoted here by V and can be expressed as

$$V = k_1(CF_3OOCF_3) - k_2(CF_3O)^2 \quad (a)$$

$$V = k_3(CF_3O) - k_4(F)(CF_2O) \quad (b)$$

$$V = k_5(CF_3O)(F) - k_6(CF_3OF) \quad (c)$$

It is then possible to solve, from eq a, for (CF_3O).

$$(CF_3O) = \left(\frac{k_1(CF_3OOCF_3) - V}{k_2}\right)^{1/2} \quad (d)$$

By inserting (d) into (c) the expression for (F) is found.

$$(F) = \frac{V + k_6(CF_3OF)}{k_5\left(\frac{(k_1(CF_3OOCF_3) - V}{k_2}\right)^{1/2}} \quad (e)$$

It is then possible to insert (d) and (e) into (b) and, after some rearrangement of terms, to arrive at the expression

$$V = \frac{k_1k_3k_5(CF_3OOCF_3) - k_2k_4k_6(CF_3OF)(CF_2O)}{k_2k_4(CF_2O) + k_2k_5\left[\frac{k_3}{k_2} + \left(\frac{k_1CF_3OOCF_3) - V}{k_2}\right)^{1/2}\right]} \quad (f)$$

When $V = 0$, *i.e.*, at equilibrium, (f) reduces to the expression for the equilibrium constant.

$$\frac{(CF_3OF)_e(COF_2)_e}{(CF_3OOCF_2)_e} = \frac{k_1k_3k_5}{k_2k_4k_6} = K \quad (g)$$

Kinetics of the Initial Velocity of the Forward Reaction. When the concentrations of trifluoromethyl hypofluorite and carbonyl fluoride are considered to be negligible, (f) reduces to the expression for the initial rate of the forward reaction, V_0.

$$V_0 = \frac{k_1(CF_3OOCF_3)}{1 + \frac{k_2}{k_3}\left(\frac{(k_1(CF_3OOCF_3) - V}{k_2}\right)^{1/2}} \quad (h)$$

The second term in the denominator, from expression d, can be seen to be equal to V_2/V_3, *i.e.*

$$\frac{k_2(CF_3O)}{k_3} = \frac{k_2(CF_3O)^2}{k_3(CF_3O)} = \frac{V_2}{V_3}$$

where the subscripts refer to the elementary steps of the same number in the mechanism. When $V_2/V_3 \ll 1$ expression h reduces to the simple expression

$$V_0 = k_1(CF_3OOCF_3) \quad (i)$$

This condition will clearly be favored by lower peroxide pressures, *i.e.*, lower (CF_3O) at any one temperature, and by higher temperatures at any given peroxide pressure. The latter follows from the fact that the activation energy of step 3 is significant while that for step 2 can be set equal to zero. The Arrhenius expression written above for k_1 is thus referred to step 1, the cleavage of the oxygen–oxygen bond.

When $V_2/V_3 \gg 1$ the initial rate expression becomes

$$V_0 = \frac{k_1(CF_3OOCF_3)}{\frac{k_2}{k_3}\left(\frac{(k_1(CF_3OOCF_3) - V_0}{k_2}\right)^{1/2}} \quad (j)$$

It can be seen, however, that if $V_2 \gg V_3$, then $k_1(CF_3OOCF_3) \gg V_0$ and (j) becomes

$$V = k_3\left(\frac{k_1}{k_2}\right)^{1/2}(CF_3OOCF_3)^{1/2} \quad (k)$$

This is the rate expression that the data shown for the higher pressures in Table I and Figure 1 are approaching. Although the high-pressure points in Figure 1 correspond fairly well to the lines drawn with a slope of one-half, it is clear that they do not satisfy the

(6) H. L. Roberts, *J. Chem. Soc.*, 4538 (1964).

(7) Independent studies of the forward reaction alone have been reported by Descamps and Forst[8] and of the reverse reaction by Czarnowski and Schumacher.[9] The experimental results of Descamps and Forst[8] are similar to ours but their interpretation differs. Czarnowski and Schumacher[9] also found similar results to ours for the reverse reaction and proposed the same steps as are proposed here; they investigated the reaction only over a 10° interval, from 223 to 233°.

(8) B. Descamps and W. Forst, Abstracts of Papers Presented before Division of Fluorine Chemistry, 162nd National Meeting of the American Chemical Society, Washington, D. C., 1971.

(9) J. Czarnowski and H. J. Schumacher, *Z. Phys. Chem. (Frankfurt am Main)*, **73**, 68 (1970).

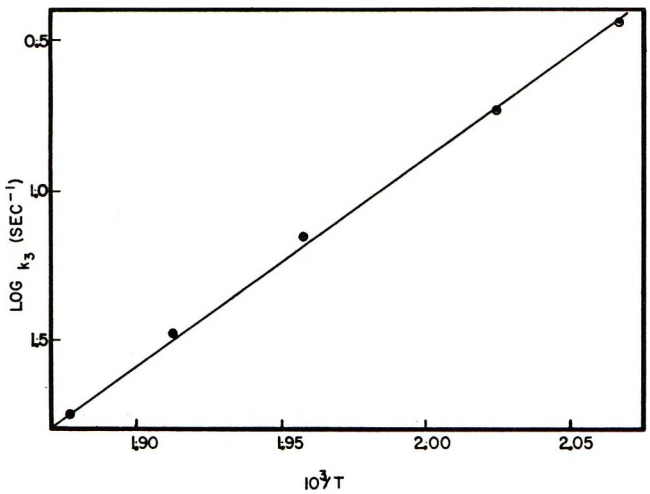

Figure 4. Arrhenius plot for k_3.

condition that $k_1(CF_3OOCF_3)/V_0 \gg 1$. For example, for the highest pressure at 221°, $k_1(CF_3OOCF_3)/V_0 \cong 4.5$.

To evaluate k_3, recourse was had to the observation that, as the pressure of bistrifluoromethyl peroxide was increased, a point would be reached at which the observed velocity would have fallen to $^1/_2\ k_1(CF_3OOCF_3)$. By plotting initial velocity *vs.* initial peroxide pressure this point can be accurately determined. At this point, from expression h

$$\begin{aligned} V_2 &= V_3 \\ (CF_3O) &= k_3/k_2 \end{aligned} \qquad (l)$$

Since for the initial velocity of the forward reaction it is always true that

$$V_0 = k_3(CF_3O) \qquad (m)$$

it follows that

$$k_3 = (k_2V_0^*)^{1/2} = (^1/_2k_1k_2(CF_3OOCF_3)^*)^{1/2} \qquad (n)$$

where $(CF_3OOCF_3)^*$ is the concentration of peroxide at which the initial velocity is just one-half that calculated on the basis of eq i, the simple first-order expression, and V_0^* is the corresponding initial velocity.

Values of k_3 found in this way are tabulated in Table IV and plotted in Figure 4. They yield the rate expression

$$k_3 = 10^{14.5 \pm 0.2}10^{-31,000 \pm 500/4.57T}\ \text{sec}^{-1} \qquad (o)$$

Kinetics of the Initial Velocity of the Reverse Reaction. When (CF_3OOCF_3) is considered negligible, expression f reduces to

$$-V_0 = \frac{k_6(CF_3OF)}{1 + \dfrac{k_5k_3}{k_2k_4(CF_2O)} + \dfrac{k_5(CF_3O)}{k_4(CF_2O)}} \qquad (p)$$

where $-V_0$ = initial velocity of the reverse reaction. The denominator is now $1 + [k_3k_5/k_2k_4(CF_2O)] +$ (V_5/V_4) and the effect of increasing (COF_2) is to make the denominator approach a value of one. Thus the kinetics observed with the addition of increasing amounts of carbonyl fluoride, *i.e.*, first-order dependence on trifluoromethyl hypofluorite, are assigned to step 6 and it is for this reason that the corresponding Arrhenius expression given in the Results for the reverse reaction is denoted as k_6. This interpretation is supported by the close correspondence of that expression for k_6 with the corresponding rate constant measured independently by Czarnowski and Schumacher.[9]

$$k_6 = 10^{14.5}10^{-43,500/4.57T}\ \text{sec}^{-1}$$

The data points reported in the latter work are shown in Figure 3.

Table IV: Calculated Values of k_3 from Initial Velocities in the Pyrolysis of Bistrifluoromethyl Peroxide

Temp, °C	Critical peroxide pressure, P_0^*, Torr[a]	$k_1 \times 10^5$, sec^{-1}	$k_2 \times 10^{-4}$, Torr^{-1} sec^{-1}	$k_3 = (^1/_2P_0^*k_1k_2)^{1/2}$, sec^{-1}
211	94 ± 5	0.209	8.28	2.85 ± 0.15
221	140 ± 5	0.544	8.11	5.56 ± 0.1
238	210 ± 10	2.61	7.84	14.6 ± 0.3
250	340 ± 10	7.42	7.66	31.1 ± 0.5
260	520 ± 20	17.2	7.52	58.0 ± 1.1

[a] See text for explanation of P_0^*.

Kinetics for Noninitial Conditions. From expressions f and g the general expression for the rate of disappearance of peroxide, V, can be written

$$V = k_1 \times \frac{K(CF_3OOCF_3) - (COF_2)(CF_3OF)}{\dfrac{k_1}{k_6}(CF_2O) + K\left[1 + \dfrac{k_2}{k_3}\left(\dfrac{(k_1(CF_3OOCF_3 - V}{k_2}\right)^{1/2}\right]} \qquad (q)$$

Since all the constants are known, it is possible to test this expression over the entire course of the reaction. This is done for the two temperatures 269 and 308° in Figures 5 and 6. The lines drawn have been constrained to pass through the origins and have been drawn with slopes that correspond to values of k_1 calculated from the Arrhenius expression for k_1 given in the Results section. The points fall well on the lines and give good support to the mechanism.

Rate Parameters for Individual Reactions. There is sufficient information available in the present results to allow calculation of all six rate constants of the mechanism. Expressions for k_1, k_3, and k_6 have already been given. The assumption can be made that the activation energies E_2 and E_5 are zero[10] since they correspond to recombination reactions of simple free radicals. The calculation of k_2 follows from the expression

(10) S. W. Benson, *J. Chem. Educ.*, **42**, 502 (1965).

$$RT \ln \frac{k_1}{k_2} = T\Delta S^\circ_{1,2} - \Delta H^\circ_{1,2}$$

where the standard entropy change and enthalpy change are evaluated for the given temperature. A similar expression can be written for the (5) (6) equilibrium. The quantity $\Delta H^\circ_{1,2}$ can be equated to activation energy E_1 since[3]

$$\Delta E^\circ_{1,2} = E_1 - RT$$

and

$$\Delta H^\circ_{1,2} = \Delta E^\circ_{1,2} + RT$$

The standard entropy for the peroxide can be taken from our earlier paper while that for CF_3O is here estimated by subtracting from the tabulated value for CF_3OF the difference between the tabulated values for OF_2 and OF.[11] Examination of this procedure shows that ΔH° and ΔS° are virtually unchanged from 500 to 600°K. The values used here are 46.2 kcal mol^{-1} and 34.0 eu mol^{-1}, respectively. (The values for $\Delta H^\circ_{f,550}$ and S°_{550} obtained in this way for CF_3O, and which will figure in the further discussion, are -156.8 ± 2 kcal mol^{-1} and 78.4 ± 1.0 eu mol^{-1}, respectively.) These yield at 550°K, $\Delta G^\circ_{1,2} = 26.5$ kcal mol^{-1} and $k_1/k_2 = 10^{-10.5}$ atm. Insertion of the experimental value for k_1 and conversion to concentration units yield $k_2 = 2.5 \times 10^9\ M^{-1}\ \text{sec}^{-1}$. In this same way it is found that $k_5 = 3.1 \times 10^9\ M^{-1}\ \text{sec}^{-1}$. These results are compared in Table V with values reported for other similar radicals. It is clear that trifluoromethoxy radicals combine at about the same rate as alkoxy or alkyl radicals.

Table V: Radical Recombination Rate Constants

Radicals	Log A, M^{-1} sec^{-1}	Ref
CH_3O, $(CH_3)_2CHO$, $(CH_3)_3CO$	9.3	12
CF_3	10.4	3
CH_3, C_2H_5	10.5	3
CF_3O	9.4	Present work
$CF_3O + F$	9.5	Present work

The value given earlier for k_3 refers to the decomposition of CF_3O and it is necessary to consider whether the reaction is in the first-order region or in the fall-off region. The evidence is that the reaction is in the first-order region. Thus the addition of inert gases in rather large amounts, *e.g.*, the data at 260°, Table I, causes no significant effect on the rate in peroxide pressure regions where k_3 is involved. In the same way no total pressure effects are indicated by the trend of the data for 221° where peroxide pressures up to 921 Torr were used. It may also be noted that the preexponential factor shown for k_3 is reasonable for a molecule of this complexity.[3] We therefore treat the above ex-

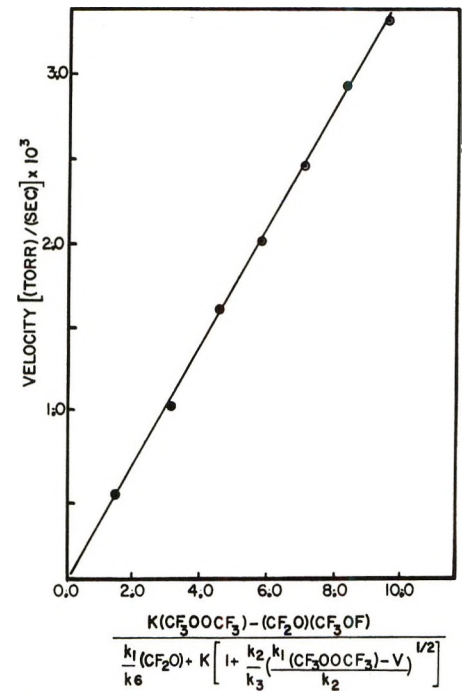

Figure 5. Plot of the rate of decomposition of bistrifluoromethyl peroxide at 269° *vs.* the rate predicted by the general expression q.

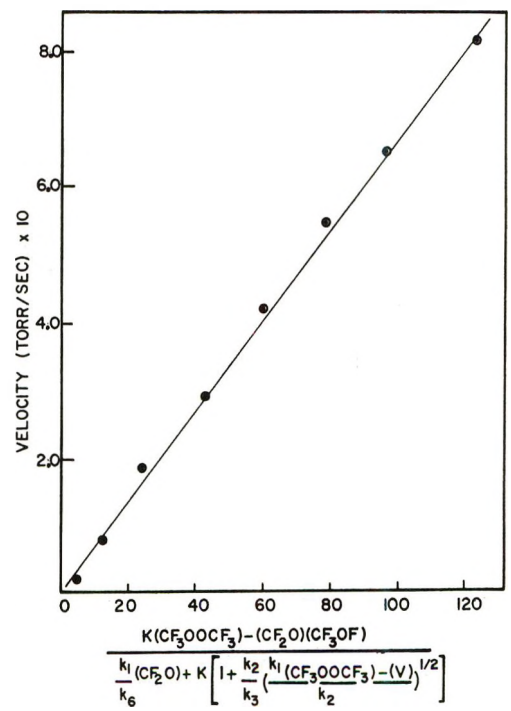

Figure 6. Plot of the rate of decomposition of bistrifluoromethyl peroxide at 308° *vs.* the rate predicted by the general expression q.

(11) "JANAF Thermochemical Tables," Thermal Research Laboratory, Dow Chemical Co., Midland, Mich., 1965.

pression as that for the first-order regime for this reaction rather than the second order. (It may be noted that if the reaction is not quite up into the first-order range, the observed activation energy would still not be expected to differ from that for the unimolecular reaction by more than about 1 kcal.)[12]

It is now possible to calculate k_4 since the equilibrium constant k_3/k_4 can be calculated from the standard entropy and heat content calculated above for CF_3O at 550°K, and the known values for F and CF_2O. The value for k_3/k_4 found is

$$k_3/k_4 = 10^{5.1\pm0.2}10^{-22,900\pm500/4.57T}\ M$$

This yields $k_4 = 10^{9.4\pm0.2}10^{-8100\pm500/4.57T}\ M^{-1}\ \text{sec}^{-1}$. These are the only kinetic parameters we know of for the reaction of F atoms with the carbonyl bond. The activation energy for the reaction

$$H + CH_2O \longrightarrow CH_3O$$

is estimated as about 8 kcal mol^{-1} by Gray, Shaw, and Thynne,[13] and the activation energy for the reaction

$$F + CF_3CF{=}CF_2 \longrightarrow CF_3{-}CF{-}CF_3$$

is estimated by Rodgers[14] as near zero. It may be noted that the exothermicity of the present reaction is very close to that of the $H\text{-}CH_2O$ reaction, 22 kcal mol^{-1},[13] and much less than that of the $F\text{-}C_3F_6$ reaction, ~50 kcal mol^{-1}.[14]

Disproportionation Reaction. The disproportionation reaction for trifluoromethoxy radicals is written, as step 7.

$$2CF_3O \underset{k_8}{\overset{k_7}{\rightleftharpoons}} CF_3OF + COF_2$$

For alkyl or alkoxy radicals this reaction appears to proceed with zero activation energy and about as fast as the recombination.[15] For perfluoroalkyl radicals the available[16,17] evidence is that the disproportionation reaction is very slow compared to recombination reactions. It is clear that the above reaction plays no significant role in the present system. Thus, if step 7 is significant, then step 8 is too; however, if step 8 occurred, limiting first-order behavior would not be found in the pyrolysis of $CF_3OF\text{-}COF_2$ mixtures. On the other hand, if step 7 occurred, the forward reaction would not show a change in kinetic order as the peroxide pressure was increased. If the assumption is made, as is generally done,[13] that the preexponential factor for k_7 is about that for k_2, then it is clear that $E_7 > 0$. Our data do not permit a quantitative evaluation of E_7 but a reasonable lower limit for E_7 is probably about $2RT$ or 2–3 kcal mol^{-1}. Conceivably E_7 could be much higher than this.

Bond Dissociation Energies. The evaluation of bond dissociation energies from the kinetics of pyrolysis reactions is a well-established procedure.[18] In the present work the bond dissociation energies for the oxygen–fluorine bond in trifluoromethyl hypofluorite and for the oxygen–oxygen bond in bistrifluoromethyl peroxide are defined by the quantities denoted earlier as $\Delta H^\circ_{1,2}$ and $\Delta H^\circ_{5,6}$, respectively. When these are converted to 298°K,[3] the values found are for the peroxide 46.7 ± 0.8 kcal mol^{-1} and for the hypofluorite 44.5 ± 0.8 kcal mol^{-1}.[19] The latter value can be compounded to the results reported by Czarnowski and Schumacher[9] of 43.1 kcal mol^{-1} and the value, 47 kcal mol^{-1} estimated by Porter and Cady.[20] The kinetics values are felt to be more accurate.

The oxygen-oxygen bond dissociation energy in bistrifluoromethyl peroxide is compared to those of other peroxides in Table VI.[21]

Table VI: Bond Dissociation Energies RO–OR

R	$D_{O-O,298}$, kcal mol^{-1}	Ref
CH_3	36.1 ± 1	18
C_2H_5	34.1 ± 4	18
$t\text{-}C_4H_9$	37.4	18
CF_3	46.7 ± 0.8	Present work
H	51	18
F	70 ± 10	21

The central bond in bistrifluoromethyl peroxide is thus significantly stronger than those in alkyl peroxides. The oxygen–oxygen bonding in peroxides has received considerable attention in recent years, largely because of the observation that the central bond in dioxygen difluoride is so strong.[22–25] In valence bond terms,[22] one would assign the increased bond strength in $CF_3\text{-}OOCF_3$, *vs.*, for example, CH_3OOCH_3, to contributions from the resonance structure $CF_3^-\ \ddot{O}{=}\ddot{O}^+CF_3$. The

(12) D. M. Golden, R. K. Solly, and S. W. Benson, *J. Phys. Chem.* **75**, 1333 (1971).

(13) P. Gray, R. Shaw, and J. C. J. Thynne, *Progr. React. Kinet.*, **4**, 63 (1967).

(14) A. S. Rodgers, *J. Phys. Chem.*, **67**, 2799 (1963).

(15) J. A. Kerr and A. F. Trotman-Dickenson, *Progr. React. Kinet.*, **1**, 111 (1961).

(16) G. O. Pritchard, G. H. Miller, and J. R. Dacey, *Can. J. Chem.*, **39**, 1968 (1961).

(17) E. J. Lehmann and J. B. Levy, *J. Amer. Chem. Soc.*, **93**, 5790 (1971).

(18) J. A. Kerr, *Chem. Rev.*, **66**, 465 (1966).

(19) The $H_T^\circ - H^\circ_{298}$ data for bistrifluoromethyl peroxide are given in the earlier paper.[1] The limits of error have been increased from 0.3 to 0.8 kcal mol^{-1} to encompass the chance that the correction to 298° might add an error of ±0.5 kcal mol^{-1}.

(20) R. S. Porter and G. H. Cady, *J. Amer. Chem. Soc.*, **79**, 5628 (1957).

(21) Calculated from the standard heats of formation of O_2F_2 and OF.[3]

(22) R. H. Jackson, *J. Chem. Soc.*, 4585 (1962).

(23) P. H. Kasai and A. D. Kirshenbaum, *J. Amer. Chem. Soc.*, **87**, 3069 (1965).

(24) S. J. Turner and R. D. Harcourt, *Chem. Commun.*, 4 (1967).

(25) R. D. Spratley and G. C. Pimentel, *J. Amer. Chem. Soc.*, **88**, 2394 (1966).

discussion of peroxides in molecular orbital terms[22,25] has described the R-O bond in ROOR in terms of electron donation from R to a π^* antibonding orbital of oxygen which contains an electron from oxygen. Clearly highly electronegative groups, such as fluorine atom, would donate less electron density to the antibonding orbital than would a group like methyl and hence the oxygen–oxygen bonding would be weakened less in the former case. For either explanation one would predict that the strength of the oxygen-oxygen bond in bistrifluoromethyl peroxide would be between that in O_2F_2 and that in dialkyl peroxides. It is worth noting that the present data offer support to the importance of the electronegativities of the attached groups in peroxides in determining the central oxygen–oxygen bond strengths. The group electronegativities of the trifluoromethyl and methyl groups have been calculated as 3.29 and 2.30,[26] respectively, while that for the fluorine is 4.0.[27] The electronegativity of the trifluoromethyl group is 37% of the way along from that of the methyl group to that of fluorine. The bond dissociation energy for bistrifluoromethyl peroxide is 32% of the way along from the value for the corresponding bond in dimethyl peroxide to that in dioxygen difluoride.

The molecular orbital picture also serves to give some insight into the bonding in polyoxides. The investigations of di-*tert*-butyl tri- and tetroxides have shown that these are both considerably less stable than the peroxides, with the tetroxides being least stable.[28–31] Since the bond in the trioxide could be pictured as involving interaction of one nonbonding orbital (from RO_2) and one p or sp^3 orbital (from RO) while that in the tetroxide would involve two of the former types it is quite reasonable that the bond strengths would show the observed trend. Here too the effect of terminal CF_3 groups would be predicted to be bond-strengthening relative to alkyl groups. The available data are shown in Table VII and are consistent with all of these qualitative productions.

Table VII: O–O Bond Strengths in Polyoxides (kcal mol^{-1})

R	ROOR	ROOOR	ROOOOR
t-C_4H_9	36	~23[a]	~9[b]
CF_3	45	~30	?

[a] References 28, 29, and 31. [b] References 29 and 31.

Experimental Section

Apparatus and Procedure. The initial experiments of the investigation were carried out in a 500-cc spherical Monel vessel. However, there was evidence that a heterogeneous wall reaction influenced the observed rates. Previous work had shown that aluminum fluoride is one of the less active metal fluoride catalysts for the addition of fluorine to carbonyl fluoride. Consequently, a 3-in. diameter cylindrical aluminum vessel of 1000-cc volume was constructed with all joints aluminum welded and was used for all of the experiments reported here except for those performed in the aluminum tubular reactor. The reactor surface was passivated only with CF_3OF at the temperatures used for the rate determinations. The vessel was connected by 0.25-in. o.d. aluminum tubing to a Pace Model V7 pressure transducer. In order to test for heterogeneous surface effects some experiments were carried out in a tubular reactor constructed from a 12-ft length of 0.25-in. o.d. aluminum tubing. The tubular reactor was considerably more difficult to passivate than the cylindrical reactor had been. First the surface was treated with 200-mm pressure of CF_3OF at 260° for 24 hr several times. Finally, the surface was conditioned with 1.5-atm pressure of CF_3OF at 300° for 24 hr, and the process was repeated with elemental F_2. Once the reactor had been sufficiently conditioned, the rates of CF_3OOCF_3 pyrolysis were essentially the same as in the cylindrical reactor (see Table I). All the experiments reported here were performed in these two aluminum reactors. The pressure-measuring techniques and the constant-temperature bath used have been described previously.[1] A Hoke 482 M Monel valve connected the system to a small volume Monel manifold used to evacuate and introduce samples to the vessel.

Experiments were performed by filling the thermostated vessel with a measured pressure of the peroxide or a previously prepared mixture of known stoichiometry including two of the three gases used: bistrifluoromethyl peroxide, trifluoromethyl hypofluorite, and carbonyl fluoride. Pressure–time curves were then recorded and the results interpreted. Instantaneous rates were calculated from tangents drawn to these curves. Experiments in which the peroxide decomposition reaction was allowed to proceed to equilibrium in the conditioned reactors gave final pressures corresponding to those calculated from the reported equilibrium constants.

Chemicals. Bistrifluoromethyl peroxide, trifluoromethyl hypofluorite, and carbonyl fluoride were obtained from Peninsular ChemResearch and were used as received. Bistrifluoromethyl peroxide (99.5%) and carbonyl fluoride (99%) were analyzed by gas chromatography and mass spectrometry, respectively.

(26) J. Hinze, M. Whitehead, and H. H. Jaffe, *J. Amer. Chem. Soc.*, 85, 147 (1963).

(27) L. Pauling, "Nature of the Chemical Bond," 3d ed, Cornell University Press, Ithaca, N. Y., 1960, p 93.

(28) P. D. Bartlett and P. Günther, *J. Amer. Chem. Soc.*, 88, 3288 (1966).

(29) P. D. Bartlett and G. Guaraldi, *ibid.*, 89, 4799 (1967).

(30) P. G. Thompson, *ibid.*, 89, 4316 (1967).

(31) K. Adamic, J. A. Howard, and K. U. Ingold, *Can. J. Chem.*, 47, 3803 (1969).

Analysis of the trifluoromethyl hypofluorite by idiometric titration[11] showed 89% purity. The nature of the experiments was such that only bistrifluoromethyl peroxide and carbon fluoride presented any difficulties as possible impurities. Since the measurements made for experiments with trifluoromethyl hypofluorite were initial rate measurements, the presence of small (~1%) amounts of bistrifluoromethyl peroxide presented no problem. Since, in addition, these experiments were carried out with substantial amounts of added carbonyl fluoride, the presence of small amounts of carbonyl fluoride as an impurity in the trifluoromethyl hypofluorite was likewise not a source of difficulty. The procedure adopted was to use the trifluoromethyl hypofluorite, as received, and to correct for the fact that it was only 89% pure.

Acknowledgment. This work was supported by Grant No. AFOSR 70-1939 of the Air Force Office of Scientific Research, Office of Aerospace Research, USAF. The United States Government is authorized to reproduce and distribute reprints for Governmental purposes notwithstanding any copyright notation hereon.

Apparent Molal Volumes of Sodium Chloride and Magnesium Chloride in Aqueous Solution

by Henry E. Wirth* and Frederick K. Bangert

Department of Chemistry, Syracuse University, Syracuse, New York 13210 *(Received November 19, 1971)*

Publication costs assisted by Syracuse University

The apparent molal volumes of sodium chloride and magnesium chloride in aqueous solution at 25° were determined for the concentration range 0–4 *m* using a modified form of the Geffcken dilatometer. The data obtained at low concentrations (ionic strength less than 0.4) were treated by the extended forms of the Debye–Hückel and Friedman equations. The calculated apparent molal volumes at infinite dilution of magnesium chloride were 14.47 (Debye–Hückel) and 14.52 cm³/mol (Friedman).

Introduction

Preliminary to the determination of the volume changes on mixing solutions of magnesium chloride and sodium chloride, the apparent molal volumes of magnesium chloride in aqueous solution were determined at concentrations up to 4 *m*. As a check on the precision of the dilatometer method used, the apparent molal volumes of sodium chloride were determined.

Experimental Section

A stock solution approximately 4 *m* in sodium chloride (Fisher Certified) was made up and analyzed by evaporation and drying to constant weight at 220°. A similar stock solution of magnesium chloride (Baker and Adamson) was analyzed by precipitation of the chloride as silver chloride. All weights were corrected to vacuum. The densities of the stock solutions were determined by the sinker method, using a "supplementary bob."[1] The sinkers used were made of Vycor and had approximate volumes of 300 cm³.

The apparent molal volumes of dilute solutions were determined using a modified Geffcken dilatometer.[2–4] The apparent molal volume (ϕ) is obtained from the observed change in volume (Δv) when stock solution is added to water by means of the relation

$$\phi = \phi_{ref} + \frac{\Delta v}{n_2} \quad (1)$$

where n_2 is the number of moles of electrolyte added, and ϕ_{ref} is the apparent molal volume of the electrolyte in the stock solution. The molality of the solution is $1000\, n_2/(m'_1 + m_1)$, where m'_1 is the weight of the water to which the stock solution (containing n_2 moles of salt and m_1 grams of water) is added. With the Geffcken apparatus a series of additions can be made, so that a

(1) H. E. Wirth and F. N. Collier, Jr., *J. Amer. Chem. Soc.*, **72**, 5292 (1950).

(2) W. Geffcken, A. Kruis, and L. Solana, *Z. Phys. Chem., Abt. B (Leipzig)*, **35**, 317 (1937).

(3) H. E. Wirth, R. E. Lindstrom, and J. N. Johnson, *J. Phys. Chem.*, **67**, 2339 (1963).

(4) H. E. Wirth, *ibid.*, **71**, 2922 (1967).

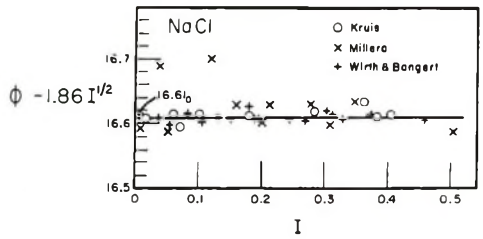

Figure 1. Evaluation of $\phi°$ for sodium chloride. The observed apparent molal volumes minus the limiting law plotted *vs.* the ionic strength are compared with the results of Kruis[5] and Millero.[6]

number of data points are obtained from a single loading of the dilatometer.

In some experiments a more dilute reference solution ($m \simeq 1$) was employed. The apparent molal volume of the electrolyte in these solutions was obtained from the dilution experiments with the stock solutions. The apparent molal volume of solutions between 2 and 4 m were obtained from the volume change observed when water was added to the stock solution.

The thermostat used for both the density determinations and the dilatometer experiments was maintained at 25.00 ± 0.01°, and was held constant within ±0.0005° during the course of a single series of observations.

Results and Discussion

Sodium Chloride. The apparent molal volume at infinite dilution ($\phi°$) was determined in the usual manner by plotting $\phi_{corr} = \phi_{obsd} - 1.86\,I^{1/2}$ (where I = ionic strength on a molal basis) *vs.* I (Figure 1). Based on 18 points ($I < 0.46$), $\phi° = 16.610 \pm 0.006$ cm³/mol, where ±0.006 is the root mean square deviation (rmsd) between the observed and calculated values, assuming the slope of ϕ_{corr} *vs.* I is zero. The results are in good agreement with values reported previously by Kruis,[5] by Millero,[6] and by Vaslow.[7]

A deviation plot for all the experimental points is given in Figure 2.

We were concerned that our present results are higher than those of Vaslow[7] and previous results of Wirth[8] by approximately 0.06 cm³/mol at concentrations above 2 m, although they do agree within the experimental error with the results of Geffcken.[9] An error of 0.02% in the density or an error of 0.2% in the molality is required to give this difference in the apparent molal volume. An error of 0.02% in the density is very unlikely, so it is possible that differences in the molality, perhaps due to impurities in the salts used, are the sources of the discrepancy. Since in our procedure an error of 0.06 cm³/mol in the determination of the apparent molal volume of the reference solution would lead to an equal error in the apparent molal volume of the dilute solutions (eq 1), and since our values in dilute solution agree so well with other authors, we believe our new values are to be preferred.

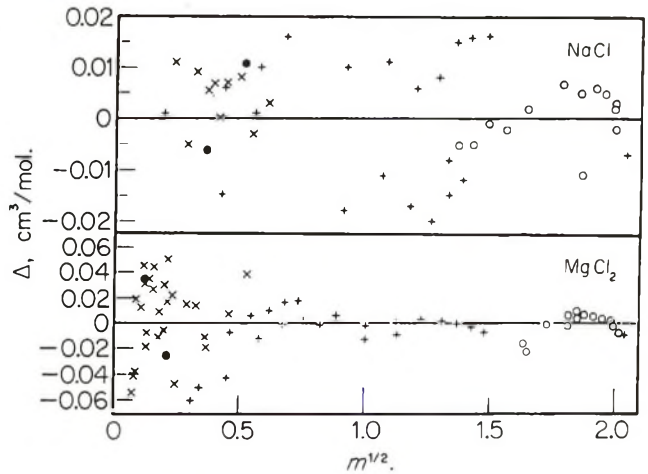

Figure 2. Deviation plot of $\Delta(= \phi_{calcd} - \phi_{obsd})$ *vs.* the square root of the molality. For NaCl (upper plot), $\phi_{calcd} = 16.610 + 1.86I^{1/2} + 0.0084_8I + 0.0452_8I^2 - 0.00809I^3$, an equation which represents all 47 experimental points (0–4I) with an rmsd of ±0.010 cm³/mol. Data points were obtained by adding a solution ($m = 1.129_2$, $\phi = 18.64_8$) to water (×), by adding a solution ($m = 0.7665$, $\phi = 18.27_1$) to water (●), by adding reference solution ($m = 4.1780$, $\phi = 20.655$) to water (+), and by adding water to reference solution (○). For $MgCl_2$ (lower plot), $\phi_{calcd} = 14.517 + 3.9511I^{1/2} - 0.56294I + 0.084783I^2 - 0.004741I^3$, an equation which represents the 45 data points between 0 and 4I with an rmsd of ±0.028 cm³/mol, and $\phi_{calcd} = 15.245 + 2.4072I^{1/2} + 0.3295I - 0.008198I^2 - 0.0002276I^3$, representing the 35 observations between I = 0.6 and I = 12 with an rmsd of ±0.012 cm³/mol. Comparison of experimental values with calculated values from the latter equation are given only for $I > 4$ ($m^{1/2} > 1.15$) in the above deviation plot. Data points were obtained by adding a solution ($m = 1.011$, $\phi = 20.34_4$) to water (×), by adding a solution ($m = 1.000$, $\phi = 20.31_2$) to water (●), by adding reference solution ($m = 4.167_8$, $\phi = 26.15_8$) to water (+), and by adding water to reference solution (○).

As Millero[6] has pointed out, the partial molal volume of a 1–1 electrolyte should be given by the extended Debye–Hückel equation including the ion-size parameter $\mathring{a}$

$$\bar{v}_2 - \bar{v}_2° = \frac{1.5S_v\sqrt{c}}{1 + A\mathring{a}\sqrt{c}} + Kc + \ldots \qquad (2)$$

where $S_v = 1.86$ at 25°.[10] The corresponding equation for apparent molal volume (in terms of m) is

$$\phi - \phi° = \frac{S_v\sqrt{m}}{1 + A\mathring{a}\sqrt{m}} + K'm + \ldots \qquad (3)$$

The fact that the experimental results for sodium chloride at 25° would imply that $\mathring{a} = 0$ (and $K' = 0$) in the concentration range 0–0.5 m (Figure 1) is explained by

(5) A. Kruis, *Z. Phys. Chem.* (*Leipzig*), **134**, 1 (1936).
(6) F. J. Millero, *J. Phys. Chem.*, **74**, 356 (1970).
(7) F. Vaslow, *ibid.*, **70**, 2286 (1966).
(8) H. E. Wirth, *J. Amer. Chem. Soc.*, **62**, 1128 (1940).
(9) W. Geffcken, *Z. Phys. Chem., Abt. B* (*Leipzig*) **5**, 81 (1929).
(10) O. Redlich and D. Meyer, *Chem. Rev.*, **64**, 221 (1964).

Table I: Constants in the Equation $\phi_{corr} = \phi^\circ + BI + CI^{3/2} + DI^2$

Equation	ϕ_{corr}, cm³/mol	ϕ°, cm³/mol	B	C	D	rmsd
I	$\phi_{obsd} - 5.58I^{1/2}$	14.464	−12.06	27.59	−20.88	±0.029
IIa	$\phi_{obsd} - \frac{5.58I^{1/2}}{1 + 1.65I^{1/2}}$	14.389	1.318	0.7989	0	±0.034
IIb	$\phi_{obsd} - \frac{5.58I^{1/2}}{1 + 1.65I^{1/2}}$	14.382	1.605	0	0.577	±0.035
IIc	$\phi_{obsd} - \frac{5.58I^{1/2}}{1 + 1.65I^{1/2}}$	14.471	−3.743	18.91	−16.71	±0.029
III	$\phi_{obsd} - \frac{5.58I^{1/2}}{1 + 2.15I^{1/2}}$	14.475	−1.709	14.94	−14.08	±0.029
IVa	$\phi_{obsd} - 5.58I^{1/2} - 7.545I \log I$	14.474	4.199	−6.520	0	±0.030
IVb	$\phi_{obsd} - 5.58I^{1/2} - 7.545I \log I$	14.502	2.388	0	−6.041	±0.028
IVc	$\phi_{obsd} - 5.58I^{1/2} - 7.545I \log I$	14.517	1.524	3.053	−8.823	±0.028

Millero as being due to association of Na^+ and Cl^- ions. He estimates the stoichiometric association constant to be 0.18 at 25°. Since in dilute solution the apparent molal volumes of most of the alkali halides can be represented by the relation $\phi_{obsd} - 1.86\sqrt{m} = \phi^\circ + K'm$ (Vaslow[7]), similar large association constants are implied for these salts. Hydrochloric acid, on the other hand, shows the type of behavior predicted by the extended Debye–Hückel equation[8] and would be assigned a small association constant.

The extended equation of Friedman[11]

$$\phi_I - \phi_I^\circ = \frac{V^{ex}}{I} = 1.86I^{1/2} + 2.514\left(\frac{n_3}{n_2}\right)^2 I \log I + O(I) \quad (4)$$

where ϕ_I is the apparent ional volume (apparent volume per ionic strength unit), V^{ex} is the excess volume per kilogram of solvent, and $n_m = \Sigma_s c_s z_s{}^m/c$ is the reduced mth moment of the concentration of charge types (c_s = concentration of species s, z_s = ionic charge of species s, and c = total concentration). For solutions of symmetric electrolytes the term involving I log I vanishes; for NaCl ($m = I$) the equation becomes

$$\phi = \phi^\circ + 1.86m^{1/2} + O(m) \quad (5)$$

The term $O(m)$ involves the volumes $\bar{v}_{Na,Cl}{}^*$, $\bar{v}_{Na,Na}{}^*$, and $\bar{v}_{Cl,Cl}{}^*$ where $\bar{v}_{ij}{}^*$ is the part of the volume which changes on mixing due to structural effects when ion i is in the neighborhood of ion j.[12] The observed behavior of the apparent molal volume of sodium chloride at 25° may then be interpreted as being due to the balancing out of the volume effects due to cation–anion interaction (assumed to be positive in agreement with Millero's[8] view) by volume effects due to cation–cation and anion–anion interaction (assumed to be negative). Furthermore, the results of Millero at 0°, and at 55°, may be interpreted as indicating that the temperature coefficient for cation–anion interactions is larger than the temperature coefficient for cation–cation and anion–anion interactions.

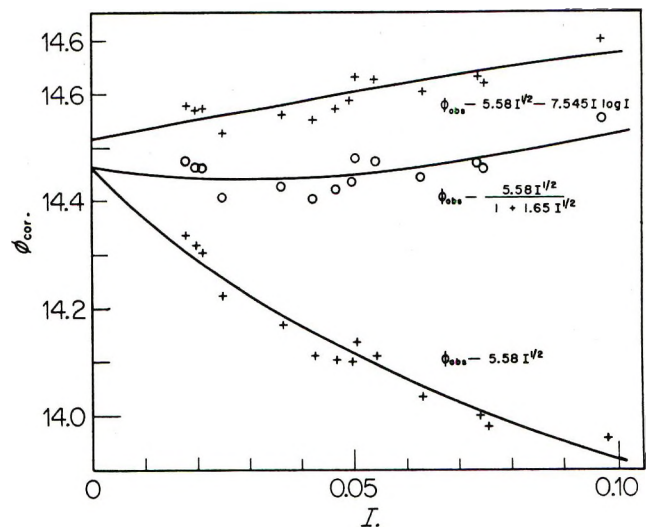

Figure 3. Evaluation of ϕ° for magnesium chloride by extrapolation of various functions to $I = 0$. The two lower curves are for two forms of the Debye–Hückel equation, I and IIc (Table I), and the upper curve is for the Friedman equation, IVc.

The apparent molal volume of sodium chloride (and other alkali halides) therefore provides clear differences of interpretation which may help in the choice between the two ionic solution theories. If the extended Debye–Hückel theory is correct, then considerable cation–cation pairing (up to 13% in 1 M solutions, according to Millero's estimates) seems to be the most reasonable interpretation.

Magnesium Chloride. The evaluation of ϕ° for magnesium chloride is more difficult than for sodium chlo-

(11) H. L. Friedman, "Ionic Solution Theory," Interscience, New York, N. Y., 1962, pp 209 and 211. The constants in the equations have been calculated using the values of d ln D/dP (D = dielectric constant, P = pressure) and of β (coefficient of compressibility) recommended by Redlich and Meyer.[10]

(12) W.-Y. Wen and K. Nara, *J. Phys. Chem.*, **71**, 3907 (1967).

ride, as $\phi_{obsd} - 5.58I^{1/2}$ is not a linear function of I and cannot be readily extrapolated to zero concentration (Figure 3).

In Table I, the constants in various forms of the Debye–Hückel equation (eq I, IIa, b, and c, and III) and of the Friedman equation (eq IV) are given. In eq II, $\mathring{a}$ was taken to be 5 Å, the value used by Robinson and Stokes[13] to represent activity coefficient data. The Debye–Hückel eq I, IIc, and III yield values of ϕ° of 14.47 cm³/mol, while the Friedman equation with the same number of arbitrary constants (IVc) gives 14.52 cm³/mol as the value of ϕ°. This difference is too small to permit a choice of the best extrapolation equation. The Friedman equation is better in that the value of ϕ° obtained is less sensitive to the choice of the powers of I to be included in the equation (compare eq IIa, b, c with eq IVa, b, c).

Dunn[14] estimates ϕ° of magnesium chloride to be 14.49 cm³/mol. However, his experimental values in the range $0.003 < I < 0.06$ are from 0.06 to 0.17 cm³/mol larger than those calculated from eq I (Table I). His values are based on those of Shedlovsky and Brown[15] at higher concentrations which are in good agreement with those reported here.

A deviation plot for all the data is given in Figure 2.

Acknowledgment. Portions of this work were supported by the Office of Saline Water, Grant No. 14-01-0001-623.

(13) R. A. Robinson and R. H. Stokes, "Electrolyte Solutions," 2nd ed, Academic Press, New York, N. Y., 1959, p 246.

(14) L. A. Dunn, *Trans. Faraday Soc.*, **62**, 2348 (1966).

(15) T. Shedlovsky and A. S. Brown, *J. Amer. Chem. Soc.*, **56**, 1066 (1934).

Volume Changes on Mixing Solutions of Magnesium Chloride and Sodium Chloride

by Henry E. Wirth* and Frederick K. Bangert

Department of Chemistry, Syracuse University, Syracuse, New York 13210 *(Received November 19, 1971)*

Publication costs assisted by Syracuse University

The volume changes on mixing magnesium chloride and sodium chloride solutions of equal molality ($m = 4$), of equal weight normality ($E = 4$), and of equal ionic strength ($I = 1.00, 1.56, 2.25, 3.06$, and 4.00) have been determined. All the results of mixing at constant ionic strength can be represented by the relation $D'' = -0.195I^{1/2}y(1 - y) + 0.080y^2(1 - y)$, where D'' (in cm³/ionic strength unit) is the correction term in Young's rule, and y is the ionic strength fraction of sodium chloride. On the assumption that the equation for D'' can be applied to ionic strengths above 4, the apparent molal volume of sodium chloride in pure solution has been estimated for ionic strengths between 4 and 11+ from the results of mixing at constant molality. The volume change on mixing a solution containing 500 g of water and 2.0 mol of sodium chloride with a solution containing 500 g of water and n_3 mol of magnesium chloride is a minimum when $n_3 = 0.9$.

Introduction

In previous work the volume changes in mixing of the $HCl–HClO_4–NaCl–NaClO_4$[1] and the $Na_2SO_4–NaCl–LiCl–Li_2SO_4$[2] systems have been investigated. In the present work, the system $MgCl_2–NaCl$ has been looked at in greater detail than in previous systems, in that the effects of mixing at constant molality, at constant weight normality, and at constant ionic strength have all been determined, and the mixings have been made at a number of constant ionic strengths.

Experimental Section

Solutions of magnesium chloride and of sodium chloride of the appropriate concentrations were prepared by weight dilution of the stock solutions described in the previous paper.[3]

The volume changes in mixing were determined using the modified Geffcken[2] apparatus.

Results

Mixing at Constant Ionic Strength. The volume changes (Δv) on mixing a solution of magnesium chlo-

(1) H. E. Wirth, R. E. Lindstrom, and J. N. Johnson, *J. Phys. Chem.*, **67**, 2339 (1963).

(2) H. E. Wirth and W. L. Mills, *J. Chem. Eng. Data*, **13**, 102 (1968).

(3) H. E. Wirth and F. K. Bangert, *J. Phys. Chem.*, **76**, 3488 (1972).

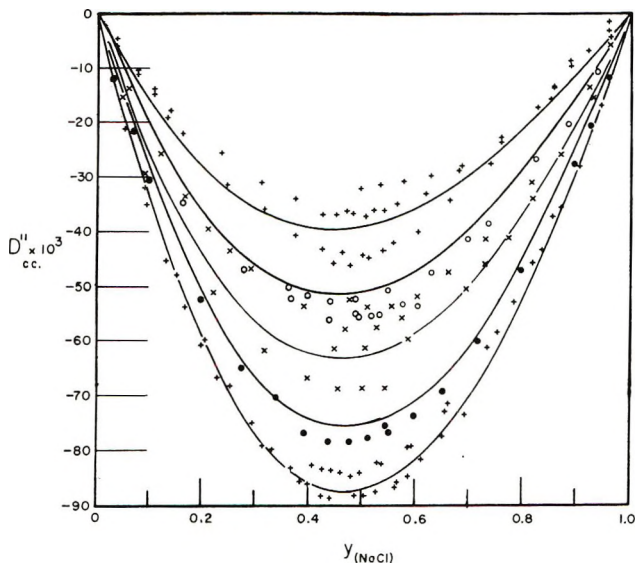

Figure 1. Volume change (cubic centimeters per ionic strength unit) on mixing solutions of $MgCl_2$ and NaCl at constant total ionic strengths of 1.00 (+), 1.56 (O), 2.25 (×), 3.06 (●), and 4.00 (+) *vs.* the ionic strength fraction (y) of NaCl. The curves are calculated from the equation: $D'' = -0.195I^{1/2}y(1 - y) + 0.080y^2(1 - y)$.

ride with a solution of sodium chloride of the same ionic strength were determined for solutions of ionic strength (I) = 1.00, 1.56, 2.25, 3.06, and 4.00. The observed volume change divided by the number of ionic strength units in the mixture gives the value of D'' in Young's rule, written as

$$\Phi_I = y(\phi_I)_{NaCl} + (1 - y)(\phi_I)_{MgCl_2} + D'' \quad (1)$$

where Φ_I is the mean apparent ional volume of the mixture of electrolytes, $(\phi_I)_{NaCl}$ is the apparent ional volume (= apparent molal volume) of sodium chloride in a pure solution of ionic strength I, $(\phi_I)_{MgCl_2}$ is the apparent ional volume of magnesium chloride (= one-third the apparent molal volume) in a solution of ionic strength I containing only magnesium chloride, and y is the ionic strength fraction of sodium chloride in the mixture. The excess volume change on mixing ($(\Delta_M V^{ex})_I$, Friedman[4]) in cubic centimeters per kilogram of water is equal to $D''I$.

The observed values of D'' (Figure 1) are of the same order of magnitude as previously observed for HCl–NaCl and for LiCl–NaCl, and can be represented at a given ionic strength by the equation $D'' = Ay(1 - y) + By^2(1 - y)$ (Table I). All of the experimental points could be represented by an equation in which $A = -0.195I^{1/2}$ and $B = 0.080$.

Mixing at Constant Molality and Constant Weight Normality. In addition to the mixings at constant ionic strength, sodium chloride and magnesium chloride were mixed at a constant molality of 4.00 and at a constant weight normality of 4.00. The observed volume changes were divided by the number of moles

Table I: Mixing at Constant Ionic Strength
$D'' = Ay(1 - y) + By^2(1 - y)$

I, ionic strength units/kg of H_2O	A	B	No. of exptl points	rmsd,[a] cm³/ ionic strength unit
1.00	−0.198	0.099	54	0.004
1.56	−0.252	0.071	22	0.002
2.25	−0.275	0.071	38	0.005
3.06	−0.338	0.050	22	0.001
4.00	−0.397	0.104	54	0.002
(1–4.00)	$(-0.195I^{1/2})$	(0.080)	(190)	(0.004)

[a] Root mean square deviation between observed and calculated values.

or the number of equivalents in the resulting mixture to give D or D', respectively, in the equations

$$\Phi = S_2\phi_{NaCl} + (1 - S_2)\phi_{MgCl_2} + D \quad (2)$$

$$\Phi_E = E_2(\phi_E)_{NaCl} + (1 - E_2)(\phi_E)_{MgCl_2} + D' \quad (3)$$

where Φ is the mean apparent molal volume of the electrolytes in the mixture, ϕ_{NaCl} and ϕ_{MgCl_2} are the apparent molal volumes of NaCl and $MgCl_2$ in pure solution at a given molality, and S_2 is the mole fraction of NaCl present in the mixture. Φ_E is the mean apparent equivalent volume of the electrolytes, $(\phi_E)_{NaCl}$ and $(\phi_E)_{MgCl_2}$ are the apparent equivalent volumes of NaCl and $MgCl_2$ in pure solution at a given weight normality, and E_2 is the equivalent fraction of NaCl in the mixture. Equations 2 and 3 arise naturally from the experimental treatment of volume changes on mixing solutions of equal molality or weight normality.[1] They should not be confused with Young's rule which applies only to mixings at constant ionic strength.

The excess volume on mixing ($\Delta_m V^{ex}$) is obtained by multiplying D by the total molality, or D' by the total weight normality. Observed values of $\Delta_m V^{ex}$ are given in Figure 2 and may be represented by the equations

$$m = 4;\ (\Delta_m V^{ex})_m = -5.967S_2(1 - S_2) - 0.965S_2^2(1 - S_2) \quad (25 \text{ points}) \quad (4)$$

$$E = 4;\ (\Delta_m V^{ex})_E = -1.224E_2(1 - E_2) + 0.389E_2^2(1 - E_2) \quad (26 \text{ points}) \quad (5)$$

with an rmsd of ±0.004 cm³/kg of H_2O.

Apparent Molal Volume of Sodium Chloride at High Concentrations. From the results on mixing at a constant molality of 4, the volume occupied by a solution containing 1 kg of water, n_2 moles of NaCl and n_3 moles of $MgCl_2$ ($n_2 + n_3 = 4$) is given by

$$V = 55.51\bar{v}_1^\circ + n_2(\phi_{NaCl})_{m_2=4} + n_3(\phi_{MgCl_2})_{m_3=4} + (\Delta_m V^{ex})_{m=4} \quad (6)$$

(4) H. L. Freidman, "Ionic Solution Theory," Interscience, New York, N. Y., 1962.

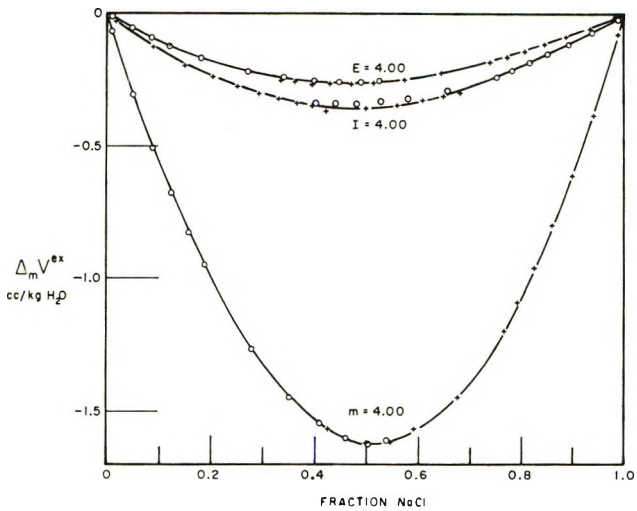

Figure 2. Observed excess volume of mixing at a constant weight normality (E), at constant molality (m), and at constant ionic strength (I) *vs.* the equivalent, mole, or ionic strength fraction, respectively.

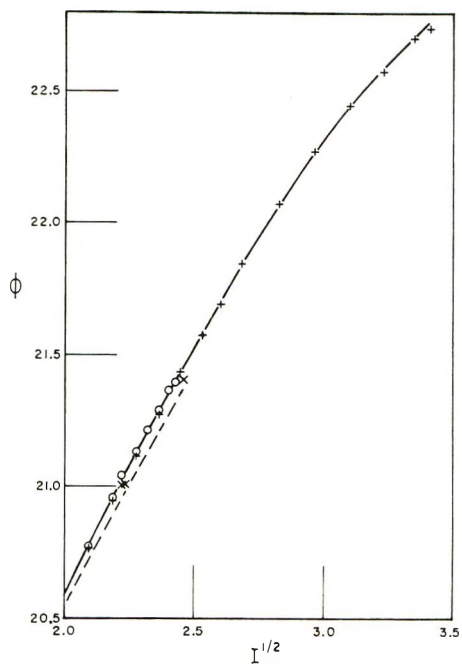

Figure 3. The apparent molal volume of sodium chloride (ϕ) for ionic strengths above 4, as calculated from mixing at constant molality (+) and from mixing at constant weight normality (○). Experimental values of Geffcken[5] are indicated by ×, and the dashed line is the value calculated from density data in ICT[6] between 4 m and saturation.

This same solution can be considered as being prepared by mixing solutions of sodium chloride and magnesium chloride of equal ionic strengths, where $I = n_2 + 3n_3$, and

$$V = 55.51\bar{v}_1^\circ + n_2(\phi_{NaCl})_I + n_3(\phi_{MgCl_2})_I + (\Delta_m V^{ex})_I \quad (7)$$

If these two values for V are equated, the only unknown in the resulting equation is $(\phi_{NaCl})_I$ if $(\Delta_m V^{ex})_I$ is extrapolated to ionic strengths above 4 by use of the general equation in Table I.

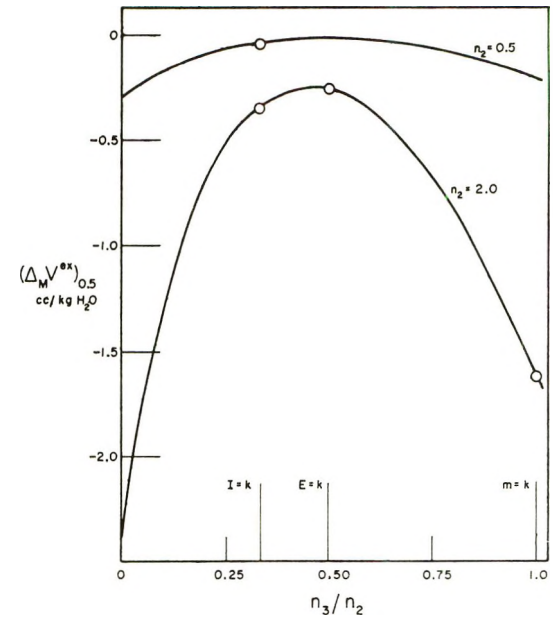

Figure 4. Estimated volume changes on mixing a solution contining 500 g of water and n_2 moles of sodium chloride (n_2 = 0.5 or 2.0) with solutions containing 500 g of water and n_3 moles of magnesium chloride ($0 < n_3 < 0.5$ and $0 < n_3 < 2.0$, respectively) as a function of n_3/n_2. Experimental values of the volume changes on mixing at constant ionic strength ($n_2 = n_3/3$) are indicated by open circles for both n_2 = 0.5 and n_2 = 2.0. Experimental values for mixing at constant weight normality and constant molality are also given for n_2 = 2.0.

For example, if S_2 is taken as 0.1, then n_2 = 0.4, n_3 = 3.6, I = 11.2, and y_2 = 0.0357. For m = 4.0, ϕ_{NaCl} = 20.57_1,[3] ϕ_{MgCl_2} = 25.96_3,[3] and $(\Delta_m V^{ex})_m$ = −0.546; for I = 11.2, ϕ_{MgCl_2} = 25.64_3,[3] and $(\Delta_m V^{ex})_I$ = −0.251. The estimated value of $(\phi_{NaCl})_I$ is then 22.71 cm³/mol. Values for ϕ_{NaCl} for ionic strengths above 4 are given in Figure 3,[5,6] along with values calculated by a similar procedure from the results of mixing at constant weight normality. The comparison with other values between 4 m and saturation indicates that the calculated values are valid to at least ±0.05 cm³/mol in this range. Above saturation, we believe the estimated values are good to ±0.10 cm³/mol.

Other 50–50 Mixings. The results given in Figure 2 suggest that there is a minimum volume change on mixing solutions at constant weight normality. To see if this is the true minimum, the volume change on mixing a solution containing 500 g of water and 2 mol of sodium chloride (m_2 = 4) with a solution containing 500 g of water and n_3 moles of magnesium chloride ($m_3 = 2n_3$) has been calculated for values of n_3 between 0 and 2. This volume change ($(\Delta_m V^{ex})_{0.5}$) is given by an equation similar to eq 6

(5) W. Geffcken, *Z. Phys. Chem., Abt. B*, 5, 81 (1929).

(6) "International Critical Tables," McGraw-Hill, New York, N. Y., 1926.

$$V = 55.51\bar{v}_1^\circ + 2(\phi_{NaCl})_{m_2=4} + n_3(\phi_{MgCl_2})_{m_3} + (\Delta_m V^{ex})_{0.5} \quad (8)$$

Combining this with eq 7, in which $I = n_2 + 3n_3$, the relation

$$(\Delta_m V^{ex})_{0.5} = 2[(\phi_{NaCl})_I - (\phi_{NaCl})_{m_2=4}] + n_2[(\phi_{MgCl_2})_I - (\phi_{MgCl_2})_{m_3}] + D''I \quad (9)$$

is obtained. For values of $I > 4$, D'' was estimated assuming that the general equation in Table I was valid, and $(\phi_{NaCl})_I$ as calculated in the previous section was used. The results (Figure 4) indicate that the true minimum corresponds to a value of n_3/n_2 of about 0.45. At a lower concentration ($n_2 = 0.5$) the minimum is poorly defined and appears to lie between 0.40 and 0.55.

Discussion

The heats of mixing of aqueous solutions of magnesium chloride with solutions of various alkali metal chlorides have been determined by Wood, Patton, and Ghamkhar.[7] While the observed heats were comparable in magnitude to the heats of mixing of two alkali chloride solutions, the quantity h_0 tended to become more positive in lower concentrations as predicted by the Friedman limiting law in the case of a charge-asymmetric mixture. To compare with these results, the volume changes on mixing magnesium chloride with sodium chloride must be expressed by equations analogous to that used by Wood, *et al.*

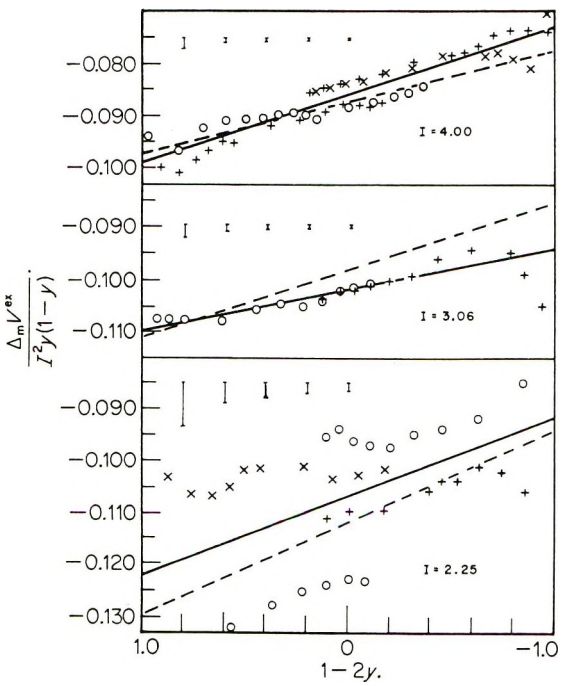

Figure 5. The function $\Delta_m V^{ex}/[I^2y(1 - y)]$ (cm³ kg (ionic strength unit)$^{-2}$) *vs.* $(1 - 2y)$ for ionic strengths of 4.00, 3.06, and 2.25. The lengths of the vertical bars indicate at each mole fraction the error in the function due to an error of 2×10^{-4} cm³ in the observed volume change. The solid lines are calculated from the individual equations and the dotted line from the general equation given in Table I.

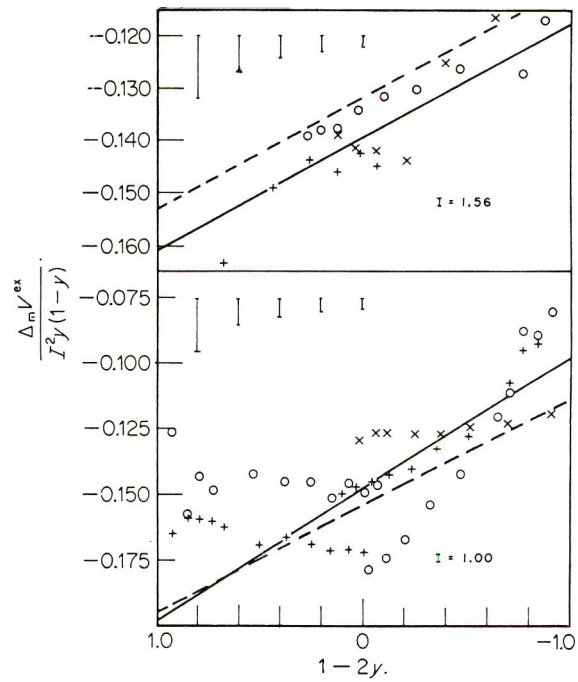

Figure 6. The function $\Delta_m V^{ex}/[I^2y(1 - y)]$ (cm³ kg (ionic strength unit)$^{-2}$) *vs.* $(1 - 2y)$ for ionic strengths of 1.56 and 1.00. The lengths of the vertical bars indicate at each mole fraction the error in the function due to an error of 2×10^{-4} cm³ in the observed volume change. The solid lines are calculated from the individual equations and the dotted lines from the general equation given in Table I.

The excess volume on mixing is given by

$$\Delta_m V^{ex} = I^2y(1 - y)[v_0 + (1 - 2y)v_1] \quad (10)$$

where the term v_0 is analogous to h_0 for heats of mixing and is equal to $-2.514 \log I$ at 25° (limiting law). Since $\Delta_m V^{ex}$ is also equal to $D''I$, it can be shown that $v_0 = (A + B/2)/I = -0.195/I^{1/2} + 0.040/I$ and $v_1 = -B/2I = -0.040/I$ (from Table I). In the concentration range studied, v_0 becomes increasingly negative as the concentration decreases. However, the equation used to represent the data does meet the requirement that v_0 approaches $+\infty$ as I approaches zero.

Plots of the relationship expressed by eq 10 are given in Figures 5 and 6. While the scatter of the experimental points apparently increases with decreasing ionic strength, the deviations represent about the same experimental error in the determination of Δv.

Acknowledgment. This work was supported in part by Grant No. 14-01-0001-623 from the Office of Saline Water.

(7) R. H. Wood, J. D. Patton, and H. Ghamkhar, *J. Phys. Chem.*, **73**, 346 (1969).

Ultrasonic and Brillouin Scattering Study of Viscoelastic Relaxation in a Concentrated Aqueous Calcium Nitrate Solution

by Judith H. Ambrus,*

Naval Ordnance Laboratory, White Oak, Silver Spring, Maryland 20910

Henry Dardy, and Cornelius T. Moynihan

Vitreous State Laboratory, The Catholic University of America, Washington, D. C. 20017 *(Received June 9, 1972)*

Publication costs assisted by the Naval Ordnance Laboratory

Ultrasonic and Brillouin scattering experiments were performed on a highly concentrated aqueous $Ca(NO_3)_2$ solution (6.908 *m*, R = 8.035). Propagating velocity and absorption coefficient of ultrasound were measured in the frequency range 30–190 MHz. Additional velocity data were obtained at 3 MHz, and Brillouin scattering yielded data in the GHz range. The temperature range of the measurements was room temperature to glass transition temperature (−90°). A strong relaxation effect was observed in both absorption and velocity. Calculations show that the data are consistent with the treatment of this relaxation as a viscoelastic rather than a thermal effect. The relaxation is characterized by a broad distribution of relaxation times. The distribution is symmetric (log gaussian, b = 0.34) and appears to be temperature independent in the range of our experiments. A comparison of the average longitudinal and conductivity relaxation times shows that while relaxation of mechanical and electrical stress seem to occur on the same time scale at temperatures of low viscosity, as the temperature decreases toward the glass transition temperature, the time for mechanical relaxation becomes much slower than that for electrical conduction.

I. Introduction

Shear and structural relaxation experiments on liquids yield information on the time scale and mechanism of diffusive rearrangements of the liquid quasi-lattice in response to mechanical stress. They are usually carried out by studying the frequency dependence of the velocity and absorption of ultrasonic shear and longitudinal waves in the frequency range 2 to 200 MHz.[1] For this frequency range pronounced viscoelastic relaxation effects are generally observed when the liquid shear viscosity, η_s, attains values of 10 P and greater, although in cases where the process must be described by a broad distribution of relaxation times viscoelastic effects on the ultrasonic velocity and absorption may become prominent at viscosities as low as 1 P.

In the past few years, notice has been taken of the fact that supercooled highly concentrated aqueous electrolyte solutions exhibit viscosities approaching and exceeding 1 P, and a number of ultrasonic velocity and absorption studies have been carried out on systems of this sort. Darbari and Petrucci[2] reported a longitudinal ultrasonic study on calcium nitrate–water solutions over the viscosity range 0.2 to 2 P and the concentration range R = 4–5, where

$$R = \text{moles of water/mole of salt}$$

They observed a frequency dispersion in α/f^2, the ratio of the longitudinal absorption coefficient to the square of the frequency, which they attributed to an unspecified chemical relaxation process involving ionic hydration. In a subsequent study[3] of a more concentrated calcium nitrate–water solution (R = 3.2) over the viscosity range 15–115 P the observed dispersion in α/f^3 could be attributed to a viscoelastic relaxation; a dispersion in the shear velocity was also reported at one temperature for this solution. In a study[4] of $ZnCl_2$–H_2O solutions covering the range R = 2.3–547 the observed dispersion in α/f^2 was attributed to a chloride ion complexation reaction. However, at the highest $ZnCl_2$ concentration the solution viscosities were in the 1 P range and the beginning of a shear viscoelastic relaxation could be detected in the frequency range of the relaxation attributed to the complexation reaction. Moynihan, *et al.*,[5] have reported shear impedance measurements for concentrated LiCl solutions (R = 4.83–5.77) at 88 MHz over the viscosity range 10–10^8 P; a shear viscoelastic relaxation exhibiting a broad asymmetric distribution of relaxation times was observed.

In all of these previous studies the relaxations in viscous highly concentrated aqueous electrolyte solu-

(1) T. A. Litovitz and C. M. Davis, "Physical Acoustics," Vol. IIA, W. P. Mason, Ed., Academic Press, New York, N. Y., 1965, pp 281–349.

(2) G. S. Darbari and S. Petrucci, *J. Phys. Chem.*, **73**, 921 (1969).

(3) G. S. Darbari, M. R. Richelson, and S. Petrucci, *J. Chem. Phys.*, **55**, 4351 (1971).

(4) G. S. Darbari, M. R. Richelson, and S. Petrucci, *ibid.*, **53**, 859 (1970).

(5) C. T. Moynihan, N. Balitactac, L. Boone, and T. A. Litovitz, *ibid.*, **55**, 3013 (1971).

tions have been poorly characterized because of the limited frequency range employed and/or because the investigation was carried out over a limited viscosity (temperature) regime. In an effort to obtain a better characterization of processes of this sort, we report in the present paper a study of the velocity and absorption of longitudinal waves in a concentrated calcium nitrate–water solution (R = 8). We have augmented the frequency range available by ultrasonic techniques with Brillouin light scattering measurements which yield longitudinal velocity values in the 10-GHz region. In addition, the ability of the $Ca(NO_3)_2 \cdot 8H_2O$ solution to withstand considerable supercooling for long periods of time without crystallizing has allowed us to obtain data extending from the temperature region of high fluidity ($\eta_s \sim 10^{-1}$ P) down to the glass transition region ($\eta_s \sim 10^{13}$ P).

II. Experimental Methods and Results

A. Sample Preparation and Characterization. The solution was prepared from reagent grade calcium nitrate tetrahydrate and deionized water and was filtered through a 5-μm pore filter prior to use. Other details of sample preparation and analysis have been described previously,[6] along with measurements of the density, shear viscosity, and electrical conductivity. The exact solution composition was R = 8.035 (6.908 m). An equation expressing the density as a function of temperature is given in Table I. Representative solution viscosities obtained by using the Fulcher equation as a smoothing function for data over short viscosity intervals[6] are included in Table II. The glass transition temperature for this solution is −90°.[7]

Table I: Density, Refractive Index, and Limiting Low- and High-Frequency Longitudinal Modulus Equations for $Ca(NO_3)_2 \cdot 8H_2O$ Solution

Density	$\rho(g/cm^3) = 1.541 - 8.6 \times 10^{-4} t(°C)$
Refractive index	$\frac{n^2 - 1}{n^2 + 2} = 0.1709\rho$
Low-frequency modulus	$M_0(dyn/cm^2) = 5.02 \times 10^{10} - 0.68 \times 10^8 t(°C)$
High-frequency modulus	$M_\infty(dyn/cm^2) = 9.5 \times 10^{10} - 12.7 \times 10^8 t(°C)$

B. Brillouin Scattering and Refractive Index. When a beam of monochromatic light is scattered through an angle θ by a solid or liquid, the scattered light exhibits intensity maxima at frequencies $f_0 \pm f_B$ symmetrically placed about the original light frequency f_0. These spectral lines, known as Brillouin lines, result from light scattering from thermally generated hypersonic waves of frequency f_B. The longitudinal sound velocity at frequency f_B is given by[8,9]

$$V = cf_B/2nf_0 \sin(\theta/2) \quad (1)$$

where c is the velocity of light in a vacuum, θ is the angle between the incident and scattered light beams, and n is the refractive index at frequency f_0.

Table II: Longitudinal Velocities and Frequencies Obtained from Brillouin Scattering Measurements and Shear Viscosities as a Function of Temperature for $Ca(NO_3)_2 \cdot 8H_2O$ Solution

t, °C	f_B, GHz	$10^{-5}V$, cm/sec	η_s, P
40.0	7.2	1.83	
20.0	7.3	1.84	1.26×10^{-1}
15.5	7.5	1.89	1.49×10^{-1}
10.0	7.7	1.94	1.88×10^{-1}
−1.0	8.0	2.02	3.23×10^{-1}
−10.0	8.5	2.15	5.53×10^{-1}
−20.0	9.6	2.43	1.16
−30.0	10.6	2.66	2.99
−40.0	11.5	2.88	1.06×10^1
−50.0	12.3	3.08	5.6×10^1
−60.0	13.1	3.27	5.4×10^2
−70.0	13.6	3.39	1.76×10^4
−80.0	14.0	3.48	4.1×10^6
−90.0	14.5	3.60	
−100.0	14.8	3.67	

Brillouin scattering experiments were carried out for the $Ca(NO_3)_2 \cdot 8H_2O$ solution over the temperature range from −100 to 40°. Temperatures for this experiment and for the ultrasonic experiments described below were measured with copper–constantan thermocouples to an accuracy of ±0.1°. The Brillouin scattering apparatus was a slightly modified version of that described by Pinnow, *et al.*[9] The light source, an argon ion laser with a power of approximately 1 W, was operated in a single mode at 5145 Å. Brillouin spectra representing a typical temperature run are shown in Figure 1. Brillouin shift data (f_B) at the higher temperatures, where the central and Brillouin peaks are not completely separated, were obtained by decomposing the two peaks into two Lorentzians by computer.

Refractive index values needed for the calculation of V *via* eq 1 were measured at the laser wavelength over the temperature range from −30 to 40° with an Abbe refractometer. The refractometer prisms were thermostated by circulating liquid through the jackets surrounding them; this part of the instrument was enclosed in a nitrogen-filled glove bag to prevent water or ice condensation on the optics at the lower tem-

(6) J. H. Ambrus, C. T. Moynihan, and P. B. Macedo, *J. Electrochem. Soc.*, **119**, 192 (1972).

(7) C. A. Angell and E. J. Sare, *J. Chem. Phys.*, **52**, 1058 (1970).

(8) C. J. Montrose, V. A. Solovyev, and T. A. Litovitz, *J. Acoust. Soc. Amer.*, **43**, 117 (1968).

(9) D. A. Pinnow, S. J. Candau, J. T. LaMacchia, and T. A. Litovitz, *ibid.*, **43**, 131 (1968).

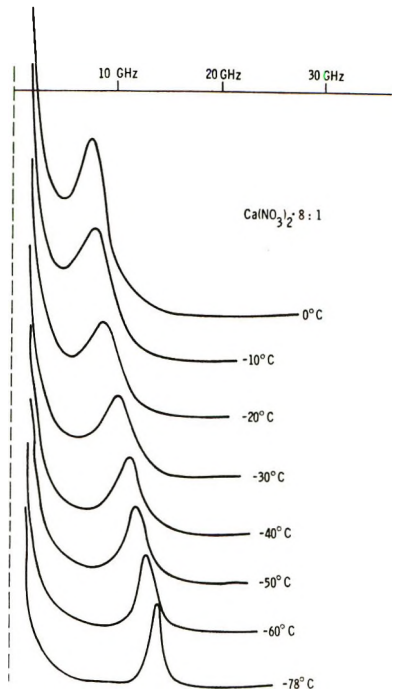

Figure 1. Brillouin scattering spectra for $Ca(NO_3)_2 \cdot 8H_2O$ solution.

peratures. The refractometer was calibrated with distilled water at 18° ($n_{18}^{[5146]}$ 1.3354).[10] Within experimental error the refractive index as a function of temperature for the $Ca(NO_3)_2 \cdot 8H_2O$ solution could be related to the density *via* the Lorentz–Lorenz equation. The experimental relation between n and ρ is given in Table I.

Brillouin shift frequencies and longitudinal velocities calculated from eq 1 are listed in Table II and are accurate to ±2%.

C. Ultrasonic Velocity and Absorption. The standard pulse technique was used to determine the longitudinal ultrasonic velocity V and absorption coefficient α of the $Ca(NO_3)_2 \cdot 8H_2O$ solution over the frequency range 30–190 MHz. Velocities were measured using an interferometric technique[11] in which the number of maxima (or minima) in the interference pattern between the pulse through the sample and a reference pulse is counted as the path length through the sample is changed by a given amount. The absorption coefficient α was determined by comparing the amplitude of the signal transmitted through the sample for various path lengths with a standard pulse from a calibrated signal generator. The design of the interferometer used in these experiments was based on an apparatus described by Hunter, *et al.*[12] The cell block was High Perma 49 stainless steel whose thermal expansion coefficient closely matches that of crystalline quartz, the material used for the delay lines. A single hole was machined through the steel block to accept a specific pair of quartz rods which would just enter the hole in a close, sliding fit. The bottom delay rod was mounted

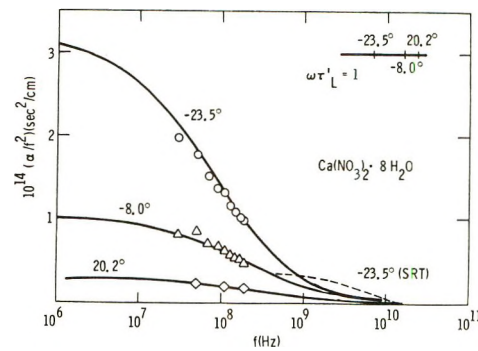

Figure 2. α/f^2 *vs.* frequency at three temperatures for $Ca(NO_3)_2 \cdot 8H_2O$ solution: ——, α/f^2 *vs.* f curves calculated for log gaussian distribution function with $b = 0.34$, $\tau_L' = 1.11\eta_s/M_r$, and M_0 and M_∞ taken from Table I; – – –, α/f^2 *vs.* f curve at −23.5° calculated for single relaxation time with $\tau_L' = 1.11\eta_s/M_r$, and M_0 and M_∞ taken from Table I.

permanently, while the position of the top rod could be varied by means of a micrometer screw. The advantage of this arrangement was that the parallelism of the transducers mounted at the ends of the rods could be maintained without special leveling procedures. The disadvantage was that, if the liquid is highly viscous, the liquid between the rod and the wall of the shaft acted as a brake and prevented sliding of the rod; this limited measurements to temperatures at which the sample viscosity was below approximately 70 P. Additional details on the experimental measurement of α and V have been given elsewhere.[13]

Longitudinal velocity and absorption coefficient values for the $Ca(NO_3)_2 \cdot 8H_2O$ solution at various temperatures and frequencies of 50, 110, and 190 MHz are listed in Table III. Additional absorption coefficient measurements at −23.5 and −8.0° are shown in Figure 2 in the form of a plot of α/f^2 *vs.* frequency. The estimated accuracy of the velocity values ranges from ±0.3% at the highest temperatures to ±1.5% at the lowest temperatures. The absorption coefficient values are accurate to ±1–3%.

Longitudinal ultrasonic velocities at 3 MHz were measured over the temperature range from 38 to −34° using a "sing-around" cell of the type described by Garnsey, *et al.*[14] The 3-MHz velocities are listed as a function of temperature in Table III.

III. Data Analysis

The complex longitudinal modulus M^* is given by[1]

$$M^* = M' + iM'' = \rho V^2 + i(2\rho V^3\alpha/\omega) \qquad (2)$$

(10) E. D. Washburn, Ed., "International Critical Tables," Vol. III, McGraw-Hill, New York, N. Y., 1928, p 13.

(11) T. A. Litovitz, T. Lyon, and L. Peselnick, *J. Acoust. Soc. Amer.*, **26**, 566 (1954).

(12) J. L. Hunter and H. D. Dardy, *ibid.*, **36**, 1914 (1964).

(13) J. H. Ambrus, Ph.D. Thesis, University of Maryland, 1970.

(14) R. Garnsey, R. J. Boe, R. Mahoney, and T. A. Litovitz, *J. Chem. Phys.*, **50**, 5222 (1969).

Table III: Ultrasonic Longitudinal Velocities and Absorption Coefficients as a Function of Temperature and Frequency for $Ca(NO_3)_2 \cdot 8H_2O$ Solution

3 MHz		50 MHz			110 MHz			190 MHz		
t, °C	$10^{-5}V$, cm/sec	t, °C	$10^{-5}V$, cm/sec	α, cm^{-1}	t, °C	$10^{-5}V$, cm/sec	α, cm^{-1}	t, °C	$10^{-5}V$, cm/sec	α, cm^{-1}
38.1	1.772	37.8	1.781	2.98	37.8	1.781	13.2	37.8	1.779	37.1
27.8	1.782	20.2	1.799	5.48	20.2	1.798	22.9	20.2	1.795	63.2
19.1	1.790	0.2	1.812	12.63	15.2	1.800	27.6	2.2	1.820	130
8.1	1.798	−20.5	1.820	35.1	5.8	1.803	43.4	0.2	1.835	140
−1.1	1.805	−36.0	1.90	137.1	0.2	1.814	54.4	−6.4	1.845	168
−12.7	1.813	−42.8	1.98	140	−10.5	1.830	86.2	−11.5	1.854	180
−23.6	1.819	−45.7	2.09	149	−21.0	1.864	125.4	−17.3	1.889	279
−33.9	1.825	−49.0	2.18	170	−31.8	1.92	161	−21.0	1.907	397
					−38.7	2.02	337	−22.0	1.910	345
					−40.3	2.07	350	−39.2	2.15	
					−43.7	2.24	412	−39.3	2.18	695
					−47.7	2.30	375	−44.0	2.34	626
								−49.0	2.42	614
								−49.6	2.50	561

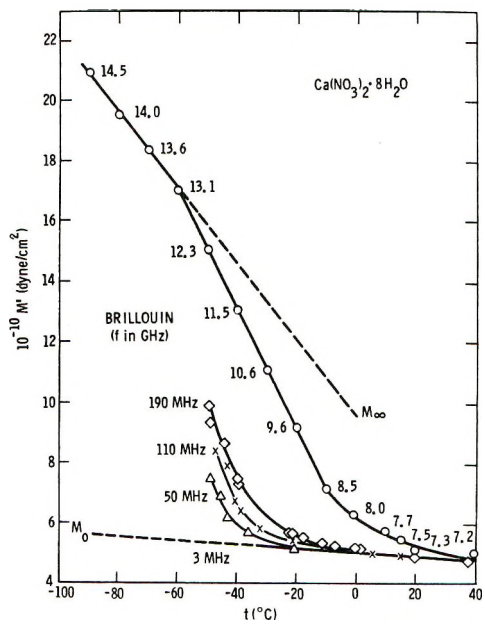

Figure 3. Real part of longitudinal modulus, M', *vs.* temperature at different frequencies for $Ca(NO_3)_2 \cdot 8H_2O$. Data points are not shown for 3-MHz measurements.

where ω is the angular frequency. The real part of the modulus M' for the $Ca(NO_3)_2 \cdot 8H_2O$ solution is plotted as a function of temperature for different frequencies in Figure 3. A strong dispersion in M' at the ultrasonic frequencies 50–190 MHz is observed in the viscosity region 3–60 P (−30 to −50°), which dispersion may be identified with the viscoelastic relaxation of the solusion (see Introduction). The viscoelastic relaxation of the longitudinal modulus may in turn be characterized by the equation[1]

$$M^* = M_0 + M_r \int_0^\infty \mathrm{d}\left(\frac{\tau_L}{\tau_L'}\right) g\left(\frac{\tau_L}{\tau_L'}\right)\left(\frac{(\omega\tau_L)^2}{1 + (\omega\tau_L)^2}\right) + iM_r \int_0^\infty \mathrm{d}\left(\frac{\tau_L}{\tau_L'}\right) g\left(\frac{\tau_L}{\tau_L'}\right)\left(\frac{\omega\tau_L}{1 + (\omega\tau_L)^2}\right) \quad (3)$$

τ_L is a longitudinal stress relaxation time, and $g(\tau_L/\tau_L')$ is a distribution function for the relaxation times normalized to reference time τ_L'. M_0, M_∞, and M_r are respectively the limiting low-frequency, limiting high-frequency, and relaxational longitudinal moduli

$$M_0 = \lim_{\omega\langle\tau_L\rangle \ll 1} M'$$

$$M_\infty = \lim_{\omega\langle\tau_L\rangle \gg 1} M'$$

$$M_r = M_\infty - M_0 \quad (4)$$

where the average longitudinal relaxation time $\langle\tau_L\rangle$ is defined by

$$\langle\tau_L\rangle = \int_0^\infty \mathrm{d}\left(\frac{\tau_L}{\tau_L'}\right) g\left(\frac{\tau_L}{\tau_L'}\right) \tau_L$$

$\langle\tau_L\rangle$ is related to the average structural or volume relaxation time $\langle\tau_v\rangle$ and the average shear relaxation time $\langle\tau_s\rangle$ by[1]

$$M_r\langle\tau_L\rangle = K_r\langle\tau_v\rangle + {}^4/_3 G_\infty\langle\tau_s\rangle = \eta_v + {}^4/_3\eta_s \quad (5)$$

where K_r is the relaxational part of the bulk modulus, G_∞ the limiting high-frequency shear modulus, and η_v the volume or bulk viscosity.

The limiting low-frequency modulus M_0 was evaluated using M' values calculated from the 3-MHz velocity measurements, since, as may be seen from Figure 3, no frequency dispersion in M' is detectable experimentally above −20° and below 50 MHz. The M_0 values so determined were found to be a linear function of temperature in the range measured and are given in this form in Table I. In order to estimate the limiting high-frequency modulus, M_∞, the reasonable assumption has to be made that the average shear and longitudinal relaxation times are comparable in magnitude. Using the shear viscosities and Brillouin

frequencies from Table II and a nominal value[1,5] of $G_\infty \sim 10^{10}$ dyn/cm², we find that

$$\omega\langle\tau_L\rangle \sim \omega\langle\tau_s\rangle = \frac{\omega\eta_s}{G_\infty} \geq 5 \times 10^3$$

at temperatures of −60° and below. Even if an extremely broad distribution of relaxation times exists in this system, at such high values of $\omega\langle\tau_L\rangle$ the M' values for the liquid can safely be considered to be the unrelaxed, limiting high-frequency modulus, M_∞. As shown in Figure 3, M_∞ determined in this fashion is a linear function of temperature at and below −60° and is given in this form in Table I. For the further reduction of data both M_0 and M_∞ have been linearly extrapolated into the relaxation region, as shown in Figure 3.

To remove the temperature dependence of M^* in eq 3 arising from the temperature dependences of M_0 and M_∞, it is convenient to define a normalized relaxational longitudinal modulus, N^*

$$N^* = \frac{M^* - M_0}{M_r} = N' + iN''$$

$$= \frac{M' - M_0}{M_r} + i\frac{M''}{M_r} \qquad (6)$$

Provided that the distribution function $g(\tau_L/\tau_L')$ is temperature independent, N' and N'' are explicit functions only of $\omega\langle\tau_L\rangle$, and if plots are made of N' and N'' *vs.* $\omega\langle\tau_L\rangle$ data points from all temperatures should fall on the same pair of reduced curves. If the assumption is also made that the ratios M_r/G_∞ and $\langle\tau_L\rangle/\langle\tau_s\rangle$ are temperature independent, it may be seen from eq 5 that $\omega\eta_s/M_r$ is proportional to $\omega\langle\tau_L\rangle$ and may be used in place of $\omega\langle\tau_L\rangle$ in the reduced plots of N' and N''.

In Figure 4 reduced plots of N' and N'' *vs.* $\omega\eta_s/M_r$ are shown for the experimental data between −10 and −60°. N' and N'' were calculated from eq 2 and 6 using M_r values determined from eq 4 and the expressions for M_0 and M_∞ given in Table I. All data points

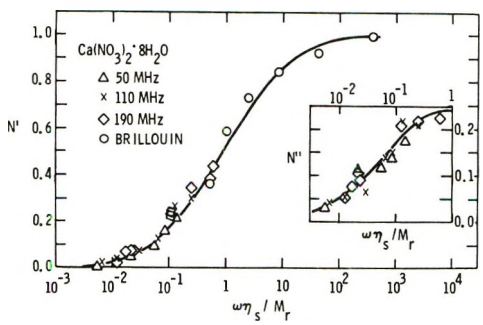

Figure 4. Plots of normalized real and imaginary parts of relaxational longitudinal modulus *vs.* reduced frequency $\omega\eta_s/M_r$ for $Ca(NO_3)_2 \cdot 8H_2O$ solution data between −10 and −60°. Solid curves calculated for log gaussian distribution function with $b = 0.34$, $\tau_L' = 1.11\eta_s/M_r$, and M_0 and M_∞ taken from Table I.

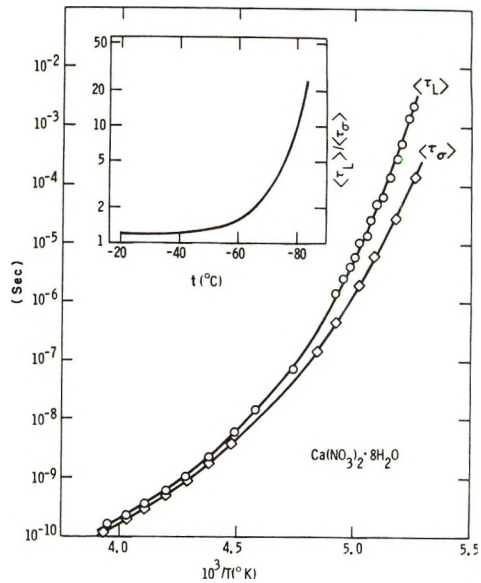

Figure 5. Arrhenius plot of average longitudinal and conductivity relaxation times. Inset shows $<\tau_L>/<\tau_\sigma>$ ratio *vs.* temperature.

in the N' and N'' plots of Figure 4 appear to fall on the same respective curves with no systematic scatter, showing that the data are consistent with the assumptions that the relaxation time distribution function and the M_r/G_∞ and $\langle\tau_L\rangle/\langle\tau_s\rangle$ ratios are temperature independent.

The reduced N' plot is symmetric about its midpoint ($N' = 0.5$), suggesting a relaxation time distribution function symmetric on a logarithmic time scale such as a log gaussian distribution.[1] The curves drawn through the N' and N'' plots of Figure 5 were calculated using a log gaussian distribution of relaxation times for which

$$N' = \int_{-\infty}^{\infty} d\left(\ln\frac{\tau_L}{\tau_L'}\right) g\left(\ln\frac{\tau_L}{\tau_L'}\right)\left(\frac{(\omega\tau_L)^2}{1 + (\omega\tau_L)^2}\right) \qquad (7a)$$

$$N'' = \int_{-\infty}^{\infty} d\left(\ln\frac{\tau_L}{\tau_L'}\right) g\left(\ln\frac{\tau_L}{\tau_L'}\right)\left(\frac{\omega\tau_L}{1 + (\omega\tau_L)^2}\right) \qquad (7b)$$

$$g\left(\ln\frac{\tau_L}{\tau_L'}\right) = \frac{b}{\sqrt{\pi}} \exp\left(-b^2 \ln^2\frac{\tau_L}{\tau_L'}\right) \qquad (7c)$$

The most probable relaxation time τ_L' and the width parameter b used in the calculation were

$$\tau_L' = 1.11\eta_s/M_r \qquad (8)$$

and

$$b = 0.34$$

The average relaxation time is related to the most probable time for a log gaussian distribution by $\langle\tau_L\rangle = \tau_L' \exp(1/4b^2)$.[1] Hence, using $b = 0.34$, we find that the average longitudinal relaxation time for the $Ca(NO_3)_2 \cdot 8H_2O$ solution is

$$\langle\tau_L\rangle = 9.6\eta_s/M_r \qquad (9)$$

The solid curves drawn through the experimental α/f^2 *vs.* f plots of Figure 2 were calculated from the above log gaussian distribution function and parameters using the equation[1]

$$\frac{\alpha}{f^2} = \frac{\pi\rho^{1/2}}{f} \frac{M_r N''}{(M_0 + M_r N')^{3/2}} \tag{10}$$

The agreement between the calculated and observed α/f^2 plots is good, showing that the log gaussian distribution function for relaxation of the longitudinal stress also accounts for the observed dispersion in α/f^2. The shear to volume viscosity ratio, η_v/η_s, calculated from eq 5 and 9, is 8.3 for the $Ca(NO_3)_2 \cdot 8H_2O$ solution.

IV. Discussion Section

The width of the relaxation time distribution found for the viscoelastic relaxation of M^* in the $Ca(NO_3)_2 \cdot 8H_2O$ solution is extremely broad, but it is comparable to the width found at low temperatures for an anhydrous $0.4Ca(NO_3)_2$–$0.6KNO_3$ melt.[15] This fused salt was also found to exhibit a symmetric, log gaussian distribution of longitudinal stress relaxation times which was attributed to a distribution of molecular environments in the liquid. The width of the relaxation time distribution for the $0.4Ca(NO_3)_2$–$0.6KNO_3$ melt, however, was highly temperature dependent, while in the range covered by the present measurements the data are consistent with a temperature-independent distribution width.

The effect of the distribution of longitudinal stress relaxation times on the dispersion in α/f^2 is of considerable interest, since, as indicated in the Introduction, most previously reported ultrasonic relaxation studies for concentrated electrolyte solutions have been confined primarily to characterizing the α/f^2 dispersion. In Figure 2 the frequency for which the condition $\omega\tau_L' = 1$ is fulfilled is indicated for each of the three temperatures for which data are shown. For a log gaussian distribution of relaxation times this frequency corresponds to the midpoint of the N' curve and to the peak of the N'' curve in Figure 4. In Figure 2 we also show a dispersion curve for α/f^2 at $-23.5°$ calculated from eq 10 using a τ_L' value from eq 8, M_0 and M_∞ values from Table I, but using a single relaxation time distribution function ($g(\tau_L/\tau_L') = \delta(\tau_L - \tau_L')$). As may thus be seen from Figure 2, the effect of a distribution of longitudinal stress relaxation times for the $Ca(NO_3)_2 \cdot 8H_2O$ solution at a given temperature is to enhance the strength of the dispersion in α/f^2, to broaden the frequency range over which the dispersion takes place and, most significantly, to shift the region in which the dispersion in α/f^2 is most prominent some two decades lower in frequency than the dispersion region for the real and imaginary parts of the modulus, M' and M''.

The α/f^2 dispersion curves of Figure 2 are very similar in appearance to the α/f^2 curves obtained in the same viscosity and frequency range by Darbari and Petrucci[2] for $Ca(NO_3)_2$–H_2O solutions in the concentration range $R = 4$–5. On the assumption that the viscoelastic relaxation was governed by a single relaxation time distribution function, so that the viscoelastic dispersion in α/f^2 would be expected at frequencies much higher than their experimental frequencies, they tentatively attributed the observed dispersion in α/f^2 to a chemical relaxation arising from some ionic hydration process distinct in nature from the viscoelastic relaxation. However, on the basis of the present results and the generally ubiquitous occurrence of broad distributions of relaxation times in viscoelastic relaxation processes in liquids,[1,15] it seems much more likely that the α/f^2 dispersions observed by Darbari and Petrucci[2] were a manifestation of the viscoelastic relaxation process shifted to lower frequencies than the modulus or velocity dispersions by the effect of a distribution of relaxation times. This does not necessarily imply that hydration or association reactions such as the exchange of water and anion in the first coordination sphere of a cation may not be part of the diffusive motions involved in the viscoelastic relaxation of concentrated aqueous electrolyte solutions. Indeed, the study of Darbari, *et al.*,[4] of the chloride ion complexation process in zinc chloride solutions suggests that at very high electrolyte concentrations the hydration and association processes and the viscoelastic relaxation become indistinguishable.

The dispersion in α/f^2 observed by Darbari, *et al.*,[3] for a $Ca(NO_3)_2 \cdot 3.2H_2O$ solution in the frequency range 3–150 MHz was attributed to a viscoelastic relaxation and analyzed using a single relaxation time distribution function. Taking their analysis at face value, their results tend to indicate that the distribution of relaxation times for the $Ca(NO_3)_2 \cdot 3.2H_2O$ solution is considerably narrower than that for the more dilute $Ca(NO_3)_2 \cdot 8H_2O$ solution. However, since their data cover a comparatively limited frequency and temperature range and since they were unable to obtain measurements of the dispersion in the longitudinal velocity, it is our opinion that the viscoelastic relaxation in this solution is not sufficiently well characterized at the moment to allow any firm conclusions to be drawn in regard to the width and shape of the distribution of relaxation times.[15a]

(15) R. Weiler, R. Bose, and P. B. Macedo, *J. Chem. Phys.*, **53**, 1258 (1970).

(15a) Note Added in Proof. Recently additional measurements of α/f^2 *vs.* frequency were reported by Yeager and coworkers [S. Smedley, C. Hall, and E. Yeager *J. Phys. Chem.*, **76**, 1506 (1972)] on $Ca(NO_3)_2$–H_2O solutions in the vicinity of composition $R = 4$. Although these data do not agree with those reported by Petrucci and coworkers [G. S. Darbari, M. R. Richelson, and S. Petrucci, *J. Phys. Chem.*, **76**, 1507 (1972); see also ref 2] they also seem to indicate that the distribution of viscoelastic relaxation times is considerably narrower at concentrations around $R = 4$ then for the $R = 8$ solutions. Clearly more work is required on these solutions before it will be possible to make any firm statement on the effect of composition on the details of the viscoelastic relaxation process.

In Figure 5 is shown an Arrhenius plot of the average longitudinal relaxation times $\langle\tau_L\rangle$ for the $Ca(NO_3)_2 \cdot 8H_2O$ solution calculated from eq 9 using the experimental shear viscosities[6] and M_0 and M_∞ values obtained from Table I. Also plotted in Figure 5 are the average conductivity relaxation times $\langle\tau_\sigma\rangle$ for the solution calculated from the equation[5,16]

$$\langle\tau_\sigma\rangle = \frac{e_0\epsilon_s}{\sigma_0}$$

where σ_0 is the limiting low-frequency or dc conductivity, e_0 the permittivity of free space (8.854×10^{-14} F/cm), and ϵ_s is the contribution to the dielectric constant of the solution from polarization mechanisms not connected with the long-range ionic diffusion process. σ_0 values were taken from a previous study,[6] while the value of $\epsilon_s(= 10 \pm 2)$ was estimated from dielectric constant measurements as a function of frequency for the $Ca(NO_3)_2 \cdot 8H_2O$ solution near the glass transition temperature.[13] The ϵ_s value was assumed to be temperature independent.

As explained in previous papers,[5,16] $\langle\tau_\sigma\rangle$ is the time constant for the decay of the electric field in the solution to zero by the ionic conduction process, in the same sense that $\langle\tau_L\rangle$ is the time constant for the decay of the longitudinal stress. In an ionic liquid (a fused salt or a concentrated electrolyte solution in which most of the solvent is strongly bound in the coordination spheres of the ions) in which all of the mobile particles are electrically charged $\langle\tau_L\rangle$ and $\langle\tau_\sigma\rangle$ are expected to be of comparable magnitude provided that all of the particles have comparable mobilities. The $Ca(NO_3)_2 \cdot 8H_2O$ solution is sufficiently concentrated that it can be considered an ionic liquid. In the insert of Figure 5 the $\langle\tau_L\rangle/\langle\tau_\sigma\rangle$ ratio is plotted *vs.* temperature. The $\langle\tau_L\rangle/\langle\tau_\sigma\rangle$ ratio is seen to be close to unity at high temperatures, but below $-50°$ begins an accelerated increase with decreasing temperature, reaching a value in excess of 20 at the lowest temperatures for which data are available, and possibly becoming greater than 1000 at the glass transition temperature ($-90°$). As noted in previous papers,[5,16] this sort of behavior seems to be a common feature of ionic liquids: the mechanical stress and electric field relaxation times are comparable at high temperatures and low viscosities, but at low temperatures and high viscosities the electric field relaxes by ionic conduction considerably faster than does the mechanical stress. One possible explanation for this is that at high viscosities there develops a considerable mobility difference between the component ions of the liquid. The rate of relaxation of the electric field is determined by the mobility of the more mobile ion, while the rate of mechanical stress relaxation and viscous flow, which demands a rearrangement of the liquid structure as a whole, is determined by the mobility of the less mobile ion.

It is interesting to note that in the temperature range (roughly -10 to $-50°$) of the present study, the width of the longitudinal relaxation time distribution was temperature independent and the $\langle\tau_L\rangle/\langle\tau_\sigma\rangle$ ratio was constant and approximately equal to unity for the $Ca(NO_3)_2 \cdot 8H_2O$ solution. On the other hand, the width of the longitudinal relaxation time distribution for the previously studied $0.4Ca(NO_3)_2$–$0.6KNO_3$ melt is highly temperature dependent,[15] while in the temperature range of that study the $\langle\tau_L\rangle/\langle\tau_\sigma\rangle$ ratio is considerably larger than unity and markedly temperature dependent.[17,18] Although there are a number of interesting speculations in which one could indulge in regard to the source and significance of this observation, we prefer to reserve these for a time when further studies have established more clearly the existence or nonexistence of correlations between the temperature dependence of the width of stress relaxation time distributions and the behavior of the $\langle\tau_L\rangle/\langle\tau_\sigma\rangle$ ratio for ionic liquids.

Acknowledgments. This research was supported by the Naval Ordnance Laboratory Independent Research Program and by a Themis Grant from the Office of Naval Research. The authors wish to thank Professors T. A. Litovitz and C. J. Montrose for a number of helpful comments on the manuscript and Dr. F. Scott Howell for his experimental assistance.

(16) C. T. Moynihan, R. D. Bressel, and C. A. Angell, *J. Chem. Phys.*, **55**, 4414 (1971).

(17) R. Bose, R. Weiler, and P. B. Macedo, *Phys. Chem. Glasses*, **11**, 117 (1970).

(18) F. S. Howell, Ph.D. Thesis, Catholic University of America, (1972).

Thermodynamics of Hydrogen Bond Formation between Phenol and Some Diazine *N*-Oxides

by Norman Kulevsky* and Lyman Lewis

Chemistry Department, University of North Dakota, Grand Forks, North Dakota 58201 *(Received May 8, 1972)*

Equilibrium constants and ΔH° values for the interactions of phenol with azine *N*-oxides in $CHCl_2$ indicate that the relative order of basicity is pyridine *N*-oxide > pyrimidine *N*-oxide > pyridazine *N*-oxide > pyrazine *N*-oxide. With the exception of pyrazine *N*-oxide, the order toward phenol parallels that found toward I_2. These data are interpreted on the basis of oxygen being the donor site and discussed in terms of the forces involved in forming the hydrogen bond. Pyridine *N*-oxide is found to be a stronger base than pyridine and this is explained in terms of the solvent effect of CH_2Cl_2 on the equilibrium.

The relative electron-donor abilities of the mono *N*-oxides of some heterocyclic diazines toward molecular iodine have recently been studied.[1,2] For these compounds, arguments based upon frequency shifts in the infrared and the trend of equilibrium constants for formation of the iodine complexes lead to the conclusion that it is oxygen and not the pyridine like nitrogen that acts as the donor site toward iodine. In this paper we shall discuss an investigation of the stability of the H-bonded complexes of phenol with these same bases which was undertaken in order to see what changes would occur in the relative basic strengths when an acid is used whose electronic and steric requirements are different from iodine. The effect of a hydrogen-bonding solvent on the relative complexing ability of pyridine and its oxide is also discussed.

Experimental Section

The donor species were prepared and purified by procedures given in a previous paper.[2] Reagent grade phenol was fractionally crystallized and vacuum distilled. Spectral grade solvents were stored over molecular sieve before use. All solutions were prepared in a drybox. The concentrations were obtained by weight.

The association constants were obtained by spectroscopic techniques previously used by other workers.[3] The optical densities were obtained at the maximum of the first overtone of the free O–H stretching mode in the near-infrared at 1.4 m. A Cary Model 14 spectrophotometer equipped with a thermostated cell holder was used to obtain these measurements. The cells used were matched silica with 10-cm path length.

The molar absorption coefficient was obtained by measuring optical densities of from six to ten solutions at six different temperatures ranging from 11.0 to 31.9°. The concentration of phenol in CH_2Cl_2 ranged from 6×10^{-3} to 26×10^{-3} M. Plots of optical density against concentration at each temperature were linear with zero intercept, indicating that there is no self-association over this concentration range. The slopes of the plots were taken as the absorption coefficient.

To obtain the equilibrium constants, solutions of phenol within this range were prepared with several different concentrations of base added. For each of the bases, the concentration ranges were 16×10^{-3} to 42×10^{-3} M. Using the previously determined absorption coefficient, the concentration of free phenol in the equilibrium mixture was calculated. Then using the stoichiometric relations the concentrations of free base, complex, and the equilibrium constant were calculated.

Results and Discussion

Equilibrium constants as a function of temperature for the formation of the H-bonded complexes of phenol with pyridine and the *N*-oxides are given in Table I. Each of the values is the average of values obtained from measurements on from four to seven different solutions in which the concentration of base mixed with a constant concentration of phenol was varied by a factor of 2.5. The error limits, which are standard deviations, are *ca.* 2%, although a few are higher. No discernable trends in K values could be observed over the range of base concentrations used, indicating that the stoichiometry for all the complexes is 1:1 even in those cases where, as for the diazine *N*-oxides, the base has two potential donor sites. The values of ΔH° obtained from the plot of ln K *vs.* $1/T$ are given in Table II. The values obtained for the pyridine–phenol interaction are also included in these tables and the agreement between them and the value of K_{25} given by Rubin and Panson[4] is quite reasonable.

(1) N. Kulevsky and R. G. Severson, Jr., *Spectrochim. Acta, Part A*, **26**, 2227 (1970).

(2) N. Kulevsky and R. G. Severson, Jr., *J. Phys. Chem.*, **75**, 2504 (1971).

(3) D. L. Powell and R. West, *Spectrochim. Acta*, **20**, 983 (1964).

(4) J. Rubin and G. S. Panson, *J. Phys. Chem.*, **69**, 3089 (1965).

Table I: Association Constants (M^{-1}) as a Function of Temperature for Phenol Complexes in CH_2Cl_2

T, °C	Pyridine	Pyridine *N*-oxide	Pyridazine *N*-oxide	Pyrimidine *N*-oxide	Pyrazine *N*-oxide
11.0	28.1 ± 0.2	99.1 ± 0.8	13.8 ± 0.1	19.1 ± 0.3	10.7 ± 0.3
15.0	23.7 ± 0.6	85.9 ± 1.5	12.4 ± 0.3	16.9 ± 0.3	9.6 ± 0.2
19.7	22.3 ± 0.6	72.1 ± 2.2	11.4 ± 0.2	14.7 ± 0.4	9.0 ± 0.1
24.0	19.4 ± 0.6	63.3 ± 3.3	10.0 ± 0.2	13.0 ± 0.2	8.0 ± 0.1
28.0	15.1 ± 0.4	54.9 ± 1.1	8.2 ± 0.3	11.6 ± 0.5	6.9 ± 0.5
31.9	13.4 ± 0.2	49.3 ± 0.6	7.7 ± 0.3	10.4 ± 0.2	6.6 ± 0.2

Table II: Enthalpy of Association for Phenol Complexes in CH_2Cl_2

	$-\Delta H°$, kcal/mol
Pyridine	5.9 ± 0.2
Pyridine *N*-oxide	5.8 ± 0.1
Pyridazine *N*-oxide	5.0 ± 0.3
Pyrimidine *N*-oxide	4.9 ± 0.3
Pyrazine *N*-oxide	4.2 ± 0.3

From the data given in the two tables, the relative base strength is pyridine *N*-oxide > pyrimidine *N*-oxide > pyridazine *N*-oxide > pyrazine *N*-oxide. From the values of K this order is unequivocal, although the $\Delta H°$ values are, in some cases, very close. This order is similar to the one found when iodine is the reference acid, except for the position of pyridazine *N*-oxide which forms the weakest iodine complex. If the values of $\Delta G°$ for the iodine and phenol complexes, exclusive of pyridazine *N*-oxide, are plotted against one another a linear relationship can be observed. Since there are only three points in this correlation a statistical analysis of this relationship does not seem valuable to report here. This relationship would indicate that for pyrimidine and pyrazine *N*-oxides it is oxygen which is the donor site toward phenol as well as toward iodine. Since the equilibrium constants for iodine interactions correlate with Hammet σ constants, the failure of this correlation for the phenol pyridazine *N*-oxide indicates that if oxygen is the donor site, the σ value for the ortho position given by Katritzky and Swinbourne[5] is not valid for the phenol interactions. The reason for this observation could be the differences in the types of interaction the base undergoes with the two acids. Iodine, a nonpolar species, forms a charge-transfer complex whose stability is to a large extent determined by the amount of overlap between donor and acceptor orbitals and the electron density in the donor orbital. Thus, for the iodine complexes the trend in stability follows the π electron density at the oxygen atom previously calculated by MO theory.[6] On the other hand, the hydrogen-bonding strength is determined to a large extent by dipole–dipole forces. If dipole–dipole forces are the determining factor then for pyridazine *N*-oxide and pyrazine *N*-oxide where the dipole moments are 5.21 D and 1.66 D,[6] respectively, pyridazine *N*-oxide should have the stronger interaction with phenol. This would also imply that for pyridazine *N*-oxide the hydrogen of phenol is interacting with both the oxygen- and the pyridine-like nitrogen, which was not apparent for the iodine interaction.

One anomaly is apparent if the data for pyridine and its oxide are compared. According to the values of K and $\Delta H°$ given in the tables, pyridine is less basic than its oxide. However, the reverse order of basicity is exhibited toward both aqueous acid[7] and iodine[8] in CCl_4. One possible reason for this reversal could be solvent effects. Rubin, *et al.*,[4] found that association constants for phenol–pyridine varied a great deal as the solvent was changed although there was no correlation of these constants with the dielectric constant of the solvent. Since the values of K were the same in both CH_2Cl_2 and $CHCl_3$ and lower than the value in CCl_4 (by a factor of 0.5) it is possible that the hydrogen bonding of CH_2Cl_2 or $CHCl_3$ to the free base causes the large change in K values observed by them. Because in most cases pyridine *N*-oxide is a weaker base than pyridine it is possible that hydrogen bonding of the solvent to the free bases would not affect the equilibrium constant for the oxide as much as it does for pyridine. Therefore, the association with phenol in CH_2Cl_2 could appear larger for the oxide than for pyridine.

(5) A. R. Katritzky and F. J. Swinbourne, *J. Chem. Soc.*, 6707 (1965).

(6) T. Kubota and H. Watanabe, *Bull. Chem. Soc. Jap.*, **36**, 1093 (1963).

(7) (a) A. Albert, R. Goldacre, and J. Phillips, *J. Chem. Soc.*, 2240 (1948); (b) H. H. Jaffe and G. O. Doaks, *J. Amer. Chem. Soc.*, **77**, 4441 (1955).

(8) (a) W. McKinney and A. I. Popov, *ibid.*, **91**, 5215 (1969), and references therein; (b) T. Kubota, *ibid.*, **87**, 458 (1965).

Determination of the Heat of Formation of Diazirine by Photon Impact

by Allan H. Laufer* and Hideo Okabe

Physical Chemistry Division, National Bureau of Standards, Washington, D. C. 20234 *(Received May 9, 1972)*

Publication costs assisted by the National Bureau of Standards

Threshold energies of the incident photons required to initiate three primary processes in diazirine (I, II, and III) have been measured yielding 8.6, 7.6, and 11.8 eV, respectively. A lower limit for the heat of formation of diazirine may then be derived, namely, $\Delta H_f°(c\text{-}CH_2N_2) \geq 60.6$ kcal/mol. A probable upper limit of $\Delta H_f°(c\text{-}CH_2N_2) \leq 66$ kcal/mol is obtained from the observation that process I does not occur as a result of Xe (147 nm) photolysis. The difference between the photon impact and previous electron impact value is discussed. The absorption coefficient of diazirine in the region from 125 to 200 nm has been measured.

Introduction

A thorough understanding of methylene radical chemistry requires accurate thermodynamic parameters for methylene itself and its precursors. The heat of formation of methylene, 93 kcal/mol, has been established with a probable error limit of ±2 kcal/mol by photoionization of various sources.[1-3]

Common precursors for methylene are ketene, diazomethane, and diazirine. Of these, heats of formation of ketene[4] and diazomethane[5] have already been determined. An electron impact value for $\Delta H_f°(c\text{-}CH_2N_2)$ has been reported based upon the appearance potential of CH_2^+ from the parent molecule. The value of $\Delta H_f°$ so obtained is 79.3 kcal/mol.[6] In view of the inherent uncertainty involved in the determination of threshold energies by electron impact, another independent measurement is highly desirable.

In the present work the threshold energies of photons required to produce the products $CH(A^2\Delta)$, $N_2(A^3\Sigma_u^+)$, and CH_2^+ from diazirine (processes I–III) were measured from which three values of $\Delta H_f°(c\text{-}CH_2N_2)$ were derived. The same technique has been used to obtain the heat of formation of diazomethane.[5]

$$c\text{-}CH_2N_2 \xrightarrow{h\nu} CH(A^2\Delta) + H + N_2 \quad (I)$$

$$c\text{-}CH_2N_2 \xrightarrow{h\nu} N_2(A^3\Sigma_u^+) + CH_2(X^3\Sigma) \quad (II)$$

$$c\text{-}CH_2N_2 \xrightarrow{h\nu} CH_2^+ + N_2(X^1\Sigma_g^+) + e \quad (III)$$

Experimental Section

The experimental apparatus for the fluorescence experiments has been previously described.[5] Briefly two different measurements were made utilizing a 1-m vacuum monochromator: (a) the fluorescence spectrum excited by a Kr resonance lamp was directly observed by a 13-stage photomultiplier placed at the exit slit of the monochromator; (b) the fluorescence intensity was measured as a function of incident wavelength with a hydrogen lamp as the light source. The hydrogen emission, in the wavelength region of interest, is a continuum upon which is superimposed a many-lined spectrum. For the detection of the $CH(A^2\Delta)$ fluorescence produced by process I, an interference filter centered at 431.5 nm (7 nm FWHM) was used in front of a photomultiplier. The filter has an optical density of greater than 2.5 outside of the region from 422 to 437 nm.

The $N_2(A^3\Sigma_u^+)$ formed by process II was detected by the NO γ emission produced from the reaction

$$N_2(A^3\Sigma_u^+) + NO(X^2\Pi) \longrightarrow N_2(X^1\Sigma_g^+) + NO(A^2\Sigma^+)$$

which is known to be very efficient.[7] For the detection of the γ emission a filter, transmitting light of wavelength from 230 to 420 nm, was placed in front of the photomultiplier. The CH_2^+ ions formed from process III were detected by a mass spectrometer attached to a reaction vessel.[8] The light source used for the production of CH_2^+ ions was an Ar resonance lamp emitting light at 104.8 and 106.7 nm.

The absorption spectrum of diazirine has been analyzed in the near-ultraviolet.[9,10] The vacuum ultraviolet absorption spectrum has not been measured although it is reported to have an intense absorption band below 200 nm.[11] Absorption coefficients of

(1) V. H. Dibeler, M. Krauss, R. M. Reese, and F. N. Harllee, *J. Chem. Phys.*, **42**, 3791 (1965).

(2) W. A. Chupka and C. Lifshitz, *ibid.*, **48**, 1109 (1968).

(3) W. A. Chupka, J. Berkowitz, and K. M. A. Refaey, *ibid.*, **50**, 1938 (1969).

(4) R. L. Nuttall, A. H. Laufer, and M. V. Kilday, *J. Chem. Thermodyn.*, **3**, 167 (1971).

(5) A. H. Laufer and H. Okabe, *J. Amer. Chem. Soc.*, **93**, 4137 (1971).

(6) G. S. Paulett and R. Ettinger, *J. Chem. Phys.*, **39**, 825, 3534 (1963).

(7) R. A. Young and G. A. St. John, *ibid.*, **48**, 898 (1968).

(8) L. W. Sieck, S. Searles, and P. Ausloos, *J. Amer. Chem. Soc.*, **91**, 7627 (1969).

(9) L. C. Robertson and J. A. Merritt, *J. Mol. Spectrosc.*, **19**, 372 (1966).

(10) A. Lau, *Spectrochim. Acta*, **20**, 97 (1964).

(11) H. M. Frey, *Advan. Photochem.*, **4**, 225 (1966).

diazirine were measured at 0.3-nm intervals with an absorption cell of 6.95 ± 0.01 cm length. The pressure of diazirine was about 0.2 Torr. The H_2 continuum was used as a light source from 210 to 175 nm and from 175 to 125 nm the Xe and Kr continuum lamps were employed.[12]

Diazirine was prepared following the method of Ohme and Schmitz.[13] The material is explosive when solidified so only millimole quantities were prepared and stored above −140°, the melting point.[14] The intensities and wavelengths of the sharp peaks in the ultraviolet absorption spectrum agreed quite well with those in the literature.[9,15]

Results and Discussion

Mass spectrometric analysis at 70 eV produced a cracking pattern significantly different from that previously reported,[6,15] as shown in Table I.

Table I: 70-eV Cracking Pattern of Diazirine

	Rel intensity	
m/e	This work	Ref 6
12	6.2	10.8
13	14.7	23.5
14	66.4	100.0
26	2.7	2.3
27	7.9	6.6
28	13.7	8.5
29	2.2	1.9
40	3.8	2.1
41	19.5	10.7
42	100.0	48.1
43	2.6	0.8

The absorption coefficient of diazirine measured at a resolution of 0.3 nm in the vacuum ultraviolet is shown in Figure 1, where ϵ is defined as $I/I_0 = \exp(-\epsilon px)$. I and I_0 are the transmitted and incident light intensities, p is the pressure in atmospheres at 25°, and x is the path length in cm. The curve shown in the figure is an average of several runs where the maximum deviation of any point was less than 10%. The spectrum is clearly divided into two regions centered about 143.5 nm. Above this wavelength there exists a strong but diffuse continuum and below, a similar continuum upon which weak bands are superimposed.

Two band systems in fluorescence were observed from the photolysis of diazirine with a Kr resonance lamp (123.6 nm, 10 eV). These were the $CH(A^2\Delta-X^2\Pi)$ system at 431.5 nm and the $CN(B^2\Sigma^+-X^2\Sigma^+)$ violet system.[16] The (0,0) transition of the latter is at 388.4 nm. The CN emission was presumably caused by an impurity as it was reduced by a factor of 20 after passing the diazirine through an ascarite-containing tube (NaOH impregnated asbestos). It is presumed the CH emission arises from

$$c\text{-}CH_2N_2 \longrightarrow CH(A^2\Delta) + H + N_2 \qquad (I)$$

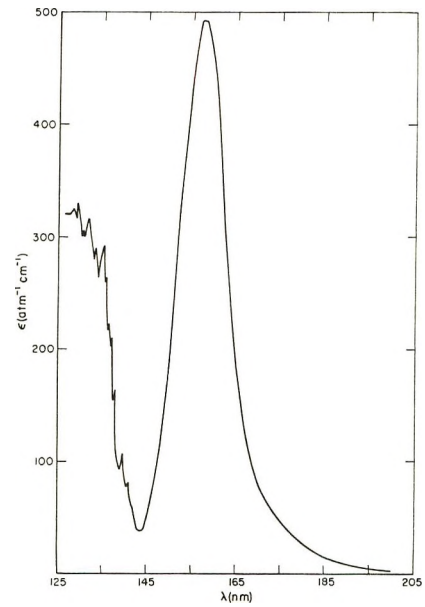

Figure 1. Absorption coefficients of diazirine. ϵ is defined by $I/I_0 = \exp(-\epsilon px)$.

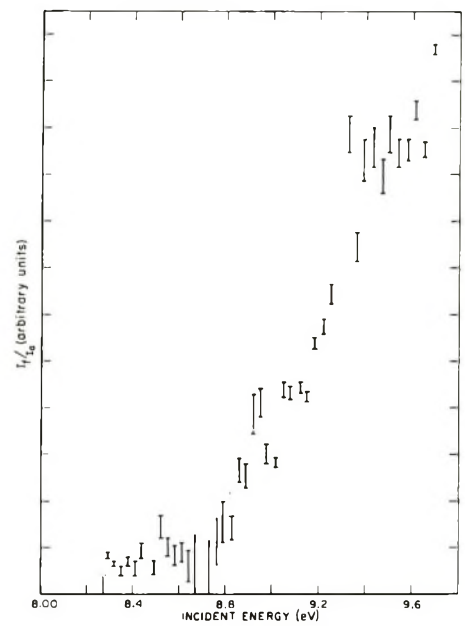

Figure 2. Fluorescence intensity of $CH(A^2\Delta-X^2\pi)$ as a function of incident photon energy corrected for diazirine absorption.

(12) P. G. Wilkinson and E. T. Bryam, *Appl. Opt.*, **4**, 581 (1965).
(13) R. Ohme and E. Schmitz, *Chem. Ber.*, **97**, 297 (1964).
(14) L. S. Wood, private communication.
(15) W. H. Graham, *J. Amer. Chem. Soc.*, **84**, 1063 (1962).
(16) R. W. Pearse and A. G. Gaydon, "The Identification of Molecular Spectra," 3rd ed, Wiley, New York, N. Y., 1963, p 112.

Table II: Thermochemical Data of Diazirine from Photon Impact

Method	Process	Threshold energy, eV	Threshold energy, kcal/mol	$\Delta H_f°$(c-CH_2N_2), kcal/mol	Ref
Photodissociation	c-CH_2N_2 − $CH(A^2\Delta)$ + H + N_2	$8.4 < h\nu < 8.6$	$194 < h\nu < 198$	$66 > \Delta H_f° > 61.7$	This work
Photodissociation	c-CH_2N_2 → $N_2(A^3\Sigma_u^+)$ + $CH_2(X^3\Sigma)$	<7.6	<174	>61	This work
Photoionization	c-CH_2N_2 → CH_2^+ + N_2 + e	<11.8	<272	>60.6	This work
Electron impact	c-CH_2N_2 → CH_2^+ + N_2 + e	11.0 ± 0.1	230 ± 2	79.3	6
	c-CH_2N_2 → $N_2(X^1\Sigma)$ + $CH_2(X^3\Sigma)$	1.2–1.4	27–33		Calcd from $\Delta H_f°$ (c-CH_2N_2)

Figure 2 shows the intensity of the fluorescence of the $CH(A^2\Delta–X^2\Pi)$ system corrected for absorption by diazirine (I_a), as a function of incident energy at a resolution of 0.3 nm. The actual onset has been chosen at the value of the abscissa where there is a distinct change of slope, *i.e.*, 8.6 eV (144.2 nm) with an estimated error limit of ±0.1 eV or 198.3 ± 2 kcal/mol. The value so obtained is a lower limit for $\Delta H_f°$(c-CH_2N_2).

$$\Delta H_f°_0(\text{c-}CH_2N_2) \rightarrow \Delta H_f°_0(CH) + E_0[CH(A^2\Delta)] + \Delta H_f°_0(H) + \Delta H_f°_0(N_2) - h\nu$$

where $h\nu$ is the observed inset = 198.3 ± 2 kcal/mol, $E_0(CH\ A^2\Delta)$ = 66.25 kcal/mol,[17] the electronic energy of the $CH(A^2\Delta_{v=0})$ state, $\Delta H_f°_0(CH)$ = 142.1[5] and $\Delta H_f°_0(H)$ = 51.63 kcal/mol,[18] respectively. Then $\Delta H_f°_0(\text{c-}CH_2N_2) \geq 61.7 \pm 2$ kcal/mol is derived. The observed threshold for $CH(A^2\Delta)$ production correlates remarkably well with the long-wavelength edge of the band region of the absorption spectrum in Figure 1 suggesting that the second absorption band is responsible for process I. The actual edge of the band lies further to the red but is buried beneath the adjoining band. It was possible to check further for fluorescence at slightly higher wavelength. A 50-fold increase in light intensity at 147 nm (8.44 eV or 194.6 kcal/mol) was obtained by use of a Xe resonance lamp at the entrance of the monochromator. Both entrance and exit slits of the monochromator could be set at 2 nm, the widest available, without affecting the bandwidth of the incident light. No emission attributable to $CH(A^2\Delta–X^2\Pi)$ was observed which suggests the probable upper limit for $\Delta H_f°_0(\text{c-}CH_2N_2)$. It must be realized, however, that determination of an upper limit for $\Delta H_f°_0$ of a reactant molecule *via* the fluorescence technique is not unequivocal. It is possible that fluorescence does occur at lower energies but is undetected due to lack of instrument sensitivity. Similarly, in spite of the increase in total absorption at lower energies, the absorption process (spectral transition) leading to the formation of $CH(A^2\Delta)$ may be weaker; thus the fluorescence may be absorption limited although energetically possible. Subject to these qualifications an upper limiting value equal to 65.4 kcal/mol is obtained for $\Delta H_f°_0(\text{c-}CH_2N_2)$.

Another independent value for $\Delta H_f°_0(\text{c-}CH_2N_2)$ may be obtained from process II, which is spin allowed

$$\text{c-}CH_2N_2 \xrightarrow{h\nu} N_2(A^3\Sigma_u^+ +) + {}^3CH_2 \qquad \text{(II)}$$

and

$$\Delta H_f°_0(\text{c-}CH_2N_2) \geq \Delta H_f°_0(CH_2) + E_0(N_2A^3\Sigma) - h\nu$$

The threshold energy of photons required for process II was determined by the sensitized fluorescence of NO by $N_2(A^3\Sigma_u^+)$, when various amounts of NO were added to diazirine. The direct fluorescence of NO in this region is well established. The measurement therefore involved the enhancement of the existing NO emission on a point-by-point basis involving fresh samples of both NO and diazirine at each wavelength. An increase in intensity was observed at 164 nm or 174.3 kcal/mol. Using values of $E_0(N_2A^3\Sigma_u^+{}_{v=0})$ = 142.3 kcal/mol[17] and $\Delta H_f°_0(CH_2)$ = 93 kcal/mol,[1-3] $\Delta H_f(\text{c-}CH_2N_2) \geq 61.0$ kcal/mol is derived.

A photoionization mass spectrometric experiment employing an Ar resonance lamp (11.6 and 11.8 eV) placed a further limit on $\Delta H_f°_0(\text{c-}CH_2N_2)$ which may be obtained from the photon energy required for process III.

$$\text{c-}CH_2N_2 \xrightarrow{h\nu} CH_2^+ + N_2 + e \qquad \text{(III)}$$

$$\Delta H_f°_0(\text{c-}CH_2N_2) \geq \Delta H_f°(CH_2) + IP(CH_2) - h\nu$$

The photoionization yield of CH_2^+ at the Ar lines amounted to 20% of the total primary ionization which indicates that the threshold is ≤11.8 eV or 272.1 kcal/mol. The ionization potential of CH_2 has been accu-

(17) L. Wallace, *Astrophys. J., Suppl. Ser.*, **6**, 445 (1962).

(18) D. D. Wagman, W. H. Evans, V. B. Parker, I. Halow, S. M. Bailey, and R. H. Schumm, *Nat. Bur. Stand. (U. S.), Tech. Note*, 270-3 (1968).

rately determined to be 10.396 eV (239.8 kcal/mol)[19] from which $\Delta H_f°(c\text{-}CH_2N_2) \geq 60.6$ kcal/mol is obtained.

Combining the results from the three independent processes allows us to place a lower limit for $\Delta H_f°_0(c\text{-}CH_2N_2)$ at 61 kcal/mol. The fact that the heat of formation of diazirine resulting from the measured onsets for processes I, II, and III all lie within 1 kcal/mol of each other is indicative that the true value of $\Delta H_f°_0(c\text{-}CH_2N_2)$ is close to our lower limit. As previously discussed, it is doubtful if $\Delta H_f°_0(c\text{-}CH_2N_2)$ is greater than 66 kcal/mol. $\Delta H_f°(c\text{-}CH_2N_2)$ obtained previously (79.3 kcal/mol) by electron impact[6] is definitely outside of the above limits. From Table I, it is apparent that the CH_2^+ (m/e 14) peak obtained by Paulett and Ettinger is twice as large as the parent ion, whereas our data show that the CH_2^+ peak is only 66% of the parent. The other peak ratios are quite comparable. It is therefore possible that extensive pyrolysis may have taken place in their reaction chamber to produce $CH_2 + N_2$ prior to ionization. The appearance potential of 11.0 eV which they measure may be due to "free" CH_2, which leads to a much higher value of $\Delta H_f°(c\text{-}CH_2N_2)$. The results are summarized in Table II.

Acknowledgment. The authors would like to thank Dr. L. Wayne Sieck of the Physical Chemistry Division for performing the photoionization experiments.

(19) G. Herzberg, *Can. J. Phys.*, **39**, 1511 (1961).

COMMUNICATIONS TO THE EDITOR

On the pK_a of the $^+H_3N\dot{C}HCOOH$ Radical

Publication costs assisted by Carnegie–Mellon University and the U. S. Atomic Energy Commission

Sir: The proton dissociation of the radical obtained by hydrogen abstraction from glycine by OH radicals has been studied both by pulse radiolysis and by electron spin resonance. In the pulse radiolysis experiments[1] the transient optical absorption formed after a short pulse of radiation was found to change with pH in three steps. These changes were interpreted in terms of two dissociation constants of the radical $^+H_3N\dot{C}HCOOH$, with pK_a values in the region 3–6, and a third change in alkaline solution owing to abstraction from the amino group.[1] However, the esr spectrum of the radical produced by hydrogen abstraction from glycine in *acid* solution, both in the radiolysis experiments[2] and in the Ti^{3+}–H_2O_2 rapid mixing experiments,[3-6] showed the presence of an NH_2 group and not an NH_3^+ group. Experiments in D_2O confirmed these findings.[2] It became clear that the pulse radiolysis and the esr experiments were not in agreement. More recently, Paul and Fischer[7] have determined the second pK_a value for the equilibria

$$^+H_3N\dot{C}HCOOH \underset{H^+}{\rightleftharpoons} H_2N\dot{C}HCOOH \underset{H^+}{\rightleftharpoons} H_2N\dot{C}HCOO^- \quad (1)$$

as 6.6. The first pK_a is well below 1, as inferred from the various esr experiments.[2-7] Although the second pK_a is in reasonable agreement with that suggested from the pulse radiolysis study,[1] a clear contradiction appears concerning the first pK_a. At this stage it seemed desirable to reexamine the pulse radiolysis interpretation.

In the pulse radiolysis experiments[1] the quantitative conversion of the primary radicals of water radiolysis into the glycine radical, *via* hydrogen abstraction by OH or by H in acidic solutions, is a prerequisite for the interpretation of the effect of pH. On the basis of the rate constants as known at that time for the various reactions, quantitative formation of the glycine radical was expected. However, in a recent competition study[8] it was found that the rate constant for the reaction of e_{aq}^- with glycine changes from $9 \times 10^6\ M^{-1}\ sec^{-1}$ at pH 7 up to $4 \times 10^9\ M^{-1}\ sec^{-1}$ at pH <2. This new finding suggests that the decrease[1] in optical density with decrease in pH between pH 4 and 1 could be a result of enhanced competition of glycine, relative to N_2O and H^+ for the hydrated electrons, and that no

(1) P. Neta, M. Simic, and E. Hayon, *J. Phys. Chem.*, **74**, 1214 (1970).

(2) P. Neta and R. W. Fessenden, *ibid.*, **75**, 738 (1971).

(3) H. Paul and H. Fischer, *Ber. Busenges. Phys. Chem.*, **73**, 972 (1969).

(4) W. A. Armstrong and W. G. Humphreys, *Can. J. Chem.*, **45**, 2589 (1967).

(5) P. Smith, W. M. Fox, D. J. McGinty, and R. D. Stevens, *ibid.*, **48**, 480 (1970).

(6) H. Taniguchi, K. Fukui, S. Ohnishi, H. Hatano, H. Hasegawa, and T. Maruyama, *J. Phys. Chem.*, **72**, 1926 (1968).

(7) H. Paul and H. Fischer, *Helv. Chim. Acta*, **54**, 485 (1971).

(8) F. A. Peter and P. Neta, *J. Phys. Chem.*, **76**, 630 (1972).

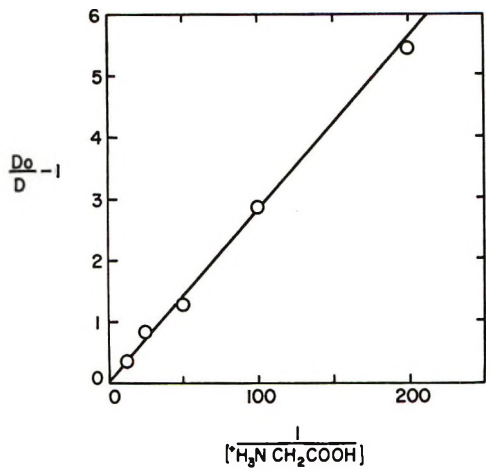

Figure 1. A competition plot of the optical density at 320 nm observed ~0.1 μsec after a 30-nsec electron pulse (2.4 krads/pulse) at a constant pH of 2.3 as a function of the glycine concentration. The concentration of the acid form of glycine is used in the plot and the very small contribution by the zwitterion is neglected. The fact that only ~50% of the e_{aq}^- reacting with glycine yield the observed $\dot{C}H_2COOH$ radical[1] does not affect the competition. The plot yields $k(e_{aq}^- + {}^+H_3NCH_2COOH)/k(e_{aq}^- + H^+) = 0.18$.

change in the state of protonation of the radical takes place in this region provided that the product of e_{aq}^- reaction with glycine has lower optical absorption at 250 nm, where the changes were recorded. Calculation of the expected competition agrees reasonably well with the absorbance measurements.[1] However, no quantitative experiment can be carried out to show the absence of this disputed pK_a. In order to obtain quantitative agreement between the measured initial optical density and the rate constants for the reactions of e_{aq}^- with the various solutes, the experiments should be devised differently.

In the present experiments no N_2O was added so that competition for e_{aq}^- occurs between glycine and H_3O^+ only

$$^+H_3NCH_2COOH + e_{aq}^- \longrightarrow NH_3 + \dot{C}H_3COOH \quad (2)$$
$$\searrow H + H_2NCH_2COOH \quad (2a)$$

$$H_3O^+ + e_{aq}^- \longrightarrow H + H_2O \quad (3)$$

while OH and H react with *tert*-butyl alcohol. The radical product of reaction 2 has absorption maximum at 320 nm[1,9] while the radical from *tert*-butyl alcohol has no optical absorption at this wavelength region. Varying the concentration of glycine at a constant pH of 2.3 ($pK_a = 2.3$, *i.e.*, half the glycine is in the acid form) and following the initial optical absorption at 320 nm yields a good competition plot, as shown in Figure 1. Using the concentration of the acid form of glycine as the competitor for e_{aq}^- and neglecting the very small contribution (0.2%) by the zwitterion form,[8] the rate constant calculated from Figure 1 is $k_{(e_{aq}^- + {}^+H_3NCH_2COOH)} = 4.1 \times 10^9\ M^{-1}\ sec^{-1}$ determined by reference to $k_{(e_{aq}^- + H^+)} = 2.3 \times 10^{10}\ M^{-1}\ sec^{-1}$. The rate constant measured by this competition is in very good agreement with that recently reported.[8]

This experiment thus offers a different interpretation of the earlier pulse radiolysis results,[1] which brings them into full agreement with the esr results, namely that the $H_2N\dot{C}HCOOH$ radical does not undergo protonation even at pH 1. It is interesting to note, however, that the pK_a of the radical $^+H_3N\dot{C}HCONH_2$, obtained by pulse radiolysis of glycine amide, is 4.3.[10]

Acknowledgment. We wish to thank Drs. R. W. Fessenden and J. Lilie for helpful discussions and the U. S. Atomic Energy Commission for partial support.

(9) P. Neta, M. Simic, and E. Hayon, *J. Phys. Chem.*, **73**, 4207 (1969).
(10) P. S. Rao and E. Hayon, manuscript in preparation.

RADIATION RESEARCH LABORATORIES AND CENTER FOR SPECIAL STUDIES
MELLON INSTITUTE OF SCIENCE
CARNEGIE-MELLON UNIVERSITY
PITTSBURGH, PENNSYLVANIA 15213
P. NETA*

DEPARTMENT OF ZOOLOGY
UNIVERSITY OF TEXAS
AUSTIN, TEXAS 78712
M. SIMIC

PIONEERING RESEARCH LABORATORIES
U. S. ARMY NATICK LABORATORIES
NATICK, MASSACHUSETTS 01760
E. HAYON

RECEIVED AUGUST 11, 1972

obtain pore volume, pore area distributions; BET surface areas AUTOMATICALLY with the Aminco Adsorptomat

The commercial model of an instrument developed for catalyst research by the Gulf Research and Development Co., the Adsorptomat completely automates determination of pore volume, pore-size distribution, and total surface area of catalyst, adsorbents, etc.
The instrument records a complete nitrogen adsorption/desorption isotherm for each sample, as well as data printout suitable for application to a computer. A Fortran program is supplied with the instrument.
A multiple-sample attachment permits automatic sequential analysis of up to five samples, without interruption or shut-down. Once the operator has introduced the sample(s) and adjusted the necessary controls, no further attention or control is required. The unit covers the pore-diameter range of 14 A to 600 A. (For porosity determinations in the range of 0.012 to 100 microns, Aminco offers the Aminco Winslow mercury-intrusion Porosimeter.)
Send for literature Portfolio which provides complete information on all three instruments.

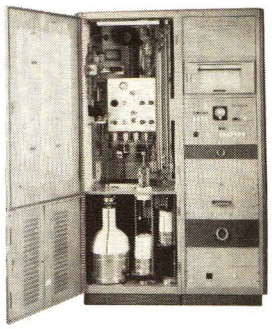

multi-point BET surface area determinations ECONOMICALLY, with the Aminco Sor-BET

This new instrument performs rapid, accurate BET determinations by the classic measurement of pressure decrease after adsorption of nitrogen by the sample. It differs from the conventional method in the fact that nitrogen is selectively adsorbed from a binary gas mixture. The method is rapid because equilibration is achieved under dynamic conditions, and accuracy is maintained because measurements are made under static conditions.
Operation is simple and direct, requiring no vacuum, no mercury manometers, no traps. Piping and sample are purged by helium flow.
The unit is compact (35 x 25½ x 16 in. high) and self-contained, having a recirculating gas pump that cycles a mixture of helium and nitrogen through the sample at liquid-nitrogen temperature. Depending on sample characteristics, up to 16 three-point determinations per day may be processed (without data reduction) on samples of from 0.1 to 20 g or higher (from 0.1 to 1500 m^2/g).

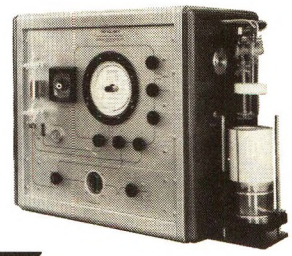

AMERICAN INSTRUMENT COMPANY
DIVISION OF TRAVENOL LABORATORIES, INC.
Silver Spring, Maryland 20910

Molecular Sieve Zeolites

ADVANCES IN CHEMISTRY
SERIES No. 101 and 102

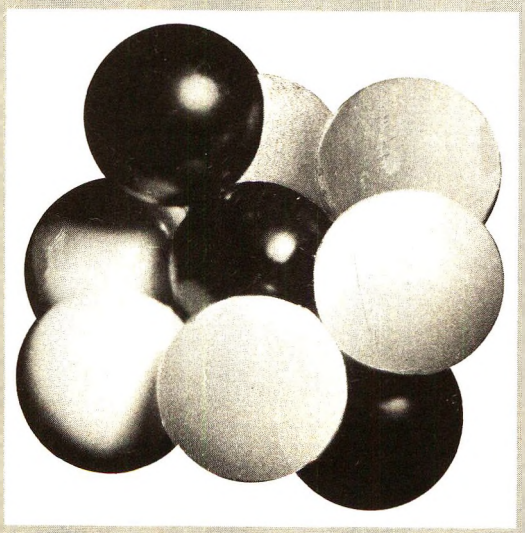

Seventy-seven papers from a symposium co-sponsored by the Divisions of Colloid and Surface Chemistry, Petroleum Chemistry, and Physical Chemistry of the American Chemical Society and Worcester Polytechnic Institute, Edith M. Flanigen and Leonard B. Sand, co-chairmen.

Do you need a group of substances that can remove radioactive isotopes from nuclear wastes, remove ammonia from secondary sewage effluents, remove sulfur dioxide from waste gases, foster formation of actinides, or disrupt bacterial cells? These and many other possibilities are available through research on molecular sieve zeolites. For example, they are used for:

- separating hydrogen isotopes
- solubilizing enzymes
- carrying active catalysts in curing of plastics
- transporting soil nutrients in fertilizers
- filtering tars from cigarette smoke

"Molecular Sieve Zeolites" reports recent advances in this rapidly developing field. Volume I offers 41 papers devoted to the synthesis, structure, mineralogy, and modification of sieve zeolites. These are followed in Volume II by 36 papers discussing sorption and catalysts.

Volume I: 526 pages with index Cloth (1971) $16.00
Volume II: 459 pages with index Cloth (1971) $16.00
No. 101 and 102 ordered together $30.00
Postpaid in U.S. and Canada; plus 40 cents elsewhere.
Set of L.C. cards with library orders upon request.

Order from:
Special Issues Sales
American Chemical Society
1155 Sixteenth St., N.W.
Washington, D.C. 20036